

Thierry Duffar
Editor

Crystal Growth Processes Based on Capillarity

Czochralski, Floating Zone,
Shaping and Crucible Techniques

 WILEY



Crystal Growth Processes Based on Capillarity

Crystal Growth Processes Based on Capillarity

Czochralski, Floating Zone,
Shaping and Crucible Techniques

Edited by

THIERRY DUFFAR

*Laboratoire SIMaP-EPM
INP Grenoble
Saint Martin d'Hères
France*

 **WILEY**

A John Wiley & Sons, Ltd., Publication

This edition first published 2010
© 2010 John Wiley & Sons Ltd

Registered office

John Wiley & Sons Ltd, The Atrium, Southern Gate, Chichester, West Sussex, PO19 8SQ, United Kingdom

For details of our global editorial offices, for customer services and for information about how to apply for permission to reuse the copyright material in this book please see our website at www.wiley.com.

The right of the author to be identified as the author of this work has been asserted in accordance with the Copyright, Designs and Patents Act 1988.

All rights reserved. No part of this publication may be reproduced, stored in a retrieval system, or transmitted, in any form or by any means, electronic, mechanical, photocopying, recording or otherwise, except as permitted by the UK Copyright, Designs and Patents Act 1988, without the prior permission of the publisher.

Wiley also publishes its books in a variety of electronic formats. Some content that appears in print may not be available in electronic books.

Designations used by companies to distinguish their products are often claimed as trademarks. All brand names and product names used in this book are trade names, service marks, trademarks or registered trademarks of their respective owners. The publisher is not associated with any product or vendor mentioned in this book. This publication is designed to provide accurate and authoritative information in regard to the subject matter covered. It is sold on the understanding that the publisher is not engaged in rendering professional services. If professional advice or other expert assistance is required, the services of a competent professional should be sought.

The publisher and the author make no representations or warranties with respect to the accuracy or completeness of the contents of this work and specifically disclaim all warranties, including without limitation any implied warranties of fitness for a particular purpose. This work is sold with the understanding that the publisher is not engaged in rendering professional services. The advice and strategies contained herein may not be suitable for every situation. In view of ongoing research, equipment modifications, changes in governmental regulations, and the constant flow of information relating to the use of experimental reagents, equipment, and devices, the reader is urged to review and evaluate the information provided in the package insert or instructions for each chemical, piece of equipment, reagent, or device for, among other things, any changes in the instructions or indication of usage and for added warnings and precautions. The fact that an organization or Website is referred to in this work as a citation and/or a potential source of further information does not mean that the author or the publisher endorses the information the organization or Website may provide or recommendations it may make. Further, readers should be aware that Internet Websites listed in this work may have changed or disappeared between when this work was written and when it is read. No warranty may be created or extended by any promotional statements for this work. Neither the publisher nor the author shall be liable for any damages arising herefrom.

Library of Congress Cataloging-in-Publication Data

Crystal growth processes based on capillarity : czochralski, floating zone, shaping and crucible techniques / edited by Thierry Duffar.

p. cm.

Includes bibliographical references and index.

ISBN 978-0-470-71244-3 (cloth)

1. Crystal growth. I. Duffar, Thierry.

QD921.C765 2010

548'.5—dc22

2009045996

A catalogue record for this book is available from the British Library.

ISBN HB: 9780470712443

Set in 10/12 Times by Toppan Best-set Premedia Limited

Printed and bound in Great Britain by Antony Rowe Ltd, Chippenham, Wiltshire

*This book is dedicated to my previous, present and future PhD students.
Each of them, with his/her personality, improved my perception of crystal growth and
inclined my scientific activity toward a human adventure.
Thank you!*

Contents

<i>Preface</i>	<i>page</i> xiii
<i>Introduction</i>	xv
<i>Acknowledgements</i>	xxv
<i>Nomenclature</i>	xxvii
<i>Contributors</i>	xxxii
1. Basic Principles of Capillarity in Relation to Crystal Growth	1
<i>Nicolas Eustathopoulos, Béatrice Drevet, Simon Brandon and Alexander Virozub</i>	
1.1 Definitions	1
1.1.1 Characteristic Energies of Surfaces and Interfaces	1
1.1.2 Capillary Pressure	3
1.1.3 Surface Energy versus Surface Tension	4
1.2 Contact Angles	4
1.2.1 Thermodynamics	5
1.2.2 Dynamics of Wetting	12
1.2.3 Measurements of Contact Angle and Surface Tension by the Sessile Drop Technique	16
1.2.4 Selected Data for the Contact Angle for Systems of Interest for Crystal Growth	17
1.3 Growth Angles	28
1.3.1 Theory	28
1.3.2 Measurements of Growth Angles: Methods and Values	35
1.3.3 Application of the Growth Angle Condition in Simulations of Crystal Growth	38
1.3.4 Summary	45
Acknowledgements	45
References	46
2. The Possibility of Shape Stability in Capillary Crystal Growth and Practical Realization of Shaped Crystals	51
<i>Vitali A. Tatartchenko</i>	
2.1 Crucible-Free Crystal Growth – Capillary Shaping Techniques	52
2.2 Dynamic Stability of Crystallization – the Basis of Shaped Crystal Growth by CST	54
2.2.1 Lyapunov Equations	57
2.2.2 Capillary Problem – Common Approach	59
2.2.3 Equation of Crystal Dimension Change Rate	62

2.2.4	Equation of Crystallization Front Displacement Rate	63
2.2.5	Stability Analysis in a System with Two Degrees of Freedom	64
2.3	Stability Analysis and Growth of Shaped Crystals by the Cz Technique	65
2.3.1	Capillary Problem	65
2.3.2	Temperature Distribution in the Crystal–Melt System	65
2.3.3	Stability Analysis and Shaped Crystal Growth	68
2.3.4	Dynamic Stability Problem for the Kyropoulos Technique	69
2.4	Stability Analysis and Growth of Shaped Crystals by the Verneuil Technique	70
2.4.1	Principal Schemes of Growth	70
2.4.2	Theoretical Investigation	71
2.4.3	Practical Results of the Theoretical Analysis	76
2.4.4	Stability Analysis-Based Automation	78
2.5	Stability Analysis and Growth of Shaped Crystals by the FZ Technique	80
2.6	TPS Techniques: Capillary Shaping and Impurity Distribution	81
2.6.1	Capillary Boundary Problem for TPS	81
2.6.2	Stability Analysis	92
2.6.3	Experimental Tests of the Capillary Shaping Theory Statements	94
2.6.4	Impurity Distribution	100
2.6.5	Definition of TPS	104
2.6.6	Brief History of TPS	104
2.7	Shaped Growth of Ge, Sapphire, Si, and Metals: a Brief Presentation	108
2.7.1	Ge	108
2.7.2	Sapphire	109
2.7.3	Si	109
2.7.4	Metals and Alloys	110
2.8	TPS Peculiarities	110
	References	111
3	Czochralski Process Dynamics and Control Design	115
	<i>Jan Winkler, Michael Neubert, Joachim Rudolph, Ning Duanmu and Michael Gevelber</i>	
3.1	Introduction and Motivation	116
3.1.1	Overview of Cz Control Issues	116
3.1.2	Diameter Control	117
3.1.3	Growth Rate Control	117
3.1.4	Reconstruction of Quantities not Directly Measured	117
3.1.5	Specific Problems for Control in Cz Crystal Growth	118
3.1.6	PID Control vs. Model-Based Control	121
3.1.7	Components of a Control System	122
3.1.8	Modelling in Crystal Growth Analysis and Control	123
3.2	Cz Control Approaches	124

3.2.1	Proper Choice of Manipulated Variables	124
3.2.2	Feedforward Control	125
3.2.3	Model-Based Analysis of the Process	126
3.2.4	Stability	127
3.2.5	Model-Based Control	127
3.2.6	Identification	130
3.2.7	Measurement Issues and State Estimation	130
3.3	Mathematical Model	132
3.3.1	Hydromechanical–Geometrical Model	133
3.3.2	Model of Thermal Behaviour	142
3.3.3	Linear System Model Analysis	148
3.4	Process Dynamics Analysis for Control	150
3.4.1	Operating Regime and Batch Implications	152
3.4.2	Actuator Performance Analysis	154
3.4.3	Curved Interface	157
3.4.4	Nonlinear Dynamics	157
3.5	Conventional Control Design	161
3.5.1	Control Based on Optical Diameter Estimation	161
3.5.2	Weight-Based Control	164
3.6	Geometry-Based Nonlinear Control Design	170
3.6.1	Basic Idea	170
3.6.2	Parametrization of the Hydromechanical–Geometrical Model in Crystal Length	171
3.6.3	Flatness and Model-Based Feedback Control of the Length-Parametrized Model	172
3.6.4	Control of Radius and Growth Rate	176
3.7	Advanced Techniques	181
3.7.1	Linear Observer Design	182
3.7.2	Nonlinear Observer Design	183
3.7.3	Control Structure Design for Batch Disturbance Rejection	194
	References	199
4	Floating Zone Crystal Growth	203
	<i>Anke Lüdge, Helge Riemann, Michael Wünscher, Günter Behr, Wolfgang Löser, Andris Muiznieks and Arne Cröll</i>	
4.1	FZ Processes with RF Heating	207
4.1.1	FZ Method for Si by RF Heating	207
4.1.2	FZ Growth for Metallic Melts	220
4.2	FZ Growth with Optical Heating	230
4.2.1	Introduction	230
4.2.2	Image Furnaces	230
4.2.3	Laser Heating	240
4.2.4	FZ Growth for Oxide Melts	242
4.3	Numerical Analysis of the Needle-Eye FZ Process	247
4.3.1	Literature Overview	248

4.3.2	Quasi-Stationary Axisymmetric Mathematical Model of the Shape of the Molten Zone	249
4.3.3	Numerical Investigation of the Influence of Growth Parameters on the Shape of the Molten Zone	256
4.3.4	Nonstationary Axisymmetric Mathematical Model for Transient Crystal Growth Processes	258
	Appendix: Code for Calculating the Free Surface During a FZ Process in Python	267
	References	270
5	Shaped Crystal Growth	277
	<i>Vladimir N. Kurlov, Sergei N. Rossolenko, Nikolai V. Abrosimov and Kheirreddine Lebbou</i>	
5.1	Introduction	277
5.2	Shaped Si	279
5.2.1	EFG Method	281
5.2.2	Dendritic Web Growth	286
5.2.3	String Ribbon	288
5.2.4	Ribbon Growth on Substrate (RGS)	290
5.3	Sapphire Shaped Crystal Growth	292
5.3.1	EFG	293
5.3.2	Variable Shaping Technique (VST)	295
5.3.3	Noncapillary Shaping (NCS)	297
5.3.4	Growth from an Element of Shape (GES)	307
5.3.5	Modulation-Doped Shaped Crystal Growth Techniques	312
5.3.6	Automated Control of Shaped Crystal Growth	319
5.4	Shaped Crystals Grown by the Micro-Pulling Down Technique (μ -PD)	333
5.4.1	Crucible–Melt Relation During Crystal Growth by the μ -PD Technique	339
5.4.2	Examples of Crystals Grown by the μ -PD Technique	340
5.5	Conclusions	347
	References	347
6	Vertical Bridgman Technique and Dewetting	355
	<i>Thierry Duffar and Lamine Sylla</i>	
6.1	Peculiarities and Drawbacks of the Bridgman Processes	356
6.1.1	Thermal Interface Curvature	356
6.1.2	Melt–Crystal–Crucible Contact Angle	358
6.1.3	Crystal–Crucible Adhesion and Thermomechanical Detachment	360
6.1.4	Spurious Nucleation on Crucible Walls	363
6.2	Full Encapsulation	366
6.2.1	Introduction	366
6.2.2	LiCl–KCl Encapsulant for Antimonides	368
6.2.3	B ₂ O ₃ Encapsulant	371
6.2.4	Conclusion	372

6.3	The Dewetting Process: a Modified VB Technique	373
6.3.1	Introduction	373
6.3.2	Dewetting in Microgravity	374
6.3.3	Dewetting in Normal Gravity	378
6.3.4	Theoretical Models of Dewetting	394
6.3.5	Stability Analysis	404
6.4	Conclusion and Outlook	407
	References	408
7	Marangoni Convection in Crystal Growth	413
	<i>Arne Cröll, Taketoshi Hibiya, Suguru Shiratori, Koichi Kakimoto and Lijun Liu</i>	
7.1	Thermocapillary Convection in Float Zones	417
7.1.1	Model Materials	417
7.1.2	Semiconductors and Metals	417
7.1.3	Effect of Oxygen Partial Pressure on Thermocapillary Flow in Si	419
7.1.4	Fluid Dynamics of Thermocapillary Flow in Half-Zones	422
7.1.5	Full Float Zones	435
7.1.6	The Critical Marangoni Number Ma_{c2}	435
7.1.7	Controlling Thermocapillary Convection in Float Zones	443
7.2	Thermocapillary Convection in Cz Crystal Growth of Si	448
7.2.1	Introduction	448
7.2.2	Surface Tension-Driven Flow in Cz Growth	448
7.2.3	Numerical Model	449
7.2.4	Calculation Results	452
7.2.5	Summary of Cz Results	456
7.3	Thermocapillary Convection in EFG Set-Ups	456
7.4	Thermocapillary Convection in Bridgman and Related Set-Ups	457
7.5	Solutocapillary Convection	457
	References	460
8	Mathematical and Numerical Analysis of Capillarity Problems and Processes	465
	<i>Liliana Braescu, Simona Epure and Thierry Duffar</i>	
8.1	Mathematical Formulation of the Capillary Problem	468
8.1.1	Boundary Value Problems for the Young–Laplace Equation	468
8.1.2	Initial and Boundary Conditions of the Meniscus Problem	472
8.1.3	Approximate Solutions of the Axisymmetric Meniscus Problem	473
8.2	Analytical and Numerical Solutions for the Meniscus Equation in the Cz Method	476
8.3	Analytical and Numerical Solutions for the Meniscus Equation in the EFG Method	486
8.3.1	Sheets	486
8.3.2	Cylindrical Crystals	493

8.4 Analytical and Numerical Solutions for the Meniscus Equation in the Dewetted Bridgman Method	500
8.4.1 Zero Gravity	502
8.4.2 Normal Gravity	508
8.5 Conclusions	517
Appendix: Runge–Kutta Methods	518
A.1 Fourth-Order Runge–Kutta Method (RK4)	518
A.2 Rkfixed and Rkadapt Routines for Solving IVP	520
References	523

<i>Index</i>	525
---------------------	------------

Preface

The idea of this book came to me in the course of a long ski journey across the Alps. Perhaps the extended contact with rocks, ice and snow flakes inclined my mind toward my professional and scientific activity in crystal growth, so that, after some days, the general outline was ready and, when I returned back to my office, I began contacting potential authors.

It may seem surprising to the reader that capillarity is the backbone of this book, as it refers to the liquid state, which seems like the opposite of the crystalline state. The idea that crystals are grown in crucibles is common, probably because metallic alloys are cast in moulds; in fact, most crystals are produced without contact with a crucible wall and their shape is controlled by capillary forces. The aim of this book is, above all, to explain how much and in what way the crystal growth techniques are dependent on liquid surface phenomena.

All the aspects of capillarity that are of interest to the crystal grower have been reviewed in this book. The authors' main wish is that it will be useful to a range of people, including researchers at the start of their career looking for fundamental principles or working on laboratory experiments; industrial engineers; and advanced senior researchers looking for detailed information.

Thierry Duffar
Saint Martin d'Hères, France
October 2009

Introduction

Thierry Duffar
SIMaP-EPM

The historical development of crystal growth processes is a good reflection of the importance of capillarity and crucible-free concepts. The first technique that was used for producing crystals was described by Verneuil at the turn of the 20th century [Verneuil 1902, 1904, 1910] but there is evidence that the so called ‘Geneva ruby’ was grown by a similar technique almost 20 years earlier [Nassau 1969]. Verneuil in fact wished to study the properties of ruby and other alumina-based crystals and was aware of the very high melting temperature of these materials (*c.*2000 °C), which prevented the use of any crucible material known at that time. By melting alumina powder in a hydrogen–oxygen flame and solidifying the droplets on a colder seed, he got artificial ruby crystals (Figure 1). Obviously a melt layer, sustained by surface tension, exists at the hot side of the growing crystal where the droplets arrive and merge. Thousands of furnaces, little changed from that used by Verneuil, are used nowadays for the industrial production of sapphire and spinel crystals.

The second technique for crystal growth was introduced by Czochralski a few years later [Czochralski 1918]. In order to study the growth kinetics of metals, Czochralski needed materials with small dimensions in order to dissipate the latent heat of solidification efficiently and rapidly. He pulled thin wires from the melt at various speeds and obtained single crystals. As can be seen in Figure 2, this technique for the growth of bulk semiconductor single crystals, beginning in the 1950s, eventually developed into the complex technology required in order to obtain the large-diameter perfect crystals that are the raw material for the electronics industry. In this case, capillarity acts on the small meniscus that joins the liquid surface in the crucible to the crystal and is of paramount importance in the problem of crystal diameter control.

In Czochralski’s time, controlling the dimensions of the crystal was very difficult. It was in order to stabilize crystal growth that Gomperz had the idea of using a shaping device floating on the melt surface [Gomperz 1922]; he used a drilled mica plate. Since

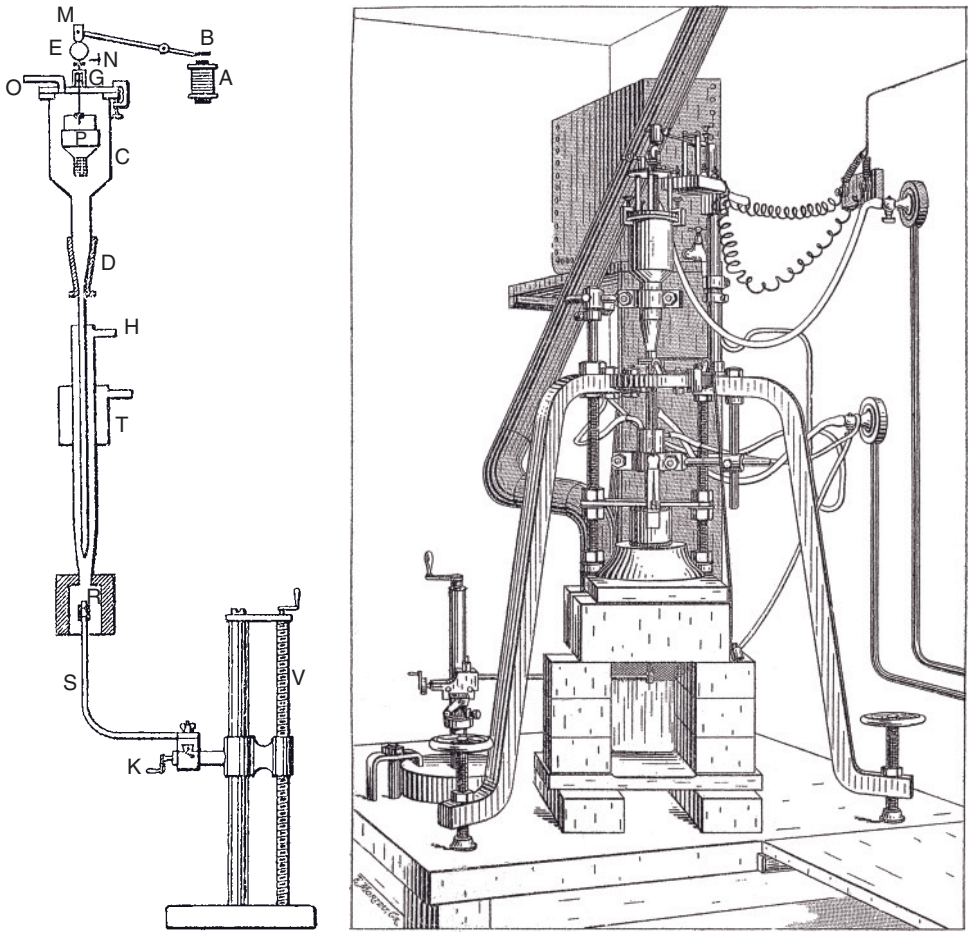


Figure 1 Schematic of Verneuil's method and drawing of the equipment used in his laboratory (Reprinted with permission from [Verneuil 1904], copyright (1904)). The seed is held on the shaft *S*, powder is supplied by the feeder *C–D*, and gases are provided through the torch entries *H* and *T*.

that time, numerous types of shaping devices have been devised in order to get crystals of various shapes (Figure 3).

After the important growth processes based on capillarity, historically the next development was the Bridgman method, aiming to increase crystal size and consisting of growing crystals in a crucible [Bridgman 1925]. In spite of the great advantage of solving the problem of crystal shape control, contact between the growing crystal and a crucible wall has numerous associated drawbacks such as the crystal adhering to the crucible or the appearance of defects in the crystal. Bridgman was perfectly aware of these problems; in order to avoid adhesion he suggested greasing and flaming the crucible before the experiment. However, it is not clear from his explanation whether he invented encapsulation or crucible wall coating.

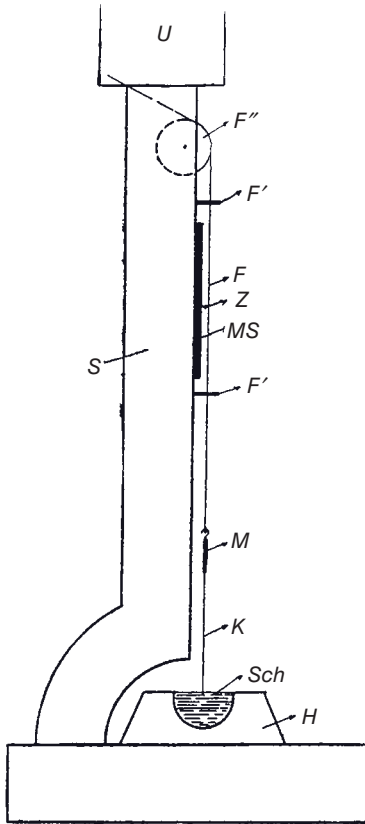


Figure 2 Schematic of Czochralski's method of pulling single crystal wires of metals (K) from the melt (Sch) (Reprinted with permission from [Czochralski 1918], copyright (1918) Oldenbourg Wissenschaftsverlag). On the right, view of a 300-mm, 250-kg silicon single crystal grown by Czochralski's method (Reproduced with permission from Siltronic AG).

The next method to be invented was the floating zone (FZ) technique. Initially used for material purification, it was later patented for the growth of single crystals without a crucible [Theuerer 1952]. It is a purely capillary-based technique, because the liquid column from which the crystal is grown is supported entirely by surface tension. As can be seen in Figure 4, controlling the shape of the crystal is very difficult in this case and a lot of research and development effort was required to find efficient solutions.

Since then various modifications of these basic methods have been proposed, such as pedestal growth, the EFG process, micro-pulling down and others, all based on the use of capillary forces in order to maintain and shape the liquid. A tentative classification can be proposed, based on the presence or absence of a crucible or shaping die in contact with the molten material and on the direction of pulling (Figure 5). This clearly shows that, from the capillarity point of view, the techniques proceed from one to the next by changing one parameter at a time, and consequently this specific point of view links all the processes in a unique way.

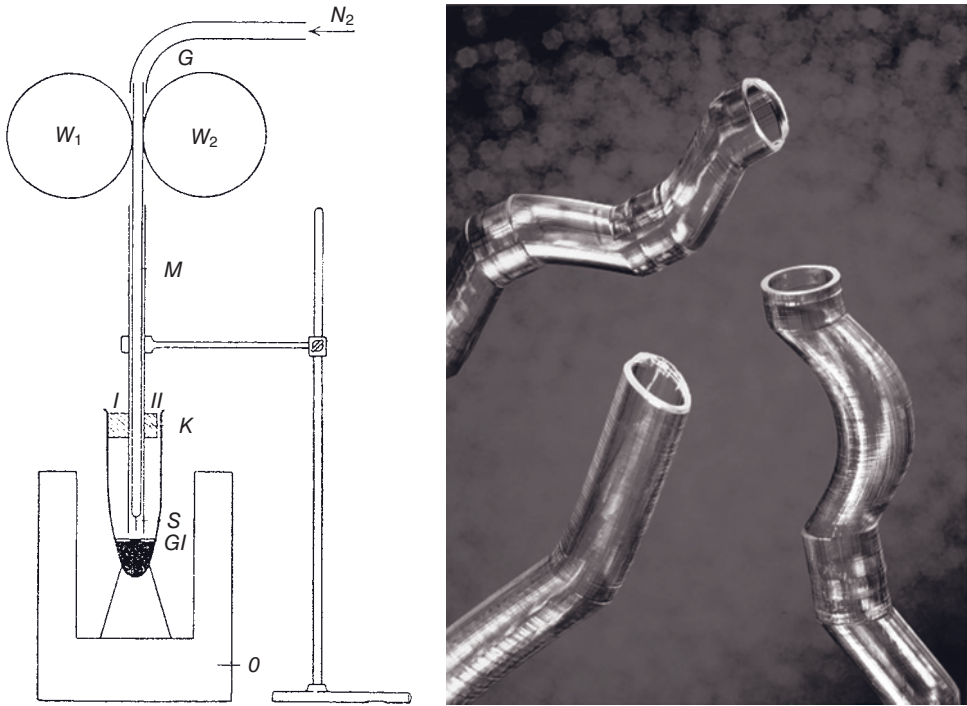


Figure 3 Schematic of Gomperz's method of pulling single crystal wires of metals (S) through a floating open disc (Gl) (Reprinted with permission from [Gompertz 1922], copyright (1922) Springer Science + Business Media). On the right, some bent single crystal tubes of sapphire obtained by a modified shaping method (Reproduced with permission from the Commissariat à L'Energie Atomique).

In recent years there has been a succession of good books dealing with crystal growth. The *Handbook of Crystal Growth* [Hurle 1993] is certainly the most comprehensive of them, treating all aspects of the fundamental and practical questions in crystal growth; capillarity issues are of course developed in some detail, but because of the size of the book and the large variety of topics covered, they do not appear as a link between bulk growth techniques. Some books are organized by classes of materials, so that readers can easily find out the most appropriate method to grow the material of their choice [Capper 2005, Scheel 2003]. Experimental, technical and theoretical topics including important recent improvements can also be found in [Scheel 2003]. Finally, the only book that deals entirely with capillarity aspects [Tatartchenko 1993] focuses principally on the study of the stability of the various processes and does not cover all the aspects relating to capillarity in crystal growth. It is the purpose of the present book to present all the growth techniques in a unified way. I hope that it will be useful to a wide range of readers, with its various chapters covering in turn fundamental capillary effects, detailed experimental developments or technically important processes, and some associated software. Because of such different points of view, there is a certain amount of overlap between the chapters but this is intentional, with the hope that it will help the reader to get a full coverage of the topic.

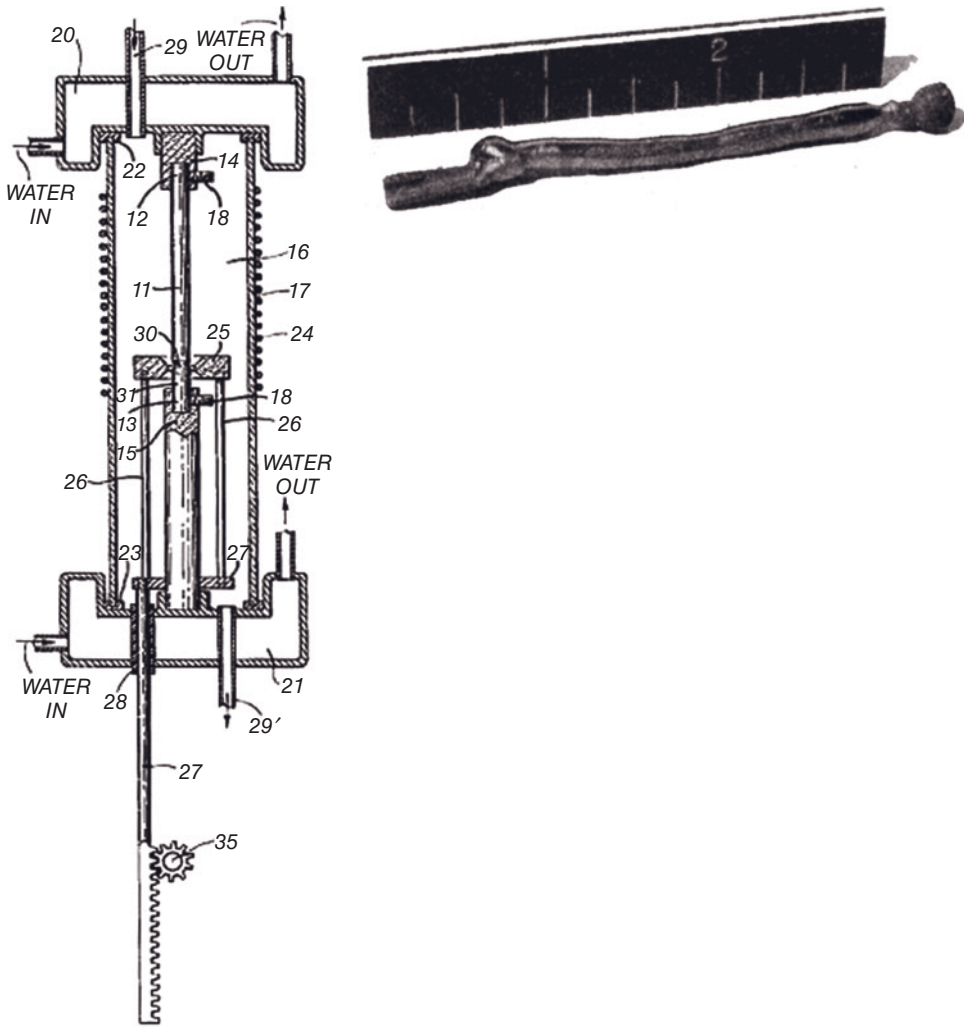


Figure 4 Principle of the floating zone crystal growth process (Reprinted with permission from [Theurer 1952], copyright (1952) H. C. Theurer), where 25 is a graphite resistance heater, 11 the silicon or germanium rod. On the right, the first published silicon floating zone crystal (Reprinted with permission from [Keck 1953], copyright (1953) American Physical Society).

Some crystal growers are not totally familiar with the concepts involved in capillarity, namely surface tension and wetting. The purpose of the first part of *Chapter 1* is to give a strict definition of these concepts in a clear way, based on physical sense rather than on mathematical developments. N. Eustathopoulos and B. Drevet were certainly the right people to write this account. They have both worked for a long time in the field of high-temperature capillarity and it has always been a pleasure for me to work with them, because of the way they really introduced me to capillary matters. In the second part of the chapter they discuss wetting, a very important aspect of surface science which is in

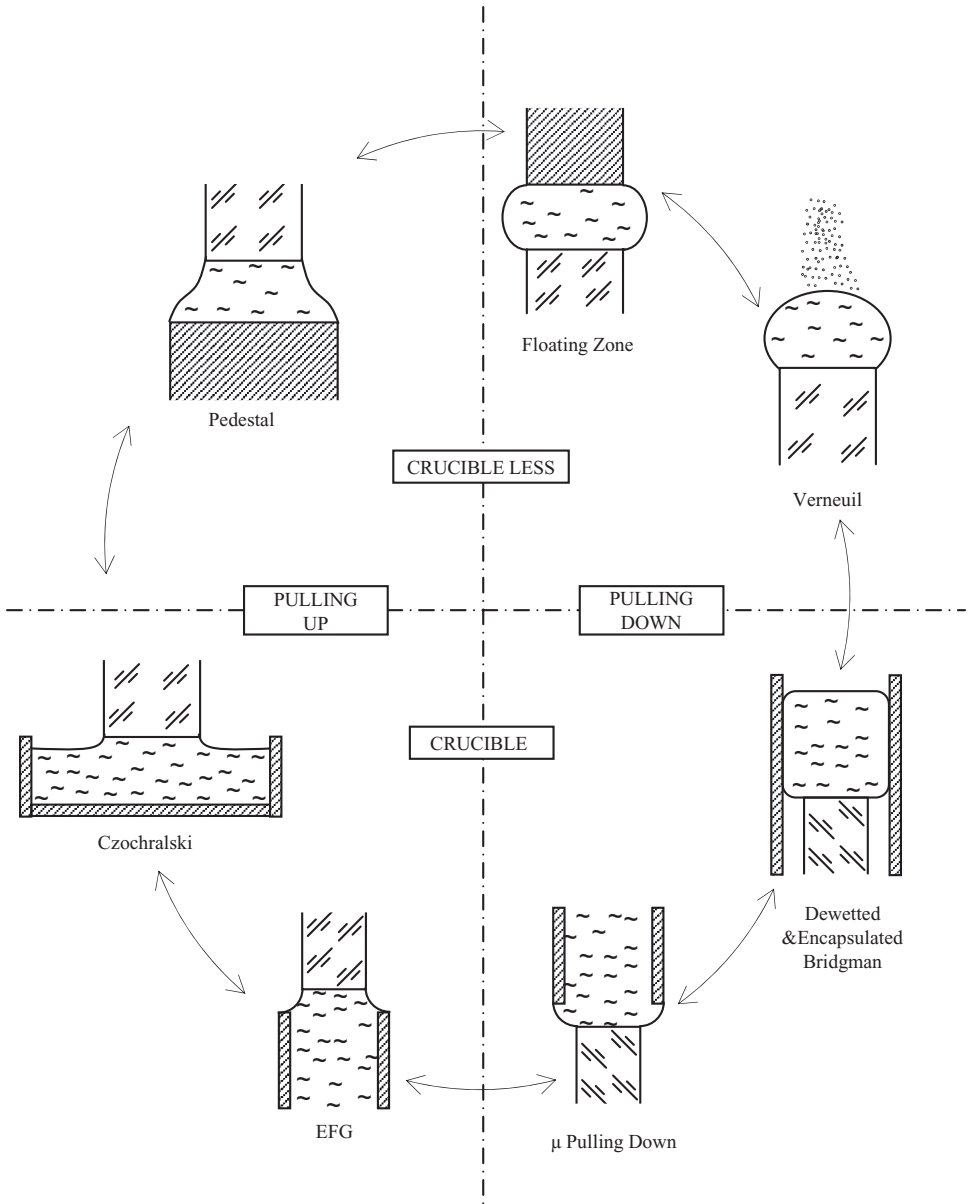


Figure 5 Classification of the various crystal growth processes using capillary forces for maintaining or shaping the molten material.

fact a measure of the interaction between a melt and a solid. Their critical analysis of the available data concerning wetting of molten materials on the crucibles used in crystal growth is quite original and will be useful to anyone looking for reliable and up-to-date values of wetting angles. One specific wetting behaviour concerns the liquid on its own solid, i.e. the melt on the crystal. A measure of this interaction is the growth angle, a

concept which is central to the whole book, involved in stability analysis, shape control, technical achievements and numerical simulation. S. Brandon and A. Virozub have recently improved the understanding of this phenomenon and of the related measurement methods, and they provide a full coverage of the topic.

The book written by V.A. Tatartchenko has already been cited as the only one specifically dealing with capillarity in crystal growth. Obviously it was necessary to cover the aspect of shape stability in the present book and I was very pleased when he agreed to write *Chapter 2*, summarizing his earlier book and including new aspects. All techniques involving capillarity are analysed in this chapter, including Verneuil's process. There is some overlap with other chapters, but this gives a great unity and clarity to the stability analysis approach. In the last part of his chapter, Tatartchenko gives a historical view of his career. He first worked with Stepanov, recognized as the father of shaping techniques, spent too short a time in my laboratory in Grenoble, and now continues his activity in Western-based companies, including Saphikon in the USA, which uses developments of the EFG method, previously recognized as the Western challenger to the Soviet Stepanov method. It is a pleasure to include these historical details in the book.

Chapter 3 will be the most interesting for all readers trying to control the diameter of the crystals grown by the Czochralski (Cz) process. In fact the problem is not only to control the diameter of the crystal but also, as a consequence, to improve its quality, which is always damaged when the growth rate is not perfectly stable. It is a difficult control problem whatever the measurement technique used – weighting of the crystal or optical observation of the liquid meniscus. These difficulties are first explained in detail, based on the physics of the process, and the reader is then introduced to the control techniques and vocabulary. Two approaches are described in detail. The first is the linear approach, as developed during the 1980s and 1990s and benefiting from the involvement of M. Gevelber and N. Duanmu. The second approach is a recent nonlinear model based on up-to-date developments in control science. It was developed at the Leibniz Institute of Crystal Growth in Berlin by J. Winkler and M. Neubert with the help of J. Rudolph from the University of Dresden. The two different approaches give good results in term of diameter control and consequently of crystal quality, showing that there are always several ways of solving a given problem. The authors succeeded in combining the two approaches and finally delivered a clear and convincing chapter, in spite of the difficulty of the topic, which is not familiar to crystal growers. I am particularly grateful to J. Winkler for his energy and involvement and to M. Gevelber for the difficult task of coordinating the chapter.

As explained in *Chapter 4*, in the floating zone process the liquid is essentially stabilized and maintained by the forces of surface tension. This makes this technique central one to the book, with a very important application to the growth of single silicon crystals of high purity and high structural quality. A. Lüdge, H. Riemann and M. Wünschler agreed to write this part of the chapter, with very detailed technical explanations. They are members of the team at the Leibniz Institute for Crystal Growth in Berlin, now the world's leading centre in silicon floating zone research and development. The development of the technique for the growth of large-diameter crystals on a large scale has been possible with the help of numerical simulation. This is a very difficult task, as it is necessary to compute the shape of three free surfaces, as well as their interaction with electromagnetic forces. A. Muiznieks has been working on this for many years and has succeeded in giving clear explanations of the tricky numerical problems. The floating zone technique is also

employed in many laboratories for the growth of pure or alloyed metallic and intermetallic materials and also for oxide growth. The team at the University of Dresden, G. Behr and W. Löser, is famous for the growth of this type of materials and they explain the problems, and related solutions, associated with the specificity of these materials. Often the furnace used is an optical heating device and A. Cröll has written a very detailed and comprehensive review of this specific technique, the first as far as I know.

Chapter 5 is remarkable. V.N. Kurlov and S.N. Rossolenko give a fascinating description of the ingenious methods they use in order to grow sapphire crystals of very different shapes and qualities. It seems that there is no limit to their ability to use dies in order to control the liquid shape and consequently the form of the crystals. This is a shining illustration of the potential of capillary-based crystal growth techniques for the production of shaped crystals. The part concerning process control is also new and very interesting. N.V. Abrosimov describes how silicon can be shaped in ribbons or tubes, for the very useful application of photovoltaic cells. It is worth noting the specific twinned crystal structure that naturally appears in these silicon ribbons and tubes and which periodically changes its orientation in order to follow the shape of the growing crystal. Such phenomena can only be studied in the case of capillary shaping. Micro-pulling down is one of the most recent crystal growth techniques to have emerged. K. Lebbou gives a comprehensive survey of the technical details and crystal fibres that are currently grown in this way.

Perhaps surprisingly, *Chapter 6* is devoted to the Bridgman technique and some variants. This was in fact a good place to discuss the problems related to crystal–crucible contact and then, in comparison, to highlight the positive aspects of capillary techniques. In fact capillary-based variants, such as full encapsulation, are commonly used in an attempt to get the advantage of the method without the defects. L. Sylla recently finished a PhD thesis on the dewetting phenomenon and process, and this part of the chapter forms a natural sequel. First discovered as a result of experiments under microgravity conditions, dewetting evolved toward a terrestrial variant of the Bridgman process where crucible contact does not occur. So far it has not found industrial application but it is useful to give a review of this process, including the theoretical and experimental details.

Capillarity involves liquid free surfaces that are submitted to temperature and concentration gradients. This generates the Marangoni convection, which in turn impacts the crystal growth process. *Chapter 7* is devoted to the coverage of this fluid flow problem, which is absolutely capillary dependent. In order to study this phenomenon thoroughly, without perturbation due to buoyancy convection, A. Cröll performed many experiments under microgravity conditions. In parallel, T. Hibiya and S. Shiratori studied the effect of Marangoni convection on silicon floating zones and especially how this changes when oxygen contamination occurs. One important practical and theoretical problem is the onset of the different fluid flow regimes that occur successively when the Marangoni convection increases from laminar to fully turbulent convection. The authors' discussion clearly explains how the critical values are observed, measured and simulated. There is no doubt that this chapter will be of interest not only to crystal growers but also to those interested in fluid mechanics. Marangoni convection also impacts the Czochralski process and has been studied in details with the help of numerical simulation by K. Kakimoto and L. Liu as detailed in this chapter, as well as the effect of this convection on the EFG and Bridgman processes.

Chapter 8 is devoted to the resolution of the Young–Laplace equation that was introduced in Chapter 1. This equation relates the pressure inside the liquid to the curvature of the liquid surface, and then allows computation of the shape of liquid menisci or liquid columns involved in the crystal growth processes. However it is a highly nonlinear equation which has analytical solutions only in very rare configurations. Specific mathematical methods must then be used in order to study the solutions. In the most general cases only numerical methods can help in solving the problem. L. Braescu and S. Epure are working on the mathematical aspects of these solutions and have chosen the Czochralski, EFG and dewetting configurations in order to give detailed examples of the exact, approximated and numerical solutions that are known in these cases. The preferred numerical method used in these problems is the Runge–Kutta method, and an appendix describes in detail how this technique works and can be implemented on a computer. We hope that readers will be able to find useful solutions for their specific problems, based on these examples.

References

- [Bridgman 1925] Bridgman P.W., *Proc. Am. Acad. Arts Sci.* **20** (1925) 305–383.
 [Capper 2005] Capper P. (ed.) *Bulk Crystal Growth of Electronic, Optical and Optoelectronic Materials*, John Wiley & Sons Ltd, New York (2005).
 [Czochralski 1918] Czochralski J., *Z. Phy. Chem.* **92** (1918) 219–221.
 [Gompertz 1922] Gomperz E.V., *Z. Phys.* **8** (1922) 184–190.
 [Hurle 1993] Hurle D.T.J. (ed.), *Handbook of Crystal Growth*, Elsevier, Amsterdam (1993).
 [Keck 1953] Keck P.H., Golay M.J.E., *Phys. Rev.* **89** (1953) 1297.
 [Nassau 1969] Nassau K., *J. Cryst. Growth* **5** (1969) 338–344.
 [Scheel 2003] Scheel H.J., Fukuda T. (eds), *Crystal Growth Technology*, John Wiley & Sons Ltd, New York (2003).
 [Tatartchenko 1993] Tatartchenko Y.A., *Shaped Crystal Growth*, Kluwer Academic Publishers, Dordrecht (1993).
 [Theurer 1952] Theurer H.C., US Patent No. 3060123 V, 17 December 1952.
 [Verneuil 1902] Verneuil A., *Comptes Rendus (Paris)* **135** (1902) 791–794.
 [Verneuil 1904] Verneuil A., *Ann. Chim. Phys.* **8**(3) (1904) 20–48.
 [Verneuil 1910] Verneuil A., *Comptes Rendus (Paris)* **151** (1910) 131–132.

Acknowledgements

The main actors in this book are obviously the authors themselves. It is very gratifying that they all enthusiastically agreed to embark on this adventure. They really did their best to deliver comprehensive, up to date and well-written chapters, submitted on time. I thank all of them for their involvement and for their gracious acceptance of my endless recommendations, deadline warnings and remarks. Above all, I am deeply grateful to those who accepted the hard task of coordinating the chapters. It has been a very exiting experience to gather all these authors from around the world and finally merge all their contributions into a single book; I'm convinced that it would not have been so successful without the friendly relationship that I have with most of them.

On the publishing side, I am very pleased to thank John Wiley & Sons for agreeing to publish the book and for the help of the editorial team, Alexandra Carrick, Richard Davies and Emma Strickland.

The editing process has been long and tedious, because I wanted to achieve consistency of style and nomenclature throughout the chapters. This would not have been possible without the invaluable and passionate help of Simona Epure who spent some nights (following the days) on the project; I'm profoundly indebted to her for this hard work and also to Najib Kacem for his help in fitting all the figures to the publisher's format. This editing activity has been made possible by the financial help, reflecting more importantly their interest, of the companies Cyberstar and Siltronix, and of my laboratory SIMaP, including support from the EPM group.

<http://www.cyberstar.fr/>

<http://www.siltronix.com/>

<http://simap.grenoble-inp.fr/>



Last in this list but first in my heart, I cannot forget my deep gratitude to Bernadette for her patience, interest and support for the project and her *petit clown* gift that makes life so amazing.

Nomenclature

As far as possible the nomenclature has been harmonized between the various chapters. However, because of the wide range of physical phenomena involved, some chapters have used specific symbols for the sake of clarity.

a	lattice parameter; also capillary constant
b	Burgers vector
c	chemical composition
c_p	heat capacity
d	diameter
e	gap thickness
f	solidified fraction; frequency of the induction current (Chapter 4)
g	gravitational acceleration
h	meniscus height
k	segregation coefficient
k_B	Boltzmann constant
m	liquidus or solidus slopes; mode of rotational wave
p_0	reference pressure in the melt
p_v	gas pressure
p	pressure
r	radial coordinate
r_a	ampoule/crucible radius
r_c	crystal radius
s	arc length
t	time, also ribbon thickness
u	fluid velocity
v	pulling rate
v_c	solid-liquid interface velocity (crystallization rate)
w	die half thickness
x, y, z	axis
A	surface, area
B	magnetic field
Bi	Biot number
Bo	Bond number
D_{th}	thermal diffusivity
E	Young's modulus
Gr	Grashof number

H	magnetic induction; distance from the shaper edge to the coordinate plane (Chapter 2)
Ha	Hartmann number
H_m	length of the melt column
I	nucleation rate (s^{-1})
L	crystal length
La	Laplace number
M	mass
Ma	Marangoni number
N	a number (of nuclei, of particles, etc.)
P	heating power
Pe	Peclet number
Pr	Prandtl number
Re	Reynolds number
Sc	Schmidt number
T	temperature
T_a	ambient temperature
V	volume (V_a , atomic volume)
We	Weber number
X	mole fraction
W	ribbon width, also weight of crystal
\mathcal{D}	thermal diffusivity
\mathcal{P}	powder charge flow rate
ζ	latent heat of melting
Ω	rotation rate
α	growth angle
α_0	angle between the tangent to the meniscus and the vertical axis
β	angle between the shaper wall and the horizontal; dilatation coefficient also coefficient of mass flow rate prescribed by the feeder
γ	surface energy (solid liquid, liquid gas, etc.)
δ	boundary layer thickness
ε	fluctuation, perturbation; strain, emissivity
κ	curvature ($1/R$)
σ	stress; also Stefan–Boltzmann constant;
σ_{el}	electrical conductivity of the melt
θ	wetting angle (Young, or apparent, etc.)
ν	kinematic viscosity
λ	thermal conductivity, also surface mass transport coefficient (Chapter 1)
ρ	density; resistivity
μ	dynamic <i>viscosity</i> , also permeability
ϕ	angle between the tangent to the meniscus and the horizontal axis
$\delta\phi_0$	angle of crystal tapering at any moment
φ	angular polar coordinate, also the angle between the pulling direction and the vertical direction (Chapter 5)
ψ	angle between the vertical axis and the l/v interface (Chapter 1)
Φ	electrical potential; also heat flux (Chapter 3, Chapter 6)

ω	frequency
Γ	Gibbs parameter ($\gamma/\Delta S$; K m)
J, j	flux and flux density
G	Gibbs free energy
H	enthalpy
S	entropy
$\Delta G, \Delta H, \Delta S$	differences of formation/migration/etc. energy or entropy
ΔT	undercooling
Δc	supersaturation
∇	gradient

Subscripts

s	solid
l	liquid
i	at the solid/liquid interface
m	melting
c	crystal
e	environment/encapsulant; also boron oxide layer (Chapter 3)
0	reference
ch	chemical
T or th	thermal
t	time
v	vapour

Vectors are in **bold**.

Contributors

Nikolai V. Abrosimov, Leibniz-Institut für Kristallzüchtung im Forschungsverbund Berlin e.V., Berlin, Germany

Günter Behr, Leibniz-Institut für Festkörper- und Werkstoffforschung, Dresden, Germany

Liliana Braescu, Department of Computer Science, West University of Timisoara, Romania

Simon Brandon, Department of Chemical Engineering, Technion–Israel Institute of Technology, Haifa, Israel

Arne Cröll, University of Freiburg, Kristallographie-Geowissenschaftliches Institut, Freiburg, Germany

Béatrice Drevet, CEA-INES/RDI, Le Bourget du Lac, France

Thierry Duffar, Laboratoire SIMaP-EPM, INP Grenoble, Saint Martin d'Hères, France

Simona Epure, SIMaP-EPM, Saint Martin d'Hères, France and Department of Computer Science, West University of Timisoara, Romania

Nicolas Eustathopoulos, Laboratoire SIMaP, Saint Martin d'Hères, France

Michael Gevelber, Boston University, Mechanical Engineering Department, Boston, USA

Taketoshi Hibiya, Tokyo Metropolitan Institute of Technology, Department of Aerospace Engineering, Tokyo, Japan

Koichi Kakimoto, Kyushu University, Research Institute for Applied Mechanics, Fukuoka, Japan

Vladimir N. Kurlov, Institute of Solid State Physics RAS, Chernogolovka, Russia

Kheirreddine Lebbou, LPCML-CNRS, Université de Lyon I, France

Lijun Liu, Kyushu University, Research Institute for Applied Mechanics, Fukuoka, Japan

Wolfgang Löser, Leibniz-Institut für Festkörper- und Werkstoffforschung, Dresden, Germany

Anke Lüdge, Leibniz-Institut für Kristallzüchtung im Forschungsverbund Berlin e.V., Berlin, Germany

Andris Muiznieks, Department of Physics, University of Latvia, Riga, Latvia

Michael Neubert, Leibniz-Institut für Kristallzüchtung im Forschungsverbund Berlin e.V., Berlin, Germany

Duanmu Ning, GT Solar International, Merrimack, New Hampshire, USA

Helge Riemann, Leibniz-Institut für Kristallzüchtung im Forschungsverbund Berlin e.V., Berlin, Germany

Sergei N. Rossolenko, Institute of Solid State Physics RAS, Chernogolovka, Russia

Joachim Rudolph, Lehrstuhl für Systemtheorie und Regelungstechnik, Universität des Saarlandes, Saarbrücken, Germany

Suguru Shiratori, Tokyo Metropolitan Institute of Technology, Department of Aerospace Engineering, Tokyo, Japan.

Lamine Sylla, Freiburger Materialforschungszentrum FMF, Albert-Ludwigs-Universität Freiburg, Germany

Vitali A. Tatartchenko, Saint-Gobain Crystal, Nemours, France

Alexander Virozub, Department of Chemical Engineering, Technion–Israel Institute of Technology, Haifa, Israel

Jan Winkler, Institut für Regelungs- und Steuerungstheorie, Technische Universität Dresden, Germany

Michael Wünscher, Leibniz-Institut für Kristallzüchtung im Forschungsverbund Berlin e.V., Berlin, Germany

1

Basic Principles of Capillarity in Relation to Crystal Growth

Nicolas Eustathopoulos
Laboratoire SIMaP

Béatrice Drevet
CEA-INES/RDI

Simon Brandon and Alexander Virozub
Technion–Israel Institute of Technology

The first part of this chapter (1.1) contains a brief definition of characteristic energies of surfaces and interfaces, as well as of capillary pressure. The second part (1.2) presents the basic principles of wettability and selected data for surface tension and contact angle for liquids of interest in crystal growth on various solid substrates. The third part (1.3) deals with growth angles, i.e. the contact angles formed by liquids on their own crystal, and the role of these angles in melt growth processes.

1.1 Definitions

1.1.1 Characteristic Energies of Surfaces and Interfaces

In order to define the characteristic energies of surfaces and interfaces, let us consider two bodies, solid (s) and liquid (l) respectively, that have a unit cross-sectional area. The

2 Crystal Growth Processes Based on Capillarity

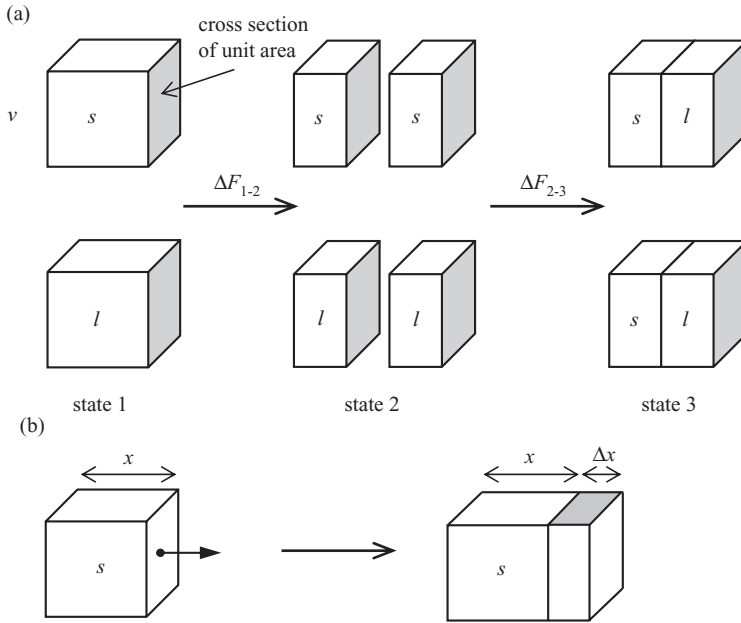


Figure 1.1 (a) Formation of two solid/liquid interfaces of unit area from pure solid and liquid bodies. (b) Formation of solid surface by elastic deformation.

solid and the liquid are surrounded by a vapour phase (v) at constant temperature. The free energy change corresponding to the reversible creation, without any elastic or plastic deformation, of two new surfaces of solid and liquid, by the process schematized in Figure 1.1.a, is:

$$\Delta F_{1-2} = 2(\gamma_{sv} + \gamma_{lv}) \quad (1.1)$$

In this expression, the quantities γ_{sv} and γ_{lv} define the surface energy of the solid and the liquid respectively. Consider now the transformation 2–3 consisting in joining two surfaces of solid and liquid. The free energy change is equal to:

$$\Delta F_{2-3} = 2(\gamma_{sl} - \gamma_{sv} - \gamma_{lv}) \quad (1.2)$$

Finally, the transformation 1–3 corresponds to:

$$\Delta F_{1-3} = \Delta F_{1-2} + \Delta F_{2-3} = 2\gamma_{sl} \quad (1.3)$$

where γ_{sl} is the solid/liquid interface energy.

For pure liquids and solids, the quantity $2\gamma_{lv}$ or $2\gamma_{sv}$ defines the *work of cohesion* W_c of the liquid ($W_c^l = 2\gamma_{lv}$) or the solid ($W_c^s = 2\gamma_{sv}$). The values of these quantities are proportional to the evaporation and sublimation energies per unit area respectively. In Equation

(1.2), the quantity $(\gamma_{sl} - \gamma_{sv} - \gamma_{lv})$ is equal but opposite in sign to the *work of adhesion* W_a defined by Dupré [Dupré 1869]:

$$W_a = \gamma_{sv} + \gamma_{lv} - \gamma_{sl} \tag{1.4}$$

Accordingly, the magnitude of W_a directly reflects the intensity of interactions between atoms in the liquid and solid states across the common interface.

1.1.2 Capillary Pressure

Consider a spherical liquid (l) drop of radius r in a vapour v. The volume of this drop is increased slowly, for instance by using a syringe to inject fresh liquid into the drop (Figure 1.2a). The increase of drop radius from r to $(r + dr)$ leads to an increase of the surface energy of the system equal to $d(4\pi r^2 \gamma_v) = 8\pi r \gamma_v dr$. If P_l is the pressure inside the drop and P_v the pressure in the vapour, the increase of r is associated with an amount of mechanical work to move the surface by a distance dr , i.e. $(P_l - P_v)4\pi r^2 dr$. Equating the two amounts of work leads to the expression of capillary pressure ΔP_c given by Laplace [Laplace 1805]:

$$\Delta P_c = P_l - P_v = 2 \gamma_{lv} / r \tag{1.5}$$

In the general case of a surface characterized by principal radii R_1 and R_2 (Figure 1.2.b), the curvature at each point Q of the liquid/vapour surface has to satisfy:

$$P_l^Q - P_v^Q = \gamma_{lv} \left(\frac{1}{R_1} + \frac{1}{R_2} \right) \tag{1.6}$$

The various mathematical forms of Laplace’s equation are discussed in Chapter 8. The capillary pressure ΔP_c preponderates over the hydrostatic pressure of a liquid of density ρ for liquid sizes less than a characteristic length called the *capillary length* and defined by $(\gamma_{lv}/(\rho g))^{1/2}$ where g is the acceleration due to gravity.

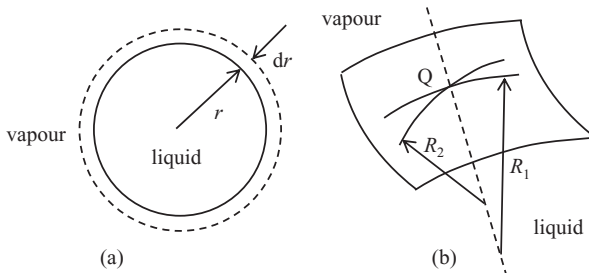


Figure 1.2 (a) Displacement of a liquid surface allowing derivation of the Laplace equation. (b) The principal radii of curvature R_1 and R_2 at a point Q on a curved liquid surface.

1.1.3 Surface Energy versus Surface Tension

In Figure 1.1.a, the two new solid/vapour surfaces are created by breaking bonds to increase the number of solid atoms (or molecules) which belong to the surface. A typical example of such a process is cleavage achieved without any elastic or plastic deformation of the solid. An alternative process to create a new solid/vapour surface is by purely elastic strain of the solid (Figure 1.1b), i.e. *without increasing the number of surface atoms*. The extra stress due to the surface, called ‘surface tension’ or ‘surface stress’, is denoted by σ_{sv} and expressed as a force per unit length.

For liquids, σ_{lv} and γ_{lv} are equal because the reversible stretching of a liquid surface is identical to the reversible creation of new surface. In both cases, the liquid can increase its surface area only by the addition of new atoms to the surface. Note that, from a dimensional point of view, an energy per unit area is equivalent to a force per unit length and the values are numerically equal when γ_{lv} is measured in Jm^{-2} and σ_{lv} is measured in Nm^{-1} .

For solids, σ_{sv} and γ_{sv} are different quantities. For instance, for each crystal face, there is a unique value of γ_{sv} (which is a scalar) while σ_{sv} depends also on the orientation along the face. Moreover, γ_{sv} is always a positive quantity (breaking bonds needs work) while σ_{sv} can be either positive or negative [Nolfi 1972]. For high symmetry surfaces, the surface tension is related to the surface energy by the equation [Shuttleworth 1950]:

$$\sigma_{sv} = \gamma_{sv} + d\gamma_{sv}/d\varepsilon \quad (1.7)$$

where ε is a macroscopic elastic strain. The physical origin of the difference between γ_{sv} and σ_{sv} , i.e. of the term $d\gamma_{sv}/d\varepsilon$ in Equation (1.7), can be explained taking into account the atomistic origin of γ_{sv} . For instance, for monoatomic solids, γ_{sv} is proportional to the difference in potential energy between an atom of the surface and an atom of the bulk solid. When a new surface is created by stretching the solid (Figure 1.1b), this difference does not remain constant. Indeed, because surface atoms are bonded weakly compared to those in the bulk, the work needed to stretch the surface is less than for the bulk material.

From now on, for solid/vapour and solid/liquid boundaries, only the surface and interface energies γ_{sv} and γ_{sl} will be considered. For liquid/vapour boundaries, both the surface tension σ_{lv} and surface energy γ_{lv} will be used interchangeably depending on the context.

1.2 Contact Angles

In this part (sections 1.2.1–1.2.4), the fundamental equations describing the wetting of ideal surfaces in chemically inert systems are given. Then the wetting of real surfaces is presented, taking into account the effects of roughness and chemical heterogeneities of the solid surface. The dynamics of wetting will be presented mainly for nonreactive solid/liquid systems and more briefly for reactive ones. After a short description of methods for measuring contact angles and surface tensions at high temperature, selected data are

given and discussed for molten semiconductors, oxides and halides on solid oxides, carbon, nitrides and metallic substrates.

1.2.1 Thermodynamics

1.2.1.1 Ideal Solid Surfaces

Young's and Young–Dupré equations. Consider a flat, undeformable, perfectly smooth and chemically homogeneous solid surface in contact with a nonreactive liquid in the presence of a vapour phase. If the liquid does not completely cover the solid, the liquid surface will intersect the solid surface at a 'contact angle' θ . The equilibrium value of θ , used to define the wetting behaviour of the liquid, obeys the classical Young's equation [Young 1805]:

$$\cos\theta_Y = \frac{\gamma_{sv} - \gamma_{sl}}{\gamma_{lv}} \quad (1.8)$$

In this chapter, a contact angle of less than 90° will identify a wetting liquid, while a greater value will identify a nonwetting liquid. If the contact angle is zero, the liquid will be considered to be perfectly wetting.

Equation (1.8) can be easily derived by calculating the variation of the *surface* free energy F_s of the system caused by a small displacement δx of the solid/liquid/vapour *triple phase line* (TPL). In Figure 1.3, the TPL is perpendicular to the plane of the figure and assumed to be a straight line, rendering the problem two-dimensional. Thus, the total length of the TPL is constant during its displacement, as in the case of a meniscus formed on a vertical plate. Moreover, the radius r of the TPL region considered in this derivation (Figure 1.3) is much larger than the range of atomic (or molecular) interactions in the

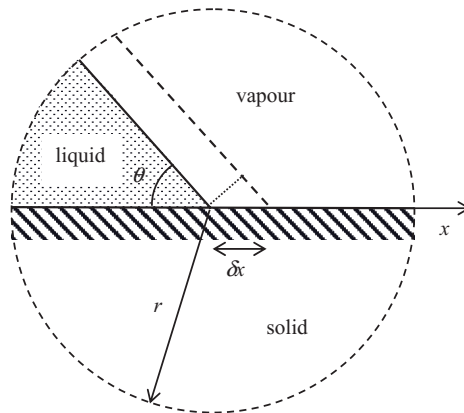


Figure 1.3 Displacement of a triple line around its equilibrium position that allows derivation of Young's equation. Only a small region close to the triple line is taken into account to neglect the curvature of the liquid/vapour surface.

system ($r \gg 10\text{ nm}$) and small compared to a characteristic dimension of the liquid, for instance the average drop base radius R in the sessile drop configuration (see Figure 1.15a) or the maximum height of a meniscus formed on a vertical solid wall which are both typically in the millimetre range. With these assumptions, the variation of interfacial free energy per unit length of the TPL, resulting from a small linear displacement δx of the TPL, is

$$F_s(x + \delta x) - F_s(x) = \delta F_s = (\gamma_{sl} - \gamma_{sv})\delta x + \cos(\theta)\gamma_{lv}\delta x$$

and the equilibrium condition $d(\delta F_s)/d(\delta x) = 0$ leads to Equation (1.7). Young's equation was shown also to be valid in the presence of the gravitational field for the configuration of a meniscus formed on a vertical plate [Neumann 1972, Eustathopoulos 1999 p. 12], and for the classical configuration of an axisymmetric sessile drop [Garandet 1998].

By combining Equation (1.4) of W_a and the Young Equation (1.8), the following fundamental equation of wetting, known as the Young–Dupré equation, is obtained:

$$\cos\theta = \frac{W_a}{\gamma_{lv}} - 1 \quad (1.9)$$

Taking into account the transformation ΔF_{3-2} of Figure 1.1a, this equation shows that the contact angle results from the competition of two types of forces: cohesion forces responsible for γ_{lv} ($\gamma_{lv} = W_c/2$) and adhesion forces responsible for W_a .

System Size Effects. In the sessile drop configuration, the increase of the drop base radius during wetting leads not only to a change of surface and interface areas but also to the increase of the TPL length. The TPL can be considered as a line defect, similar to the step energy in crystal growth, with a specific excess energy τ [Eustathopoulos 1999 p. 10]. Therefore, the contact angle is in principle a function not only of surface energies γ_{ij} but also of τ . However, the importance of τ decreases when the drop size increases, and becomes negligible for a droplet radius of more than a few tens of nm [Chizhik 1985, Eustathopoulos 1999 p. 11].

Metastable and Stable Contact Angles. Young's equation is derived from minimization of the free energy of the system carried out by considering only displacements of the triple line parallel to a solid/vapour surface assumed to be undeformable (Figure 1.4b). Therefore, θ_Y corresponds to a metastable equilibrium configuration. For isotropic solid/vapour and solid/liquid surface and interfacial energies, the local stable equilibrium shown in Figure 1.4c is described by the Smith equation by means of three dihedral angles θ_l , θ_v and θ_s [Smith 1948]:

$$\frac{\gamma_{sv}}{\sin\theta_l} = \frac{\gamma_{sl}}{\sin\theta_v} = \frac{\gamma_{lv}}{\sin\theta_s} \quad (1.10)$$

For a simple derivation of this equation, the interested reader can refer to [Eustathopoulos 1999 p. 16].

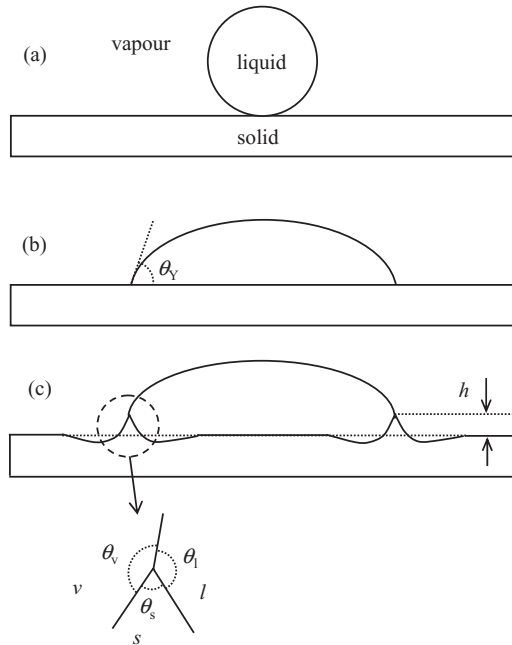


Figure 1.4 Metastable (b) and stable (c) equilibrium angles at a solid/liquid/vapour junction obtained after spreading of a liquid droplet (a).

For fluids with low viscosity (a few mPas), such as molten metals and semiconductors or certain oxide melts at high temperature, the approach to the local stable equilibrium occurs in two stages with very different rates. In the first rapid stage (spreading time for millimetre-sized droplets of the order of 10^{-1} or 10^{-2} s, see section 1.2.2.1), the macroscopic contact angle approaches θ_Y . This stage is followed by a much slower process occurring at the vicinity of the triple line to satisfy the Smith equation. As discussed in [Saiz 1998], the growth of the ‘wetting ridge’ of height h (Figure 1.4c) can take place by mechanisms similar to those occurring during grain boundary grooving as described by Mullins [Mullins 1957, 1960]. An example is millimetre-size Cu droplets on Al_2O_3 surfaces in Ar at 1150°C . While the Young contact angle is reached in a few ms, a wetting ridge with $h = 10$ nm is formed after 2 h. Clearly, such a wetting ridge has a negligible effect on the value of the contact angle. Therefore, the area of the solid/liquid and liquid/vapour interfaces at equilibrium is determined essentially by the value of θ_Y .

For vitreous solids, such as SiO_2 , viscosity decreases strongly close to the melting point. In this case, the solid ridge can be formed by viscous flow and the height h can reach easily measurable sizes in quite short times. For example, wetting of a Ni droplet on a SiO_2 substrate at 1470°C is accompanied by the formation, in about 20 min, of an easily observable SiO_2 meniscus on the Ni drop ($h = 5\text{--}10\ \mu\text{m}$) [Merlin 1992].

1.2.1.2 Effect of Roughness

The roughness of solid surfaces affects wetting as a result of two different effects: the first is the fact that the actual surface area is increased and the second is pinning of the triple line by sharp edges.

Effect of Increased Surface Area – Wenzel Equation. If s_r denotes the ratio of the actual area to the planar area ($s_r > 1$), for a surface with a small asperity wavelength compared to the capillary length, the macroscopic equilibrium contact angle denoted by θ_w is given by the equation of Wenzel [Wenzel 1936]:

$$\cos \theta_w = s_r \cos \theta_Y \quad (1.11)$$

According to this equation, for $\theta_w < 90^\circ$ and if $s_r > 1/\cos \theta_w$, perfect wetting will be observed.

Effect of Sharp Edges – Hysteresis of Contact Angle. Sharp edges can pin the triple line at positions far from stable equilibrium, i.e. at contact angles markedly different from θ_Y . This effect is illustrated schematically in Figure 1.5 where a solid substrate with an horizontal surface A_1 and another surface A_2 inclined at an angle β is considered. The initial equilibrium configuration of the liquid surface, marked (1) in Figure 1.5, corresponds to a contact angle on the A_1 surface $\theta(A_1) = \theta_Y$. Then, if the liquid volume is increased slowly enough for the liquid to retain capillary equilibrium, the TPL will advance on surface A_1 and reach configuration (2) where the contact angle at point N is $\theta_N(A_1) = \theta_Y$. Thereafter, the TPL will be pinned at point N and the macroscopic contact angle on A_1 , $\theta_N(A_1)$, will increase until the liquid surface assumes configuration (3) where $\theta_N(A_1) = \theta_Y + \beta$, which corresponds to the establishment of the Young contact angle on the A_2 surface, i.e. $\theta_N(A_2) = \theta_Y$. Any further increase in the liquid volume will produce a movement of the TPL on the A_2 surface, for example to configuration (4) with $\theta(A_2) = \theta_Y$.

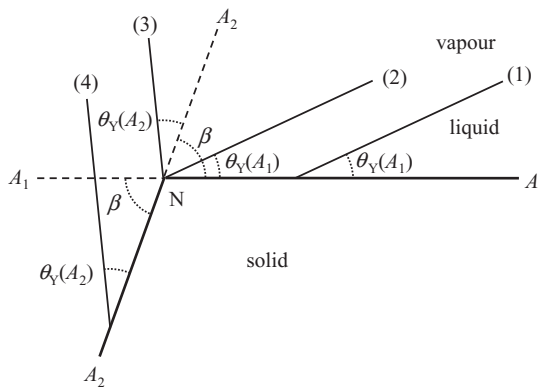


Figure 1.5 Effect of a sharp edge on the contact angle when a triple line advances on a solid surface. (1), (2), (3) and (4) denote the successive configurations of the liquid surface when the liquid volume is increased.

Thus, the liquid can form an infinite number of *advancing* contact angles at point N on the A_1 surface lying between θ_Y and $\theta_Y + \beta$. This last value defines the maximum advancing contact angle on A_1 :

$$\theta_a(\max) = \theta_Y + \beta \tag{1.12a}$$

Consider now that configuration (4) in Figure 1.5 represents the initial liquid surface and that the liquid volume is slowly decreased. Using similar arguments for the retreat of the liquid on the A_2 surface, it can be shown that the liquid can form an infinite number of *receding* contact angles at point N on the A_2 surface lying between θ_Y and $\theta_Y - \beta$. This last value defines the minimum receding contact angle on A_2 :

$$\theta_r(\min) = \theta_Y - \beta \tag{1.12b}$$

When these considerations are applied to a rough surface consisting of grooves parallel to the moving triple line, one can identify the maximum advancing contact angle and the minimum receding contact angle, as shown in Figure 1.6:

$$\theta_a(\max) = \theta_Y + \beta_{\max} \tag{1.13a}$$

$$\theta_r(\min) = \theta_Y - \beta_{\max} \tag{1.13b}$$

The range of angles lying between $\theta_a(\max)$ and $\theta_r(\min)$ defines the hysteresis domain of contact angle. For a given system and roughness, a large number of angles belonging to the hysteresis domain and corresponding to metastable equilibrium states can be observed. Vibrations help the triple line to overcome the energy barriers caused by roughness and to approach the stable equilibrium state, i.e. the Wenzel contact angle (Equation (1.11)). In practice, for random roughness surfaces with average roughness parameter R_a of about 100nm, the excess $(\theta_a - \theta_Y)$ values are a few degrees, while for R_a close to 1 μm the excess $(\theta_a - \theta_Y)$ values for various nonwetting liquids can be as much as 20° [Hitchcock 1981, Eustathopoulos 2005] (Figure 1.7).

Composite Wetting. For solid surfaces with high roughness, a liquid forming large nonwetting contact angles ($\theta \gg 90^\circ$) cannot infiltrate surface cavities, resulting in the

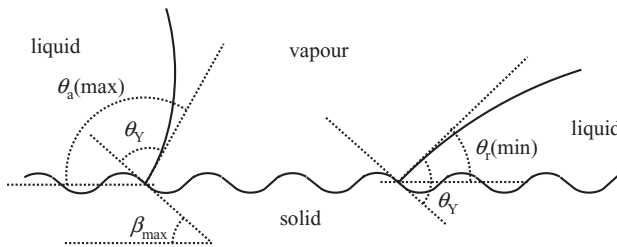


Figure 1.6 Identification of the maximum advancing contact angle $\theta_a(\max)$ and minimum receding contact angle $\theta_r(\min)$ on a rough surface.

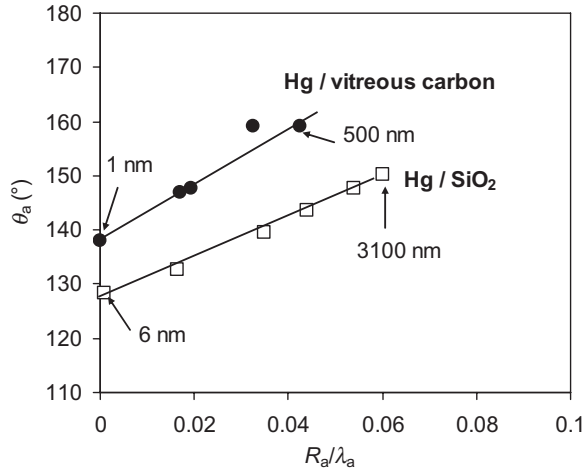


Figure 1.7 Advancing contact angle θ_a measured by the sessile drop technique as a function of R_a/λ_a , a quantity proportional to the average slope of the surface profile where R_a is the average roughness and λ_a the average wavelength of the asperities, for Hg on abraded SiO_2 and C_v ; the arrows indicate R_a values. θ_y values for Hg on these substrates are the values at $R_a/\lambda_a = 0$ [Eustathopoulos 2005a]. Data from work reported in [Hitchcock 1981].

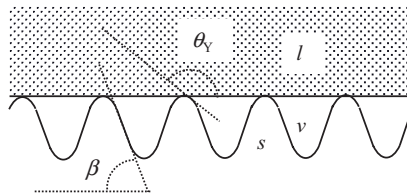


Figure 1.8 Formation of a composite interface in a nonwetting system.

formation of a composite interface, i.e. a mixed solid/liquid interface and solid/vapour surface (Figure 1.8). A characteristic of such an interface is the disappearance of the energy barriers to the movement of the TPL. Indeed, the liquid surface contacts the solid only at a limited number of points so that no pinning of the TPL can occur, explaining why the difference $(\theta_a - \theta_r)$ tends towards zero in this case. Thus, Hg droplets on ceramic surfaces are very mobile. Indeed, owing to the poor wetting by Hg and the formation of composite interface, droplets are never pinned and move easily.

The condition for the transition from a solid/liquid to a composite interface is given by [Eustathopoulos 1999 p. 34]:

$$\beta > 180^\circ - \theta_y \quad (1.14)$$

where β is the maximal average slope of the surface. In practice, θ_y values of metals and semiconductors are rarely greater than 150° . In this case, composite interfaces can be obtained only with very rough surfaces ($\beta > 30^\circ$).

Sticking. When composite interfaces are formed, no sticking is observed during cooling at room temperature, whatever the thermomechanical characteristics of the system. Typical examples are nonreactive metals (e.g. Cu, Ag) on polycrystalline graphite, or soda-lime glasses on steel moulds lubricated with a porous layer of carbon [Pech 2005].

When a true interface is established at any point of the common area, the behaviour of the interface on cooling depends on several material parameters, as well as system geometry and cooling rate. Sticking is favoured by (i) a high adhesion energy W_a and (ii) a low thermoelastic energy stored in the system during cooling due to thermal contraction mismatch ($\Delta\alpha = \alpha_A - \alpha_B$) between the substrate A and the solidified liquid B. For a given $\Delta T = T_{\text{sol}} - T_{\text{room}}$ (where T_{sol} is the temperature of solidification and T_{room} the room temperature), this energy increases proportionally to $(\Delta\alpha)^2$ and to $E_A E_B^2 / (E_A + E_B)^2$ where E is Young's modulus [Pech 2004]. Ductility of one of the contacting phases in a certain range of temperature contributes to decrease, by plastic deformation, the driving force for detachment. Many semiconductors (e.g. Si, InSb, GaSb) are brittle materials, such that energy dissipation by plastic deformation is small. In this case, the mechanical response of the system during cooling depends critically on the adhesion energy of the solidified liquid/substrate couple. For instance, for Si on Si_3N_4 and SiC, the adhesion energy is high (Si wets well both these ceramics; see Tables 1.4 and 1.5) resulting in sticking or cohesive fracture [Drevet 2009]. Conversely, the adhesion energy of GaSb and InSb on vitreous carbon is very low (see Table 1.4) leading during cooling to detachment by a purely interfacial separation [Harter 1993, Boiton 1999]. See also Chapter 6, section 6.1.3.

1.2.1.3 Wetting on Heterogeneous Surfaces

Many materials of practical interest are multiphase solids with heterogeneous surfaces that can be either regular (oriented eutectics, unidirectional composites, etc.) or random ('hard' alloys processed by liquid phase sintering, alloys strengthened by precipitation, etc.).

Consider an horizontal solid consisting of two macroscopic phases α and β separated by a plane intersecting the solid surface by a vertical straight line (Figure 1.9). The intrinsic contact angles on the two phases are such that $\theta_\alpha > \theta_\beta$, and for the sake of clarity $\theta_\alpha > 90^\circ$ and $\theta_\beta < 90^\circ$. The initial position of the liquid surface is on the β phase with a macroscopic contact angle θ_M equal to θ_β (configuration (1) on Figure 1.9). If the liquid volume is increased, when the TPL reaches the line of separation from β to α , it will be pinned at this position by the nonwetted α phase (configuration (2)). When the volume of the liquid is increased again, the TPL does not move until configuration (3) is obtained

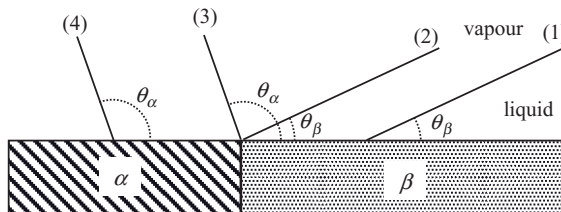


Figure 1.9 Successive configurations of the liquid surface on a solid surface consisting of two macroscopic phases α and β when the liquid volume is increased.

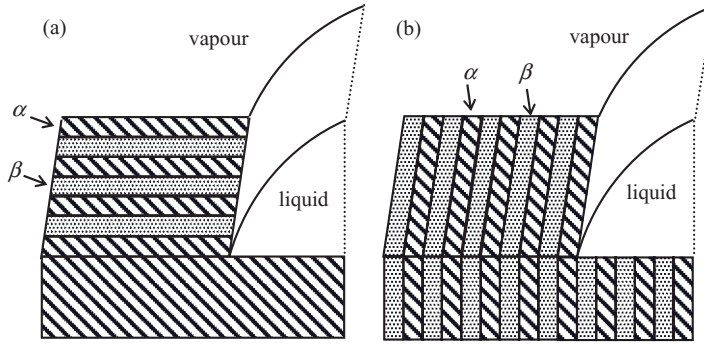


Figure 1.10 Composite solid consisting of alternate strips perpendicular (a) and parallel (b) to the triple line.

where $\theta_M = \theta_\alpha$. If the liquid volume is further increased, the TPL will move on the α surface while θ_M will remain equal to θ_α (configuration (4)).

Consider now the case of a composite solid consisting of alternate strips of α and β phases, with contact angles θ_α and θ_β , such that the surface area fractions are f_α and f_β . The width of the strips is assumed small compared to the capillary length, so that the macroscopic TPL is a straight line which is either perpendicular (Figure 1.10a) or parallel (Figure 1.10b) to the strips. For the first situation, it has been shown that there are no metastable states and, as a consequence, no hysteresis of contact angle [Johnson 1993, Neumann 1972]. The macroscopic contact angle that would be observed at equilibrium, denoted θ_C , is then given by Cassie's equation [Cassie 1948]:

$$\cos \theta_C = f_\alpha \cos \theta_\alpha + (1 - f_\alpha) \cos \theta_\beta \quad (1.15)$$

This equation, which is an analog of the Wenzel equation for rough surfaces (Equation (1.11)), gives the stable equilibrium contact angle for any heterogeneous surface.

When the TPL is parallel to the strips, a situation analogous to a rough surface with grooves parallel to the TPL (Figure 1.6), free energy change calculations [Johnson 1993, Neumann 1972] indicate the existence of metastable states separated by energy barriers for any position of the TPL corresponding to a macroscopic contact angle θ_M between θ_α and θ_β . Consequently, the maximum advancing and minimum receding contact angles are given by the equations:

$$\theta_a(\max) = \theta_\alpha \quad (1.16a)$$

$$\theta_r(\min) = \theta_\beta \quad (1.16b)$$

which are analogous to equations (1.13) for rough surfaces.

1.2.2 Dynamics of Wetting

In this section, spreading kinetics will be presented first for nonreactive solid/liquid systems and then for reactive ones. In view of the systems of interest in crystal growth,

the reactive case will be presented briefly. Nonreactive systems exhibit a reactivity low enough such that the resulting solid/liquid interface remains flat at the macroscopic scale and reactivity has a negligible effect on the interfacial energies. Under this last condition, interfacial energies can be taken constant with time during the wetting process.

1.2.2.1 Nonreactive Spreading

Consider a drop of millimetre size spreading on a flat surface spontaneously, i.e. in the absence of any external force. The triple line velocity $U = dR/dt$, where R is the drop base radius, results from a balance of forces that drive and resist to spreading. The driving force for wetting per unit length of triple line is given by the change in the surface and interfacial energies of the system resulting from a lateral displacement of the triple line:

$$\gamma_{sv} - \gamma_{sl} - \gamma_{lv} \cos \theta = \gamma_{lv} (\cos \theta_F - \cos \theta) \quad (1.17)$$

where θ_F is the final, equilibrium, contact angle. In the so-called hydrodynamic models of wetting, energy dissipation is supposed to occur by viscous friction in a macroscopic wedge near the triple line of typical width 0.1 mm. The resulting expression for U for $\theta < 135^\circ$ is:

$$U = \frac{\gamma_{lv}}{\mu K} (\theta^3 - \theta_F^3) \quad (1.18)$$

where μ is the dynamic viscosity, K is a constant close to 100 and θ is expressed in radians [de Gennes 1985, Cox 1986, Kistler 1993]. It has been shown that this equation does not depend on the configuration (sessile drop or meniscus formed on a vertical wall). Moreover, this equation is valid for both spontaneous and forced spreading. An example of forced spreading is the steady immersion (or withdrawal) of a plate in a liquid bath at an *imposed rate* U . Then, the observed contact angle would be the value $\theta(U)$ given by Equation (1.18). Finally, for θ_F close to zero, Equation (1.18) can be written as:

$$\theta \cong \left(\frac{K\mu U}{\gamma_{lv}} \right)^{1/3} = K^{1/3} Ca^{1/3} \quad (1.19)$$

where Ca is the capillary number. Accordingly, for all liquids with $\theta_F \cong 0$, the experimental $\theta = f(Ca)$ results would lie on the same ‘universal’ curve.

Molten metals and semiconductors are low viscosity liquids, their viscosity close to the melting point being a few mPas. For this type of liquid, the experimental average U is very high, of the order of 1 m s^{-1} . For millimetre-sized droplets, this leads to spreading times t_s of a few ms [Eustathopoulos 1999 p. 54]. The analysis of experimental results obtained in the sessile drop configuration shows that values $U(\theta)$ predicted by Equation (1.18) consist in an upper limit. Overestimation of U is particularly high for $\theta > 30^\circ$. For instance, in the liquid Sn/solid Ge system at 600° in which the final contact angle is about 40° [Naidich 1992], the spreading rate at $\theta = 80^\circ$ is about 0.5 m s^{-1} , while the value calculated by Equation (1.18), taking $\gamma_{lv} = 0.5 \text{ J m}^{-2}$ and $\mu = 1.1 \text{ mPas}$, is 11 m s^{-1} . For low viscosity liquids and large θ , it is likely that the spreading rate is limited not by viscous

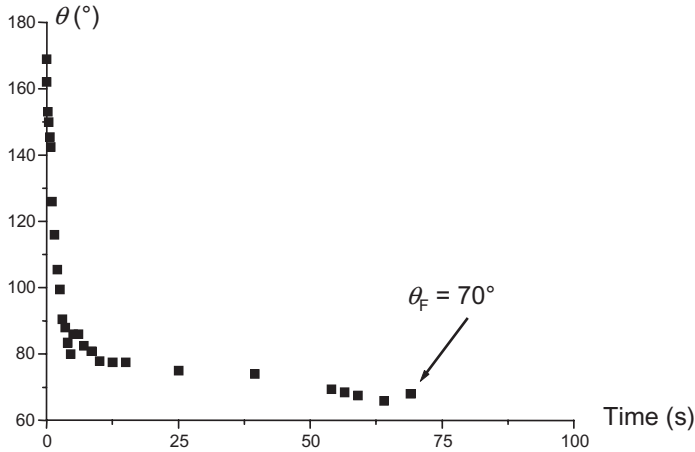


Figure 1.11 Wetting kinetics of a drop of soda-lime glass (13.4 wt% Na_2O , 10.9 wt% CaO , 1.6 wt% Al_2O_3 , 1.4 wt% MgO , SiO_2 bal.) on steel at 1200 °C ($\mu = 10^2 \text{ Pas}$) [J. Pech, M. Jeymond, N. Eustathopoulos, unpublished work].

flow but by the movement of atoms at the solid/liquid interface close to the triple line, as proposed by Blake [Blake 1993], who considered spreading as an adsorption–desorption process of the liquid atoms on the substrate surface. The values of U calculated by Blake’s model are very sensitive to the value of a model parameter, i.e. the activation energy of wetting which is an unknown quantity.

The viscosity of molten oxides is often several orders of magnitude greater than that of molten metals. As a consequence, the spreading time t_s for millimetre-sized droplets can attain several seconds or hundreds of seconds (vs a few ms for metals) and even more. In agreement with Equation (1.18), the wetting rate is very high at short times (i.e. for high θ values) and decreases strongly at longer times (Figure 1.11). Finally, the experimental wetting curves obtained for the same molten oxide/solid metal couple by varying the temperature by 240 ° (implying a variation of μ by more than two orders of magnitude) are plotted as $\theta = f(Ca)$ on Figure 1.12. In agreement with Equation (1.18), a unique curve is obtained (note that in these experiments the change of θ_F with temperature is negligible) [Pech 2004].

1.2.2.2 Reactive Spreading

In this type of spreading, wetting is accompanied by (and in many cases coupled to) a reaction forming a new compound at the interface. The fundamentals of reactive wetting (driving force, limiting process) have been studied mainly for molten metals and alloys on ceramics and are reviewed in [Eustathopoulos 2005b]. In these systems, the observed spreading times are in the range 10^1 – 10^3 s (Figure 1.13), corresponding to spreading rates U several orders of magnitude lower than those measured for molten metals in nonreactive spreading. Therefore, in reactive spreading, U is limited by the interfacial reaction itself. Actually it has been shown that the relevant region is not the two-dimensional solid/liquid interface but the solid/liquid/vapour triple line. Indeed, at this line where the liquid

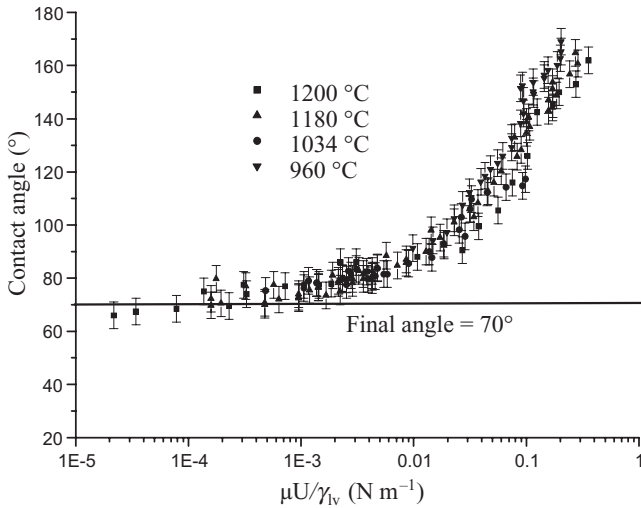


Figure 1.12 Contact angle as a function of $Ca = \mu U / \gamma_{lv}$ for the glass 13.4 wt% Na_2O , 10.9 wt% CaO , 1.6 wt% Al_2O_3 , 1.4 wt% MgO , bal. SiO_2 on steel at different temperatures (Reprinted with permission from [Pech 2004], copyright (2004) Elsevier Ltd).

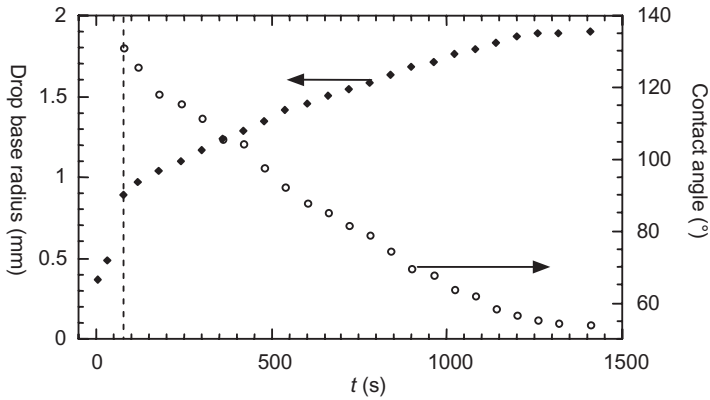


Figure 1.13 Variation of drop base radius and contact angle with time for Ge-20 at.% Si alloy on vitreous carbon at 1231 °C under high vacuum (the dashed vertical line indicates the moment of drop detachment from the capillary end in the dispensed drop apparatus of Figure 1.15b) (Reprinted with kind permission from [Dezellus 2000], copyright (2000) O. Dezellus). In this system, wetting is promoted by the formation at the interface of a wettable SiC layer.

contacts directly a fresh surface of the solid substrate, the growth rate of the reaction product is maximal (Figure 1.14). Far behind the triple line, thickening of the reaction product continues but this process is slow as it occurs by solid state diffusion. Two regimes of reactive spreading have been identified depending on the relative rate of the two successive steps: (i) diffusion of the reactive solute from the liquid bulk to the triple

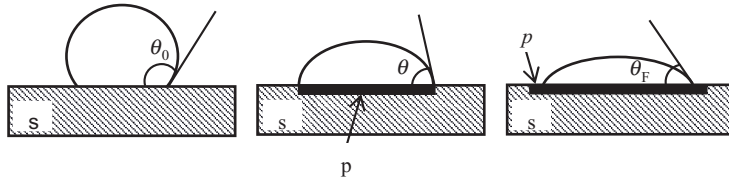


Figure 1.14 Schematic representation of the ‘reaction product control’ model. The initial contact angle θ_0 is the contact angle on the unreacted ceramic substrate surface s . After a transient stage, a quasi-state configuration is established at the triple line where the advance of the liquid is hindered by the presence of a nonwetable substrate in front of the triple line. Thus, the only way to move ahead is by lateral growth of the wettable reaction product layer p until the macroscopic contact angle equals the equilibrium contact angle θ_F of the liquid on the reaction product (Reproduced with permission from [Eustathopoulos 1998], copyright (1998) Elsevier Ltd).

line and (ii) the local process at the triple line. When the local process at the triple line is the slowest one, the spreading rate U was found to be nearly constant in a large domain of the $\theta(t)$ curve (linear spreading) (Figure 1.13). Conversely, nonlinear spreading is predicted for diffusion controlled reactive spreading (drop base radius $R \sim t^{1/4}$) [Mortensen 1997].

1.2.3 Measurements of Contact Angle and Surface Tension by the Sessile Drop Technique

A critical review of the state of knowledge in high temperature contact angle measurement is given in [Eustathopoulos 1999 p. 106, Eustathopoulos 2005a]. Briefly, the technique most widely used for wetting experiments is the sessile drop method. In its classical form, shown in Figure 1.15a, a small piece of solid, typically some tens or hundreds of milligrams, is placed on a substrate and then heated above its melting temperature. In another variant, a metal or alloy is melted in an unwetted and chemically inert ceramic tube and is dispensed on the substrate surface through a small hole in the tube end by applying a back pressure of inert gas or using a piston (Figure 1.15b). One advantage of this technique is that oxide films on liquid metals are disrupted during liquid extrusion from the crucible through the capillary. In the ‘transferred drop’ technique (Figure 1.15c), a sessile drop can be melted on an inert substrate, which is then raised so that the top of the drop contacts a fresh solid surface. The liquid can be transferred to the top substrate provided it is better wetted than the inert bottom substrate. In all the above techniques, values of advancing contact angles θ_a are measured and they are attained by an irreversible movement of the triple line from $\theta \sim 180^\circ$ to θ_a .

When it is possible, single crystal or amorphous substrates with a random roughness less than 100 nm are preferred in order to achieve an acceptable accuracy of θ (a few degrees). The experiments are conducted in controlled furnace conditions under either high vacuum or gases with low or known oxygen partial pressure. For contact angles greater than 90° , the sessile drop technique allows the surface tension of the liquid to be determined with an accuracy of 2–3% by fitting the shape of the droplet to the Laplace

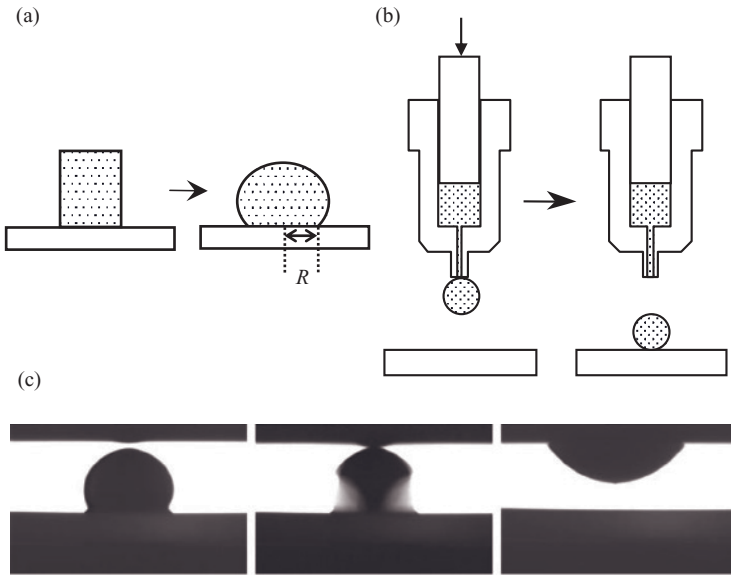


Figure 1.15 (a) Classical sessile drop method. (b) Dispensed drop method. (c) Example of the transferred drop method: Pb drop transferred from an Al_2O_3 substrate (bottom) to a Fe substrate (top) at $400^\circ C$.

equation, i.e. by expressing at each point of the drop surface the balance between the hydrostatic pressure and the capillary pressure. This is often performed by automatic imaging procedures that give also a reliable value of the contact angle. Table 1.1 gives the value of γ_v for a number of semiconductors and compounds relevant in crystal growth.

1.2.4 Selected Data for the Contact Angle for Systems of Interest for Crystal Growth

1.2.4.1 Semiconductor/Ceramic Systems

Semiconductors on Oxides. The wettability of ionocovalent oxides by molten metals and semiconductors depends critically on their reactivity at the common interface. This can be quantified by the molar fraction of oxygen in the liquid metal, X_O^l , provided by the dissolution of the oxide at the solid/liquid interface I. For SiO_2 , the dissolution reaction is:



where the parentheses mean that the species are in the liquid state. It has been found in [Eustathopoulos 1998, Eustathopoulos 1999 p. 198] that for all metal/oxide couples with $X_O^l < 10^{-5}$, the observed equilibrium contact angles are in the range $115-135^\circ$ whatever the value of X_O^l . In these systems, considered as nonreactive from the point of view of

Table 1.1 Values of surface tension for compounds of interest in crystal growth

Compound	T_m (°C)	γ_v (mJm ⁻²)	Reference
Ge	937	587–0.105 ($T - T_m$)	[Eustathopoulos 1999 p. 149]
Si ^a	1412	827–0.48 ($T - T_m$) 749–0.15 ($T - T_m$)	[Eustathopoulos 1999 p. 149]
GaSb	711	453–0.14 ($T - T_m$)	[Harter 1993]
InSb	530	434–0.08 ($T - T_m$)	[Harter 1993]
CdTe	1092	181 at T_m $d\gamma_v/dT = -0.16$	[Shetty 1990a]
Pb _{0.8} Sn _{0.2} Te	$T_l = 905$	186 at 1100°C	[Katty 1992]
GaAs	1238	230–0.17 ($T - 905$ °C) 465 at T_m $d\gamma_v/dT = -0.96$	[Kinoshita 1989] [Shetty 1990b]
Al ₂ O ₃	2047	630 at T_m	[Eustathopoulos 1999 p. 165]
SiO ₂	1720	307 at T_m	[Eustathopoulos 1999 p. 165]
CaF ₂	1418	387 at T_m	[Tanaka 1996]
BaF ₂	1290	253 at T_m	[Tanaka 1996]
LiF	848	236 at T_m	[Tanaka 1996]
NaF	992	186 at T_m	[Tanaka 1996]
CsI	621	72 at T_m	[Tanaka 1996]
NaI	660	86 at T_m	[Tanaka 1996]
LiNbO ₃	1250	192 at 1300°C	[Shi 1980]

T_l , temperature of liquidus; T_m , melting temperature.

^aTwo groups of values for both $\gamma_v(T_m)$ and $d\gamma_v/dT$ have been found.

wettability, adhesion is ensured mainly by weak, van der Waals, interactions. Typical examples are the noble metals Ag, Au, Cu and the low melting point metals Ga, In, Pb, Sn on SiO₂ or Al₂O₃ substrates. Note that for these systems, the contact angle decreases with temperature only slightly ($d\theta/dT \cong 10^{-2}/K$). The molten Ge/SiO₂ couple in high vacuum belongs to this type of system (Table 1.2).

For a given metal/oxide couple, the concentration of oxygen in the liquid metal can be increased above the value imposed by the interfacial equilibrium (1.20) by increasing the oxygen partial pressure P_{O_2} in the furnace atmosphere. Indeed, according to Henry's law (i.e. constant activity coefficient of the diluted solute), at constant temperature $X_O = K(T)P_{O_2}^{1/2}$, where $K(T)$ is a constant depending on the metal. As shown in Figure 1.16, when X_O becomes higher than $X_O^w \cong 10^{-5}$, the contact angle decreases from its 'plateau' value, and for elements such as Ag, Cu or Ni dissolving enough oxygen, contact angles as low as 80–100° have been observed on Al₂O₃. A similar 'wetting transition' was found for molten Pb on SiO₂ [Sangiorgi 1995]. As discussed in [Naidich 1981, Eustathopoulos 1999 p. 220, Eustathopoulos 2001], the improvement of wetting by dissolved oxygen results from the development of chemical interactions between the oxide surface and oxygen–metal clusters formed in the liquid.

Oxidation of the liquid metal M surface can occur when P_{O_2} in the furnace becomes equal to $P_{O_2}^{ox}$ corresponding to the reaction $(M) + n/2[O_2] \rightarrow <MO_n>$. When the MO_n oxide is solid, the skin formed around the metal prevents direct contact between the liquid and the substrate resulting in very large, obtuse, contact angles (typically 150–160°) (Figure 1.16). As long as such oxide skins exist, no sticking is observed on cooling.

Table 1.2 Contact angle of semiconductors on SiO₂

Semiconductor	T (°C)	Atmosphere	θ_f (°)	Reference
Ge	1100	High vacuum	115	[Kaiser 2001]
		Ar	155	
Si	1420	Ar ($P_{O_2} = 10^{-15}$ Pa)	85	[Yuan 2004]
Ge-4.6 at.% Si	1100	High vacuum	105	[Cröll 2002]
Ge-10.7 at.% Si			100	
GaSb	920	High vacuum	119	[Harter 1993]
GaSb	710–910	H ₂	132	[Cröll 2003]
InSb	800	High vacuum	110	[Harter 1993]
InP	1065	High vacuum + P vapour	140–150	[Shimizu 2002]
GaAs	1238	High vacuum + As vapour	115	[Shetty 1990b]
CdTe	1092	High vacuum + Cd vapour	83	[Shetty 1990a]

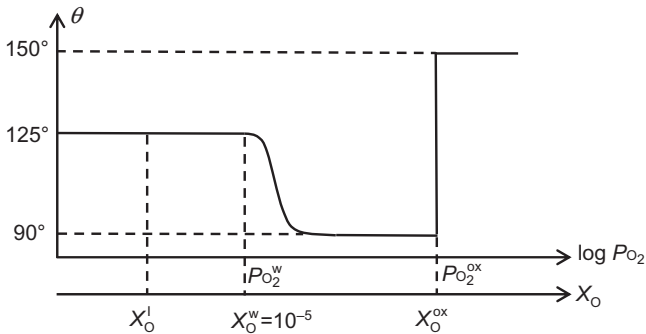


Figure 1.16 Schematic representation of the variation of θ with $\log P_{O_2}$ at constant temperature for a given metal/oxide couple. The wetting transition occurs at $P_{O_2}^w$ and X_O^w . When the metal changes, X_O^I and X_O^{ox} change too but X_O^w remains nearly constant [Eustathopoulos 2001]. However, the value of $P_{O_2}^w$ is different from metal to metal.

Classical examples are Al on Al₂O₃ [Laurent 1988] or molten silicides on SiC [Mailliart 2008] (see also Figure 6.28). Figure 1.17 shows the contact angle vs time curve for Ge on fused SiO₂ under high vacuum or Ar containing a few ppm of oxygen. In high vacuum, steady contact angles close to 115° are observed. When Ar is introduced the contact angle increases strongly towards 155°, indicating liquid oxidation. As a general rule, the effect of a skin on wetting predominates in the low temperature–high P_{O_2} ranges. As shown in Table 1.3, the $P_{O_2}^{ox}$ value in equilibrium with the oxide of the metal at a temperature close to its melting point is much lower than typical P_{O_2} values in regular neutral gas atmospheres (10^{-6} – 10^{-8} atm), resulting in skin formation. Some elements such as Al and Si can form volatile suboxides. Then, the reaction between the skin and the underlying metal (for instance the reaction $(Si) + <SiO_2>_{skin} \rightarrow 2[SiO]$) favors deoxidation which can occur at P_{O_2} values in the furnace much higher than $P_{O_2}^{ox}$ [Laurent 1988, Castello 1994]. Obtaining clean surfaces is much easier in high vacuum where the removal of SiO (or Al₂O) gaseous species far from the metal surface is much easier than in neutral gas

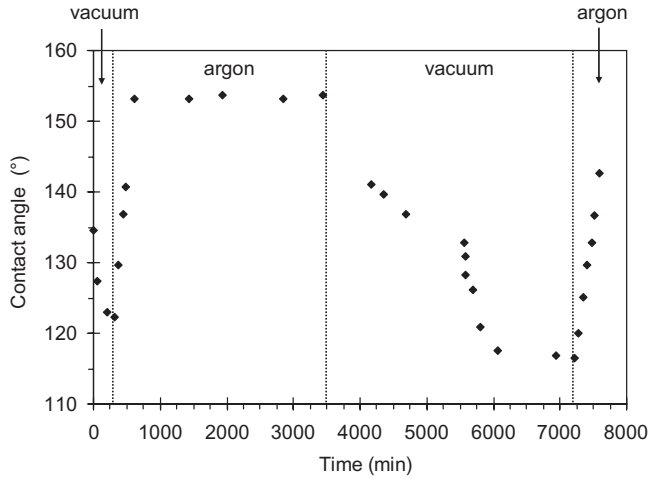


Figure 1.17 Contact angle of Ge on fused silica showing the effect of a change between dynamic vacuum and 1040mbar Ar on the wetting angle. Data from work reported in (Reprinted with permission from [Kaiser 2001], copyright (2001) Elsevier Ltd).

Table 1.3 Partial pressure of oxygen in equilibrium with the oxide of the metal at the temperature of fusion of the metal T_m^M and at 1000 °C

Metal/metal oxide	T_m^M (°C)	$P_{O_2}^{ox}$ (T_m^M) (atm)	$P_{O_2}^{ox}$ (1000 °C) (atm)
Al/Al ₂ O ₃	660	3×10^{-52}	10^{-35}
Pb/PbO	327	2×10^{-28}	8×10^{-9}
Sn/SnO ₂	232	10^{-50}	6×10^{-14}
Si/SiO ₂	1412	10^{-19}	10^{-28}
Ge/GeO ₂	950	2×10^{-15}	2×10^{-14}
Ga/Ga ₂ O ₃	30	2×10^{-113}	6×10^{-19}
In/In ₂ O ₃	157	9×10^{-63}	10^{-14}
Sb/Sb ₂ O ₃	631	10^{-18}	4×10^{-11}
Cd/CdO	321	8×10^{-43}	8×10^{-9}
Te/TeO ₂	450	2×10^{-14}	10^{-4}

atmospheres [Mailliart 2008]. In some cases, the metal oxide is liquid and can react with the oxide substrate, thus promoting wetting and adhesion. On cooling, sticking can be observed. An example is PbO formed during wetting of Pb on SiO₂ substrates [Sangiorgi 1995, Eustathopoulos 1999 p. 230].

The above considerations concern metals (M) for which the thermodynamic stability of the MO_n oxide, as reflected by its Gibbs energy of formation ΔG_0^f , is much lower than that of the oxide substrate (see also the values of $P_{O_2}^{ox}$ at 1000 °C in Table 1.3, which are calculated from ΔG_0^f). This is no longer the case for molten Si on SiO₂. Indeed, the value of X_O^1 for the Si/SiO₂ system at a temperature close to the melting point of Si is in the range 5×10^{-5} – 15×10^{-5} , i.e. above the X_O^w value defining the wetting transition

(Figure 1.16). This can explain the contact angles close to 90° observed for molten Si on SiO_2 (Table 1.2) and also on Al_2O_3 , MgO and ZrO_2 [Maeda 1986, Yuan 2004]. However, it is likely that Si (like Al) also modifies the surface chemistry and structure of the oxide substrate itself, as discussed in [Eustathopoulos 1998, Eustathopoulos 1999 p. 216].

Consider now an alloying element added in a nonreactive, nonwetting matrix M on a ionocovalent oxide. If the alloying element develops weak, van der Waals, interactions with the oxide substrate, as the matrix M, the effect of the alloying element on wetting is expected to be small and even negligible. This is consistent with the thermodynamic model of Li *et al.* [Li 1989]. This explains the small variation of contact angle for Ga–Sb on SiO_2 when varying the composition of the liquid between pure Ga ($\theta = 136^\circ$) and pure Sb ($\theta = 132^\circ$) [Cröll 2003]. A similar behaviour has been observed for In–Sb mixtures [Harter 1993].

A more significant effect can be observed by the addition of an element developing, by adsorption, chemical interaction with the oxide substrate, such as Si in Ge (see Table 1.2). This effect is important for the first few per cent of the addition, further addition having much less effect.

Note that in Table 1.2 differences of about 10° in θ values measured in the same system by different teams are not surprising, taking into account differences in P_{O_2} , substrate roughness, experimental procedure and method for obtaining θ values from drop images. Among the results presented in Table 1.2, the case of CdTe is rather puzzling. In the absence of oxygen in the quartz ampoule containing the sessile drop, Cd and Te cannot react with SiO_2 as their $P_{\text{O}_2}^{\text{ox}}$ values are much higher than the value for Si (Table 1.3). Therefore, according to the previous developments, in the absence of oxygen the equilibrium contact angle would be much higher than 90° . Oxygen present in the ampoule can dissolve in CdTe, thus reducing the contact angle. However, to our knowledge, no data exist showing a significant solubility of O in CdTe. Moreover, an explanation based on dissolved oxygen can hardly explain the comparatively marked decrease of θ (15°) observed in [Shetty 1990a] for a limited increase of temperature (60 K). Indeed, for a given value of P_{O_2} , the molar fraction of oxygen dissolved in a liquid metal or alloy decreases when the temperature increases. Another possibility for the oxygen in the ampoule is to form a liquid oxide such as TeO_2 likely to react with SiO_2 , thus improving wetting and adhesion. Such an effect was observed by Yasuda *et al.* [Yasuda 1990], cited in [Cobb 1999], who found that TeO_2 in the starting charge of CdTe ingots reacted with the quartz ampoule, causing adhesion. The same situation was likely to occur with ZnO_2 and SeO_2 when solidifying $\text{Hg}_{1-x}\text{Zn}_x\text{Se}$ alloys in quartz ampoules [Cobb 1999].

Semiconductors on Carbon-Based Substrates. The wettability of carbon-based substrates by liquid metals and semiconductors depends on the liquid/carbon reactivity. Three cases can be distinguished [Eustathopoulos 1999 p. 317]: (i) very low solubility of carbon in the liquid (typically <100 ppm), (ii) high solubility, and (iii) formation of metal carbide at the interface. Only (i) and (iii) are considered here.

Nonreactive pure metals (such as In, Ga, Sb, Pb, Sn, Cu, Ag) do not wet carbon substrates ($\theta \gg 90^\circ$) whatever the type of carbon: vitreous carbon (C_v), graphite (C_g), or diamond (C_d). As for ionocovalent oxides, adhesion in these systems is ensured by weak, van der Waals, interactions. As a result, for a given system, θ changes only slightly with temperature (typically by $1\text{--}2^\circ$ for every 100 K). Moreover, the addition of a nonreactive

element in a nonreactive matrix produces a change in θ of only 5–15° [Eustathopoulos 1999 p. 324]. All the semiconductors listed in Table 1.4, except Si and Ge–Si alloys, belong to this type of nonreactive, nonwetting, system. Note that for a given element, the contact angles on smooth surfaces of C_v are higher by 15–20° than those on basal faces of monocrystalline graphite because of the lower atomic density of vitreous carbon [Dezellus 1999]. For polycrystalline graphite, very large contact angles are often observed (150–160°). However, these values are due to its high roughness (it is difficult to prepare polycrystalline graphite surfaces with an average roughness less than 100 nm) and also to porosity (in nonwetting systems pores act as a second phase with $\theta_\beta = 180^\circ$ in Cassie's Equation (1.15)).

Reactive wetting will be considered only for pure Si and Ge–Si alloys. Si reacts with C forming at the interface a continuous layer of SiC, a few microns in thickness. Figure 1.18 shows the change with the logarithm of time of the contact angle of Si on a smooth surface of C_v . When time tends towards zero, the contact angle tends towards 150°, which is the contact angle of Si on unreacted carbon (see also Figure 1.14). The final contact angle of 36° is very close to the contact angle of Si on SiC. As a general rule, reported values for polycrystalline graphite are in the range 5–15°, i.e. lower than those on C_v .

Table 1.4 *Contact angle of semiconductors on carbon-based substrates*

Semiconductor	Substrate	Temperature (°C)	Atmosphere	θ_f (°)	Reference
Ge	C_v	1100	High vacuum	157	[Kaiser 2001]
				166	
Ge	C_g	1000	High vacuum	139	[Naidich 1968]
Ge	C_d CVD	1100	High vacuum	146	[Kaiser 2001]
Ge	C_d	1000	High vacuum	136	[Naidich 1981]
GaSb	C_v	920	High vacuum	128	[Harter 1993]
				no sticking	
InSb	C_v	800	High vacuum	124	[Harter 1993]
CdTe	C_v	1100	High vacuum + Cd vapour	116	[Katty 1992]
				no sticking	
$Cd_{0.96}Zn_{0.04}Te$	C_v	1100	High vacuum + Cd vapour	126	[Katty 1992]
GaAs	C-coated SiO_2	1238	High vacuum + As vapour	120	[Shetty 1990b]
Ga–In–As	C_g	632	H_2	148	[König 1984]
InP	C_g	632	H_2	144	[König 1984]
Si	C_g	1450	High vacuum	15	[Naidich 1981]
Si	C_v	1430	High vacuum	36	[Dezellus 2005]
Ge-4.6 at.% Si	C_v -coated C_g	1100	High vacuum	103	[Cröll 2002]
Ge-20 at.% Si	C_v	1231	High vacuum	55	[Dezellus 2000]

C_d , diamond; C_g , graphite; C_v , vitreous carbon.

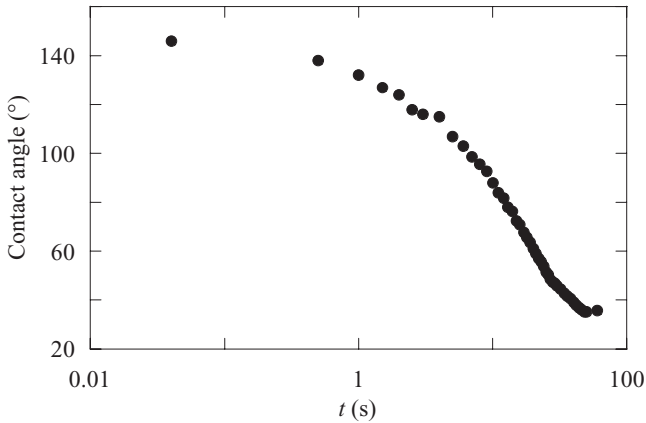


Figure 1.18 Variation of contact angle with time for Si on C_v at 1430 °C (Reprinted with kind permission from [Dezellus 2005], copyright (2005) Springer).

Indeed, for wetting systems ($\theta \ll 90^\circ$), roughness favours wetting, as indicated by the Wenzel Equation (1.11). Moreover, Si can infiltrate the open porosity of graphite ahead of the drop triple line. In this case, filled pores act as a second phase with $\theta_\beta = 0^\circ$ in Cassie's Equation (1.15). Finally, infiltration decreases the drop volume leading to a receding contact angle instead of an advancing one.

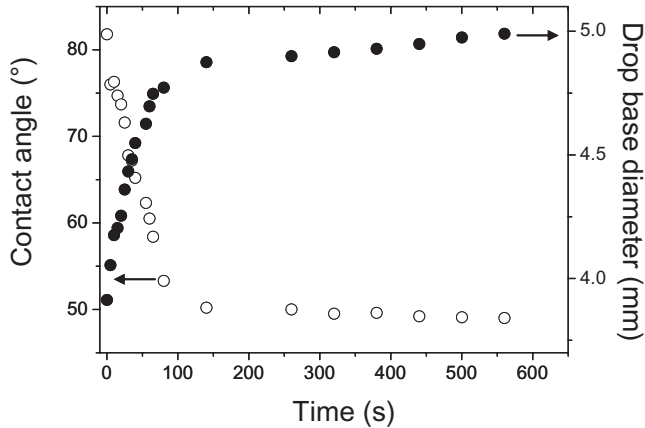
Ge does not wet C_v (Table 1.4) but the addition of Si promotes wetting by forming a wettable SiC layer at the solid/liquid interface. For the Ge-20 at.% Si alloy, a steady contact angle of 55° is reached in 1300 s at 1231 °C (Figure 1.13). However, for the Ge-4.6 at.% Si alloy, the driving force of the interfacial reaction at 1100 °C is much lower, resulting in very slow spreading kinetics : the contact angle decreases from an initial value of 150° to a value close to 110° within a day [Cröll 2002]. However, it is possible that the value of 103° reported in Table 1.4 is not a steady angle.

Semiconductors on Nitrides. Al and Si nitrides are nonoxide but oxidizable ceramics. Indeed, even a very short time (1–2 min) in contact with air at room temperature leads to the formation of nanometre-thick oxide or oxi-nitride layers. These layers are stable even in high vacuum environments. For instance, in the case of Si_3N_4 , several hours at 1140 °C in an ultrahigh vacuum are needed to remove oxygen. Therefore, at temperatures lower than 1100 °C, in neutral gas or standard vacuum environments employed in crystal growth, wettability of Al and Si nitrides is imposed by oxygen-rich surface layers. As a consequence, the contact angle of nonreactive metals such as In, Sn, Ga, Pb, Sb, Ag on these nitrides is in the range 110 – 140° , as on ionocovalent oxides. Among semiconductors, Ge and GaSb form also nonwetting contact angles (Table 1.5).

The initial contact angle of Si on Si_3N_4 is close to 80° , as on SiO_2 substrates (see Table 1.2). However, the contact angle decreases rapidly with time and tends towards 49° , which is close to the intrinsic contact angle of Si on Si_3N_4 (Figure 1.19). The spreading kinetics in this system are controlled by substrate deoxidation occurring by reaction between liquid Si and the oxide layer at the triple line with formation of volatile SiO [Drevet 2009]. For Ge–Si alloys on Si_3N_4 , Cröll *et al.* [Cröll 2002] also observed a

Table 1.5 Contact angle of semiconductors on Al and Si nitrides

Semiconductor	Nitride	Temperature (°C)	Atmosphere	θ_F (°)	Reference
Ge	AlN sintered	950	High vacuum	122	[Naidich 1995]
Ge	AlN sintered	1100	Vacuum/Ar	153	[Kaiser 2001]
Si	AlN CVD	1430	H ₂ $P_{O_2} = 8.7 \times 10^{-16}$ Pa	45	[Barsoum 1981]
Si	AlN sintered	1412	High vacuum	48	[Naidich 1995]
Ge-6.3 at.% Si	AlN sintered	1100	Vacuum/Ar	124	[Cröll 2002]
GaSb	AlN pyrolytic	820	High vacuum	103	[Harter 1993]
Ge	Si ₃ N ₄ sintered	1100	Vacuum/Ar	136	[Kaiser 2001]
Si	Si ₃ N ₄ CVD	1430	H ₂ $P_{O_2} = 10^{-15}$ Pa	48–52	[Barsoum 1981]
Si	Si ₃ N ₄ sintered	1430	Ar	49	[Drevet 2009]
Ge-6.2 at.% Si	Si ₃ N ₄ sintered	1100	Vacuum/Ar	96	[Cröll 2002]

**Figure 1.19** Contact angle and drop base diameter as a function of time for a Si drop on sintered Si₃N₄ at 1430 °C (Reprinted with permission from [Drevet 2009], copyright (2009) Elsevier Ltd).

decrease of the contact angle from 150° towards 96° (Table 1.5) probably occurring by a similar process. However, due to the low thermodynamic activity of Si and the comparatively low temperature, the spreading time is very high (several hundreds of minutes). Similar phenomena occur with Ge–Si alloys on AlN [Cröll 2002].

BN is also an oxidizable ceramic but boron oxide, B₂O₃, which is liquid above 450 °C, is a volatile oxide such that clean BN surfaces are expected to form at higher temperatures, especially in high vacuum. Nonreactive metals such as Ga, Sn, Ag, Au do not wet BN at temperatures of 1000–1100 °C, the contact angle being in the range 130–150° [Naidich 1981]. No significant differences in wettability have been found between hexagonal and cubic BN [Naidich 1981]. Even higher contact angle values, close to 160–170°, have

Table 1.6 Contact angle of semiconductors on BN

Semiconductor	Substrate	Temperature (°C)	Atmosphere	θ_f (°)	Reference
Ge	BN pyrolytic	1100	Ar-2% H ₂	173	[Kaiser 2001]
Ge	BN cubic	1100	High vacuum	138	[Naidich 1981]
	BN hexagonal	1100	High vacuum	139	
Si	BN pyrolytic	1430	Ar	117	[Drevet 2009]
Si	BN cubic	1500	High vacuum	95	[Naidich 1981]
	BN hexagonal	1500	High vacuum	110	
Si	BN pyrolytic	1500	High vacuum	105	[Champion 1973]
Ge-7.1 at.% Si	BN pyrolytic	1100	vacuum/Ar	168	[Cröll 2002]
GaSb	BN pyrolytic	920	High vacuum	129	[Harter 1993]
InSb	BN pyrolytic	800	High vacuum	134	[Harter 1993]
InP	BN pyrolytic	1065	High vacuum + P vapour	140–150	[Shimizu 2002]
CdTe	BN pyrolytic	1092	High vacuum + Cd vapour	132	[Shetty 1990a]
GaAs	BN pyrolytic	1238	High vacuum + As vapour	155	[Shetty 1990b]

been reported in the literature, mainly due to roughness effect. The wetting of Ge, GaSb, InSb, InP, CdTe and GaAs on BN is the same as that of nonreactive metals (Table 1.6).

Molten Si does not wet the different forms of BN, but the contact angles are significantly lower than for nonreactive semiconductors (Table 1.6). Moreover, despite this nonwetting behaviour, sticking has been observed in the Si/BN system. These phenomena were explained in [Drevet 2009] by the reaction between Si and BN leading to the formation of Si₃N₄ at the interface ($3(\text{Si}) + 4\langle\text{BN}\rangle \rightarrow \langle\text{Si}_3\text{N}_4\rangle + 4(\text{B})$). However, the reactivity in the Si/BN system is so weak that chemical equilibrium (i.e. saturation of liquid Si with B) is established well before the equilibrium contact angle on the reaction product (i.e. Si₃N₄) is attained.

Ge–Si alloys with a low Si content are nonreactive with BN, such that the presence of Si in the melt does not affect the contact angle of Ge on BN (Table 1.6).

1.2.4.2 Oxide/Metal and Oxide/Carbon Systems

Although several articles have been devoted to crystal growth of oxides in contact with refractory metals (Pt, Ir, Mo, W), only a few give measurements of contact angles. In contrast, a significant number of wettability studies has been performed with oxide slags and glasses. One can reasonably expect that the conclusions drawn from these studies can also be applied to oxide/metal systems that are relevant in crystal growth.

In nonreactive molten oxide/solid metal systems, as in nonreactive liquid metal/ionocovalent oxide ones, adhesion results from weak, van der Waals, interactions leading to values of work of adhesion W_a of a few hundreds of mJ m⁻². However, while liquid metals do not wet ionocovalent oxides, molten oxides wet metallic substrates ($\theta < 90^\circ$, Table 1.7). The reason for this difference is the very different values of surface tension between

Table 1.7 Contact angles of soda-lime glass (13.4 wt% Na₂O, 10.9 wt% CaO, 1.6 wt% Al₂O₃, 1.4 wt% MgO, SiO₂ bal.) on different substrates at temperatures close to 1000 °C

Substrate	Atmosphere	θ_f (°)
X25V steel	He	65 ± 3
Pt	He	75 ± 3
Au	N ₂	60 ± 3

Reprinted with permission from [Pech 2004], copyright (2004) Elsevier Ltd.

molten metals and molten oxides. For instance, γ_{lv} of molten SiO₂ at 1720 °C is 300 mJ m⁻² while at the same temperature γ_{lv} of molten Ni is six times higher. Thus, for liquid metals, γ_{lv} is higher than W_a , resulting in nonwetting according to the Young–Dupré Equation (1.9). Conversely, for molten oxides, $\gamma_{lv} < W_a$, leading to $\theta < 90^\circ$. The physical reason for which the surface tension of molten oxides is low, comparatively to their cohesion energy, is discussed in [Eustathopoulos 1999 p. 164].

A feature of van der Waals interactions is lack of selectivity. For instance, the contact angle of soda-lime glass on a stainless steel rich in Cr, a metal with a high affinity for oxygen, is close to the contact angle observed for the same glass on the noble metals Pt and Au (Table 1.7). However, the mechanical behaviour of the solid oxide/metal substrate system on cooling is very different. Indeed, soda-lime glass adheres on Pt but not on steel substrates. The adhesion energy in these systems is very close, as well as the elastic modulus of contacting phases. However, $\Delta\alpha$ is very different, close to zero in the case of Pt ($< 0.2 \mu\text{m m}^{-1} \text{K}^{-1}$) and very high in the case of stainless steel ($\cong 10 \mu\text{m m}^{-1} \text{K}^{-1}$) [Pech 2004].

For a given mixture of oxides on Pt substrate, when the wetting experiments are performed in air, the contact angles are found systematically lower by 10–30° than those measured in a neutral gas atmosphere (50–80°). This effect was attributed to the formation on the metal surface of a layer of chemisorbed oxygen [Eustathopoulos 1999 p. 345]. Indeed, with metal atoms adsorbed oxygen forms a partially ionocovalent bond that increases the adhesion energy of the solid metal with the molten oxide. Such an adsorption effect on adhesion was evidenced by Ownby *et al.* [Ownby 1995] who found a significant decrease in contact angle, occurring above a given value of P_{O_2} in the gas, in a range where no oxidation of the W substrate takes place (Figure 1.20). Oxidation of the solid metal can enhance wetting, but this usually leads to dissolution of the oxide layer in the molten oxide, which may locally increase the viscosity and thus reduce the spreading rate. Duffar *et al.* [Duffar 2009] report melting studies of BGO in Ir where an increase of P_{O_2} above 0.1 mbar promotes Ir oxidation, leading to a decrease in the contact angle (from 70° to 0°) and sticking.

Nonreactive oxides do not wet carbon. Indeed, contact angles as high as 130–140° have been observed for various oxides on vitreous carbon or graphite [Ellefson 1938, Towers 1954, Pech 2005]. Reactivity promotes wetting. For instance, molten B₂O₃ reacts with C_s, leading to contact angles as low as 30–40° [Wery 2008]. In this system, it seems that wettability is improved by the formation at the interface of B₄C, a compound wettable by the oxide.

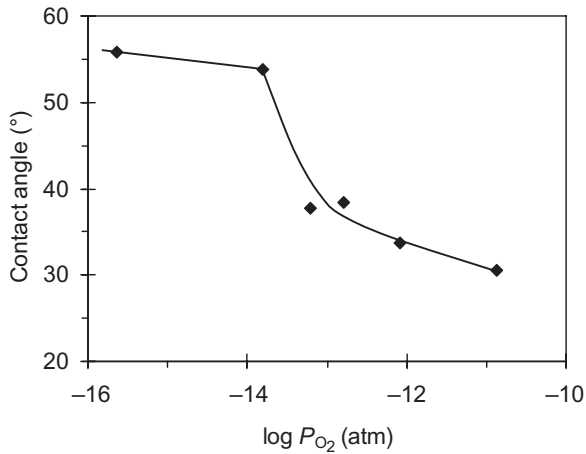


Figure 1.20 Contact angle values as a function of $\log P_{O_2}$ for $SiO_2-20Al_2O_3-10CaO-10MgO$ (wt.%) on W at $1400^\circ C$. Data from work reported in [Ownby 1995].

Table 1.8 Contact angles of molten salts measured on graphite immediately after melting

Salt	Temperature ($^\circ C$)	θ ($^\circ$)	γ_v ($mJ m^{-2}$)
NaCl	810	113	114
KCl	780	78	99
RbCl	740	58	95
CsCl	645	31	92

Reprinted with permission from [Baumli 2008], copyright (2008) Elsevier Ltd.

1.2.4.3 Halide/Ceramic Systems

Molten halides have low γ_v values (in the range $50-250 mJ m^{-2}$) comparatively to other molten substances, such as metals and even oxides. The thermodynamic adhesion of molten halides on carbon is weak, as ensured solely by physical interactions [Baumli 2008]. From modelling molten halide/graphite interactions, it was shown that for the same type of halides (for instance chlorides), when the surface tension decreases, the work of adhesion increases rapidly. According to the Young–Dupré Equation (1.9), this implies a strong decrease in the contact angle (Table 1.8). Similarly, while large nonwetting contact angles ($130-150^\circ$) were found for LiF ($\gamma_v = 236 mJ m^{-2}$) and NaF ($\gamma_v = 186 mJ m^{-2}$), the contact angle of KF ($\gamma_v = 144 mJ m^{-2}$) was found to be 80° and that of CsF ($\gamma_v = 106 mJ m^{-2}$) was 41° [Morel 1970].

Like molten oxides, molten halides seem to wet metallic substrates. An example is molten LiF on various metals. In all cases, $\theta < 90^\circ$ but significant differences were found, for instance between Ta ($\theta = 4^\circ$) and Ni ($\theta = 62^\circ$) or Pt ($\theta = 68^\circ$) [Jaworske 1989].

1.3 Growth Angles

This section begins with a review of the basic theory underlying the concept of the growth angle, important in meniscus-defined melt growth systems, in the case of both isotropic and anisotropic interfacial energies. Next, various methods for measuring growth angles are discussed and data resulting from such measurements are presented. This is followed by a brief report on the application of the growth angle condition in simulations of crystal growth, as well as by the description and application, in a number of systems, of a method for determining and rigorously verifying the growth angle (assumed constant). The constant angle assumption, as well as the impact of heat transport and interface-attachment kinetics on the verification procedure (effectively involving a small-scale crystal growth simulation), are also discussed.

1.3.1 Theory

The concept of the growth angle stems from the early work on equilibrium at a junction between several phases. Consider Figure 1.21, which depicts the case relevant to this section: three phases (solid, liquid, and vapour) in equilibrium with one another along their line of mutual contact, the TPL, which is normal to the plane of the figure. Herring used an energy minimization approach [Herring 1951] to derive a vector condition, which in our case is given by the following sum of coplanar vectors:

$$\gamma_{sl}\mathbf{e}_{sl} + \gamma_{sv}\mathbf{e}_{sv} + \gamma_{lv}\mathbf{e}_{lv} + \gamma'_{sl}\mathbf{e}_{sl}^{\dagger} + \gamma'_{sv}\mathbf{e}_{sv}^{\dagger} + \gamma'_{lv}\mathbf{e}_{lv}^{\dagger} = \mathbf{0}. \quad (1.21)$$

The first three terms of Equation (1.21), containing the three interfacial energies together with the unit vectors tangent to the three interfaces, are related to the system's tendency

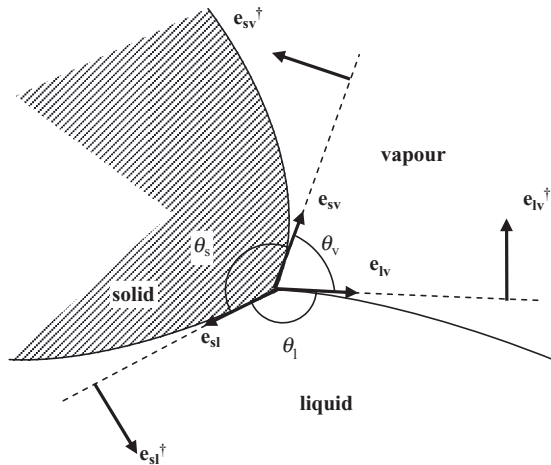


Figure 1.21 The triple phase line (TPL) with associated vectors and angles between interfaces.

to minimize the area of the more energetically expensive interfaces via contraction. The last three terms involve the derivative of the three energies with respect to the angular coordinate (measured in a counterclockwise sense around the TPL), together with unit vectors normal to the interfaces. These so called ‘torque terms’ reflect the system’s resistance to the change of interfacial orientation in a manner leading to the increase of energy due to its angular dependence.

1.3.1.1 Isotropic Interfacial Energies

The liquid/vapour interfacial energy is isotropic (i.e. $\gamma'_{lv} = 0$) and therefore the last term on the left-hand side of Equation (1.21) can be dropped. Now consider the case where both the solid/fluid interfacial energies do not depend on orientation ($\gamma'_{sl} = \gamma'_{sv} = 0$), yielding the isotropic form of the Herring equation. The resultant vector equation is often presented as two independent scalar equations relating interfacial energies and angles between interfaces. One form, originally proposed by Smith [Smith 1948], is given by Equation (1.10). A different representation of the same conditions is given [Voronkov 1963, Bardsley 1974] by:

$$\cos \alpha = \frac{\gamma_{sv}^2 + \gamma_{lv}^2 - \gamma_{sl}^2}{2\gamma_{sv}\gamma_{lv}}, \quad \cos \beta = \frac{\gamma_{sv}^2 + \gamma_{sl}^2 - \gamma_{lv}^2}{2\gamma_{sv}\gamma_{sl}} \quad (1.22)$$

where the first angle, defined as $\alpha = \pi - \theta_v$, is the growth angle and the second angle is defined as $\beta = \pi - \theta_s$.

The two isotropic relations for α and β given in Equation (1.22), together with the trivial equality $\theta_v + \theta_l + \theta_s = 2\pi$, provide the *intrinsic* values of the three angles between the interfaces as a function of the three interfacial energies. However, when viewing the TPL from a macroscopic viewpoint, it is not obvious that these angles will be preserved. This depends on the distance from the TPL over which the slope of the interface (i.e. its orientation) can be assumed constant. In the case of the liquid/vapour interface the relevant distance (see e.g. [de Gennes 2004]) is of the order of the capillary length ($l_c = \sqrt{\gamma_{lv}/\rho_l g}$), where ρ_l and g are, respectively, the liquid phase density and the acceleration due to gravity. Since, in typical crystal growth systems, the resultant value of l_c is of the order of millimetres, it is reasonable to assume that the slope of this interface at the TPL can be observed from a macroscopic viewpoint.

The solid/liquid interface typically conforms to the melting point isotherm (whose shape and position is governed by heat transport) except near the TPL where it must curve away from the isotherm to satisfy Equation (1.22) at the TPL. The curvature is related to the local undercooling at the TPL via the Gibbs–Thomson equation (see e.g. [Flemings 1974]), where the distance from the TPL over which the deviation from the isotherm occurs typically ranges from a few microns to several hundredths of a micron (see e.g. [Voronkov 1978, Voronkov 1981]).

Most interesting is the possibility of local (close to the TPL) variations in the slope of the solid/vapour interface. Following Voronkov [Voronkov 1978], consider the curvature of the solid/vapour interface, whose value at the TPL can be associated with the undercooling at this point. The surface gradient of this curvature can be related to a process of surface transport and deposition of mass from the liquid phase at the TPL to a point far

from the TPL where the curvature is negligible and the solid/vapour interface can be considered ‘finally formed’. The resultant deviation between the intrinsic growth angle α and the (effective) growth angle α^* , measured with respect to the slope at this point, is depicted in Figure 1.22. Quantification of this deviation [Voronkov 1978], assuming steady-state solidification and an isotropic solid/vapour interfacial energy near the TPL, yields:

$$\alpha^* = \alpha - \chi_0 = \alpha - Cv^{-1/3} \Delta T. \tag{1.23}$$

The angle χ_0 appearing in this equation is marked in Figure 1.22, ΔT (given by $\Delta T = T_m - T$) is the undercooling at the TPL, T is the temperature at the TPL, T_m is the material’s melting point, v is the crystal growth rate in the direction tangent to the solid/vapour interface far from the TPL, and C is a coefficient given by:

$$C = \frac{\Delta H}{T_m} \left[\frac{\lambda}{(\gamma_{sv} \hat{N})^2} \right]^{1/3}. \tag{1.24}$$

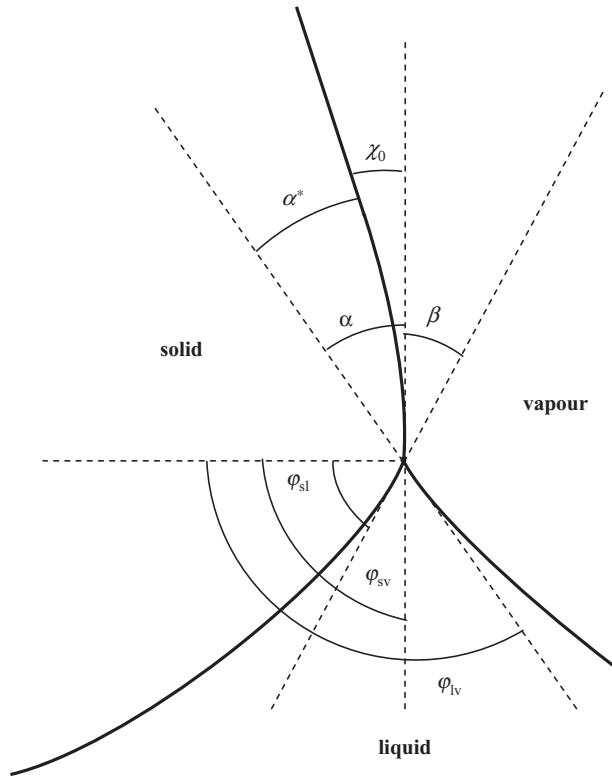


Figure 1.22 Important angles at the TPL.

In Equation (1.24) ΔH is the volumetric latent heat of fusion of the crystal, \hat{N} is the atomic density of the crystal and λ is the surface mass transport coefficient. Assuming a surface diffusion mechanism of mass transport yields:

$$\lambda = \frac{D_s \hat{N}_s}{k_B T}, \quad (1.25)$$

where D_s , \hat{N}_s and k_B are, respectively, the surface diffusion coefficient, the atomic surface density of the crystal and the Boltzmann constant. In the next section, concerned with anisotropic interfacial energies, an example related to the growth of silicon is used to obtain a feel for values of χ_0 in typical semiconductor growth systems (with and without isotropic interfacial energies).

1.3.1.2 Anisotropic Interfacial Energies

Consider the more general case of anisotropic fluid/crystal interfacial energies. Following Bardsley *et al.* [Bardsley 1974], a scalar multiplication of the relevant form of the Herring equation (Equation (1.21) with $\gamma'_{lv} = 0$) with the unit vectors \mathbf{e}_{sv} and \mathbf{e}_{lv} yields two relations uniquely defining α and β :

$$\begin{aligned} \gamma_{sv} - \gamma_{lv} \cos \alpha - \gamma_{sl} \cos \beta - (\gamma'_{sl}|_{\varphi_{sl}}) \sin \beta &= 0 \\ \gamma_{lv} - \gamma_{sv} \cos \alpha + \gamma_{sl} \cos(\alpha + \beta) - (\gamma'_{sv}|_{\pi + \varphi_{sv}}) \sin \alpha + (\gamma'_{sl}|_{\varphi_{sl}}) \sin(\alpha + \beta) &= 0, \end{aligned} \quad (1.26)$$

where, following Figure 1.22, the angular derivatives of the interfacial energies are taken with respect to φ , which is measured counterclockwise from the horizontal.

Using Equation (1.26) allows for the determination of α and β provided all three interfacial energies are known where, in the case of the two solid/fluid interfaces, the angular dependence of these energies is also required. Alternatively, Equation (1.26) can be used, together with experimental and calculated data for average values of the interfacial energies and angles α and β , to obtain rough estimates for the contributions of the torque terms in these two relations (see e.g. [Bardsley 1974] for such an estimate in the case of the growth angle of Ge).

The relations in Equation (1.26) specify the intrinsic angles α and β as long as the two solid/fluid interfacial energies (γ_{sl} , γ_{sv}) are continuously differentiable at the relevant angular orientation of these interfaces (φ_{sl} and $\pi + \varphi_{sv}$; see Figure 1.22). As in the case of isotropic energies, there is the possibility that macroscopically observed angles will differ from their intrinsic values. The above discussion of this issue is still relevant though certain restrictions apply (related to anisotropy of the solid/vapour interface). Of special interest is the case where a facet exists on the solid/liquid interface near the TPL. The resultant typically nonnegligible value of ΔT at the TPL associated with such a facet is often associated with an appreciable difference between α and α^* according to Equation (1.23).

To obtain a feeling for values of χ_0 in typical semiconductor growth systems, consider the case of a dislocation-free silicon crystal grown by the Czochralski method in the $\langle 111 \rangle$ direction, where a ring-shaped facet appears on the solid/liquid interface near the TPL

(see e.g. [Voronkov 1975]). The undercooling at the TPL is $\Delta T = 3.7^\circ\text{C}$ and the experimentally based estimated value of χ_0 is of the order of 20° (see [Voronkov 1978] and references therein). In the event that a facet is not present near the TPL, the undercooling is two orders of magnitude smaller (see e.g. [Voronkov 1974]). Assuming a similar growth velocity and treating C (in Equation (1.23)) as a constant suggests that the value of χ_0 is negligible and the effective observable growth angle is, in this case, equal to α . This important conclusion implies that a typical semiconductor crystal growth system, whose growth front is facet-free in the vicinity of the TPL and whose solid/vapour interfacial energy can be assumed isotropic, is likely to exhibit a macroscopically observable growth angle which is the thermodynamic constant α given by Equation (1.26); in the event that both solid/fluid interfacial energies are isotropic the growth angle will be given by Equation (1.22).

Systems exhibiting facets in contact with the TPL cannot be analysed using Equation (1.26) since the interfacial energy associated with faceted surfaces is not continuously differentiable with respect to orientation at the relevant value of φ . In this case it is useful to consider graphical solutions to Equation (1.21). Two similar approaches have been proposed, the first in [Hoffman 1972] and the second in [Voronkov 1980; Voronkov 1981]. In the following the approach described in [Voronkov 1981] is presented.

First, two two-dimensional polar (Wulff) plots are constructed, one for γ_{sl} and the other for γ_{sv} . For each surface orientation \mathbf{n}_{ij} a segment of length $\gamma_{ij}(\mathbf{n}_{ij})$ is drawn from the origin in the direction of \mathbf{n}_{ij} ($ij = \text{sl}$ or sv); note that (see Figure 1.21) $\mathbf{n}_{\text{sl}} = \mathbf{e}_{\text{sl}}^\dagger$ and $\mathbf{n}_{\text{sv}} = -\mathbf{e}_{\text{sv}}^\dagger$. Next, a straight line perpendicular to this segment is drawn at its end. The family of these straight lines defines an inner closed form whose boundary is denoted by Γ_{ij} ($ij = \text{sl}$ or sv). Examples of the two resultant forms are depicted in Figure 1.23. Note that in this specific case a system has been chosen which exhibits one singular orientation (identical for both solid/fluid interfaces), associated with a cusp in the two Wulff plots.

Consider a vector \mathbf{g}_{ij} drawn from the origin to some point on Γ_{ij} ($ij = \text{sl}$ or sv). It can be shown (see e.g. [Voronkov 1980]) that:

$$\mathbf{g}_{ij} = \gamma_{ij}\mathbf{n}_{ij} + \gamma'_{ij}\mathbf{n}_{ij}^\dagger \quad (ij = \text{sl}, \text{sv}, \text{lv}), \quad (1.27)$$

where (see Figure 1.21) $\mathbf{n}_{\text{sl}}^\dagger = -\mathbf{e}_{\text{sl}}$, $\mathbf{n}_{\text{sv}}^\dagger = \mathbf{e}_{\text{sv}}$, $\mathbf{n}_{\text{lv}}^\dagger = -\mathbf{e}_{\text{lv}}$ and $\mathbf{n}_{\text{lv}} = \mathbf{e}_{\text{lv}}^\dagger$; notice that the definition of the vector \mathbf{g}_{ij} is given for all three interfaces ($ij = \text{sl}, \text{sv}, \text{lv}$). Let us now rotate the Herring equation, Equation (1.21), by $\pi/2$ in the counterclockwise direction where this can be achieved by performing a scalar multiplication of this equation (with $\gamma'_{\text{lv}} = 0$) from the left by an appropriately chosen dyadic. Inserting into the resultant vector equation, for all three interfaces, the relation given by Equation (1.27) yields:

$$\mathbf{g}_{\text{sl}} - \mathbf{g}_{\text{sv}} + \mathbf{g}_{\text{lv}} = \mathbf{0}. \quad (1.28)$$

Following Voronkov [Voronkov 1981], for a given solid/vapour interfacial orientation at the TPL (\mathbf{n}_{sv}), assuming the three interfacial energies are known (as a function of orientation), it is possible to use Equation (1.28) together with the two Γ plots in Figure 1.23 to obtain the other two interfacial orientations \mathbf{n}_{sl} and \mathbf{n}_{lv} . First, the point on Γ_{sv} whose ori-

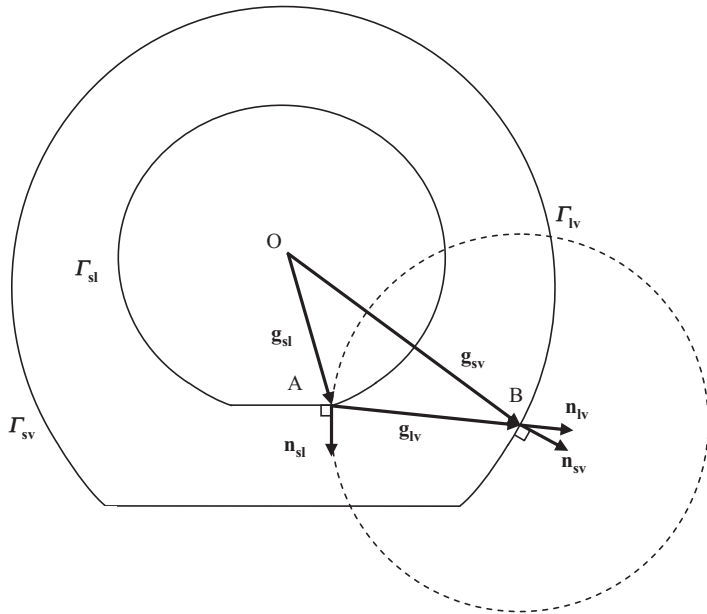


Figure 1.23 Geometric representation associated with the Herring equation (Equation (1.21)).

entation is \mathbf{n}_{sv} (point B) is located, where OB is the corresponding \mathbf{g}_{sv} vector. Drawing from point B a circle whose radius is equal to g_{lv} (i.e. γ_{lv}), determines point A which is the intersection of this circle with Γ_{sl} . The obtained vectors OA and AB are, respectively, equal to \mathbf{g}_{sl} and \mathbf{g}_{lv} , where the resultant closed triangle constructed by the three vectors is a graphical representation of Equation (1.28) and now all three orientations (\mathbf{n}_{sl} , \mathbf{n}_{lv} , \mathbf{n}_{sv} or φ_{sl} , φ_{lv} , φ_{sv}) are known. This result immediately yields the two intrinsic angles $\alpha = \varphi_{lv} - \varphi_{sv}$ and $\beta = \varphi_{sv} - \varphi_{sl}$. Finally, note (in Figure 1.23) the additional intersection point of the circle with Γ_{sl} . Although this point admits an additional solution to Equation (1.28), it must be rejected because the resultant interfacial orientations are not consistent with the physical picture involving, when moving in a counterclockwise direction around the TPL, a crossover from solid to liquid to vapour and back again to solid (see Figures 1.21 and 1.22).

The specific triangle of vectors in Figure 1.23 reflects the orientations of the three interfaces at a given point in time where, in the case of steady-state growth, all orientations are time-independent and the growth angle α is a constant. It is possible to think of several positions for point B, each with different corresponding orientations of the three interfaces. Plotting the resultant solid/fluid interfacial orientation angles (φ_{sl} , φ_{sv}) as a function of the angular orientation of the liquid/vapour interface (φ_{lv}) yields a useful figure of the type proposed in [Voronkov 1980]. A schematic of such a plot, qualitatively consistent with Figure 1.23 is shown in Figure 1.24; the point corresponding to the specific OAB triangle shown in Figure 1.23 is marked in Figure 1.24. Note that Figures 1.23 and 1.24 are not completely consistent with Figures 1.21 and 1.22, which do not show a facet

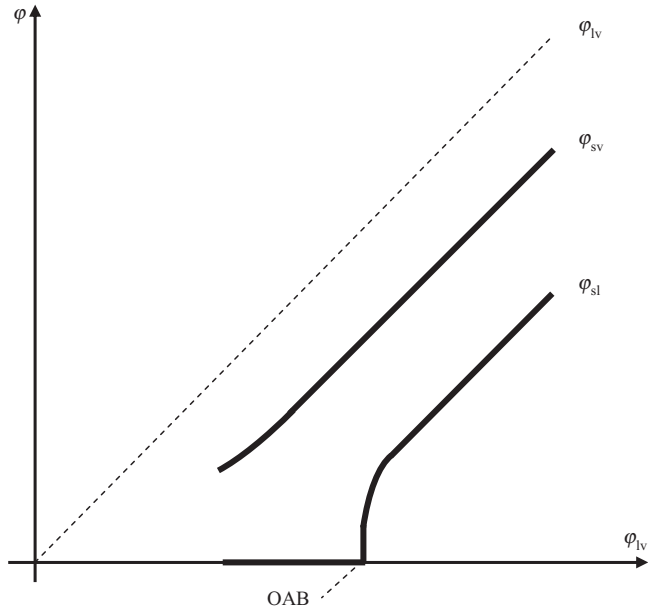


Figure 1.24 Relative orientations of the three interfaces. The dashed line corresponds to the 45° line (ϕ_{lv} vs ϕ_{lv}) and the point corresponding to the OAB construction in Figure 1.23 is marked.

on the solid/vapour interface at the TPL. In addition, it is important to note that the curves in Figure 1.24 are associated with a limited range of interfacial orientations and do not cover all possibilities that can be derived from Figure 1.23 (e.g. facets on the solid/vapour interface).

It is possible to relate γ'_{sl} to the relevant step energy (normalized by the step height) of a vicinal surface associated with the singular direction characterized by the specific \mathbf{n}_{sl} vector shown in Figure 1.23. As described in [Voronkov 1981], and consistent with Figure 1.23, γ'_{sl} on the singular surface jumps from the negative value associated with a negative vicinal surface slope to a positive value associated with a positive vicinal surface slope. As can be understood from Figures 1.23 and 1.24, a faceted solid/liquid surface in contact with the TPL may theoretically be associated with a variety of growth angles whose range can be related to the negative and positive vicinal slope step energy values. Interestingly, in [Yuferev 2005] it is shown how this phenomenon (in the context of a facet on the solid/vapour interface) may result in two distinctly different growth angles on the two sides of a sapphire ribbon grown by the EFG technique. Finally, in the case of isotropic energies, the two Γ plots are circular, the size and relative orientation (one with respect to the other) of the three vectors remain constant and, consistent with Equation (1.22), α and β also remain constant regardless of the position of point B. This situation can be observed in Figure 1.24 for large values of ϕ_{lv} at which the curves are parallel to one another (recall that $\alpha = \phi_{lv} - \phi_{sv}$ and $\beta = \phi_{sv} - \phi_{sl}$).

The above relatively simple picture of the graphical approach to the determination of the growth angle is misleading. First of all, real quantitative data on both Γ plots is not usually available. In addition, significant differences between the values of α and α^* can be expected in certain cases, providing further complications to the analysis. Additional nontrivial issues such as the possibility for metastable solutions are discussed in [Voronkov 1981]. Such complications lead to the practical approach according to which growth angles are typically measured from experiments. The analysis of the results of these can, however, benefit from an understanding of the above theoretical considerations.

1.3.2 Measurements of Growth Angles: Methods and Values

Over the past four decades there have been several efforts to measure growth angles in a number of melt growth systems. The measurement techniques can usually be classified as belonging to one of two main approaches, observation of the TPL region during growth (method 1) or an *a posteriori* analysis of solidified material (method 2). Method 1 involves either direct observation and measurement of the angle between tangents to the meniscus (liquid/vapour interface) and the solid/vapour interface at the TPL, or a mathematical analysis of the observed meniscus (and in some cases the solid/vapour interface) leading to the determination of the growth angle. Related measurements of contact angles of melt drops placed on substrates (e.g. relevant to liquid phase epitaxy [König 1983, König 1984]) are not discussed here.

In the following, several studies involving the application of methods 1 and 2 to the measurement of growth angles in a variety of systems are briefly discussed. Measured values, sorted according to the type of crystalline material studied, are listed in Table 1.9. Note also that partial lists of growth angles are reviewed in the literature ([Bohm 1994, Hurle 1994, Hurle 1995, Duffar 1997, Kuandykov 2001]).

The early measurements date back to the 1960s. Antonov [Antonov 1965] photographed the meniscus (including the TPL) of Ge growing by the Czochralski technique. He directly measured the angle between the tangent to the meniscus and the horizontal and, in addition, showed that two different values of this angle give a good fit to an approximate solution of the Young–Laplace equation for two different sets of experimental measurements of crystal diameter and meniscus height. The angles determined are equal to $\pi/2 - \alpha$ (where α is the growth angle) only if the measurements can be assumed to have involved a time-independent crystal diameter. Shashkov and Mel'inkov [Shashkov 1965] filmed the Czochralski growth process, applied to Ge and Si, to obtain direct observations of the growth angles of these materials. Further measurements using method 1 are reported by Wenzl *et al.* [Wenzl 1976, Wenzl 1978] who used a Czochralski growth process to determine the growth angles of Cu [Wenzl 1976] and Ga [Wenzl 1978]. The angle in the case of Ga was measured both with He as the vapour phase and with an aqueous solution of HCl replacing the vapour phase (value not shown in Table 1.9). Additional similar measurements for Ge and Au are reported in [Wenzl 1978].

The direct viewing approach (method 1) was used in a number of additional investigations. The growth angle of sapphire was measured, using this method, by Satunkin and

Table 1.9 Values of growth angles reported in the literature

Material ^a	α (°)	Surface ^b	References	Method
Si {111}	11 ± 1	Nonfaceted	[Surek 1975]	2
	11 ± 1.5	Nonfaceted	[Hamidi 1983]	2
	11.4–19.9	Nonfaceted	[Antonov 2002] ^c	2
	12 ± 1	Unknown	[Satunkin 1980]	2
Si {110}	11 ± 1.5	Nonfaceted	[Hamidi 1983]	2
Si	12 ± 1	Isotropic	[Satunkin 2003]	2
	10	Isotropic	[Virozub 2008] ^d	2
	8.5–9	Polycrystalline	[Surek 1975]	2
	9.5 ± 1.5	Polycrystalline	[Hamidi 1983]	2
Ge {111}	15–20	Unknown	[Shashkov 1965]	1
	13 ± 1	Nonfaceted	[Surek 1975, 1976]	2
	12 ± 1	Facet	[Satunkin 2003]	2
Ge {110}	14 ± 1	Facet	[Satunkin 2003]	2
Ge	8	Polycrystalline	[Surek 1975]	2
	8–10.3	Polycrystalline	[Antonov 2002] ^c	2
	14 ± 1	Isotropic	[Satunkin 2003]	2
	12 ± 1	Isotropic	[Satunkin 1980]	2
	14.3	Isotropic	[Virozub 2008] ^d	2
	7 ± 3	Unknown	[Wenzl 1978]	1
InSb ($\bar{1}\bar{1}\bar{1}$)	25 ± 1	Facet	[Satunkin 1980]	2
	25.5 ± 0.5	Facet	[Antonov 2002] ^e	2
	25–30	Facet	[Satunkin 2003]	2
LiNbO ₃	0	Unknown	[Satunkin 1986]	1
NaNO ₂	7 ± 1	Unknown	[Ivantsov 1986]	1
LiF	19 ± 2	Unknown	[Ivantsov 1986]	1
Sapphire {0001}	35 ± 4	Facet	[Dreeben 1980]	1
Sapphire	17 ± 4	Nonfaceted periphery	[Dreeben 1980]	1
Sapphire	20 ± 5	Unknown	[Tatarchenko 1977]	1
Sapphire	12 ± 1	Unknown	[Satunkin 1980]	1
Cu	0	Nonfaceted	[Wenzl 1976]	1
Ga	0	Facet	[Wenzl 1978]	1
Au	0	Unknown	[Wenzl 1978]	1
GaP (111)	9.8 ± 0.5	Facet	[Antonov 2002]	2
InP (111)	7.0 ± 0.5	Facet	[Antonov 2002]	2
GaSb	30.7 ± 2	Unknown	[Tegetmeier 1996]	1
GaSb (μg)	28	Unknown	[Tegetmeier 1996]	1
W	20 ± 5	Unknown	[Glebovsky 1989]	1
GaAs	16	Unknown	[Satunkin 2003]	2

^aIn some cases the nominal orientation of the solid/liquid interface (i.e. the growth direction) is provided.

^bThis is the quality of the solid/liquid interface which, if reported, is typically known only at the onset of solidification.

^cBased on data from [Surek 1975].

^dBased on data from [Satunkin 2003].

^eBased on data from [Satunkin 1980].

co-workers [Tatarchenko 1977, Satunkin 1980]. The measurement system involved pulling thin crystalline rods through a shaper, where the growth angle was determined by a number of different analysis techniques applied to data on solid/vapour and liquid/vapour interfaces obtained by direct observation of the TPL and shaper regions. The

application of method 1 to sapphire growth is also reported in [Dreeben 1980], in which case the crystals were grown in a laser-heated float zone system. In [Satunkin 1986] Satunkin and co-workers emphasize the fact that their (type 1) method, applied to the pulling of thin lithium niobate rods from a shaper, does not require knowledge of the position of the TPL. The method described in [Satunkin 1986] is applicable to crystals of uniform diameter. The constant diameter assumption is also necessary when using the type 1 method applied in [Ivantsov 1986] for the determination of the growth angles of LiF and NaNO₂.

Two more studies involve the application of method 1 in the measurement of growth angles of W [Glebovsky 1989] and GaSb [Tegetmeier 1996]. The growth angle was determined in [Glebovsky 1989] using an approximate analytical solution for the meniscus between tube-shaped feed and crystalline rods in an electron-beam zone melting system. The analysis in [Tegetmeier 1996] involved fitting lines to the meniscus and solid/vapour interface to determine the growth angle in a floating zone system, both under normal conditions and in microgravity. Finally, an example of method 1 applied to the case of floating zone growth of Si can be found in Chapter 4 of this book.

The *a posteriori* analysis of solidified material (method 2) was, to the best of our knowledge, pioneered by Surek and Chalmers [Surek 1975]. These authors determined growth angle values based on a careful examination of a re-solidified small circular region of melt created in a thin crystalline wafer using an electron gun. Gravity was ignored in the analysis and the solid/liquid interface was assumed planar. This technique was applied to the case of Si and Ge [Surek 1975, Surek 1976], where in [Surek 1976] a rough estimate of gravitational effects was mentioned.

In [Satunkin 1980] Satunkin *et al.* presented a study of InSb, where the measurement was based on the *a posteriori* analysis of directionally solidified drops obtained when Czochralski-grown crystals were pulled free (i.e. separated) from the melt. The analysis involved approximating the solid/vapour interface to be parabolic in shape, an assumption of negligible effect of gravity on the liquid/vapour interface form, as well as a planar solid/liquid (growth) interface. Interestingly, in their later publication [Satunkin 1986], Satunkin and co-workers mentioned that transparent materials such as LiNbO₃ or sapphire cannot be analysed using this method since solidification in this case is not unidirectional from the base (original crystallization front) to the tip.

The method proposed in [Surek 1975] was used in [Hamidi 1983] to determine angles of Si both in vacuum and under Ar atmosphere. Antonov and Selin [Antonov 2002] proposed an elegant method for determining the growth angle from directionally solidified drops based on their cone angle and the assumptions of negligible gravitational effect on meniscus shape as well as a planar solidification front. This method was applied to GaP and InP systems as well as to photographs from the literature of InSb [Satunkin 1980], Ge [Surek 1975] and Si [Surek 1975]. Interestingly, the comparison with results of Surek [Surek 1975] was in some cases excellent in spite of the fact that the solidification geometry in [Surek 1975] is different from that of a solidifying drop.

An extensive report on measurements of growth angles using method 2 applied to Ge, Si and InSb is given in [Satunkin 2003]. A number of analysis techniques are applied. In particular, the assumption of constant growth angle is tested and is found to be valid for Si and Ge but not for InSb. Finally, in [Virozub 2008] method 2 was applied to data on Ge and Si drops from [Satunkin 2003] in a manner that requires no assumptions regarding

the shape of the solidification front. Once determined, the accuracy of the growth angle value and the possibility that it can be assumed constant were both verified using a detailed dynamic growth simulation involving coupled heat transport and capillarity. Results highlight the possible importance of gravity in these problems. In addition, this reference suggests that solidified drop shapes may not be very sensitive to the shape of the solid/liquid interface during growth.

Although (as can be seen in Table 1.9) several measurements were made on systems with a known crystallographic orientation, it is not always obvious if the solidification interface near or at the TPL is faceted or atomically rough. As can be understood from section 1.3.1 as well as from [Voronkov 1981, Satunkin 2003], although knowledge of the exact nature of the solid/liquid and solid/vapour interfaces at the TPL may not always be necessary for growth angle measurement, this information is important for the interpretation of measured values.

1.3.3 Application of the Growth Angle Condition in Simulations of Crystal Growth

Rigorous simulations of meniscus-defined crystal growth processes, in which the liquid/vapour interface shape is calculated, should be consistent with the growth angle as dictated by the application of the physics, described in section 1.3.1, to the system at hand. Relevant modelling efforts of melt growth systems, coupling heat transport and capillarity in a self-consistent manner, can be traced back to the mid 1980s. Some of the earliest studies include a quasi-steady-state model for the edge-defined film-fed (EFG) growth of Si [Ettouney 1983], a steady-state description of small-scale floating-zone growth of Si [Duranceau 1986] and a dynamic analysis of the Czochralski growth of Ge [Crowley 1983]. In [Ettouney 1983] the growth angle value is enforced as a boundary condition in the numerical solution of the Young–Laplace equation for the liquid/vapour interface shape, in [Duranceau 1986] this boundary condition is used to determine the *a priori* unknown pressure jump across the liquid/vapour interface, and in [Crowley 1983] the growth angle value is implemented by a dynamic equation relating the changing crystal diameter to the crystal growth rate at the TPL. This equation, important when considering the stability of growth (see Chapter 2 of this book) and control of crystal diameter (see [Hurle 1994] and Chapter 3), is given by:

$$\frac{dr_c}{dt} = v_g \tan(\psi - \alpha), \quad (1.29)$$

where r_c is the crystal radius at the TPL, ψ is the angle between the vertical and the liquid/vapour interface, and v_g is the crystal growth rate at the TPL; note that in Czochralski growth systems this growth rate is equal to the difference between the pull rate and the rate of change of melt height below the TPL.

It is interesting to note, that in the case of a floating zone system (discussed in [Duranceau 1986]), in which two TPLs exist, the growth angle is enforced only at the TPL associated with growth. No angles are specified at the TPL on the melting solid/vapour interface (i.e. on the feed rod). A relevant discussion of this issue is presented, in

relation to back-melting during Czochralski growth, in [Van den Bogaert 1996]. Following the discussion in this reference, it is probably best to restrict growth angle measurements to experiments in which it is verified that growth actually takes place at the relevant TPL.

The field of crystal growth modelling has advanced considerably since the mid-1980s. Highly sophisticated modelling efforts have been reported in the literature, many of which involve simulation of meniscus-defined systems in which transport-phenomena and capillarity are rigorously coupled. Physically consistent methods, accounting for the growth angle condition in these studies, are typically based on the principles laid down in the three above-mentioned references and other early works. A description of the development and application of relevant modelling efforts, which is beyond the scope of this chapter, is given in several review articles and book chapters published since the mid 1980s (e.g. [Brown 1988, Dupret 1994, Yeckel 2005]). In addition, note that a discussion related to the application of modelling to the floating zone technique can be found in Chapter 4 of this book.

1.3.3.1 Constant Growth Angle Approximation

Almost all of the computational analyses of meniscus-defined growth, accounting for the growth angle, assume it to be constant in both time and space. Exceptions include the analysis of a directionally solidifying sessile water drop [Anderson 1996] in which a dynamic angle was used to fit experimental data, and the calculation of a nonaxisymmetric cross-section of crystals pulled from the melt [Pet'kov 1993] which involved growth angle anisotropy in the plane perpendicular to the growth direction. However, in [Anderson 1996] heat transport was not accounted for in the analysis. As indicated in [Schultz 2001] and shown in [Virozub 2008], agreement with experimentally observed features in this particular case (involving solidification of a sessile water drop) can be obtained when heat transport is accounted for in the analysis without the need for relaxing the constant growth angle approximation. In addition, although the basic reasoning behind the analysis in [Pet'kov 1993] is sound, this two-dimensional study is limited to the cross-sectional plane of the crystal with no account for heat transport in the formulation.

In [Virozub 2008] a method is discussed for the estimation and verification of growth angle values based on experimentally obtained directionally solidified sessile or pendant drops. The estimation refers to the angle exhibited at the initial stages of drop solidification while the verification is based on the constant growth angle assumption. The two examples shown in this reference, of Si and Ge solidifying on isotropic fronts of Czochralski-grown crystals pulled free from the melt, suggest that this assumption is satisfactory in these systems. Following the discussion in section 1.3.1, it is theoretically possible for this assumption to fail in systems exhibiting anisotropy of interfacial energies, significant undercooling at the TPL, or a combination of both. It is important to note however, that even in cases where one or both of these phenomena occur, the angle may still remain constant throughout growth due to *time-independent* conditions at the TPL. Finally, as discussed above in relation to [Pet'kov 1993], three-dimensional effects, such as those involving anisotropy of interfacial energies in the plane perpendicular to the growth direction, may lead to nonuniform growth angle values along the TPL.

The following involves the application of an approach based on the method presented in [Virozub 2008], further probing issues related to the constant growth angle

approximation. In particular a situation is examined, where a facet dominates the solid/liquid interface. Since the method and related equations are given in detail in [Virozub 2008], they are only briefly mentioned here. Additional information, associated with anisotropic interfacial attachment growth kinetics, is briefly discussed below with more detail provided in [Weinstein 2004].

Computational Approach to the Estimation and Verification of Growth Angle Values. Our starting point is a solidified pendant or sessile drop whose shape, which is known, is used for the determination of the solid drop volume as well as the angle of contact between the solid/vapour interface and the substrate. The solidified material volume is multiplied by the solid-to-liquid density ratio thus providing a value for the original liquid drop volume. This is then used, together with the known drop/substrate (circular) interfacial area, to determine the liquid drop's shape by numerical solution of the Young–Laplace equation with gravity (see Chapter 8 for the various forms of the Young–Laplace equation):

$$\frac{1}{r} \frac{d}{dr} \left\{ r \frac{dz_l}{dr} \left[1 + \left(\frac{dz_l}{dr} \right)^2 \right]^{-1/2} \right\} = \frac{\rho_l (z_{la} - z_l)}{\gamma_{lv}} (\mathbf{g} \cdot \mathbf{e}_z) - \frac{2}{b} \quad (1.30)$$

The coordinate system used here is the same as the one described below (see Figure 1.25) in the context of drop-solidification calculations, where $z_l(r)$ is the z -coordinate value of the liquid/vapour interfacial profile at a given radial position. In Equation (1.30) $1/b$ is the drop's mean curvature at its apex ($r = 0, z_l = z_{la}$), z_{la} is the vertical distance of the drop apex from its base, \mathbf{e}_z is the unit vector in the z coordinate direction and \mathbf{g} is the gravity vector. Boundary conditions applied in this case are a symmetry (zero slope) condition at $r = 0$ and the fact that, at $r = R_0$, the liquid/vapour interface's vertical position is fixed at $z_l = 0$. In addition, the parameter $1/b$ is determined by coupling the solution of Equation (1.30) with that of an additional equation enforcing the pre-determined liquid

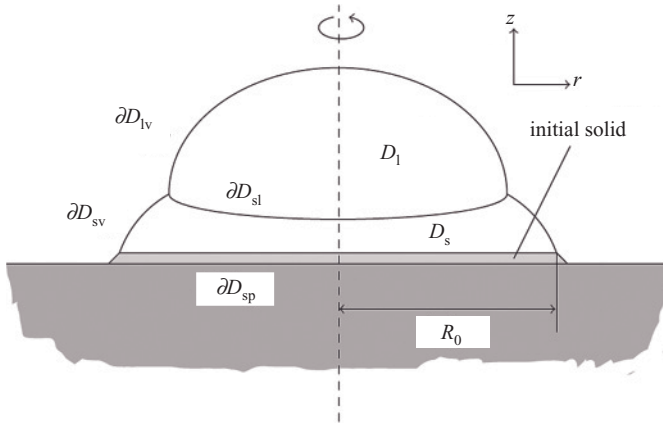


Figure 1.25 Mathematical representation of model system for drop solidification.

volume. Once the shape, $z_i(r)$, is known it is possible to evaluate the angle of contact between the liquid/vapour interface and the substrate. Finally, the difference between this angle and the previously obtained contact angle of the solidified drop is the estimated growth angle.

Verification of the estimated growth angle, assuming it is constant, is obtained by solving the coupled problem of heat transport, phase-change and capillarity during the directional solidification of the drop. A mathematical representation of the axially-symmetric model system used in these calculations is shown in Figure 1.25.

The evolution of the temperature field in the solid (D_s) and liquid (D_l) phases during solidification is assumed to be governed by the heat equation:

$$\rho_i C_{pi} \frac{\partial T}{\partial t} = \nabla \cdot k_i \nabla T \quad (i = l, s), \quad (1.31)$$

where ρ_i , C_{pi} , and k_i are, respectively, the density, heat capacity and thermal conductivity of phase i , while T , t and ∇ represent temperature, time and the gradient operator. Note that in this analysis of small-scale systems with relatively low-valued temperature gradients, we have neglected the impact, on the thermal field, of melt flow driven either by buoyancy or by surface tension gradients.

External boundary conditions for this problem include a prescribed ($T = T_0$) temperature along the interface between the drop and the cold substrate (∂D_{sp}) and heating by the environment at the liquid/vapour (∂D_{lv}) and solid/vapour (∂D_{sv}) interfaces according to:

$$-k_i \nabla T \cdot \mathbf{n}_{ij} = h(T - T_a) \quad (ij = lv, sv), \quad (1.32)$$

where \mathbf{n}_{ij} is the unit normal vector pointing from the interface towards the environment, T_a is the ambient temperature and h is the convective heat transfer coefficient enhanced due to radiative transport effects.

Along the solidification interface (∂D_{sl}) a balance of heat fluxes requires adherence to the Stefan condition given by:

$$[(k_s \nabla T)_s - (k_l \nabla T)_l] \cdot \mathbf{n}_{sl} = \Delta H v_n, \quad (1.33)$$

where the subscripts l and s respectively denote quantities evaluated on the liquid and solid sides of the solid/liquid interface, the volumetric heat of fusion is given by ΔH , v_n is the normal growth rate and \mathbf{n}_{sl} is the unit normal vector pointing from the interface into the liquid phase. In [Virozub 2008] the solid/liquid interface is assumed to coincide with the melting point isotherm. This assumption, which is consistent with extremely fast interfacial attachment growth kinetics, is relaxed (where necessary) in the following to allow for the formation of a kinetically driven facet during solidification; see e.g. [Weinstein 2004] for a full discussion of our approach to the problem of faceting. In this case, the simple isotherm condition ($T = T_m$ on ∂D_{sl}) in [Virozub 2008] is replaced here by the more general equation:

$$v_n = \beta_k \Delta T, \quad (1.34)$$

where ΔT is the undercooling on ∂D_{sl} and β_k is the kinetic coefficient (which is not necessarily constant). In the common event of an atomically rough solid/liquid interface, kinetics of growth are extremely fast (β_k is relatively large), the resultant undercooling value is negligible ($\Delta T \rightarrow 0$), and the isotherm condition used in [Virozub 2008] is recovered. However, when (at some point on the solid/liquid interface) crystal growth occurs along a singular orientation, a facet may appear, molecular attachment kinetics become relatively slow and the resultant nonnegligible undercooling must be accounted for. This is done via Equation (1.34) where the kinetic coefficient now depends on the undercooling as well as on the deviation from the singular orientation (δ), in accordance with basic crystal growth mechanisms characteristic of growth in the vicinity of an atomically smooth singular surface.

As described in detail in [Weinstein 2004], a general expression for the kinetic coefficient near a singular surface can be formulated using a combination of the following expressions:

$$\beta_k(\Delta T, \delta) = \begin{cases} \beta_r & \text{rough surface} \\ \beta_{st} |\sin \delta| & \text{vicinal surface} \\ C(\cos \delta) \Delta T & \text{screw dislocation} \\ B(\cos \delta) e^{-A/\Delta T} & \text{two-dimensional nucleation} \end{cases} \quad (1.35)$$

where β_r is a large-valued rough growth kinetic coefficient (practically enforcing the isotherm condition), β_{st} is a step kinetic coefficient and A , B and C are additional parameters which, together with β_r and β_{st} , can be treated as constants. In the most simple (yet robust) approximation, each mechanism is enforced separately depending on the local crystallographic orientation and (in the case of extremely small values of δ) on the nature of the singular surface. For large enough values of δ rough surface kinetics are used, for intermediate δ values vicinal kinetics are enforced, and below a certain value of δ either screw dislocation or two-dimensional nucleation kinetics are applied depending on the availability of screw dislocations on the surface. In [Weinstein 2004] (and here) the crossover from step source (screw dislocation or two-dimensional nucleation) to vicinal surface kinetics for $\langle 111 \rangle$ Si is modelled as occurring at misorientation values on the order of 0.001° , while switching to rough growth kinetics is enforced at δ values on the order of 0.5° .

The liquid/vapour interface shape is calculated, as a function of time, by solving Equation (1.30) coupled with an overall mass conservation equation for the determination of l/b , where a zero interfacial slope condition is imposed at the liquid drop's apex and the edge of the drop is positioned to coincide with the TPL. Finally, self-consistency with the thermal field calculation is enforced by applying the growth angle condition according to which α is equal to the difference between the inverse tangent (arctan) values of the solid/vapour and liquid/vapour interfacial slopes at the TPL.

The finite-element based numerical procedures for solution of the equations presented above are mostly given in [Virozub 2008]. When enforcing the isotherm condition (as in [Virozub 2008]), an iterative procedure is used, involving an empirically determined interface motion coefficient. However, when modelling a solid/liquid interface which exhibits a facet, this interface motion procedure is replaced with the algorithm described

in detail in [Weinstein 2004]. Details of mesh and time-step sizes as well as other numerical parameters are the same as in [Virozub 2008] except for when Equation (1.34) is applied. In this case a reduced time-step size ($\Delta t = 0.00025$ s) is used with approximately 70 substeps employed for advancement of the interface at each time-step.

As already discussed above, in [Virozub 2008] the growth angles for Si and Ge were estimated (and verified to be constant), based on experiments reported in [Satunkin 2003]. Here additional data from [Satunkin 2003] is used to estimate the growth angle for InSb ($\bar{1}\bar{1}\bar{1}$). The resultant growth angle value, obtained using the procedure briefly described above (and in more detail in [Virozub 2008]), is found to be given by $\alpha = 25^\circ$. Next the verification procedure is applied while assuming the isotherm condition to be applicable (i.e. ignoring effects of interface attachment kinetics). System parameters and physical coefficients are given, respectively, by the following values of estimated base undercooling, estimated ambient overheating, liquid density [Kozhemyakin 1995], solid density [Vaidya 2006], heat of fusion [Vaidya 2006], solid conductivity [Vaidya 2006], liquid conductivity [Roussopoulos 2004], volumetric liquid heat capacity [Kozhemyakin 1995], volumetric solid heat capacity [Vaidya 2006], liquid/vapour interfacial energy [Hurle 1995] and estimated heat transfer coefficient: $T_m - T_0 = 10$ K, $T_a - T_m = 12$ K, $\rho_l = 6430$ kg/m³, $\rho_s = 5640$ kg/m³, $\Delta H = 1.3 \times 10^9$ J/m³, $k_s = 4.57$ W/mK, $k_l = 12.3$ W/mK, $\rho_l C_{pl} = 1.68 \times 10^6$ J/m³K, $\rho_s C_{ps} = 1.5 \times 10^6$ J/m³K, $\gamma_v = 0.434$ J/m², $h = 115$ W/m²K.

A plot of the predicted solidified drop profile, obtained with the above estimated angle value, is shown in Figure 1.26 together with the relevant experimental data from [Satunkin 2008]. For comparison, this figure contains a similar plot for the case of Ge grown on an isotropic growth front, obtained using the angle $\alpha = 14.3^\circ$ which was determined and verified in [Virozub 2008]. The agreement between experiment and simulation is excellent, suggesting that the growth angle is indeed constant. However, in the case of InSb, numerical difficulties limited the ability to simulate solidification beyond the level shown in Figure 1.26. Consider the nonnegligible size of the residual liquid drop in this case ($\sim 4\%$ of original volume as compared with less than 0.5% in the case of Ge). It is theoretically possible that, if achievable, continued simulated solidification may reveal a discrepancy between experimental and simulated profiles for small values of the radial coordinate. It is important to consider this possibility in this case since Satunkin’s analysis

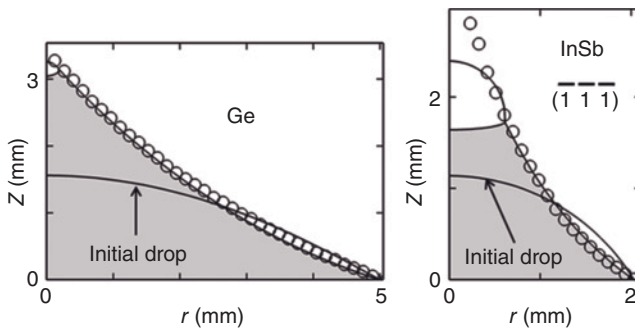


Figure 1.26 Experimental (circles) and simulated (solid lines) directionally solidified pendant drop profiles. Shaded regions are the final (simulated) solid drop shapes. The small regions above the simulated solid drops are the residual liquid.

[Satunkin 2003] determined the growth angle of this material to be nonconstant (see Table 1.9). In addition, as mentioned above, the verifications exhibited in Figure 1.26 were made using the isotherm condition at the interface. Strictly speaking, this approach is incorrect in the event (possibly relevant in the case of InSb shown in Figure 1.26) that a facet appears on the solid/liquid interface during the solidification process.

The importance of using the rigorous boundary condition, Equation (1.34), in cases involving facets at the solid/liquid interface is investigated using a hypothetical case of Si drop solidification in the $\langle 111 \rangle$ direction. Here parameters are the same as those used in [Virozub 2008] for the case of Si growing on an isotropic growth front. Since the actual value of the growth angle is not truly known in this case, the same value ($\alpha = 10^\circ$) as that determined in [Virozub 2008], is chosen. Solidification is simulated twice. First an analysis identical to that employed in [Virozub 2008] is applied. Next, the solidified drop profile is recalculated, this time using the rigorous approach involving Equation (1.34) which accounts for interface attachment kinetics on a facet, should it evolve. In this case it was assumed that a two-dimensional nucleation mechanism dominates step generation. Parameters relevant to Equation (1.35) are $\beta_s = 0.001$ m/sK, $\beta_{sl} = 0.63$ m/sK, $B = 4.8 \times 10^8$ m/sK and $A = 140$ K. Looking at the results, shown in Figure 1.27, it is interesting to note that, although the more rigorous calculation predicts the solid/liquid interface to be dominated by a $\{111\}$ facet, this result has almost no impact on the shape of the solidified drop. This suggests that the commonly used approach of assuming the solid/liquid interface to be planar, when estimating the growth angle, may yield accurate results even in some of the cases where this assumption is clearly incorrect. Additional calculations (not exhibited here), showing a surprising insensitivity of the solidified drop shape to variations in k_s , k_l , h , T_0 and T_a , provide further support for this conclusion at least with respect to the Si system considered here.

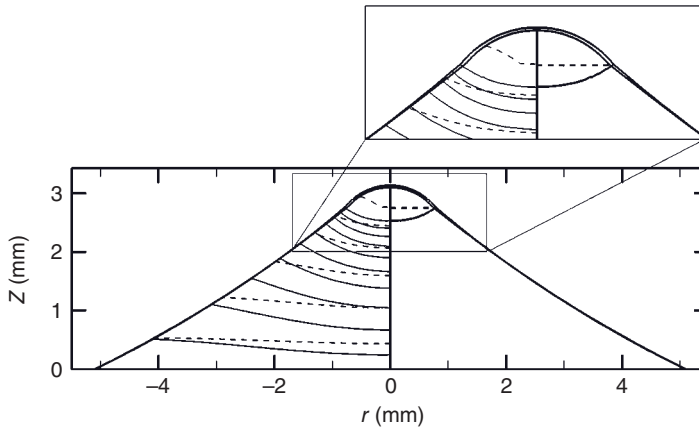


Figure 1.27 Thermal fields and interfacial profiles during simulated solidification of Si in the $\langle 111 \rangle$ direction assuming $\alpha = 10^\circ$. Right-hand side (both of main figure and of inset) depicts solid/vapour, residual liquid/vapour and solid/liquid interfacial profiles; the dashed line demarks the solid/liquid interface when faceting is accounted for. Left-hand side depicts isotherms spaced 1 K apart. Dashed lines correspond to the faceted growth calculation and solid lines to those obtained using the isotherm condition.

1.3.4 Summary

The concept of the growth angle, its measurement and relevant crystal growth simulations are reviewed. The constant growth angle approximation appears valid in cases where significant anisotropy is not present near the TPL. The existence of a facet (associated with significant anisotropy) at or near the TPL may lead to variations in the value of the growth angle. However, if steady-state growth conditions are maintained near the TPL, this growth angle value may remain constant throughout most of the solidification process.

The agreement between different measurements of growth angle values for a given material is not always satisfactory (see Table 1.9). There may be a number of reasons for the discrepancies. Although some of the relevant references include information on the quality of the solid/liquid interface (faceted, polycrystalline, nonfaceted), it is not necessarily simple to verify that this information is accurate throughout the solidification process. In particular, the quality of the interface at the TPL (e.g. the nature of contact between a solid/liquid interfacial facet and the TPL) is not easy to resolve. An additional complication is related to the accuracy of the estimation methods employed. Systematic errors may be introduced due to the use of approximate solutions of relevant equations. For example, as shown in [Virozub 2008], when neglecting the effect of gravity in the analysis of solidifying drops it is important to make sure that the Bond number is small (to be on the safe side it is probably best to neglect gravity only when $Bo < 0.1$). Assuming the solid/liquid interface to be planar when calculating solidification profiles is probably incorrect in many cases considered in the growth angle measurement literature. However, the rigorous growth angle verification procedure, applied here for a hypothetical case of a $\langle 111 \rangle$ Si drop solidification process, shows almost no change in the solidification profile when simulating a faceted (flat) as compared to a curved (non-faceted) solid/liquid interface (using the same value of the growth angle in both cases). Further manipulation of system parameters indicates that the solidification profile is, in this case, relatively insensitive to heat transport. This result, which is in contradiction with the situation described for solidification of a sessile water drop ([Virozub 2008] as compared with [Anderson 1996]), suggests that a more complete investigation of this issue is necessary.

Anisotropy and the possibility of a nonconstant growth angle are important issues which require further attention. Understanding the three-dimensional picture of a meniscus-defined growth process often requires the consideration of anisotropy in the plane of solidification (along the TPL). The coupling of capillarity with kinetics associated with faceted growth near the TPL in relevant systems (see e.g. [Santos 1996]), is a nontrivial problem which must be addressed when considering the three-dimensional analysis of such processes.

Acknowledgements

S.B. and A.V. thank G.A. Satunkin for providing them with original versions of the photographs exhibited in [Satunkin 2003] and would also like to thank Dr I.G. Rasin for his assistance in resolving numerical problems.

References

- [Anderson 1996] Anderson D.M., Grae Worster M., Davis S.H., *J. Cryst. Growth* **163** (1996) 329.
- [Antonov 1965] Antonov P.I., *Sb. Rost. Kristallov.* **6** (1965) 158 (Consultants Bureau Report No. IRN1031619X).
- [Antonov 2002] Antonov V.A., Selin V.V., *J. Cryst. Growth* **241** (2002) 507.
- [Bardsley 1974] Bardsley W., Frank F.C., Green G.W., Hurle D.T.J., *J. Cryst. Growth* **23** (1974) 341.
- [Barsoum 1981] Barsoum M.W., Ownby P.D., In: *Surfaces and Interfaces in Ceramic and Ceramic-Metal Systems*, Materials Science Research, Volume 14, ed. J. Pask and A. Evans, Plenum Press, New York (1981), pp. 457–466.
- [Baumli 2008] Baumli P., Kaptay G., *Mater. Sci. Eng. A* **495** (2008) 192–196.
- [Blake 1993] Blake T.D., In: *Wettability*, ed. J.C. Berg, Marcel Dekker, New York (1993), pp. 251–309.
- [Bohm 1994] Bohm J., Lüdge A., Schröder W., In: *Handbook of Crystal Growth Vol. 2a – Bulk Crystal Growth: Basic Techniques*, ed. D.T.J. Hurle, North Holland, Amsterdam (1994), pp. 213–257.
- [Boiton 1999] Boiton P., Giacometti N., Duffar T., Sentailler J.L., Dusserre P., Nabot J.P., *J. Cryst. Growth* **206** (1999) 159–165.
- [Brown 1988] Brown R.A., *AIChE J* **34**(6) (1988) 881.
- [Cassie 1948] Cassie A.B.D., *Discuss. Faraday Soc.* **3** (1948) 11–16.
- [Castello 1994] Castello P., Ricci E., Passerone A., Costa P., *J. Mater. Sci.* **29** (1994) 6104–6114.
- [Champion 1973] Champion J.A., Keene B.J., Allen S., *J. Mater. Sci.* **8** (1973) 423–426.
- [Chizhik 1985] Chizhik S.P., Gladkikh N.T., Larin V.I., Grigor'eva L.K., Dukarov S.V., Stepanova S.V., *Poverkhnost* **12** (1985) 111–121 (in Russian).
- [Cobb 1999] Cobb S.D., Szofran F.R., Jones K.S., Lehoczy S.L., *J. Electron. Mater.* **28** (1999) 732–739.
- [Cox 1986] Cox R.G., *J. Fluid Mech.* **168** (1986) 169–194.
- [Cröll 2002] Cröll A., Salk N., Szofran F.R., Cobb S.D., Volz M.P., *J. Cryst. Growth* **242** (2002) 45–54.
- [Cröll 2003] Cröll A., Lantzsch R., Kitanov S., Salk N., Szofran F.R., Tegetmeier A., *Cryst. Res. Technol.* **38** (2003) 669–675.
- [Crowley 1983] Crowley A.B., *IMA J. Appl. Math.* **30** (1983) 173.
- [de Gennes 1985] de Gennes P.G., *Rev. Modern Phys.* **57** (1985) 827–863.
- [de Gennes 2004] de Gennes P.G., Brochard-Wyart F., Quéré D., *Capillarity and Wetting Phenomena: Drops, Bubbles, Pearls, Waves*, Springer, New York (2004).
- [Dezellus 1999] Dezellus O., Eustathopoulos N., *Scripta Mater.* **40** (1999) 1283–1288.
- [Dezellus 2000] Dezellus O., PhD thesis, INP-Grenoble, France (2000) (in French).
- [Dezellus 2005] Dezellus O., Jacques S., Hodaj F., Eustathopoulos N., *J. Mater. Sci.* **40** (2005) 2307–2311.
- [Dreeben 1980] Dreeben A.B., Kim K.M., Schujko A., *J. Cryst. Growth* **50** (1980) 126.
- [Drevet 2009] Drevet B., Voytovych R., Israel R., Eustathopoulos N., *J. Eur. Ceram. Soc.* **29** (2009) 2363–2367.
- [Duffar 1997] Duffar T., Boiton P., Dusserre P., Abadie J., *J. Cryst. Growth* **179** (1997) 397.
- [Duffar 2009] Duffar T., Bochu O., Dusserre P., *J. Mater. Sci.*, DOI: 10.1007/s10853-009-4041-3
- [Dupré 1869] Dupré A., *Théorie Mécanique de la Chaleur*, Chapter IX, Gauthier-Villars, Paris (1869).
- [Dupret 1994] Dupret F., Van den Bogaert N., In: *Handbook of Crystal Growth, Vol. 2b – Bulk Crystal Growth: Growth Mechanisms and Dynamics*, ed. D.T.J. Hurle, North Holland, Amsterdam (1994), pp. 875–1010.
- [Duranceau 1986] Duranceau J.L., Brown R. A., *J. Cryst. Growth* **75** (1986) 367.
- [Ellefson 1938] Ellefson B.S., Taylor N. W., *J. Am. Ceram. Soc.* **21** (1938) 193–205.

- [Ettouney 1983] Ettouney H.M., Brown R.A., Kalejs J.P., *J. Cryst. Growth* **62** (1983) 230.
- [Eustathopoulos 1998] Eustathopoulos N., Drevet B., *Mater. Sci. Eng. A* **249** (1998) 176–183.
- [Eustathopoulos 1999] Eustathopoulos N., Drevet B., Nicholas M., *Wettability at High Temperatures*, Pergamon, Oxford (1999).
- [Eustathopoulos 2001] Eustathopoulos N., Drevet B., Muolo M.L., *Mater. Sci. Eng. A* **300** (2001) 34–40.
- [Eustathopoulos 2005a] Eustathopoulos N., Sobczak N., Passerone A., Nogi K., *J. Mater. Sci.* **40** (2005) 2271–2280.
- [Eustathopoulos 2005b] Eustathopoulos N., *Curr. Opin. Solid State Mater. Sci.* **9** (2005) 152–160.
- [Flemings 1974] Flemings M.C., *Solidification Processing*, McGraw-Hill, New York (1974).
- [Garandet 1998] Garandet J.P., Drevet B., Eustathopoulos N., *Scripta Mater.* **38** (1998) 1391–1397.
- [Glebovsky 1989] Glebovsky V.G., Semenov V.N., Lomeyko V.V., *J. Cryst. Growth* **98** (1989) 487.
- [Hamidi 1983] Hamidi M., Rodot H., *Rev. Phys. Appl.* **18** (1983) 75.
- [Harter 1993] Harter I., Dusserre P., Duffar T., Nabot J.P., Eustathopoulos N., *J. Cryst. Growth* **131** (1993) 157–164.
- [Herring 1951] Herring C., In: *The Physics of Powder Metallurgy*, ed. W.E. Kingston, McGraw-Hill, New York (1951), pp. 143–179.
- [Hitchcock 1981] Hitchcock S.J., Carroll N.T., Nicholas M.G., *J. Mater. Sci.* **16** (1981) 714–732.
- [Hoffman 1972] Hoffman D.W., Cahn J.W., *Surf. Sci.* **31** (1972) 368.
- [Hurle 1994] Hurle D.T.J., Cockayne B., In: *Handbook of Crystal Growth Vol. 2a – Bulk Crystal Growth: Basic Techniques*, ed. D.T.J. Hurle, North Holland, Amsterdam (1994), pp. 99–211.
- [Hurle 1995] Hurle D.T.J., *J. Cryst. Growth* **147** (1995) 239.
- [Ivantsov 1986] Ivantsov V.A., Antonov P.I., Panov M.F., USSR. Mat. Vses. Soveshch. Poluch. Profilirovannykh Krist. Izdelii Sposobom Stepanova Ikh Primen. Nar. Khoz. (1986), Meeting Date 1985, pp. 138–142 (in Russian).
- [Jaworske 1989] Jaworske D.A., Perry W.D., *AIAA 24th Thermophysics Conference*, Buffalo, NY, 12–14 June 1989, *AIAA-89-1756*, (1989).
- [Johnson 1993] Johnson R.E., Dettre R.H., In: *Wettability*, ed. J.C. Berg, Marcel Dekker, New York (1993), pp. 1–73.
- [Kaiser 2001] Kaiser N., Cröll A., Szofran F.R., Cobb S.D., Benz K.W., *J. Cryst. Growth* **231** (2001) 448–457.
- [Katty 1992] Katty A., Dusserre P., Triboulet R., Duffar T., *J. Cryst. Growth* **118** (1992) 470–472.
- [Kinoshita 1989] Kinoshita K., Yamada T., *J. Cryst. Growth* **96** (1989) 953–956.
- [Kistler 1993] Kistler S.F., In: *Wettability*, ed. J.C. Berg, Marcel Dekker, New York (1993), pp. 311–429.
- [König 1983] König U., Keck W., *J. Electrochem. Soc.* **130** (1983) 685.
- [König 1984] König U., Keck W., Kricks A., *J. Cryst. Growth* **68** (1984) 545–549.
- [Kozhemyakin 1995] Kozhemyakin G., *J. Cryst. Growth* **149** (1995) 266.
- [Kuandykov 2001] Kuandykov L.L., Antonov P.I., *J. Cryst. Growth* **222** (2001) 852.
- [Laplace 1805] Laplace P.S. (Marquis), *Traité de Mécanique Céleste*, Vol. 4, first section (théorie de l'action capillaire) of the supplement to book 10 (sur divers points relatifs au système du monde), Chez Courcier, Paris (1805), (in French).
- [Laurent 1988] Laurent V., Chatain D., Chatillon C., Eustathopoulos N., *Acta Metall.* **36** (1988) 1797–1803.
- [Li 1989] Li J.G., Coudurier L., Eustathopoulos N., *J. Mater. Sci.* **24** (1989) 1109–1116.
- [Maeda 1986] Maeda Y., Yokoyama T., Hide I., Matsuyama T., Sawaya K., *J. Electrochem. Soc.*, **133** (1986) 440–443.
- [Mailliar 2008] Mailliar O., Hodaj F., Chaumat V., Eustathopoulos N., *Mater. Sci. Eng. A* **495** (2008) 174–180.
- [Merlin 1992] Merlin V., PhD thesis, INP-Grenoble, France (1992) (in French).

- [Morel 1970] Morel C.F., *Surface Tensions of Molten Salts and Contact Angle Measurements of Molten Salts on Solids*, EUR 4482e, Commission of the European Communities–Euratom, Joint Nuclear Research Centre, Petten Establishment, Netherlands (1970).
- [Mortensen 1997] Mortensen A., Drevet B., Eustathopoulos N., *Scripta Mater.* **36** (1997) 645–651.
- [Mullins 1957] Mullins W.W., *J. Appl. Phys.* **28** (1957) 333–339.
- [Mullins 1960] Mullins W.W., *Trans. Met. Soc. AIME* **218** (1960) 354–361.
- [Naidich 1968] Naidich Y.V., Kolesnichenko G.A., *Russ. Metall.* **4** (1968) 141–149.
- [Naidich 1981] Naidich Y.V., In: *Progress in Surface and Membrane Science*, Vol. 14, ed. D.A. Cadenhead and J.F. Danielli, Academic Press, New York (1981), pp. 353–484.
- [Naidich 1992] Naidich Y.V., Sabuga W., Perevertailo V., *Adgeziya Raspl. Pajka Mat.* **27** (1992) 23–34 (in Russian).
- [Naidich 1995] Naidich J.V., Taranets N.Y., *Proc. 1st Int. Conf. High Temperature Capillarity*, Smolenice Castle, 8–11 May 1994, ed. N. Eustathopoulos (Reprint, Bratislava, 1995), pp. 138–142.
- [Neumann 1972] Neumann A.W., Good R.J., *J. Colloid Interface Sci.* **38** (1972) 341–358.
- [Nolfi 1972] Nolfi F.V., Johnson C.A., *Acta Metall.* **20** (1972) 769–778.
- [Ownby 1995] Ownby P.D., Weirauch D.A., Lazaroff J.E., *Proc. 1st Int. Conf. High Temperature Capillarity*, Smolenice Castle, 8–11 May 1994, ed. N. Eustathopoulos (Reprint, Bratislava, 1995), pp. 330–334.
- [Pech 2004] Pech J., Braccini M., Mortensen A., Eustathopoulos N., *Mater. Sci. Eng. A* **384** (2004) 117–128.
- [Pech 2005] Pech J., Berthomé G., Jeymond M., Eustathopoulos N., *Glass Sci. Technol.* **78** (2005) 54–62.
- [Pet'kov 1993] Pet'kov I.S., Red'kin B.S., *J. Cryst. Growth* **131** (1993) 598.
- [Roussopoulos 2004] Roussopoulos G., Rubini P., *J. Crystal Growth* **271** (2004) 333.
- [Saiz 1998] Saiz E., Tomsia A.P., Cannon R.M., *Acta Mater.* **46** (1998) 2349–2361.
- [Sangiorgi 1995] Sangiorgi R., Muolo M.L., Eustathopoulos N., *Proc. 1st Int. Conf. High Temperature Capillarity*, Smolenice Castle, 8–11 May 1994, ed. N. Eustathopoulos (Reprint, Bratislava, 1995), pp. 148–154.
- [Santos 1996] Santos M.T., Marin C., Diéguez E., *J. Cryst. Growth* **160** (1996) 283.
- [Satunkin 1980] Satunkin G.A., Tatartchenko V.A., Shaitanov V.I., *J. Cryst. Growth* **50** (1980) 133.
- [Satunkin 1986] Satunkin G.A., Red'kin B.S., Kurlov V.N., Rossolenko S.N., Tatartchenko V.A., Tufin Yu.A., *Cryst. Res. Technol.* **21** (1986) 995.
- [Satunkin 2003] Satunkin G.A., *J. Cryst. Growth* **255** (2003) 170.
- [Schultz 2001] Schultz W.W., Grae Worster M., Anderson D.M., In: *Interactive Dynamics of Convection and Solidification*, ed. P. Ehrhard, D.S. Riley, P.H. Steen, Kluwer, Dordrecht (2001), pp. 209–226.
- [Shashkov 1965] Shashkov Yu. M., Mel'nikov E.V., *Russ. J. Phys. Chem.* **39** (10) (1965) 1364.
- [Shetty 1990a] Shetty R., Balasubramanian R., Wilcox W. R., *J. Cryst. Growth* **100** (1990) 51–57.
- [Shetty 1990b] Shetty R., Balasubramanian R., Wilcox W. R., *J. Cryst. Growth* **100** (1990) 58–62.
- [Shi 1980] Shi Z.J., He Z.G., Ying C.F., *Ultrasonics* **18** (1980) 57–60.
- [Shimizu 2002] Shimizu A., Nishizawa J., Oyama Y., Suto K., *J. Cryst. Growth* **237–239** (2002) 1697–1700.
- [Shuttleworth 1950] Shuttleworth R., *Proc. Phys. Soc.* **A63** (1950) 444–457.
- [Smith 1948] Smith C.S., *Trans. AIME* **175** (1948) 15–51.
- [Surek 1975] Surek T., Chalmers B., *J. Cryst. Growth* **29** (1975) 1.
- [Surek 1976] Surek T., *Scripta Met.* **10** (1976) 425.
- [Tanaka 1996] Tanaka T., Hack K., Iida T., Hara S., *Z. Metallkd.* **87** (1996) 380–389.
- [Tatarchenko 1977] Tatarchenko V.A., Satunkin G.A., *J. Cryst. Growth* **37**(3) (1977) 285.
- [Tegetmeier 1996] Tegetmeier A., Cröll A., Danilewsky A., Benz K.W., *J. Cryst. Growth* **166** (1996) 651.

- [Towers 1954] Towers H., *Br. Ceram. Soc. Trans.* **53** (1954) 180–202.
- [Vaidya 2006] Vaidya N., Huang H., Liang D., *Comm. Comp. Phys.* **1** (3) (2006) 511.
- [Van den Bogaert 1996] Van den Bogaert N., Dupret F., *J. Cryst. Growth* **166** (1996) 446.
- [Virozub 2008] Virozub A., Rasin I.G., Brandon S., *J. Cryst. Growth* **310** (2008) 5416.
- [Voronkov 1963] Voronkov V.V., *Fizika Tverdogo Tela* **5** (2) (1963) 571 (in Russian; English translation *Sov. Phys. Solid State* **5** (2) (1963) 415).
- [Voronkov 1974] Voronkov V.V., *Krystallografiya* **19** (1974) 922 (in Russian; English translation *Sov. Phys. Crystallogr* **19** (5) (1975) 573).
- [Voronkov 1975] Voronkov V.V., Pankov V.M., *Krystallografiya* **20** (1975) 1145 (in Russian; English translation *Sov. Phys. Crystallogr* **20** (6) (1975) 697).
- [Voronkov 1978] Voronkov V.V., *Krystallografiya* **23** (1978) 249 (in Russian; English translation *Sov. Phys. Crystallogr.* **23** (2) (1978) 137).
- [Voronkov 1980] Voronkov V.V., *Izv. Akad. Nauk. SSSR, Ser. Fiz.* **44** (2) (1980) 226 (in Russian).
- [Voronkov 1981] Voronkov V.V., *J. Cryst. Growth* **52** (1981) 311.
- [Weinstein 2004] Weinstein O., Brandon S., *J. Cryst. Growth* **268** (2004) 299.
- [Wenzel 1936] Wenzel R.N., *Ind. Eng. Chem.* **28** (1936) 988–994.
- [Wenzl 1976] Wenzl H., Fattah A., Uelhoff W., *J. Cryst. Growth* **36** (1976) 319.
- [Wenzl 1978] Wenzl H., Fattah A., Gustin D., Mihelcic M., Uelhoff W., *J. Cryst. Growth* **43** (1978) 607.
- [Wery 2008] Wery S., PhD thesis, Université de Perpignan, France (2008) (in French).
- [Yasuda 1990] Yasuda K., Iwakami Y., Saji M., *J. Cryst. Growth* **99** (1990) 727–730.
- [Yeckel 2005] Yeckel A., Derby J.J., In: *Bulk Crystal Growth of Electronic, Optical and Optoelectronic Materials*, ed. P. Capper, John Wiley & Sons Ltd., Chichester (2005) pp. 73–119.
- [Young 1805] Young T., *Phil. Trans. R. Soc. Lond.* **94** (1805) 65–87.
- [Yuan 2004] Yuan Z., Huang W.L., Mukai K., *Appl. Phys. A* **78** (2004) 617–622.
- [Yuferev 2005] Yuferev V.S., Krymov V.M., Kuandykov L.L., Bakholdin S.I., Nosov Yu.G., Shulpina I.L., Antonov P.I., *J. Cryst. Growth* **275** (2005) e785.

2

The Possibility of Shape Stability in Capillary Crystal Growth and Practical Realization of Shaped Crystals

Vitali A. Tatartchenko
Saint-Gobain Crystal

As mentioned in Chapter 1, capillary crystal growth techniques have many advantages compared with crucible techniques. The main one is the absence of defect formation as a result of the contact with the crucible walls during solidification. In addition, however, crystals of specified shape and size (shaped crystals) with controlled defect and impurity structure can be grown with these techniques. Since the 1950s several hundreds of papers and patents concerned with shaped growth by crucible-free techniques have been published. This chapter does not try to enumerate the cases of successful application of shaped growth to different materials but to carry out a fundamental mathematical analysis of shaping as well as peculiarities of shaped crystal structures. Four main techniques, where the lateral surface of the crystal is shaped without any contact with container walls, are analysed here: the Czochralski (Cz) technique, the Verneuil technique, the floating zone (FZ) technique and the technique of pulling from shaper (TPS). Modifications of these techniques are also analysed. In all these techniques the shape of the melt meniscus is controlled by the forces of the surface tension – these are capillary forces, so they are classified as capillary shaping techniques (CST). For successful use, the crystal growth process in each of the CST has to be *dynamically stable*. In this case, all process perturbations attenuate and a crystal of constant cross-section is grown without any special regulation.

Dynamic stability theory of the crystal growth process for all CST is developed on the basis of Liapunov's dynamic stability theory. Liapunov's equations for the crystal growth processes come from fundamental laws. The results of the stability analysis allow us to choose stable regimes of crystal growth for all CST as well as special designs of shapers in the TPS. The experiments of shaped crystal growth by Cz, Verneuil and FZ techniques are discussed, but the main consideration is given to TPS and the history of the TPS is also described. Shapers allow us not only to grow crystals of very complicated cross-section but to provide special distributions of impurities. The crystal growth of silicon, and some other materials, including crystal growth in space, are briefly discussed. More technical details can be found in Chapter 5.

2.1 Crucible-Free Crystal Growth – Capillary Shaping Techniques

Modern engineering makes much use of components fabricated from crystals, mainly in the shape of plates, rods or tubes although sometimes the shapes can be more complicated. Traditional methods of fabrication (growth of a bulk crystal and its machining) incur a loss of expensive material (often up to 90%) as well as the appearance of structure defects. Crystals of specified shape and size with controlled defect and impurity structure are therefore desirable; they can be used as final products with minimal additional machining, if any.

The problem of shaped crystal growth seems to be simply solved by profiled container crystallization, just as in the case of casting. Indeed, it is possible to find a realization of this idea by the vertical or horizontal Bridgman techniques for growth of silicon, sapphire, fluorides and YAG as well as other crystals with crucibles of different cross-sections (see, for instance [Bagdasarov 1977], [Petrova 1990], [Horowitz 1993]). But these techniques have many disadvantages, mentioned in Chapter 6 of this book. The main problem is that the crucible material must satisfy certain requirements – it should neither react with the melt nor be wetted by it. Even if all these requirements are fulfilled, the growth of perfect crystals is not assured: the crucible serves as a source of uncontrolled nucleation as well as internal residual stresses. In addition, if the crucible material is wetted by the melt, the crucible should be made from a thin foil and used only once.

The techniques of crystal lateral surface shaping without contact with the container walls therefore have to be considered as candidates for shaped crystal growth. Since the late 1950s, both the theoretical and practical aspects of shaped crystal growth by these techniques have been developed and published in books and reviews [Antonov 1981, Tatartchenko 1988, 1993, 1994-1, 2001-1, 2001-2, 2005], in the proceedings of three international conferences [Cullen 1980, Kalejs 1987, 1990], in the thirteen published proceedings of Russian national workshops [Voinova 1968, Antonov 1969, 1971, 1972, 1976, 1979, 1982, 1983, 1985, 1989, 1994, 1999, 2004] and in hundreds of papers.

The few 'classical' techniques of this type are well known: the Cz technique (Figure 2.1), the Verneuil technique (Figure 2.2) and the FZ technique (Figure 2.3). For all these

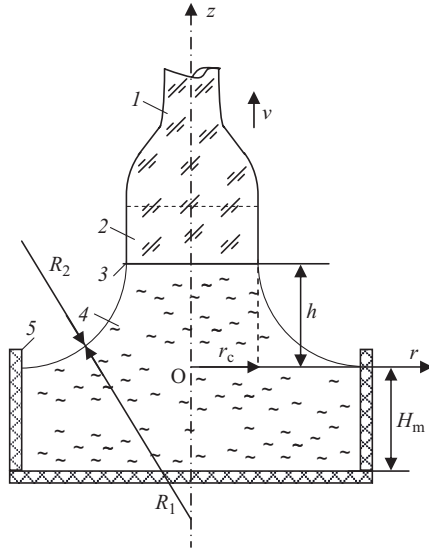


Figure 2.1 Crystal growth by the Czochralski technique (Cz). 1, seed; 2, crystal; 3, crystallization front; 4, melt; 5, crucible; r_c , crystal radius; h , crystallization front height; v , crystal pulling rate; H_m , melt level in the crucible; zOr , nondimensional coordinate system; R_1 and R_2 , main radii of liquid surface curvature.

techniques, the shapes and the dimensions of the grown crystals are controlled by the shapes and the dimensions of the melt meniscus existing at the vicinity of the crystal–melt interface. The shape of the meniscus is controlled by the surface tension forces of the melt – capillary forces. The above-mentioned techniques (some ‘nonclassical’ ones will be added later) are classified as capillary shaping techniques (CST). As a rule, all these techniques are used to grow crystals of irregular shape, but all of them have been used for shaped crystal growth as well. For shaped crystal growth it is necessary to guarantee a special shape for the melt meniscus and dynamical stability of the crystal growth process. But in any case, all of the above-mentioned techniques allow us to obtain only simple shaped crystals (cylinders, plates or tubes) and have to be modified to allow growth of more complicated shapes. The ‘classical’ Kyropoulos technique also belongs to the CST category, but the problem of stability for this technique is in fact a very specific one (discussed in section 2.3.4 below); in addition, the Kyropoulos technique has never been used for growth of shaped crystals.

Some variants of ‘classical’ CST are shown in Figure 2.4. All of them are characterized by the presence of a shaper. The schemes in Figure 2.4a–e, h, i may be classified as modified Cz techniques; and they differ from the standard Cz technique by the presence of a shaper in the melt. The schemes in Figure 2.4f, g, j may be classified as modified FZ techniques with lowering, where the melting rod is replaced by a shaper with the melt inside. The scheme in Figure 2.4k may be classified as a modified Verneuil technique where the melt layer is augmented by using a shaper with the melt inside.

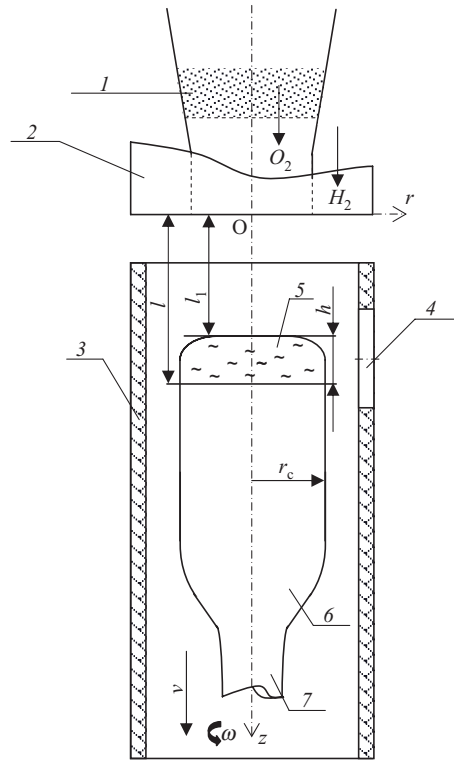


Figure 2.2 Cylindrical crystal growth by the Verneuil technique. 1, powder stock bin; 2, burner, H_2 , hydrogen flow, O_2 , mixed oxygen and powder flow; 3, furnace thermal insulation; 4, peep-hole; 5, melt layer; 6, crystal; 7, seed; r_c , crystal radius; l_1 , melt surface position relative to the burner; l , crystallization front position relative to the burner; $h = l - l_1$, melt meniscus height; zOr , coordinate system; v , crystal displacement rate; ω , crystal rotation rate.

2.2 Dynamic Stability of Crystallization – the Basis of Shaped Crystal Growth by CST

As the crystal is not restricted by crucible walls, its cross-section depends on the growth regime. Any deviations of the rate of pulling or lowering (for downward growth), as well as heat transfer field, result in changes of the crystal cross-section (pinch formation). Many defects (increased amount of inclusions, nonuniform impurity distributions, sub-grain formation) are observed at the pinch locations. It is not the pinches themselves that seem to cause defect formation, but some deviation from optimal growth conditions (mainly the crystallization rate), indicated by a change in the crystal dimensions. Therefore, stabilization of the crystal cross-section and of the position of the crystallization front has to be achieved. Why is the stabilization of the position of the crystallization front so important? We can see from the CST schemes shown in Figure 2.1 that if the position of

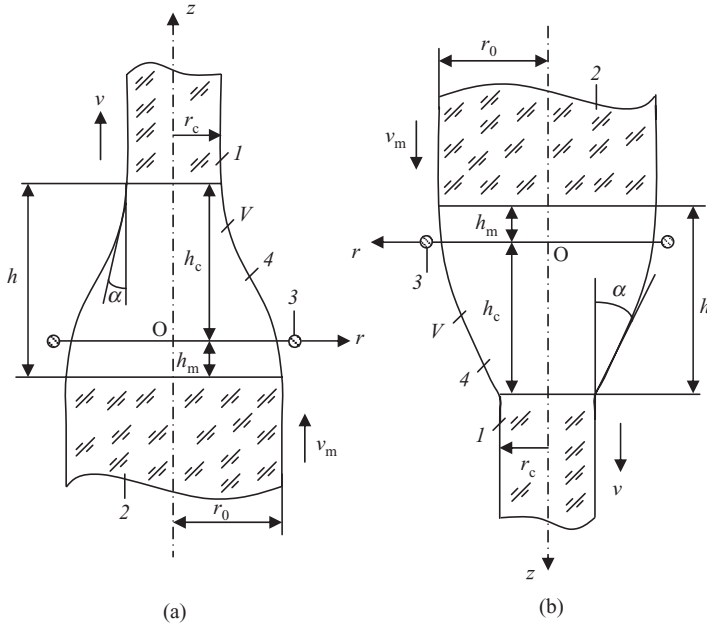


Figure 2.3 Cylindrical crystal growth by the FZ technique: (a) pulling up; (b) lowering). 1, growing crystal with radius r_c ; 2, feeding rod with radius r_0 ; 3, heater; 4, melted zone; h_c , h_m , positions of crystallization front and melting front relative to the heater, respectively; $h = h_c + h_m$, length of the melted zone, V , volume of the melted zone, α , growth angle; v , rate of growing crystal displacement relative to the induction heater; v_m , the same for feeding rod.

the crystallization front is stationary, the crystal growth rate is exactly equal to the speed of pulling or lowering the seed. A displacement of the crystallization front position changes the real crystal growth speed – see Equation (2.10) below. As a result, in spite of stabilization of the pulling or lowering speed, there is defect formation.

The modern systems of control using weight or crystal diameter detectors make it possible to obtain cylindrical crystals by CST. These systems act on a change of heating power or of pulling rate. Sometimes the regulation is not stable, and there is a permanent perturbation of the crystallization front position. The solution is to analyse theoretically the dynamic stability of practical configurations of crystal growth and to select the stable ones on the basis of this analysis. In a dynamically stable system, the perturbations of parameters attenuate because of internal processes and without any additional active regulation; it is possible to provide crystals of specified shape and controlled cross-section. If an active regulator is included in the system under investigation, this dynamically stable system can improve the shape and quality of crystals.

A comparative theoretical analysis of the dynamic stability of the crystallization process for the Cz technique and TPS was carried out for the first time by the present author in 1971 [Tatartchenko 1973-1]. This explains why it is difficult to pull crystals of constant cross-section by the Cz technique but easy by TPS: the use of a shaper permits dynamic

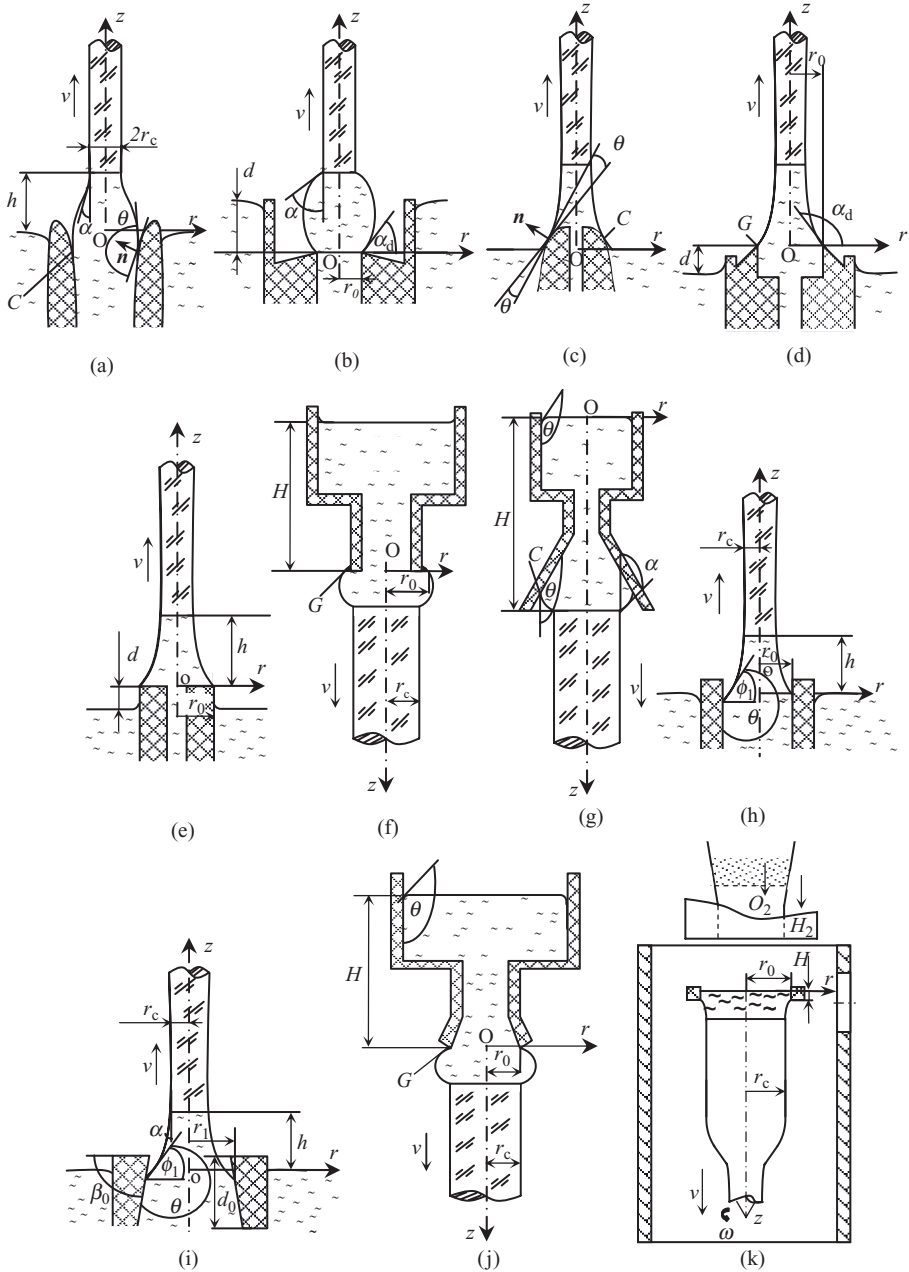


Figure 2.4 TPS melt growth of crystalline rod with shapers: pulling up (a–e, h, i) or lowering (f, g, j, k) with rate v ; shaping on the shaper surfaces (a, c, g–i); shaping on the shaper edges (b, d–f, j, k); positive melt pressure of value d (b, f, g, j, k), negative melt pressure of value d (d, e), undetermined melt pressure (a, c, h, i), fixed point (G) and nonfixed point (C) of contact of the meniscus with the shaper, \mathbf{n} , normal vector to the shaper wall, d_0 , shaper depth, r_c , crystal radius; r_0 , edge contour radius, h , crystallization front height, θ , wetting angle, α , growth angle, α_d , meniscus inclination angle with respect to positive r direction at the point of contact with the shaper, $\alpha_1 = \pi - \alpha_d$, β , angle of cone shaper wall inclination, r_1 , cone radius on the melt free surface level.

capillary stability (see below) of the crystal growth process to be obtained. The first paper on the investigation of dynamic stability in the Verneuil technique was published in the same year [Tatartchenko 1973-2]. The investigation of stability in the Cz, TPS, Verneuil and FZ techniques was presented at the 4th International Conference on Crystal Growth in Japan [Tatartchenko 1974]. The detailed analysis of capillary and heat stability using Lyapunov's approach was published for the first time in [Tatartchenko 1976]. In 1976, T. Surek published a paper on capillary stability analysis only [Surek 1976] repeating the main results for the Cz technique and TPS [Tatartchenko 1973-1, 1974], but without any reference to these papers.

2.2.1 Lyapunov Equations

The main results of stability analysis for all CST [Tatartchenko 1976-1, 1977-1, 1987, 1988, 1991, 1993, 1994-1, 1994-2, 1997, 2000, 2001-1, 2005] were obtained by application of the Lyapunov approach [Korn 1961]. In this approach, the crystallization techniques under consideration are characterized by a finite number, n , of variables (degrees of freedom), X_i , which can be arbitrarily varied in the process of crystallization. Each CST has to include, as a minimum, crystal dimension r_c and crystallization front position h as degrees of freedom, i.e. the minimum number of degrees of freedom, $\min n$, is 2. Depending on the configuration, this may be sufficient for the dynamic stability analysis (see Figure 2.1 for the Cz technique and Figure 2.4 for TPS). But for the Verneuil technique, $\min n = 3$ (Figure 2.2): r_c, l, h ; and for the FZ technique, $\min n = 4$ (Figure 2.3): r_c, V, h_c, h_m . In addition, $\min n$ depends on the cross-section of the crystal to be grown. For instance, for a tube crystal, the internal diameter and the external diameter are both degrees of freedom and therefore $\min n = 3$ for Cz tube pulling and for TPS of tubes.

If n exceeds $\min n$, the analysis is more fruitful. Sometimes several iterations can be used. The first iteration can include the stability investigation for $\min n$. After that, one or more variables can be added. For instance, in [Tatartchenko 1993 pp. 71–145], the stability of TPS as a system with $\min n$ was investigated. As a second step ([Tatartchenko 1993 pp. 155–9]), the melt pressure was added as a third degree of freedom and complementary information concerning the influence of pressure perturbation on the stability of growth was obtained. So, $n \geq \min n = 2$, but there is no simple way of choosing n ; in every case, it has been the result of specific investigations.

To carry out a mathematical analysis of stability, a set of equations (2.1) for derivation of each degree of freedom X_i with respect to time t as a function of all n degrees of freedom X_1, \dots, X_n , their $n - 1$ derivatives (except i), time t , and parameters of process C (temperature of the melt, pulling velocity, cooling regime, etc.) must be obtained:

$$\frac{dX_i}{dt} = f_i \left(X_1, X_2, \dots, X_n, \frac{dX_1}{dt}, \frac{dX_2}{dt}, \dots, \frac{dX_{n-1}}{dt}, t, C \right), \quad i = 1, 2, \dots, n. \quad (2.1)$$

To find the explicit function f_i , a set of fundamental physical laws has to be used. This set could include (among others):

- the Navier–Stokes equation for the melt with the boundary conditions on the meniscus free surface (Laplace's capillary equation);

- the continuity equation (law of crystallizing substance mass conservation);
- the heat transfer equations for the liquid and the solid phases with the equations of heat balance at the crystallization front and at the melting front as boundary conditions (law of energy conservation);
- the diffusion equation (impurity mass conservation);
- the growth angle existence condition.

This set of equations is general for all the crystallization techniques under consideration (but it does not mean that all of them are used in each case), while the specific features of each crystallization configuration are characterized by the set of boundary conditions and concrete values of the parameters included in the equations.

Equation (2.1) with zero left-hand side corresponds to the system under conditions of equilibrium ($X_i = X_i^0$): growth of crystal of constant cross-section X_1^0 with stationary crystallization front position X_2^0 , etc.

$$f_i(X_1^0, X_2^0, \dots, X_n^0, t, C) = 0. \quad (2.2)$$

Stable solutions of Equation (2.1) are sought. According to Lyapunov [Korn 1961] the solutions of (2.1) are stable if they are stable for the linearized set of equations:

$$\delta \dot{X}_i = \sum_{k=1}^n \frac{\partial f_i}{\partial X_k} \cdot \delta X_k = \sum_{k=1}^n A_{ik} \cdot \delta X_k \quad (2.3)$$

Here $\delta X_k = X_k - X_k^0$, $\partial f_i / \partial X_k = A_{ik}$, and all partial derivatives are taken with $X_k = X_k^0$.

The stability of (2.3), in turn, is observed when all the roots S of the characteristic equation (2.4):

$$\det \left(\frac{\partial f_i}{\partial X_k} - S \delta_{ik} \right) = 0 \quad (2.4)$$

have negative real components (δ_{ik} is the Kronecker delta [Korn 1961]). The equilibrium is unstable if (2.4) has at least one root with a positive real component. If an imaginary number is found among the roots, additional investigation including a consideration of the nonlinear terms in (2.3) is required.

Calculation of the time-dependent nonstationary functions f_i is usually rather difficult. These difficulties can be avoided using a quasi-stationary approach. This approach has been used successfully in the most of the CST dynamic stability investigations and in other cases. For instance, Mullins and Sekerka [Mullins 1964] applied it to the temperature and impurity distribution problem while studying the morphological stability of the crystallization-front shape. However, in each particular case, the quasi-stationary approach has to be justified.

A number of constraints imposed on the systems and on the perturbations occurring in the course of the Lyapunov stability study should be noted. Stability is examined over an infinitely long period of time. In this case, the perturbations are considered to be small and are imposed only on the initial conditions: the same forces and energy sources affect the system after the perturbations as before.

2.2.2 Capillary Problem – Common Approach

2.2.2.1 Melt Meniscus Shaping Conditions

For CST, the crystal cross-section is determined by the melt meniscus section formed by the crystallization surface. The melt meniscus shape can be calculated on the basis of the Navier–Stocks equation, the Laplace capillary equation being the free-surface boundary condition.

The complete solution of this problem poses considerable mathematical difficulties. To simplify formulation of the problem, the contributions of various factors to meniscus shaping should therefore be estimated: the inertial forces associated with the melt flow, capillary forces, gravitational forces, viscous and thermocapillary forces [Tatartchenko 1987, 1993]. The relative effect of the first three factors can be estimated by means of dimensionless numbers:

- the *Weber number* $We = \rho_l u^2 L / \gamma_v$, characterizing comparative action of the inertial and capillary forces;
- the *Froude number* $Fr = u / (gL)^{1/2}$, characterizing comparative action of the inertial and gravity forces;
- the *Bond number* $Bo = \rho g L^2 / \gamma_v$, characterizing comparative action of the gravity and capillary forces.

Here ρ_l denotes the liquid density, L the liquid meniscus characteristic dimensions, γ_v the liquid surface tension coefficient, u the liquid flow rate, and g is the acceleration due to gravity.

When the Weber and Froude numbers are small, the melt flow can be neglected. The Bond number defines the region of capillary or gravity force predominance (Figure 2.5).

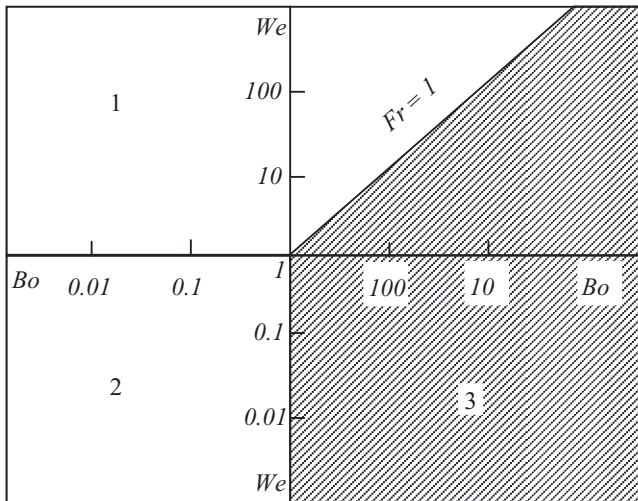


Figure 2.5 Inertial (1), capillary (2), and gravitational (3) force effects on the melt column shaping (We , Bo , Fr are the characteristic Weber, Bond and Froud numbers, respectively) (Reprinted with permission from [Tatartchenko 1987], copyright (1987) Elsevier Ltd).

If the liquid flow rate is considered to be of the order of the crystallization rate, the effect of the inertial force as compared to the gravity and capillary forces proves to be negligible. Indeed, if the linear dimensions of the meniscus lie within the range of 10^{-3} – 10^{-2} m, $\rho_l \cong 10^3 \text{ kg m}^{-3}$ and $\gamma_{lv} \cong 1 \text{ N m}^{-1}$, the liquid meniscus shaping can be investigated using the hydrostatic approximation up to fluid speeds of 0.1 – 1.0 ms^{-1} .

Convective flows, whose rates can substantially exceed the crystallization rate, can occur in a liquid column in addition to the flow associated with crystallization. This flow has effects on meniscus shaping and on liquid-phase heat transfer [Tatartchenko 1993].

2.2.2.2 *Meniscus Surface Equation*

In the hydrostatic approximation, the equilibrium shape of the liquid surface is described by the Laplace capillary equation [Landau 1971]:

$$\frac{\gamma_{lv}}{R_1} + \frac{\gamma_{lv}}{R_2} + \rho_l g \tilde{z} = \text{const.} \quad (2.5)$$

Here R_1 and R_2 denote the main radii of liquid surface curvature, which must be located in two perpendicular planes. As a rule, one of the planes coincides with the plane of the diagram (R_2 in Figure 2.1) and the second one is perpendicular to it (R_1 in Figure 2.1). The \tilde{z} -axis is directed vertically upwards. The value of the constant depends on the selection of the origin of the \tilde{z} -coordinate and is equal to the difference between the pressure p in the liquid at $\tilde{z} = 0$ and the pressure of the gas p_v . In particular, if the \tilde{z} -coordinate origin coincides with the plane of the liquid surface, the constant is equal to zero (Figure 2.1).

In this chapter our study is restricted to a meniscus possessing axial symmetry (Figures 2.1–2.4). Such a meniscus is obtained during melt pulling of a straight circular cylinder, or a tube-shaped crystal. The equation of such a meniscus surface is found by introducing the cylindrical coordinates \tilde{z} , \tilde{r} . The problem of calculating the shape of the liquid meniscus for an axially symmetric meniscus is reduced to finding the shape of a profile curve $\tilde{z} = f(\tilde{r})$. The liquid surface meniscus for cylindrical or tubular crystals is obtained by rotating the profile curve around the \tilde{z} -axis.

Equation (2.5) is also appropriate for the flat part of a ribbon if $R_1 \rightarrow \infty$. In this case, the profile curve $\tilde{z} = f(\tilde{r})$ is the equation of its meniscus. This equation will also be used for growing large-diameter crystals.

Now let us introduce the capillary constant, a , and move on to the dimensionless coordinates and parameters:

$$(2\gamma_{lv}/\rho_l g)^{1/2} = a, \quad \tilde{z}/a = z, \quad \tilde{r}/a = r, \quad p \cdot a/(2\gamma_{lv}) = d.$$

Now the capillary constant serves as the unit of linear dimension, and the weight of the melt column of the height a corresponds to unit pressure. This approach allows the results to be applied to any substance and any magnitude of gravity, with a simple scale change. Then, after calculation of the radii of curvature, (2.5) takes the form:

$$z''r + z'(1 + z'^2) + 2(d - z)(1 + z'^2)^{3/2} \quad r = 0, \text{ if } z' < 0 \quad (2.6a)$$

$$z''r + z'(1 + z'^2) - 2(d - z)(1 + z'^2)^{3/2} \quad r = 0, \text{ if } z' > 0. \quad (2.6b)$$

For large Bond numbers ($Bo \gg 1$, Figure 2.5), gravity prevails and (2.6) can be simplified:

$$z''r \pm 2(d-z)(1+z'^2)^{3/2} \quad r = 0. \quad (2.7)$$

This condition corresponds to $R_1 \rightarrow \infty$. As mentioned above, Equation (2.7) can be applied to the flat part of ribbon growth and the growth of large-diameter crystals with $r_c \geq 5a$.

For small Bond numbers ($Bo \ll 1$, Figure 2.5), capillarity prevails (this condition corresponds to growing small-diameter crystals ($r_c < a$) and is also easily satisfied in TPS experiments on space stations [Tatartchenko 1993] where the capillary constant is high) and (2.6) can also be simplified:

$$z''r + z'(1+z'^2) \pm 2d(1+z'^2)^{3/2} \quad r = 0. \quad (2.8)$$

Static stability of the melt meniscus, as well as the dynamic stability of the crystal growth process, should apply. Static stability means that the melt meniscus exists for all values of crystallization parameters. A stability analysis can be carried out by a method based on Jacobi's equation. For the TPS, this analysis was realized in [Tatartchenko 1993, 1997, 2000].

2.2.2.3 Growth Angle Existence – Common Boundary Condition for CST

As the Laplace capillary equation is a second-order differential equation, the formulation of the boundary problem for calculating melt meniscus shape requires the assignment of two boundary conditions. The first of these is determined by the geometry of each specific CST and will be analysed in detail below, but the second boundary condition (the crystal–melt interface condition) is common to all CST. This condition follows from the existence of the growth angle.

The growth angle α (Figures 2.3, 2.4a, b) is the angle between the line tangent to the meniscus and the lateral surface of the growing crystal. It is discussed in detail in Chapter 1 of this book and should not be confused with the wetting angle, which characterizes particular equilibrium relative to the liquid movement along a solid body and is not directly associated with crystallization [Tatartchenko 1993]. In the earliest studies of the Cz technique and TPS, a crystal of constant cross-section was considered to grow in the case $\alpha = 0$. Judging by a purely geometric diagram of the liquid–solid phase conjugation, this assumption is quite natural. However, experimental and theoretical investigations of the crystal growth process showed that the geometrical condition $\alpha = 0$ is not satisfied while growing crystals of constant cross-sections, and α is a physical characteristic of the melt–crystal system. The particular case $\alpha = 0$ occurs only for some metals. Experimental determinations of α have included direct measurements as well as indirect calculations. The indirect techniques are more precise, as a rule [Tatartchenko 1993]. In [Satunkin 1980, Tatartchenko 1993], shapes of crystallized drops were studied, obtained on the bottom of Si, Ge and InSb crystals detached from the melts at the end of pulling by the Cz technique. Values of $\alpha = 25^\circ \pm 1^\circ$ for InSb, $\alpha = 11^\circ \pm 1^\circ$ for Si, and $\alpha = 12^\circ \pm 1^\circ$ for Ge were obtained. The problem is discussed in detail in section 1.3 of

this book, where it is shown in particular that α is an anisotropic value as well as depending on the crystallization speed. In this chapter, for the dynamic stability analysis, the value of α will be considered as a constant for the crystal to be grown.

2.2.3 Equation of Crystal Dimension Change Rate

From the growth angle boundary condition, an equation for the crystal characteristic dimension change rate, $\partial r_c / \partial t$, common to all CST, is obtained. In Figure 2.6 a vector \mathbf{r}_c is located within the diagram plane and represents the radius of a straight circular cylinder-shaped crystal. For a plate it is its half-thickness. Now we introduce the angles made by the line tangent to the meniscus on the three-phase line with the horizontal, ϕ_0 , and with the vertical, α_0 (the crystal grows in the vertical direction). When the angles ϕ_0 and α add up to $\pi/2$, a crystal of constant cross-section, r_c^0 , grows. In this case, the angle α_0 is equal to the growth angle α and the value of the angle ϕ_0 is denoted by ϕ_c . If $\alpha_0 \neq \alpha$ the crystal lateral surface declines from the vertical on the angle $\alpha - \alpha_0 = \phi_0 - \phi_c = \delta\phi_0$, the crystal changes its dimension, $\delta r_c = r_c - r_c^0$, in accordance with the equation (Figure 2.6):

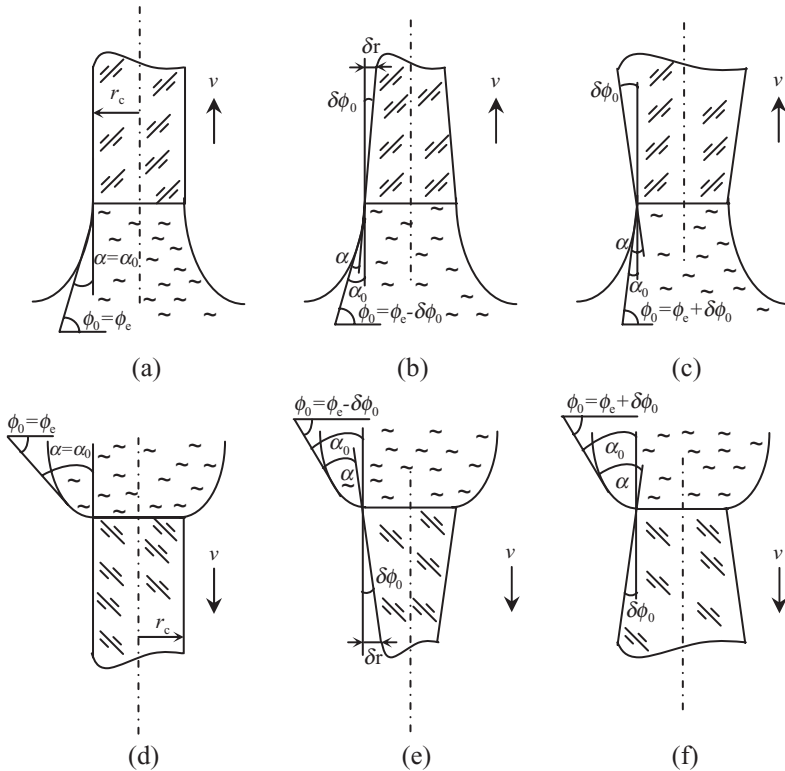


Figure 2.6 Crystal growth by CST: pulling up (a–c); lowering (d–f); $\phi_0 = \phi_c$, growth of a crystal with constant cross-section (a, d); $\phi_0 < \phi_c$, growth of a widening crystal (b, e); $\phi_0 > \phi_c$, growth of a narrowing crystal (c, f); v is the crystal displacement rate; other symbols as in the text.

$$\delta \dot{r}_c = v_c \tan(\delta \phi_0) = v_c \tan(\phi_0 - \phi_c). \quad (2.9)$$

The angle $\delta \phi_0$ is the angle of crystal tapering at any moment, and the crystallization rate v_c is equal to the difference in rates between pulling and displacement of the front:

$$v_c = v - dh/dt. \quad (2.10)$$

Near the stationary state ($r_c = r_c^0$, $h = h^0$), that we need for (2.3), deviations dh/dt as well as $\delta \phi_0$ have to be negligible. Hence, the crystallization rate v_c can be replaced by the rate of pulling v and $\tan(\delta \phi_0) \approx \delta \phi_0$. The angle ϕ_0 , together with the meniscus shape as a function of r_c , h and other parameters, can be determined by solving the capillary boundary problem whose equation was discussed above. Assuming that the capillary problem is solved, i.e. the function $\phi_0(X_1^0, X_2^0, \dots, X_n^0, t, C) = 0$ is found, Equation (2.9) can be written as:

$$\delta \dot{r}_c = v \sum_{k=1}^n \partial \phi_0 / \partial X_k \cdot \delta X_k = \sum_{k=1}^n A_{ik} \cdot \delta X_k. \quad (2.11)$$

2.2.4 Equation of Crystallization Front Displacement Rate

The equation of the crystallization front displacement rate belongs to the set (2.3) and, like (2.11), is common to all CST. It follows from the heat-balance condition on the crystallization front:

$$-\lambda_s G_s(h) + \lambda_l G_l(h) = \zeta v_c \quad (2.12)$$

Here λ_s and λ_l denote thermal conductivities of the solid and liquid phases respectively, $G_s(h)$ and $G_l(h)$ are the temperature gradients in the solid and liquid phases at the crystallization front, h is the crystallization front position, ζ denotes the latent heat of melting per unit volume of material and v_c is the crystallization rate. In accordance with (2.10), we obtain a (2.1)-type equation for dh/dt :

$$dh/dt = v - \zeta^{-1} (\lambda_l G_l(h) - \lambda_s G_s(h)). \quad (2.13)$$

The corresponding (2.3)-type equation is:

$$\delta \dot{h} = \zeta^{-1} \sum_{k=1}^n [\lambda_s (\partial G_s / \partial X_k) - \lambda_l (\partial G_l / \partial X_k)] \delta X_k. \quad (2.14)$$

Now the functions $G_s(h)$ and $G_l(h)$ have to be found, which can be done by solving the Stefan problem – a nonstationary thermal conductivity problem with the solid–liquid interface as a heat source.

2.2.5 Stability Analysis in a System with Two Degrees of Freedom

If only the crystal radius r_c and the crystallization front position h are regarded as variable parameters, Equations (2.11) and (2.14) have the following form:

$$\delta \dot{r}_c = A_{rr} \delta r_c + A_{rh} \delta h \quad (2.15)$$

$$\delta \dot{h} = A_{hr} \delta r_c + A_{hh} \delta h \quad (2.16)$$

with

$$A_{rr} = -v(\partial \phi_0 / \partial r_c);$$

$$A_{rh} = -v(\partial \phi_0 / \partial h);$$

$$A_{hr} = \zeta^{-1} [\lambda_s (\partial G_s / \partial r_c) - \lambda_l (\partial G_l / \partial r_c)];$$

$$A_{hh} = \zeta^{-1} [\lambda_s (\partial G_s / \partial h) - \lambda_l (\partial G_l / \partial h)].$$

The solutions of the set of equations (2.15), (2.16) are:

$$\delta r_c = C_1 \exp(S_1 t) + C_2 \exp(S_2 t), \quad (2.17)$$

$$\delta h = C_3 \exp(S_1 t) + C_4 \exp(S_2 t). \quad (2.18)$$

Here S_1 and S_2 are the roots of the characteristic equation (2.4), which for this case is:

$$S^2 - (A_{rr} + A_{hh})S + (A_{rr}A_{hh} - A_{rh}A_{hr}) = 0. \quad (2.19)$$

To estimate the stability of the set of equations (2.15) and (2.16) there is no need to solve the equations themselves: the Routh–Hurwitz conditions [Korn 1961] can be used. The set (2.15) and (2.16) is stable if and only if the equation coefficients satisfy the following inequalities:

$$A_{rr} + A_{hh} < 0, \quad (2.20)$$

$$A_{rr}A_{hh} - A_{rh}A_{hr} > 0. \quad (2.21)$$

This type of stability is robust in the sense that the stability of the system remains unchanged within a wide range of values of the coefficients A_{ik} ($i, k = r, h$).

If at least one of the inequalities (2.20), (2.21) is replaced by an equality, the roots of the characteristic equation (2.19) are either imaginary or zero. In this case the system stability can not be judged from its linear approximation, and a nonlinear model must be used.

The coefficients A_{rr} and A_{hh} indicate direct correlation between $\partial r_c / \partial t$ and δr_c , as well as $\partial h / \partial t$ and δh , i.e. self-stability of the parameters. The coefficients A_{rh} and A_{hr} represent the effect of the change in one value on the rate of change of the other value, i.e. inter-stability of the parameters. It can be concluded from the analysis of (2.20) and (2.21) that the crystal growth system is stable if:

$$A_{rr} < 0, A_{hh} < 0, A_{rh}A_{hr} < 0, \quad (2.22)$$

$$A_{rr} < 0, A_{hh} < 0, A_{rh}A_{hr} > 0, |A_{rr}A_{hh}| > |A_{rh}A_{hr}|, \quad (2.23)$$

$$A_{rr} < 0, A_{hh} > 0, |A_{rr}| > |A_{hh}|, A_{rh}A_{hr} < 0, |A_{rr}A_{hh}| < |A_{rh}A_{hr}|, \quad (2.24)$$

$$A_{rr} > 0, A_{hh} < 0, |A_{rr}| < |A_{hh}|, A_{rh}A_{hr} < 0, |A_{rr}A_{hh}| < |A_{rh}A_{hr}|. \quad (2.25)$$

It can be seen that negative values of A_{rr} and A_{hh} are a very important condition for the stability of the crystal growth system. The following terminology will be used in what follows: there is *capillary stability* in the system if $A_{rr} < 0$ and there is *heat stability* if $A_{hh} < 0$.

2.3 Stability Analysis and Growth of Shaped Crystals by the Cz Technique

2.3.1 Capillary Problem

Solving the boundary capillary problem allows us to find the coefficients A_{rr} and A_{rh} . The problem is investigated in details in [Tatartchenko 1967, 1968, 1969-1, 1976-1, 1976-2, 1977-1, 1977-2, 1987, 1991, 1993, 1994-1, 1994-2, 1995, 1997, 2000]; only a few of the results are given here. The problem includes Equation (2.6) with $d = 0$ and two boundary conditions:

$$dz/dr|_{r=r_c} = -\tan\phi_0, \quad (2.26)$$

$$z|_{r \rightarrow \infty} = 0. \quad (2.27)$$

Because of the particular choice of origin we have $p(\bar{z} = 0) = p_v$ and $d = 0$.

The numerical solution of the boundary problem is given in Figure 2.7 and shows that:

$$A_{rr} > 0; A_{rr}|_{r \rightarrow \infty} \rightarrow 0, \quad (2.28)$$

$$A_{rh} < 0; A_{rh}|_{r \rightarrow \infty} \rightarrow \sim 4v. \quad (2.29)$$

For numerical calculation, the dimensionality of A_{ik} is s^{-1} ; all angles have to be measured in radians; the unit of length is the capillary constant a , and the speed of pulling is $a s^{-1}$.

2.3.2 Temperature Distribution in the Crystal–Melt System

Solving the boundary heat problem allows us to find the coefficients A_{hh} and A_{hr} . Much research has been devoted to calculation of the temperature field in the crystal–melt system. It forms a group of the Stefan problems in which the crystal–melt interface is a heat source. However, because of the variety of growth configurations and the presence

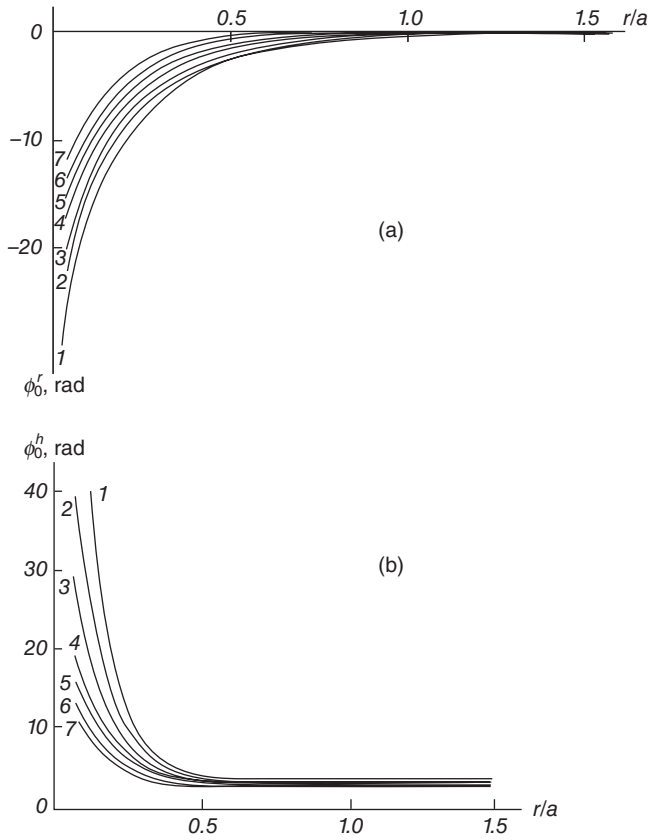


Figure 2.7 For the Cz technique (a) $(\partial\phi_0/\partial r_c) \cdot a$ (denoted by ϕ_0^r) and (b) $(\partial\phi_0/\partial h) \cdot a$ (denoted by ϕ_0^h) vs crystal radius for various values of the growth angles α : (1) -15° ; (2) -5° ; (3) 0° ; (4) 10° ; (5) 20° ; (6) 30° ; (7) 40° . The capillary constant, a , is used as a unit of all dimensions (Reprinted with permission from [Tatartchenko 1988], copyright (1988) Springer Science + Business Media).

of a great number of factors that have to be taken into account for the thermal conductivity problems (complex temperature dependence of the thermophysical properties of various materials, convective flows in the melt, etc.) a complete mathematical description of heat patterns during crystal growth is very difficult. Analytical solutions are usually achieved by significant simplifications. With this end in view, the following equation from [Carslaw 1959] allowing simple analytical solutions will be used to analyse the heat conditions in the crystallization process:

$$D_{th,i}^{-1} \partial T_i / \partial t = d^2 T_i / dz^2 - \nu k_i^{-1} dT_i / dz - \mu_i \lambda_i^{-1} F (T_i - T_a) \quad (2.30)$$

Here $i = 1, s$ ($i = 1$ for the liquid, $i = s$ for the solid body), T_i denotes the temperature, $D_{th,i}$ is the thermal diffusivity coefficient, z is the vertical coordinate, μ_i denotes the coefficient of heat exchange with the environment, F denotes the crystal perimeter to area

ratio at the interface, T_a is the ambient temperature and λ_i is the thermal conductivity coefficient.

Equation (2.30) has a few peculiarities:

- It describes the temperature distribution of the crystal–melt system in a one-dimensional approximation that means that the temperature in the crystal (meniscus) cross-section is averaged and isotherms are flat.
- The heat exchange with the environment is described not as boundary conditions but by introducing heat losses on the lateral surface in the form of an additional term in the equation.
- It gives a good description of real temperature distribution for small Biot numbers ($Bi = \mu_i r_c \lambda_i^{-1} \ll 1$) – this is the case during growth of crystals of small diameter or wall thickness, for low coefficients of convective heat transfer from the crystal (melt) surface, and for high thermal conductivities.
- Heat exchange is described by the Newtonian law, which means that the convective heat exchange is much higher than the heat losses caused by radiation (the heat losses caused by free convection are comparable to the heat losses caused by radiation for a surface temperature up to 1000 °C and even higher in the case where the crystal surface is cooled by forced convection).
- The equation is not applicable to refractory materials pulled under vacuum; radiation heat exchange (the Stefan–Boltzmann law) must be used, which leads to considerable nonlinearity of the problem. In this case a linearization of the crystal-surface radiation law described in [Tatartchenko 1993] can be applied that allows the use of Equation (2.30) for temperatures up to 2000 °C.

In section 2.2.1 we discussed the possibility of using a quasi-stationary approximation, according to which temperature distribution in the crystal–melt system at any moment of time satisfies the stationary thermal conductivity equation with instantaneous values of all the process parameters. For this approximation to be applied, the time for relaxation of the crystallization front to the stationary state should be significantly longer than the characteristic of temperature relaxation time. As a rule, this condition is satisfied [Tatartchenko 1993]. Thus, Equation (2.30) with zero left-hand side can be used for the calculation of G_s and G_l .

As an example of the calculation of A_{hh} and A_{hr} , consider the growth of a long crystal (the limiting case is continuous pulling), with good thermal screening of the melt column. So, Equation (2.30) is used with zero left-hand side for the crystal as well as for the melt meniscus with $\mu_l = 0$. The boundary conditions of the problem are the following:

- The melt temperature at the bottom of the liquid column at the level of the melt free surface is fixed: $T_l|_{z=0} = T_0$.
- The crystallization-front temperature is equal to the melting temperature T_m : $T_l|_{z=h} = T_s|_{z=h} = T_m$.
- The temperature of the end of the crystal is equal to the ambient temperature: $T_s|_{z \rightarrow \infty} = T_a$.

The solution of Equation (2.30) with these boundary conditions (the solution for other boundary conditions can be found in [Tatartchenko 1993]) allows us to obtain A_{hh} and A_{hr} :

$$A_{hh} = -\zeta^{-1} \lambda_1 h^{-2} (T_0 - T_m), \tag{2.31}$$

$$A_{hr} = \zeta^{-1} \mu_s r_c^{-2} \zeta_s^{-1} (T_m - T_a), \text{ where } \zeta_s = \left(\frac{1}{4} v^2 k_s^{-2} + 2 \mu_s \lambda_s^{-2} r_c^{-1} \right)^{1/2}. \tag{2.32}$$

So, based on the solution of the capillary and heat boundary problems, the signs and the values of the growth stability coefficients for the Cz technique are found. If the melt is superheated ($T_0 > T_m$), the signs are as follows: $A_{rr} > 0$; $A_{rh} < 0$; $A_{hr} > 0$; $A_{hh} < 0$.

2.3.3 Stability Analysis and Shaped Crystal Growth

2.3.3.1 Capillary Stability

First we introduce the notion of capillary stability. Consider the case where a change in crystal dimensions and crystallization front position does not lead to a change in liquid- and solid-phase temperature gradients at the crystallization front. In this case, the system stability can be provided only by capillary effects (capillary stability). In practice, a crystallization system with one degree of freedom is considered in this case and the set of equations (2.3) describing stability reduces to the simple relation $\partial r_c / \partial t = A_{rr} \delta r_c$. A necessary and sufficient condition to attain capillary stability is $A_{rr} < 0$. In this case, any crystal dimension perturbation will attenuate.

The positive value of the coefficient A_{rr} found in section 2.3.1 is indicative of the absence of capillary stability during crystal pulling by the Cz technique. This is illustrated in Figure 2.8. Let the point A characterizes constant-diameter crystal growth ($\phi_0 = \phi_c$). An arbitrary change in the crystal dimensions (upward tapering A' , downward tapering

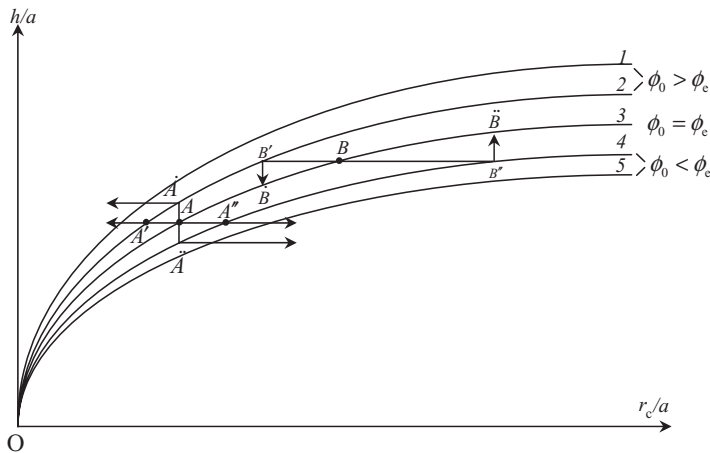


Figure 2.8 Heights of profile curves vs crystal radius for various growth angles α : (1) -10° ; (2) 0° ; (3) 10° ; (4) 20° ; (5) 30° . A, scheme of capillary instability; B, scheme of thermal stability. (Reprinted with permission from [Tatartchenko 1988], copyright (1988) Springer Science + Business Media).

A''), or in the position of the crystallization front (rise \dot{A} , fall \dot{A}), will cause a change in the angle ϕ_0 such that it will lead to further crystal tapering according to Figure 2.6.

2.3.3.2 Stability Analysis

On the basis of the two previous sections, it can be concluded that for the Cz technique:

- Capillary stability is absent for all crystal diameters.
- Heat stability can be realized.
- There is a possibility of satisfying the conditions (2.25) and to have a stable crystal growth if the following two inequalities can be fulfilled:

$$|\partial\phi_0/\partial r_c| < \lambda_1 v^{-1} \zeta^{-1} h^{-2} (T_0 - T_m), \quad (2.33)$$

$$|\partial\phi_0/\partial r_c| < |\partial\phi_0/\partial h| h^2 \mu_s r_c^{-2} \lambda_1^{-1} \zeta_s^{-1} (T_m - T_a)(T_0 - T_m)^{-1}. \quad (2.34)$$

In this case, a change in crystal dimension (points B' or B'' in Figure 2.8) results in a change in the position of the crystallization front (points \dot{B} and \ddot{B} in Figure 2.8) such that it provides growth of a crystal with slightly changed dimensions, with the liquid–solid phase conjunction angle equal to the growth angle. In practice this means that a constant crystal of cross-section with an immovable interface position can be grown if the diameter of the crystal is bigger than the melt capillary constant and if the melt is superheated, i.e. high thermal gradients are applied. If the crystal has a smaller diameter, superheating has to be greater and a special combination of the crystal growth process parameters has to hold, given by the inequalities (2.33) and (2.34).

2.3.3.3 Shaped Crystal Growth

Our experience of the Cz technique crystal growth without any special diameter regulation as well as the growth of cylindrical crystals of Ag [Bachmann 1970] and of large-diameter Si tubes [Alioshin 1990] confirms the conclusions of the above analysis. The necessity of very good stabilization of the pulling speed must be mentioned: it has been shown [Tatartchenko 1967] that even a stable system cannot compensate for a sudden change of speed, and pinch formation is the result. The problem of control in the Cz technique is discussed in detail in Chapter 3, where technical solutions are given.

2.3.4 Dynamic Stability Problem for the Kyropoulos Technique

It was mentioned earlier that the ‘classical’ Kyropoulos technique also belongs to CST and is formally very similar to the Cz technique. But, in fact, the problem of crystal growth in dynamically stable regimes is a very specific one for the Kyropoulos technique. As already explained, crystal growth using CST in stable regimes makes it possible to eliminate the appearance of defects, especially in the case of crystallization speed perturbations. On the other hand, the condition (2.33) shows that much superheating and, as a result, large temperature gradients near the interface, is one of the necessary conditions for stable growth by the Cz technique. This means that the generation of defects

(especially dislocations) resulting from the large temperature gradients is very probable during crystal growth by the Cz technique in stable regimes. The Kyropoulos technique differs from the Cz technique by using very low temperature gradients and consequent annealing of crystals in the same growth zone. As a result, there is no dynamically stable growth in the Kyropoulos technique and it has never been used for shaped growth. Thus, to choose whether the Cz shaped growth technique or the Kyropoulos technique is preferable for a specific material it is necessary to compare them from this point of view. Such a comparison is made for sapphire in the review [Tatartchenko 2005], for example.

2.4 Stability Analysis and Growth of Shaped Crystals by the Verneuil Technique

2.4.1 Principal Schemes of Growth

Figure 2.2 illustrates the Verneuil crystal growth technique. A fine powder of the material from which the crystal is to be grown is fed into a burner with an oxy-hydrogen flame. The powder melts, partially or completely, forming a melt layer on the surface of the seed crystal. The powder must be extremely fine, with particle size 1–20 μm . The crystal grows by consecutive melt crystallization as a result of downward pulling of the crystal toward the colder zone.

Until the middle of the 20th century this technique was used mainly to grow precious gemstones (corundum, i.e. ruby and sapphire) 20mm in diameter. Alumina powder is used for corundum crystals grown by the Verneuil technique. The pure aluminium oxide is α -alumina. Different degrees of hydration give β -alumina, γ -alumina, and so on. For instance, γ -alumina is $5\text{Al}_2\text{O}_3 \cdot \text{H}_2\text{O}$. Both α - and γ -alumina can be used for crystal growth. A widely used process for powder fabrication includes purification of alum ($\text{KAl}(\text{SO}_4)_2 \cdot 12\text{H}_2\text{O}$) by recrystallization and decomposition of the alum to α - or γ -alumina by heating. The optimal temperature of heating to obtain α -alumina is 1000 °C.

The equipment (see Figure 2.2) was originally very simple because of the absence of any special requirement for crystal quality, but the use of ruby crystals in lasers changed the situation dramatically. It was necessary to increase the crystal dimensions and to improve the crystal quality. This was achieved by modifying the equipment on the basis of theoretical investigation of the crystal growth process. Modern furnaces for the Verneuil technique include several oxygen and hydrogen channels for more homogeneous burning of the hydrogen, preliminary heating of the gases, special heating of the furnace, thermal insulation and automatic growth regulation.

It is clear why the Verneuil technique has been the most widespread technique for production of laser elements. Its main advantage is the absence of a crucible and, as a result, absence of contamination of the crystal by the crucible material. In addition, the Verneuil technique can be used for growth of crystalline plates with large surface area. Several modifications of the classical configuration (Figure 2.2) were used for this purpose. Some patents are cited in our review [Tatartchenko 2005]: using rotation of the seed crystal around a horizontal axis made it possible to obtain a single crystal sapphire disc with an area up to 180 cm^2 ; reciprocating motion of the seeding crystal in relation to

the gas burner enabled the production of plates about 70 cm² in size; a split burner model was used to grow plate-shaped crystals up to 240 cm². In our experience all these techniques have had major problems with crystals cracking because of internal tension due to periodic changes of temperature for each crystal volume and inhomogeneous temperature distribution in the growth zone. There are versions of the Verneuil technique using plasma, laser radiation and Ir resistive heating, but they do not have a wide application. In an unpublished technique, combined ruby–sapphire crystals have been grown for a laser application: ruby crystals with sapphire ends. This only requires changing the feed from doped to undoped powder.

2.4.2 Theoretical Investigation

In the early 1970s, our attention was drawn to the experimental fact that it is easy to grow small-diameter corundum crystals (~5 mm); they are grown especially as seed crystals. In practice, the growth regime required no correction by an operator. The crystals had smooth surfaces and cylindrical shapes. This stimulated our investigation of dynamic stability in the Verneuil technique. As mentioned above, for cylindrical crystals, the analysis should be carried out with three degrees of freedom (Figure 2.2): (i) r_c , the crystal radius; (ii) l , the crystallization front position relative to the burner; (iii) $h = l - l_1$, the melt meniscus height, where l_1 is the melt surface position relative to the burner.

In the present case the linearized set of equations (2.3) defined from the Lyapunov criteria of growth process stability takes the following form:

$$\delta \dot{r}_c = A_{rr} \delta r_c + A_{rh} \delta h + A_{rl} \delta l, \quad (2.35)$$

$$\delta \dot{h} = A_{hr} \delta r_c + A_{hh} \delta h + A_{hl} \delta l, \quad (2.36)$$

$$\delta \dot{l} = A_{lr} \delta r_c + A_{lh} \delta h + A_{ll} \delta l. \quad (2.37)$$

The explicit form of the coefficients of the system must now be found.

2.4.2.1 Determination of the Coefficients A_{rr} , A_{rh} , A_{rl}

Comparison of Equations (2.35) and (2.11) gives:

$$A_{rr} = -v(\partial \phi_0 / \partial r_c); A_{rh} = -v(\partial \phi_0 / \partial h); A_{rl} = -v(\partial \phi_0 / \partial l). \quad (2.38)$$

$A_{rl} = 0$ as the meniscus shape and the angle ϕ_0 do not explicitly depend on the position of the liquid–gas interface. The functional relation between the angle ϕ_0 , the crystal radius r_c , and the meniscus height h is defined from the Laplace capillary equation (2.6).

The specificity of the capillary shaping by the Verneuil technique appears in the following way:

- The line tangent to the melt surface is horizontal at the peak point of the melted layer (Figure 2.9):

$$dz/dr|_{r=0} = 0. \quad (2.39)$$

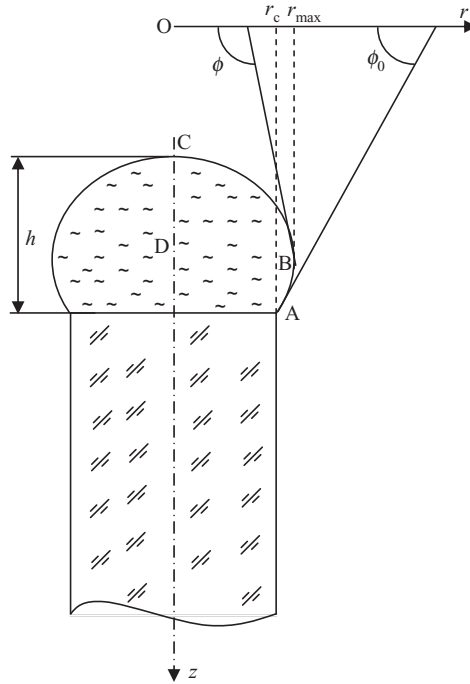


Figure 2.9 Capillary shaping for the Verneuil technique (see text for explanation) (Reprinted with permission from [Tatartchenko 1988], copyright (1988) Springer Science + Business Media).

- The second boundary condition is specified at the solid–liquid interface and follows from the condition of growth angle existence:

$$dz/dr|_{r=r_c} = -\tan\phi_0 \quad (2.40)$$

- The shape of the melt zone is obtained by rotation of the profile curve AC around the z -axis. The curve AC consists of two portions, AB and BC. Each of them is described by the proper differential form of the Laplace capillary equations (2.6a) and (2.6b).
- The maximum radius of the melted layer cross-section BD is denoted by r_{\max} in Figure 2.9. The point B is selected in such a way that the line tangent to it is vertical. At point B:

$$dz/dr|_{r=r_m} = \infty. \quad (2.41)$$

In the usual case the Laplace equation (2.6) is not solvable by quadrature and numerical calculation is required. However, a semiquantitative solution of the problem can be estimated in the following way. For the meniscus with $r_c < a$ and $r_c > a$, analytical solutions can be obtained (here r_c is the dimensional crystal radius). Then by joining the functions and their derivatives at the point $r_c = a$, a common solution can be obtained.

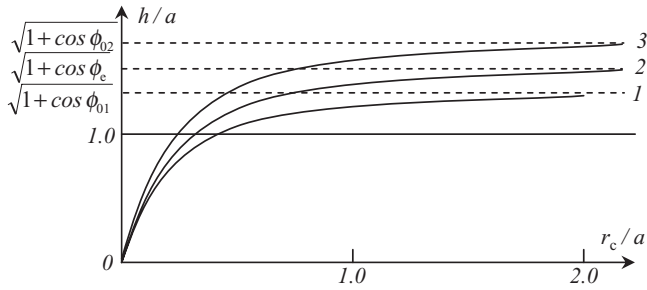


Figure 2.10 Nondimensional melt meniscus height h/a vs crystal radius r_c/a for various angles ϕ_0 : $\phi_{01} > \phi_e > \phi_{02}$ (Reprinted with permission from [Tatarchenko 1988], copyright (1988) Springer Science + Business Media).

Small Bond Number ($r_c < a$). First, the case where the crystal radius is considerably smaller than the capillary constant will be discussed. Then the melt weight in the Laplace equation (2.6) can be disregarded; it takes the form (2.8). The function describing the shape of curve AB satisfies the equation

$$z'' = -r^{-1}(1 + z'^2)^{3/2} (\sin \phi - 2dr) \tag{2.42}$$

with the boundary conditions (2.40) and (2.41). For curve BC, this equation takes the form

$$z'' = r^{-1}(1 + z'^2)^{3/2} (\sin \phi - 2dr) \tag{2.43}$$

with the boundary conditions (2.39) and (2.41).

The meniscus height h can be obtained as a result of mutual solution of these boundary condition problems (Figure 2.10, range $r_c < a$):

$$h = r_c(1 + \cos \phi_0)(\sin \phi_0)^{-1}. \tag{2.44}$$

Large Bond Number ($r_c > a$). Secondly, the case where the crystal radius is considerably bigger than the capillary constant will be discussed. Then the Laplace equation takes the form (2.7) with boundary conditions (2.39)–(2.41). The meniscus height h proves to tend asymptotically to the value $(1 + \cos \phi_0)^{1/2}$ with increasing r_c (Figure 2.10, range $r_c > a$). In this approach the greatest deviation from the true relation $h(r_c)$ is observed in the vicinity of the point $r_c/a = 1$, however it allows us to avoid the difficulties of the numerical methods and provides a qualitative representation of the relation behaviour (Figure 2.10).

The capillary coefficients for the first case have the following forms:

$$A_{rr} = -v(\partial \phi_0 / \partial r_c) = -vr_c^{-1} \sin \phi_0 < 0, \tag{2.45}$$

$$A_{hh} = -v(\partial \phi_0 / \partial h) = -vr_c^{-1} \sin \phi_0 (1 + \cos \phi_0)^{-1} > 0. \tag{2.46}$$

For the second case:

$$A_{rr} < 0; A_{rr}|_{r \rightarrow \infty} \rightarrow 0^-, \quad (2.47)$$

$$A_{rh} > 0; A_{rh}|_{r \rightarrow \infty} \rightarrow v(1 + \cos \phi_0)^{1/2} (\sin \phi_0)^{-1}. \quad (2.48)$$

Thus, formally, $A_{rr} < 0$ for all ranges of crystal dimensions and the Verneuil technique possesses capillary stability. But its effect on the crystal growth is very important only for small crystal diameters, where the value of A_{rr} is large. For large crystal dimensions, the influence of capillary effects on dynamic stability is insignificant: $A_{rr}|_{r \rightarrow \infty} \rightarrow 0^-$.

2.4.2.2 Determination of the Coefficients A_{lr} , A_{lh} , A_{ll}

The coefficients A_{lr} , A_{lh} , A_{ll} can be found from mass-balance conditions in the powder–crystal–melt system, which can be represented in the following form:

$$W_0 = \pi \rho_s r_c^2 (v - dl_1/dt) + \pi \rho_l r_c^2 (dl_1/dt - dl/dt). \quad (2.49)$$

Here W_0 is the charge mass fed into the melted layer per unit time, and ρ_s and ρ_l are solid- and liquid-phase densities, respectively. The first term on the right-hand side of (2.49) denotes the substance mass crystallizing per unit time, while the second component is the change in mass of the melted layer. Assuming that $\rho_s = \rho_l = \rho$, for simplicity, gives:

$$dl/dt = -W_0 (\pi \rho r_c^2)^{-1} + v \quad (2.50)$$

Linearization of (2.50) gives:

$$\partial l / \partial t = 2W_0 (\pi \rho r_c^3)^{-1} \delta r_c \quad (2.51)$$

Comparing this equation with (2.37) we obtain:

$$A_{lr} = 2W_0 (\pi \rho r_c^3)^{-1} > 0, A_{lh} = 0, A_{ll} = 0.$$

When calculating the coefficient A_{lr} , the charge-mass distribution in the falling flow was assumed to be localized close to the z -axis (Figure 2.11, curve 1), and with changing crystal radius the amount of substance fed to the melt remains unchanged. In a real situation the charge-mass distribution in the flow along the muffle cross-section in the crystallization area depends on a number of factors (in particular, on the design of the equipment used – Figure 2.11, curves 2–4) and the mass of substance fed into the melt per unit time depends on the crystal diameter:

$$W_0 = 2\pi\beta \int_0^{r_c} F(r) dr, \quad (2.52)$$

where β denotes the coefficient of mass flow rate prescribed by the feeder. Substitution of Equation (2.52) into Equation (2.50) and subsequent linearization gives

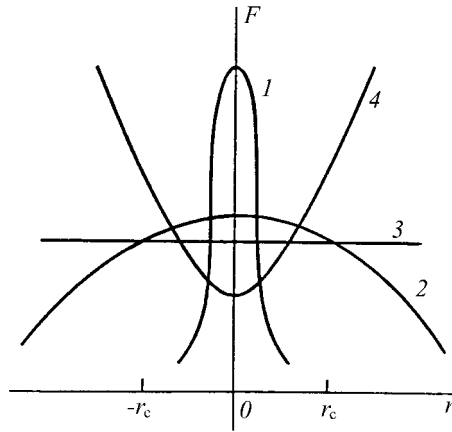


Figure 2.11 Function $F(r)$ of the charge distribution in the gas flow depending on the burner design (see text for details) (Reprinted with permission from [Tatartchenko 1988], copyright (1988) Springer Science + Business Media).

$$A_{lr} = \beta r_c^{-3} \left(2 \int_0^{r_c} F(r) dr - r_c^2 F(r_c) \right). \quad (2.53)$$

Possible forms of the function $F(r)$ are shown in Figure 2.11. If $F(r) = \text{const}$ then $A_{lr} = 0$. It is obvious that if the function $F(r)$ reaches its extremum when $r = 0$ the sign of A_{lr} will not change with changing r_c . If the extremum is a minimum, $A_{lr} < 0$. Finally, when the charge is fed from the central nozzle of the burner (the most widely used case in practice) the maximum of the charge distribution in the flow lies in the centre of the burner muffle (curves 1, 2, Figure 2.11), therefore $A_{lr} > 0$.

2.4.2.3 Determination of the Coefficients A_{hb} , A_{hb} , A_{hl}

As usual, these coefficients have to be found as a result of the heat boundary problem solution for the crystal–melt system. First, we note some peculiarities of the heat problem formulation for the Verneuil technique and the main conclusions. When formulating the heat problem for crystal growth from melts, the melt temperature has been specified as the boundary condition (see section 2.3.2). This boundary condition for the Verneuil technique does not correspond to the real situation. Crystal displacement in the furnace muffle results in a temperature change on the melt surface. This is why the heat conditions of the technique under consideration will be defined through the density Q of the heat flow fed from the burner on to the surface of the melted layer. With the gas flow specified, the density of the heat flow Q depends on the distance between the burner and the level of the melt surface $Q(l)$. The function $Q(l)$ is determined by the burner design and the gas flow.

Space limitations in this chapter do not allow giving further details about the theoretical model. They can be found in [Tatartchenko 1988, 1993, 1994].

2.4.3 Practical Results of the Theoretical Analysis

2.4.3.1 Cylindrical Crystals

For the process to be stable the following three conditions have to be fulfilled:

- The diameter of the crystal, $2r_c$, has to be small ($r_c < a$). We can see that this result is opposite to the case of Cz technique.
- Variation of the heat flow density $Q(l)$ along the furnace muffle in the vicinity of the growth zone, at a distance of the order of r_c , should not exceed the latent heat of crystallization.
- The heat flow density value $Q(l)$ in the vicinity of the growth zone has to be decreased if the distance between the melt surface and the burner, l_1 , is increased.

The results of the theoretical investigation explain why growing corundum crystals of small diameters (~ 5 mm) is easy. They grow in the dynamically stable regime; this means that there are internal mechanisms for the attenuation of perturbations. Using our terminology, capillary stability exists for $r_c < a$ ($a = 6$ mm for sapphire melt).

In spite of the fact that capillary stable growth is impossible for cylindrical sapphire crystals with diameter more than 12 mm, the theoretical model allows us to minimize the crystallization process perturbations while growing large-diameter crystals. For this, the previous two conditions have to be fulfilled (evidently, without the crystal dimension limitation) and also:

- The temperature of the muffle wall has to be as high as possible.
- Irregularities of the density distribution of the charge flow falling on the melted layer have to be kept as small as possible.

These requirements for the crystallization conditions (classified as optimized conditions) are in good agreement with experimental results [Tatartchenko 1973-2, Romanova 1976]. In the experiments, rates of hydrogen and oxygen flow in a three-channel burner resulted in crystals with a larger diameter growing closer to the burner. This corresponds to an increase in heat-flow density when approaching the burner. Preheating the gas before feeding it into the burner and increasing the furnace muffle temperature were also used. As a rule, no parameter control was required to keep the cross-section of the crystal constant. Crystals grown under these conditions had a smoother surface and improved optical and structural characteristics. Figure 2.12 shows corundum crystals of 40 mm diameter, grown in 1972 without any automatic control by the present author with collaborators from the Leningrad State Optical Institute.

Several crystal growth experiments were carried out using a shaper (see Figure 2.4k). The advantage of this scheme is evident – it is possible to have a thicker melt layer and, as a result, better crystal quality. In addition, as will be shown below, this configuration shows capillary stability for all dimensions of grown crystals. On the other hand, the very important advantage of the Verneuil technique – the absence of a crucible – is lost. It is difficult to discuss the experimental results because no shaper material resistant to the hydrogen–oxygen flame was found; It was more or less usable, but contamination-free crystals were not obtained.

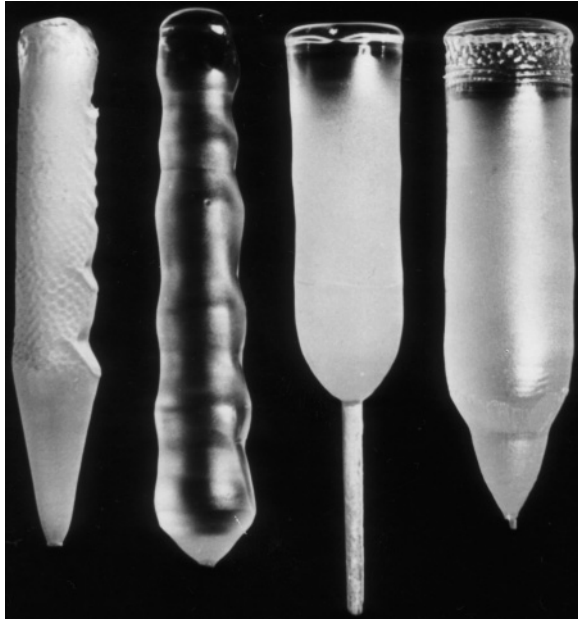


Figure 2.12 Corundum cylindrical crystals grown by the Verneuil technique in optimized (right) and nonoptimized (left) regimes (Reprinted with permission from [Tatartchenko 1988], copyright (1988) Springer Science + Business Media).

2.4.3.2 Tubular Crystals

The theoretical analysis [Tatartchenko 1988, 1993] states that crystallization of tubes of arbitrary outer diameters by the Verneuil technique is stable if the tube wall thickness is less than a critical value. This critical thickness is smaller than the capillary constant, a , and depends both on the heat conditions of the process and on the outer diameter of the tube. It increases as the outer diameter increases. In the experiments [Borodin 1982-2, Tatartchenko 1993] tubes with an outer diameter of 17–25 mm with walls 3–4 mm thick were grown (Figure 2.13). A crystallization apparatus fitted with a four-channel burner providing charge supply via the central and peripheral channels was used. The optimal gas distribution in the burner channels has been experimentally determined as oxygen–hydrogen–oxygen–hydrogen. Crystal growth was initiated from a seed 3–4 mm in diameter. First, a seed cone was grown. The cone was widened by feeding the charge through the central channel, the peripheral oxygen flow rate being increased. As soon as the crystal diameter reached the specified value (20–22 mm) the charge was additionally fed through the peripheral channel. A little later (10–15 min) the charge supply from the central tank was cut off, and the rate of the central oxygen flow was reduced within 30–60 min. This growth regime provided a smooth transition from a bulk crystal to a tube. The lowering rate was gradually increased and after that a stationary growth process continued. Tubes up to 120 mm long were grown. Usually no parameter control was required to keep the cross-section of the tube constant, i.e. the theoretically predicted stable growth conditions were attained. Figure 2.13 shows some of the tubes grown in 1981 by the present author



Figure 2.13 Six corundum single crystals (five tubes and one bulk cylindrical crystal, on the right) grown by the Verneuil technique in the same regime. (Reprinted with permission from [Tatartchenko 1993], copyright (1993) Springer).

with collaborators from the Solid State Institute of the Russian Academy of Science. Three of the tubes are cut (one of them along the axis, and two obliquely) to show the tube walls. For comparison, a cylindrical crystal of the same outer diameter, grown in the same furnace, is also shown. The irregular shape of the bulk crystal indicates that this regime is not optimal from the point of view of stability for the bulk crystal growth of this diameter. This corresponds to the theoretical prediction.

2.4.3.3 Plate-Shaped Crystals

The theoretical results are applicable for the growth of plate-shaped crystals: growth of crystal plates of less than two capillary constant thicknesses (12 mm for sapphire) is stable. Information of corundum crystal plate growth by the Verneuil technique can be found in the review [Tatartchenko 2005].

2.4.4 Stability Analysis-Based Automation

As shown above, crystallization stability is lost when crystal diameter exceeds two capillary constants. In practice this means that the crystallization front position and crystal dimensions change during the crystal growth process. In this case, an operator has to control the parameters by changing the gas rate, charge feed rate and crystal lowering rate using experience and intuition. An automatic control system provides better results. When developing crystal growth systems with automatic diameter control, the problem of finding the rules for automatic control of the process parameters versus changes in crystal dimensions arises. Before we carried out our investigations, the required rules of parameter control had been obtained as results of empirical trial and errors. Later they were defined on the basis of the crystal growth stability analysis [Borodin 1981, Tatartchenko 1988, 1993, 1994]. In this instance, controllable parameters should be added



Figure 2.14 Corundum crystals grown by the Verneuil technique with automatic regulation under stable (a) and unstable (b) laws of powder charge control.

to the crystal diameter, liquid–gas interface position and melt meniscus height as the degrees of freedom of the crystal growth process. For the Verneuil technique the density of the heat flow from the burner Q (which is regulated by changing the gas rate Π), the rate of crystal lowering ν and the powder charge flow rate \mathcal{P} can be used as controllable parameters. Usually, Π and \mathcal{P} are used as controllable parameters for the crystal widening stage. After the crystal has already widened from the seed dimension up to the desired diameter, the control is provided by regulation of \mathcal{P} only. In the theoretical approach, \mathcal{P} has to be regarded as an additional fourth degree of freedom for the cylindrical crystal. But the coefficients of the linear equation for \mathcal{P} are unknown; they have to be found from the necessary and sufficient conditions of the set of four stability equations of the same type as (2.3). The problem can have several solutions, each of which can be used as the regulation law for the control system. In this case the system of crystal growth, including the regulator, is stable. In [Borodin 1981, Tatartchenko 1988, 1993, 1994] three different \mathcal{P} change laws allowing stable growth were found. Figure 2.14 compares a corundum crystal grown with one of the stable laws of \mathcal{P} regulation to another crystal grown with a simple proportional control law. These crystals were grown in 1979 by the present author with collaborators from the Institute of Crystallography and Solid State Physics

Institute of the Russian Academy of Science. A standard industrial Verneuil furnace was used for the experiments. Comparing Figure 2.14 with Figure 2.12 shows that a furnace designed in agreement with optimized growth conditions, from the stability point of view, can provide the same crystal quality as an automatic control system (or even better).

2.5 Stability Analysis and Growth of Shaped Crystals by the FZ Technique

The FZ technique is described in detail in Chapter 4 of this book. It has been widely used for crystal growth of different materials, especially semiconductors (RF heating), high-melting metals and dielectrics (electron beam, plasma or laser heating and mirror furnaces). There are a lot of publications concerning the theoretical study of the FZ technique, but only two aspects have been the subject of investigation: the static meniscus stability, melt flows included, and impurity segregation. Only few papers have been devoted to the dynamic stability analysis, and [Surek 1976] was the first of them. However, this analysis is incomplete as the heat conditions of crystallization are not been taken into account and the capillary aspect of the problem has been simplified. As a result, in [Surek 1976], capillary stability was shown to exist in all versions of the FZ technique. Analysis based on Lyapunov's theory [Tatartchenko 1988, 1993, 1994] shows that this is not correct. The latter approach is more detailed and includes the following main points:

- A value of $\min n = 4$ was chosen (Figure 2.3).
- Pulling up as well as pulling down of the crystal, with different crystal/feed rod diameter ratios, was analysed.
- Equation (2.11) for $\delta\dot{r}_c$ was obtained as a result of the capillary boundary problem with the boundary condition of the growth angle on the crystallization front.
- It has been shown that the growth angle boundary condition does not apply at the melting front [Tatartchenko 1988, 1993].
- The equation for $\partial V/\partial t$ was obtained from the mass balance of melted and crystallized substances.
- Equation (2.14) for $\delta\dot{h}_c$ and $\delta\dot{h}_m$ were obtained as a result of the solution of Equation (2.30) near the crystallization front and near the melting front consequently.

The analysis of the results is rather complicated because four Routh–Hurwitz inequalities have to be satisfied simultaneously; see [Tatartchenko 1988, 1993]. The main conclusions are as follows:

- Capillary stability exists ($A_{rr} < 0$) for large diameters of the growing crystal and feed rod ($r_c > a$, $r_0 > a$) for all r_c/r_0 ratios.
- For small crystal and rod diameters ($r_c < a$, $r_0 < a$), $A_{rr} < 0$ if $r_c \geq 1/2r_0$.
- The largest negative value of the A_{rr} coefficient corresponds to $r_c = r_0$.
- Capillary stability exists for both directions of growth (up or down), but pulling downwards is preferable.

In terms of practical use of the FZ technique for shaped crystal growth, besides the widely prepared cylindrical rods, the ribbon-to ribbon (RTR) technique [Lesk 1976] has

to be mentioned. A sintered powder ribbon was used to feed a growing ribbon crystal. This method achieved silicon ribbons (for use in solar cells) of width 75 mm, thickness 0.1 mm, and $3\text{--}9\text{ cm min}^{-1}$ growth rate with use of laser heating.

2.6 TPS Techniques: Capillary Shaping and Impurity Distribution

In the beginning, TPS are analysed as a system with two degrees of freedom (r_c and h). Therefore, Equations (2.15)–(2.25) have to be used. The first step is the analysis of the melt-column shaping conditions in TPS.

2.6.1 Capillary Boundary Problem for TPS

For the axisymmetrical case, the Laplace capillary equations (2.6)–(2.8) will be used in the analysis. As mentioned above, each of them is a second-order differential equation and the boundary problem for the melt meniscus shape calculation strictly requires assignment of two boundary conditions. The first of these is (2.26), which is common to all CST, but the second one is determined by the structural features of each specific TPS. A shaper is used for melt-column shaping in the TPS (Figure 2.4). The functions of the shaper in the TPS are numerous, and will be discussed later. At the moment, the shaper is characterized only as a device to control the melt-column shape. This problem is a fundamental one for dynamic stability analysis of shaped crystal growth by the TPS and it will be discussed in detail. In a mathematical description of the problem, the shaper function determines the meniscus shape by imposing the second boundary condition of the capillary problem. The characterization of shapers from this point of view was first accomplished in 1967 [Tatartchenko 1968]. In most cases, the shaper (Figure 2.4h, i) is characterized by its wall or free edge curvature radius r_0 in the horizontal plane, and the angle β made by its wall with the horizontal. The wetting angle θ , formed by the melt and the shaper surface, is a very important shaper characteristic (Figure 2.4a, c, g, h, i). If this angle exceeds 90° , the shaper material is not wetted by the melt (Figure 2.4a, g, h, i); if it is smaller, the melt wets the shaper material (Figure 2.4c). Shaping is accomplished either on the surfaces of the shaper (Figure 2.4a, c, g–i) or on its sharp edges (Figure 2.4b, d–f, j, k). This corresponds to two different boundary conditions of the capillary boundary problem discussed in the following.

2.6.1.1 Catching Boundary Condition

In the case where the shaper material is wetted by the melt, the melt is easily caught by the sharp edges of the shaper. This boundary condition is therefore termed the *catching condition*. There is a possibility of providing catching conditions on nonwetable free edges of the shaper, which will be discussed below. The catching condition means that a contour line on the meniscus surface is fixed by the edge of the shaper, i.e. it coincides with the edge contour of the shaper. It does not matter whether the edge contour is concave (Figure 2.4b, d, j, k) or convex (Figure 2.4e, f), or whether the crystal is pulled up (Figure 2.4b, d, e) or down (Figure 2.4f, j, k). In the general case the shaper may not be flat, i.e.

the height of the catching point is not necessarily constant all around the shaper. If the coordinate plane coincides with the free level of the melt (Figure 2.4a, c, g, h, i, k) the catching condition has the following mathematical form in the cylindrical coordinate system:

$$z|_G = H(r, \varphi) \quad (2.54)$$

because in this case in the Laplace capillary equations (2.5)–(2.8) $\text{const} = d = 0$. Here G is the contour of the shaper edge and H is the distance from the shaper edge to the coordinate plane. If the shaper is flat and is positioned parallel to the melt plane, $H = \text{const}$. For axisymmetric flat shaper edges the condition (2.54) has the following form:

$$z|_{r=r_0} = \text{const} = H, \quad (2.55)$$

where r_0 is the contour radius of the shaper edge.

Thus, in this case, H defines the pressure of feeding the melt to the shaper, and it is included in the boundary condition. The nondimensional pressure H/a is denoted by d .

If the coordinate plane coincides with the shaper edge plane (Figure 2.4b, d–f, j) the right part of (2.55) is equal to zero and the pressure d is included in the Laplace capillary equations (2.5)–(2.8) as a parameter ($\text{const} = d$). If the pressure is positive, the shaper edges are positioned below the melt free-surface level, and vice versa.

2.6.1.2 Angle Fixation Boundary Condition (Wetting Condition)

If the melt contacts with the shaper surface, the angle it makes with the surface is the wetting angle, θ (Figure 2.4a, c, g–i). This boundary condition will be termed the *angle fixation condition* or *wetting condition*. It can be realized for nonwetable shaper materials (Figure 2.4a, g–i) as well as for wettable ones (Figure 2.4c), and for pulling up (Figure 2.4a, c, h, i) as well as for lowering (Figure 2.4g) shaped crystal growth. The condition means that the shaper fixes the meniscus angle on a line belonging to the shaper surface, where the angle of wetting is satisfied. The condition has the following forms:

- In the general case, where \mathbf{n} denotes the direction of the normal towards the shaper wall, C is the line of contact of the meniscus with the shaper walls:

$$\left[1 + (\partial z / \partial x)^2 + (\partial z / \partial y)^2 \right]^{-1/2} \partial z / \partial \mathbf{n}|_C = -\cos \theta. \quad (2.56)$$

Shapers with complicated surfaces (Figure 2.4a, c) can illustrate this condition although the figure shows the special case of the cylindrical symmetry system (z, r coordinates), whereas in the general case the use of a three-dimensional coordinate system is necessary.

- For an axisymmetrical problem (a rod or tube) on the vertical shaper walls (Figure 2.4h):

$$dz/dr|_{r=r_0} = -\tan(\theta - \pi/2) = -\tan \phi. \quad (2.57)$$

- For circular conical shaper walls with an angle β with the horizontal (Figure 2.4i):

$$dz/dr|_{r=\eta-z\cotan\beta} = -\tan(\theta + \beta - \pi/2) = -\tan\phi_1. \quad (2.58)$$

For the wetting boundary condition, the coordinate plane has to coincide with the free level of the melt (Figure 2.4a, c, h, i). In the Laplace capillary equation, $\text{const} = 0$. The position of the line of contact of the melt with the shaper surface will be found as a result of the boundary problem solution (to be discussed below).

2.6.1.3 Wetting-to-Catching Condition Transition

With the melt pressure increasing, the catching boundary condition on the nonwettable free edges of the shaper can be obtained. Figure 2.15a illustrates this transition with increasing the pressure by gradual immersion of the shaper into the melt. The diagram is based on a description [Adams 1941] of particle buoyancy conditions for flotation processes. A nonwettable shaper, with a hole of depth d_0 and vertical walls, is considered. The angle between the line tangent to the liquid surface and the shaper wall is denoted by χ . We can now analyse a number of successive positions of the shaper. In *position A*, the shaper touches the melt with its lower plane. The lower-plane immersion depth is equal to zero. The line tangent to the liquid surface coincides with the liquid surface. The angle χ is $\pi/2$. The catching condition holds at the lower free edge of the shaper. When the shaper is now immersed into the liquid, the angle χ increases, and when the shaper

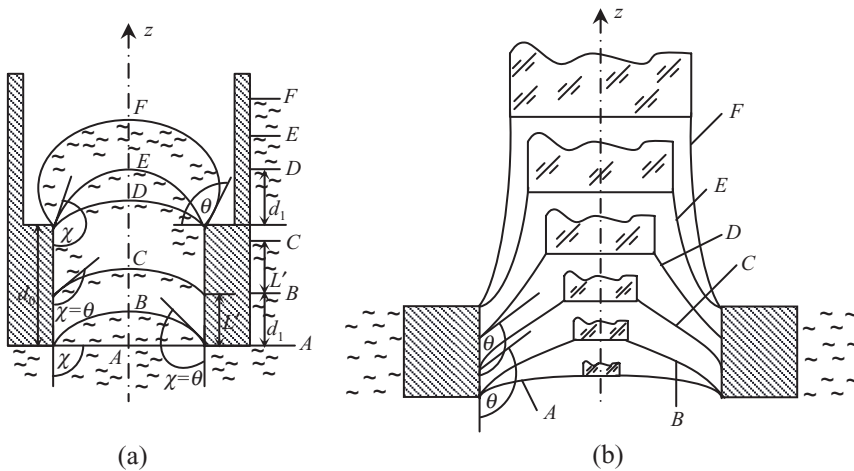


Figure 2.15 Transition of the shaper lower free-edge catching boundary condition (meniscus A) to the wetting condition (meniscus B, C, D) and further to the shaper upper free-edge catching condition (meniscus E, F). (a) Pressure changes (the external horizontal lines denote successive positions of the liquid free surface). (b) The seed-shaper dimension ratio changes; χ is the angle between the line tangent to the melt surface and the shaper wall, θ is the wetting angle. (Reprinted with permission from [Tatartchenko 1988], copyright (1988) Springer Science + Business Media).

lower plane reaches some depth d_1 , (*position B*) the angle χ will be equal to the wetting angle θ (within the immersion depth range from 0 to d_1 the catching condition holds at the lower free edge). With further shaper immersion into the liquid, χ remains equal to the wetting angle θ . The liquid–shaper wall contact line goes up by the value of L' , the shaper immersion depth, the distance between this line and the free surface level remaining equal to d_1 (*position C*). As soon as the immersion depth is equal to $d_0 + d_1$, the liquid–shaper contact line coincides with the sharp edge of the shaper (*position D*), and with further pressure increase, the catching condition at the upper free edge of the shaper holds (*position E*). In this case the angle χ will increase until the wetting angle θ is formed by the liquid and the shaper surface. For the horizontal shaper surface, $\chi = \pi/2 + \theta$ (*position F*). Further increase in pressure is not considered as it will lead to liquid spreading over the shaper surface and the shaper will not operate properly. But if the free edges of the shaper are really sharp (Figure 2.4b), pressure increase is possible up to the point where the static stability of the meniscus is lost.

The presence of a seed or a profiled crystal considerably changes the conditions of the transition described above. This means that the condition at the upper boundary (along the crystal–melt contact line) can affect the condition at the lower boundary (along the melt–shaper contact line). A diagram, which will be proved when solving the boundary problem, is shown in Figure 2.15b. By changing only the seed/shaper diameter ratio, the catching boundary condition at the lower free edge (meniscus A, B), the wetting condition on the shaper walls (meniscus C, D) and the catching boundary condition at the upper free edge (meniscus E, F) can be achieved. The very important conclusion is the following: the wetting boundary condition means that the angle χ is fixed but the line of contact of the meniscus with the shaper can move. Its position on the shaper walls depends on the melt pressure and on the crystal–shaper dimension ratio. Certainly, the melt pressure can be changed in any other way and the growth direction does not matter. For instance, by changing the melt pressure or the crystal–shaper edge dimension ratio, it is possible to get either the configuration Figure 2.4g or Figure 2.4j.

A comparison of the Figures 2.15a and 2.15b shows that there are two very different situations: before seeding and after seeding (during pulling). In the second case, even for nonwetable shaper walls, the meniscus changes its curvature, thus causing an internal negative pressure which raises the melt above the shaper edge, up to the crystallization front (the same situation exists in the Cz technique).

Later it will be shown that the catching boundary condition usually leads to a process that is more stable from the capillary point of view, so the ways of achieving the catching condition at the free edges of the shaper in the TPS should be specified:

- *First*, a melt-wetable material should be used for the shaper, and the latter should be designed in such a way that the melt can rise up to the free edges of the shaper as a result of capillary forces (Figure 2.4d–f).
- *Secondly*, for melt-nonwetable materials, the melt column should be under external pressure, providing additional pressure on the liquid to have the melt–shaper contact line at the sharp edge of the shaper (Figure 2.4b, j).
- *Thirdly*, for poorly wettable shaper materials, the crystal–shaper dimension ratio should be used in order to ensure contact of the melt column with the shaper sharp edges – compare Figures 2.4g and 2.4j.

2.6.1.4 Influence of Wetting-Angle Hysteresis on the Capillary Boundary Conditions

While analysing the capillary effects, the existence of wetting-angle hysteresis should be taken into consideration. The wetting angle hysteresis is discussed in Chapter 1. It reveals itself in the fact that the wetting angle of a liquid spreading onto a solid body is larger than for the same liquid receding from the surface of the solid body. This means that the stationary wetting angle depends on the process of meniscus formation (run-on or run-off). This results, for example, in the fact that a higher pressure has to be applied to create the catching condition at the free edge of the shaper than is required to keep it unchanged. In the case where the catching condition is created by the seed, this condition can remain unchanged in the growth process, although the gap between the free edge of the shaper and the growing crystal changes.

2.6.1.5 Comparison of the Catching Boundary Condition and the Angle Fixation Condition

The previous description of the transition from one to the other forms a basis for comparison. It shows that there is a big difference between these two boundary conditions. The catching condition fixes the coordinate of the end of the meniscus line, but the angle of inclination of the meniscus is not fixed. The wetting condition fixes the angle of inclination of the end of the meniscus at the contact line, but not its coordinate. In this case the meniscus is movable (Figure 2.15b). Its position on the shaper wall depends on the second boundary condition (seed or growing crystal presence, as well as the growing crystal dimensions and growth angle) and can be found as a result of the capillary boundary problem solution. So, for capillary shaping by walls, shaper design has to take account of this phenomenon as well as the wetting-angle hysteresis.

This difference needs to be explained carefully because there is considerable misunderstanding of this key problem in capillary shaping. Let's analyse some wrong approaches. In [Tsivinskii 1970] the idea from [Tsivinskii 1962] has been used for the solution of the boundary capillary problem. For the axisymmetrical meniscus described by the Laplace equation (2.5), Tsivinski *et al.* suggested replacing $1/R_2$ (Figure 2.1) by a linear function of the vertical coordinate. There are at least four mistakes in this approach (Figure 2.16):

- The axisymmetrical meniscus is applied for the growth of crystals with arbitrary cross-section.
- *A priori*, it is necessary to know if the meniscus is concave, convex or concave-convex.
- *A priori*, for a concave-convex meniscus, it is necessary to know the coordinates of the point of inflection.
- y_0 , α_0 and α_{01} (Figure 2.16) should be known. This is the worst mistake. Indeed, fixing these parameters means that three boundary conditions for the second-order differential equation should be used: fixation of the growth angle on the crystal-melt boundary and (in our terminology) the catching condition as well as the wetting boundary condition on the shaper. But this is nonsense. The authors' main argument is that this approach is applied for the Cz technique – there is a lot of experimental evidence for it. But the reason why the approach is applicable for the Cz technique is clear: the second

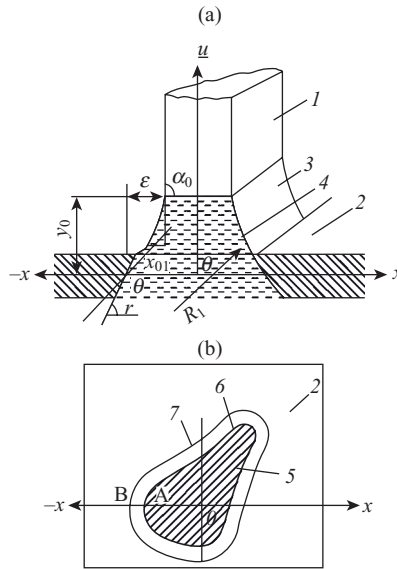


Figure 2.16 Arrangement for producing a crystal with cross-section of arbitrary form: (1) crystal; (2) shape former; (3) column of melt; (4) melt column profile curve; (5) cross-section of the crystal being pulled; (6, 7) contours of crystal cross-section and of opening in the shape former. Melt column parameters: y_0 represents the melt column height, α is the inclination of the profile curve tangent to the x-axis (α_0 at $y = 0$ and α_{01} at $y = y_0$), and R_1 the radius of curvature of the melt column surface, lying in a plane perpendicular to the tangent (R^0 at $y = 0$ and R^{01} at $y = y_0$). (Reprinted with permission from [Tsivinskii 1970], copyright (1970) Nauka).

boundary condition for Cz technique (2.27) states that the vertical coordinate tends toward zero at infinity. Automatically this means that the first derivative also tends toward zero at the infinity. So, this is a well-known mathematical peculiarity of the boundary condition at infinity and, as a result, there are three boundary conditions. The nonapplicability of this approach to the TPS was first explained in [Tatartchenko 1969-2] and later in the reviews [Tatartchenko 1988, 1993, 1994-1]. Unfortunately, many journals have continued to publish this kind of mistake (see for instance [Pet'kov 1990], an investigation of the dynamic stability of shaped growth, published in the special issue of the *Journal of Crystal Growth* on shaped crystals [Kalejs 1990]). The nonapplicability of this approach was explained again in the paper [Tatartchenko 1995].

2.6.1.6 More Precise Definition of the Catching Boundary Condition

The misunderstanding is as follows: from the formal point of view, the mathematical formulation of the problem requires two boundary conditions. But from the physical point of view, the melt has to form a wetting angle with the shaper surface. This discrepancy was explained in the paper [Tatartchenko 1997], which presents a well-grounded mathematical proof. Here only the main idea is illustrated.

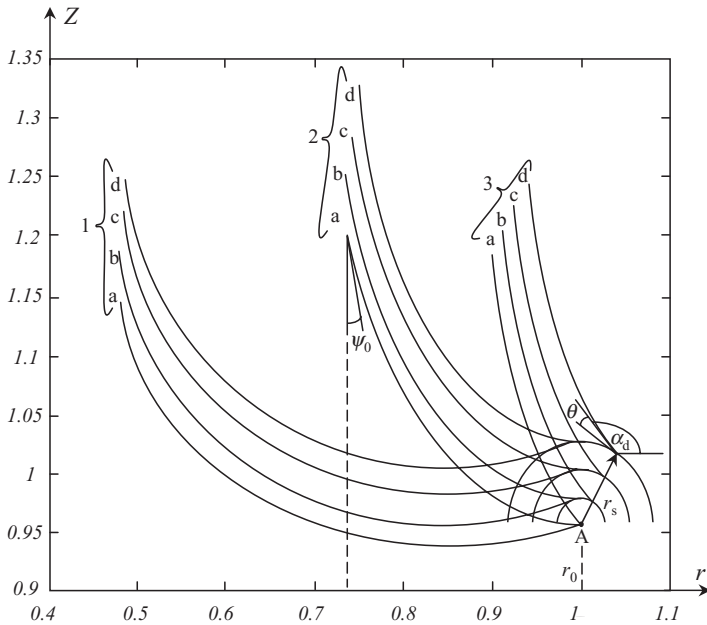


Figure 2.17 Mid-range Bo : profile curves $z(r)$, starting from a sharp edge of the shaper (a) and from surfaces of different radius r_s torus (b–d): (1) $r_c = 0.45$; (2) $r_c = 0.7$; (3) $r_c = 0.9$.

Figure 2.17 presents one specific case: the growth of a cylindrical crystal with respect to the scheme of Figure 2.4d. The shaper edge is replaced by a circular coaxial torus in four cases with four different radii r_s , the last $r_s \rightarrow 0$ (Figure 2.17a). The example corresponds to a middle-range Bond number, $Bo \approx 1$. The dimensionless shaper radius $r_0 = 1$. The unit of length measurement is the capillary constant a , which is 7.6 mm for Si, 6 mm for sapphire, 4.8 mm for Ge and 3.7 mm for InSb [Tatartchenko 1993]. This means that for Si the diameter of the shaper edge circle is about 15.2 mm, for sapphire 12 mm, etc. The origin of the z -coordinate is located on the free surface of the melt (not shown). The negative melt pressure is $d = -1$, e.g. the free surface of the melt is located at a distance a lower than the shaper edge (Figure 2.4d). Three sets of profile curves (a profile curve is a section of the meniscus by the figure plane) are shown in Figure 2.17. All sets are characterized by the same value of the angle α_d , the meniscus inclination angle with respect to the positive r direction at the point of contact with the shaper, and each set has four profile curves for the four values of r_s . The lower end of each profile curve is located on the surface of the torus and forms the wetting angle $\theta = 10^\circ$ with the surface of the torus. Each torus corresponds to a shaper edge with a different radius of curvature r_s : $r_s = 0.09$ (0.68 mm for Si) for all three profile curves of set d, $r_s = 0.06$ (0.46 mm for Si) for the curves c, $r_s = 0.03$ (0.23 mm for Si) for curves b, $r_s \rightarrow 0$ for curves a. The upper end of each profile curve forms an angle of 10° with the vertical. It corresponds to crystal growth of the respective dimension with a growth angle $\alpha = 10^\circ$: $r_c \approx 0.45$ (a crystal of 7 mm diameter for Si) for set 1, $r_c \approx 0.7$ (the crystal of 10.6 mm diameter for

Si) for set 2, $r_c \approx 0.9$ (a crystal of 17 mm diameter for Si) for set 3. The crystallization front is located at a height (from the plane of the shaper edges) of approximately 0.20 (1.5 mm for Si) for sets 1 and 3, and approximately 0.30 (2.2 mm for Si) for set 2.

So, at the micro scale, the melt forms a wetting angle with the torus surface which is a normal physical wetting condition. If the crystal dimension changes, the contact point also changes its position on the torus surface but, in any case, its position will be in the vicinity (torus radius r_s) of the point A. With r_s decreasing, the location of the lower end of the profile curve comes closer and closer to the point A with the coordinates ($r_0 = 1$, $z = 1$). If the torus radius is infinitely small then, in the macroscopic sense, the meniscus catches on the sharp shaper edge (at point A). So, *the catching condition is just a useful mathematical approach to satisfy the capillary boundary problem. From the physical point of view it defines a wetting boundary condition on the sharp edges of the shaper.* Unfortunately, in spite of the publication [Tatartchenko 1997], the history of applying the approach used in [Tsivinski 1962] to the TPS is not yet complete: see [Kuandykov 2001] or [Balint 2005].

2.6.1.7 Capillary Boundary Problem Solution

The solution of the problem will be discussed in three parts relating to large, intermediate and small values of the Bond number, Bo . For large and small Bo , the Laplace equation takes the forms (2.7) and (2.8) respectively. A solution of the boundary problems for both of these can be obtained in analytical form (sometimes with the use of special elliptical functions). For a mid-range Bo , a numerical solution is needed. A comparison of the analytical and numerical solutions shows that, in practice, with a sufficient accuracy, these approximations can be used:

- The large Bo approximation for the growth of cylindrical solid rods or tubes of $10a$ minimal diameter (this corresponds to 76 mm for Si, 60 mm for sapphire) as well as for the flat part of a ribbon growth.
- The small Bo approximation for the growth of cylindrical solid rods or tubes of $1a$ maximal diameter (this corresponds 7.6 mm for Si, 6 mm for sapphire) on the Earth's surface, as well as for very largediameter crystals grown under microgravity conditions.

Solution of the boundary capillary problem allows us to obtain very interesting information concerning the capillary shaping as a function of the shaper design, melt pressure and wetting angle. The information can include [Tatartchenko 1988, 1993, 1994]:

- the shape of the meniscus – conditions of existence of concave, convex and convexo-concave ones;
- the range of parameters for the existence of catching and wetting boundary conditions;
- the design of the shaper and the range of parameters for the existence of a meniscus with a definite growth angle α ;
- the design of the shaper and the range of parameters for the existence of a meniscus with a fixed crystallization front position;
- the signs and values of the A_{rr} and A_{rn} coefficients.

Here are few examples of this kind.

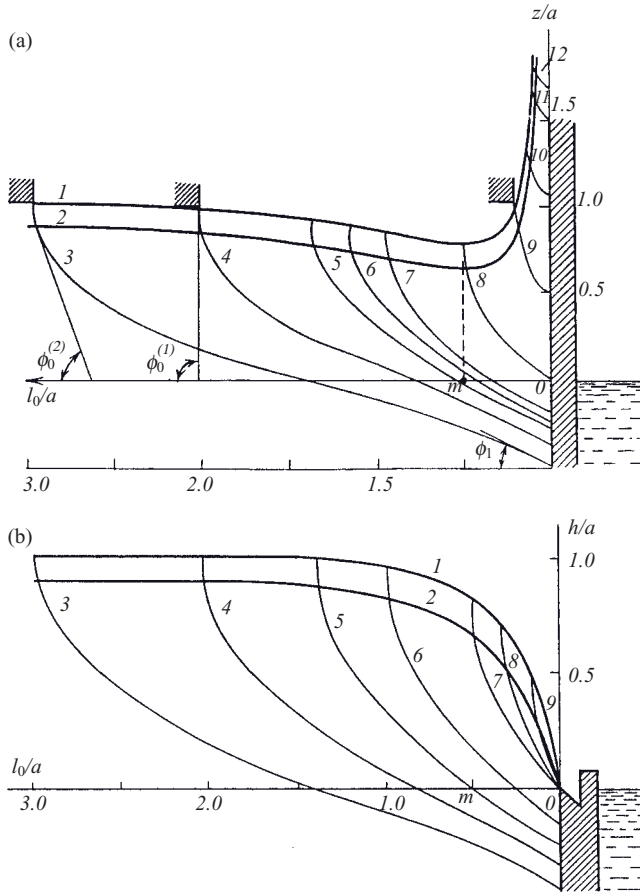


Figure 2.18 Large Bo : (a) wetting boundary condition ($\theta = 135^\circ$); convex-concave (3–7) and concave (8–12) profile curves $z(l_0)$ (l_0 is the gap between the crystal edge and the shaper: $l_0 = r_0 - r_c$) and (1, 2) boundary curves $h(l_0)$: 1 ($\alpha = 0$) and 2 ($\alpha = 15^\circ$); (b) transition from the wetting boundary condition (profile curves 3–6) to the catching one (profile curves 7–9) by changing the shaper design (Reprinted with permission from [Tatartchenko 1988], copyright (1988) Springer Science + Business Media).

Large Bo . First, we formulate the following crystal growth conditions (Figure 2.18) which correspond to the scheme in Figure 2.4h [Tatartchenko 1988, 1993]: the nonwetted shaper wall is located to the right, where $r = r_0$. The tangent to the melt surface at the melt-shaper contact point makes the wetting angle θ with the shaper wall. We now introduce the angle $\phi_1 = \theta - \pi/2$. The edge of a melt-growing flat crystalline ribbon or that of a circular cylindrical crystal of large diameter is situated to the left, where $r = r_c$. Let the angle ϕ_0 (Figure 2.6a), between the tangent to the melt surface at the melt-crystal growing contact point and the negative direction of the r -axis, be specified (while growing crystals of constant cross-section, the angle $\phi_0 = \pi/2 - \alpha$). Let l_0 denotes the gap between the crystal edge and the shaper: $l_0 = r_0 - r_c$. Now consider which process parameter data

can be obtained with such problem formulation. According to the terminology defined above, the angle-fixation boundary conditions (or wetting conditions) apply on both ends of the l_0 variation interval: Equation (2.7), with boundary conditions (2.26) and (2.57). The analytical solution of the problem was obtained with the help of Legendre's elliptical functions (see, for instance, [Tatartchenko 1988, 1993]) and is shown in Figure 2.18a for the following parameter values: $\theta = 135^\circ$ ($\phi_1 = 45^\circ$), $\alpha = 15^\circ$ ($\phi_0 = 75^\circ$) and $\alpha = 0$ ($\phi_0 = 90^\circ$). The origin of the z -coordinate coincides with the free melt surface. The profile curves 3–12 are the sections of the melt meniscus cut by the diagram plane. Each profile curve corresponds to a definite distance l_0 between the growing crystal and the shaper wall. The edges of the crystals are located on one of the two boundary curves $h(l_0)$ corresponding to two different growth angles: (1) for $\alpha = 0$ and (2) for $\alpha = 15^\circ$. Based on this boundary problem solution, the following results are established:

- With the angle fixation boundary condition satisfied at both ends of the l_0 -variation interval, the vertical coordinates of the liquid–solid phase contact points (melt–crystals and melt–shaper) with respect to the melt free surface are not fixed but depend on the relation between the angles at both ends of the meniscus and on the value of the gap between the shaper and the crystal being pulled. This is a confirmation of the scheme in Figure 2.15b.
- There exists some specific value m of the gap l_0 between the shaper and the crystal being pulled (it is equal approximately to one capillary constant a for the set of parameter values used). When $l_0 > m$, the meniscus is located partly above and partly below the melt free surface. When $l_0 < m$, the line of meniscus contact with the shaper wall is located higher than the melt free surface.
- The part of the meniscus located below the melt surface is convex; the part located above the melt surface is concave.
- A higher crystallization front position corresponds to a smaller growth angle.
- For a crystal–shaper gap larger than the capillary constant, a , the crystallization front height does not exceed the capillary constant. For smaller gaps, the crystallization front height can be larger, tending toward infinity with a vanishing gap.
- Any change in the melt level during pulling will have the following effect on the crystal dimensions: with the level decreasing, the ribbon thickness (or the rod diameter) can be kept unchanged only if the crystallization front is lowered by the same value. With the crystallization front position kept unchanged, the ribbon thickness or the crystal diameter will decrease with the lowering of the melt and vice versa. This means that the melt level can be qualified as one of the degrees of freedom. These phenomena were investigated in [Tatartchenko 1988, 1993].
- The capillary coefficients of stability A_{rr} and A_{rh} of the set of equations (2.15) and (2.16) can be defined. It follows from Figure 2.18a that $|\partial\phi_0/\partial h| > 0$; $|\partial\phi_0/\partial r_c| > 0$ for $l_0 < m$; $|\partial\phi_0/\partial r_c| < 0$ for $l_0 > m$. This means that there is a capillary stability ($A_{rr} < 0$) only if the gap between the shaper wall and the pulling crystal is larger than the capillary constant ($l_0 > m \approx a$).

Now, we modify the shaper design and locate a sharp shaper edge at the melt free surface level. The solution of the new boundary problem is shown in Figure 2.18b. This gives new results:

- For $l_0 > m \approx a$, the situation is the same as in the previous case.
- But for $l_0 < m \approx a$, the situation is dramatically changed: the catching boundary condition is realized (this is a second confirmation of the scheme of Figure 2.15b). In this case, and also for $l_0 < m \approx a$, $|\partial\phi_0/\partial r_c| > 0$ and as a result $A_{rr} < 0$), i.e. capillary stability exists for the whole range of l_0 variations.
- On the other hand, the crystallization front $h(l_0)$ has to be located much lower than in the previous case. In particular, $h(l_0)|_{l_0 \rightarrow 0} \rightarrow 0$.

Mid-Range Bo. For intermediate values of Bo ($Bo \approx 1$), the three profile curves (a) of sets 1–3 in Figure 2.17 give an example of the numerical solution of the capillary boundary problem with the catching boundary condition that corresponds to Figure 2.4d. Therefore, the meniscus shape is given by Equation (2.6) and the boundary conditions (2.26) and (2.55). The results were discussed in section 2.6.1.6 above, but two peculiarities must be mentioned:

- A central part of the meniscus corresponding to the crystal radius $r_c \approx 0.5$ is located lower than the shaper edge.
- The crystal radius $r_c \approx 0.7$ is peculiar. First of all, the highest crystallization front position corresponds to this crystal radius. Secondly, if $r_c > 0.7$ then $\partial\phi_0/\partial r_c > 0$, i.e. $A_{rr} < 0$, and if $r_c < 0.7$ then $|\partial\phi_0/\partial r_c| < 0$, i.e. $A_{rr} > 0$. Thus, there is capillary stability for crystals with ratio $r_c/r_0 > 0.7$ but there is no capillary stability for crystals with ratio $r_c/r_0 < 0.7$. Thus, for $r_c/r_0 < 0.7$ the shaper has no influence on the capillary shaping. In practice, this is a realization of the Cz technique.

Small Bo. The influence of the melt pressure on the shape of the profile curves $z(r)$ is presented as an example of the capillary boundary problem solution for a small Bo ($Bo \ll 1$), which is studied in detail in the analytical form using Legendre elliptical functions in [Tatartchenko 1988, 1993]. In Figure 2.19 the catching boundary condition is fixed at the point r_0 (shaper radius $r_0 = 0.05$). The boundary curves $h(r_c)$ (1–4) are shown, corresponding to the growth angle $\alpha = 0$ as well as several profile curves. Hence, the set of equations of interest consists of Equation (2.8) with the boundary conditions (2.26) and (2.55). It is very important to mention that in the capillary problem with small Bo , the influence of gravity is neglected. This is why these results are applicable to the growth of crystals of different sizes in microgravity conditions. For growth in normal gravity, the results are applicable for filament growth (for sapphire, for instance, the case under consideration corresponds to growth of a filament of 0.6 mm diameter) with pulling up as well as lowering. Consequently, the schemes Figure 2.4b, d, e, f, j are described in the framework of this model. Here are some peculiarities of the results presented in Figure 2.19:

- The order of magnitude of the crystallization front position is the same as the shaper radius for all values of pressures under investigation. In the example, $r_0 = 0.05$, e.g. for sapphire, the crystallization front is located at the distance of 0.5–0.6 mm from the plane of sharp shaper edges.
- For all boundary curves, except 4, $h(r_c)|_{r_c \rightarrow r_0} \rightarrow 0$.
- Boundary curve 4 is a special one: if pressure d corresponds to the value giving $2dr_0 = 1$, the boundary curves for all r_0 values (but only in the range of small Bo values)

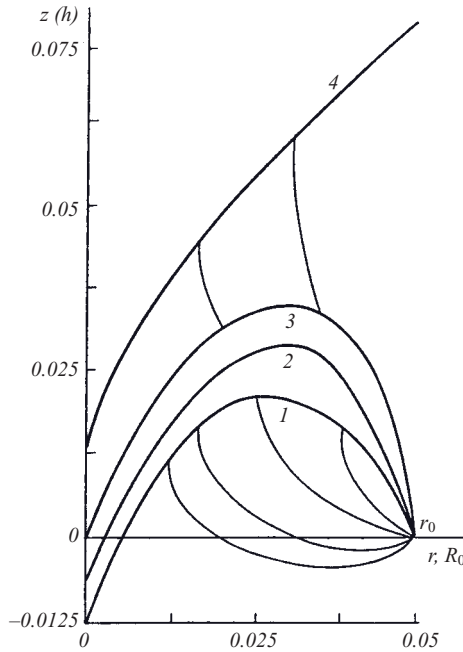


Figure 2.19 Small Bo : boundary curves $h(r_c)$ 1–4 and some profile curves $z(r)$ for a shaper with $r_0 = 0.05$, under various pressures d : -10 (curve 1), -5 (curve 2), 0 (curve 3), 10 (curve 4) (Reprinted with permission from [Tatartchenko 1988], copyright (1988) Springer Science + Business Media).

should have a shape similar to curve 4. The main particularity of this curve is $h(r_c)|_{r_c=r_0} = 0.5\pi r_0$. Hence, for this particular pressure, if the diameter of the pulled crystal is equal to the shaper edge diameter, the very special meniscus has the shape of a right circular cylinder.

- All boundary curves, except 4, have a maximum. The maximum position corresponds to $r_c = r_m \approx 0.7r_0$ and it divides the range of the crystal dimensions in two parts for which $\partial\phi_0/\partial r_c > 0$ if $r_c > r_m$ and $\partial\phi_0/\partial r_c < 0$ if $r_c < r_m$. It means that for d values such that $2dr_0 < 1$, there is capillary stability ($A_{rr} < 0$) only if the gap between the shaper edge and the pulling crystal is less than $0.3r_0$. Hence, it exactly corresponds to the mid-range Bo .

2.6.2 Stability Analysis

For the different Bond numbers and boundary conditions, the signs of the capillary coefficients A_{rr} and A_{rh} are listed in Table 2.1. For stability estimation, Equations (2.31) and (2.32) for heat coefficients can be used: $A_{hh} < 0$, $A_{hr} > 0$. From Table 2.1, we can see that a shaper can be designed in order to have capillary stability: $A_{rr} < 0$, $A_{rh} < 0$. The inequalities (2.22) are thus fulfilled, and dynamic stability of the shaped crystal growth is attained.

Here only the simplest case of dynamic stability investigation (growth of a solid cylindrical crystal in the thermal conditions described by the one-dimensional thermoconduc-

Table 2.1 Cz technique and TPS capillary coefficients for different Bo and capillary boundary conditions

Conditions of crystallization				A_{rr}	A_{rh}
Method	Bond number	Boundary condition	Parameter values		
Cz					
TPS	Small	Catching	$\sin\phi_0 < 2r_0d$ $\sin\phi_0 > 2r_0d$	<0	<0
		Wetting	$\phi_0 < \phi_1$ $\phi_0 > \phi_1$	<0 >0	<0
	Large	Catching	Single- and doubled-valued meniscus Double-valued meniscus $r_c \approx r_0$	<0	<0 >0
		Wetting	$\phi_0 < \phi_1$ $\phi_0 > \phi_1, r_0 - r_c > m$ $\phi_0 > \phi_1, r_0 - r_c < m$	<0 >0	<0

Source: Reprinted with permission from [Tatartchenko 1988], copyright (1988) Springer Science + Business Media.

tivity equation (2.30)) has been analysed. Additional information on the topic can be found in reviews and papers by the present author [Tatartchenko 1988, 1993, 1994-1, 1997, 2000]. They include:

- Investigation of the meniscus static stability.
- Investigation of tube growth dynamic stability. It is a stability problem with three degrees of freedom where the internal tube diameter is the third degree of freedom.
- Investigation of the influence of melt pressure on the dynamic stability. It is a stability problem with three degrees of freedom where the melt pressure is the third degree of freedom.
- Crystal cross-section shape stability.

Although some problems have been solved, a lot of theoretical problems remain. Important ones are the stability of crystal growth for complicated shapes and the influence of crystallographic anisotropy. Now, before the experimental work begins rough estimations are used for preliminary analysis of the capillary shaping conditions. For instance, for ribbon growth, an approximation including three steps was proposed in [Tatartchenko 1988, 1993]:

- Solution of the capillary problem with large Bo for flat part of the ribbon.
- Solution of the capillary problem with small Bo for the edge of the ribbon.
- Joining up the two solutions on the corner at the edge of the ribbon, with the condition that the growth angle is the same on both parts.

To conclude this section, the use of computer modelling for calculation of non-axisymmetric shapers [Babik 1999, Despreaux 2000] must be mentioned.

2.6.3 Experimental Tests of the Capillary Shaping Theory Statements

Here some experimental confirmations of the main statements of the capillary shaping theory presented above are discussed.

2.6.3.1 Existence of a Growth Angle

The existence of a growth angle during crystal growth from the melt is one of the main foundations of capillary shaping theory, which is why special experiments were carried out to examine it [Tatartchenko 1988, 1993]. Thin sapphire crystals were grown from a shaper of 0.8 mm diameter (Figure 2.20). By changing the slope between the crystallization front and the surface of the skew shaper by means of differential heating, various boundary conditions were created for the left and right sides of the same crystal. In Figure 2.20a a rod of a constant cross-section grows: the angles α_1 between the crystallization front and the growth direction are different on the left and on the right crystal sides; constancy of the diameter is provided by maintaining the angle $\phi_0 = \phi_e$ ($\phi_e = \pi/2 - \alpha$) all over the perimeter. In Figure 2.20b, $\phi_0 = \phi_e$ on the left and $\phi_0 < \phi_e$ on the right; the right side of the crystal widens. In Figure 2.20c, the deviation ϕ_0 from the equilibrium value ϕ_e on the right has led to crystal contraction. In the transient region, the crystal surface is convex in Figure 2.20b and concave in Figure 2.20c, which corresponds to the capillary stability effect.

If in the process of crystal dimension change the growth angle α remains constant, the following relation should be valid for the crystal lateral surface (Figure 2.6):

$$dr_c/dz = \tan(\phi_e - \phi_0). \tag{2.59}$$

Integrating Equation (2.59) in the range of the crystal radius r_c changing from r_c^0 to the final value r_c^{01} for small deviation of the angle ϕ_0 from the angle of growth ϕ_e gives the following:

$$\ln D = -(d\phi_0/dr_c)z \text{ where } D = (r_c - r_c^{01})(r_c^0 - r_c^{01}). \tag{2.60}$$

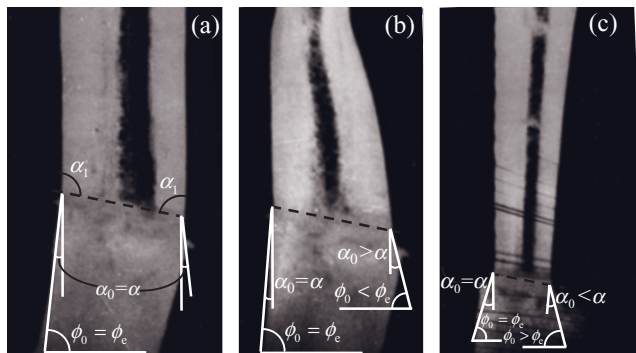


Figure 2.20 TPS growth of a thin sapphire filament with skewed shaper: (a) constant cross-section, (b) convex widening from the right, (c) concave constriction from the right (Reprinted with permission from [Tatartchenko 1988], copyright (1988) Springer Science + Business Media).

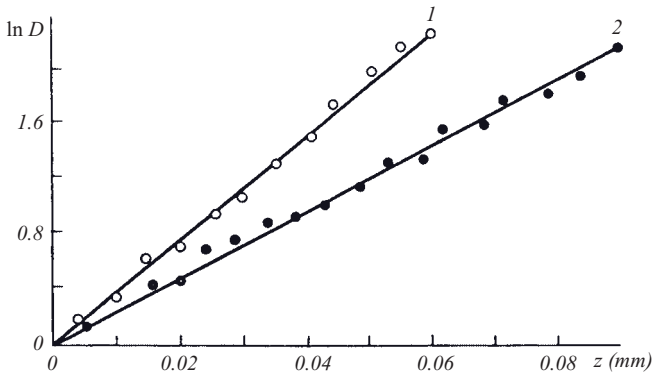


Figure 2.21 Sapphire filament constriction (1) and widening (2) in the transient range (Reprinted with permission from [Tatartchenko 1988], copyright (1988) Springer Science + Business Media).

Figure 2.21 presents the data processed from Figure 2.20b, c. The linear dependence of $\ln D$ on z is a proof of the correctness of (2.59) and then of the existence and constancy of the growth angle.

2.6.3.2 Microgravity Experiments

Model experiments have been carried out in microgravity conditions (small Bo) to test some capillary shaping theory statements [Tatartchenko 1988, 1993].

Simulation Experiments. Crystal growth experiments under microgravity conditions in space were preceded by simulating the liquid column shape by using immiscible liquids of equal densities. A meniscus of an alcohol–water solution was formed between two glass tubes (1 and 3), surrounded by a mineral oil with same density (Figure 2.22). The pressure d in the meniscus was equal to the weight of the column of the alcohol solution in the upper tube (1). The lower tube (3), of constant diameter $2r_0 = 13.12$ mm, imitated the shaper, and the upper one (1), of diameter $2r_c$, the crystal. The spherical meniscus (4) at the end of the lower tube (3) was used for the pressure estimation as well as, under a certain known pressure, for calculation of the value of the surface tension at the boundary of the two liquids. A convex meniscus (2) (Figure 2.22b) was formed under the pressure of 27.14 dyn/cm². For existence of a right circular cylindrical meniscus (2) with $2r_c = 2r_0$, a pressure of 16.8 dyn/cm² was determined (Figure 2.22a). Some experiments were carried out on board a flying laboratory with 20 s microgravity time.

Crystallization of Cu Under Short-Term Microgravity Conditions. The simulation experiments with isodense liquids were only the first step in estimating the real conditions of crystal growth. Moreover, we began to doubt that shaped crystal growth could be obtained under microgravity because in the simulation experiments the liquid sometimes flew on to the crystal surface. Therefore, Cu was crystallized by capillary shaping on a high-altitude rocket with 20 min microgravity time [Tatartchenko 1988, 1993]. This metal has a relatively low melting point (1083°C), resistance to stress (which is important for

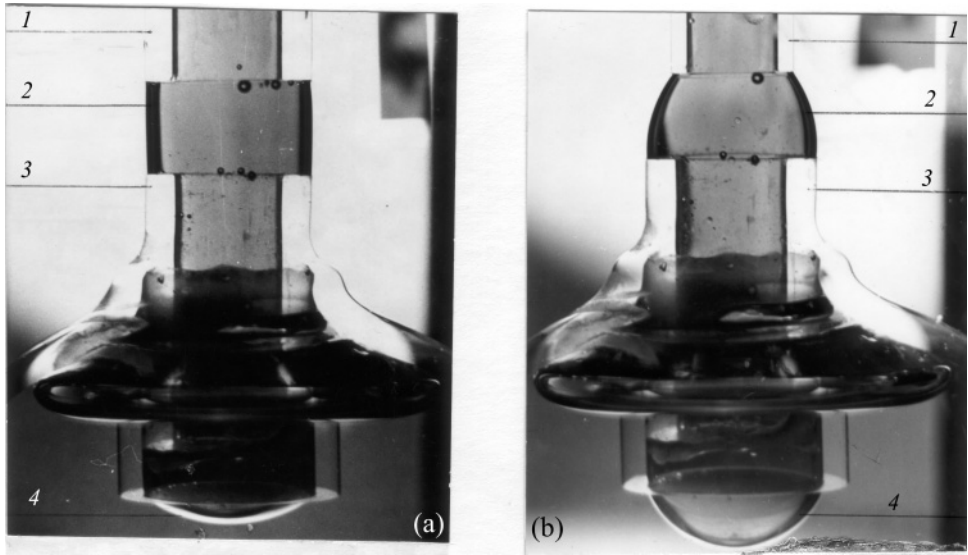


Figure 2.22 Experiment with two isodense immiscible fluids. Meniscus model that appears on pulling a circular rod under zero-gravity condition: right circular cylinder (a), convex meniscus (b).

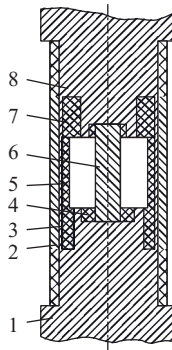


Figure 2.23 Design of the capsule used to investigate the crystallization process from the melt under microgravity conditions (notation as in the text) (Reprinted with permission from [Tatartchenko 1993], copyright (1993) Springer Science + Business Media).

rocket launching as well as for capsule landing), and its physicochemical properties are well known.

The technique of capillary shaping was first used to produce a rod specimen under vacuum. This enabled us to reduce the amount of gas in the metal. The specimen (6), in the form of a cylinder 5–8 mm in diameter and about 5–6 cm long (Figure 2.23), was placed between two Mo shapers (1) and (8) into which Cu (4) was fused and solidified beforehand. This guaranteed complete wetting of the shaper during the microgravity experiment. Two graphite guard rings (3) and (7) were introduced to prevent the melt

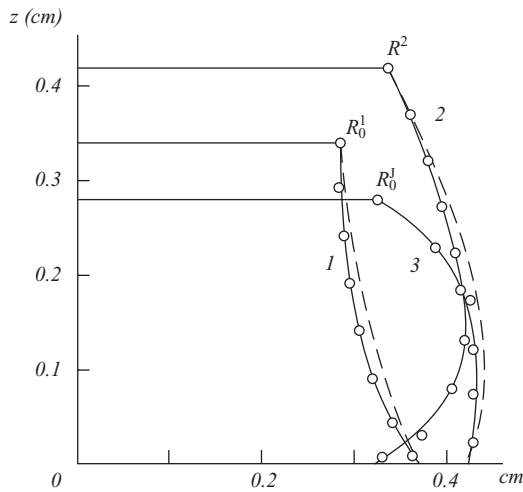


Figure 2.24 Calculated profile curves of the melted copper columns (dashed line) and crystallized specimens (solid line) for different pressures (1, 2, 3) within the meniscus; experimental data of crystallized specimen shape (open circles) (Reprinted with permission from [Tatartchenko 1993], copyright (1993) Springer Science + Business Media).

escaping beyond the sharp lip of the shaper. These rings were supported by the graphite spacer (5), which also acted as a thermal shield. Both shapers were pushed into the coupling tube (2). The above design ensured rigidity, simplicity of assembly, and constant separation between the shapers. W–Rh thermocouples were mounted near the ends of the specimen to estimate the temperature distribution along its length. The capsule was inserted into an exothermic heating device that contained no moving parts.

The experiment was carried out in the following way. When microgravity conditions were achieved, the specimen was completely melted. After that, during the microgravity phase, a directional crystallization of the melt column was realized by heat removal from the upper shaper. On these high-altitude rockets there were no photographic facilities for recording the crystallization process so the shapes of the crystallized specimens were examined experimentally after the flight and were compared to the calculated shapes for $\alpha = 0$.

The results are presented in Figure 2.24 which confirms that:

- With a crystallization speed of 5–7 mm/min as computed from the thermocouple recordings, $\alpha = 0$ for Cu crystallization.
- The melt did not flow on the crystal surface during crystallization.

These results suggested that crucible-free zone melting and capillary shaping crystal growth could be realized in space.

The next crystallization processes were realized in the ‘Shape’ and ‘Ribbon’ experiments.

‘Shape’ Experiment. The main idea of the experiment was to grow a crystal by using a right cylindrical melt column which cannot exist in the terrestrial conditions (except for

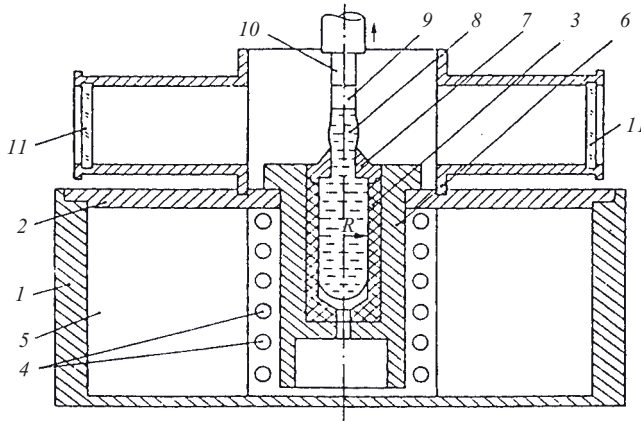


Figure 2.25 *Experimental set-up for crystal growth in space (notation as in the text) (Reprinted with permission from [Tatartchenko 1988], copyright (1988) Springer Science + Business Media).*

small-diameter filament growth). Under microgravity (Figures 2.19, 2.22a), such a melt column is formed if $r_c = r_0$; $\phi_0 = \pi/2$ under a pressure d , satisfying the equality $2dr_0 = 1$, but on increasing h up to $h \approx \pi r_0$ it loses static stability and transforms first into a meniscus, the profile of which has an ambiguous projection onto the abscissa axis, and then, with further increasing h , it breaks into two independent menisci. For $h < \pi r_0$ and $d = 0$, the meniscus is a catenoid; with increasing pressure its curvature in the axial cross-section decreases, reaching infinity at $2dr_0 = 1$. When the pressure increases above this value the meniscus becomes convex (Figure 2.22b). A cylindrical meniscus can be used for crystal growth only for $\alpha = 0$, which means that a metal should be chosen for the material to be grown in the experiment (the angle of growth for metals is usually close to zero). In 1984, under microgravity in the Salyut orbital space station, the crystallization of In was carried out by a large group of Russian scientists; see [Tatartchenko 1988, 1993]. The advantage of In is its low melting temperature (156°C), which is very important for the simplicity of the space furnace and the limited energy available on the spacecraft. Some other physical characteristics of In are a comparatively high density in solid state (7.28 g/cm^3), which differs only slightly from that of the melt (7.03 g/cm^3); surface tension of the melt $\gamma_{lv} = 0.592\text{ J m}^{-2}$; and capillary constant under terrestrial conditions $a = 0.41\text{ cm}$.

Figure 2.25 shows a schematic of the growth device. A plastic case (1) with a lid (2) has a graphite container (3) previously filled with In. A resistive heater (4), insulated by a layer of polyurethane foam (5), is used. The heat is delivered to the container through a Cu capsule (6), which also serves to holding a Cu cap (7) which is also the shaper, with a hole to ensure equality of the inert gas pressure inside and outside the container (3). The meniscus of melt (8) is formed first between the initial Cu rod (9), fastened to a rod (10), and the edge of the shaper (7). The meniscus shape is recorded by a camera through illuminated windows (11). The most important part of this set-up was the system of maintaining the pressure inside the meniscus by means of a melt meniscus formed near the bottom of the crucible. The pressure depends on the radius r_a of the graphite container and on the wetting angle. This idea was used also for the ‘Ribbon’ experiments. Figure 2.26 depicts the shape of a drop (a), formed at the edge of the shaper, and of the melt

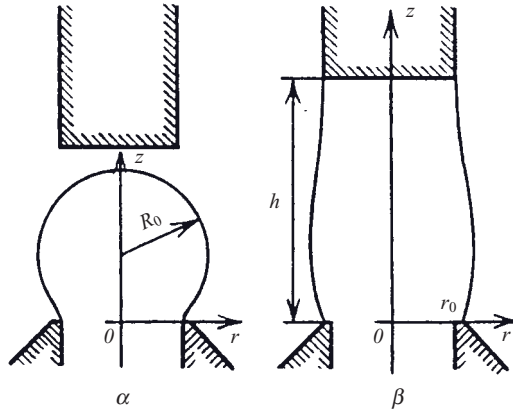


Figure 2.26 The melt drop at the edge of the shaper (a) and the meniscus formed there (b) (Reprinted with permission from [Tatartchenko 1988], copyright (1988) Springer Science + Business Media).

meniscus (b). The pressure, which was determined from the shape of the drop (Figure 2.26a), exceeded by approximately 40% that required for the formation of a cylindrical column. There are a lot of error factors, including those governed by the wetting angle hysteresis. Some of them were encountered only under real space conditions and could not have been predicted. Unfortunately, we did not have any possibility of repeating the same experiment with a suitable correction. Nevertheless, the main aim of the experiment was achieved: the typical shape of the meniscus had the ratio $h/r_0 \approx 3.6$ ($h = 10\text{ mm}$) that exceeded terrestrial TPS growth conditions by an order of magnitude. After the seed rod was wetted with the melt, it was pulled at the speed $v \sim 3\text{ mm/min}$. The pulling speed of the test In specimen grown with an analogous device in terrestrial conditions could not be increased above 0.2 mm/min . The diameter of the flight specimen was approximately 5.6 mm , whereas for the test one it was $2.9\text{--}3.2\text{ mm}$. No special regulation systems were used, but it is evident that both pulling processes were stable. Both samples were mainly single crystals in structure.

‘Ribbon’ Experiment. The crystallization of ribbons of Ge and GaAs from the melt in the orbital station Mir in 1990 is the next example of TPS realization under microgravity conditions [Tatartchenko 1993]. The melt is placed in a fixed gap between two nonwetable flat plates (Figure 2.27). The right part of the melt has a free surface of curvature $1/R$ which depends on the wetting angle and on the distance $2r_0$ between the plates. The same idea had previously been used in the ‘Shape’ experiment: to maintain a positive pressure inside the growth meniscus by the curvature of the melt free surface. The growth meniscus projections in the gaps between the walls and the growing crystal are circular arcs of same radius r . This is the realization of TPS with the wetting boundary conditions on the walls of the shaper. The use of nonwetted walls is successful if the following inequality is fulfilled:

$$\phi_1 = \theta - \pi/2 > \phi_0 = \pi/2 - \alpha$$

i.e. $\theta > \pi - \alpha$, where θ is the wetting angle and α is the growth angle.

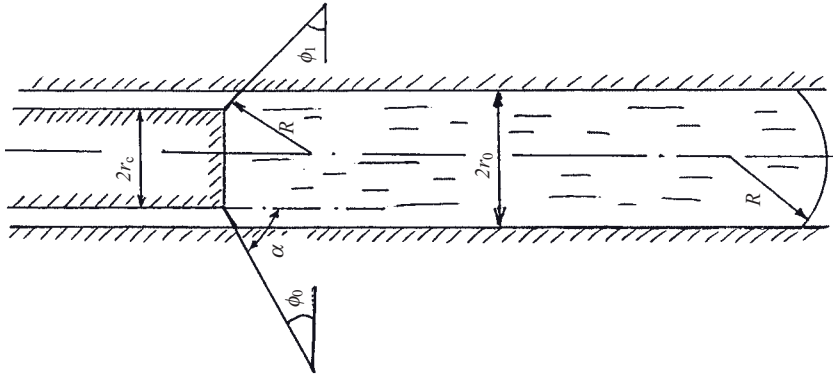


Figure 2.27 Schematic drawing of the Ribbon growth space experiment (Reprinted with permission from [Tatartchenko 1993], copyright (1993) Springer Science + Business Media).

The ribbon thickness $2r_c$ and the capillary coefficients A_{rr} and A_{rh} are given by:

$$2r_c = 2r_0 \sin \phi_0 / \sin \phi_1, \quad (2.61)$$

$$A_{rr} = -v \sin \phi_1 / (r_0 \cos \phi_0), \quad (2.62)$$

$$A_{rh} = -v \sin \phi_1 / (r_0 \sin \phi_0). \quad (2.63)$$

Both capillary coefficients are negative and there is capillary stability.

For the usual dynamic stability estimation, the heat coefficients (2.31) and (2.32) can be disregarded, because, without gravity, the position of the solid–liquid interface has no effect on the meniscus shape and thus on r_c . Therefore, with the inequalities (2.22) fulfilled, the dynamic stability of the scheme under investigation is ensured.

In the flight experiments, Ge and GaAs ribbons were grown between pyrocarbon plates. Unfortunately, the heating regime was not optimal, the seeds were melted and the ribbon structures were polycrystalline; see picture in [Tatartchenko 1993]. But the smooth surfaces and constant thickness of the ribbons, grown without any special regulation, are evidence of the stability of the process. This is further confirmed by the dewetting configurations, which are spontaneous and stable in microgravity as fully described in Chapter 6.

2.6.4 Impurity Distribution

The shapers used in the TPS technique provide possibilities for regulation of the impurity distribution along the crystal as well as in its cross-section. We analyse these possibilities first for thin ribbon growth. Impurity distribution in crystals grown by the Bridgman, Cz and FZ techniques has been studied quite thoroughly, but extension of the known mechanisms to thin-profile growth using TPS can lead to erroneous conclusions. Application of the Burton–Prim–Slichter equation [Burton 1953] to calculation of the impurity distribu-

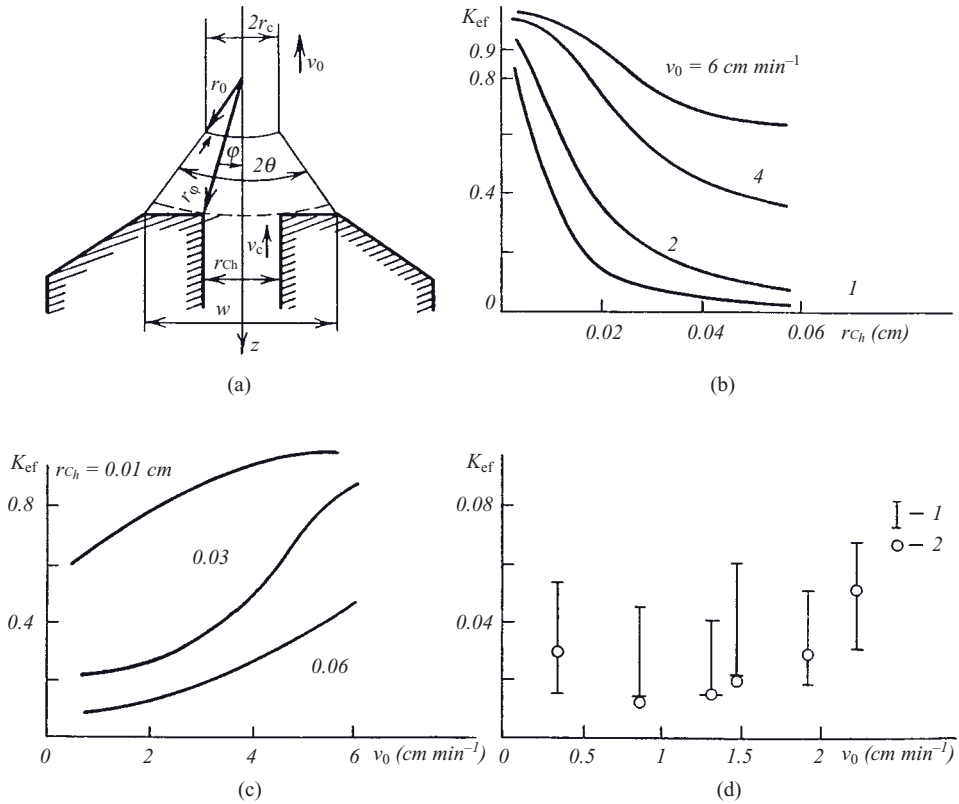


Figure 2.28 Configuration for calculation of the impurity distribution effective coefficient: (a) diagram; (b) $K_{ef} = f(r_{ch})$ – calculated; (c) $K_{ef} = f(v_0)$ – calculated; (d) comparison of experimental values (1) with calculated ones (2) from Equation (2.69) of the *In* distribution effective coefficient for thin-walled shaped Si crystal growth (Reprinted with permission from [Tatartchenko 1988], copyright (1988) Springer Science + Business Media).

tion effective coefficient K_{ef} requires specification of the thickness of the diffusive boundary layer. If this thickness is assumed to be equal to the total height of the meniscus and of the shaper capillary channel, $K_{ef} = 1$ for any impurity [Swartz 1975], which does not correspond to reality. The present section gives a model of impurity transfer for the TPS under conditions that allow relating K_{ef} to the of capillary shaping and feeding parameters [Brantov 1983, Tatartchenko 1988, 1993]. Figure 2.28a illustrates the growth of a thin tape.

A stationary process is considered; it is assumed that the melt in the zone of the meniscus and the capillary channel is not stirred and that complete stirring occurs in the crucible. Under these assumptions, the stationary impurity transfer in the meniscus is described by the equation written in the polar coordinates of the Figure 2.28a:

$$D(d^2c/dr^2 + r^{-1}dc/dr) = -vdc/dr, \tag{2.64}$$

with the following boundary condition at the crystallization front:

$$-D dc/dr|_{r=r_0} = v_0(1 - K_0)c(r_0), \quad (2.65)$$

where c denotes the impurity concentration in the melt, D is the diffusion coefficient and K_0 is the impurity distribution equilibrium coefficient; others notation is obvious from Figure 2.28a.

The polar coordinate system chosen allows easy specification of the melt flow rate distribution in the meniscus $v(r) = v_0 r_0 / r$. Then Equation (2.64) is rearranged:

$$d^2c/dr^2 + r^{-1}(1 + v_0 r_0 / D) dc/dr = 0. \quad (2.66)$$

Impurity transfer in the capillary channel is described by the equation in the linear coordinate z :

$$D d^2c/dz^2 = -v_c dc/dz \quad (2.67)$$

with the following boundary condition:

$$c|_{z \rightarrow \infty} \rightarrow c_\infty. \quad (2.68)$$

It is assumed that the impurity concentration in the bulk of the melt c_∞ is constant in the process of tape growth. The solution of the problem relates the value of the impurity distribution effective coefficient K_{ef} to the parameters of the crystallization conditions (v_0 and $2r_c$), with the conditions of capillary shaping (w , r_{Ch} , θ) and the impurity characteristics (D and K_0):

$$K_{\text{ef}} = K_0 / \{K_0 [1 + (\theta r_{\text{Ch}} / \varphi w - 1) \cos \varphi] + (1 - K_0)(1 - \cos \varphi)(2r_c / w)\}^{v_0 r_c / D \sin \theta}. \quad (2.69)$$

If the width of the capillary channel r_{Ch} reaches its maximum value w , Equation (2.69) is reduced to:

$$K_{\text{ef}} = K_0 / \{K_0 [1 + (1 - K_0)(1 - \cos \varphi)(2r_c / w)]\}^{v_0 r_c / D \sin \theta} \quad (2.70)$$

It should be mentioned that [Seidensticker 1979] used a similar approach for solute partitioning during silicon dendritic WEB growth.

Figure 2.28b shows $K_{\text{ef}} = f(r_{\text{Ch}})$ calculated for Al impurities in Si. The following values are used: $K_0 = 0.002$, $D = 0.53 \times 10^{-3} \text{ cm}^2 \text{ s}^{-1}$, $2r_c = 0.03 \text{ cm}$, $w = 0.06 \text{ cm}$. Figure 2.28c shows $K_{\text{ef}} = f(v)$ calculated from Equation (2.70) for various values of r_{Ch} . It is obvious that K_{ef} increases with v (and as a result v_c) increasing. Under actual conditions of growing thin-walled profiled Si crystals, $K_{\text{Al}} \ll 1$. Processing the data of [Kalejs 1978] gives a value of $K_{\text{Al}} = 0.039$ in Si, which agrees very well with the value of $K_{\text{Al}} = 0.03\text{--}0.04$ calculated from Equation (2.69) with the parameters and data values of [Kalejs 1978].

Figure 2.29 gives data on sulfur distribution along the axis of a TPS Si tape obtained by laser emission microanalysis (LEM). The ratio of the sulfur spectral line strength J_{S} to that of silicon J_{Si} (the ratio is proportional to the concentration of the element analysed

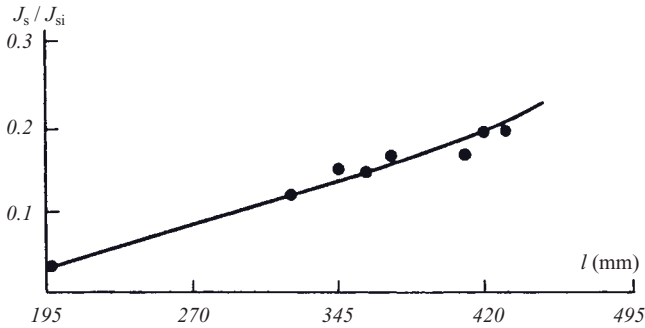


Figure 2.29 Sulfur distribution along the length of a silicon tape (LEM data) (Reprinted with permission from [Tatartchenko 1988], copyright (1988) Springer Science + Business Media).

in the Si matrix) is plotted on the ordinate. The rate of tape pulling was 12 mm/min. Increase of sulfur concentration in the Si tape in the process of pulling shows that $K_S < 1$ (it is assumed that $K_0 = 1 \times 10^{-5}$ for sulfur impurity in Si). No explicit regularities were observed while analysing other impurities.

To verify the main equation (2.69) several In-doped (0.01 wt%) Si tapes were grown. The mass of each tape did not exceed 7% of that of Si charged into the crucible. The tape thickness $2r_c$, the shaper transverse dimension w , the capillary slot dimension r_{ch} and the growth rate v were measured. Photometric spectral lines of In in the grown crystals and in the crucible residue were then determined. The measurement accuracy of the In distribution effective coefficient was 40–50%. The results obtained are shown in Figure 2.28d. Vertical arrows indicate experimental results, circles show the values calculated from Equation (2.69) in accordance with the above-mentioned parameters. The values of $D = 5.2 \times 10^{-4} \text{ cm}^2 \text{ s}^{-1}$, $K_0 = 4 \times 10^{-4}$ are assumed for In impurity in Si. The results shown in Figure 2.28d do not allow plotting K versus the growth rate, v_0 , since the thickness of the silicon tape, $2r_c$, decreases with increasing v_0 (the value of $2r_c v_0$ was practically constant in the experiments), and they can only demonstrate satisfactory agreement between calculated and experimental values. The values of K calculated from the Burton–Prim–Slichter equation are 0.8–0.9, i.e., they are one order of magnitude greater than the experimental values.

Distribution of impurities along the widths of profiled crystals is to a great extent determined by the technique used to feed the melt to the growth meniscus. In Figure 2.30a, b distributions of resistivity, ρ , across Si tapes grown under the conditions of two versions of meniscus melt feeding are compared. The shaper shown in Figure 2.30d had one long capillary slot, while the shaper shown in Figure 2.30e had two small slots at its end faces. The same feeding system was used for sapphire ribbon growth. The diffusion of reflected light (Figure 2.30c) indicates a bubble concentration at the centre of the ribbon. The following explanation of the nonuniformity of the impurity distribution across the crystal (Figure 2.30a–c) can be proposed. In the case of horizontal melt flow in the meniscus from the shaper edges towards its centre, impurities with $K < 1$ rejected by the growing crystal accumulate in the central part of the meniscus where they are pushed by the liquid flows. Hence, a corresponding distribution of capillary channels in the shaper allows control of the impurity distribution in the cross-section of the grown crystals.

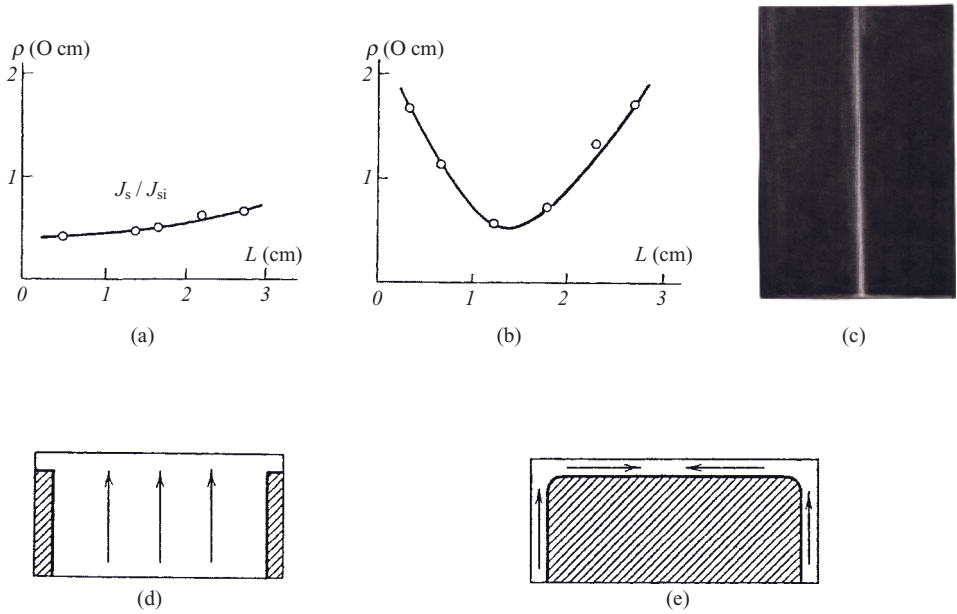


Figure 2.30 Impurity distribution across ribbons using two different versions of melt feeding of the meniscus: (a) Si ribbon and (d) corresponding feeding scheme; (b) Si as well as (c) sapphire ribbon and (e) corresponding feeding scheme (Reprinted with permission from [Tatartchenko 1988], copyright (1988) Springer Science + Business Media).

2.6.5 Definition of TPS

On the basis of the theoretical analysis above, a definition of TPS can be proposed:

TPS are shape crystal growth techniques which use a solid body (shaper) to define a melt meniscus shape by means of either a catching (on shaper edges) or a wetting (on shaper surfaces) capillary boundary condition in order to obtain a crystal of predetermined cross-section and impurity distribution as a result of pulling it in a dynamically stable regime.

This definition follows from our analysis of capillary catching and wetting boundary conditions, completed in 1967 [Tatartchenko 1968], as well as from our dynamical stability analysis with capillary shaping, completed in 1970 [Tatartchenko 1973-1].

2.6.6 Brief History of TPS

With the definition of TPS in mind, we can analyse the development history of the technique. This is why the history is placed here rather than at the beginning of this section.

The development of shaped crystal growth for industrial applications began from a group of papers published in 1958–1959 [Goltsman 1958, 1959; Shakch-Budagov

1959; Stepanov 1959-1, 1959-2]. These papers described how the Russian scientist A.V. Stepanov had carried out experiments concerning pulling of shaped polycrystalline and single-crystalline specimens (sheets, tubes and others) from melts of some metals, especially Al and its alloys, in the Physical and Technical Institute of the USSR Academy of Sciences in 1938–1941. The Second World War interrupted these experiments, but they have continued since the 1950s. In 1950–58, some of Stepanov's collaborators, especially postgraduate students A.L. Shakch-Budagov and B.M. Goltsman, continued these experiments with metals and alkaline halides. The present author of this chapter has taken part in these events since 1959 when he began his scientific activity as an undergraduate student in the Stepanov laboratory of the Leningrad Physical and Technical Institute of the USSR Academy of Sciences.

In 1963 A.V. Stepanov formulated his global idea [Stepanov 1963]: it is necessary to find a way to pull all types of industrial profiles from melts of metals and alloys. It could save energy, and eliminate extruding, rolling, cutting and many other types of mechanical treatments. This was the basis of practical investigations carried out in Stepanov's laboratory. Two main directions have been developed: (i) polycrystalline metals and alloys and (ii) semiconductor single crystals.

2.6.6.1 Shaped Metal Profiles

The present author of this chapter was put in charge of work on polycrystalline metals and alloys. First of all, Stepanov and I decided to demonstrate the possibilities of the technique. For this, we designed equipment for the continuous production of Al tubes and the installation was completed in 1963. During development of this apparatus, many technical problems were solved [Tatartchenko 1971-1]. The equipment contained two connected crucibles: the first for feeding and the second for the pulling of a 6-mm diameter tube with 0.5-mm wall thickness, automatically wound on a coil. During testing of the installation, we obtained specimens of tubes 4000 m long with a growth speed of 15 m h^{-1} . The installation was made very compact so that its operation could be demonstrated at various exhibitions. In 1964, the present author showed it at the Industrial Exhibition of the Soviet Union in Genoa, Italy. It was a great success: many articles described this new metallurgical technique. After that, we developed a second version of the installation for production of Al profiles of various complicated cross-sections with lengths up to 3 m [Antonov 1981]. The author demonstrated the working installation at exhibitions in Hungary (twice in 1967), in Italy (1968) and in Czechoslovakia (1971). Examples of aluminium profiles obtained with this installation are shown in Figure 2.31. The possibility of using the technique for pulling steel profiles was also demonstrated [Tatartchenko 1971-2] (Figure 2.32a).

2.6.6.2 Shaped Ge Crystals

For the application of the technique to single-crystal pulling, the laboratory was working intensively with the huge industrial Ge project. The present author participated by developing the theory described above as well as its application to the process (see, for instance, [Sachkov 1973]). Some industrial laboratories and plants were included in the project and, in the former Soviet Union in the late 1960s, about 85% of Ge was produced as shaped crystals. For instance, for electronic applications, instead of pulling one crystal

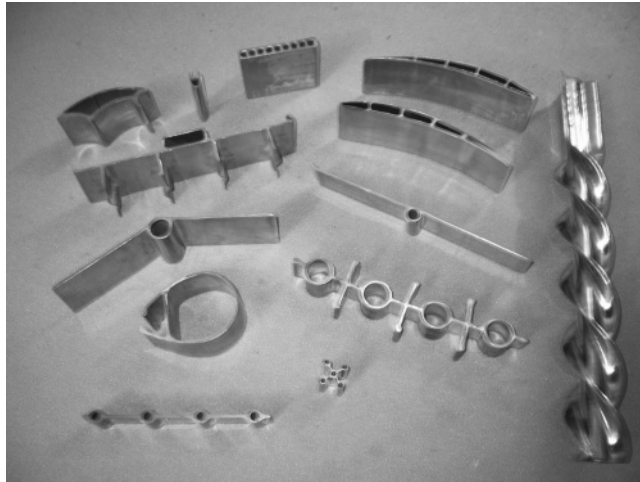


Figure 2.31 Al heat exchangers and other profiles TPS-grown by the author of this chapter in collaboration with A.S. Kostigov at the Physical and Technical Institute of the USSR Academy of Sciences in 1964–1972.

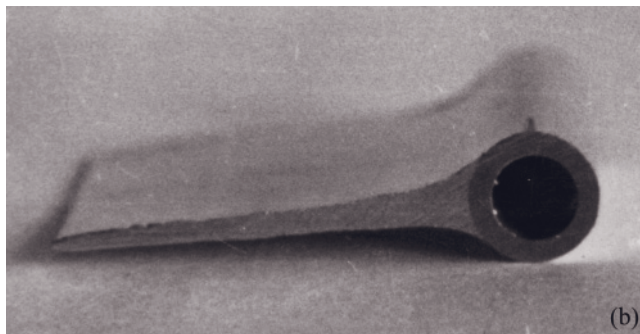
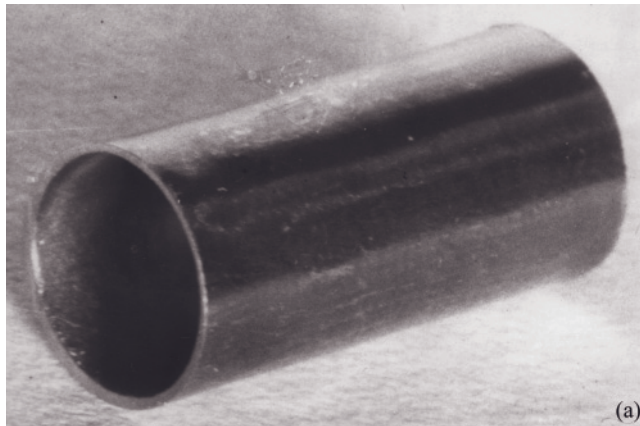


Figure 2.32 Steel tube (a) and steel tube with Al rib (b) TPS-grown by the author of this chapter at the Physical and Technical Institute of the USSR Academy of Sciences.

by the Cz technique, we pulled, from the same crucible, without any special control, 26 round cylindrical crystals with a diameter of 10.0 ± 0.1 mm [Antonov 1981].

2.6.6.3 *Development of TPS*

Until 1967 shaped crystal growth had been developed only in the former Soviet Union. The publication of information concerning shaped filament growth [La Belle 1967] and especially edge-defined film-fed growth (EFG) [La Belle 1971-1, 1971-2] changed the situation dramatically: shaped crystal growth now appeared in the USA. After that, interest in shaped crystal growth spread to many research groups, especially for the growth of sapphire and silicon. In the former Soviet Union, these crystal growth techniques have continued to develop. Every year since 1968, the laboratory has organized Russian national conferences with published proceedings (see, for instance, [Voinova 1968]) as well as special issues of the *Bulletin of the Academy of Sciences of the USSR, Physical Series* (see, for instance, [Antonov 1969]).

A.V. Stepanov died in 1972 but the work in his laboratory has continued. All types of methods involving pulling from a shaper were called Stepanov techniques. As for the present author, he organized the Shaped Crystal Growth Laboratory with a staff of 40 within the Solid State Physics Institute of the Academy of Sciences of the USSR in Chernogolovka, near Moscow. Many theoretical and experimental aspects of shaped growth, including microgravity experiments, were developed there. For a long time our main competitor during was the Tyco laboratory in the USA, where EFG growth was being developed for sapphire and Si. In 1978, the present author visited the Tyco laboratory and had very interesting discussions with La Belle. At that time, it was impossible to imagine that he would come to work in that laboratory (later Saphikon, then Saint-Gobain Crystal) as the chief scientist 24 years later. Now, shaped crystal growth is widespread but a lot of names are used, especially EFG and Stepanov technique. Since 1980, the author has preferred to use the name TPS rather than Stepanov or EFG techniques. Here are the reasons for that.

2.6.6.4 *Initiation of TPS Development and Some Peculiarities*

The priority in using a shaper (holes in plates placed onto the melt surface for shaping melt-pulled crystals) belongs to Gomperz [Gomperz 1922]. He was the first to have used mica plates floating on melt surfaces for pulling Pb, Zn, Sn, Al, Cd, Bi thin filaments through holes in the plates. Sometimes the filaments had a single crystalline structure. In 1923 and 1924, the same technique was also used for filament pulling by [Mark 1923, Grüneisen 1924]. In 1929, for growth of Zn single-crystalline filaments, a single crystalline seed was used for the first time [Hoyem 1929]. In 1929, the technique was named the Czochralski–Gomperz technique [Hoyem 1929, 1931]. In 1928, P. Kapitza, later awarded the Nobel Prize, used this technique for growth of Bi rods [Kapitza 1928]. So, between 1922 and 1931 period, six papers concerned with the use of shapers for crystal pulling were published. Moreover, the technique was described as a variant of the Cz technique, the Czochralski–Gomperz technique. Hence, Stepanov does not have the priority. However, he never referred to these papers in his publications. He did not seem to be interested in the functions of the shaper from the physical point of view. For example, he is one of the co-authors of the papers [Tatartchenko 1968, 1969-1], which explain

catching and wetting boundary conditions, and on the other hand, he is a co-author of [Tsivinskii 1970], the inconsistency of which has been discussed in section 2.6.1.5 above. What makes the situation more absurd is that he also co-authored the paper where this inconsistency is demonstrated [Tatartchenko 1969-2].

In [Stepanov 1963] Stepanov claimed to have invented ‘the principle of shape formation from a melt, using capillary forces or some other actions (other than crucible walls) on the melt, of the cross-section or an element of a cross-section of solid profile following crystallization’. This formulation covers the Cz, Verneuil and FZ techniques as well as electromagnetic, ultrasonic, inertial and other possibilities of shaping. In the same book we read: ‘A shaper should be distinguished from a die. A die is the embodiment of a brute force. A shaper is a more spiritual system. Its aim, first of all, is to provide a delicate effect on the curvature and shape of the mobile column of the liquid melt stretching itself behind the crystal by creating new boundary conditions along its contour’. We agree that there is a big difference between a die and a shaper, but in spite of Stepanov’s important role in the dissemination of TPS [Tatartchenko 2001-2], ‘new boundary conditions’ were never been specified in his papers. On the contrary, our capillary shaping analysis of the TPS and theoretical explanation of the determining role of the influence of boundary conditions on dynamic stability, carried out in 1967 and 1970 [Tatartchenko 1968, 1969-1, 1973], are complete: if a shaper is used to pull shaped crystal, it is impossible to suggest conditions other than catching or wetting. From this point of view, the EFG technique is only a variant using catching boundary condition. It is probably because of a low level of expertise in patent offices that the independent EFG patent exists: the edge-defined condition for meniscus was published in the paper [Tatartchenko 1968, 1969-1] as ‘catching boundary conditions’ before the EFG patent was deposited. Capillary feeding was, however, described for the first time in the EFG patent. Certainly, many shaped growth schemes have some peculiarities. Among them, principally the variable shaping technique (VST) and local shaping technique (LST), developed with the participation of the present author, should be mentioned. They are discussed in Chapter 5.

2.7 Shaped Growth of Ge, Sapphire, Si, and Metals: a Brief Presentation

The widest industrial application of the TPS has been for the growth of Ge, sapphire, and Si.

2.7.1 Ge

In the 1960s and 1970s, Ge was one of the main materials used for electronics. It is a rare and expensive material, and is no longer used for this purpose. The development of TPS for Ge at that time has been mentioned above, and information concerning TPS Ge growth can be found in the review and proceedings of the Russian national workshops [Voinova 1968, Antonov 1969, 1971, 1972, 1976, 1979, 1981, 1982, 1983, 1985].

2.7.2 Sapphire

Information concerning TPS growth of sapphire and peculiarities of its structure and application can be found in Chapter 5 of this book and also in the reviews [Tatartchenko 1993, 2005].

2.7.3 Si

The third example of the successful industrial application TPS is Si. But, unlike sapphire, all of the numerous attempts to grow shaped Si crystals of electronic grade have been unsuccessful. Shaped Si is characterized by the presence of a specific defect structure (parallel twins) influencing its electronic properties. However, the quality of the large-area thin sheets obtained was acceptable for industrial production of cheap solar cells. Information concerning the TPS growth of Si and peculiarities of its structure and application can be found in Chapter 5 of this book, in reviews [Tatartchenko 1988, 1993] and also in the proceedings of three international conferences [Cullen 1980, Kalejs 1987, 1990].

Using the example of Si shaped growth, we now show how stability theory can be used to characterize a crystal growth process. In Figure 2.33 three schemes of shaped growth are compared: classical schemes of rod and tape growth with the catching boundary condition, and the two shaping elements technique (TSET) – horizontal growth on a substrate where the substrate is used as a part of a solar cell. This variant of shaped Si growth was suggested 25 years ago [Brantov 1984]. An outline of the technique can be seen in Figure 2.33. When a graphite cloth is used as the substrate the technique is called ‘silicon on cloth’ (SOC). Figure 2.33 shows the attenuation curves for perturbation of the crystallization front. It is clear that the TSET shows better behaviour than the other techniques.

Special experiments were carried out for TSET. The relocation time was calculated as a function of the growth speed. It was found to be decreased when the growth speed increased up to 6cm/min but unchanged with a further speed increase. Two speeds

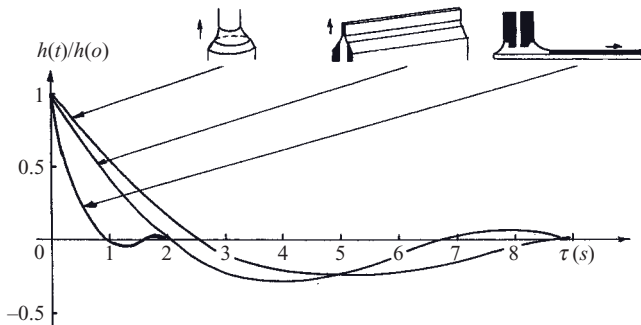


Figure 2.33 Calculated curves of attenuation of crystallization front perturbation for Si shaped growth techniques.

(1.5 and 6 cm/min) were used in the experiments. The surface quality of the ribbons grown at a speed of 6 cm/min was much better; the roughness amplitude was five times less.

2.7.4 Metals and Alloys

In the author's experience, profiles can be pulled from pure metals and eutectic alloys when a proper material for the shaper is found, either wetted or nonwetted, but chemically inert. The profiles have good surface quality (sometimes mirror-like). It is easy to grow low-melting metal single crystals by this technique, but they have not found any technical applications. For single crystals of refractory metals, for instance Mo, which is used in foil production by subsequent forming, it is very difficult to find a shaper material.

Polycrystalline metal profiles could be used for many applications, for instance heat-exchangers from Al alloys (see Figure 2.31). But when alloys with good mechanical properties are needed, the composition of the alloy is complicated. There is a big gap between the temperatures of liquidus and solidus. Dendrite crystals appear in the meniscus and the problem of profile pulling is rather difficult, both from the point of view of surface quality and internal structure. So, it is difficult for TPS to compete with extrusion. On the other hand, the structure and mechanical properties of TPS profiles are better than those of cast profiles. The story is not over yet. The problem of industrial application is not easy, and a lot research effort is required. First of all, alloys of special compositions have to be developed. Success in TPS applications for special steel [Tatartchenko 1971-2] (Figure 2.32a) and for steel tubes with Al rib (Figure 2.32b) was promising. These last profiles (previously unpublished) were pulled by the author, but unfortunately investigations have not been continued.

2.8 TPS Peculiarities

In conclusion, the peculiarities of TPS are as follows:

- The crystals have the shape that is needed for the most rational practical use.
- The technique can be applied to any material if a suitable shaper material (either wetted or nonwetted, but chemically inert) can be found.
- The range of crystal dimensions is large: filaments of 0.02 mm diameter; tubes of 0.5 m diameter; plates $480 \times 320 \times 10$ mm.
- The growth speed, as a rule, is much higher than in other crystal growth techniques.
- The crystal, as a rule, has a special structure concerned with the interface faceting (see Chapter 5).
- The shaper influences the interface shape.
- The separation of the growth zone from the melt in the crucible allows continuous feeding by raw material during the growth process. As a result, brief presence of the melt in the crucible before growth is possible, if necessary. Periodic change of doping is also possible.

- The distribution of impurities along the axis of the crystal is more uniform. Indeed, if the coefficient of distribution of impurities is not equal to 1 during crystal growth, the concentration of impurities changes along the axis of crystals in most of the crystal growth techniques. A solution to this problem can be found by localizing part of the melt at the growth zone without stirring it in with the other melt volume. This situation is realized, for instance, in using an additional small-volume crucible for the Cz technique. More effective results are achieved by capillary feeding of the TPS.
- The distribution of impurities in the cross-section of the crystal can be controlled by the use of special systems of capillaries for feeding.
- A combination of doped and undoped areas can be achieved in the same crystal (see Chapter 5).
- The dynamic stability theory, developed for the TPS, was successfully used for other CST as well as for analysis of cylindrical pores (negative crystals) growth and radial instability of vapour whisker growth [Tatartchenko 1988, 1993, 1994-1, 1994-2].

References

- [Adams 1941] Adams N.K., *The Physics and Chemistry of Surfaces*, Cambridge University Press, Cambridge (1941).
- [Alioshin 1990] Alioshin A.A., Bletsan N.I., Bogatyriov S.I., Fedorenko V.N., *J. Cryst. Growth* **104** (1990) 130–135.
- [Antonov 1969] Antonov P.I. (ed.), *Proc. 2nd Conf. Stepanov's Growth of Semiconductor Single Crystals, April 1968, Izv. Akad. Nauk SSSR Ser. Fiz.* **33** (1969) 1945–2040 (in Russian; English translation in *Bull. Acad. Sci. USSR Phys. Ser.*).
- [Antonov 1971] Antonov P.I. (ed.), *Proc. 4th Conf. Stepanov's Growth of Semiconductor Single Crystals, March 1970, Izv. Akad. Nauk SSSR Ser. Fiz.* **35** (1971) 441–552 (in Russian; English translation in *Bull. Acad. Sci. USSR Phys. Ser.*).
- [Antonov 1972] Antonov P.I. (ed.), *Proc. 5th Conf. Stepanov's Growth of Semiconductor Single Crystals, March 1971, Izv. Akad. Nauk SSSR Ser. Fiz.* **36** (1972) 457–618 (in Russian; English translation in *Bull. Acad. Sci. USSR Phys. Ser.*).
- [Antonov 1976] Antonov P.I. (ed.), *Proc. 7th Conf. Stepanov's Growth of Semiconductor Single Crystals, March 1976, Izv. Akad. Nauk SSSR Ser. Fiz.* **40** (1976) 1321–1547 (in Russian; English translation in *Bull. Acad. Sci. USSR Phys. Ser.*).
- [Antonov 1979] Antonov P.I. (ed.), *Proceedings of the 8th Conference on Stepanov's Growth of Shaped Single Crystals and profiles, March 1979, Izv. Akad. Nauk SSSR Ser. Fiz.* **43** (1979) 1925–2009 and **44** (1980) 225–414 (in Russian; English translation in *Bull. Acad. Sci. USSR Phys. Ser.*).
- [Antonov 1981] Antonov P.I., Zatulovskiy L.M., Kostigov A.S., Levinzon D.I., Nikanorov S.P., Peller V.V., Tatarchenko V.A., Juferev V.S., *Preparation of Shaped Single Crystals and Products by Stepanov's Technique*, Nauka Science, Moscow (1981) (in Russian).
- [Antonov 1982] Antonov P.I., Nosov Yu.G., Spivak L.N., Pivina M.E. (eds), *Proc. 9th Conf. Stepanov's Growth of Shaped Single Crystals and Profiles, March 1982, Institute of Nuclear Physics, Leningrad* (1982), pp. 1–348 (in Russian).
- [Antonov 1983] Antonov P.I. (ed.), *Proc. 9th Conf. Stepanov's Growth of Shaped Single Crystals and Profiles, March 1982, Izv. Akad. Nauk SSSR Ser. Fiz.* **47** (1983) 209–411 (in Russian; English translation in *Bull. Acad. Sci. USSR Phys. Ser.*).
- [Antonov 1985] Antonov P.I. (ed.), *Proc. Conf. Stepanov's Growth of Shaped Single Crystals and Profiles, March 1985, Izv. Akad. Nauk SSSR Ser. Fiz.* **49** (1985) 2289–2472 (in Russian; English translation in *Bull. Acad. Sci. USSR Phys. Ser.*).

- [Antonov 1989] Antonov P.I. (ed.), *Proc. Conf. Stepanov's Growth of Shaped Single Crystals and Profiles*, March 1988, Physical and Technical Institute, Leningrad (1989), pp. 1–285 (in Russian).
- [Antonov 1994] Antonov P.I. (ed.), *Proc. Conf. Stepanov's Growth of Crystal Profiles, Plasticity and Strength of Crystals, November 1993*, *Izv. Akad. Nauk SSSR Ser. Fiz.* **58** (9) (1994) 1–190 (in Russian; English translation in *Bull. Acad. Sci. USSR Phys. Ser.*).
- [Antonov 1999] Antonov P.I. (ed.), *Proc. Conf. Stepanov's Growth of Crystal Profiles, Plasticity and Strength of Crystals, October 1998*, *Izv. Aka. Nauk SSSR Ser. Fiz.* **63** (9) (1999) 1681–1882 (in Russian; English translation in *Bull. Acad. Sci. USSR Phys. Ser.*).
- [Antonov 2004] Antonov P.I. (ed.), *Proc. Conf. Stepanov's Growth of Crystal Profiles, Plasticity and Strength of Crystals, October 2003*, *Izv. Akad. Nauk SSSR Ser. Fiz.* **68** (6) (2004) 758–911 (in Russian; English translation in *Bull. Acad. Sci. USSR Phys. Ser.*).
- [Babik 1999] Babik F., Duffar T., Witomski P., Nabo J.P., *Izv. Akad. Nauk SSSR, Ser. Fiz.* **63**(9) (1999) 1699–1704 (in Russian; English translation in *Bull. Acad. Sci. USSR Phys. Ser.*).
- [Bachmann 1970] Bachmann K.J., Kirsch H.J., Vetter K.J., *J. Cryst. Growth* **7** (1970) 290–295.
- [Bagdasarov 1977] Bagdasarov Ch.S., In: *Rost Kristallov* **11**, ed. E.I. Givargizov, Erevan State University, Erevan (1977), pp. 179–195 (in Russian; English translation: *Growth of Crystals*, Consultants Bureau, New York, 1978).
- [Balint 2005] Balint S., Braescu L., Balint A.M., Szabo R., *J. Cryst. Growth* **283** (2005) 15.
- [Borodin 1981] Borodin V.A., Brener E.A., Tatarchenko V.A., Gusev V.I., Tsigler I.N., *J. Cryst. Growth* **52** (1981) 505–508.
- [Borodin 1982-2] Borodin V.A., Brener E.A., Steriopolu T.A., Tatarchenko V.A., Chernishova L.I., *Crys. Res. Technol.* **17** (1982) 1199–1207.
- [Brantov 1983] Brantov S.K., Tatarchenko V.A., *Cryst. Res. Technol.* **18** (1983) K59–K64.
- [Brantov 1984] Brantov S.K., Epelbaum B.M., Tatarchenko V.A., *Mater. Lett.* **2** (4A) (1984) 274–277.
- [Burton 1953] Burton J.A., Prim P.C., Slichter W.P., *J. Chem. Phys.* **21** (1953) 1987–1991.
- [Carslaw 1959] Carslaw H.S., Jaeger J.C., *Conduction of Heat in Solids*, Clarendon Press, Oxford (1959), p. 148.
- [Cullen 1980] Cullen G.W., Surek T., Antonov P.I. (eds), *Shaped crystal growth. J. Cryst. Growth* **50** (1980) 1–396.
- [Despreaux 2000] Despreaux S., Witomski P., Duffar T., *J. Cryst. Growth* **209** (2000) 983–993.
- [Goltsman 1958] Goltsman B.M., *Opt. Mech. Ind.* **11** (1958) 45–46 (in Russian).
- [Goltsman 1959] Goltsman B.M., Stepanov A.V., *Bull. Acad. Sci. USSR Metall. Fuel Ser.* **5** (1959) 49–53 (in Russian).
- [Gompertz 1922] Gompertz E.V., *Z. Phys.* **8** (1922) 184–190.
- [Grüneisen 1924] Grüneisen E., Goens E., *Z. Phys.* **26** (4/5) (1924) 235–273.
- [Horowitz 1993] Horowitz A., Biderman S., Gazit D., *et al. J. Cryst. Growth* **128** (1993) 824–828.
- [Hoyem 1929] Hoyem A.G., Tyndall E.P.T., *Phys. Rev.* **33** (1929) 81–89.
- [Hoyem 1931] Hoyem A.G., *Phys. Rev.* **38** (1931) 1357–1371.
- [Kalejs 1978] Kalejs J.P., *J. Cryst. Growth* **44** (1978) 329–334.
- [Kalejs 1987] Kalejs J.P., Surek T., Tatartchenko V.A. (eds), *Shaped crystal growth. J. Cryst. Growth* **82** (1987) 1–278.
- [Kalejs 1990] Kalejs J.P., Surek T. (eds): *Shaped crystal growth. J. Cryst. Growth* **104** (1990) 1–200.
- [Kapitza 1928] Kapitza P., *Proc. R. Soc. London A* **119** (1928) 358–443.
- [Korn 1961] Korn G.A., Korn T.M., *Mathematical Handbook for Scientists and Engineers*, McGraw-Hill, New York (1961), pp. 282–284.
- [Kuandykov 2001] Kuandykov L.L., Antonov P.I., *J. Cryst. Growth* **222** (2001) 852–861.
- [La Belle 1967] La Belle H.E., Mlavsky A.I., *Nature* **216** (1967) 574–575.
- [La Belle 1971-1] La Belle H.E., Mlavsky A.I., *Mater. Res. Bull.* **6** (1971) 571–580.
- [La Belle 1971-2] La Belle H.E., Mlavsky A.I., *Mater. Res. Bull.* **6** (1971) 581–590.
- [Landau 1971] Landau L.D., Lifchits E.M., *Mécanique des Fluides*, Mir, Moscow (1971) (in French).

- [Lesk 1976] Lesk I.A., Baghdadi A., Gurtler R.W., Ellis R.J., Wise J.A., Colmen M.G., *12th IEEE Photovoltaic Specialists Conf. Record*, IEEE, New York (1976), pp. 173–177.
- [Mark 1923] Mark H., Polanyi M., Schmid E., *Z. Phys.* **12** (1923) 58–77.
- [Mullins 1964] Mullins V.W., Sekerka F.R., *J. Appl. Phys.* **35** (1964) 444–455.
- [Pet'kov 1990] Pet'kov I.S., Red'kin B.S., *J. Cryst. Growth* **104** (1990) 20–22.
- [Petrova 1990] Petrova D., Pavloff O., Marinov P., *J. Cryst. Growth* **99** (1990) 841–844.
- [Romanova 1976] Romanova G.I., Tatarchenko V.A., Tichonova N.P., *Trudi Goi* **54** (188) (1976) 10–13 (in Russian; Soviet Proceedings of State Optical Institute, Leningrad).
- [Sachkov 1973] Sachkov G.V., Tatarchenko V.A., Levinzon D.I., *Izv.Akad. Nauk SSSR Ser. Fiz.* **37** (1973) 2288–2291 (in Russian; English translation *Bull. Acad. Sci. USSR Phys. Ser.*).
- [Satunkin 1980] Satunkin G.A., Tatarchenko V.A., Shaitanov V.I., *J. Cryst. Growth* **50** (1980) 133–139.
- [Seidensticker 1979] Seidensticker R.G., Stewart A.M., Hopkins R.H., *J. Cryst. Growth* **46** (1979) 51–54.
- [Shakh-Budagov 1959] Shakh-Budagov A.L., Stepanov A.V., *J. Tech. Phys.* **29** (1959) 394–405 (in Russian; English translation *Sov. Phys. Tech. Phys.*).
- [Stepanov 1959-1] Stepanov A.V., *J. Tech. Phys.* **29** (1959) 382–393 (in Russian; English translation *Sov. Phys. Tech. Phys.*).
- [Stepanov 1959-2] Stepanov A.V., *Mech. Eng. Bull.* **11** (1959) 47–50 (in Russian).
- [Stepanov 1963] Stepanov A.V., *The Future of Metals Machining*, Lenizdat, Leningrad (1963) (in Russian).
- [Surek 1976] Surek T., *J. Appl. Phys.* **47** (1976) 4384–4393.
- [Swartz 1975] Swartz J.C., Surek T., Chalmers B., *J. Electron. Mater.* **4** (1975) 255–264.
- [Tatartchenko 1967] Tatarchenko V.A., Saet A.I., *J. Eng. Phys.* **13**(2) (1967) 255–258 (in Russian; English translation in *J. Eng. Phys. USA*).
- [Tatartchenko 1968] Tatarchenko V.A., Saet A.I., Stepanov A.V., *Proc. 1st Conf. Stepanov's Growth of Semiconductor Single Crystals*, Physical Technical Institute, Leningrad (1968), pp. 83–97 (in Russian).
- [Tatartchenko 1969-1] Tatarchenko V.A., Saet A.I., Stepanov A.V., *Izv.Akad. Nauk SSSR Ser. Fiz.* **33** (1969) 1954–1959 (in Russian; English translation *Bull. Acad. Sci. USSR Phys. Ser.*).
- [Tatartchenko 1969-2] Tatarchenko V.A., Stepanov A.V., *Izv. Akad.Nauk SSSR Ser. Fiz.* **33** (1969) 1960–1962 (in Russian; English translation *Bull. Acad. Sci. USSR Phys. Ser.*).
- [Tatartchenko 1971-1] Tatarchenko V.A., Stepanov A.V., In: *Machines and Devices for Testing of Materials*. Metallurgy, Moscow (1971). (in Russian).
- [Tatartchenko 1971-2] Tatarchenko V.A., Vakhrushev V.V., Kostygov A.S., Stepanov A.V., *Izv. Akad. Nauk SSSR Ser. Fiz.* **35** (1971) 511–513 (in Russian; English translation *Bull. Acad. Sci. USSR Phys. Ser.*).
- [Tatartchenko 1973-1] Tatarchenko V.A., *Phys. Chem. Mat. Treat.* **6** (1973) 47–53 (in Russian).
- [Tatartchenko 1973-2] Tatarchenko V.A., Romanova G.I., In: *Single Crystals and Technique* **2** (1973) 48–53 (in Russian).
- [Tatartchenko 1974] Tatarchenko V.A., *4th Int. Conf. Crystal Growth*, Tokyo (1974), abstracts, pp. 521–522.
- [Tatartchenko 1976-1] Tatarchenko V.A., Brener E.A., *Bull. Acad. Sci. USSR Phys. Ser.* **40** (7) (1976) 106–115.
- [Tatartchenko 1976-2] Tatarchenko V.A., Brantov S.K., *Bull. Acad. Sci. USSR Phys. Ser.* **40** (7) (1976) 116–129.
- [Tatartchenko 1977-1] Tatarchenko V.A., *J. Cryst. Growth* **37** (1977) 272–284.
- [Tatartchenko 1977-2] Tatarchenko V.A., Satunkin G.A., *J. Cryst. Growth* **37** (1977) 285–288.
- [Tatartchenko 1987] Tatarchenko V.A., *J. Cryst. Growth* **82** (1987) 74–80.
- [Tatartchenko 1988] Tatarchenko V.A., *Stable Crystal Growth*, Nauka Science, Moscow (1988) (in Russian) Distributed by Springer Science + Business Media.
- [Tatartchenko 1991] Tatarchenko V.A., *Adv. Space Res.* **11**(7) (1991) 307–321.
- [Tatartchenko 1993] Tatarchenko Y.A., *Shaped Crystal Growth* (Kluwer, Dordrecht, 1993).
- [Tatartchenko 1994-1] Tatarchenko V.A., In: *Handbook of Crystal Growth*, Vol. 2b, ed. D.T.J. Hurler, North-Holland, Amsterdam (1994), pp. 1011–1110.

- [Tatartchenko 1994-2] Tatarchenko V.A., *J. Cryst. Growth* **143** (1994) 294–300.
- [Tatartchenko 1995] Tatarchenko V.A., Nabot J.Ph., Duffar T., Tatartchenko E.V., Roux B., *J. Cryst. Growth* **148** (1995) 415–420.
- [Tatartchenko 1997] Tatarchenko V.A., Uspenski V.S., Tatartchenko E.V., Nabot J.Ph., Duffar T., Roux B., *J. Cryst. Growth* **180** (1997) 615–626.
- [Tatartchenko 2000] Tatarchenko V.A., Uspenski V.S., Tatartchenko E.V., Roux B., *J. Cryst. Growth* **220** (2000) 301–307.
- [Tatartchenko 2001-1] Tatarchenko V.A., In: *Encyclopedia of Materials: Science and Technology*, Elsevier Science, Amsterdam (2001), pp. 3697–3703.
- [Tatartchenko 2001-2] Tatarchenko V.A., *J. Jpn Assoc. Cryst. Growth* **28** (2001) 55–59.
- [Tatartchenko 2005] Tatarchenko V.A., In: *Bulk Crystal Growth of Electronic, Optical and Optoelectronic Materials*, ed. P. Capper, John Wiley & Sons, Ltd, Chichester (2005), pp. 299–338.
- [Tsivinskii 1962] Tsivinskii S.V., *J. Eng. Phys.* **5**(9) (1962) 59–63 (in Russian; English translation *J. Eng. Phys. USA*).
- [Tsivinskii 1970] Tsivinskii S.V., Antonov P.I., Stepanov A.V., *Sov. Phys.Tech. Phys.* **15** (1970) 274–277.
- [Voinova 1968] Voinova N.A. (ed.), *Proc. 1st Conf. Stepanov's Growth of Semiconductor Single Crystals*, April 1967, Physical-Technical Institute, Leningrad (1968), pp. 1–209 (in Russian).

3

Czochralski Process Dynamics and Control Design

Jan Winkler

Technische Universität Dresden

Michael Neubert

Leibniz-Institut für Kristallzüchtung, Berlin

Joachim Rudolph

Universität des Saarlandes

Ning Duanmu

GT Solar International

Michael Gevelber

Boston University

This chapter presents many of the critical concepts and practices needed to design and implement modern control for the Czochralski (Cz) process. An overview of important process modelling and control issues is provided in sections 3.1 and 3.2. Mathematical modelling for analysis and controller design is presented in section 3.3. Critical to developing an appropriate control design is an understanding of the fundamental dynamics and input/output coupling of the process, which is provided in section 3.4. Here, in particular,

it is important to understand the relation of the process dynamics (e.g. how fast the process states respond to an input change and the nature of this response) to both the specific operating regime selected, and important process characteristics such as gradients, process physics, system design, and materials characteristics. Two conventional control approaches are presented in section 3.5: PID control using the diameter of the bright meniscus ring as the measured variable, as used in Si crystal growth, and weight-based control using PID controllers, as commonly used when crystal imaging is not available or possible (e.g. in growth of compound semiconductors by the liquid encapsulated Cz (LEC) method). Although these approaches are widely used in industry, they have some important limitations, which are discussed in detail.

A modern geometry-based nonlinear control approach which at least partially overcomes these problems and limitations is presented in section 3.6. The main idea of this approach is not to rely on a complex mathematical model of the overall process. Such a model usually suffers from many unknown parameters, boundary and initial conditions as well as doubtful assumptions. Instead, only those parts of the process are modelled and used for control design which describe the behaviour of the crystal geometry and the hydromechanics. The hydromechanical modelling of the system has been thoroughly explored in the literature, its parameters are known with sufficient accuracy, and its structure is sufficiently precise. The model-based controller is the core of the control concept. Some conventional PI controllers are grouped around this model-based controller in order to compensate for the missing knowledge about the thermal behaviour.

Finally, the use of an observer scheme to reconstruct process state variables not explicitly measured is presented in section 3.7, in terms of linear dynamics as well as those from a model based on the geometric coordinate frame. This section also shows how an alternative control structure can enhance the ability to reject disturbances.

3.1 Introduction and Motivation

This section presents an overview on the motivation and requirements of control for Czochralski crystal growth. Furthermore, some basic principles of control theory are presented to provide a framework.

3.1.1 Overview of Cz Control Issues

Early closed-loop control for the Cz process focused on implementing automatic diameter control (ADC) using a variety of different sensors and actuators. The goal was to reduce the variations of diameter, replacing the constant attention required by highly skilled operators. Early pioneers included Levinson, who used a weight measurement of the crucible or growing crystal to control heater power [Levinson 1959], and Patzner, Dessauer, and Poponiak who used an optical sensor to manipulate pull rate for Silicon (Si) [Patzner 1967]. Since then, diameter control has been developed for a variety of different materials and system configurations, where many complex problems have been identified such as those relating to use of a liquid encapsulant for the process, materials

with hard-to-control conditions that resulted in either high dislocation densities or large growth and shape variations, as well as the challenges in the scale-up of the process for larger crystal sizes. More recently, the focus of control design has been extended to maintain additional degrees of freedom which affect crystal quality such as growth rate, as well as crystal shape during the neck, shoulder, and tail sections in addition to the main body. In this section these requirements are described and the components of a modern control system needed to meet them are discussed.

3.1.2 Diameter Control

Crystal diameter is important mainly in matters of technological requirements. The better it meets the desired value and the better its constancy, the less material has to be cut off after growth [Hurle 1990]. Marked radius changes may also influence the structural properties of the crystal [Jordan 1981, Jordan 1984, Motakef 1991, Neubert 2001]. However, since Cz is a batch process (meaning there is no constant operating point due to the decrease in melt height) the dynamics of which cannot be captured in a linear model [Gevlber 1987-1, Hurle 1990]. In addition, in LEC growth there are time delays, making diameter control even more difficult [Johansen 1987-2, Jordan 1983]. Furthermore, more sophisticated variants of the Cz process, like the vapor pressure controlled Czochralski (VCz) method [Azuma 1983], intentionally lead to reduced axial and radial temperature gradients. This again results in increasing problems of diameter control and could thus benefit from a more sophisticated control concept. Consequently, the performance of diameter control based on the use of linear PID controllers with heuristically chosen parameters can be limited [Gevlber 1987-2, Gevlber 1988, Gevlber 1994-1, Gevlber 1994-2], as seen in Figure 3.1.

3.1.3 Growth Rate Control

Apart from tracking crystal radius along a desired trajectory, control of the crystal growth rate is also of special interest because it directly influences the properties of the growing crystal. With increasing demand for very narrow tolerances in structural, electrical and optical material properties, the growth rate becomes more and more important. It correlates directly with the amount of imperfections, like polycrystalline growth, twins and dislocations, as well as the number of native point defects and residual impurities and the amount of intentionally introduced dopants [Gevlber 1987-2, Voronkov 2002, Hurle 1991, Neubert 2001]. Consequently, there is an interest in growth rate control [Gevlber 2001], especially in Si crystal growth where the relation between growth rate and thermal gradients at the interface is of great importance in ensuring an extremely low point defect content [Falster 2000, Voronkov 1982, Voronkov 2002].

3.1.4 Reconstruction of Quantities not Directly Measured

Another challenging task results from the fact that, at least for the LEC process, the crystal diameter is not directly measured, because of the boron oxide layer. The measured

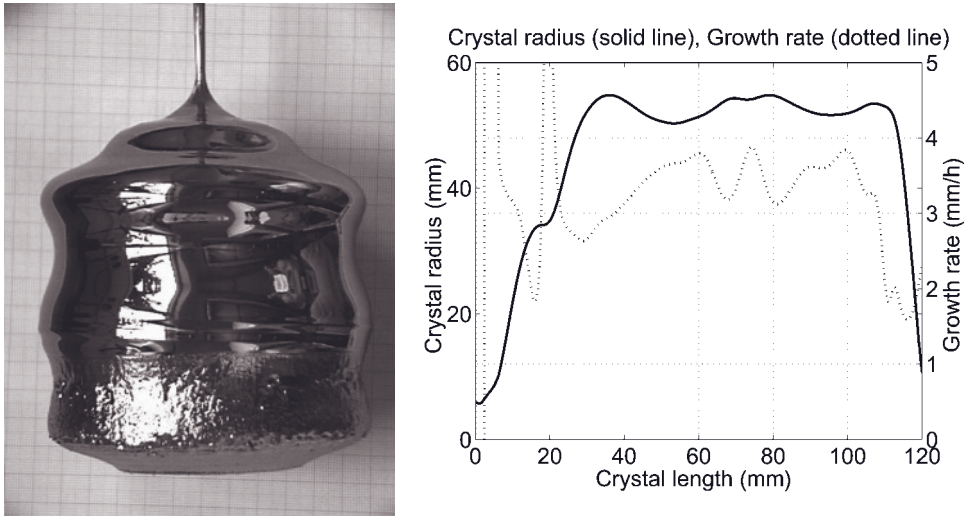


Figure 3.1 4" GaAs crystal grown by the vapour pressure controlled Cz (VCz) method. Left: Poor diameter control even though much effort has been spent in parametrization of a conventional control system. Right: Trajectory of radius and growth rate. Considerable fluctuations in growth rate can be observed, especially in the conical part.

quantity most commonly used in that case is the first time derivative of the force acting on a load cell mounted at the top of the pulling rod [Levinson 1959, Rummel 1966]. Because this quantity is also influenced by forces resulting from the meniscus and the boron oxide layer, the crystal diameter cannot be calculated easily from this signal [Bardsley 1974-1, Johansen 1992-1, Johansen 1992-2, Jordan 1983]. Furthermore, if the density of the solid is less than the density of the liquid, a well-known anomaly comes into play: an increasing diameter temporarily results in a decreasing first time derivative of the force measured by the load cell [Bardsley 1974-2, Bardsley 1977-1, Bardsley 1977-2, Gevelber 1988] (see Figure 3.2). The same holds for materials of which the melt does not completely wet its solid (see Chapter 1). Unfortunately, all commonly grown semiconducting materials show both effects. Measurement of the diameter of the bright meniscus ring [Digges 1975], as widely used in Si growth, can also be affected by a similar anomaly due to the so-called right-half-plane zero of the interface height [Gevelber 1988, Gevelber 1994-1]. From this it follows that reconstruction of crystal diameter and growth rate is a challenging task requiring comprehensive knowledge of the model. Details can be found in sections 3.5.2 and 3.7.

The anomaly also leads to crucial problems during the transfer from the shoulder into cylindrical growth: see Figure 3.3 (left). Furthermore, in case of LEC growth, the influence of the boron oxide layer comes into play, resulting in additional dynamical effects, as shown in Figure 3.3 (right).

3.1.5 Specific Problems for Control in Cz Crystal Growth

The most important region in Cz crystal growth is the meniscus, the interconnection between melt and crystal (Figure 3.4). The meniscus and its shape result from

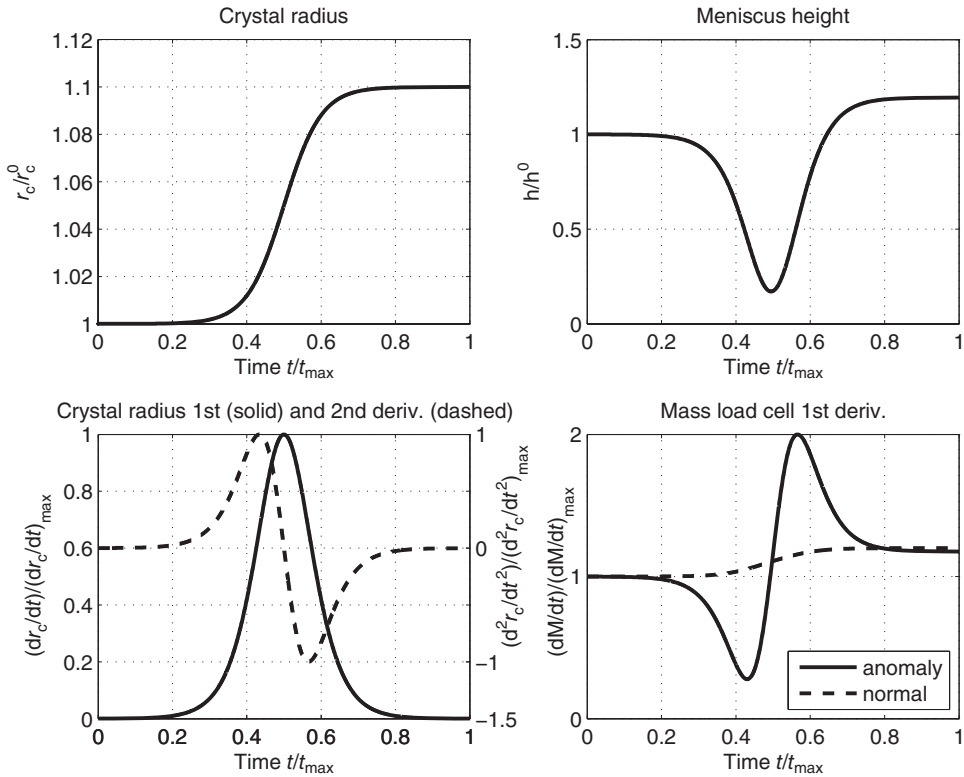


Figure 3.2 Anomaly of the differential weight gain signal illustrated by the example of a small perturbation of the crystal radius (based on conditions reported in [Bardsley 1977-1]). Top left: increase of crystal radius. Bottom left: corresponding first (solid line) and second (dashed line) derivative of the crystal radius. Top right: corresponding reaction of the meniscus height. Bottom right: Derivative of the force acting on the load cell with respect to time in case of anomalous (solid line) or normal behaviour (dashed line, i.e. the density of the solid is larger than the density of the liquid and the melt wets its solid). Radius and meniscus height are normalized on their unperturbed values, derivatives are normalized on the maximum values occurring during the perturbation.

gravitational forces and surface tension. At its upper end the so-called phase boundary, or interface is located. Here crystallization takes place and thereby heat of fusion (latent heat) is released. Because the crystal is pulled upwards into colder regions of the furnace a temperature gradient is established, which leads to a heat flow by conduction from the hot interface into the colder crystal [Derby 1986-1]. By this mechanism, crystallization is maintained throughout the growing process.

The amount of heat transported into the crystal consists of two components: The amount of heat transported from the meniscus region into the interface with radius r_c and the amount of heat released by crystallization. In general, the following relation holds for the vector \vec{v}_c of the growth rate along the phase boundary described by $z = Z(r)$, $r \in [0, r_c]$:

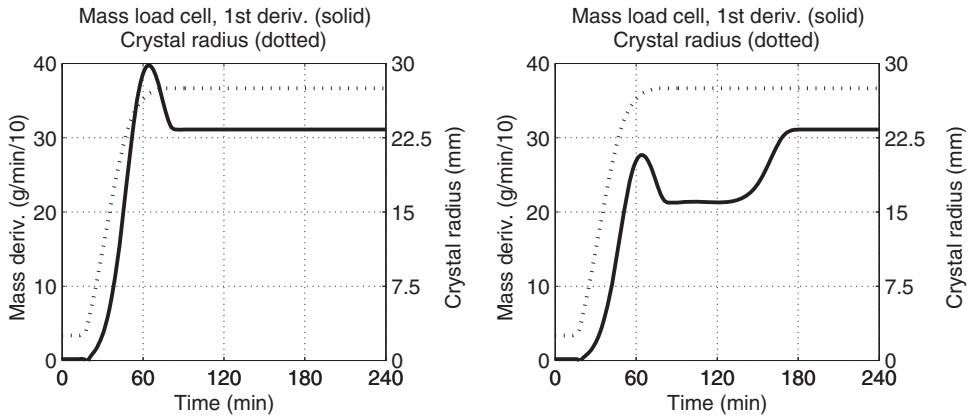


Figure 3.3 Left: Increase of the derivative of the force acting on the load cell with respect to time before the radius reaches its maximum. Right: For the LEC process an “aftershock” occurs in the differential weight gain signal because of the boron oxide layer. For clarity, the corresponding trajectory of the radius is shown as a dashed line (from [Winkler 2010-1]).

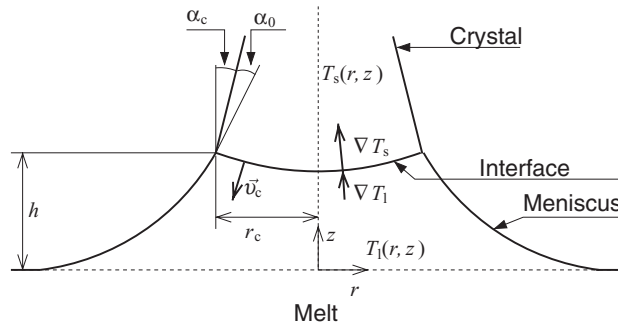


Figure 3.4 Sketch of the interface region with important physical quantities (from [Winkler 2010-1]).

$$\vec{v}_c(r, Z(r)) = \frac{1}{\rho_s \Delta H} (\lambda_l \nabla T_l(r, Z(r)) - \lambda_s \nabla T_s(r, Z(r))), \quad r \in [0, r_c]. \quad (3.1)$$

In this equation the specific latent heat is denoted by ΔH , the heat conductivities of the solid and the liquid are given by λ_s and λ_l , respectively, and $T_s(r, z)$ and $T_l(r, z)$ represent the temperature in the solid and the melt. The density of the crystal at the interface (at melting temperature T_i) is given by ρ_s . A necessary condition for growth is that the growth rate is positive, i.e. the heat flux is directed from the melt into the crystal.

Changes in the temperature gradients on the liquid or solid side of the phase boundary lead to an immediate change of growth rate, as can be easily seen from Equation (3.1). On the one hand, a local change of growth rate results in a deformation of the phase boundary, and in a change of the crystal diameter if this deformation is located at the rim of the interface. On the other hand, a change in interface geometry initiates a change in

heat transport. This consideration leads to the conclusion that the demand to grow crystals of well-defined shape makes necessary exact control of thermal conditions in the interface region. This is quite complicated because of disturbances in heat transport (initiated by convection of gas and melt or changes of material properties during growth) as well as by the batch character of the process which causes an ever-changing heat input from the heaters (see e.g. [Kim 1983]). Furthermore, the shape of the meniscus strongly depends on the radius r_c of the crystal at the interface as well as on the growth angle α ; see section 1.3 and Chapter 2 or [Boucher 1980, Mika 1975, Surek 1980]. This means that changes in the meniscus shape initiated by changes in geometry result in an immediate change of the heat balance in this region, with the consequences described above.

3.1.6 PID Control vs. Model-Based Control

It is common practice to realize feedback control by means of a PID controller. The PID controller processes a deviation $e(t)$ between the desired and the real value of the variable to be controlled in order to calculate a change $\Delta u(t)$ of the manipulated variable at time t :

$$\Delta u(t) = K_p e(t) + K_i \int_{t_0}^t e(\tau) d\tau + K_d \frac{de}{dt}(t). \quad (3.2)$$

The dynamic behaviour of the PID controller is parametrized using the three real constants K_p , K_i , and K_d . The PID controller has several advantages: (i) its operating principle is simple, (ii) it can be easily implemented, (iii) if certain conditions hold it can be adjusted using some simple rules, (iv) it is suitable for a wide range of technological systems found in practice. However, there are some drawbacks as well: (i) The PID controller is a linear controller. This means that its parametrization is adjusted for a certain operating point of the process. If this operating point changes (as is the case in Cz growth) parameters may have to be scheduled. The same holds for trajectory tracking, e.g. if the system is intentionally driven from one operating point to another. (ii) Because of their linear character, the performance of PID controllers is limited if the system shows nonlinear behaviour. The reason for this is the fact that a change of the manipulated variable is processed nonlinearly resulting in ‘unexpected’ reactions of the system (in comparison to a linear one). (iii) The situation worsens if the system contains time delays (e.g. $y(t) = u(t - \tau)$ with delay time τ). In this case, any reaction of the system to a change of the manipulated variable appears delayed by the delay time τ . This may result in an increasing integral in the PID algorithm (see Equation (3.2)). In Cz crystal growth, the LEC process belongs to the class of delay systems (see Figure 3.3, right). (iv) In summary, a PID controller does not necessarily reflect the dynamics of the system, especially if the order of the system is greater than 2. Therefore, it may be very time consuming to find appropriate parameters.

Generally speaking, one may overcome these limitations by empirical methods for parameter scheduling and parameter tuning rules. However, most often the controller has to be parametrized very weakly and with scheduled parameters. Thus, control performance becomes poor.

Fortunately, the theory and application of control systems have developed very rapidly in recent decades. The increasing capacity of microcontrollers and programmable logic controllers (PLC) combined with powerful mathematical control design methods prepared the ground for the use of sophisticated model-based controllers in practice. A model-based controller uses a mathematical model of the system, i.e. its structure and parameters are fitted to the system. This means that the controller can be used in a wide range of operating points and reflects the nonlinear system characteristics as well as time delays. In addition, parametrization effort is dramatically reduced. Anyhow, a model-based controller performs well only if the model is appropriate.

In addition, improved performance can be achieved by combining a feedback control law with additional components such as feedforward control or sophisticated trajectory planning. Therefore, in the next section a brief survey of the components of a current control system and the way of using mathematical models in control applications is provided.

3.1.7 Components of a Control System

A modern control system consists of more than a simple PID controller, as explained in detail in what follows (see Figure 3.5).

- Depending on time or crystal length, a *reference trajectory generator* calculates reference values for crystal radius and growth rate or other useful quantities. In the simplest case, the trajectory generator holds a fixed value, often called the setpoint or ‘hand value’. The planning of trajectories has to consider the physical properties of the system in order to avoid impossible values for the control inputs, for example. Furthermore, one cannot request physically impossible behaviour from the system, such as steps in any of the system quantities or their derivatives. It may be useful to reschedule the reference trajectories during growth to guarantee smooth behaviour of the controller.

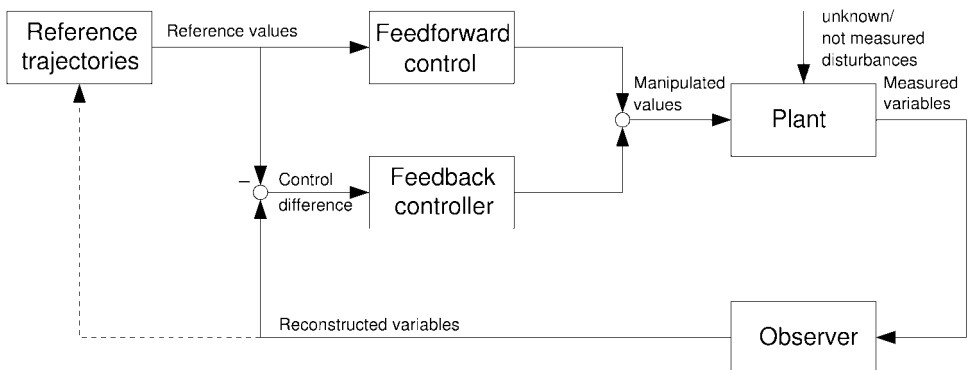


Figure 3.5 Sketch of a modern feedback control loop consisting of an observer for reconstruction of quantities which are not directly measured, a reference trajectory generator, a feedforward control and a feedback controller.

- The *feedforward control* calculates the control inputs (such as heater power or crystal pulling speed) from the reference values provided by the trajectory generator. This can be done empirically or by means of a mathematical model describing the system behaviour [Hagenmeyer 2005]. Using the values from the feedforward control one might be able to *steer* the system along its reference trajectory if the system is stable, only small perturbations are acting on the system, and the model is accurate enough. In the simplest case, the feedforward control is a constant value for the control inputs, commonly referred to as the setpoint.
- The *feedback controller* compensates for disturbances acting on the process. Furthermore, it is responsible for the correction of modelling imprecisions resulting in inaccuracies of the feedforward control. This is achieved by feedback of the measured variable (or an estimate of the latter) and a correction of the input calculated by the feedforward control. Unstable systems are stabilized by means of the feedback controller.
- Finally, it is not always possible to measure the controlled variable (e.g. the radius, for the Cz method) directly. In that case one can reconstruct this variable from the measured variable by means of a (possibly nonlinear) *observer* if a suitable model of the system is available and the system is observable (a system property discussed later in section 3.7).

All of these four components have to be adjusted carefully in order to obtain a high performance of the feedback control system. As one can see, modelling is an important task in developing a control system. For this reason, this topic is detailed in the following section.

3.1.8 Modelling in Crystal Growth Analysis and Control

Today, modelling and computer simulation play an important role in crystal growth as well as in control applications. A short comparison of how models are used in automatic control in contrast to numerical approaches in crystal growth will be given here, since the approaches and requirements differ quite a lot between the two fields.

A mathematical model which takes the spatial distribution as well as the time dependency of material parameters into account leads to a system of coupled *partial* differential equations with the corresponding initial, boundary, and compatibility conditions. They form a so-called infinite-dimensional or distributed-parameter system. Such systems are usually solved numerically using finite element methods (FEM). Using this approach, one can obtain results reflecting reality quite accurately. FEM is an absolutely essential resource in solving problems in plant design, thermal and stress analysis, etc. However, computational effort increases dramatically depending on the accuracy required, especially for solving *time-dependent* problems.

The approach used in model-based control is to keep the models as simple as possible. This is done in order to be able to run the models on the limited computer hardware usually available at the growth furnaces. It is achieved by partitioning the system under consideration into domains which may reasonably be considered as homogeneous, i.e. the material parameters of which are assumed to be constant. Heat and mass transfer between these domains are calculated from appropriate mass and energy balance equations. Since spatial dependence of the parameters is neglected, one ends up with a set of

ordinary differential equations forming a finite-dimensional or lumped-parameter model. Using such models one can calculate the basic system behaviour, leading to a qualitatively and quantitatively satisfactory insight into the process. Powerful methods for controller and observer design, trajectory planning and dynamic analysis exist for this class of models. The lack of accuracy can be mitigated by the introduction of feedback.

3.2 Cz Control Approaches

After Jan Czochralski's discovery, it took about 40 years for the Cz process to be introduced into industry [Teal 1950]. Since then, the development and improvement of diameter control has been on the agenda. In the following, we give a brief review of some of the most important articles published in the last 30 years dealing with the components of a control system for Cz crystal growth.

3.2.1 Proper Choice of Manipulated Variables

As explained in section 3.1.5, the main task of process control is to keep the thermal conditions in the interface region under control. Therefore, a proper choice of the manipulated variables is very important. The most obvious manipulated variables are the heat flows injected into the system by the heaters [Domey 1971], the translation speeds of the pulling and crucible rod [Patzner 1967], and the rotation rates of crystal and crucible (which change convection patterns in the melt and consequently the heat entry into the interface region). It is important to understand that a change in pulling speed indirectly effects the growth rate. Hence, the amount of latent heat released by the crystallization influences the heat balance at the interface, resulting in changing growth conditions; see Equation (3.1). Furthermore, it has to be considered which of these manipulated variables have a long-term, short-term, or only temporary effect. This strongly depends on thermodynamic conditions and parameters of the system [Derby 1987].

Apart from these quantities, several special inputs are presented in the literature: In [Ekhult 1986] the heat entry into the meniscus is directly manipulated by infrared radiators; [Brice 1970] suggests an apparatus blowing inert gas of well-defined temperature along the surface of the crystal in order to vary the heat flow through the crystal. This method is theoretically investigated in [Srivastava 1986]. The Peltier effect is used to initiate local temperature modifications at the interface in [Vojdani 1974].

In Si crystal growth heater power and pulling speed are usually both used as control inputs [Domey 1971], while in growth of III–V compound semiconductors the pulling speed is traditionally kept at low and constant values (In contrast to the elemental semiconductor Si, compound semiconductors are grown at low pulling speeds in order to avoid constitutional supercooling and thermoelastic stress [Riedling 1988, Thomas 1989, Wilke 1988].) However, small growth rates mean a small heat flux released from latent heat compared to the fluxes inside the melt and the crystal (Equation (3.1)). Thus, changes in pulling speed may not greatly affect the heat balance at the interface.

3.2.2 Feedforward Control

As described in section 3.1.7, feedforward control is an essential part of the overall control system. In crystal growth, a common method in practice is to determine the feedforward control by careful analysis of repeated growth runs, resulting in a trajectory for the control inputs which can then be used as part of the recipe.

Although this method is widely accepted it suffers from the fact that it is extremely time consuming and, thus, expensive, but it works well if the same conditions are repeated and there are no significant variations from run to run. However, any change in plant setup or change in desired crystal cylinder diameter means repeating this procedure. Finally, not all details of the system dynamics can be determined by this empirical approach. If a sufficiently exact model of the process is available this model can be used as a basis for determining proper feedforward control trajectories which can then be empirically fine tuned afterwards [Riedling 1988].

In case of a lumped-parameter model the system equations describe the time dependency of some system variables x , e.g. the temperature of a heater or the radius of the crystal. The behaviour of these quantities depends on initial values x_0 and control inputs u , such as heater power. A very specific example of such a model may be given by

$$\dot{x}(t) = f(x(t), u(t)), \quad x(0) = x_0, \quad (x(t), u(t)) \in \mathbb{R}^n \times \mathbb{R}^n. \quad (3.3)$$

Using this model, as the number of controls u equals the number of components of the state x , the trajectories $u_{\text{ref}}(t)$ of the inputs can be directly calculated from reference trajectories $x_{\text{ref}}(t)$. In order to achieve this, (3.3) must be solved for u :

$$u_{\text{ref}}(t) = g(x_{\text{ref}}(t), \dot{x}_{\text{ref}}(t)). \quad (3.4)$$

The desired inputs are calculated from given trajectories of the system quantities x_{ref} . This can be used for a model-based feedforward control. This strategy is also known as the solution of the *inverse problem*, in contrast to the *forward problem* which consists of the solution of (3.3) depending on initial values x_0 and given trajectories $u(t)$ for the input.

If the system equations are more complicated the solution of the inverse problem becomes difficult. Such a lumped-parameter approach is presented in [Kim 1983] (4" Si), [Masi 2000] (InP) and [Nalbandyan 1984]. However, in the case of feedforward control the performance of lumped-parameter models is limited because these models neglect the spatial distribution of system properties (see section 3.1.8). Most often one ends up with introducing some empirical corrections (e.g. in [Masi 2000]) to fit the model to reality. However, if these fit parameters are chosen properly the feedforward control performs quite well.

In order to overcome such limitations one may describe the system behaviour without neglecting the spatial dependence of some of the system properties. Then one is confronted with the problem of numerically solving a set of time-dependent partial differential equations with free boundary conditions. Even though powerful FEM for solving such problems exist, and computational performance has dramatically increased in recent years, the time-dependent solution of the inverse free-boundary problem still is one of the most challenging tasks [Brown 1989]. The situation gets even worse if feedforward

trajectories need to be rescheduled during growth, for instance in order to react to some perturbations. If such behaviour is required, the solution of the inverse problem should be available in real time [Voigt 2000]. Extensive studies on this task can be found in [Dornberger 1996, van den Bogaert 1997-1, van den Bogaert 1997-2], using the growth of large-diameter Si and Ge crystals as examples.

In order to reduce the computational effort one might restrict the problem to the quasi-stationary case. In this approach, a sequence of steady state solutions is used to form the feedforward trajectory. The strategy is presented in detail by Derby and Brown in [Derby 1986-1, Derby 1986-2], cf. section 3.7.3 for further discussion, also.

3.2.3 Model-Based Analysis of the Process

The aim of model-based analysis of a system is to gain insight into its dynamical behaviour using powerful methods provided by systems theory. A wide range of analysis methods exist, especially for lumped-parameter systems. Model-based analyses of the principal system behaviour were first presented in the 1970s [Bardsley 1972, Bardsley 1974-1, Bardsley 1974-2, Bardsley 1977-1, Bardsley 1977-2]. They used lumped-parameter models of selected components of the process in order to improve diameter feedback control. In particular, they addressed the anomaly of the weight gain signal (see section 3.1.4) and its consideration in control system design. They identified the physics related to the weight measurement signal (see section 3.1.4) and its adverse impact on controller tuning. This anomaly was later identified as corresponding to the right-half-plane zero characteristics of the weight measurement and interface dynamics, which set a fundamental limitation on achievable control performance [Gevlber 1988, Gevlber 1994-1]; see also sections 3.3.3 and 3.5.

A *global* lumped-parameter model of the overall Cz crystal growth system was first presented by [Steel 1975]. In order to simplify and improve parametrization of PID controllers they analysed a linearized model in terms of a transfer function in several growth stages. The central idea of their approach consists of partitioning the Cz system into four areas: melt, meniscus, crystal, ambient. This is still the basis of all lumped-parameter models of the Cz process used to date. Using their method an *a priori* controller design could be dramatically improved, thus avoiding time-consuming empirical parametrization of PID controllers. However, this requires sufficient accuracy of the model.

Analysis of steady state conditions, the dynamics of the process, and optimal control design using lumped-parameter models (in terms of a state space model) is subject of investigations presented by Satunkin *et al.* for the standard Cz process [Satunkin 1986-1] as well as for the LEC process [Satunkin 1995]. Optimal reference trajectory planning based on such models has been considered by the same author in [Satunkin 1986-2].

A very comprehensive and detailed model-based analysis of the global Cz system is presented in [Gevlber 1987-2, Gevlber 1988, Gevlber 1994-1, Gevlber 1994-2]. The first two of these publications are based on a seventh-order lumped-parameter model of the process, while the latter ones make use of a more refined one.

One might also use distributed-parameter models for such an analysis. Thorough analysis approaches based on such models (treated for the quasi-stationary case) have been presented in [Derby 1985, Derby 1987, Thomas 1989]. The great advantage of these

approaches is the fact that the heat flow in the plant can be modelled quite accurately. On the other hand, much effort is required to adapt the models to the actual plant design and to determine the physical parameters needed in the model with sufficient accuracy.

3.2.4 Stability

An important issue in control theory is the question of whether the system under consideration is stable or not, since unstable systems have a limitation on achievable control performance. When discussing this subject it is very important what type of model is used for stability analysis and which physical effects are included in the model: Surek's initial stability analysis was only of the capillary problem, i.e. of the meniscus region [Surek 1976]. He came to the conclusion that the capillary system is unstable. However, if the heat fluxes are taken into account, one comes to a different conclusion, depending on the assumptions made during modelling. Thus, [Surek 1980, Tatartchenko 1980] as well as [Derby 1987] show stable behaviour of the growth system under certain operating conditions. [Crowley 1983] and [Johansen 1991] show that the system is unstable for the cases they evaluated, even if the thermal effects are included in the analysis. This shows that the assumptions made for the thermal model (and for the plant set-up) are extremely important if one wishes to determine which of the two effects is dominant, i.e. whether the real process under consideration is stable or not. Sections 2.3 and 3.3 deal with the conditions for determining open-loop stability, and that stability is determined by how the heat flows in the interface-region vary with changes in radius.

3.2.5 Model-Based Control

As stated in section 3.1.8, for model-based control it is very important that the underlying model of the controller is accurate enough to make the controller(s) work properly. Indeed, this is the crux of all model-based approaches. Especially in Cz growth with its free boundary conditions and very complicated heat transfer mechanisms, it is almost impossible to derive a lumped-parameter model of the overall process that is suitable for implementing feedforward control and is robust in practice. However, at least each approach gives some insight into the process dynamics and some valuable considerations for parametrization of the control system.

Gewelber has proposed a multi-loop control system [Gewelber 1987-2, Gevelber 1988, Gevelber 1994-1, Gevelber 1994-2] based on a model analysis of the process in order not only to ensure a correct diameter over the whole process but also to ensure that identifiable disturbances are compensated for before they affect the growth dynamics. Two main disturbances are identified, both related to the melt drop: the thermal state of the melt, which changes the heat flux entering the interface, and the thermal environment that the crystal experiences, affecting the heat flux from the interface and, thus, the growth dynamics.

For example, by adding a closed loop around the melt temperature, the impact of this disturbance is significantly reduced, enabling tighter control of diameter and minimizing growth rate variations in a robust manner (e.g. insensitive to model uncertainties or process variations). Additionally, this work analysed the importance of controlling the

interface shape in addition to crystal diameter, in terms of meeting additional control objectives such as keeping thermal stress below a limit in order to minimize dislocation defects. Controlling interface shape as well as diameter requires the use of additional actuators, and an important part of the design task is to select an actuator set that can control both degrees of freedom relatively independently. To obtain further design insight, Gevelber *et al.* derive a model which, in particular, reflects the influence of heat transfer by radiation within the furnace as exactly as possible within a lumped-parameter model.

An interesting approach based on model predictive control can be found in [Irizarry-Rivera 1997-1, Irizarry-Rivera 1997-2]. The model used in this approach is of the lumped-parameter type. It includes melt convection, which requires very strict assumptions to be fulfilled in order to make the model applicable. Roughly speaking, model predictive control makes use of a dynamic model of the process also, but the way of calculating values for the manipulated variable is based on optimization methods. The solution of such optimization problems is well known and widely used in mathematics. For this purpose, in each time step the set of control activities recorded so far is evaluated in order to predict the values of the manipulated variable over a finite prediction horizon. The optimization criteria, in some sense the ‘parameters’ of a model predictive controller, reflect, for example, the dynamics of the deviation between desired and real values [Allgöwer 2007, Camacho 2004].

Another approach to establish such a model-based control on the basis of a lumped-parameter model has been published by [Voronkov 2002, Voronkov 2004]. It is closely related to the v_c/G theory [Falster 2000, Voronkov 1982] which requires very precise tracking of the growth rate v_c . This approach will be presented in a bit more detail since it shows an elegant compromise between completely model-based and empirical control. They propose a system for the control of both crystal radius and growth rate simultaneously by means of the heater power P and the pulling speed v . The heat transfer mechanism in the growth furnace is not explicitly modelled. Instead, it is assumed that the growth rate v_c directly depends on the meniscus height h and the heater power P . Then the following relation holds approximately in a neighborhood of an operating point (v_c^0, h^0, P^0) :

$$v_c(t) = v_{c0} + \underbrace{\frac{\partial v_c}{\partial h} \Big|_{(h^0, P^0)}}_{:=A_h > 0} (h(t) - h^0) + \underbrace{\frac{\partial v_c}{\partial P} \Big|_{(h^0, P^0)}}_{:=A_P < 0} (P(t) - P^0) \quad (3.5)$$

with the two important control parameters A_h, A_P . Such an assumption is reasonable since, as will be discussed in detail in section 3.3.2, the value of the growth rate is directly related to the temperature gradient G_1 in the melt at the interface. For this the approximation [Hurle 1986]

$$G_1 \approx \frac{T_1 - T_m}{h} \quad (3.6)$$

holds. Here one has the meniscus base temperature T_1 (which is directly influenced by the heater power) and the melting point temperature T_m .

As will be discussed later, trajectories of the crystal radius r_c and the meniscus height h can be calculated by solving appropriate differential equations:

$$\dot{r}_c(t) = R(h(t), v_c(t), v(t), A_h, \dots) \quad r_c(0) = r_{c0}, \quad (3.7)$$

$$\dot{h}(t) = H(h(t), v_c(t), v(t), A_h, \dots) \quad h(0) = h_0, \quad (3.8)$$

which, among other quantities, depend on the growth rate v_c .

If one assumes that Equation (3.5) is valid and the heater power is constant over a certain interval of time, these differential equations can be solved analytically on this interval, i.e. we obtain *algebraic* equations for calculation of r_c and h :

$$r_c(t) = R^*(r_{c0}, h_0, h(t), v, v_c, \dots), \quad (3.9)$$

$$h(t) = H^*(h_0, v, v_c, \dots). \quad (3.10)$$

Now, over a certain observation period $\Theta = [t - t_{p1}, t]$, $t_{p1} > 0$, the pulling speed v and the heater power P are kept constant and the trajectory of the radius $r_c(\tau)$, $\tau \in \Theta$ is measured. Subsequently, those trends of h and v_c are numerically determined which are an optimal approximation of the measured trajectory $r_c(\tau)$, $\tau \in \Theta$. This is done by using a ‘best fit routine’ [Voronkov 2004] working on Equation (3.9). As a result, at the end of the observation period values for the meniscus height h^* and the growth rate v_c^* are available. On the basis of these values a controller calculates values of the manipulated variables v and P valid for the next observation period:

- Roughly speaking, based on Equations (3.9), (3.10) the new value for the pulling speed v is calculated such that crystal radius and meniscus height tend to their reference values.
- The heater power is changed by δP such that the growth rate tends to its reference value $v_{c,\text{ref}}$, i.e. deviations of v from its feedforward value are compensated, too:

$$\delta P = -\frac{v_c^* - v_{c,\text{ref}}}{A_p} \quad (\text{note that } A_p < 0). \quad (3.11)$$

The constants A_h and A_p as well as the observation period t_{p1} (and some other parameters) have to be ‘chosen appropriately’ [Voronkov 2002].

The strategy of excluding problematic parts of the system from modelling is presented by other authors, too. [Wilde 1991] introduces a nonlinear PID controller the parameters of which are defined on intervals, for instance

$$K_p = \begin{cases} K_{p1} & \text{if } e(t)\dot{e}(t) > 0 \\ K_{p2} & \text{if } e(t)\dot{e}(t) < 0 \end{cases}$$

in Equation (3.2). This is combined with a heuristic limitation of the manipulated variable during growth of strontium niobate ($\text{Sr}_2\text{Nb}_2\text{O}_7$) crystals.

3.2.6 Identification

In the publications mentioned above, models are derived from theoretical considerations. A different approach consists of deriving the model from experimental investigations. Here, the trajectories of selected output variables generated by well-defined trajectories of the input variables are carefully analysed, resulting in a model of the process. This method is commonly referred to as *identification* [Ljung 1987]. A transfer function describing the growth of Si crystals at a certain operating point has been experimentally determined by [Hurle 1986], while in [Looze 1995] an approach for growth of GaAs in a LEC furnace is presented. The results presented in both papers are valid in the neighborhood of an operating point. Usually, the phase of cylindrical growth is taken as the operating point.

3.2.7 Measurement Issues and State Estimation

For Cz crystal growth the measurement of the variable(s) to be controlled is quite a complex task. This may be shown for example on the most important variable, the crystal radius at the solid–melt interface. There are three different approaches:

- Optical capturing of the meniscus shape, typically by detecting the bright meniscus ring [Digges 1975, Gross 1972, Lorenzini 1974, Patzner 1967].
- Image processing of the whole crystal [Bachmann 1970, van Dijk 1974].
- Evaluation of the force acting on a load cell mounted at the top of the pulling rod [Bardsley 1972, Bardsley 1974-1, Bardsley 1977-1, Bardsley 1977-2, Levinson 1959, Rummel 1966]. Weighing of the crucible is also possible [Valentino 1974, Zinnes 1973].

Optical imaging of the bright meniscus ring, which results from reflections of light emitted by the heaters, is the most important measuring technique used in Si crystal growth. This seems quite easy, since the radius is directly available in the control system. However, one has to take into account that what is measured is the diameter of the meniscus at a certain height, not the crystal diameter at the three-phase boundary. This means that the anomaly (see section 3.1.4) also comes into play: if the crystal radius begins to decrease, the meniscus height will increase first [Gevlber 1988, Gevlber 1994-1]. This means that the measured diameter of the bright meniscus ring will increase, which might result in incorrect reactions of the controller if it is not adapted to this behaviour.

The second method has no technological relevance; one reason is that it is very complicated to apply, and another one is that it detects changes in growth only when they have already influenced the crystal (which is not the case for the first and third technique, where changes in the meniscus precede a change in the crystal are detected) [Hurle 1993].

In the case of the LEC process where melt and meniscus are covered by a layer of boron oxide, only the third technique can be applied. It is based on the idea that the gravitational force F_c of a rotationally symmetric crystal of length l and density ρ_s can be calculated by integration:

$$F_c = \pi g \rho_s \int_0^l r_c^2(\lambda) d\lambda \quad (3.12)$$

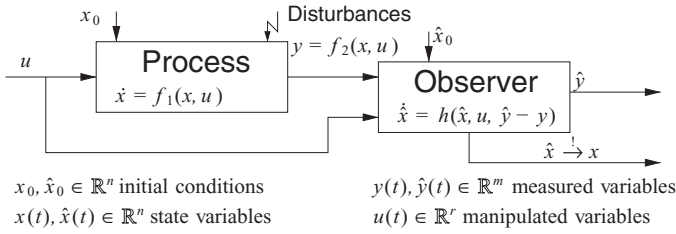


Figure 3.6 Possible structure of an observer for reconstruction of the not directly measured quantities x by injection of the measured quantities y and the manipulated quantities u .

with crystal radius r_c and gravitational acceleration g . The force measured by the load cell is not actually equal to F_c in Equation (3.12); in practice it is also influenced by forces resulting from the surface tension of the meniscus, the hydrostatic pressure of the melt raised over the melt level, and in the case of LEC by the buoyancy forces resulting from the liquid boron oxide. This makes things considerably more complicated than a first glance at Equation (3.12) might suggest. Details are discussed in section 3.3.1.8.

In order to overcome this difficulty one has to reconstruct the crystal radius from the measured force. This can be done by a so-called ‘observer’, as shown in Figure 3.6. It is based on the following idea. Assume a mathematical model

$$\begin{aligned} \dot{x}(t) &= f_1(x(t), u(t)), & x(0) &= x_0 \\ y(t) &= f_2(x(t), u(t)) \end{aligned}$$

of a process with $(x(t), u(t)) \in \mathbb{R}^n \times \mathbb{R}^r$ and $y(t) \in \mathbb{R}^m$. If some components of x are not directly measured one might implement a ‘copy’

$$\begin{aligned} \dot{\hat{x}}(t) &= f_1(\hat{x}(t), u(t)), & \hat{x}(0) &= \hat{x}_0 \\ \hat{y}(t) &= f_2(\hat{x}(t), u(t)) \end{aligned}$$

of the system model in a computer program. The trajectories of the manipulated variables u acting on the real system are also fed into this computer program. Then one has access to all components of \hat{x} . Since the initial values of \hat{x} are not known, i.e. $\hat{x}_0 \neq x_0$, and because of model inaccuracies as well as disturbances acting on the system, the values calculated for \hat{x} will generally not be equal to the real values x . However, under certain circumstances it is possible to inject the error $\hat{y} - y$ between the estimated value \hat{y} and the measured value y in such a way that the difference between the calculated value \hat{x} and the real value x will converge to zero as time increases [Luenberger 1964]. In this case the system

$$\begin{aligned} \dot{\hat{x}}(t) &= h(\hat{x}(t), u(t), \hat{y}(t) - y(t)), & \hat{x}(0) &= \hat{x}_0 \\ \hat{y}(t) &= f_2(\hat{x}(t), u(t)) \end{aligned}$$

is called an *observer*.

The design and dimensioning of the error relating to the measured variable is the key task when developing an observer. However, it is important to know whether it is possible to reconstruct a quantity from the measured variable at all. This property is commonly referred to as ‘observability’.

For Cz crystal growth several publications deal with this problem. Satunkin and Leonov discuss the question of observability in case of the Cz and LEC growth in [Satunkin 1990]. The discussion is based on a linearized model of the overall process which is bound to the knowledge of some thermodynamical parameters. An elegant approach is presented in [Abrosimov 2003, Rossolenko 1992] where, roughly speaking, an iteration algorithm is used that fits the theoretically calculated mass of the load cell to its real value by heuristically changing the crystal diameter at every step. However, this algorithm again contains a parameter which must be empirically determined to guarantee convergence.

If the influence of the changing meniscus can be more or less neglected, a simple approach is presented in [Kubota 1999, Masi 2000]. Here the basic idea is to exclude the meniscus dynamics from the model, making it easy to solve the remaining equations for the radius. This method is useful for the reconstruction of the radius during cylindrical growth and for crystals with slowly increasing diameter in the cone. For crystals with large slope angles in the shoulder this method fails, especially at the point where it tapers into the cylinder (see Figure 3.3).

3.3 Mathematical Model

The objective for developing a system model is to capture the dominant nonlinear and time-varying heat transfer conditions that determine the system’s eigenstructure, input/output gains, and couplings that are needed to design an appropriate control algorithm. Furthermore, the purpose is to develop an advanced control system, one that considers multiple objectives beyond diameter control and addresses choice of control structure [Gevlber 1999] (e.g. selection of input/output pairings). A *low-order* control volume-based approach is used [Jaluria 1986] to derive the system equations where each of the system components is subdivided into smaller ‘lumps’.

A low-order modelling (LOM) technique is used since it easily reveals how the dominant dynamics and coupling scale with design parameters and operating regime selection. While not providing the accuracy achieved by higher-order models, high open loop accuracy is not required for real-time, measurement-based feedback control, since feedback can provide robustness both for model errors and uncertainties of material properties and to boundary conditions (see section 3.1.8).

As we will see, this model can be split into two parts: a first part (section 3.3.1) describing the dynamics of the hydromechanical–geometrical system and a second part representing the dynamics of the temperatures and heat fluxes (section 3.3.2). The focus of the thermal LOM presented is to relate the interface dynamics to the local and global thermal dynamics. Section 3.3.3 closes this modelling discussion with a short analysis of some important dynamic properties of the linearized model.

Table 3.1 Assumptions made during modelling of the hydromechanical–geometrical system and resulting limitations

Subject	Assumption	Constraint
Crystal shape Interface	Rotationally symmetric Planar (However, influence of curved interface is discussed in sections 3.3.1.9 and 3.3.2.2)	Faceted growth is not described. Negligence of buoyancy effects resulting from convex/concave interface Force resulting from surface tension of the meniscus may be calculated incorrectly
Meniscus height	Calculated from approximation formulas	Cut-off of meniscus according to [Mika 1975] not described Inaccuracies for extreme growth angles ($\alpha \rightarrow \pm 90^\circ$) For LEC growth, buoyancy and boron oxide height calculated incorrectly
Growth angle α_0	Constant	Force measured at load cell may be interpreted incorrectly
Crucible	Constant radius	Influence of crucible calotte not included, i.e. melt height calculated incorrectly
Melt	Surface is free (not influenced by crucible)	Volume of meniscus and height of melt incorrect

Table 3.1 lists the assumptions made during modelling. Unless specified otherwise the model equations refer to both standard Cz and LEC crystal growth. Furthermore, it must be recalled (see section 1.3 and Chapter 2) that the growth angle α is defined as

$$\alpha = \alpha_0 + \alpha_c \quad (3.13)$$

with α_0 as the growth angle for cylindrical growth and α_c as the so-called slope angle (angle between the tangent to the crystal surface at the interface and the vertical, i.e. during cylindrical growth $\alpha_c = 0$). The choice of the symbol α_c is in contrast to Chapter 2 where the symbol $\delta\phi_0 = \alpha - \alpha_0$ is used instead for α_c . This is done in order to avoid notational conflicts when linearizing the models, where δ denotes the deviation of a quantity from a reference (not necessarily equilibrium!) value.

3.3.1 Hydromechanical–Geometrical Model

The hydromechanical–geometrical model describes the behaviour of the meniscus (in terms of the geometric conditions), the melt height, the forces resulting from the growing crystal that determined the measured weight, and the crystal radius depending on crystal pulling speed, crucible translation speed, and growth rate. These model equations are particularly useful for developing the nonlinear control system described in section 3.6 and the observer presented in section 3.7.

3.3.1.1 Crystal

The rate of change of the crystal length l is described by the growth rate $v_c = dl/dt$. Assuming a planar interface, the growth rate can be calculated from the following equation:

$$v_c = \frac{dl}{dt} = v - v_{\text{cruc}} - \dot{h} - \dot{H}_m \tag{3.14}$$

with pulling rate v , crucible translation rate v_{cruc} and rates of change \dot{h} and \dot{H}_m of meniscus and melt height, respectively.

Assuming rotational symmetry, the rate of change of the crystal mass M_c is given by

$$\dot{M}_c = \pi \rho_s r_c^2 v_c. \tag{3.15}$$

Here r_c is the radius of the crystal at the solid–melt interface and ρ_s is the density of the solid at the melting point temperature T_m .

Furthermore, one has

$$V_s = \pi \int_0^l R^2(\lambda) d\lambda \tag{3.16}$$

for the crystal volume, where $R:[0, l] \rightarrow \mathbb{R}$ describes the dependency of the crystal radius on the crystal length (see Figure 3.7)

From geometric considerations [Gevlber 1987-2] the following relation describing the behaviour of the crystal radius can be derived:

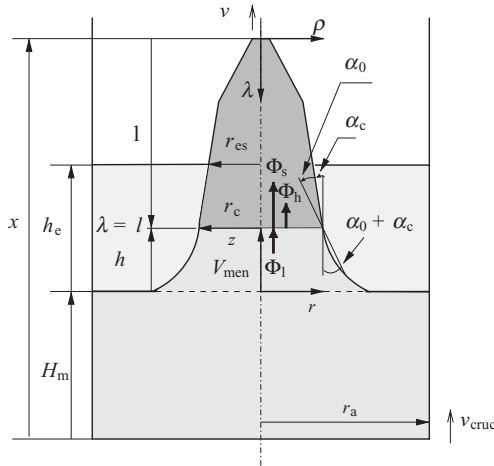


Figure 3.7 Quantities used in the model.

$$\dot{r}_c = v_c \tan(\alpha_c) \quad (3.17)$$

with the crystal slope angle α_c (see Figure 3.7).

3.3.1.2 Meniscus Height

For further calculations the height h of the meniscus at the interface is of interest. Under steady state conditions the shape of the meniscus is described by the *Young–Laplace equation* (see section 8.2). Instead of solving the Young–Laplace equation numerically it is better to rely on analytical approximations describing the meniscus height as a function of the crystal radius r_c and the slope angle $\alpha_c := \alpha - \alpha_0$. For example, Boucher derived the following formula [Boucher 1980]:

$$h = a \sqrt{\frac{1 - \sin(\alpha_0 + \alpha_c)}{1 + a/(\sqrt{2}r_c)}}. \quad (3.18)$$

An advantage of this approximation (in contrast to others) is the fact that it can be explicitly solved for α_c . Here, the parameter a is the capillary length, often called the *Laplace constant* (cf. section 2.2.2.2). This material-specific parameter depends on the surface tension γ_e between melt and environment (the boron oxide for LEC growth, otherwise the relevant atmosphere) and the densities ρ_1 of the melt and, in case of LEC growth, additionally ρ_e of the boron oxide [Egorov 1976]. The angle α_0 is assumed to be constant. Details of these approximations are discussed in section 8.2, with respect to the growth angle in section 1.3.

The derivative \dot{h} of the meniscus height follows from

$$\dot{h} = \frac{\partial h}{\partial r_c} \dot{r}_c + \frac{\partial h}{\partial \alpha_c} \dot{\alpha}_c \quad (3.19)$$

with \dot{r}_c according to Equation (3.17). An expression for $\dot{\alpha}_c$ will be derived in section 3.3.1.5.

3.3.1.3 Meniscus Mass

In this section an expression for the mass of the meniscus is derived. This is needed for the mass balance (3.26) in order to derive a differential equation for the crystal slope angle α_c . The force F_{men} resulting from the meniscus acting on the crystal consists of two components if no boron oxide layer is present:

- The melt elevated over the free melt level in the crucible causes a hydrostatic pressure drop resulting in a force acting against the pulling direction.
- On the circumference of the crystal at the interface there is a force F_σ resulting from the surface tension.

The vertical component of the latter is of interest:

$$F_\sigma = 2\pi r_c \gamma_{le} \cos(\alpha_0 + \alpha_c). \quad (3.20)$$

As a result one has the following relation describing the force F_{men} acting on the crystal (with gravitational acceleration g):

$$F_{\text{men}} = \underbrace{\pi g \rho_1 r_c^2 h}_{\text{hydrostatic pressure drop}} + \underbrace{\pi g \rho_1 a^2 r_c \cos(\alpha_0 + \alpha_c)}_{\text{vertical component of surface tension}}. \quad (3.21)$$

Formally one can derive expressions for the meniscus mass M_{men} and the meniscus volume V_{men} :

$$M_{\text{men}} = F_{\text{men}}/g \quad \text{and} \quad V_{\text{men}} = F_{\text{men}}/(g\rho_1). \quad (3.22)$$

The derivative \dot{M}_{men} of the meniscus mass with respect to time is given by

$$\begin{aligned} \dot{M}_{\text{men}} = \pi \rho_1 \left(2r_c h + r_c^2 \frac{\partial h}{\partial r_c} + a^2 \cos(\alpha_0 + \alpha_c) \right) \dot{r}_c \\ + \pi \rho_1 \left(r_c^2 \frac{\partial h}{\partial \alpha_c} - a^2 r_c \sin(\alpha_0 + \alpha_c) \right) \dot{\alpha}_c. \end{aligned} \quad (3.23)$$

At this point we must be careful: the expression (3.22) has been derived formally using the well-known relation $F = mg$ for a mass point (of mass m) in the gravitational field with gravitational acceleration g . This means that (3.22) does not really describe the meniscus volume. However, this approximation is reasonable, as discussed in [Johansen 1987-1] where a comparison with the real volume of the meniscus calculated from solving the Young–Laplace equation is performed.

3.3.1.4 Melt

The height of the melt in the crucible is denoted by H_m . With the density ρ_1 of the melt and the crucible radius r_a the derivative of the melt mass M_1 with respect to time is given by

$$\dot{M}_1 = \pi \rho_1 r_a^2 \dot{H}_m. \quad (3.24)$$

For a detailed discussion it would be necessary to consider the dependency of the crucible radius on the melt height. However, in most cases this effect is important only if the height of the melt is very small, i.e. the crucible calotte comes into play.

From the mass conservation law it follows that

$$M_0 = M_1 + M_{\text{men}} + M_c \quad (3.25)$$

with initial mass M_0 . Differentiating with respect to time leads to

$$\dot{M}_c = -(\dot{M}_{\text{men}} + \dot{M}_1). \quad (3.26)$$

Using Equations (3.15) and (3.24) we get

$$\dot{H}_m = -\frac{\pi\rho_s r_c^2 v_c + \dot{M}_{\text{men}}}{\pi\rho_l r_a^2}, \quad (3.27)$$

where expression (3.23) must be used for \dot{M}_{men} .

3.3.1.5 Crystal Slope Angle

Substituting \dot{H}_m in Equation (3.27) by Equation (3.14) and \dot{h} by (3.19) we obtain

$$\dot{\alpha}_c = \frac{v - v_{\text{cruc}} - c_{\alpha z}(r_c, \alpha_c) v_c}{c_{\alpha n}(r_c, \alpha_c)}, \quad (3.28)$$

with

$$c_{\alpha z}(r_c, \alpha_c) = 1 - \frac{\rho_s r_c^2}{\rho_l r_a^2} + \left[\left(1 - \frac{r_c^2}{r_a^2} \right) \frac{\partial h}{\partial r_c} - \frac{2r_c h}{r_a^2} - \frac{a^2}{r_a^2} \cos(\alpha_0 + \alpha_c) \right] \tan(\alpha_c) \quad (3.29)$$

and

$$c_{\alpha n}(r_c, \alpha_c) = \left(1 - \frac{r_c^2}{r_a^2} \right) \frac{\partial h}{\partial \alpha_c} + \frac{a^2 r_c}{r_a^2} \sin(\alpha_0 + \alpha_c). \quad (3.30)$$

Hence, using (3.23) and (3.28) we can rewrite Equation (3.27) as

$$\dot{H}_m = \left(1 - \frac{1}{c_{\alpha n}(r_c, \alpha_c)} \frac{\partial h}{\partial \alpha_c} \right) (v - v_{\text{cruc}}) - \left(1 + \tan(\alpha_c) \frac{\partial h}{\partial r_c} - \frac{c_{\alpha z}(r_c, \alpha_c)}{c_{\alpha n}(r_c, \alpha_c)} \frac{\partial h}{\partial \alpha_c} \right) v_c. \quad (3.31)$$

3.3.1.6 Growth Rate

An expression describing the dependency of the growth rate v_c on radius, slope angle and translations can be directly derived from Equation (3.28):

$$v_c = \frac{v - v_{\text{cruc}}}{c_{\alpha z}(r_c, \alpha_c) + c_{\alpha n}(r_c, \alpha_c) \frac{d\alpha_c}{dl}}. \quad (3.32)$$

For convenience we can write this equation in a form which directly shows the influence of the three components r_c , dr_c/dl and $d\alpha_c/dl$, respectively:

$$v_c = (v - v_{\text{cruc}}) \left(\left(1 - \frac{r_c^2}{r_a^2} \right) \rho \right) + \left[\left(1 - \frac{r_c^2}{r_a^2} \right) \frac{\partial h}{\partial r_c} - \frac{2r_c h}{r_a^2} - \frac{a^2}{r_a^2} \cos(\Theta_0 + \alpha_c) \right] \frac{dr_c}{dl} + \left[\left(1 - \frac{r_c^2}{r_a^2} \right) \frac{\partial h}{\partial \alpha_c} + \frac{a^2 r_c}{r_a^2} \sin(\Theta_0 + \alpha_c) \right] \frac{d\alpha_c}{dl} \Big)^{-1}. \quad (3.33)$$

3.3.1.7 Boron Oxide Layer

In case of LEC growth the mass M_e of the boron oxide and its density ρ_e are assumed to be constant. Because the meniscus and a part of the crystal are submerged in the boron oxide, additional buoyancy forces come into play. With the height h_e of the boron oxide layer one can write:

$$\pi r_a^2 h_e = V_{\text{sub}} + V_{\text{men}} + \frac{M_e}{\rho_e}. \quad (3.34)$$

The length L_{es} of the emerged part of the crystal results from

$$L_{\text{es}} = l - h_e + h. \quad (3.35)$$

Thus, the radius of the crystal at the surface of the boron oxide layer is given by

$$r_{\text{es}} = R(l - h_e + h). \quad (3.36)$$

The volume V_{sub} of the part of the crystal which is submerged under the boron oxide layer can be calculated from

$$V_{\text{sub}} = \pi \int_{l-h_e+h}^l R^2(\lambda) d\lambda. \quad (3.37)$$

Differentiating Equation (3.37) leads to

$$\dot{V}_{\text{sub}} = \pi(r_c^2 - r_{\text{es}}^2)v_c + \pi r_{\text{es}}^2(\dot{h}_e - \dot{h}) \quad (3.38)$$

which, together with Equation (3.34), gives an expression for the time derivative of the height of the boron oxide:

$$\dot{h}_e = \frac{(r_c^2 - r_{\text{es}}^2)v_c - r_{\text{es}}^2\dot{h} + \frac{1}{\pi}\dot{V}_{\text{men}}}{r_a^2 - r_{\text{es}}^2}. \quad (3.39)$$

From inspection of Equation (3.36) it follows that the model of the LEC process belongs to the class of delay systems: The crystal radius affects the system with a delay again corresponding to the length L_{es} (see Figure 3.3, right).

3.3.1.8 Force Acting on the Load Cell

As already mentioned in section 3.3.1.2, the force acting on the load cell does not only consist of the gravitational force of the crystal. This force is also significantly influenced by the surface tension and the hydrostatic pressure drop resulting from the meniscus as well as the buoyancy resulting from the boron oxide.

For LEC growth one has,

$$F_{\text{LEC}} = \underbrace{M_c g}_{\text{crystal}} + \underbrace{\rho_l V_{\text{men}} g}_{\text{meniscus}} - \underbrace{\rho_e (V_{\text{sub}} + V_{\text{men}}) g}_{\text{buoyancy}}. \quad (3.40)$$

After differentiation, use of Equations (3.15), (3.23), (3.38) and some algebra we get [Johansen 1992-2]

$$\dot{F}_{\text{LEC}} = \pi g r_c^2 (c_{\rho, \text{LEC}}(r_c, r_{\text{es}}) v_c + c_{r, \text{LEC}}(r_c, r_{\text{es}}, \alpha_c) \dot{r}_c + c_{\alpha, \text{LEC}}(r_c, r_{\text{es}}, \alpha_c) \dot{\alpha}_c), \quad (3.41)$$

with

$$c_{\rho, \text{LEC}}(r_c, r_{\text{es}}) = \rho_s - \frac{1 - \frac{r_{\text{es}}^2}{r_c^2}}{1 - \frac{r_{\text{es}}^2}{r_a^2}} \rho_e \quad (3.42)$$

$$\begin{aligned} c_{r, \text{LEC}}(r_c, r_{\text{es}}, \alpha_c) = & \left(\rho_l - \frac{1 - \frac{r_{\text{es}}^2}{r_c^2}}{1 - \frac{r_{\text{es}}^2}{r_a^2}} \rho_e \right) \left(\frac{\partial h}{\partial r_c} \right) \Big|_{(r_c, \alpha_c)} \\ & + \left(\rho_l - \frac{\rho_e}{1 - \frac{r_{\text{es}}^2}{r_a^2}} \right) \left(\frac{2h}{r_c} + \frac{a^2}{r_c^2} \cos(\Theta_0 + \alpha_c) \right) \end{aligned} \quad (3.43)$$

$$\begin{aligned} c_{\alpha, \text{LEC}}(r_c, r_{\text{es}}, \alpha_c) = & \left(\rho_l - \frac{1 - \frac{r_{\text{es}}^2}{r_c^2}}{1 - \frac{r_{\text{es}}^2}{r_a^2}} \rho_e \right) \left(\frac{\partial h}{\partial \alpha_c} \right) \Big|_{(r_c, \alpha_c)} \\ & - \left(\rho_l - \frac{\rho_e}{1 - \frac{r_{\text{es}}^2}{r_a^2}} \right) \frac{a^2}{r_c} \sin(\Theta_0 + \alpha_c). \end{aligned} \quad (3.44)$$

In case of growth without boron oxide the last term in Equation (3.40) can be omitted:

$$F_{\text{Cz}} = \underbrace{M_c g}_{\text{crystal}} + \underbrace{\rho_l V_{\text{men}} g}_{\text{meniscus}}, \quad (3.45)$$

and for the force F_{Cz} we obtain

$$\dot{F}_{\text{Cz}} = \pi g r_c^2 (\rho_s v_c + c_{r, \text{Cz}}(r_c, \alpha_c) \dot{r}_c + c_{\alpha, \text{Cz}}(r_c, \alpha_c) \dot{\alpha}_c), \quad (3.46)$$

with

$$c_{r, \text{Cz}}(r_c, \alpha_c) = \rho_l \left(\frac{\partial h}{\partial r_c} \Big|_{(r_c, \alpha_c)} + \frac{2h}{r_c} + \frac{a^2}{r_c^2} \cos(\Theta_0 + \alpha_c) \right) \quad (3.47)$$

$$c_{\alpha, \text{Cz}}(r_c, \alpha_c) = \rho_l \left(\frac{\partial h}{\partial \alpha_c} \Big|_{(r_c, \alpha_c)} - \frac{a^2}{r_c} \sin(\Theta_0 + \alpha_c) \right). \quad (3.48)$$

3.3.1.9 Influence of a Curved Interface on Weight Measurement

Up to now the solid–melt interface has been assumed to be planar. In this section the consequences for the weight gain signal resulting from a concave or convex interface are sketched and discussed. The main problem in modelling a curved interface is the fact that it is almost impossible to express its dynamics in terms of a lumped-parameter model, as will be shown at the end of this section. The approaches and problems discussed here were originally addressed for example in [Johansen 1992-1, Johansen 1992-2].

Concave Interface. In case of an interface which is concave to the melt, the force acting on the load cell can be expressed as follows:

$$F_{Cz} = \underbrace{M_c g}_{\text{crystal}} + \underbrace{\rho_l V_{\text{men}} g}_{\text{meniscus}} + (\rho_l - \rho_s) g \Omega_m. \quad (3.49)$$

Here Ω_m denotes the additional volume replaced by the melt within the crystal.

Convex Interface. In case of a solid–liquid interface which is convex to the melt the situation becomes a bit more complicated since it is possible for the interface to grow beyond the melt level. In this case we have

$$F_{Cz} = \underbrace{M_c g}_{\text{crystal}} + \rho_s g \Omega_s + \underbrace{2\pi r_c \gamma_{lg} \cos(\alpha_0 + \alpha_c)}_{\text{surface tension}} - F_i. \quad (3.50)$$

Here Ω_s denotes the volume of the crystal which replaces melt in, and eventually under, the meniscus. An additional buoyancy force F_i results from the melt replaced by this part of the crystal. Its value can be calculated from

$$\rho_l g \Omega_s = F_i - \pi p r_c^2 \quad (3.51)$$

with the hydrostatic pressure p at the flat top surface of Ω_s . The hydrostatic pressure at the three-junction line is $p = -\rho_l g h$. Thus, from Equation (3.51) it follows that

$$F_i = g \rho_l (\Omega_s - \pi h r_c^2). \quad (3.52)$$

Using this equation and (3.21) we obtain the final expression for the force F_{Cz} in the case of a convex interface as follows:

$$F_{Cz} = \underbrace{M_c g}_{\text{crystal}} + \underbrace{\rho_l V_{\text{men}} g}_{\text{meniscus}} + (\rho_s - \rho_l) g \Omega_s. \quad (3.53)$$

Determination of the Derivative. Up to now the expressions (3.49) and (3.53) have described the situation at the interface exactly. However, an expression describing the volumes Ω_m and Ω_s is missing although it is important to know these because otherwise we cannot determine the derivative \dot{F}_{Cz} describing the *dynamics* of the force F_{Cz} . Usually we try to overcome this problem by defining the volume Ω_s as

$$\Omega_s = \frac{\pi}{3} \omega r_c^3 \quad (3.54)$$

with an empirically chosen factor ω . Then we have

$$\dot{\Omega}_s = \omega g r_c^2 \dot{r}_c. \quad (3.55)$$

In general ω will depend strongly on the thermal conditions defining the actual shape of the interface, i.e. in reality it is time varying and Equation (3.55) is not valid. This is why the curved interface – although frequently used for some principal analysis methods – is usually not applied within control system design. Besides, it is impossible or at least very difficult to measure the deflection of the interface in real time.

3.3.1.10 Summary

The equations derived so far can be summarized as follows:

$$\dot{r}_c = v_c \tan(\alpha_c) \quad (3.56)$$

$$\dot{\alpha}_c = \frac{v - v_{\text{cruc}} - c_{\alpha z}(r_c, \alpha_c) v_c}{c_{\alpha n}(r_c, \alpha_c)} \quad (3.57)$$

$$\dot{h} = v - v_{\text{cruc}} - v_c - \dot{H}_m \quad (3.58)$$

$$\dot{H}_m = \left(1 - \frac{1}{c_{\alpha n}(r_c, \alpha_c)} \frac{\partial h}{\partial \alpha_c} \right) (v - v_{\text{cruc}}) - \left(1 + \tan(\alpha_c) \frac{\partial h}{\partial r_c} - \frac{c_{\alpha z}(r_c, \alpha_c)}{c_{\alpha n}(r_c, \alpha_c)} \frac{\partial h}{\partial \alpha_c} \right) v_c \quad (3.59)$$

$$\dot{h}_e = \frac{(r_c^2 - r_{\text{es}}^2) v_c - r_{\text{es}}^2 \dot{h} + \frac{1}{\pi} \dot{V}_{\text{men}}}{r_a^2 - r_{\text{es}}^2} \quad (\text{LEC growth only}) \quad (3.60)$$

$$\dot{F}_{\text{LEC}} = \pi g r_c^2 (c_{p,\text{LEC}}(r_c, r_{\text{es}}) v_c + c_{r,\text{LEC}}(r_c, r_{\text{es}}, \alpha_c) \dot{r}_c + c_{\alpha,\text{LEC}}(r_c, r_{\text{es}}, \alpha_c) \dot{\alpha}_c) \quad (3.61)$$

respectively

$$\dot{F}_{\text{Cz}} = \pi g r_c^2 (\rho_s v_c + c_{r,\text{Cz}}(r_c, \alpha_c) \dot{r}_c + c_{\alpha,\text{Cz}}(r_c, \alpha_c) \dot{\alpha}_c) \quad (3.62)$$

$$r_{\text{es}} = R(l - h_e + h) \quad (\text{LEC growth only}). \quad (3.63)$$

On inspecting system (3.56)–(3.63) one may conclude the following:

- What is missing is an expression describing the behaviour of the crystal growth rate and length l . For a flat interface they are related since one has $\dot{l} = v_c$. An expression for v_c can be expressed in terms of the thermal conditions found at the solid–melt interface, i.e. v_c couples the hydromechanical–geometric part with the thermal part described in the next section.
- Since there is an algebraic relation between r_c , α_c , and h , Equation (3.18)

$$h = a \sqrt{\frac{1 - \sin(\alpha_0 + \alpha_c)}{1 + a/(\sqrt{2}r_c)}},$$

we may describe the geometric behaviour of the crystal growth either by equations (3.56), (3.57) for $(\dot{r}_c, \dot{\alpha}_c)$ or by equations (3.56), (3.58) for (\dot{r}_c, \dot{h}) , respectively. The pair $(\dot{r}_c, \dot{\alpha}_c)$ is suitable for nonlinear controller design in section 3.6 while (\dot{r}_c, \dot{h}) is more advantageous for purposes of analysis in sections 3.3.3 and 3.4. Anyway, both types of system description are equivalent.

3.3.2 Model of Thermal Behaviour

As described in section 2.2.4 and Equation (3.1), the growth rate v_c depends on the thermal gradient at the interface, which in turn is determined by the thermal conditions in the growth furnace. Modelling of the thermal conditions is one of the most challenging tasks in Cz crystal growth (see section 3.1). Therefore, for control purposes, where real-time capability must be provided, the thermal behaviour is usually modelled by a LOM describing the heat fluxes at the interface.

The LOM control volume-based approach is appropriate since the dominant dynamics typically result from the slowest modes (poles) of the system which typically correspond to large length scales. To choose the number and location of the lumps in each system component, experimental data as well as the results of detailed models [Assaker 1997, Dornberger 1997, Kinney 1993] are analyzed. The models were used to identify where large temperature gradients/heat fluxes were expected to occur and, thus, the size of lumps needed to resolve the temperature gradients.

3.3.2.1 Growth Rate

An expression for the growth rate is governed by the energy and phase transformation/mass balances about the interface. Figure 3.7 illustrates the energy balance for a flat interface where the integrated heat flows across the interface are represented by Φ_s , the heat flow being taken out by the crystal, and Φ_l , the heat flow into the interface from the meniscus; their difference, Φ_h , is the rate of heat release for material solidification. The growth rate in the axial direction is given by v_c . The energy balance about the whole interface is given by:

$$\Phi_h = \Phi_s - \Phi_l = \pi r_c^2 \rho_s \Delta H v_c \quad (3.64)$$

where r_c and h are the interface radius and meniscus height at the three-phase boundary. The parameters ρ_s and ρ_l are the density of the solid and the liquid, and ΔH is the heat of fusion per cubic space. This is the lumped or integral form of the local gradient form of the interface energy balance given in equation (3.1). The growth rate is given by

$$v_c = \frac{\Phi_s - \Phi_l}{\pi r_c^2 \rho_s \Delta H}. \quad (3.65)$$

3.3.2.2 Interface Shape Modelling

Coupled to the radius dynamic state equation (3.17), the interface shape reflects the heat transfer which determines the growth rate and evolution of shape. Two approaches can be taken to model the interface dynamics, based on whether one treats the interface shape as flat or curved. Assuming a flat interface reduces the degrees of freedom and the number of equations, yet captures the dominant dynamics of the Cz growth process. Modelling a curved interface shape reveals somewhat different dynamics and reflects the variations in local thermal gradients that can affect defect formation.

For the flat interface, the axial growth rate can be expressed in terms of the local velocity of the interface as well as of the thermal conditions. Manipulation of Equations (3.14) and (3.64) yields a state equation for the meniscus height dynamics in terms of the energy balance

$$\dot{h} = v - v_{\text{cruc}} - \dot{H}_m - \frac{\Phi_s - \Phi_l}{\Delta H \rho_s \pi r_c^2} \quad (3.66)$$

which is a way of explicitly expressing the connection of the thermal model to Equations (3.14) and (3.58).

A more detailed analysis of the interface shape considers the two-dimensional temperature distribution in the melt and the crystal since the heat is released from the side surface of the crystal. The interface shape reflects the ratio of the radial to axial gradients, and it is orthogonal to the local temperature gradient and heat flow. A low-order set of equations can be developed using piecewise linear segments to represent the interface shape and a local energy balance for each segment [Gevlber 1994-1, Duanmu 2006]. Figure 3.8 shows how four pairs of geometrical variables can be used to describe the radial and axial positions for each segment.

Equations (3.67)–(3.70) describe the energy balance for the four interface segments:

$$(v - v_{\text{cruc}} - \dot{H}_m - \dot{h}) \rho_s \Delta H \pi r_c^2 = \Phi_{s1} - \Phi_{l1} \quad (3.67)$$

$$\int_{R_1}^{R_2} 2\pi r \rho_s \Delta H (v - v_{\text{cruc}} - \dot{H}_m - \dot{h}_2) dr = \Phi_{s2} - \Phi_{l2} \quad (3.68)$$

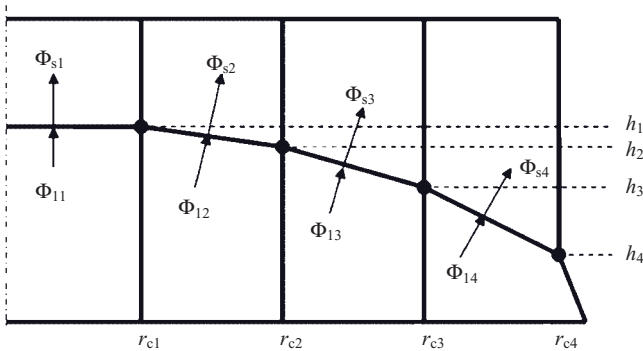


Figure 3.8 Linear segment representation of interface shape (Reprinted with permission from [Duanmu 2006], copyright (2006) Ning).

$$\int_{R_2}^{R_3} 2\pi r \rho_s \Delta H (v - v_{\text{cruc}} - \dot{H}_m - \dot{h}_3) dr = \Phi_{s3} - \Phi_{l3} \quad (3.69)$$

$$\int_{R_3}^{R_4} 2\pi r \rho_s \Delta H (v - v_{\text{cruc}} - \dot{H}_m - \dot{h}_4) dr = \Phi_{s4} - \Phi_{l4}. \quad (3.70)$$

These equations yield a set of coupled equations for the interface height for each segment. As indicated in section 3.3.2.4, the dynamics of this system becomes somewhat more oscillatory than with the flat interface equations.

3.3.2.3 *Equipment Considerations*

In order to determine the local gradients at the interface and the way how they vary throughout the batch process and as a function of operating regime (e.g. selection of heater setting and pull rate), a coupled equipment–process model is needed [Duanmu 2006]. A typical Cz crystal growth equipment configuration (Figure 3.9) is made up of four major parts: resistance heater, crucible assembly, insulation package, and water-cooled steel chamber. The crucible assembly is positioned in the central part of the furnace surrounded by the heater and supported by the crucible pedestal which lifts the crucible during the growth process. Graphite resistance heaters surround the crucible assembly and typically have a ‘picket fence’ shape.

Insulation material outside the heater is used to cut down the heat transfer from the hot zone to the steel chamber. The physical properties and the equipment geometries are

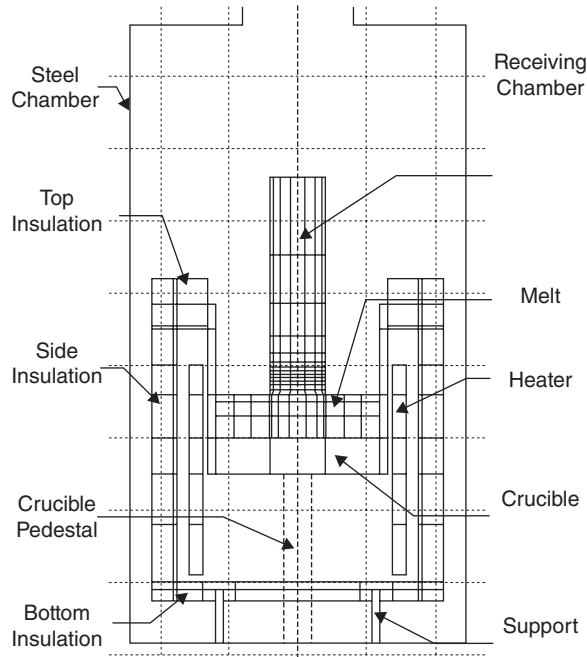


Figure 3.9 Schematic of the Cz crystal growth furnace (Reprinted with permission from [Duanmu 2006], copyright (2006) Ning).

Table 3.2 Summary of geometric parameters of equipment (all measurements in cm)

Steel chamber		Heater	
Inner radius	24.4	Inner radius	13.8
Height	60.0	Outer radius	15.8
		Height	29.0
		Empty ratio	0.4
Crucible		Top insulation	
Inner radius	12.0	Inner radius	13.2
Outer radius	13.2	Outer radius	21.6
Depth	18.5	Liner thickness	0.5
Bottom thickness (calotte)	5.0	Felt thickness	6.0
Side insulation		Bottom insulation	
Inner radius	13.2	Radius	21.6
Outer radius	21.6	Liner thickness	1.0
Liner thickness	0.5	Felt thickness	1.5
Felt thickness	6.0		

Source: [Duanmu 2006], copyright (2006) Ning.

chosen based on a small-scale commercial puller and a summary of other modelling publications [Bornside 1990, Bornside 1991]. Major parameters used in the equipment model are listed in Table 3.2.

The temperature dynamics for each thermal lump is determined by the sum of all the heat flows entering lump i from all the surrounding lumps by the relation

$$\frac{d}{dt}(C_i T_i) = \sum_{j=i}^n \Phi_{ij} \quad (3.71)$$

where C_i is the thermal capacitance of the lump, which can vary in time if the boundaries change.

The system components, including crystal, melt, crucible, heater, and insulation, are divided into 120 lumps of different dimensions (see Figure 3.9). Each lump is a control volume whose shape can be deformed (and the state equation modified to reflect this transient characteristic) and materials are allowed to flow across the boundary [Arpaci 1966]. Finer lump sizes are used where the temperature gradient is larger, especially close to the interface region.

Since the crystal normally grows in and out around the nominal diameter, the crystal contour is described by a stack of truncated conical surfaces rather than a straight cylinder. The lower part of the crystal is divided into six small axial lumps with fixed lengths to capture the temperature gradient and interface heat flow with good accuracy. The lumps in the upper part of the crystal are allowed to elongate as the crystal body grows. There are four lumps in radial direction. The radial lumps in the meniscus are aligned with the corresponding lumps in the crystal to keep the consistency of the heat flow calculation. In the outside regions of the melt that are exposed to the hot zone, the melt mass is evenly divided into three radial lumps.

Only axial lumps are formulated in the crucible side wall because the dominant temperature gradient is in the axial direction. The thermal capacity of the silica liner and the graphite container are considered together, but different material properties are taken into account in evaluating the thermal resistances. Different thermal emissivities are used in radiation calculation: graphite (.8) for the outside surface facing the heater and silica (.6) for the inside surface facing the hot zone [Gevlber 2001].

There are five axial lumps in the heater, six axial lumps in the side graphite liner and six axial lumps in the side felt. In the top and bottom insulation, the lumping strategy is designed to capture the different thermal conditions from the centre to the periphery of the equipment in the radial direction.

3.3.2.4 *Heat Transfer Modelling*

The thermal status of each individual lump is represented by one temperature state variable given by Equation (3.71). The lump is considered homogeneous in terms of physical properties such as thermal conductivity and specific thermal capacity. The lump temperature corresponds to the spatial integral of the temperature inside the lump, and thus is the average temperature. Fourier's law of heat conduction is expressed in a lumped formulation and is expressed in terms of the two neighbouring lump temperatures.

The convective influence on heat transfer is taken into account by using effective conductivity in the calculation of thermal resistance in the melt. The effective thermal conductivity in the melt is set to 1.8 times the nominal value [Sinno 2000] to take into account the mixing effects of convection. The effective conductivities of the meniscus lumps and the first layer of melt lumps underneath the meniscus are considered as linear function of the radial distance of the lump to the central line to count in the effect of crucible rotation.

Enclosures are used to model the radiative heat transfer, and are closed cavities where energy exchange happens mutually between surfaces. Six radiation enclosures are used, including a top enclosure, low enclosure, and four small side enclosures around the heater, crucible, and side insulation. Of these, the top enclosure is most important to the thermal conditions around the interface. It consists of meniscus, and melt surfaces, exposed crucible wall, part of the top insulation package, and inner surface of the steel chamber, including 30 surfaces. The view factors among these surfaces are evaluated on a dynamic basis in conjunction with geometric variation. With a noncylindrical real crystal, the effect of blocking issues is important and must be taken into account properly.

The openings in the picket fence shaped heater results direct radiation between the crucible side wall and the graphite liner of the side insulation. If the heater shape is not considered, the required heater power would differ significantly from the real system.

All surfaces inside the radiation enclosure are considered as diffuse grey surfaces, meaning their monochromatic hemispherical emissivity is independent of direction and wavelength. The calculation procedure described in [Bejan 1993] is employed to evaluate the radiation energy exchange among the enclosure surfaces.

The view factor is defined as the fraction of radiation emitted by one surface which is directly intercepted by another. It represents the geometrical characteristics of radiation enclosure. The evaluation of the view factor contributes to most of the modelling and

computational complexities for radiation heat transfer calculation in Cz crystal growth simulation [Dupret 1990], especially when the changing crystal geometry is included.

3.3.2.5 Crystal Surface Orientation

Energy interaction between the crystal side surface and the surrounding thermal environment inside the hot zone is significantly influenced by crystal geometry. Models based on simplified heat transfer assumptions treat the crystal as a straight cylinder with uniform diameter. This assumption is effective in studying the steady state of thermal conditions but it can result in incorrect process dynamics. As illustrated in Figure 3.10, the crystal surface faces a different thermal environment depending on whether it is growing inwards or outwards, and as a result, the crystal side surface radiation differs significantly. To take the effect of crystal surface orientation into account, the crystal contour is described by using a pile of truncated cones. This enables the model to capture the influence of the changing crystal surface orientation on the radiation heat transfer and, therefore, on the energy balance at the interface.

The basic concept of shape evolution is illustrated in Figure 3.11. There are some discrepancies between the real and approximated crystal shape, but for each control volume the dominant surface orientation is captured, as well as its impact on view factors and the radiation heat transfer [Duanmu 2006]. The further the crystal lump is from the interface region, the less precise the linear segment interpolation method becomes due to the lump

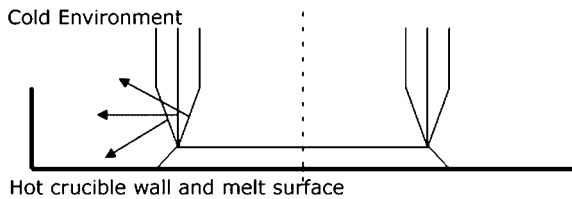


Figure 3.10 Illustration of the effect of crystal surface orientation (Reprinted with permission from [Duanmu 2006], copyright (2006) Ning).

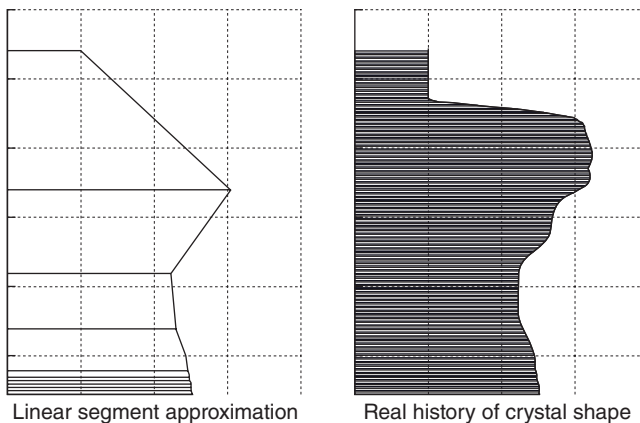


Figure 3.11 Lumped approximation of the real crystal shape history (Reprinted with permission from [Duanmu 2006], copyright (2006) Ning).

size. However, this crystal geometry error is not critical to capturing the dominant growth dynamics.

Another important model feature to capture correctly is the radiation blocking caused by the crystal standing in the central part of the hot zone. The crystal lumps block the radiation interaction among crystal melt surfaces, the interior surface of the crucible wall, and the adjacent surfaces of insulation material. It is critical to estimate how the view factor function varies with the changing crystal length while keeping it as smooth as possible to avoid discontinuity in the radiation heater transfer calculation (see [Wilson 2001] for details).

Since the body of the crystal is modelled as a pile of truncated cones rather than a straight cylinder, further computational difficulties are encountered: no analytical view factor expression is available when the blocking object is noncylindrical. The strategy for dealing with this problem is to approximate the noncylindrical object by a cylindrical shape. Its accuracy depends on how well the approximated cylinder resembles the blocking effects of cones. The accuracy can be improved by using a better approach for approximating the crystal shape.

3.3.3 Linear System Model Analysis

The most straightforward approach to obtain a linear model is full-state linearization of a nonlinear model at an equilibrium point. The partial derivatives of the nonlinear differential equation are calculated using a numerical central difference perturbation approach. Since the radiation heat transfer is incorporated, no explicit analytical solution can easily be derived for the nonlinear differential equations. The linearization results are shown in Equation (3.72), where the partial derivative terms are written in matrix form and are the Jacobian matrices

$$\dot{x} = \left. \frac{\partial f}{\partial x} \right|_{x=x_0} x + \left. \frac{\partial f}{\partial u} \right|_{u=u_0} u = Ax + Bu \quad (3.72)$$

Here $x \in \mathbb{R}^n$ is the state vector and $u \in \mathbb{R}^m$ the input vector describing a n th-order system with m inputs.

However, significant differences are observed between the linearized and nonlinear model simulations due to the changing crystal surface orientation, as shown in Figure 3.12. Although their initial transient responses (the first 40 min) are similar, the linear dynamics quickly settles down to the steady state value (the settling time is about 1.5 h), but the nonlinear dynamics exhibits slow and poorly damped oscillations (the oscillation period is about 10 h). These results are, however, similar to those found by [Atherton 1987] and [Dupret 1990].

3.3.3.1 Reduced-Order Linear Model

The state variables of the full model can be categorized into two subsets, (i) geometrical state variables that include the crystal radius and interface shape, and (ii) thermal state variables. The dominant timescale of the geometry dynamics (minutes) is much smaller than the timescale of the thermal dynamics (hours). Thus, a reduced-order linear model

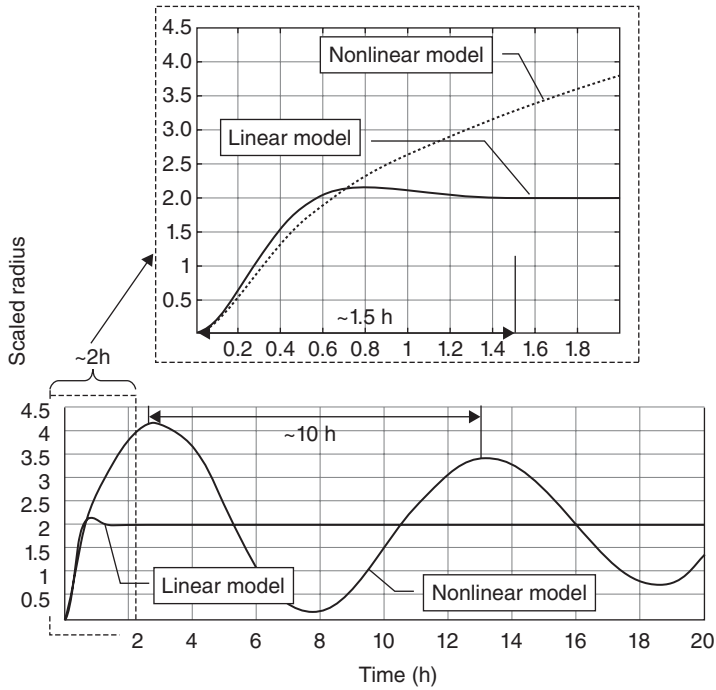


Figure 3.12 Comparison between linear and nonlinear model simulations (Reprinted with permission from [Duanmu 2006], copyright (2006) Ning).

can be found based on the dynamics of the geometrical states for constant thermal equilibrium conditions, which greatly reduces the order of the dynamic model. This reduced-order linear model does not consider the interactions between the thermal and geometrical states. Previous research for simple linear models developed by [Hurle 1993, Satunkin 1995, Johansen 1991] was based on similar modelling assumptions, including a straight cylindrical crystal.

The differential state equation (3.17) for r_c is linearized around the equilibrium point under the growth condition that the crystal is pulled up with nominal speed of v^0 and the slope angle is zero. We obtain

$$\delta \dot{r}_c = v^0 \frac{\partial \varphi}{\partial r_c} \delta r_c + v^0 \frac{\partial \varphi}{\partial h} \delta h. \tag{3.73}$$

Equation (3.73) can be transformed to a transfer function form in the Laplace domain, and describes the dynamic input–output relation between the Laplace transformed quantities $R^* = \mathcal{L}\{r_c\}$ and $H^* = \mathcal{L}\{h\}$ as:

$$R^* = \frac{A_{12}}{s - A_{11}} H^* \tag{3.74}$$

where

$$A_{11} = v^0 \frac{\partial \varphi}{\partial r_c} > 0 \quad \text{and} \quad A_{21} = v^0 \frac{\partial \varphi}{\partial h} < 0.$$

This first-order system has a positive pole and negative steady state gain. The positive pole suggests that once the interface height is perturbed, the change of the meniscus angle accelerates the initial change of the radius, instead of driving it back. For this reason, [Surek 1980] claimed that the Cz process is not stable if only the capillary effect is considered (see section 2.4).

Equation (3.74) alone, however, does not provide any indication about the growth dynamics since the energy balance equation that drives the interface movement has not been considered. Linearization of the interface height state equation about the equilibrium point yields

$$\dot{h} = -\frac{1}{\rho\Delta H} \frac{\partial(\Phi_x - \Phi_l)}{\partial r_c} \delta r_c - \frac{1}{\rho\Delta H} \frac{\partial(\Phi_x - \Phi_l)}{\partial h} \delta h + \delta v. \quad (3.75)$$

The heat fluxes Φ_s and Φ_l are considered as system parameters determined by the hot zone design, and the pulling speed v is the system input. The sensitivities of Φ_s and Φ_l to the perturbation of r_c and h are evaluated based on steady state process model simulations.

By combining Equations (3.73) and (3.75), a reduced-order linear model of the Cz process growth dynamics is obtained:

$$\begin{bmatrix} \delta \dot{r}_c \\ \delta \dot{h} \end{bmatrix} = \begin{bmatrix} v^0 \frac{\partial \varphi}{\partial r_c} & v^0 \frac{\partial \varphi}{\partial h} \\ -\frac{1}{\rho\Delta H} \frac{\partial(\Phi_x - \Phi_l)}{\partial r_c} & -\frac{1}{\rho\Delta H} \frac{\partial(\Phi_x - \Phi_l)}{\partial h} \end{bmatrix} \begin{bmatrix} \delta r_c \\ \delta h \end{bmatrix} + \begin{bmatrix} 0 \\ 1 \end{bmatrix} \delta v. \quad (3.76)$$

This form of the linear model corresponds to Equations (2.15) and (2.16) and the related stability analysis described in that section, but more explicitly shows the connection to the thermal model, and dependency on how the heat flows scale. How the eigenstructure of Equation (3.76) varies with operating point is analysed in section 3.4.

3.4 Process Dynamics Analysis for Control

To aid in developing an appropriate controller tuning strategy as well as control structure, it is desirable to understand how the eigenstructure and steady state gains vary as a function of operating conditions and throughout the batch process. This section analyses these issues for an 80–120 mm diameter Si crystal for the system described in section 3.3.2.3. Specific issues that are addressed include how the fundamental dynamics of the interface shape scale (section 3.4.1), the impact that a curved interface shape has on the dynamics and the impact of dominant nonlinear dynamics (section 3.4.4). Many of these issues are addressed for other materials such as Ge [Hurle 1990, Satunkin 1995], GaAs [Looze 1995], InP [Masi 2000], and LiNbO₃ [Satunkin 1990].

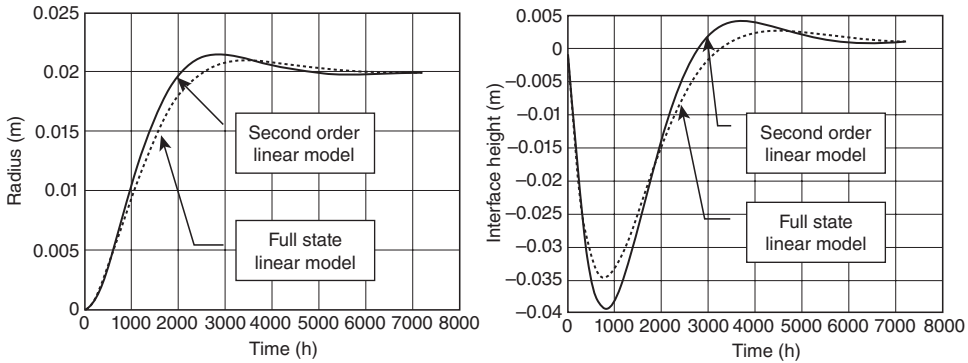


Figure 3.13 Comparison between full state and second-order linear model to a step decrease in heater power (100W) (operating conditions: $r_c = 4.0\text{ cm}$, $v = 3.0\text{ cm/h}$, $H_m = 3.0\text{ cm}$) (Reprinted with permission from [Duanmu 2006], copyright (2006) Ning).

Figure 3.13 shows the dominant crystal interface radius and interface height dynamics in response to a step decrease in heater power. The radius response has dominant second-order response characteristics with moderate overshoot and has a relatively slow settling time (i.e. the time where the output settles to within 5% of steady state) of 24 000 s (400 h). The interface height response, in contrast, clearly displays the characteristics of a so-called right-half-plane (RHP) zero, first decreasing, but in steady state, increasing relative to the initial condition. This RHP zero characteristic affects the response measured both by weight and by meniscus reflection sensors. It is significant, since it can be shown to pose a fundamental limitation on closed-loop control performance and could result in unstable (or highly oscillatory) closed-loop response if not properly addressed in controller tuning. This problem and its consequences are discussed in more detail in section 3.5.2.

Figure 3.13 also compares the response of the full linearized model to that of the reduced (second)-order model described in section 3.3. The full state linear model has a slightly less oscillatory and slower dynamic response than the reduced-order linear model. The difference is mostly due to the thermal lag in the heat transfer process captured by the full state model but neglected by the reduced-order linear model. However, the second-order model does a good job of capturing the critical timescales and dynamic features. This is achieved because the linear model is coupled to an appropriate global heat transfer model to determine the operating point, which affects how the partial derivatives in Equation (3.76) are evaluated.

Both the reduced-order linear model and full state linearized model reflect the dynamic characteristics of the nonlinear system around the equilibrium point for a small perturbation. The sensitivity of the interface heat fluxes Φ_s and Φ_l to perturbation of r_c and h is evaluated for the system geometry at the equilibrium condition, e.g. straight crystal sides. However, some nonlinear effects of the Cz process related to the global thermal–geometry interaction are not captured by either linear model (see section 3.4.4).

The dynamic relation between the pulling rate and interface radius is governed by the coupled mass and energy balance at the interface (Equation (3.76)). Figure 3.14 compares the steady state relation between the interface height and the radius (dashed line) of the

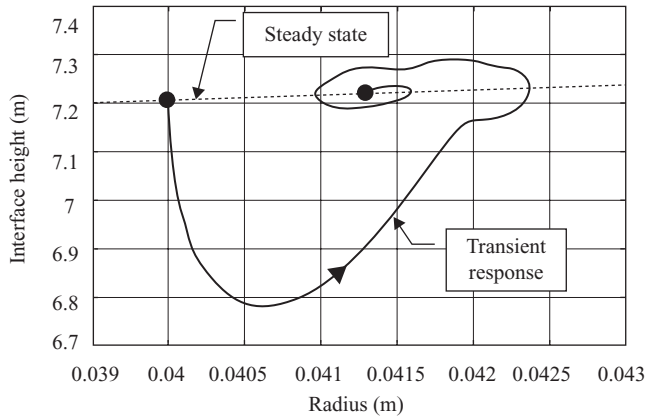


Figure 3.14 State trajectory of crystal radius (r_c) and interface height (h) from open-loop step decrease in pulling speed, nonlinear model (operating conditions: $r_c = 4.0$ cm, $v = 3.0$ cm/h, $H_m = 7.5$ cm) (Reprinted with permission from [Duanmu 2006], copyright (2006) Ning).

Young–Laplace meniscus relation (3.18) and the dynamic state trajectory of the open loop response to a 10% step decrease in pulling rate using the nonlinear model. In steady state, the interface height increases with radius and, for a constant thermal environment, this will correspond to a lower pull rate. Thus, the decrease in pulling speed will initially move the interface down as dictated by Equation (3.75). As shown in Figure 3.14, while the crystal radius dynamically increases from one equilibrium condition to another, the interface height initially moves in the opposite direction to that of the final equilibrium point. This is the characteristic of the RHP zero response shown in Figure 3.13.

3.4.1 Operating Regime and Batch Implications

In general, process dynamics vary for different operating conditions due to different thermal conditions around the interface, as well as throughout the batch process, since the melt height changes. Understanding the influence of these variations on the process dynamics provides a foundation for developing a robust process control system. In part, these different operating characteristics (e.g. temperature gradients and pulling speeds) are selected to meet process objectives related to achieving the desired material quality while optimizing throughput requirements.

A summary of how the process dynamics changes as a function of operating regime and melt level, based on the reduced-order linear model, is given in Table 3.3. The dynamic characteristics, e.g. pole locations, dominant time constants and damping ratios, as well as steady state input–output gains for pulling rate input, depend on the pulling speed, crystal radius, and melt level. Important trends include: (i) the response time becomes smaller as diameter increases and for lower pull rates, and (ii) the damping ratio (which indicates how oscillatory the response will be) decreases for faster pulling rates, lower melt heights and greater diameters. Plotting the dominant time constant as a func-

Table 3.3 Dynamic characteristics for different operating conditions (Note: K_p is the scaled steady state gain where r_c is scaled using 1% of the nominal radius and v is scaled using 10% of the nominal growth rate, τ is the time constant, ζ is the damping ratio)

Growth Condition	r_c (m)	P_{in} (W)	K_p	τ (s)	ζ
$v = 0.03$ (m/h)	0.04	28006.8	2.00	709	0.6363
$H_m = 0.030$ (m)	0.05	27147.8	2.19	835	0.4765
	0.06	26117.6	2.38	957	0.3519
$v = 0.03$ (m/h)	0.04	27839.0	1.83	678	0.7154
$H_m = 0.075$ (m)	0.05	27537.4	1.98	795	0.5260
	0.06	27374.3	2.09	898	0.4124
$v = 0.06$ (m/h)	0.04	27322.6	1.61	450	0.3244
$H_m = 0.030$ (m)	0.05	26288.2	1.71	521	0.2306
	0.06	25070.6	1.80	588	0.1595
$v = 0.06$ (m/h)	0.04	27176.9	1.51	436	0.3759
$H_m = 0.075$ (m)	0.05	26698.7	1.60	504	0.2620
	0.06	26334.1	1.65	563	0.1972

Source: [Duanmu 2006], copyright (2006) Ning.

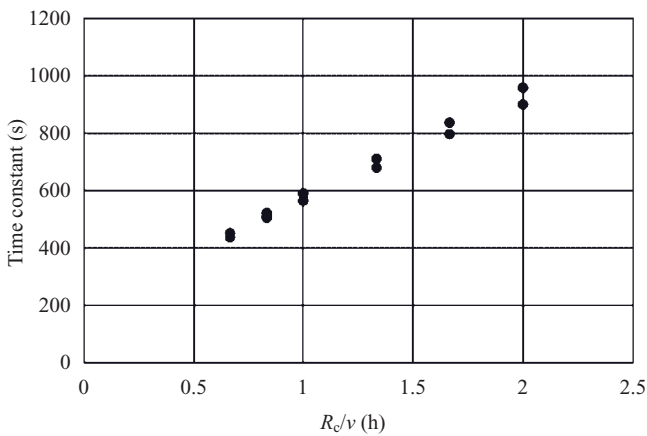


Figure 3.15 Relation of dominant time constant from the reduced-order model to the ratio of the crystal radius to pulling rate, obtained from Table 3.3 for 40–60mm radii and pull rates of 3–6 cm/h.

tion of the ratio of crystal radius to pulling rate (r_c/v) reveals that there is a linear relationship (Figure 3.15), which indicates it is an important scaling variable.

Figure 3.16 illustrates how the dynamics change for different pull rates and melt levels. For low pull rates, the system responds slower, is better damped, and has larger steady state gain. Thus, a higher pulling speed (6.0 cm/h instead of 3.0 cm/h), there is a 20% decrease in steady state gain, a 37% decrease in time constant, and a 50% decrease in damping ratio. As the system goes from high melt level to low melt level, the interface dynamic characteristics undergo moderate changes in terms of both gain and dynamic

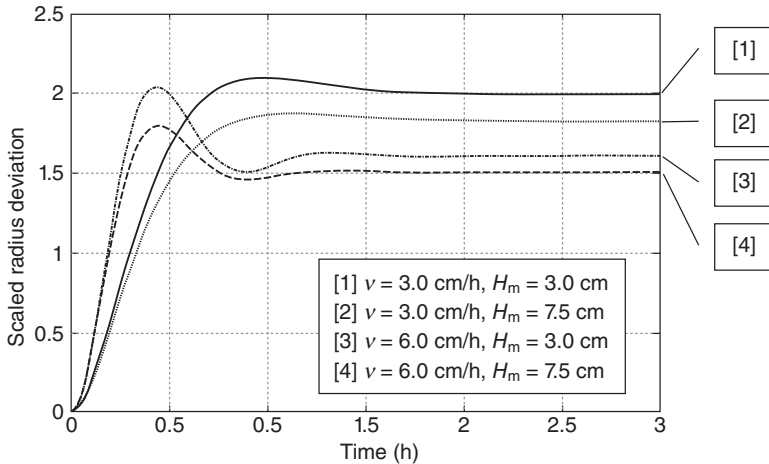


Figure 3.16 Open-loop pulling speed step response based on linear model under different operating conditions (Reprinted with permission from [Duanmu 2006], copyright (2006) Ning).

characteristics (9% decrease in steady state gain, 4% decrease in time constant, and 11% increase in damping ratio). These observations are due to by the dominant linear model eigenstructure shown in Figure 3.17.

Figure 3.18 shows how the dynamics change for open-loop heater power steps based on the linear model for different operating conditions. Similar to the open-loop pulling speed step response, at high growth rate condition, the interface responds to the heater power change faster than to the low growth rate condition. However, the system does not display the underdamped characteristics at high pull rates as was the case for low pulling rate.

The importance of designing a controller based on the specific operating point is indicated in Figure 3.19, where a PI controller designed on the basis of the low growth-rate condition does not work well for the high growth-rate condition. On the other hand, the model indicates that for the conditions evaluated, there is little need to adjust controller parameter settings at different melt levels throughout the batch process, although those results can differ, especially for low-gradient operations.

3.4.2 Actuator Performance Analysis

Pulling speed and heater power are the two major actuator inputs for the Cz crystal growth process, but they influence the material solidification process at the interface in different ways. The heater power affects the energy balance at the interface region, while pulling rate acts directly to carry the newly grown materials away. To keep the growth process operating uniformly in terms of constant crystal radius and growth rate, the pulling speed should match the growth rate for the specified heater power. Process variation happens whenever the interface energy balance is disturbed.

Changes in pulling rate impose a direct change to the interface dynamics (Equation (3.73)) and also impact the local interface heat flows. The heater power affects the

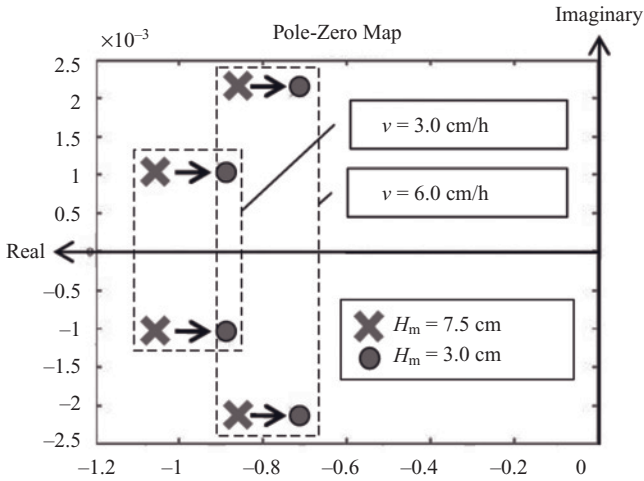


Figure 3.17 Dominant poles of linear dynamics under different operating conditions (Reprinted with permission from [Duanmu 2006], copyright (2006) Ning).

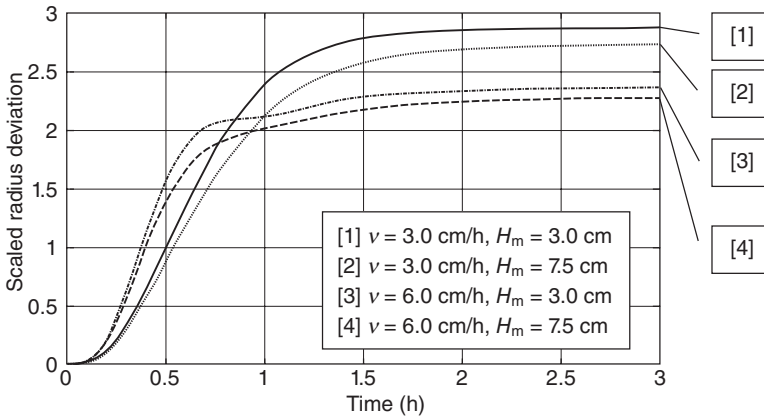


Figure 3.18 Open-loop step response for a 100-W decrease in heater power based on linear model under different operating conditions (Reprinted with permission from [Duanmu 2006], copyright (2006) Ning).

interface height by changing the interface energy balance and thus the material solidification rate. Reducing the heater power causes the crucible wall and melt temperatures to decrease, changing the heat flow around the interface. As shown by the linear model open-loop step response in Figure 3.20, the interface radius responds faster to the pulling speed change than to heater power. The difference is primarily due to the additional thermal lags in the heater–crucible–melt interface region.

The nonlinear model open-loop step response simulation (Figure 3.21) reveals some important differences from the linear model predictions. During the initial stage of the transient process, the crystal radius responds faster to the pulling speed change noticeably

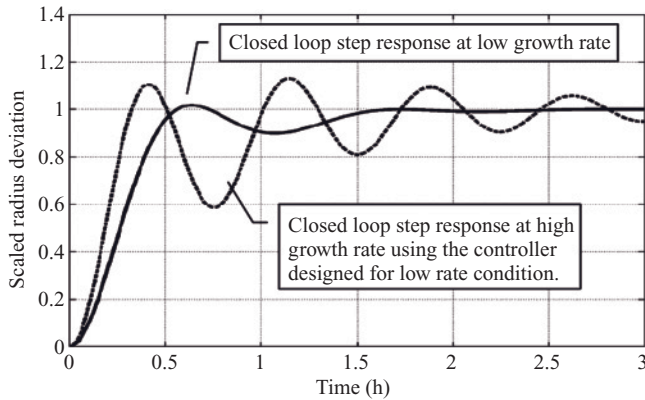


Figure 3.19 Closed-loop step response simulation based on linear mode at different growth rate (Reprinted with permission from [Duanmu 2006], copyright (2006) Ning).

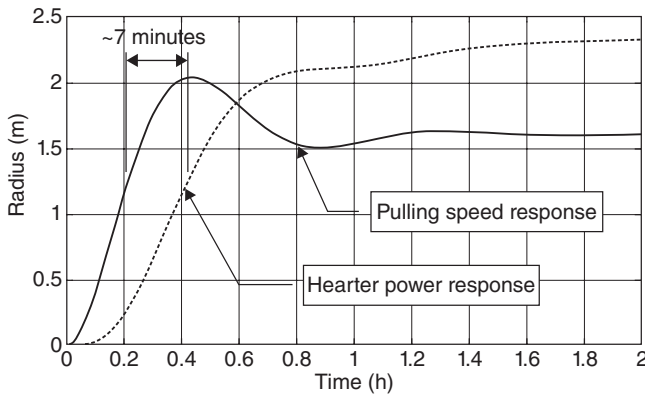


Figure 3.20 Open-loop step response for different actuators based on the linear model (Reprinted with permission from [Duanmu 2006], copyright (2006) Ning).

than the heater power (as indicated by the dashed circle). Thus, to some extent, the pulling speed can be considered to be a more effective actuator in feedback control to maintain constant crystal radius. Beyond the initial transient response, the nonlinear model reveals an additional slow oscillatory dynamic mode caused by the thermal geometry interaction. This results in there not being much difference between the peak time of v and P_{in} step responses (as indicated by arrows).

However, the use of the pull rate to control crystal diameter variations is also subject to desired acceleration constraints and possible speed limits for the pull rate actuator. In addition, [Voronkov 1982] and experimental research [Dornberger 2001, Falster 2000] also suggest that there are important limitations to pulling rate variation for growing high-quality, defect-free single crystal semiconductors, since pulling speed has to be maintained within 10% of the optimized level determined by the v_c/G theory.

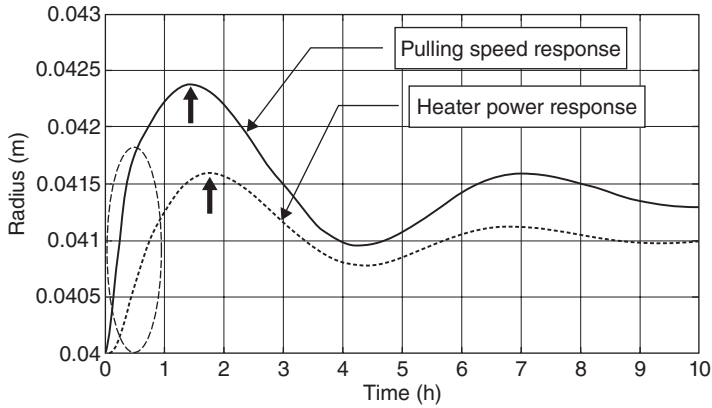


Figure 3.21 Open-loop step response based on the nonlinear model for different actuators (Reprinted with permission from [Duanmu 2006], copyright (2006) Ning).

3.4.3 Curved Interface

The importance of simulating the actual interface shape using a more complex model is that the shape reflects the local gradients which impact defect formation and the thermal stress [Frank 2000, Neubert 2001]. Large interface deflection indicates large radial temperature gradients relative to the axial gradient. Also, for wafers that are cut from the crystals, a smaller interface deflection results in more uniformly distributed material properties across the radial direction of the wafer. Thus, in general, it is desirable to control the interface shape during the growth process and it is useful to understand the impact of pulling speed and heater power on the interface shape.

The steady state interface shape shown in Figure 3.22 reveals the impact of different operating conditions (growth rate and melt height). For the same growth rate, the interface shape shows little change from high melt level to low melt level. But interface deflection is significantly larger at high growth rate than at low growth rate, due to greater crystal heat fluxes.

In terms of dynamic characteristics, nonlinear model simulations (Figure 3.23) reveal that flat interface modelling reflects the dominant dynamics of the system, although the curved interface dynamics is somewhat more oscillatory with higher overshoot.

3.4.4 Nonlinear Dynamics

3.4.4.1 Thermal-Geometry Interactions

The evolution of the crystal geometry influences the radiation energy exchange inside the hot zone since view factors are changing dynamically among different enclosure surfaces. The crystal surface orientation near the interface region strongly affects the interface energy balance (see Figure 3.10). As the crystal surface near the interface region tilts upwards when the crystal grows outwards, it becomes easier to lose heat to the cold

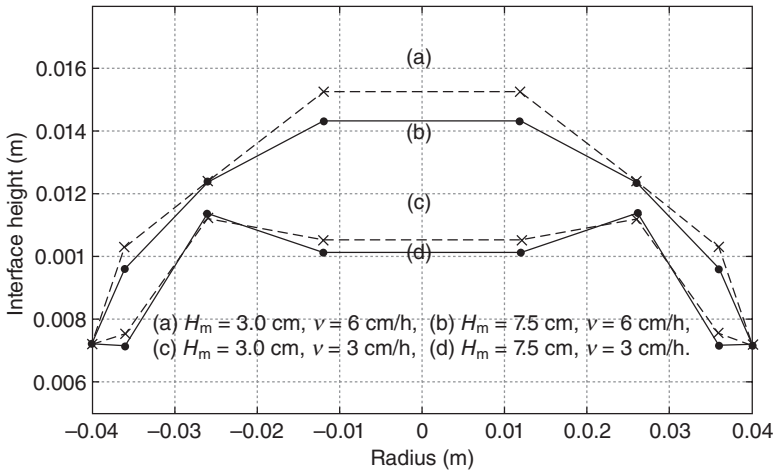


Figure 3.22 Interface shape variation under different operating conditions (Reprinted with permission from [Duanmu 2006], copyright (2006) Ning).

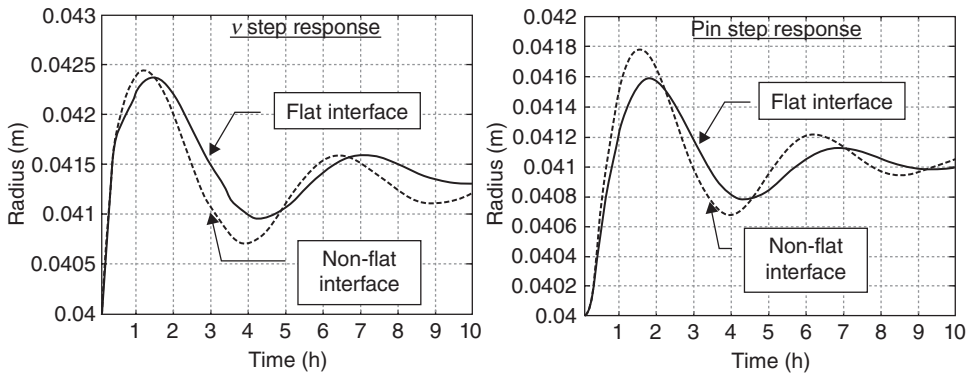


Figure 3.23 Nonlinear model step response simulations with flat and curved interface shape (Reprinted with permission from [Duanmu 2006], copyright (2006) Ning).

environment. When the crystal grows inwards, the crystal surface tilts downwards and interacts more with the hot melt surface.

Figure 3.24 shows the simulation results for crystal geometry variation and its impact on the radiation heat transfer and diameter dynamics for a 10% step decrease in pulling speed. The expansion of the outward-growing edge (labelled as edge (a) in the 4-h snapshot in Figure 3.24) makes the crystal a more efficient radiator of heat. As the interface height and crystal radius approach the equilibrium condition, the crystal stops growing larger. Similar results were found by [Atherton 1987].

However, as the edge (a) is slowly pulled further away from the interface, its cooling effect becomes weaker. Therefore, the crystal contour is not able to lose enough heat to sustain the amount of interface heat flow at the crystallization front with the interface radius at the end of edge (a), so the crystal radius starts to grow inwards. As shown in

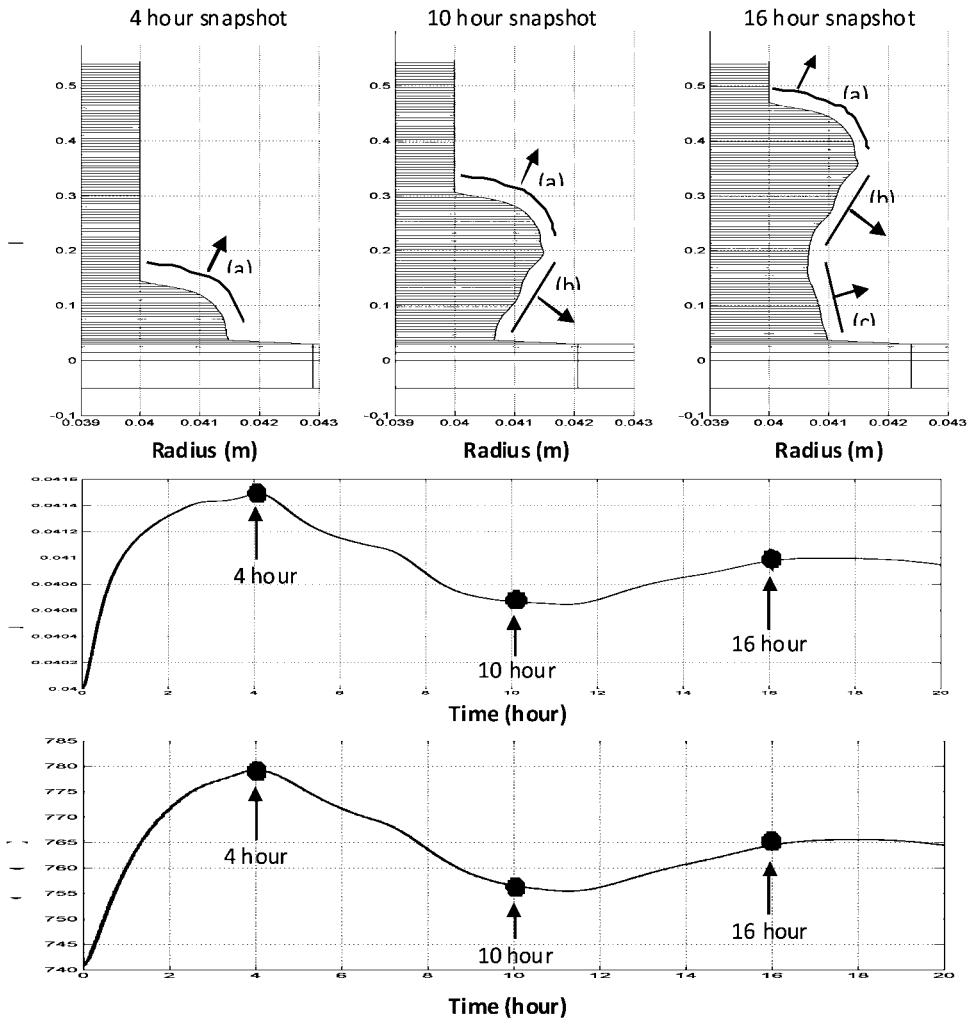


Figure 3.24 Effects of the thermal-geometry interaction using nonlinear dynamic model simulation (operating conditions: $r_c = 4.0\text{ cm}$, $v = 3.0\text{ cm/h}$, $H_m = 3.0\text{ cm}$) (Reprinted with permission from [Duanmu 2006], copyright (2006) Ning).

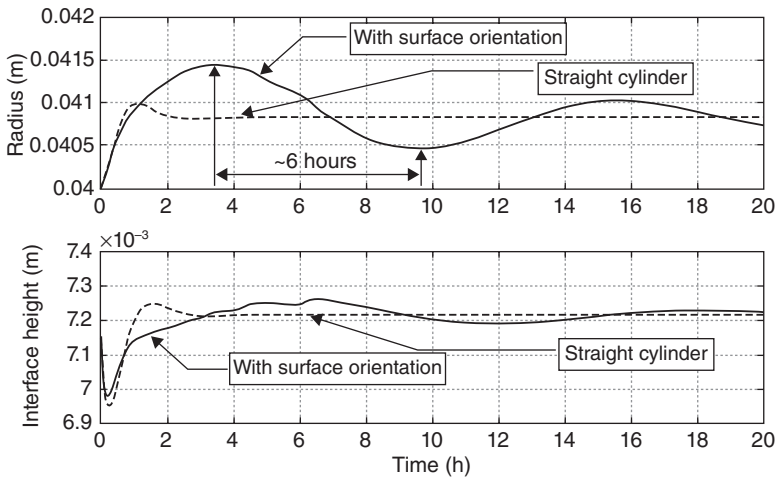


Figure 3.25 Nonlinear dynamic simulations using different modelling assumptions on crystal geometry (operating conditions: $r_c = 4$ cm, $v = 4$ cm/h, $H_m = 7.5$ cm) (Reprinted with permission from [Duanmu 2006], copyright (2006) Ning).

the 16-h snapshot in Figure 3.24, the inward-growing (b) has now developed. After the crystal radius becomes small enough to match the overall effect of edge (a) and edge (b), the interface reaches a local minimum.

The crystal geometry then grows inwards and outwards for a number of iterations before settling down at the final steady state value. By this mechanism, the crystal radius oscillates with a very long time period and small degree of damping if no control is used.

To test whether the orientation is the cause of this long-term dynamic, as well as to compare the results predicted by the common assumption that the crystal is cylindrical, the nonlinear model is run with both a varying orientation and with straight crystal sides. Figure 3.25 shows the response to a 10% step decrease in the pulling speed for both modelling approaches using the nonlinear model. The difference between the dynamic responses of the two modelling assumptions is significant. The slow evolution of crystal geometry variation gives a slow and oscillatory pattern to the overall dynamic response which is not captured by using the straight cylinder approach.

3.4.4.2 Closed-Loop Simulations

A Closed-loop nonlinear simulation of a step change in crystal diameter is illustrated in Figure 3.26. A PI controller is used, designed using the reduced linear model. This shows the surprising result that the controller design based on the reduced-order models performs well, in spite of the significant difference in long-term behaviour between the nonlinear and linear models. The reason could be that the closed-loop control limits how large the shape/orientation becomes, thus eliminating the long-term oscillatory response. This suggests that the significantly simpler linear model is useful for developing tuning strategies, while the nonlinear models are useful in understanding how local gradients and interface shape vary with different operating conditions and might be controlled.

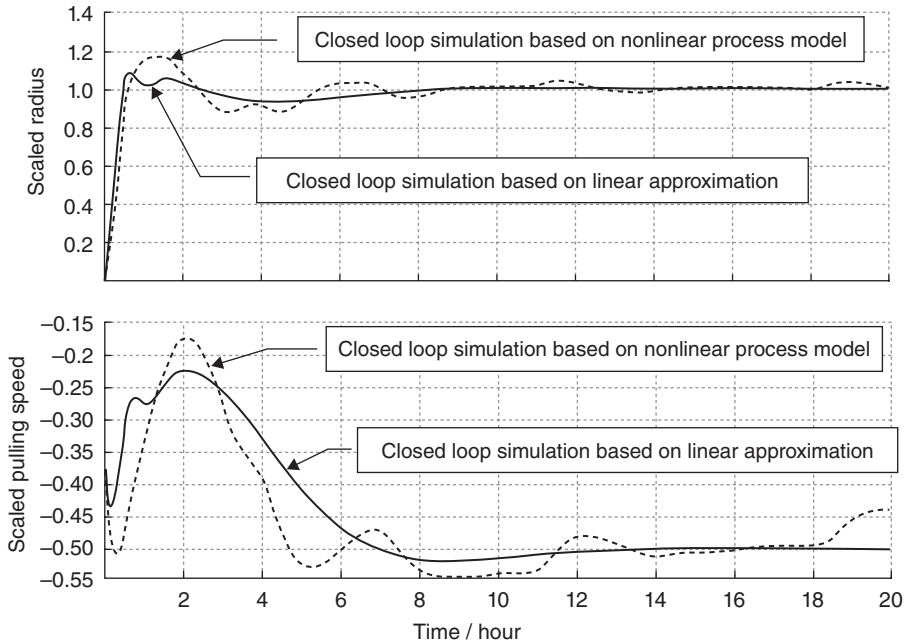


Figure 3.26 Nonlinear closed-loop simulation of control design based on linear model (Reprinted with permission from [Duanmu 2006], copyright (2006) Ning).

3.5 Conventional Control Design

This section presents two PID control approaches (section 3.1.6), commonly used in industry, utilizing optical and weight based measurements.

3.5.1 Control Based on Optical Diameter Estimation

In [Patzner 1967, Digges 1975] a method for determining an estimate of the crystal radius is presented using optical imaging. The idea is based on the fact that light emitted by the red-hot heaters is reflected upwards from the meniscus. These reflections can be seen and detected by an optical camera as a so-called ‘bright ring’. Image processing software is then able to determine the diameter of the ring in real time. This value, scaled by an empirically determined factor accounting for the difference between the measured meniscus and the expected crystal radius, is used as the measured variable in the control system. Since Si has a large Laplace constant (i.e. high surface tension and low density, resulting in large meniscus heights) and because of its metallic reflectivity, this material is an obvious candidate for this technique. Hence, although the crystal radius itself is not measured, this technique is widely and successfully used especially in Cz growth of Si [Hurle 1977, Lorenzini 1974].

3.5.1.1 Control System Structure

Using conventional PID-based control in Cz growth of Si crystals, one aims for the following objectives:

- The crystal radius has to be tracked along a given reference trajectory in order to meet requirements of post-processing steps such as wafer production. Furthermore, mechanical stress resulting from large diameter variations has to be avoided.
- The desired growth rate should be maintained throughout the batch process and changing thermal environment, in order to maintain the desired production rate.
- The growth rate has to be kept within a very narrow tolerance band in order to match important requirements of crystal quality, especially with respect to point defects (see sections 3.1.2 and 3.4.2 and [Falster 2000, Voronkov 1982, Voronkov 2002]).

When designing a control system that meets these objectives one has to reflect the different time constraints the available control inputs have on the system, as outlined in section 3.4.2: (i) changes in pulling speed affect the system quite quickly, (ii) changes in heater power need some time, depending on the thermal conditions occurring in the system [Gevelber 1987-2, Gevelber 1988]. Usually, therefore, a cascaded control structure is chosen (see Figure 3.27) [Voronkov 2002].

Deviations Δr_c from the reference value $r_{c,\text{ref}}$ of the crystal radius r_c are fed into a PID controller manipulating the reference value v_{ref} of the pulling speed by an amount Δv . This value, indicating a deviation of the real pulling speed trajectory from its pre-calculated reference value, is also fed into a second PID controller manipulating the reference value P_{ref} of the heater power by an amount ΔP . By this strategy it is ensured that the system is able to react quite quickly to perturbations in crystal diameter. Accumulated deviations in the pulling speed trajectory lead to a change of the heater power trajectory, ensuring that the system is kept in its reference state in the long term. The pulling speed especially returns to its reference level.

This control system approach requires very careful planning of the feedforward trajectories, especially for the pulling speed needed to obtain a certain growth rate trajectory. This can be achieved by using powerful numerical methods to solve the inverse problem (see section 3.2.2). Performance can be further improved by processing the knowledge gained through repeated growth runs.

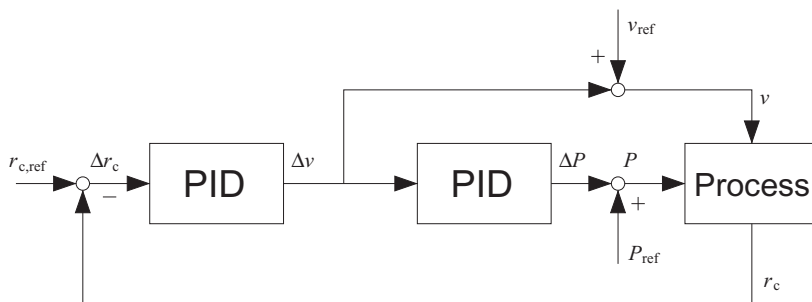


Figure 3.27 Cascaded PID-based control scheme utilizing pulling speed and heater power for diameter control (Reprinted with permission from [Voronkov 2002], copyright (2002) Ning).

3.5.1.2 Limitations

Despite its undoubtedly widespread application in industry and the fact that using this approach it is possible to grow crystals which perfectly match crystal radius requirements down to fractions of a millimeter, this approach to control system design has several important limitations.

First of all, this approach does not directly control the growth rate. Proper tracking of this value is only guaranteed if the pulling speed and the crystal radius trajectories follow their references (see Equation (3.32)). Recalling Equation (3.14),

$$v_c = v - v_{\text{cruc}} - \dot{h} - \dot{H}_m,$$

one immediately sees that further conditions must be fulfilled in order to conclude the growth rate directly from the pulling speed:

- The crucible speed must compensate for the rate of change of the melt level, i.e. $v_{\text{cruc}} = -\dot{H}_m$.
- The meniscus height must be constant, i.e. $\dot{h} = 0$, which is actually the case only on during cylindrical growth.

The first requirement can be met by an additional measurement of the melt height [Gevlber 1989], but the second one is difficult to meet since any perturbation in the crystal radius causes the meniscus height to vary. Thus, the required growth rate trajectory is matched only if the feedforward trajectory for the pulling speed is properly calculated and one can ensure that perturbations leading to long-term deviations of the pulling speed from its reference trajectory do not occur. In addition, the coupled nature of the process physics, which can limit the achievable material properties, has not been explicitly considered in designing the control structure. Closed-loop control is used to maintain diameter, but there is no explicit coordination of control to achieve the ensemble of objectives such as interface shape. Also, the process conditions required to meet advanced materials requirements become tighter and are difficult to achieve throughout the varying batch process. Finally, the conventional control system designs do not directly address important process dynamics, such as the time variation of the process due to its batch nature, and the inherent performance limitations posed by some process dynamics and measurements (e.g. the RHP zeros).

Analysis of data sets for actual growth runs in commercial puller systems reveal control requirements and complexities that might be observed from analysis of ‘idealized’ process models (both low-order and high-order methods). Figure 3.28 presents normalized plots of inputs and resulting crystal diameter from a growth run in a Kayex KX150 puller (90kg charge, 10” diameter crystal) utilizing a conventional cascaded control structure. Several important points may be observed: (i) the pulling rate set point trajectory used decreases the pull rate by half, limiting productivity; (ii) there are significant variations in pull rate (up to $\pm 17\%$), which can have adverse impact on point defect distribution; (iii) the diameter control performance changes at the beginning and the end of the growth run (indicated by the long-period oscillations), showing a need for adaptive control.

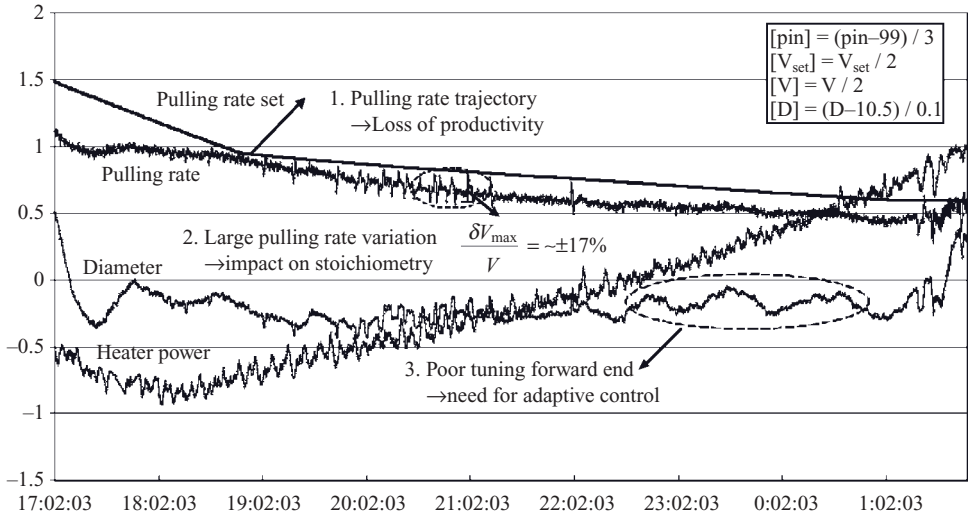


Figure 3.28 Results of a Si growth run utilizing the cascaded control structure proposed in Figure 3.27 (Reprinted with permission from [Gevlber 2001], copyright (2001) Ning).

3.5.2 Weight-Based Control

If it is not possible to capture the diameter of the bright meniscus ring, the usual control strategy is to use the crystal or the crucible ‘weight’ as the measured variable [Levinson 1959, Rummel 1966]. The basic idea is to measure the force acting on the pulling or crucible rod and to compare it with the force required, derived from the reference shape of the crystal [Bardsley 1972]. The deviation between these values is used to drive a PID controller manipulating the heater power. Crystal weighing is preferred, because of problems of material evaporating from the charge, the crucible, and the susceptor in case of crucible weighing. When RF heaters are used, additional vertical forces induced in the susceptor also come into play [Hurle 1977].

3.5.2.1 Control System Design

Operation Mode. The structure of a weight based control system is sketched in Figure 3.29. It is important to distinguish between two modes of operation [Hurle 1977]:

- *Weight mode:* The weight measured by the load cell is compared to the reference value and the difference is used as an error signal for the PID controller. Hence, in this mode the controller tries to keep the weight on its reference value, meaning that a previous error in crystal radius later results in an error of opposite sign (see Equation (3.16)). Thus, oscillations may occur. However, this mode circumvents noise generation by numerical differentiation of the force raw signal, as required in differentiated weight mode.
- *Differentiated weight mode:* The force raw signal is differentiated with respect to time and then compared to the reference value resulting from the predefined shape of the

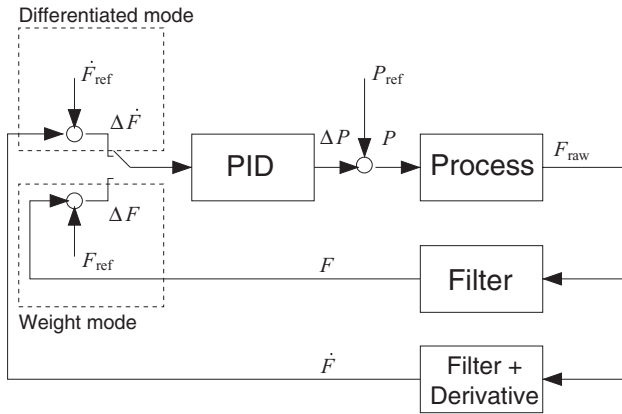


Figure 3.29 Weight-based PID control scheme utilizing heater power for diameter control.

crystal. If one neglects the dynamics of the meniscus, this signal is proportional to the crystal radius (Equation (3.15)), i.e. this mode tries to keep the radius on its reference value without being influenced by the past. The differentiation of the raw signal leads to a phase advance in the control system which tends to make the system ‘more stable’. On the other hand, sophisticated signal processing and filtering methods as well as high-resolution load cells are required.

Calculation of Reference Trajectories. When weight-based control is used, care is needed when defining the reference shape of the crystal. As already mentioned in section 3.3.1.8, influences of the meniscus and, in case of LEC growth, of the boron oxide layer have to be considered [Bardsley 1974-1, Bardsley 1974-2, Bardsley 1977-1, Bardsley 1977-2, Johansen 1987-1, Johansen 1987-2, Johansen 1992-1, Johansen 1992-2]. Given a reference trajectory for the crystal radius which is at least two times differentiable with respect to crystal length and trajectories for the pulling speed v as well as for the crucible speed v_{cruc} , one can calculate a reference trajectory for the first time derivative of the force using Equations (3.32) and (3.46) (or (3.41) in case of LEC growth). Using these equations, the complete reference meniscus dynamics (and in case of LEC growth the buoyancy) is considered. As an example, in Figure 3.30 three types of reference trajectories of the crystal radius are sketched on the left-hand side while the corresponding trajectories of the derivative \dot{M} of the weight gain signal can be found on the right-hand side (solid lines). In order to demonstrate the influence of the meniscus the trajectories of the mass of the pure crystal are also given (dashed lines). The plot at the bottom shows a very simple reference trajectory for the crystal shape on the basis of cut-lines. Such a trajectory results in steps in the reference signal fed into the controller. This means that the manipulated variable will perform a step, which may result in an unintended stimulation of the system. A more detailed discussion of reference trajectory planning issues is presented by Satunkin and Rossolenko in [Satunkin 1986-2].

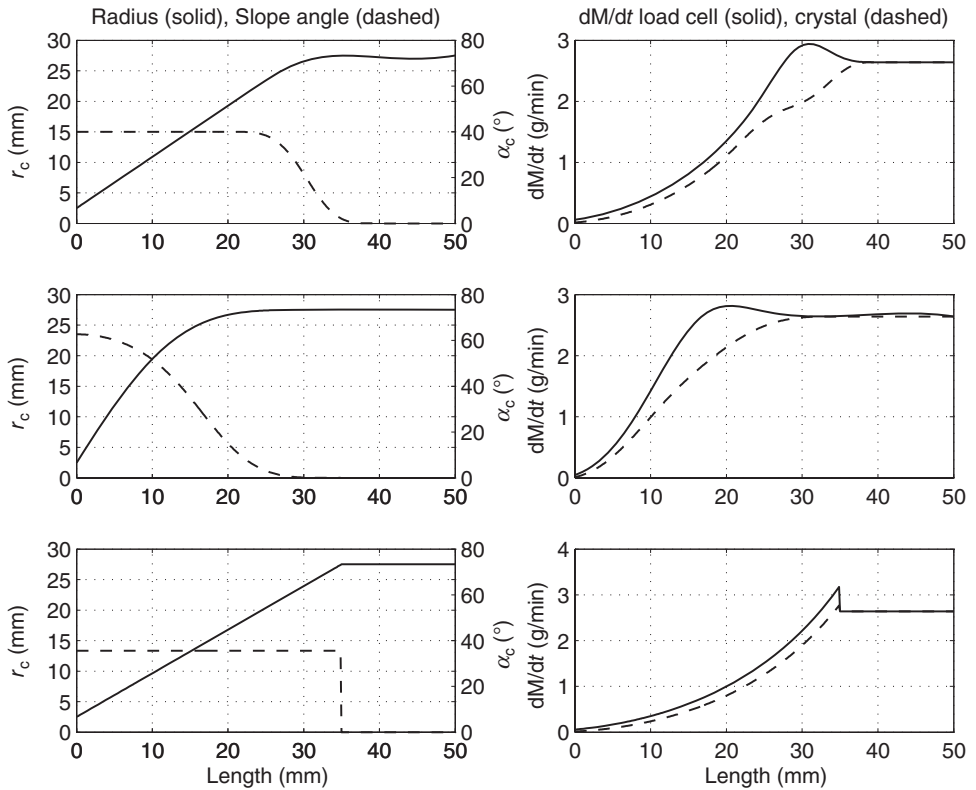


Figure 3.30 Left: Plots of different crystal shapes (solid lines: radius r_c , dashed lines: slope angle α_c). Right: Corresponding trajectories of the first time derivative of the weight gain signal (solid line) and of the first time derivative of the crystal mass (dashed line). Cz growth without boron oxide.

3.5.2.2 Problems Resulting from Anomalous Behaviour

The most crucial part of this technique is the well-known so-called *anomalous behaviour* of the elementary and III–V compound semiconductors; see section 3.1.4. Using Cz growth as an example, the topic is addressed in this section in a little bit more detail, since it fundamentally limits the performance of the weight-based control approach.

Qualitatively speaking, the reason why, for example, a decrease in the differential weight gain signal does not necessarily reflect a decrease in crystal radius is that an increasing crystal diameter first results in a decrease of the meniscus height (see Figure 3.2, top right). Since for most semiconducting materials the density of the melt is larger than the density of the solid, a decreasing meniscus volume makes the differential weight gain signal decrease at first although the crystal diameter is increasing (see Figure 3.2, bottom right). Furthermore, for materials which do not completely wet their solids, i.e. $\alpha_0 \neq 0$, an increase in crystal diameter ($\alpha_c > 0$) leads to a reduction of the influence of surface tension acting on the crystal (its vertical component is proportional to $\cos(\alpha_0 + \alpha_c)$; see Equation (3.20)), resulting in similarly incorrect information.

Such behaviour is well known in control theory and will now be analysed. More detailed discussions can also be found in [Bardsley 1977-1, Gevelber 1988, Johansen 1992-1, Satunkin 1990].

For this purpose, Equation (3.46) describing the dynamics of the force is recalled:

$$\dot{F}_{Cz} = \pi g r_c^2 (\rho_s v_c + c_{r,Cz}(r_c, \alpha_c) \dot{r}_c + c_{\alpha,Cz}(r_c, \alpha_c) \dot{\alpha}_c). \quad (3.77)$$

If $v_{\text{cruc}} = -\dot{H}_m$, we obtain from Equation (3.14)

$$v_c = v - \dot{h}. \quad (3.78)$$

Assuming only small perturbations in cylindrical growth (i.e. $\dot{h} \approx 0$), Equation (3.17) can be rewritten as $\dot{r}_c = v \alpha_c$, the time derivative of which is

$$\ddot{r}_c = v \dot{\alpha}_c. \quad (3.79)$$

Inserting Equations (3.78) and (3.79) into (3.77) while using (3.19) for \dot{h} , we obtain

$$\dot{F}_{Cz} = \pi g r_c^2 \left[\rho_s v + \left(c_{r,Cz}(r_c, \alpha_c) - \rho_s \frac{\partial h}{\partial r_c} \right) \dot{r}_c + \frac{1}{v} \left(c_{\alpha,Cz}(r_c, \alpha_c) - \rho_s \frac{\partial h}{\partial \alpha_c} \right) \ddot{r}_c \right]$$

which can be rewritten as

$$\dot{F}_{Cz} = \pi g \rho_l r_c^2 \left[\frac{\rho_s}{\rho_l} v + \phi(r_c, \alpha_c) \dot{r}_c + \frac{1}{v} \psi(r_c, \alpha_c) \ddot{r}_c \right] \quad (3.80)$$

with

$$\phi(r_c, \alpha_c) = \left(1 - \frac{\rho_s}{\rho_l} \right) \frac{\partial h}{\partial r_c} \Big|_{(r_c, \alpha_c)} + \frac{2h}{r_c} + \frac{a^2}{r_c^2} \cos(\Theta_0 + \alpha_c) \quad (3.81)$$

$$\psi(r_c, \alpha_c) = \left(1 - \frac{\rho_s}{\rho_l} \right) \frac{\partial h}{\partial \alpha_c} \Big|_{(r_c, \alpha_c)} - \frac{a^2}{r_c} \sin(\Theta_0 + \alpha_c). \quad (3.82)$$

Linearizing Equation (3.80) around some setpoint (r_c^0, α_c^0) with $\dot{r}_c = 0$, $\ddot{r}_c = 0$ and $\dot{F}_{Cz}^0 = \pi g \rho_s (r_c^0)^2 v$ as the weight gain reference value, we obtain

$$\dot{F}_{Cz} = \dot{F}_{Cz}^0 + 2\pi g \rho_s r_c^0 v \left(\delta r_c + \frac{r_c^0}{2v} \frac{\rho_l}{\rho_s} \phi(r_c^0, \alpha_c^0) \delta \dot{r}_c + \frac{r_c^0}{2v^2} \frac{\rho_l}{\rho_s} \psi(r_c^0, \alpha_c^0) \delta \ddot{r}_c \right). \quad (3.83)$$

In this equation δr_c , $\delta \dot{r}_c$ and $\delta \ddot{r}_c$ denote the deviation of the radius and its two time derivatives from the setpoint, respectively. Now it is worth defining the normalized weight error E_F as

$$E_F := \frac{\dot{F}_{Cz} - \dot{F}_{Cz}^0}{2\pi g \rho_s r_c^0 v}. \quad (3.84)$$

Using (3.84) and assuming that initial deviations δr_c , $\delta \dot{r}_c$ are zero, the Laplace transform of Equation (3.83) reads

$$\mathbf{E}^* = \left(1 + \underbrace{\frac{r_c^0}{2v} \frac{\rho_l}{\rho_s} \phi(r_c^0, \alpha_c^0)}_{\gamma} s + \underbrace{\frac{r_c^0}{2v^2} \frac{\rho_l}{\rho_s} \psi(r_c^0, \alpha_c^0)}_{\eta} s^2 \right) \mathbf{R}^* \quad (3.85)$$

with the complex frequency s and the Laplace transformed variables $\mathbf{E}^* := \mathcal{L}\{E_F\}$ and $\mathbf{R}^* := \mathcal{L}\{r_c - r_c^0\} = \mathcal{L}\{\delta r_c\}$. Thus, one can write the transfer function describing the response of the first time derivative of the normalized weight error with respect to the radius as follows:

$$G_{\mathbf{R}^*}^{\mathbf{E}^*} = \frac{\mathbf{E}^*}{\mathbf{R}^*} = \eta \left(s^2 + \frac{\gamma}{\eta} s + \frac{1}{\eta} \right). \quad (3.86)$$

In general, a transfer function $G(s)$ is a rational function

$$G(s) = \frac{N(s)}{D(s)}$$

consisting of two polynomials $N(s)$ and $D(s)$, both in the complex frequency s . The roots of the numerator $N(s)$ are called *zeros* and the roots of the denominator $D(s)$ are called *poles*. The values of these roots determine dynamic characteristics of the system such as rise time, overshooting and settling time. For example, if one of the poles has a positive real part, i.e. it lies in the RHP of the complex s -domain, the system is unstable. If there are conjugate complex poles with negative real parts, the system tends to damped oscillations. A zero with negative real part which is close to a complex pole pair with negative real part will increase overshooting, and so on [Franklin 2002-1]. Things become considerably more complicated if a zero with positive real part occurs, i.e. lying in the RHP of the complex s -domain. The effect of an RHP zero is that the initial response of such a system is in the opposite direction to the final steady state (which can be clearly seen in Figure 3.2, bottom right, solid line). Such systems are called non-minimum-phase systems or ‘systems containing an all pass’.

Unfortunately, the system under consideration belongs to this class [Gevlber 1988, Johansen 1992-1], as will be shown now in addition to the simulation results already presented in Figures 3.2 and 3.13. The transfer function (3.86) has two zeros:

$$s_{1,2} = -\frac{\gamma}{2\eta} \pm \sqrt{\frac{\gamma^2}{4\eta^2} - \frac{1}{\eta}}. \quad (3.87)$$

Now, it can be clearly seen that, if η is negative, one of these zeros is positive, i.e. it lies in the RHP. Indeed, inspecting the coefficients γ and η one comes to the conclusion that their signs depend on the signs of $\phi(r_c^0, \alpha_c^0)$ and $\psi(r_c^0, \alpha_c^0)$. These functions have been intensively studied, for example, by [Johansen 1987-2]. He concludes that $\phi(r_c^0, \alpha_c^0)$ is

always positive while the sign of $\psi(r_c^0, \alpha_c^0)$ is always negative if $\rho_1 > \rho_s$ and $\alpha_0 \neq 0$. Thus, for such materials, the anomalous behaviour is inherent. This has also been shown experimentally by Hurle *et al.* [Bardsley 1974-1, Hurle 1986] and by Bardsley [Bardsley 1977-1] who discusses the differential equation (3.83) in the time domain (instead of the Laplace domain as in this chapter). The consequence of this observation is that performance of the control system proposed in this section is fundamentally limited depending on the frequency of the RHP zero [Gevlber 1988]. Qualitatively speaking, the reason for this limitation is the fact that the controller 'is only allowed to respond carefully' to any sort of perturbation, since it could be of opposite direction and not indicating what really goes on at the interface. For example, if the radius of the crystal increases the controller would have to increase heater power in order to counteract this perturbation (i.e. the parameters K_P , K_I , K_D of the controller (3.2) must be chosen positive). However, what is first detected in this case is a decrease of the differentiated weight gain signal leading the controller to decrease heater power, thus countenancing the increase of the crystal radius. From a system theoretic point of view the problem of RHP zeros is the fact that they cannot be compensated by a pole in the corresponding controller since this pole would have to lie in the RHP, i.e. it would be unstable.

The strength of the effect depends on several factors discussed in detail in [Bardsley 1977-1]. The growth rate especially is of great importance. Roughly speaking, we can sum up by saying that the lower the pulling speed, the stronger the effect.

3.5.2.3 Improvements and Optimizations

In this section some approaches that attempt to compensate for the problems mentioned above are outlined.

Prediction of Anomalous Behaviour. [Bardsley 1977-2] presented a method based on estimating the anomalous component of the measured weight gain signal and subtracted it from the signal. The estimation is done using a linear model calculating the radius change induced by changes in heater power. This has been shown experimentally to work for some specific conditions, but no analysis was presented to show whether it can be universally implemented and with what performance implications. Specifically, the fundamental limitation posed by the RHP zero in terms of the achievable control system performance must be respected, particularly in terms of limitations to closed-loop speed. In addition, the approach presented by Bardsley *et al.* requires knowledge of a sufficiently precise model of the process, including thermal conditions, and there will be significant problems if this model is not accurate enough.

Further Optimization. Besides the RHP zero problem, a challenging task in this control approach is the determination of the parameters of the PID controller. Most often this is done by trial and error. However, there are some interesting approaches that attempt to determine optimal parameters of the PID controller on the basis of the model knowledge available. [Satunkin 1986-1, Satunkin 1990] propose an approach based on a cost functional for adjusting parameters in a single-loop as well as in a multi-loop control system, using heater power and pulling speed as manipulated variables. In [Satunkin 1990], the

same author presents a modelling approach focusing on inaccuracies of the weight sensor signal and the consideration of these in the control system.

Parameter Scheduling. As already mentioned, the dynamic characteristics of the process change during crystal growth. As a consequence, parameters of the PID controller determined for one setpoint may not produce acceptable results as the process proceeds. A strategy to overcome this problem is to change the parameters at suitable intervals. This strategy is commonly known as *parameter* or *gain scheduling* in the field of adaptive control [Åström 1994, Warwick 1988].

3.6 Geometry-Based Nonlinear Control Design

After the discussion of requirements and objectives for control of Cz growth in sections 3.1 and 3.2 and the problems arising when using conventional approaches in section 3.5, in the present section an approach for *nonlinear* model-based control of the Cz process is given. Such an approach may be useful if the approaches presented in the previous section do not provide the performance required. Usually, in that case the alternative would be a completely model-based controller as proposed in section 3.1.6. However, if the thermal parameters included in the underlying model of such a controller are not known with sufficient accuracy, or the assumptions during modelling of the thermal part are not fulfilled, such an approach may also fail. The approach derived here presents a compromise between both approaches, i.e. it tries to overcome the limitations of conventional approaches, while avoiding complete modelling of the thermal system. The usefulness of the approach is proven by several experimental results from growth of GaAs and InP crystals.

3.6.1 Basic Idea

Since one of the objectives is to have a control system which (i) is robust with respect to parameter uncertainties, (ii) can be parametrized easily, and (iii) need not be completely reparametrized when plant setup is changed (e.g. in the laboratory), a model-based approach is chosen. Now, the central idea in deriving the model-based controller is to focus only on the geometrical aspects of the growth system, avoiding explicit modelling of the thermal part (similar to the approach presented by Voronkov, see section 3.2.5). Such an approach is reasonable because of the difficulties arising in modelling the thermal part with the precision required for feedback control (see section 3.1.5). At least a time-dependent and spatially two-dimensional model would be required. Consequently, for this part, no model is used in the control system. However, the hydromechanical model of the system has been thoroughly discussed in the literature, its parameters are known with sufficient accuracy, and its structure is sufficiently precise. It can, therefore, be used for model-based control. Such an approach is possible due to a parametrization of the model in crystal length instead of time (details on this reparametrization will be discussed in the next section).

The controller based on this partial model does not cover the full process dynamics, especially the dynamics of the thermal part. Thus, it is combined with conventional PI controllers acting as a ‘substitute’ for the missing thermal model. Anyway, a large amount of model knowledge is introduced into the control system by the model-based controller. Since this regime operates directly on the crystal radius and its derivatives it is not affected by the RHP zero problem. Moreover, the time needed for finding appropriate controller parameters is reduced. In doing so, the tracking of crystal diameter and growth rate trajectories is accomplished.

It must be pointed out that for the sake of clarity, in the first instance, in this section it is assumed that crystal radius, crystal slope angle, and growth rate are available (measured) in the control system. Usually this is not the case. The reconstruction of these quantities from the measured variable (e.g. the force acting on a load cell) by means of a nonlinear observer is the subject of section 3.7.

3.6.2 Parametrization of the Hydromechanical–Geometrical Model in Crystal Length

As already explained, the control approach presented in this section is based on the hydromechanical–geometrical model only. Such a model has been presented in section 3.3.1, Equations (3.56)–(3.63). Using this model and considering the relation

$$\frac{\dot{x}}{v_c} = \frac{\frac{dx}{dt}}{\frac{dl}{dt}} = \frac{dx}{dl} = x',$$

with $v_c \neq 0$ all equations of the hydromechanical–geometrical model (3.56)–(3.63) can be divided by the growth rate $v_c = dl/dt$. As a result we obtain a model which is parametrized in crystal length instead of time. In addition, the input can be defined as

$$v_z := \frac{v - v_{\text{cruc}}}{v_c}. \quad (3.88)$$

The quantity v_z is called the *lift ratio*.

By this procedure the thermal part has been ‘hidden’ for control system design, i.e. it is implicitly included. The exact meaning and importance of this variable will be discussed in section 3.6.3.2.

The length-parametrized model reads:

$$r'_c = \tan(\alpha_c) \quad (3.89)$$

$$\alpha'_c = \frac{v_z - c_{\alpha z}(r_c, \alpha_c)}{c_{\alpha n}(r_c, \alpha_c)} \quad (3.90)$$

$$H'_m = \left(1 - \frac{1}{c_{\alpha n}(r_c, \alpha_c)} \frac{\partial h}{\partial \alpha_c}\right) v_z - \left(1 + \tan(\alpha_c) \frac{\partial h}{\partial r_c} - \frac{c_{\alpha z}(r_c, \alpha_c)}{c_{\alpha n}(r_c, \alpha_c)} \frac{\partial h}{\partial \alpha_c}\right) \quad (3.91)$$

$$h'_e = \frac{(r_c^2 - r_{es}^2) - r_{es}^2 h' + V'_{men}}{r_a^2 - r_{es}^2} \quad (\text{LEC growth only}) \quad (3.92)$$

$$F'_{LEC} = \pi g r_c^2 (c_{p,LEC}(r_c, r_{es}) + c_{r,LEC}(r_c, r_{es}, \alpha_c) r'_c + c_{\alpha,LEC}(r_c, r_{es}, \alpha_c) \alpha'_c) \quad (3.93)$$

respectively

$$F'_{Cz} = \pi g r_c^2 (\rho_s + c_{r,Cz}(r_c, \alpha_c) r'_c + c_{\alpha,Cz}(r_c, \alpha_c) \alpha'_c) \quad (3.94)$$

$$r_{es} = R(l - h_e + h) \quad (\text{LEC growth only}). \quad (3.95)$$

Parametrizing the model in terms of length still requires knowledge of the growth rate v_c . This value is needed when calculating the manipulated variables,

$$v = v_z v_c + v_{cruc},$$

and when integrating one of the equations in (3.89)–(3.95). This will be detailed in section 3.7.2.4. It must be pointed out again that the thermal model is ‘hidden’ only for controller and observer design. The thermal dynamics of the system still play the driving role in the system. Roughly speaking, the dynamics of the thermal system is expressed by the growth rate v_c .

3.6.3 Flatness and Model-Based Feedback Control of the Length-Parametrized Model

In this section the core of the proposed control system, the model-based controller, is derived. The design of this controller is based on a special system property called *flatness*. The hydromechanical–geometrical model belongs to the class of *flat systems*. Roughly speaking, the flatness of a model (consisting of a set of system variables and a set of ordinary differential equations they satisfy) means that there is a set y of variables (called a *flat output*) for which *independent* trajectories can be defined. These trajectories can be defined in such a way that all other system variables can be calculated *without* the need to solve a differential equation. This will be shown in the following sections (a formal definition can be found in [Rothfuss 1996] or, more generally, in [Fliess 1995]).

Furthermore the importance of the lift ratio v_z is discussed, and using the flatness property it is shown that both crystal radius and growth rate can be controlled independently. The composition of the overall control system is discussed in the following section 3.6.4.

3.6.3.1 Flatness of the Length-Parametrized Hydromechanical–Geometrical Model

The equations in the subsystem (3.89)–(3.90) are required for control of the crystal radius using v_z as the manipulated variable. This system is flat and a flat output is $y = r_c$. This can be seen as follows:

- All remaining system variables in (3.89)–(3.90) can be expressed by r_c and its derivatives: By defining a reference trajectory for the crystal radius r_c and its derivatives with

respect to length up to the second order one can calculate a trajectory for α_c and its derivatives from Equation (3.89) (solved for α_c) without integration. Then Equation (3.90), solved for v_z , can be used to calculate the lifting ratio v_z , again without integration.

- Since the flat output $y = r_c$ consists of one component only, it is trivial that a trajectory for r_c can be chosen freely.

The flatness property forms the basis of the controller design for the lumped-parameter model derived in the previous section. In this way, it is possible to integrate a lot of model knowledge into the control algorithm, while avoiding problems arising from modelling of the thermal part of the system. However, when the thermal part of the system is neglected it is not possible to manipulate the interaction between both parts. Thus, the strategy is to apply controllers of fixed structure (like PI controllers) where a model-based control of the thermal part would be required. With a judicious combination of model-based and PI controllers it is possible to control either growth rate and crystal shape alone or both together.

3.6.3.2 Important Role of the Lift Ratio v_z

A given value for the lift ratio defines the ratio between pulling speed and growth rate required for the crystal to grow according to the reference trajectory. From this point of view it makes no difference whether the crystal shape is controlled via pulling speed (i.e. from the mechanical side) or via growth rate (i.e. from the thermal side). This is the essential idea of the control system proposed in this section. In particular, it has to be kept in mind that during cylindrical growth (i.e. $\alpha_c = 0$, $\alpha'_c = 0$) the radius will not change as long as the lift ratio v_z is kept constant (see Equation (3.90)), i.e. in the length-parametrized system v_z is the variable solely responsible for manipulating the system.

The model-based controller derived in the next section will calculate values for v_z depending on the deviation of the crystal radius and the slope angle from their reference values. The values of v_z are calculated in such a way that they match the system dynamics under the current growth conditions. Additionally, they reflect a predefined behaviour of the error, i.e. the dynamics of its degradation. Since it is not relevant whether the trajectory of v_z is realized by manipulating the pulling speed or the growth rate (see Equation (3.88)) one is free to choose which variable is manipulated in order to adjust the desired lift ratio v_z calculated by the model-based controller. Indeed, for some materials the best manipulated variable for adjusting a desired value of v_z is the pulling speed v . For other materials the heater power or the heater temperature is better suited. This is discussed in section 3.6.4.

A simulation example is shown in Figure 3.31. The plot on the right shows the trajectory of v_z (solid line) which must be realized in order to make the crystal grow as sketched by the solid line in the left plot. At this point it is worth mentioning that in steady parts (cylindrical growth), generally $v_z < 1$. This can be illustrated as follows: If the crucible translation rate v_{cruc} is equal to zero then $v_z > v$ because of the falling melt level. If v_{cruc} is chosen in such a way that the interface position is fixed within the growth plant, then $v = v_c$ and, thus, again $v_z < 1$.

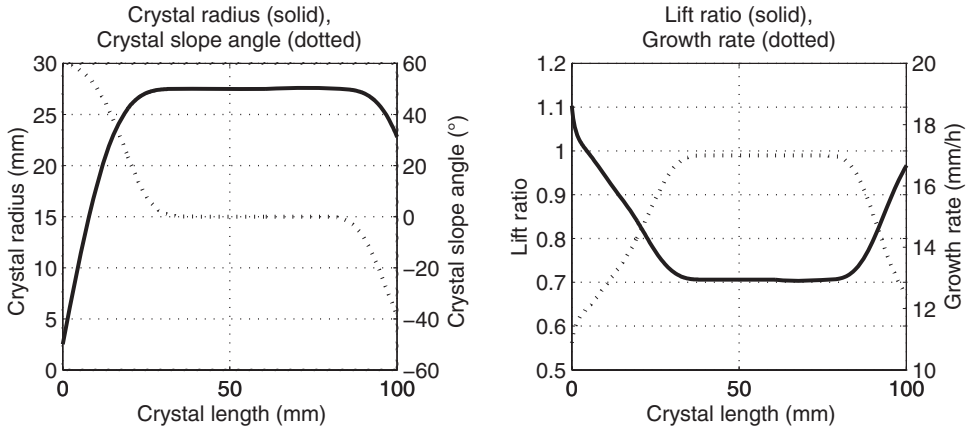


Figure 3.31 Example of trajectory planning for the length-parametrized hydromechanical-geometrical model of the Cz process. Left: trajectories of crystal radius (solid line) and slope angle (dashed line). Right: required trajectory of the lift ratio v_z (solid line) as calculated from subsystem (3.89)–(3.90) and Equation (3.88). Furthermore, the trajectory of the growth rate v_c (dashed line) is presented, which has to be realized by manipulating the heater power or the heater temperature if the pulling speed is kept constant at $v = 12 \text{ mm/h}$ and if the crystal is intended to have the form shown on the left (see Equation (3.88)) (Reprinted with permission from [Winkler 2010-1], copyright (2010) Elsevier Ltd).

3.6.3.3 Flatness-Based Controller

In this section a flatness-based controller is derived, making the crystal radius follow a given reference trajectory. In order to do so we first define the tracking error $r_c - r_{c,\text{ref}} = y - y_{\text{ref}}$. In what follows the controller is designed in such a way that the tracking error satisfies the linear second-order differential equation

$$(r_c'' - r_{c,\text{ref}}'') + \varepsilon_1 (r_c' - r_{c,\text{ref}}') + \varepsilon_0 (r_c - r_{c,\text{ref}}) = 0, \quad (3.96)$$

with $\varepsilon_0, \varepsilon_1 \in \mathbb{R} > 0$. The values of $r_{c,\text{ref}}$, $r_{c,\text{ref}}'$, and $r_{c,\text{ref}}''$ are defined by the reference trajectory of the crystal radius. The observer calculates estimated values for r_c and r_c' . If we want the dynamics of the tracking error to satisfy Equation (3.96), we *must* have

$$r_c'' = r_{c,\text{ref}}'' - \varepsilon_1 (r_c' - r_{c,\text{ref}}') - \varepsilon_0 (r_c - r_{c,\text{ref}}). \quad (3.97)$$

This can be achieved by a proper choice of v_z .

By defining a new input $\vartheta := r_c''$ with r_c'' according to (3.97) and inserting this input in the equation used for calculation of v_z (see Equation (3.90)) we obtain

$$v_z = \vartheta \frac{c_{\text{an}}(r_c, \arctan(r_c'))}{1 + (r_c')^2} + c_{\text{az}}(r_c, \arctan(r_c')). \quad (3.98)$$

This equation determines v_z in such a way that the tracking error satisfies the given error dynamics (3.96).

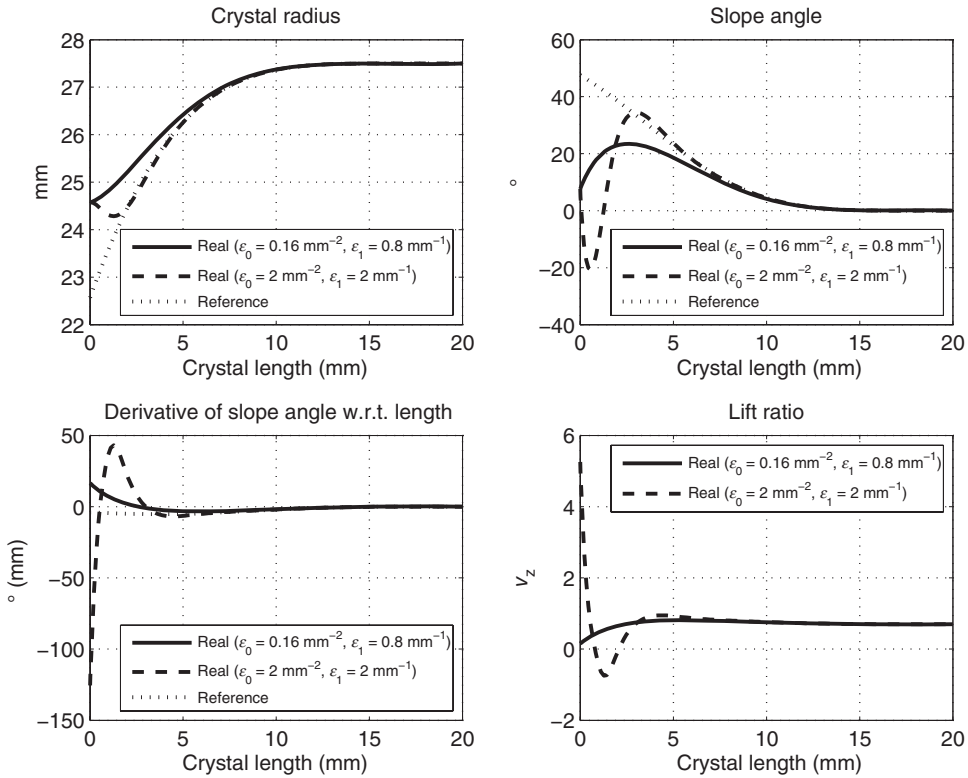


Figure 3.32 Simulation of flatness-based feedback control for different parameter sets of the flatness-based controller. Trajectories of real and reference values of the radius (top left, initial error 2 mm), of the slope angle (top right, initial error 40°) and of the derivative of the slope angle with respect to length (bottom left). The trajectories of the lift ratio v_z can be found on the bottom right figure. (Eigenvalues of the error system (3.96): parameter set 1: $p_1 = p_2 = -400 m^{-1}$ resulting in $\epsilon_0 = 0.16 mm^{-2}$, $\epsilon_1 = 0.8 mm^{-1}$ (solid lines), parameter set 2: $p_1 = -1000 m^{-1} + j1000 m^{-1}$, $p_2 = -1000 m^{-1} - j1000 m^{-1}$ resulting in $\epsilon_0 = 2.0 mm^{-2}$, $\epsilon_1 = 2.0 mm^{-1}$) (Reprinted with permission from [Winkler 2010-1], copyright (2010) Elsevier Ltd).

The coefficients ϵ_0 , ϵ_1 in Equation (3.96) are the controller parameters, the real inputs are r_c , r'_c , and the desired inputs are $r_{c,ref}$, $r'_{c,ref}$, $r''_{c,ref}$. The coefficients ϵ_0 , ϵ_1 define the dynamical behaviour of the tracking error, i.e. the way the error converges to zero. A simulation example is given in Figure 3.32 in which two sets of coefficients ϵ_0 , ϵ_1 have been chosen in order to demonstrate the impact of their choice: The first parameter set results in a very smooth trajectory of the radius and its derivatives towards their reference trajectories. The second one leads to a quite fast transfer towards the reference trajectories, but with some overshooting in the derivatives.

3.6.3.4 Possibility of Independent Control of Crystal Radius and Growth Rate

The flatness property can be used to show that crystal radius and growth rate can be controlled independently, i.e. it is reasonable to derive a control system for independent

control of these quantities. This matter is addressed in the following using the fact that the time-parametrized hydromechanical–geometrical model is flat, too.

Collecting the system equations required for the controller design in that case, we have:

$$r_c = \sqrt{\frac{\dot{V}_s}{\pi v_c}} \quad (3.99)$$

$$\alpha_c = \arctan\left(\frac{\dot{r}_c}{v_c}\right) \quad (3.100)$$

$$h = \tilde{h}(r_c, \alpha_c) \quad (3.101)$$

$$V_{\text{men}} = \pi r_c^2 h + \pi a^2 r_c \cos(\alpha_0 + \alpha_c) \quad (3.102)$$

$$H_m = \frac{M_0 - \rho_s V_s - \rho_l V_{\text{men}}}{\pi \rho_l r_a^2} \quad (3.103)$$

$$v_{\text{net}} = v_c + \dot{h} + \dot{H}_m. \quad (3.104)$$

Here, the function $\tilde{h} : (0, r_a) \times (-\pi/2, \pi/2) \rightarrow \mathbb{R}^+$ represents an arbitrary analytical formula approximating the meniscus height h depending on crystal radius r_c and crystal slope angle α_c (see Chapter 8). The difference $v - v_{\text{cruc}}$ between crystal pulling speed and crucible translation rate is denoted by v_{net} . At this point, it is worth mentioning that Equation (3.99) results from Equation (3.15) and Equation (3.100) is obtained from Equation (3.17) solving for α_c . Furthermore, one gets (3.28) for calculation of $\dot{\alpha}_c$ by inserting Equations (3.101)–(3.103) into Equation (3.104).

The system (3.99)–(3.104) consists of six equations involving the eight system variables r_c , α_c , V_s , h , V_{men} , H_m , v_c , and v_{net} . Thus, one has two degrees of freedom and a flat output (if it exists) must consist of two components. For example, $y = (V_s, v_c)$ forms one possible flat output. Inspecting (3.99)–(3.104) one may observe that:

- All remaining system variables can be expressed by V_s and v_c and their derivatives, i.e. the system can be completely parametrized by trajectories of V_s and v_c . This can be seen as follows: given trajectories for V_s , v_c , and their derivatives (\dot{V}_s , ...), and (\dot{v}_c , ...) one can immediately calculate r_c (and its derivatives \dot{r}_c , ...) from Equation (3.99) without integration. Then, using Equation (3.100), α_c can be calculated. The trajectories obtained for r_c and α_c can be used in the right hand side of Equation (3.101) in order to obtain a trajectory for h . The procedure can be continued until the last equation (3.104) is reached – without doing any integration.
- There does not exist any differential equation in $y = (V_s, v_c)$ only, i.e. the trajectories for the components of y can be chosen independently.

One conclusion resulting from this observation is the fact that the crystal shape and the growth rate can indeed be controlled independently.

3.6.4 Control of Radius and Growth Rate

The flatness-based controller presented in section 3.6.3.3 calculates a desired value for the lift ratio v_z as the ratio between pulling speed and growth rate. It has to be kept in

mind that v_z is the only manipulated variable of the length-parametrized system. Furthermore, in section 3.6.3.4 it has been shown that the radius and the growth rate can be controlled independently. The present section is concerned with the realization of the calculated *desired* value of v_z in the real process. Assuming that the *real* value of v_z is available in the control system, there are two options:

- The difference between the desired value and the real value of v_z is used as an input of a controller manipulating the pulling speed v .
- The difference between the desired value and the real value of v_z is used as an input for a controller manipulating the heater power or heater temperature.

Depending on which manipulated variable is associated to the lift ratio v_z , the remaining one can be used to control the growth rate.

As this approach omits modelling of the thermal part, controllers manipulating the system via thermal mechanisms cannot be model-based. Here, conventional PI controllers are used. One should keep in mind that, unlike conventional PI control, this approach introduces a large amount of model knowledge into the overall control system by model-based calculation of the lift ratio v_z . This is demonstrated by the following two examples. Note that here, for the sake of clarity, in the first instance only descriptive explanations of the operating principles are given. In what follows it is assumed that r_c , r'_c , v_c , and v_z are available (see section 3.7.2).

3.6.4.1 Case 1: InP

The first approach may be illustrated with simultaneous control of shape and growth rate for InP. Experimental open-loop results show that changes in pulling speed have only a very small effect on the radius; see Figure 3.33. Keeping in mind what has already been discussed in section 3.6.3.2, one can conclude that the missing radius change means that the lift ratio v_z seems to remain constant, despite the variation in pulling speed. From this it follows that pulling speed changes are directly transformed into changes of the growth rate of nearly the same amount (see Equation (3.88)).

This behaviour of InP allows us to use the pulling speed for tracking the growth rate by means of a first PI controller. The flatness-based controller calculates the lift ratio v_z required to make the crystal shape follow its reference trajectory. The difference between this desired value of v_z and the real value of v_z is fed into a second PI controller manipulating the temperature (or power).

In order to understand the working principle, especially the decoupling between both loops, the following explanations are given. For this purpose the control structure in Figure 3.34 is simplified for better understanding, as follows:

$$\begin{aligned} \text{Loop I:} & \quad \text{Growth rate} \quad \rightarrow \quad \text{PI}(v) \\ \text{Loop II:} & \quad \text{Crystal shape} \quad \rightarrow \quad \text{FBC}(v_z) \quad \rightarrow \quad \text{PI}(T). \end{aligned}$$

Here 'PI' represents a PI controller and 'FBC' a flatness-based controller, and the variables in parenthesis represent the quantities the values of which are manipulated by the corresponding controller.

It can be argued that the radius loop is decoupled from the growth rate loop since a change in pulling speed does not affect the radius (as discussed above). On the other hand,

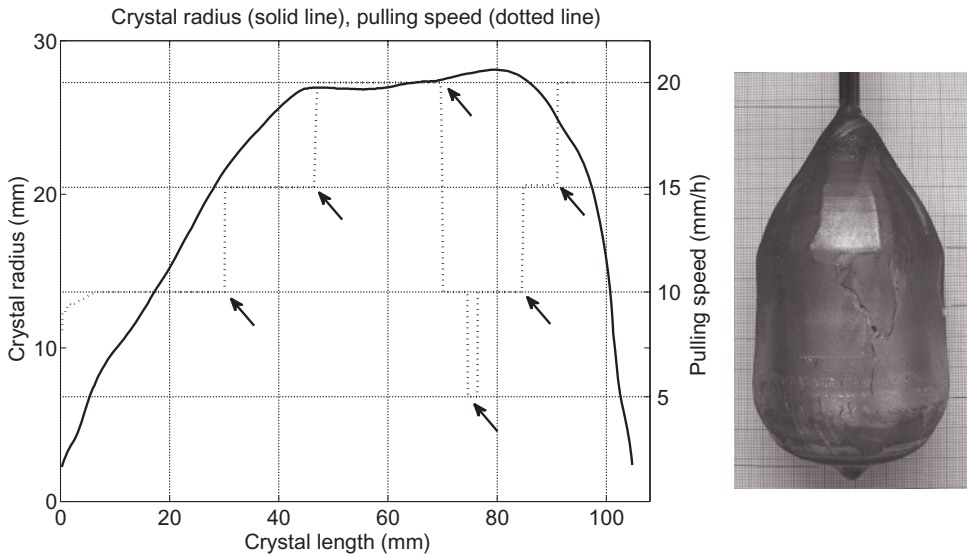


Figure 3.33 Pulling speed step response experiment during growth of a 2" InP crystal by the LEC process. The crystal has been grown without automatic diameter control using manual adjustment of the heater temperature. Steps in pulling speed (dashed line) have been applied at several stages of the process. Temperature adjustment has not been changed in the time after the steps. However, even large steps in pulling speed did not significantly influence the crystal radius (solid line) (Reprinted with permission from [Winkler 2010-1], copyright (2010) Elsevier Ltd).

a change in heater temperature will change the growth rate (see Equation (3.65)). This is immediately detected by the first control loop, resulting in a change in the pulling speed in order to compensate for the initiated growth rate change. It follows that the lift ratio v_z will change in such a way that the radius change intended by the second loop occurs while the growth rate is kept constant. The lift ratio v_z remains at the value demanded by the second loop despite the changes introduced by the first loop (Equation (3.88)). In a way one can say that the change in heater temperature is transformed into a change in pulling speed.

An example of such a system is sketched in Figure 3.34. Experimental results acquired during growth of InP by the LEC process are shown in Figure 3.35. Here one can see that after activating the control system the crystal growth rate (top right) is perfectly tracked using the pulling speed (bottom left). The desired increase of the growth rate in hours 5–7 of the experiment leads to greater cooling (bottom right, indicated by the exclamation marks). This effect is a direct consequence of the increasing amount of latent heat produced by the increasing growth rate (see Equation (3.65)).

3.6.4.2 Case 2: GaAs

The second approach is illustrated through simultaneous control of shape and growth rate for GaAs. In this case it can be shown experimentally that the crystal radius reacts quite quickly to changes in the pulling speed, as long as the crystal is not grown at too low

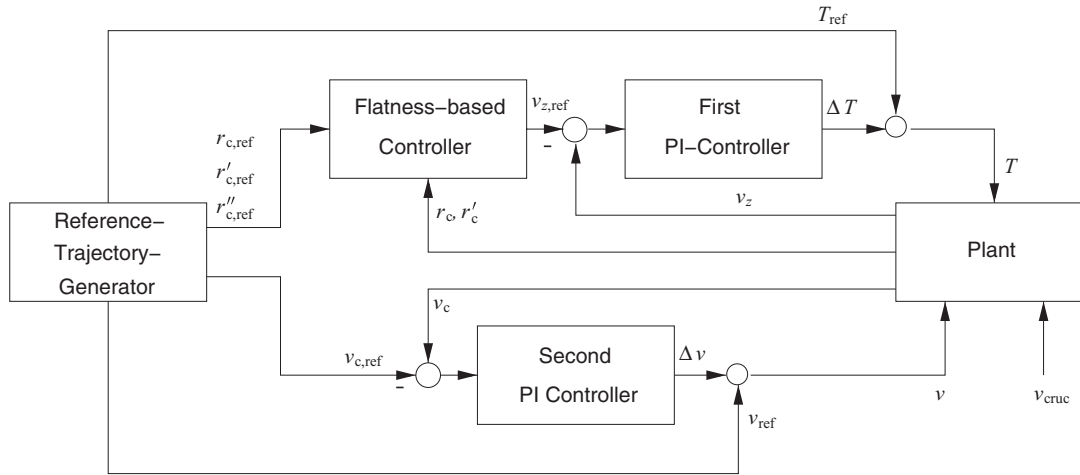


Figure 3.34 Sketch of the structure of the two-loop control system with pulling speed and heater temperature as control inputs. The observer for the reconstruction of radius, slope angle and growth rate is omitted here for simplification (Reprinted with permission from [Winkler 2010-1], copyright (2010) Elsevier Ltd).

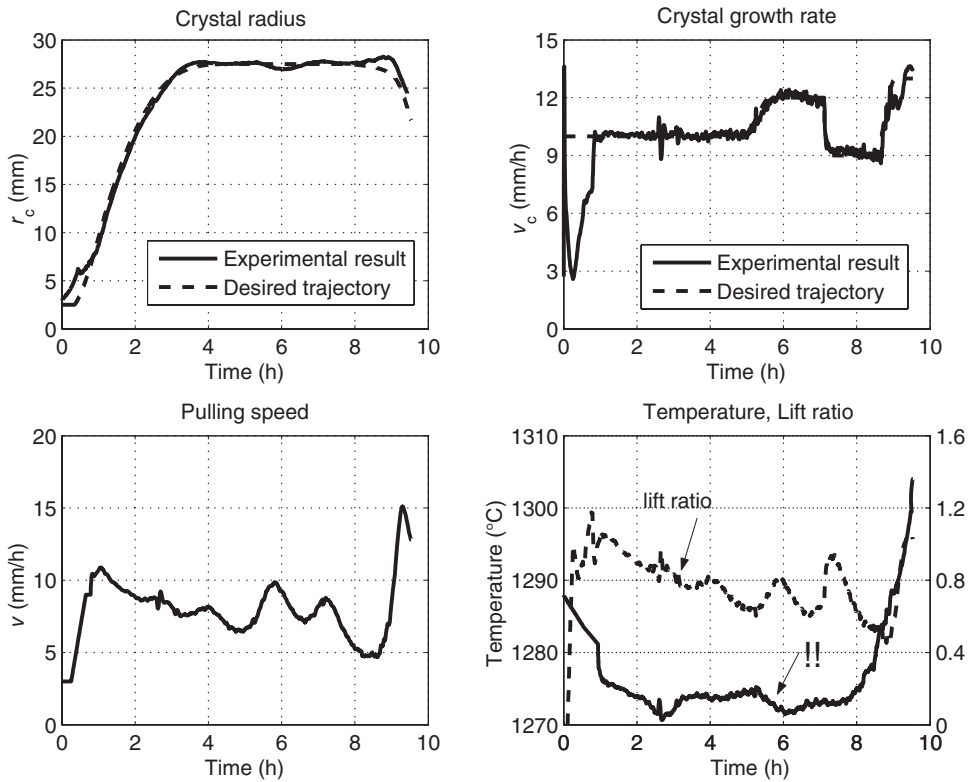


Figure 3.35 Simultaneous control of radius (top left) and growth rate (top right) for growth of a 2" InP crystal by the LEC process. Eigenvalues of flatness based controller: $-400\text{m}^{-1}, -400\text{m}^{-1}$, parameters of PI controller 1 ($v_z \rightarrow T$): $K_p = -3\text{K}$, $K_i = -0.3\text{K/min}$, parameters of PI controller 2 ($v_c \rightarrow v$): $K_p = -0.2$, $K_i = -0.35\text{min}^{-1}$ (Reprinted with permission from [Winkler 2010-1], copyright (2010)).

pulling speeds. Thus, as explained below, it is quite reasonable to interchange the outputs of the PI controllers in comparison to Figure 3.34: the PI controller responsible for tracking the lift ratio v_z now manipulates the pulling speed (instead of temperature in case of InP), and the PI controller responsible for tracking the growth rate v_c manipulates the heater temperature.

$$\begin{aligned} \text{Loop I: } & \text{Growth rate} \rightarrow \text{PI}(T) \\ \text{Loop II: } & \text{Crystal shape} \rightarrow \text{FBC}(v_z) \rightarrow \text{PI}(v). \end{aligned}$$

Now, the working principle and the decoupling between both loops can again be explained in a rather descriptive way. A change of pulling speed initiated by the PI controller of the second loop changes the crystal radius (as has been shown experimentally). This means that the lift ratio v_z changes (see discussion in section 3.6.3.2); consequently, the growth rate remains nearly constant. Hence, in some sense the growth rate loop is (temporarily) decoupled from the radius loop. The radius change will take place as required. However, after some time the growth rate will change, too, because the radius has been

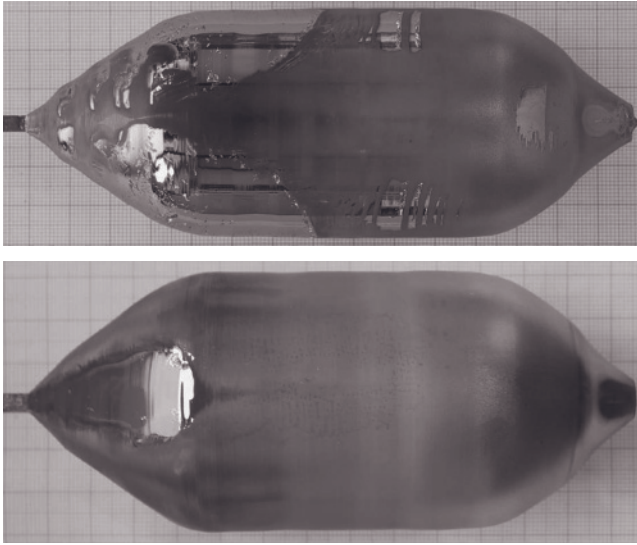


Figure 3.36 GaAs crystals grown with two-loop control according to the structure sketched in Figure 3.34 but with transposed manipulated variables. Parameters of the flatness-based controller (eigenvalues of error dynamics (3.96)): -400 m^{-1} , -400 m^{-1} . PI controller 1 ($v_z \rightarrow v$): $K_p = -5\text{ mm h}^{-1}$, $K_I = -3\text{ mm h}^{-1}\text{ min}^{-1}$. PI controller 2 ($v_c \rightarrow T$): $K_p = 0.12\text{ K mm}^{-1}\text{ h}$, $K_I = 0.06\text{ K mm}^{-1}\text{ h min}^{-1}$. Desired growth rate: 15 mm h^{-1} (Reprinted with permission from [Winkler 2010-1], copyright (2009) Elsevier Ltd).

changed; see Equation (3.32). Then the heater driven by the PI controller of the first loop will change the temperature, keeping the growth rate at its desired value, Equation (3.65). Thus, v_z is kept at the value desired by the second loop, too.

GaAs crystals grown by the LEC method using this approach are shown in Figure 3.36. Here the crystal radius is quite perfectly tracked along its reference trajectory.

3.6.4.3 Notes on Robustness

Looking at the results obtained during growth of the GaAs and InP crystals presented in the previous section, the question arises how robust the approach is. This is of particularly great interest since the model assumes a flat interface and because the thermal part of the system is not *explicitly* included in the model-based controller (however, remember that it is *implicitly* included via the lift ratio v_z). These very important questions are strongly connected with the reconstruction of quantities that are not directly measured – radius, slope angle, and growth rate. This subject is discussed in detail in section 3.7.2 dealing with nonlinear observer design.

3.7 Advanced Techniques

This section presents some advanced techniques which may be useful in control design for the Cz growth process.

The first two subsections deal with the reconstruction of quantities that are not directly measured by means of so-called observers. Such observers are especially useful if the quantities needed in the control system are not available in the process by measurements. Two different approaches in observer design are presented: a linear one based on a linear state space model and a nonlinear one based on the nonlinear hydromechanical–geometrical model. The basic idea of an observer has already been presented in section 3.2.7.

The third section addresses some important considerations for a more advanced control system.

3.7.1 Linear Observer Design

In this section a linear time-invariant Luenberger observer [Luenberger 1964] for reconstruction of the crystal radius from the weighing signal is derived. As a starting point, a linear approximation of the system behaviour can be used. For this purpose the nonlinear equations required for observer design (which have already been presented in section 3.3) need to be linearized around some operating (or steady state) values, i.e. the equations are expanded to a Taylor series which is truncated at the second order (as in section 3.3.3). For example, Equation (3.17) describing the radius dynamics,

$$\dot{r}_c = v_c \tan(\alpha_c) = f(v_c, \alpha_c),$$

can be approximated by

$$\begin{aligned} \dot{r}_c &\approx f(v_c^0, \alpha_c^0) + \left. \frac{\partial f}{\partial v_c} \right|_{v_c^0, \alpha_c^0} (v_c - v_c^0) + \left. \frac{\partial f}{\partial \alpha_c} \right|_{v_c^0, \alpha_c^0} (\alpha_c - \alpha_c^0) \\ &\approx v_c^0 \tan(\alpha_c^0) + \underbrace{\tan(\alpha_c^0)}_{=:a_{11}} (v_c - v_c^0) + v_c^0 \underbrace{\frac{1}{\cos^2(\alpha_c^0)}}_{=:a_{12}} (\alpha_c - \alpha_c^0) \end{aligned} \quad (3.105)$$

around some fixed values α_c^0 , v_c^0 . With new coordinates $\delta r_c := \dot{r}_c - v_c^0 \tan(\alpha_c^0)$, $\delta v_c = v_c - v_c^0$, and $\delta \alpha_c := \alpha_c - \alpha_c^0$ one finally obtains

$$\delta \dot{r}_c = a_{11} \delta v_c + a_{12} \delta \alpha_c. \quad (3.106)$$

In the same way one can continue with the remaining equations needed for describing the process dynamics. This has been done by [Satunkin 1986-1], for example. The linear model he derived is

$$\dot{x}(t) = Ax(t) + Bu(t) \quad (3.107)$$

$$y(t) = c^T x(t), \quad (3.108)$$

where $x \in \mathbb{R}^3$ denotes the state vector (radius, meniscus height and melt height), $u \in \mathbb{R}^2$ the input (pulling speed and temperature), and $y \in \mathbb{R}$ the force acting on the load cell. Furthermore, one has the 3×3 system matrix A , the 3×2 control matrix B and the 1×3 output matrix c^T . One has to keep in mind that the values of the state space vector x , the input vector u and the output y describe the deviation of the corresponding quantities from their operating values.

Now, for a system given in the form of Equations (3.107)–(3.108) the standard technique for deriving a *Luenberger* identity observer [Luenberger 1964] can be applied. According to [Luenberger 1964] then the observer reads

$$\hat{\dot{x}}(t) = \underbrace{A\hat{x}(t) + Bu(t)}_{\text{Copy of system}} + \underbrace{H(\hat{y}(t) - y(t))}_{\text{Corrective injection}} \quad (3.109)$$

$$\hat{y}(t) = c^T \hat{x}(t). \quad (3.110)$$

Here the hat (e.g. \hat{x}) denotes a variable the value of which is an estimate of the real value. The corrective injection $H(\hat{y}(t) - y(t))$ is introduced to ensure convergence of the observation error; see section 3.2.7. In the linear time-invariant case the values of the 3×1 matrix H must be chosen in such a way that for $t \rightarrow \infty$ the estimation error $\tilde{x} = \hat{x} - x$ with

$$\dot{\tilde{x}}(t) = (A - Hc^T) \tilde{x}(t) \quad (3.111)$$

tends to zero. This is exactly the case if the roots s_1, s_2, s_3 of the characteristic polynomial $\det(sI - A + Hc^T) = 0$ have negative real parts. System (3.111) is obtained by subtracting (3.107) from (3.109) and inserting (3.108) and (3.110). Here a key point is the fact that all elements of the matrices A, c , and H are constant. This means that the observer can only be used around a certain setpoint where the linear approximation is accurate enough.

In order to make the observer work properly (i.e. to assign the observer error dynamics as described above) the system must be *observable*. Roughly speaking, the property of observability ensures that the initial state of the system can be reconstructed from any sequence of measurements of the outputs. For a given system (3.107)–(3.108) this can be proven rigorously by the Kalman observability condition [Franklin 2002-2]:

$$\text{rank} \begin{pmatrix} c^T \\ c^T A \\ \vdots \\ c^T A^{(n-1)} \end{pmatrix} = n.$$

This has been proved to hold for the Cz and LEC system in [Satunkin 1990].

3.7.2 Nonlinear Observer Design

The advantage of a nonlinear observer is that it reflects the complex nonlinear dynamics of the process. Moreover, its use is not bound to a certain operating point, i.e. it can be used throughout the whole process, especially when growing the conical parts in which the dynamics of the process is changing greatly. Furthermore, such an approach overcomes the problems resulting from the anomaly of the weight gain signal. However, design of such an observer is rather complicated. The fundamental design method of a nonlinear observer (specific to the model of Cz crystal growth which is used in this contribution) is sketched in this section. Details can be found in [Winkler 2007, Winkler 2009-2]. The capability of the observer as well as thorough investigations regarding its robustness are illustrated using simulations and experimental results.

3.7.2.1 Nonlinear Design Procedure for Cz Growth

The observer design for Cz growth without boron oxide is based on the length parametrized equations taken from section 3.6. For the sake of clarity they are rewritten in a more genreal form using symbols f_1, f_2, f_3 for the right-hand sides of the equations:

$$r'_c = f_1(r_c, \alpha_c, v_c), \quad r_c(0) = r_{c0} \quad (3.112)$$

$$\alpha'_c = f_2(r_c, \alpha_c, v_c), \quad \alpha_c(0) = \alpha_{c0} \quad (3.113)$$

$$F'_{Cz} = f_3(r_c, \alpha_c, v_c), \quad F_{Cz}(0) = 0 \quad (3.114)$$

with initial values r_{c0}, α_{c0} for the crystal radius and the crystal slope angle, respectively. Now, by setting $y := F_{Cz}$, the design procedure consists of three steps.

Step 1. System (3.112)–(3.114) is third order. However, only the radius and the slope angle have to be reconstructed since the third quantity, y , is measured. So it seems obvious that the observer has to be second order only. Thus, the third-order nonlinear system (3.112)–(3.114) is transformed into a nonlinear second-order system with new states x_1, x_2 :

$$x'_1 = f_1(x_1, x_2, v_z) + \psi_1 f_3(x_1, x_2, v_z) \quad (3.115)$$

$$x'_2 = f_2(x_1, x_2, v_z) + \psi_2 f_3(x_1, x_2, v_z). \quad (3.116)$$

Here ψ_1, ψ_2 are design parameters which, basically, can be freely chosen and need not be constant. The functions f_1, f_2, f_3 are a result of the transition of the system (3.112)–(3.114) to new coordinates. It is worth mentioning that the transition from (r_c, α_c, y) to (x_1, x_2) implies that x_1 and x_2 do not only depend on (r_c, α_c) , but also on the measured variable y and the design parameters ψ_1 and ψ_2 . For example, a transition could be defined as

$$x_1 := r_c + \phi_1(y, \psi_1), \quad x_2 := \alpha_c + \phi_2(y, \psi_2) \quad (3.117)$$

with appropriate functions ϕ_1, ϕ_2 . This means that from x_1 and x_2 the ‘original’ values of r_c and α_c can be calculated if the values of the measured variable y and ψ_1, ψ_2 are known. For example, from (3.117) it follows that:

$$r_c = x_1 - \phi_1(y, \psi_1), \quad \alpha_c = x_2 - \phi_2(y, \psi_2). \quad (3.118)$$

Step 2. The system (3.115)–(3.116) is copied and denoted as an observer which calculates estimates \hat{x}_1, \hat{x}_2 of the new states x_1, x_2 :

$$\hat{x}'_1 = f_1(\hat{x}_1, \hat{x}_2, v_z) + \psi_1 f_3(\hat{x}_1, \hat{x}_2, v_z) \quad (3.119)$$

$$\hat{x}'_2 = f_2(\hat{x}_1, \hat{x}_2, v_z) + \psi_2 f_3(\hat{x}_1, \hat{x}_2, v_z). \quad (3.120)$$

We still have to keep in mind that \hat{x}_1 and \hat{x}_2 depend on the measured variable y and parameters ψ_1, ψ_2 . Here, the parameters ψ_1, ψ_2 play the role of so-called observer gains.

In order to ensure that system (3.119)–(3.120) is an observer for (3.115)–(3.116), i.e. $\hat{x}_1 \rightarrow x_1$, $\hat{x}_2 \rightarrow x_2$ for $l \rightarrow \infty$, the design parameters ψ_1 , ψ_2 must be chosen appropriately.

Step 3. In order to find a calculation formula for ψ_1 , ψ_2 which makes system (3.119)–(3.120) an observer for (3.115)–(3.116), both systems, (3.115)–(3.116) and (3.119)–(3.120), are linearized around the reference trajectory $l \mapsto (x_{1,\text{ref}}, x_{2,\text{ref}}, v_{z,\text{ref}})$ [Fliess 1996]. We obtain

$$\begin{aligned} x'_j(l) &= x'_{j,\text{ref}}(l) + \left. \frac{\partial f_j}{\partial r_c} \right|_{\text{ref}} (x_1(l) - x_{1,\text{ref}}(l)) + \left. \frac{\partial f_j}{\partial \alpha_c} \right|_{\text{ref}} (x_2(l) - x_{2,\text{ref}}(l)) \\ &\quad + \left. \frac{\partial f_j}{\partial v_z} \right|_{\text{ref}} (v_z(l) - v_{z,\text{ref}}(l)) + \psi_j(l) y'(l), \quad j = 1, 2 \end{aligned} \quad (3.121)$$

$$\begin{aligned} y'(l) &= y'_{\text{ref}}(l) + \left. \frac{\partial f_3}{\partial r_c} \right|_{\text{ref}} (x_1(l) - x_{1,\text{ref}}(l)) + \left. \frac{\partial f_3}{\partial \alpha_c} \right|_{\text{ref}} (x_2(l) - x_{2,\text{ref}}(l)) \\ &\quad + \left. \frac{\partial f_3}{\partial v_z} \right|_{\text{ref}} (v_z(l) - v_{z,\text{ref}}(l)). \end{aligned} \quad (3.122)$$

Similarly from (3.119)–(3.120) we obtain

$$\begin{aligned} \hat{x}'_j(l) &= x'_{j,\text{ref}}(l) + \left. \frac{\partial f_j}{\partial r_c} \right|_{\text{ref}} (\hat{x}_1(l) - x_{1,\text{ref}}(l)) + \left. \frac{\partial f_j}{\partial \alpha_c} \right|_{\text{ref}} (\hat{x}_2(l) - x_{2,\text{ref}}(l)) \\ &\quad + \left. \frac{\partial f_j}{\partial v_z} \right|_{\text{ref}} (v_z(l) - v_{z,\text{ref}}(l)) + \psi_j(l) \hat{y}'(l), \quad j = 1, 2 \end{aligned} \quad (3.123)$$

$$\begin{aligned} \hat{y}'(l) &= y'_{\text{ref}}(l) + \left. \frac{\partial f_3}{\partial r_c} \right|_{\text{ref}} (\hat{x}_1(l) - x_{1,\text{ref}}(l)) + \left. \frac{\partial f_3}{\partial \alpha_c} \right|_{\text{ref}} (\hat{x}_2(l) - x_{2,\text{ref}}(l)) \\ &\quad + \left. \frac{\partial f_3}{\partial v_z} \right|_{\text{ref}} (v_z(l) - v_{z,\text{ref}}(l)). \end{aligned} \quad (3.124)$$

After subtracting the linearized systems (3.121)–(3.122) and (3.123)–(3.124) from each other in matrix notation we obtain

$$\tilde{x}'(l) = \underbrace{(A(l) + \Psi(l)c^T(l))}_{\tilde{O}} \tilde{x}(l) \quad (3.125)$$

with

$$A(l) = \begin{pmatrix} a_{1,1}(l) & a_{1,2}(l) \\ a_{2,1}(l) & a_{2,2}(l) \end{pmatrix},$$

$$\tilde{x}(l) = \begin{pmatrix} \tilde{x}_1(l) \\ \tilde{x}_2(l) \end{pmatrix} = \begin{pmatrix} \hat{x}_1(l) - x_1(l) \\ \hat{x}_2(l) - x_2(l) \end{pmatrix},$$

$$c^T(l) = (c_1(l) \quad c_2(l)), \quad \Psi(l) = \begin{pmatrix} \psi_1(l) \\ \psi_2(l) \end{pmatrix}.$$

Here $a_{1,1}$, $a_{1,2}$, $a_{2,1}$, $a_{2,2}$, c_1 and c_2 depend on the reference trajectories, i.e. finally on crystal length.

It can be seen immediately that system (3.125) is very similar to system (3.111). They differ in that the elements of the matrices A and c are not constant in (3.125), but depend on length. Thus, the elements of Ψ need not be constant in order to ensure stability of system (3.125).

Now, the elements of Ψ have to be determined. To this end, system (3.125) is transformed into the so-called observer canonical form [Bestle 1983]:

$$\tilde{x}^{*'}(l) = (A^*(l) + \Psi^*(l)c^{*T}(l))\tilde{x}^*(l), \quad (3.126)$$

with $\Psi^*(l) = (\psi_1^*(l) \quad \psi_2^*(l))^T$, $c^{*T}(l) = (0 \ 1)$,

$$A^*(l) = \begin{pmatrix} 0 & -a_1^*(l) \\ 1 & -a_2^*(l) \end{pmatrix},$$

new coordinates $(\tilde{x}_1^*, \tilde{x}_2^*)$ and functions $a_1^*(l)$, $a_2^*(l)$. Equation (3.126) can be rewritten as

$$\tilde{x}_2^{*''}(l) + \underbrace{(a_2^*(l) - \psi_2^*(l))}_{\varepsilon_1} \tilde{x}_2^{*'} + \underbrace{(a_1^*(l) - \psi_1^*(l))}_{\varepsilon_0} \tilde{x}_2^* + \underbrace{(a_1^*(l) - \psi_1^*(l))'}_{\varepsilon_0'} \tilde{x}_2^* = 0. \quad (3.127)$$

This differential equation (like Equation (3.125)) describes the behaviour of the estimation error of the observer (in new coordinates $(\tilde{x}_1^*, \tilde{x}_2^*)$). If we choose the coefficients ε_1 , ε_0 to be constant and greater than zero, the last term in (3.127) vanishes and the error tends to zero for $l \rightarrow \infty$. This is exactly the same idea as during model-based controller design in section 3.6.3.3. The parameters ε_1 , ε_0 define the dynamical behaviour of the observer. The transformation between coordinates $(\tilde{x}_1, \tilde{x}_2)$ and $(\tilde{x}_1^*, \tilde{x}_2^*)$ and between observer gains Ψ and Ψ^* involves a lot of mathematics which it is not discussed here. Details can be found in [Winkler 2007].

One has to keep in mind that the values for Ψ depend on length and they are calculated from the reference trajectory of the radius r_c and its derivatives. This is due to the fact that systems (3.115)–(3.116) and (3.119)–(3.120) have been linearized around the reference trajectory.

The three steps discussed above are needed for calculation of the observer gains in each time-step. In the following it is shown how these values are processed within the observer (3.119)–(3.120):

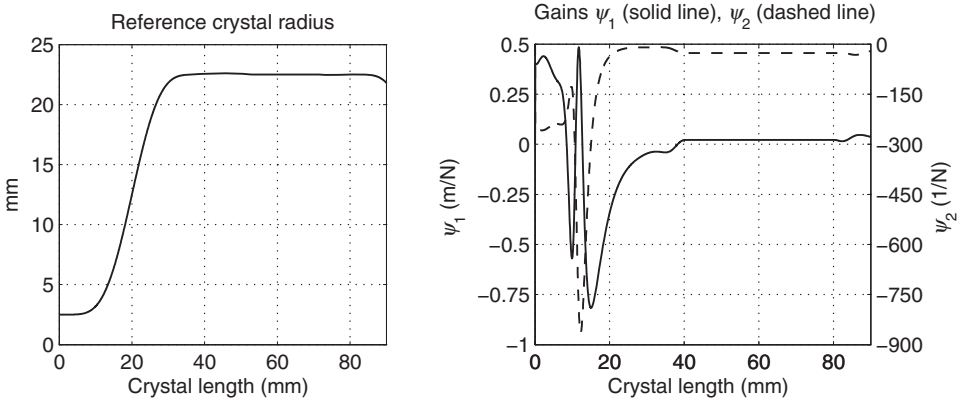


Figure 3.37 Left: reference trajectory of crystal radius used for calculation of observer gains. Right: trajectory of the observer gains ψ_1 (solid line), ψ_2 (dashed line) resulting from the trajectory plotted on the left-hand side. Note the large variations of the gains due to the dynamics of the meniscus during growth of the shoulder. Eigenvalues for error system (3.125): $p_1 = -400\text{m}^{-1}$, $p_2 = -600\text{m}^{-1}$ (Reprinted with permission from [Winkler 2010-2], copyright (2009) Elsevier Ltd).

- (i) Values for the observer gains ψ_1 , ψ_2 are calculated according to the algorithm presented above (for details see [Winkler 2007]). The values of the observer gains can be calculated in advance using the reference trajectory for crystal radius r_c and its derivatives. An example can be found in Figure 3.37.
- (ii) The values of ψ_1 , ψ_2 , the measured variable y and the input v_z are used to drive the observer

$$\hat{x}_1' = f_1(\hat{x}_1, \hat{x}_2, v_z) + \psi_1 f_3(\hat{x}_1, \hat{x}_2, v_z)$$

$$\hat{x}_2' = f_2(\hat{x}_1, \hat{x}_2, v_z) + \psi_2 f_3(\hat{x}_1, \hat{x}_2, v_z).$$

Remember that \hat{x}_1 , \hat{x}_2 depend on y and ψ_1 , ψ_2 .

- (iii) Having estimates \hat{x}_1 , \hat{x}_2 calculated by the observer, one can determine estimates \hat{r}_c , $\hat{\alpha}_c$ for the crystal radius r_c and the slope angle α_c using the inverse transition (3.118) discussed in step 1.

It is important that a suitable controller tracks the system in a neighborhood of the reference trajectory used for linearization in step 3 of the design procedure. Such an observer is called a *tracking observer* [Fliess 1996, Fliess 1997]. This condition is not too restrictive and will be discussed in more detail in section 3.7.2.5. The theoretical background of this restriction is that the observer gains calculated in the way discussed above ensure that the observer converges only locally (i.e. in a neighborhood of the reference trajectory). However, nothing can be said about the size of the domain of attraction. Therefore, the controller has to ensure that the trajectory follows the reference sufficiently closely. A necessary technical condition is that the reference trajectories comply with certain conditions: they have to be sufficiently often continuously differentiable and they have to be exponentially bounded; see [Fliess 1997]. For Cz growth these conditions are usually fulfilled.

If the matrix O in (3.125) is singular (i.e. not invertible) at a certain length l , calculation of $\psi_1(l)$ and $\psi_2(l)$ is not possible at that length. This means that reconstruction of the radius and the slope angle fails at this point. However, the elements of the matrix O depend on the reference trajectory only, and it is possible to plan these trajectories in advance. In doing so one can check in advance if reconstruction is possible for a complete growth run (i.e. if the the matrix O is regular for all l).

3.7.2.2 *Nonlinear Design Procedure for LEC Growth*

In LEC growth one has to take into account the dynamics of the boron oxide layer as well as the time delay introduced by the emerging crystal. In principle the same design method as illustrated in section 3.7.2.1 can be applied.

For this purpose one has to exchange Equation (3.114) in system (3.112)–(3.114) by Equation (3.41), parametrized in length:

$$F'_{\text{LEC}} = \pi g r_c^2 (c_{p,\text{LEC}}(r_c, r_{\text{es}}) + c_{r,\text{LEC}}(r_c, r_{\text{es}}, \alpha_c) \tan(\alpha_c) + c_{\alpha,\text{LEC}}(r_c, r_{\text{es}}, \alpha_c) \alpha'_c), \quad F_{\text{LEC}}(0) = 0. \quad (3.128)$$

Now, one can continue as in section 3.7.2.1. While determining the values of the observer gains in Steps 1, 2, and 3 one assumes that the radius r_{es} of the crystal at the top of the boron oxide layer is at its desired value in order to obtain a linear length varying error dynamics as in (3.125).

The observer itself (see Equations (3.119)–(3.120)) is

$$\hat{x}'_1 = f_1(\hat{r}_c, \hat{\alpha}_c, v_z) + \psi_1 f_3(\hat{r}_c, \hat{r}_{\text{es}}, \hat{\alpha}_c, v_z), \quad \hat{x}_1(0) = \hat{r}_{c0} \quad (3.129)$$

$$\hat{x}'_2 = f_2(\hat{r}_c, \hat{\alpha}_c, v_z) + \psi_2 f_3(\hat{r}_c, \hat{r}_{\text{es}}, \hat{\alpha}_c, v_z), \quad \hat{x}_2(0) = \hat{\alpha}_{c0}, \quad (3.130)$$

with

$$r_c = x_1 - \phi_1(y, \psi_1), \quad \alpha_c = x_2 - \phi_2(y, \psi_2) \quad (3.131)$$

and

$$\hat{r}_{\text{es}} = \mathbf{R}(l - \hat{h}_e + \hat{h}), \quad \mathbf{R}(\lambda) = r_{c0} \forall \lambda < 0. \quad (3.132)$$

Here, values for \hat{h}_e result from integration of

$$\hat{h}'_e = \frac{(\hat{r}_c^2 - \hat{r}_{\text{es}}^2) - \hat{r}_{\text{es}}^2 \hat{h}' + \frac{1}{\pi} \hat{V}'_{\text{men}}}{r_a^2 - \hat{r}_{\text{es}}^2}, \quad h_e(0) = h_{e0} \quad (3.133)$$

with h_{e0} the initial height of the boron oxide layer. Values for \hat{h} result from evaluation of (3.18) using \hat{r}_c , $\hat{\alpha}_c$. Note that this approach does not assign an error dynamics for the calculation of h_e , i.e. errors occurring during calculation of h_e are continuously summed. However, as we will see during inspection of the experimental results, this does not lead to problems.

3.7.2.3 Calculation of Growth Rate

An estimate of the growth rate can be calculated from the values \hat{r}_c and $\hat{\alpha}_c$ provided by the nonlinear observer. For this it is necessary to numerically differentiate $\hat{\alpha}_c$ with respect to crystal length in order to obtain values for α'_c . Then we can estimate the growth rate from Equation (3.32):

$$v_c = (v - v_{\text{cruc}})/N$$

with

$$N = \left(1 - \frac{r_c^2}{r_a^2} \rho\right) + \left[\left(1 - \frac{r_c^2}{r_a^2}\right) \frac{\partial h}{\partial r_c} - \frac{2r_c h}{r_a^2} - \frac{a^2}{r_a^2} \cos(\Theta_0 + \alpha_c) \right] \frac{dr_c}{dl} \\ + \left[\left(1 - \frac{r_c^2}{r_a^2}\right) \frac{\partial h}{\partial \alpha_c} + \frac{a^2 r_c}{r_a^2} \sin(\Theta_0 + \alpha_c) \right] \frac{d\alpha_c}{dl}.$$

3.7.2.4 Parametrization in Time

The observer design is based on a model of the process which is parametrized in crystal length. The advantage of this method is the elimination of the growth rate v_c and, thus, the hiding of the thermal model. In practice all calculations in the observer have to be done with respect to time parametrization. Therefore, reparametrization from length to time is required at two points:

- when calculating the input variable $v_z = (v - v_{\text{cruc}})/v_c$;
- when integrating the observer equations (3.119)–(3.120):

$$\hat{x}'_j = f_j(\hat{r}_c, \hat{\alpha}_c, v_z) + \psi_j f_3(\hat{r}_c, \hat{\alpha}_c, v_z), \quad j = 1, 2.$$

The reparametrization has to be done using the growth rate v_c . Since values of the growth rate are not known in advance it is assumed that the system is near to its reference trajectory (represented by $v_{c,\text{ref}}$):

$$v_z = \frac{v - v_{\text{cruc}}}{v_{c,\text{ref}}}.$$

This condition must be ensured by an appropriate control; see section 3.6. Then, the reference values of the growth rate can be taken for this calculation.

3.7.2.5 Simulation and Experimental Results

In the following the capability of the approach is demonstrated on the basis of results from simulations and experiments. Here the values of the crystal radius and the slope angle reconstructed by the observer are compared to the values determined manually from the crystal after the growth experiment.

Variable Observer Gains. First of all the trajectories of the observer gains for a given reference shape of the crystal are plotted in Figure 3.37. These trajectories also depend

on the choice of the two parameters ε_1 , ε_0 (see Equation (3.127)) defining the dynamics of the estimation error. It can be clearly seen that the values of the observer gains depend on the crystal length, especially in the conical part, reflecting the complex nonlinear dynamics of the system – in contrast to the linear case, where the elements of the vector H are constant. The underlying reference trajectory is plotted on the left-hand side of the figure.

Cz Growth Without Boron Oxide. Results of a simulation as well as of a real growth run are presented in Figure 3.38. Both refer to Cz growth without a boron oxide layer [Kiessling 2008]. In the simulation, the results of which can be found on the left-hand side, of the figure the observer starts with a wrong initial radius and a wrong initial slope angle. It can be seen that radius and slope angle reconstructed by the observer converge

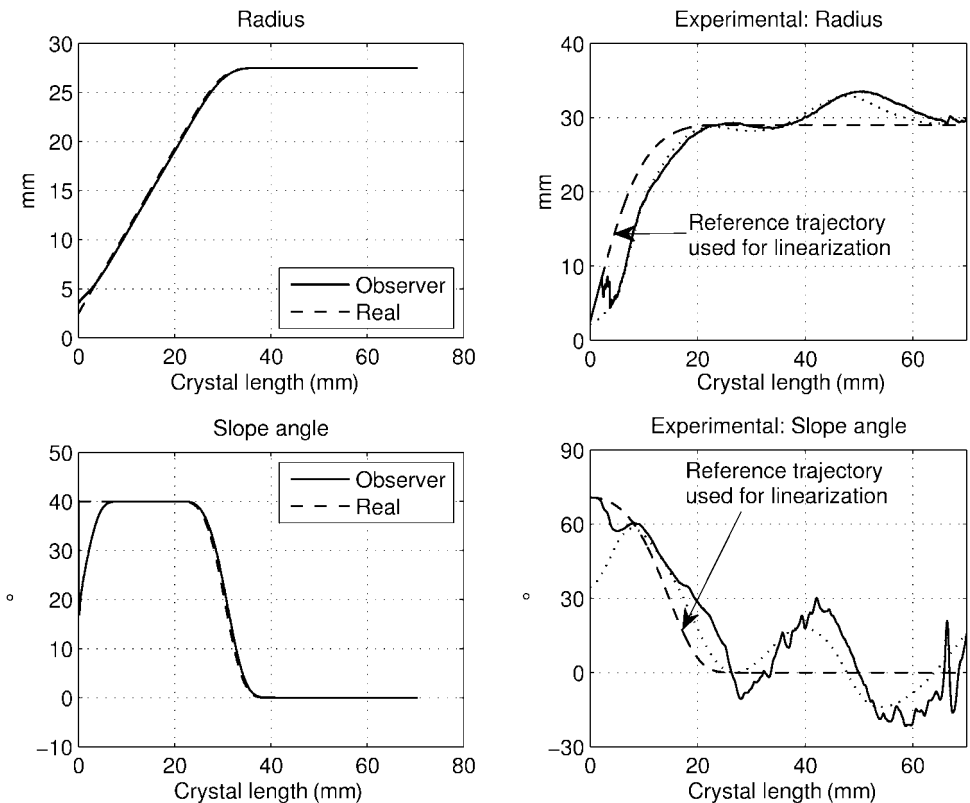


Figure 3.38 Crystal radius (top) and slope angle (bottom) reconstructed by means of the nonlinear reduced observer for growth without boron oxide. Left: simulation. Right: experimental results (2" GaAs, VCz-growth without boron oxide). The real trajectories are dotted and have been determined manually after the growth run, the reference trajectory used for calculation of the observer gains is given by the dashed line. Eigenvalues for error system (3.125): $p_1 = -400\text{ m}^{-1}$, $p_2 = -600\text{ m}^{-1}$ (Reprinted with permission from [Winkler 2010-2], copyright (2009) Elsevier Ltd).

to the real values after a few millimeters. The results obtained in a real growth run are presented on the right-hand side of the figure. The crystal has intentionally been grown without feedback control in order to show that – even if the process is away from its reference trajectory (see condition in Step 3 of section 3.7.2.1 – the observer still produces acceptable results. Just as in the simulation, the observer starts with wrong initial values and quickly converges to the real ones.

LEC Growth. An example for growth using the LEC method is shown in Figure 3.39. There, again, the growth run was intentionally done in open-loop mode demonstrating that even large differences between real and reference trajectory do not lead to serious problems.

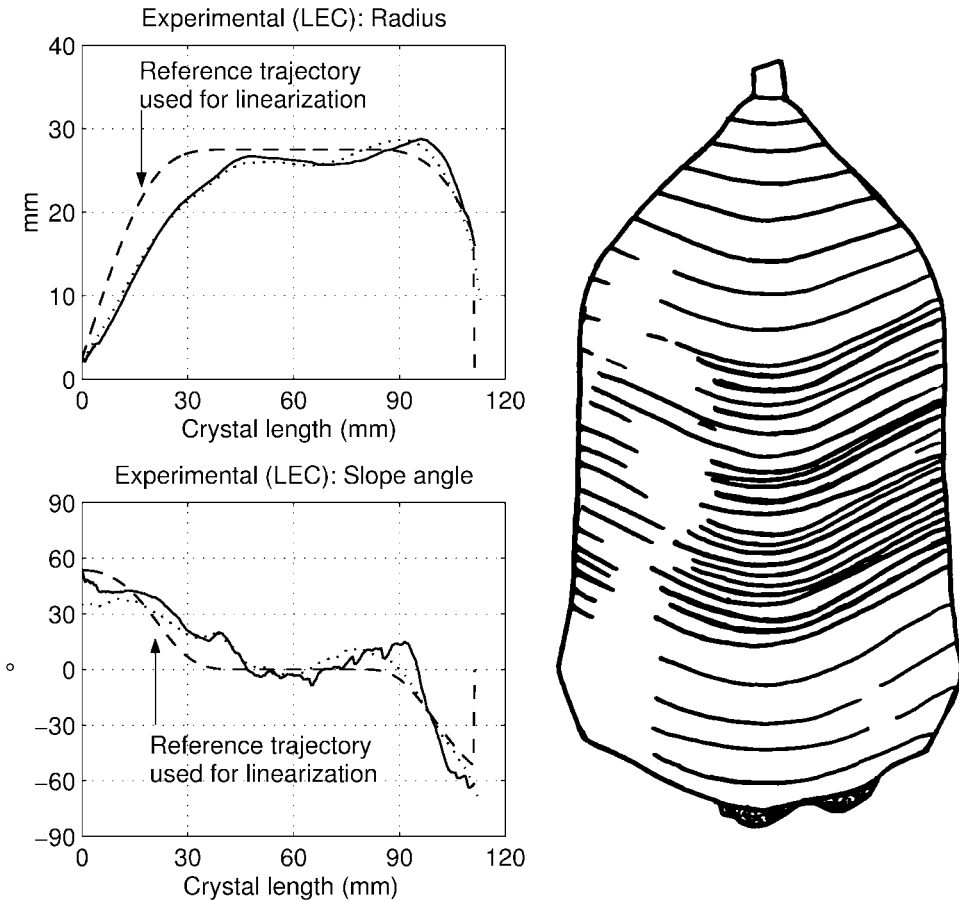


Figure 3.39 Left: reconstructed (solid lines) and real (dotted lines) trajectories of crystal radius and slope angle in case of LEC growth. The reference trajectory used for calculation of the observer gains is plotted using dashed lines. Right: striations determined from a longitudinal section of the grown crystal showing the shape of the interface during growth (Reprinted with permission from [Winkler 2010-2], copyright (2009) Elsevier Ltd).

3.7.2.6 *Robustness of the Observer*

One may wonder if the performance of the presented observer and of the overall closed loop system degrades if uncertainties in the physical parameters or a non-flat interface come into play. These problems are addressed in the present section.

Influence of a Curved Interface. The most critical assumption of the approach presented so far is the flat interface. The presence of a flat interface allows one to reparametrize the model equations in crystal length (as described in section 3.6.2). One might assume that, if the assumption is not met, the control system may fail. In fact, a nonflat interface leads to the following problems:

- A ‘lumped’ growth rate v_c cannot be defined as the derivative of crystal length with respect to time because the length of the crystal depends on the radial coordinate also, i.e. growth rate would become a spatially distributed variable.
- The curvature of the interface leads to additional terms for mass and buoyancy which have to be considered, e.g. in the equation describing the force acting on the load cell.
- Changes of the curvature of the interface during growth may introduce additional dynamics into the system.

In the literature there are some approaches that attempt to consider the effects of a nonflat interface within a *lumped-parameter* model; see e.g. [Gevlber 1994-1, Johansen 1992-1, Johansen 1992-2, Satunkin 1995] and section 3.3.1.9. Here, the main problem is that it is difficult to derive the necessary dynamic equations describing the deflection of the interface. This is a direct consequence of the lumped-parameter character: since the curvature of the interface is, broadly speaking, a result of the melting-point isotherm, it cannot be described by a single lumped parameter.

In order to check the robustness of the control system with respect to changes in the interface deflection the following simulation has been performed. It is assumed that the curvature of the interface has a form like that sketched in Figure 3.40. The degree of deflection is described by the parameter ζ . In this case the force acting on the load cell (compared to the force F when the interface is flat) is influenced by the following term:

$$\Delta F_i = \pi g (\rho_s - \rho_l) \left(\frac{1}{2} \zeta r_c^2 - \frac{1}{6} \zeta^3 \right). \quad (3.134)$$

Now, the observer (designed for a flat interface) is fed with data $F + \Delta F_i$ for the modified weighing signal. The interface is assumed to be convex, i.e. $\zeta > 0$. In the beginning of the simulation the parameter ζ is kept constant at 0.5 mm. Starting at crystal length of 60 mm the value of ζ is increased linearly up to 5 mm, i.e. an increasing deflection of the interface into the melt is simulated. The crystal radius is 27.5 mm. The effect of a changing weighing signal resulting from this increasing deflection is sketched in Figure 3.40. It can be easily seen that the additional force introduced into the system is quite small compared to the overall mass of the crystal and has not much effect on the reconstruction of the radius.

Some results of experimental investigations are shown in Figure 3.39 by way of example. Here, the reconstruction result of the observer is compared to the real values

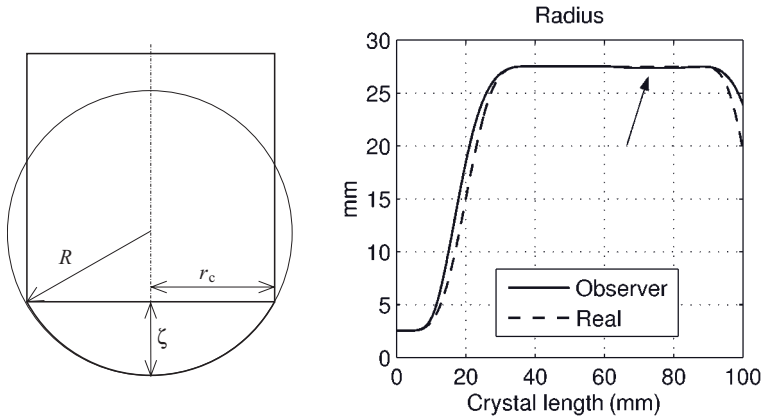


Figure 3.40 Left: parameters used for simulation of the influence of a nonflat interface. Right: simulation of the influence of a changing deflection of the interface. The change of the interface deflection ζ from 0.5 mm to 5 mm occurs between a crystal length of 60 and 80 mm. Model used for simulation taken from [Winkler 2010-1], parameters used for simulation from [Looze 1995] (Reprinted with permission from [Winkler 2010-2], copyright (2009) Elsevier Ltd).

(as determined after the growth run) of crystal radius and slope angle. The crystal has been grown using the LEC method and the observer presented in [Winkler 2007]. The grown crystal has been cut longitudinally after growth in order to determine the striations shown on the right-hand side of Figure 3.39. It can be seen that the interface is not flat and its shape has varied during growth. Despite that, the observer still shows acceptable performance, even though the experiment has been performed in open-loop mode, thus resulting in a quite large difference between reference and real trajectories.

Note that the influence of a deflected interface shape directly depends on the difference between the densities of the solid and the melt (Equation 3.134). As long as the difference $\rho_s - \rho_l$ is not too large (as is the case for a lot of semiconductor materials, e.g. GaAs, where the difference is only about 10%), the effect might be negligible. However, some materials may have a larger difference between the densities of their solid and melt and here the effect might become a problem.

Parameter Uncertainties. The following physical parameters are important for the model used in the observer: the densities of the solid and liquid phase, the crucible radius, the capillary constant, and the growth angle. The values of the densities and crucible radius are well known, but determination of the capillary constant and the growth angle might be complicated and, therefore, inaccurate. Hence, in what follows some simulation results are presented showing the effect of a non-constant growth angle even during cylindrical growth. The values and constancy of this parameter have been intensively (and controversially) discussed in the literature (see for instance [Anderson 1996, Bakovets 1998, Surek 1980, Virozub 2008] and Chapter 1.3.2).

In a simulation the growth angle α_0 was increased from its reference value of 17° to a value of 27° during growth of the cylinder from 60 to 80 mm in length, in order to show

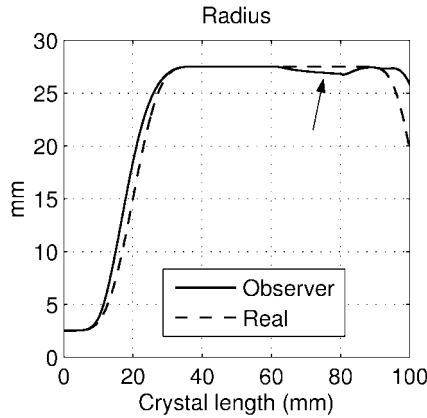


Figure 3.41 Simulation of the influence of a nonconstant growth angle during cylindrical growth on the reconstruction of the crystal radius (GaAs, model and other constant parameters as in Figure 3.40) (Reprinted with permission from [Winkler 2010-2], copyright (2009) Elsevier Ltd).

the effects of a nonconstant value. The results are shown in Figure 3.41. It can be clearly seen that the effect is not negligible, since the accuracy of the reconstructed radius rapidly degrades.

Closed-Loop Performance. Finally, some results obtained in closed-loop experiments using the controller derived in section 3.6 are presented (Figure 3.42). In these cases the controller ensured that the values of growth rate and crystal radius were close to their reference values, i.e. the observer should operate with ‘optimal’ performance. On the right-hand side of each picture a sketch of the striations made from a longitudinal section of a GaAs crystal is shown. Here, we can make two observations:

- The interface is not strictly flat as assumed in the model, but it is not heavily deflected as it might be under certain growth conditions.
- The shape of the interface does change during growth, i.e. an additional dynamical effect not included in the model is added to the weighing signal.

Despite these observations no effects on diameter control can be seen in the photographs of the grown crystals on the left.

Furthermore, in Figure 3.43 the trend of the radius as calculated by the observer and the real radius determined after the growth experiment are displayed for the crystals presented in Figure 3.42. In both cases the estimated radius is consistent with the real radius. Hence, from an experimental point of view, the approach is robust, at least to moderate deflections of the phase interface. Furthermore, we may conclude that the growth angle during cylindrical growth seems to be almost constant.

3.7.3 Control Structure Design for Batch Disturbance Rejection

So far the discussion has focused on the design and dimensioning of feedback controllers and observers. As already mentioned in section 3.1.7, a feedforward control may be

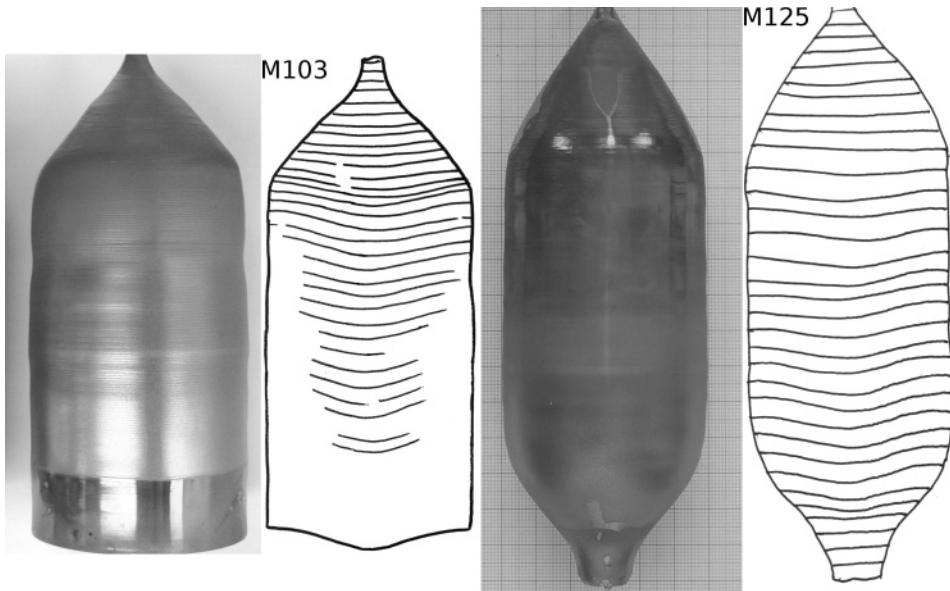


Figure 3.42 Striations and photographs of two GaAs crystals grown using diameter control via heater temperature (left) and both diameter and growth rate control via heater temperature and pulling speed, respectively (right, as in [Winkler 2010-1]). Radius, slope angle and growth rate have been reconstructed using the observer proposed in section 3.7.2 (Reprinted with permission from [Winkler 2010-2], copyright (2009) Elsevier Ltd).

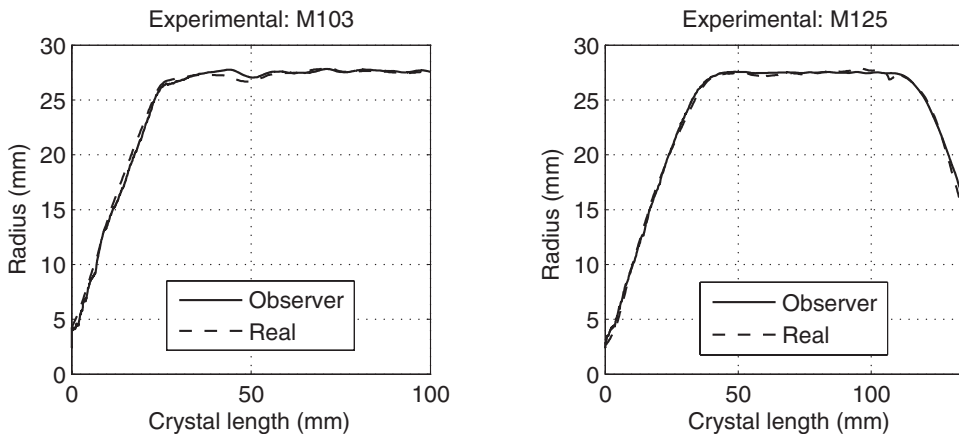


Figure 3.43 Trajectories of the radius of the crystals shown in Figure 3.42. Solid line: radius measured manually after the growth experiment. Dashed line: radius estimated by the observer during the growth run. It can be clearly seen that the two-loop control (right) shows better performance (Reprinted with permission from [Winkler 2010-2], copyright (2009) Elsevier Ltd).

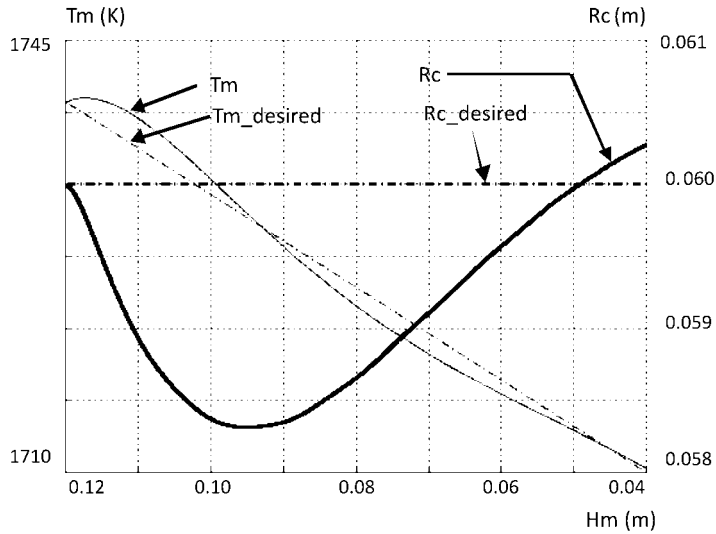


Figure 3.44 Resulting diameter and melt temperature from steady-state feedforward control (Reprinted with permission from [Gevlber 2001], copyright (2001) Elsevier Ltd).

required in order to improve the performance of the overall control system. Using the system model described in section 3.3.2, the performance of model-based feedforward heater power and pull rate trajectories for achieving diameter control is evaluated. The advantage of this control approach is that it takes the guesswork out of what those trajectories should be. The result presented here, which is consistent with the results of [Assaker 1997], is that it is critical to include the dynamics of both the equipment (primarily thermal lags that are sensitive to assumptions of insulation and radiation interactions) and the process (primarily the large lag associated with the interface dynamics). Figure 3.44 shows the melt surface temperature and resulting diameter of a dynamic simulation where the power input trajectory was derived from analysing the steady state of the model as a function of melt height. The use of steady state models has been proposed by others since it requires significantly less computational time than a full simulation of the entire batch process (due to the wide difference in timescales in the process and equipment models). While the temperature deviation is only of the order of 3 K, the resulting diameter error is 3%. The reason is that there are significant dynamics in both the equipment and process models that are ignored. Note, however, that the performance of feedforward control, even using a dynamic model, is limited by model error, plant variation, and unmodelled disturbances.

In analysing the experimental benchmarks of growth runs (as shown for example in Figure 3.28), it is observed that a decreasing pull rate trajectory was used as a reference trajectory. This might seem to be reasonable since, as the melt level decreases, the crystal is exposed to more hot crucible wall which reduces the crystal heat flux. The large initial decrease in pull rate may also be due to the fact that the shoulder, which is an effective radiator, moves further away from the interface. The model analysis, as well as others,

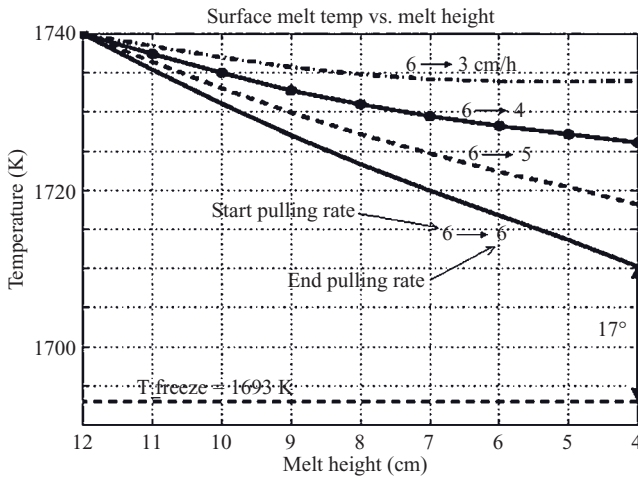


Figure 3.45 Simulation of melt surface temperatures for different pull rate trajectories (Reprinted with permission from [Gevlber 2001], copyright (2001) Elsevier Ltd).

showed, however, that it is possible to find a heater power trajectory that would enable a constant pull rate to be maintained. A reduction in pull rate might be motivated by several additional factors; for example, it might be related to a desired v/G ratio in order to achieve a desired defect structure. Additionally, the model analysis indicates that another factor might be the different resulting melt temperature trajectories. Figure 3.45 shows the resulting melt surface temperature for a series of different pull rate trajectories, starting with no decrease in pull rate to decrease by half. Maintaining a constant pull rate would result in the surface melt temperature being only 17K above the solidification temperature towards the end of growth. Such a low offset may not be desirable because of sensitivity to growth variations and crystal quality due to melt turbulence, which can be of the order of ± 5 K. In contrast, decreasing the pull rate by half results in a 40-K offset at low melt heights. Since the batch melt temperature variations are one of the batch disturbances acting on the interface to change the diameter, this analysis suggests that a more direct control strategy of maintaining the melt temperature would (i) compensate more directly for part of the batch disturbance, and (ii) enable one to operate 'closer to the edge' (i.e. limit the pull rate reduction) and achieve an increase in process productivity.

Figure 3.46 shows a new control structure [Gevlber 2001] to compensate for the batch disturbance, while meeting the desire of maintaining a desired melt temperature offset. The structure incorporates explicit control of the melt temperature, and uses feedforward input trajectories for pulling rate and heater power. In this fashion, the actuators are changed in anticipation of needed changes (i.e. the general ramp), and therefore not driven entirely by an error signal. Feedback is still used as a trim, however, e.g. to provide a corrective term to the actual heater power and pull rate implemented. Comparing the performance of the conventional control structure to the new one (Figure 3.47) reveals that to achieve the same performance, the new structure requires six times less control

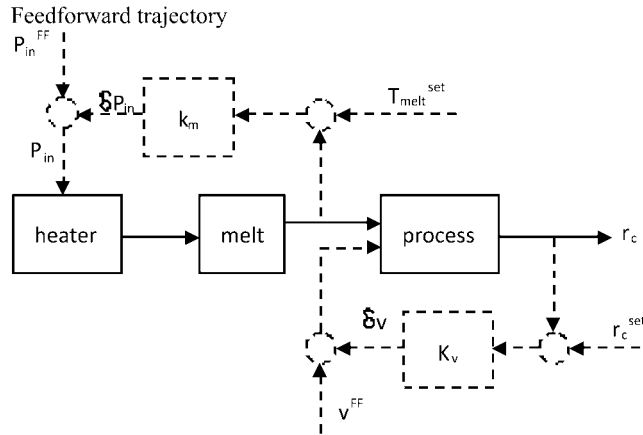


Figure 3.46 Advanced melt/diameter control structure (dashed line) (Reprinted with permission from [Gevlber 2001], copyright (2001) Elsevier Ltd).

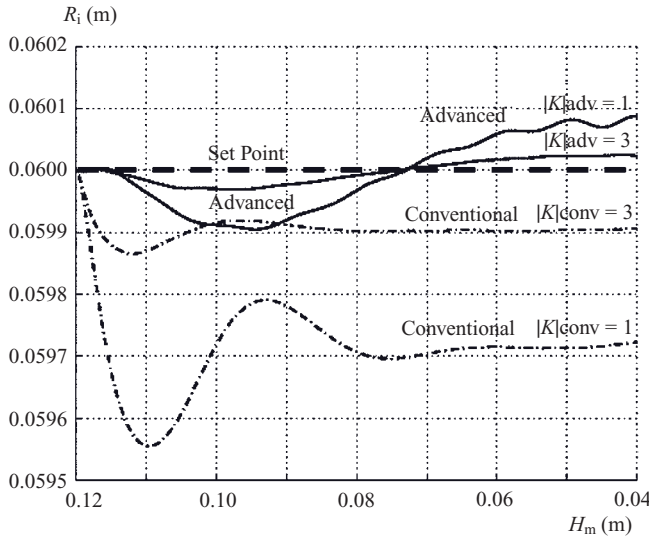


Figure 3.47 Radius performance comparison of conventional and proposed controllers for different control gains (Reprinted with permission from [Gevlber 2001], copyright (2001) Elsevier Ltd).

gain. This lower gain should significantly reduce the magnitude of the pull rate fluctuations. The gain comparison is based on the control gain required to achieve the same volumetric error in the crystal shape. In addition, the melt temperature follows the setpoint trajectory very closely (Figure 3.48), indicating that it will be safe to utilize a higher pull rate trajectory. The robustness of the proposed scheme is suggested by the fact that we used very rough feedforward trajectories (i.e. we did not use model-developed dynamic trajectories).

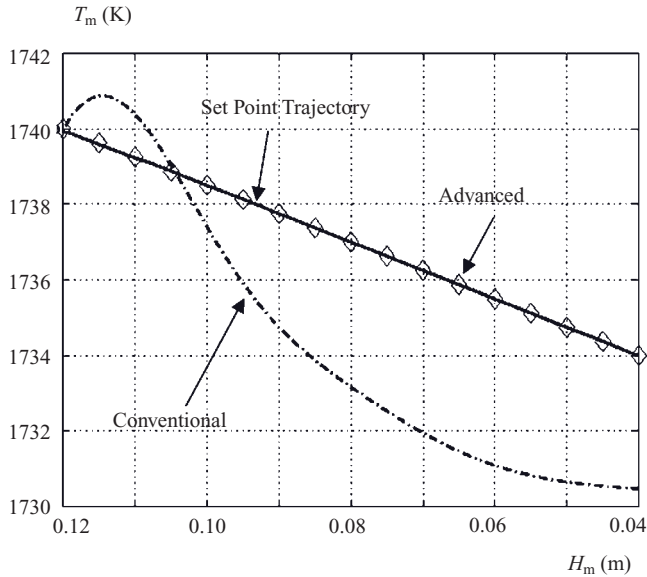


Figure 3.48 Comparison of surface temperature control (Reprinted with permission from [Gevlber 2001], copyright (2001) Elsevier Ltd).

Section 3.7.3 reprinted with permission from *Journal of Crystal Growth*, M. Gevlber, D. Wilson and N. Duanmu, 230, 1–2, 217–223 Copyright (2001) Elsevier Ltd.

References

- [Abrosimov 2003] Abrosimov N., Kurlov V., Rossolenko S., *Prog. Crystal Growth Charact. Mat.* **46** (2003) 1–57.
- [Allgöwer 2007] Allgöwer F., Zheng A. (eds.), *Nonlinear Model Predictive Control. Progress in Systems and Control Theory*. Birkhäuser Verlag, Basel (2007).
- [Anderson 1996] Anderson D., Worster M.G., Davis S., *J. Cryst. Growth* **163** (1996) 329–338.
- [Arpaci 1966] Arpaci V.S., *Conduction Heat Transfer*. Addison-Wesley, Reading, MA (1966).
- [Assaker 1997] Assaker R., van den Bogaert N., Dupret F., *J. Cryst. Growth* **180** (1997) 450–460.
- [Åström 1994] Åström K.J., Wittenmark B., *Adaptive Control*, Chapter 9. Prentice Hall, Englewood Cliffs, NJ (1994).
- [Atherton 1987] Atherton L.J., Derby J.J., Brown R.A., *J. Cryst. Growth* (1987) 57–78.
- [Azuma 1983] Azuma K., Japanese Patent No. 60–11299 (1983).
- [Bachmann 1970] Bachmann K., Kirsch H., Vetter K., *J. Cryst. Growth* **7** (1970) 290–295.
- [Bakovets 1998] Bakovets V., *J. Cryst. Growth* **193** (1998) 720–727.
- [Bardsley 1972] Bardsley W., Green G., Holliday C., Hurle D., *J. Cryst. Growth* **16** (1972) 277–279.
- [Bardsley 1974-1] Bardsley W., Cockayne B., Green G., Hurle D., Joyce G., Roslington J., Tufton P., Weber H., *J. Cryst. Growth* **24/25** (1974) 369–373.
- [Bardsley 1974-2] Bardsley W., Frank F., Green G., Hurle D., *J. Cryst. Growth* **23** (1974) 341–344.

- [Bardsley 1977-1] Bardsley W., Hurlle D., Joyce G., *J. Cryst. Growth* **40** (1977) 13–20.
- [Bardsley 1977-2] Bardsley W., Hurlle D., Joyce G., Wilson G., *J. Cryst. Growth* **40** (1977) 21–28.
- [Bejan 1993] Bejan A., *Heat Transfer*. John Wiley & Sons, Ltd, New York (1993).
- [Bestle 1983] Bestle D., Zeitz M., *Int. J. Control* **38** (1983) 419–431.
- [Bornside 1990] Bornside D., Kinney T., Brown R., Kim G., *Int. J. Numer. Meth. Eng.* **30** (1990) 133–154.
- [Bornside 1991] Bornside D., Kinney T., Brown R., *J. Cryst. Growth* **108** (1991) 779–805.
- [Boucher 1980] Boucher E., Jones T., *J. Chem. Soc. Faraday Trans. I* (1980) 1419–1432.
- [Brice 1970] Brice J., *J. Cryst. Growth* **6** (1970) 205–206.
- [Brown 1989] Brown G., Kinney T., Sackinger P., Bornside D., *J. Cryst. Growth* **97** (1989) 99–115.
- [Camacho 2004] Camacho E., Bordons C., *Model Predictive Control*. Springer, New York (2004).
- [Crowley 1983] Crowley A., *IMA J. Appl. Math.* **30** (1983) 173–189.
- [Derby 1985] Derby J., Brown R., *J. Electrochem. Soc.* (1985) 470–482.
- [Derby 1986-1] Derby J., Brown R., *J. Cryst. Growth* **74** (1986) 605–624.
- [Derby 1986-2] Derby J., Brown R., *J. Cryst. Growth* **75** (1986) 227–240.
- [Derby 1987] Derby J., Brown R., *J. Cryst. Growth* **83** (1987) 137–151.
- [Digges 1975] Digges T., Hopkins R., Seidensticker R., *J. Cryst. Growth* **29** (1975) 326.
- [Domey 1971] Domey K., *Solid State Technol.* **10** (1971) 41–45.
- [Dornberger 1996] Dornberger E., von Ammon W., van den Bogaert N., Dupret F., *J. Cryst. Growth* **166** (1996) 452–457.
- [Dornberger 1997] Dornberger E., Tomzig E., Seidl A., Schmitt S., Leister H.J., Schmitt C., Müller G., *J. Cryst. Growth* **180** (1997) 461–467.
- [Dornberger 2001] Dornberger E., Virbulis J., Hanna B., Hoelzl R., Dauba E., von Ammon W., *J. Cryst. Growth* **229** (2001) 11–16.
- [Duanmu 2006] Duanmu N., PhD thesis, College of Engineering, Boston University, USA (2006).
- [Dupret 1990] Dupret F., Nicodeme P., Ryckmans Y., Wouters P., Crochet M.J., *Int. J. Heat Mass Trans.* **33** (1990) 1849–1871.
- [Egorov 1976] Egorov L., Tsivinskii S., Zatulovskii L., *Bull. Acad. Sci. USSR Phys. Ser.* **40** (1976) 172–174.
- [Ekhult 1986] Ekhult U., Carlberg T., *J. Cryst. Growth* **76** (1986) 317–322.
- [Falster 2000] Falster R., Voronkov V., *Mater. Res. Soc. Bull.* (2000) 28–32.
- [Fliess 1995] Fliess M., Levine J., Martin P., Rouchon P., *Int. J. Control* **61** (1995) 1327–1361.
- [Fliess 1996] Fliess M., Rudolph J., *Proc. Symp. Control, Optimization, and Supervision*, IMACS Multiconference, Lille, pp. 213–217.
- [Fliess 1997] Fliess M., Rudolph J., *C.R. Acad. Sci. Paris Ser. Iib* **324** (1997) 513–519.
- [Frank 2000] Frank, Ch., Jacob K., Neubert M., Rudolph P., Fainberg J., Müller G., *J. Cryst. Growth* **213** (2000) 10–18.
- [Franklin 2002-1] Franklin G., Powell J., Emami-Naeini A., *Feedback Control of Dynamic Systems*, 4th ed., Chapter 3, Prentice Hall, Englewood Cliffs, NJ (2002), pp. 150–166.
- [Franklin 2002-2] Franklin G., Powell J., Emami-Naeini A., *Feedback Control of Dynamic Systems*, 4th ed., Appendix D, Prentice Hall, Englewood Cliffs, NJ (2002), pp. 849–856.
- [Gevlber 1987-1] Gevelber M., Stephanopoulos G., *J. Cryst. Growth* **84** (1987) 647–668.
- [Gevlber 1987-2] Gevelber M., Wargo M., Stephanopoulos G., *J. Cryst. Growth* **85** (1987) 256–263.
- [Gevlber 1988] Gevelber M., Stephanopoulos G., Wargo M., *J. Cryst. Growth* **91** (1988) 199–217.
- [Gevlber 1989] Gevelber M., Stephanopoulos G., US Patent No. 4,857,278, 15 August 1989.
- [Gevlber 1994-1] Gevelber M., *J. Cryst. Growth* **139** (1994) 271–285.
- [Gevlber 1994-2] Gevelber M., *J. Cryst. Growth* **139** (1994) 286–301.
- [Gevlber 1999] Gevelber M.A., In: *Encyclopedia of Electrical and Electronic Engineering*, John Wiley & Sons, Ltd, New York (1999), pp. 255–265.
- [Gevlber 2001] Gevelber M., Wilson D., Duanmu N., *J. Cryst. Growth* **230** (2001) 217–223.

- [Gross 1972] Gross U., Kersten R., *J. Cryst. Growth* **15** (1972) 85.
- [Hagenmeyer 2005] Graichen K., Hagenmeyer V., Zeitz M., *Automatica* **41** (2005) 2033–2041.
- [Hurle 1977] Hurle D., *J. Cryst. Growth* **42** (1977) 473–482.
- [Hurle 1986] Hurle D., Joyce G., Wilson G., Ghassempoory M., Morgan C., *J. Cryst. Growth* **74** (1986) 480–490.
- [Hurle 1990] Hurle D., Joyce G., Ghassempoory M., Crowley A., Stern E., *J. Cryst. Growth* **100** (1990) 11–25.
- [Hurle 1991] Hurle D., In: *Sir Charles Frank, OBE, FRS: An 80th Birthday Tribute*, ed. R. Chambers, J. Enderby, A. Keller, A. Lang, J. Steeds, Adam Hilger Publishing, Bristol (1991), pp. 188–206.
- [Hurle 1993] Hurle D., *J. Cryst. Growth* **128** (1993) 15–25.
- [Irizarry-Rivera 1997-1] Irizarry-Rivera R., Seider W. D., *J. Cryst. Growth* **178** (1997) 593–611.
- [Irizarry-Rivera 1997-2] Irizarry-Rivera R., Seider W. D., *J. Cryst. Growth* **178** (1997) 612–633.
- [Jaluria 1986] Jaluria Y., Torrance K.E., *Computational Heat Transfer*, Hemisphere Publishing, New York (1986).
- [Johansen 1987-1] Johansen T., *J. Cryst. Growth* **84** (1987) 609–620.
- [Johansen 1987-2] Johansen T., *J. Cryst. Growth* **80** (1987) 343–350.
- [Johansen 1991] Johansen T., *J. Cryst. Growth* **114** (1991) 27–30.
- [Johansen 1992-1] Johansen T., *J. Cryst. Growth* **118** (1992) 353–359.
- [Johansen 1992-2] Johansen T., *J. Cryst. Growth* **123** (1992) 188–194.
- [Jordan 1981] Jordan A., Caruso R., von Neida A., Nielsen J., *J. Appl. Phys.* **52** (1981) 3331–3336.
- [Jordan 1983] Jordan A., Caruso R., von Neida A., *Bell System Tech. J.* **62** (1983) 477–498.
- [Jordan 1984] Jordan A., von Neida A., Caruso R., *J. Cryst. Growth* **70** (1984) 555–573.
- [Kiessling 2008] Kiessling F.-M., Albrecht M., Irmscher K., Krause-Rehberg R., Ulricic W., Rudolph P., *J. Cryst. Growth* **310** (2008) 1418–1423.
- [Kim 1983] Kim K., Kran A., Smetana P., Schwuttke G., *J. Electrochem. Soc.* **130** (1983) 1156–1160.
- [Kinney 1993] Kinney T.A., Bornside D.E., Brown R.A., Kim K.M., *J. Cryst. Growth* **126** (1993) 413–434.
- [Kubota 1999] Kubota E., *Cryst. Res. Technol.* **34** (1999) 539–548.
- [Levinson 1959] Levinson J., US Patent No. 2,908,004, 6 October 1959.
- [Ljung 1987] Ljung L., *System Identification: Theory for the User*. Prentice Hall, Englewood Cliffs, NJ (1987).
- [Looze 1995] Looze D., Farzin A., Bernstein B., *J. Cryst. Growth* **148** (1995) 79–95.
- [Lorenzini 1974] Lorenzini R., Neff F., Blair D., *Solid State Technol.* **2** (1974) 33.
- [Luenberger 1964] Luenberger D.G., *IEEE Trans. Mil. Electron.* **8** (1964) 74–80.
- [Masi 2000] Masi M., Carra S., Polli M., Ratti M., Guadalupi G., *Mater. Chem. Phys.* **66** (2000) 236–245.
- [Mika 1975] Mika K., Uelhoff W., *J. Cryst. Growth* **30** (1975) 9–20.
- [Motakef 1991] Motakef S., Kelly K., Koai K., *J. Cryst. Growth* **113** (1991) 279–288.
- [Nalbandyan 1984] Nalbandyan H., *J. Cryst. Growth* **67** (1984) 115–118.
- [Neubert 2001] Neubert M., Rudolph P., *Prog. Cryst. Growth Charact. Mat.* (2001) 119–185.
- [Patzner 1967] Patzner E., Dessauer R., Poponiak M., *Solid State Technol.* **10** (1967) 25–30.
- [Riedling 1988] Riedling K., *J. Cryst. Growth* **89** (1988) 435–446.
- [Rossolenko 1992] Rossolenko S., Pet'kov I., Kurlov V., Red'kin B., *J. Cryst. Growth* **116** (1992) 185–190.
- [Rothfuss 1996] Rothfuss R., Rudolph J., Zeitz M., *Automatica* **32** (1996) 1433–1439.
- [Rummel 1966] Rummel T., US Patent No. 3,259,467, 5 July 1966.
- [Satunkin 1986-1] Satunkin G., Rossolenko S., *Cryst. Res. Technol.* **21** (1986) 1125–1138.
- [Satunkin 1986-2] Satunkin G., Rossolenko S., Kurlov V., Reg'kin B., Tatartchenko V., Avrutik A., *Cryst. Res. Technol.* **21** (1986) 1257–1264.
- [Satunkin 1990] Satunkin G., Leonov A., *J. Cryst. Growth* **102** (1990) 592–608.
- [Satunkin 1995] Satunkin G., *J. Cryst. Growth* **154** (1995) 172–188.

- [Sinno 2000] Sinno T., von Ammon E.D.W., Brown R.A., Dupret F., *Mater. Sci. Eng.* **28** (2000) 149–198.
- [Srivastava 1986] Srivastava R., Ramachandran P., Dudukovic M., *J. Cryst. Growth* **76** (1986) 395–407.
- [Steel 1975] Steel G., Hill M., *J. Cryst. Growth* **30** (1975) 45–53.
- [Surek 1976] Surek T., *J. Appl. Phys.* **47** (1976) 4384–4393.
- [Surek 1980] Surek T., Coriell S., Chalmers B., *J. Cryst. Growth* **50** (1980) 21–32.
- [Tatartchenko 1980] Tatartchenko V., Brener E., *J. Cryst. Growth* **50** (1980) 33–44.
- [Teal 1950] Teal G., Little J., *Phys. Rev.* **78** (1950) 647.
- [Thomas 1989] Thomas P., Derby J., Atherton L., Brown R., *J. Cryst. Growth* **96** (1989) 135–152.
- [Valentino 1974] Valentino A., Brandle C., *J. Cryst. Growth* **26** (1974) 1–5.
- [van den Bogaert 1997-1] van den Bogaert N., Dupret F., *J. Cryst. Growth* **171** (1997) 65–76.
- [van den Bogaert 1997-2] van den Bogaert N., Dupret F., *J. Cryst. Growth* **171** (1997) 77–93.
- [van Dijk 1974] van Dijk H., Jochem C., Scholl G., van der Werf P., *J. Cryst. Growth* **21** (1974) 310–312.
- [Virozub 2008] Virozub A., Rasin I., Brandon S., *J. Cryst. Growth* **310** (2008) 5416–5422.
- [Voigt 2000] Voigt A., Metzger M., Numerical simulation and control of industrial crystal growth by the Czochralski and vertical gradient freeze method. Caesar Preprint.
- [Vojdani 1974] Vojdani S., Dabiri A., Ashoori H., *J. Cryst. Growth* **24/25** (1974) 374–375.
- [Voronkov 1982] Voronkov V. V., *J. Cryst. Growth* **59** (1982) 625–643.
- [Voronkov 2002] Voronkov V., Mutti P., US Patent No. US 2002/0043208 A1 (2002).
- [Voronkov 2004] Voronkov V., Mutti P., US Patents Nos US 2002/043206 and US 6726764.
- [Warwick 1988] Warwick K., Rees D. (eds), *Industrial Digital Control Systems*, Chapter 14.7. Peter Peregrinus, Stevenage (1988).
- [Wilde 1991] Wilde J., Hesselink L., Feigelson R., *J. Cryst. Growth* **113** (1991) 337–359.
- [Wilke 1988] Wilke K., Bohm J., *Kristallzüchtung*. VEB Deutscher Verlag der Wissenschaften, Berlin (1988).
- [Wilson 2001] Wilson D., Master's thesis, Department of Electrical and Computer Engineering, Boston University, USA (2001).
- [Winkler 2007] Winkler J., *Beiträge zur Regelung des Czochralski Kristallzüchtungsprozesses zur Herstellung von Verbindungshalbleitern*. Shaker Verlag, Aachen.
- [Winkler 2010-1] Winkler J., Neubert M., Rudolph J., *J. Cryst. Growth* **312** (2010) 1005–1018.
- [Winkler 2010-2] Winkler J., Neubert M., Rudolph J., *J. Cryst. Growth* **312** (2010) 1019–1028.
- [Zinnes 1973] Zinnes A., Nevis B., *J. Cryst. Growth* **19** (1973) 187–192.

4

Floating Zone Crystal Growth

*Anke Lüdge, Helge Riemann and Michael Wünscher
Leibniz-Institut für Kristallzüchtung, Berlin*

*Günter Behr and Wolfgang Löser
Leibniz-Institut für Festkörper- und Werkstoffforschung, Dresden*

*Andris Muiznieks
University of Latvia*

*Arne Cröll
University of Freiburg*

Originally, horizontal zone melting was applied to reduce impurity levels in different materials such as metals, semiconductors and organic compounds [Pfann 1966]. A horizontal boat crucible was used to contain the material, and a molten zone was generated and passed from one end of the crucible to the other by moving a narrow heater. Multiple zone melting shifts most of the impurities to one end and purifies the remainder up to high grades. If the melt does not wet the crucible, the method can also be used to grow a single crystal, e.g. of Ge, if a seed crystal is placed at the start of the solidification. However, impurities can be newly introduced from the crucible to the melt. Some important substances such as Si react with or adhere to any crucible material, and can be neither purified nor single-crystallized in that way. So, the crucible-free floating zone (FZ) process was invented for Si in 1952 [Theuerer 1952, Keck 1953, Zulehner 2000].

The FZ crystal grows from the molten lower end of a cylindrical feed rod. A stationary molten zone between rod and crystal therefore has to be produced by contactless heating. For this, inductive heating by a radiofrequency (RF) magnetic field is widely used. The

main limitation of RF heating is the necessity for high electrical conductivity of the solid rod and the melt, which is normally fulfilled for metallic materials. For Si and some other materials with insufficient electrical conductivity at room temperature, it is often necessary to preheat the feed rod to enable the coupling with the electromagnetic (EM) field.

Other ways of heating the FZ are also possible: focused lamp radiation, laser beams, electron bombardment, electric arcs or plasma discharge.

As well as Si, single crystals of a wide variety of other substances have been grown after the FZ method. Typical examples are:

- transition metals Ni, Co, Fe and alloys such as Fe–Si [Kadečková 1963, Vaněk 1979, Vaněk 1983];
- refractory metals such as W, Ta, Mo [Berthel 1963, Otani 1990, Pfann 1966];
- rare earth borides such as LaB₆ for electron emission sources [Niemyski 1968, Shimizu 1975, Tanaka 1975] and CeB₆, SmB₆, GdB₆ [Tanaka 1980], CaB₆ [Otani 1998], CrB₂ [Otani 1999], YB₄ and YB₆ [Otani 2000];
- transition metal silicides and aluminides V₃Si [Jurisch 1977], Cr₃Si [Jurisch 1979], NiAl [Essmann 1995], RuAl [Hermann 2008];
- metal carbides such as TiC [Otani 1984] and WC [Tanaka 1988];
- complex ternary and quaternary rare earth (RE)–transition metal (TM) compounds of the type RENi₂B₂C, RE₂PdSi₃ as well as RECu₂Si₂ and REPd₂Si₂ [Behr 1999, Behr 2000, Behr 2002, Behr 2005-2, Behr 2008]. See [Pfann 1966] and [Wilke 1988-1] for comprehensive reviews of early works;
- a variety of oxides as described in section 2.4.

The possible size of the molten zone is the decisive parameter for applying the FZ method. It is determined by equating the capillary forces of surface tension and the hydrostatic pressure of the melt column. The maximum height and the shape of the zone were calculated by Heywang [Heywang 1954] under the condition that only surface tension and gravity are acting on the zone. For large rod diameters (a diameter approximately twice the maximum zone height or more), the maximum zone height L_{\max} becomes independent of the radius:

$$L_{\max} = 2.84 \sqrt{\frac{\gamma_{lv}}{\rho_l \cdot g}} \quad (4.1)$$

where γ_{lv} is the surface tension of the melt, ρ_l the density of the melt and g the acceleration due to gravity.

The maximum zone height depends on the material parameters as shown in Table 4.1. The factor 2.84 in Equation (4.1) may slightly vary between 2.62 and 3.18 according to other theoretical approaches (see [Bohm 1994], p. 219).

In general, a crucible-free method is only possible if surface tension and density of the melt enable a stable molten zone which does not spill out. Si, with its high surface tension and low density, is a unique element which allows molten zones high enough to grow the largest FZ crystals. Today, FZ Si is grown with a maximum diameter of 200 mm. This is possible with the needle-eye technique, where the waist-shaped molten zone, which is drawn through the inductor hole, does not exceed the maximum zone height (Figure 4.1a).

Table 4.1 Density of the melt ρ_l , surface tension γ_{lv} at melting point and maximum zone heights L_{max} of materials

Material	ρ_l (kg m ⁻³)	γ_{lv} (N m ⁻¹)	$\gamma_{lv}/\rho_l 10^{-4}$ (s ⁻² m ³)	L_{max} (mm)
Ti ^b	4130	1.65	4.00	18
Si ^a	2580	0.88	3.41	17
Co ^b	7750	1.87	2.42	14
Ni ^b	7900	1.78	2.25	14
Mo ^b	9099	2.25	2.47	14
Cu ^b	8000	1.30	1.63	12
Ge ^b	5490	0.62	1.13	10
Ag ^b	9330	0.97	1.04	9
GaAs ^c	5400	0.45	0.83	8
GaSb ^c	6030	0.47	0.78	8
Sn ^b	6980	0.56	0.80	8
Au ^b	17400	1.17	0.67	7
Pb ^b	10670	0.46	0.43	6

Data from ^a[Ratnieks 2008], ^b[Iida 1993] and ^c[Tegetmeier 1996].
 For many substances, such as intermetallic compounds, accurate parameters are not known.

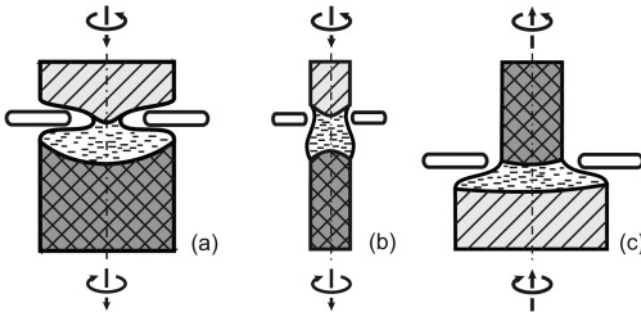


Figure 4.1 Schemes of FZ techniques: (a) with needle eye; (b) without needle eye; (c) pedestal growth. The dark hatched area is the growing crystal, the lighter hatched area is the feed rod and the white dashed area is the molten zone.

From Table 4.1, Ti seems to be just as suitable for the FZ process as Si. Irrespective of the fact that there is, so far, no important need for single-crystalline Ti, a phase transition from the cubic to hexagonal phase at about 880 °C prevents obtaining a single crystal. Other semiconductors of higher density, like Ge and GaAs, or heavy metals like Au, allow only small melting zones to be stable, leading to correspondingly small crystal diameters (e.g. <10 mm for GaAs).

In principle, higher molten zones are possible under microgravity. Nevertheless, the length of the molten zone is also limited: a liquid cylinder between two rods is not stabilized by the surface tension if its length exceeds its circumference (Rayleigh limit). In this case, a small perturbation of the melt surface allows the liquid cylinder to break down. FZ crystal growth under microgravity was investigated during space missions: e.g. a GaAs

crystal 20 mm in diameter which had a zone length of 20–24 mm when grown [Herrmann 1995] and two GaSb crystals 16 mm in diameter which had a zone length of 13–14 mm [Cröll 1998]. These zone lengths in space were more than twice the size of those possible on Earth; see section 2.2. A summary of the results concerning the dynamic stability of the FZ process can be found in Chapter 2, section 2.5.

The pedestal technique, equally crucible-free, is similar to the FZ process but with a reversed set-up. The feed rod below the inductor is molten at the top and the crystal is pulled upwards. This technique was introduced by several authors [Dash 1958, Dash 1960, Poplawsky 1960]. Here, the diameter of the growing crystal is always smaller than that of the feed rod. From the viewpoint of capillarity, the pedestal process is comparable to the Czochralski growth method as described in Chapter 3, although without a crucible.

Figure 4.1 shows schematics of possible FZ configurations. The heat transfer of the FZ technique is characterized by competition between the power for heating a narrow zone from outside and energy dissipation via the liquid and solid surfaces. Considering the heat dissipation by surface radiation and heat conduction, the power needed to establish a zone is governed by the dimensionless Biot number (Bi) independent of the mode of heating. It describes the ratio between the heat transfer by radiation and that by conduction. [Kobayashi 1978, Otani 1984].

$$Bi = \frac{\varepsilon \sigma r_c}{\lambda} T_m^3 \quad (4.2)$$

Here, ε is the emissivity, σ the Stefan–Boltzmann constant, r_c the crystal radius, λ the heat conductivity and T_m the melting point temperature. If Bi is relatively small, the heat transfer of the zone is conduction-dominated, which means that the heat is mainly dissipated through the solid–liquid interfaces, whereas a considerably larger Bi means that the heat is mainly dissipated through the outer zone surface (for materials and numbers see Table 4.2). Additional convective and conductive heat transfers to a surrounding gaseous growth are not considered in Equation (4.2) but should be considered in the

Table 4.2 *Melting temperatures of some materials and respective Biot numbers of rods with 10 mm diameter [Kobayashi 1978, Otani 1984] Copyright (1978) [Elsevier Ltd]*

Material	T_m (°C)	Bi
Cu	1083	2×10^{-4}
Mo	2610	0.02
Si	1412	0.06
Ge	937	0.03
W	3377	0.05
TaC	3527	0.12
LaB ₆	2715	0.18
TiC	2827	0.18
ZrB ₂	3037	0.19
Cr ₂ O ₃	2265	1.86

case of comparably low radiative heat dissipation (small emissivity, low crystallization temperatures).

In all FZ methods the feed rod as well as the crystal is rotated to homogenize the temperature field. Normally, feed rod and crystal are rotated in opposite directions, but co-rotation or no rotation is also possible.

In this chapter, the different crucible-free methods of crystal growth are described in detail for various heating methods and the corresponding suitable materials: RF heating in section 4.1, optical heating in section 4.2. Numerical simulation is an important aspect of modern FZ Optimization, it is described in detail for Si in section 4.3.

4.1 FZ Processes with RF Heating

4.1.1 FZ Method for Si by RF Heating

The FZ melting of Si is the most important commercial application of this technique. The basis for the growth of Si single crystals is a sufficiently pure Si feed rod of a diameter comparable to that of the crystal to be grown. Siemens started the production of polycrystalline Si rods by chemical vapour deposition in 1953. Beginning with an electrically heated Si filament, the so-called slim rod, ultra pure trichlorosilane (SiHCl_3) pyrolytically decomposes on the rod surface at about 1100°C . This process is known as the ‘Siemens process’ [Zulehner 2000]. Silane (SiH_4) can be used at about 850°C instead of trichlorosilane. With the Siemens process, feed rods of up to 200 mm diameter can be produced for FZ crystal growth.

4.1.1.1 General FZ Setup

The FZ growth chamber as shown in Figure 4.2b has to have a tightly closing chamber door and can be filled with a growth atmosphere that is inert to Si such as Ar (plus additives) or vacuum. The upper and lower vertical spindles (Figure 4.2b, c2, 9) are fed through the top and bottom walls of the growth chamber. Their ends carry mounts for the cylindrical Si feed rod at the top (Figure 4.2b, c3) and the seed crystal at the bottom. The spindles can both rotate and translate. A one-turn RF induction coil (Figure 4.2b, c5), which is connected to the RF power generator (Figure 4.2b, c12), is placed between them. The inductor is a ring-shaped one-turn coil, commonly a flat ‘pancake’ inductor (Figure 4.3). It has to be water-cooled to prevent overheating. The two important functions of the inductor are homogeneous melting of the feed rod and stable cylindrical growth of the crystal.

During the growth process, the inductor encloses the FZ without contacting it (Figure 4.2b, c11). The liquid Si molten from the feed rod flows through the inner hole of the coil and crystallizes below. For bigger crystals, the lower spindle carries a mechanical crystal-supporting device (Figure 4.2b, c8).

Optionally, special shields that reflect or back-diffract the heat radiation emitted from the Si can be placed around the crystal and/or the feed rod so as to achieve optimum temperature gradients for the crystallization and melting conditions, respectively.

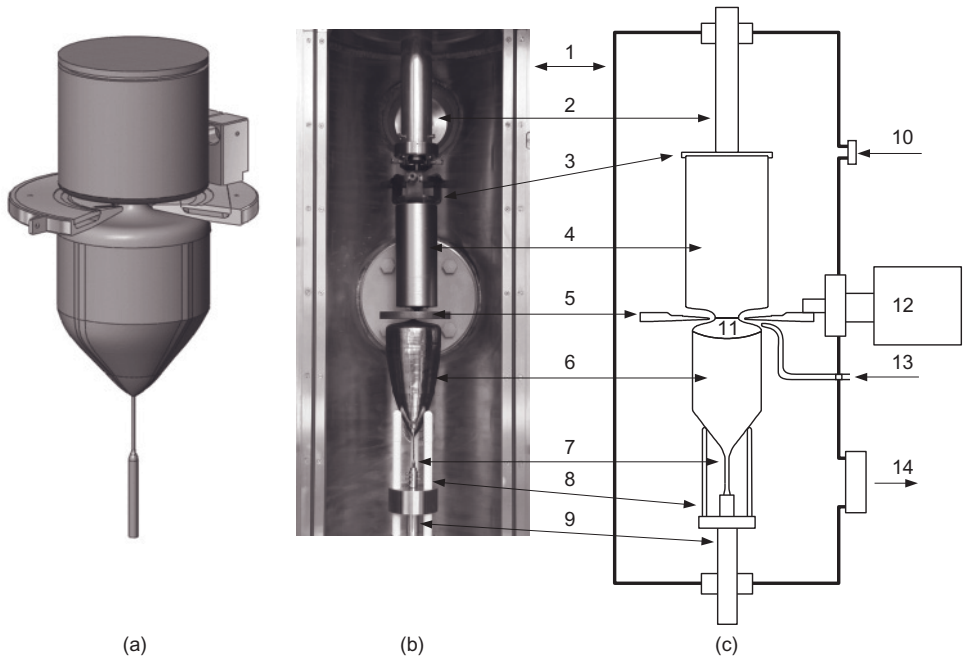


Figure 4.2 The FZ process: (a) three-dimensional scheme, (b) model set-up of the chamber, (c) cross-section through a growth chamber. 1, growth chamber; 2, upper spindle; 3, rod holder; 4, feed rod; 5, induction coil; 6, growing crystal; 7, seed with thin neck; 8, crystal support; 9, lower spindle; 10, gas inlet; 11, molten zone; 12, RF generator; 13, doping gas; 14, pump.

4.1.1.2 Basic Process Steps

After the setup is assembled, the chamber evacuated and then filled with the protective gas atmosphere, the lower end of the feed rod is preheated and inductively melted until a drop of liquid Si hangs over the inductor hole (Figure 4.4a). It does not fall because adhesion, surface tension of the melt and electrodynamic forces act against gravity and stabilize the free melt surface of the drop. Then, the rod-like crystalline Si seed of about 5 mm diameter is slowly moved upwards to the drop, dipped into it and melts back, smoothing the seed–melt interface. After this, the seed is moved downwards with a rather high pull rate of 8–16 mm/min, whereby the heating power is reduced. The reduced power lets the melt zone shrink to a diameter and height of a few millimetres. In this manner, the so-called thin neck [Dash 1958] is grown with a high crystallization rate. Under these conditions, grown-in dislocations leave the crystal when they cross the surface, and new dislocations are not generated because the thermomechanical stress is very small for a growth diameter of 2–3 mm. After a few centimetres of pull length, all line dislocations are eliminated in the thin neck. Because of their high energy of generation, new dislocations are now highly unlikely. This necking after Dash works well, if the $\langle 110 \rangle$ main direction of the dislocations is not the growth direction of the crystals. So, dislocation-free single-crystalline FZ crystals of $\langle 100 \rangle$ and $\langle 111 \rangle$ orientations can be grown, whereas the

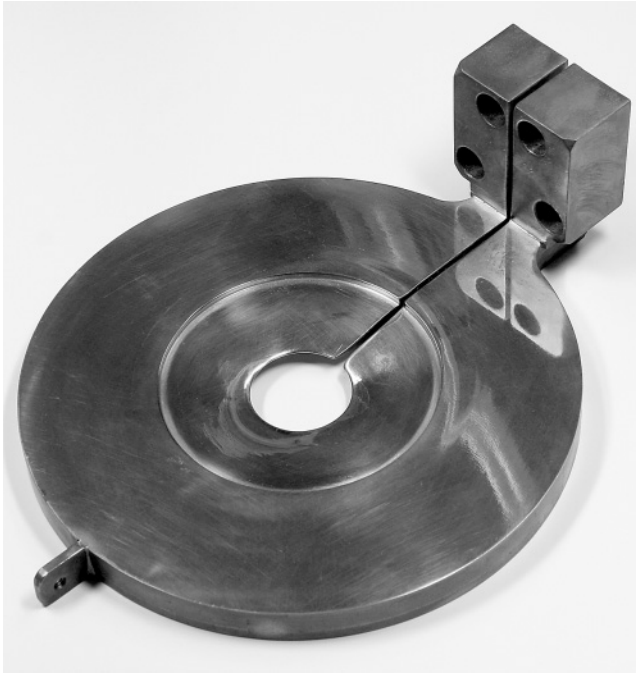


Figure 4.3 RF induction coil with central hole, slit and connecting flanges to the coaxial feed-trough and the cooling-water supply.

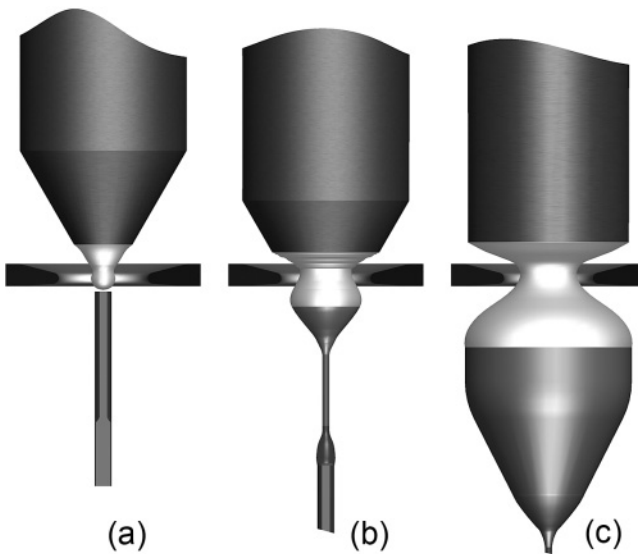


Figure 4.4 Process phases of the FZ needle-eye process (for diameters <math><30\text{ mm}</math>): (a) hanging drop; (b) growing cone; (c): stable crystal growth.

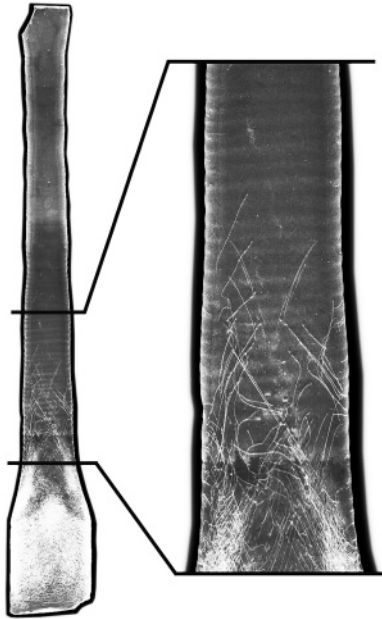


Figure 4.5 X-ray topogram of a $\langle 111 \rangle$ thin neck (5 mm \times 40 mm) with vanishing dislocations, enlargement on the right: no further dislocations after about 20 mm.

$\langle 110 \rangle$ orientation will not enable dislocation-free crystals, because not all dislocations leave the thin neck. Figure 4.5 shows the disappearing dislocations in the X-ray topogram of a grown $\langle 111 \rangle$ thin neck.

After growing the thin neck, the crystal diameter is increased. By increasing feed rate and RF power, the cone is enlarged until the final diameter of the crystal is reached (Figure 4.4). The pull rate of the crystal is lowered to typically 2–5 mm/min depending on the crystal diameter. If, for once, crystals with dislocations are acceptable, the thin-neck phase is omitted.

Commonly, feed rod and crystal are rotated in order to average thermal deviations of the rotational symmetry, e.g. of the induction heating, what results in an approximately circular crystal cross-section and a crystallization interface with only slight deviations from symmetry due to the crystal-inherent anisotropy.

4.1.1.3 Forces Acting on the Melt Zone

The forces acting on the FZ during the FZ growth process are of different physical origins: inertia, buoyancy, surface tension, thermocapillarity and electrodynamics.

The crystal rotation, which can optionally be modulated, causes centrifugal and Coriolis forces which influence the zone shape and cause melt flow. The electrodynamic laws define the RF current distribution (e.g. the skin effect) and produce temperature differences in the melt which generate buoyancy convection as well as gradients of the surface tension which are the origin of Marangoni convection.

Generally, the surface tension, which itself is temperature-dependent and so varies along the free surface, shapes the melt zone. Last but not least, the electrodynamic interaction between the RF magnetic field and the induced current field results in repulsion forces according to Lenz's rule which can deform the zone shape and drive the electrodynamic melt flow, if there are tangential forces.

4.1.1.4 Growth Angle

For the FZ crystal growth of Si, Ge, GaAs or GaSb with a constant diameter, a material-specific angle α appears between the vertical crystal surface and the tangent of the melt surface at the solid–vapor–liquid (svl) line which is independent of gravity, growth rate, diameter and some other parameters. This phenomenon is experimentally and theoretically investigated in the works of various authors, e.g. [Surek 1975, Voronkov 1963, 1974, 1978] and is described and studied in detail in Chapter 1, section 1.3. Tegetmeier [Tegetmeier 1995] worked out that, as a consequence of the minimal overall surface energy of the melt zone during crystal growth, the zone shape and especially the growth angle α is related to the ratios of the specific energies of the interfaces between the liquid, solid and gaseous phases. Under the assumption of a horizontal solid–liquid growth interface and a constant crystal diameter, we can conclude that

$$\gamma_{lv} \sin \alpha = \gamma_{sl}, \quad (4.3)$$

where γ_{lv} is the liquid–vapour interface energy (surface tension) and γ_{sl} the solid–liquid interface energy. Furthermore, Tegetmeier conducted that, for $\gamma_{sl} \ll \gamma_{lv}$, a zero growth angle, $\alpha = 0$, leads to $\gamma_{sl} = 0$ and $\gamma_{sv} = \gamma_{lv}$ which means that melt and solid (at the svl triple-phase line) do not differ with regard to the surface energies.

An experimental determination of the growth angle from photographs is difficult for Si, because it is difficult to get good photographs. Therefore, in [Tegetmeier 1995] the values for the growth angle α of Si range from 6° to over 12° . Figure 4.6a shows a new photograph of a FZ process taken by the authors which is suitable for determining this angle. Various photographs were taken at the same position during this process. Evaluating 17 photographs similar to the one in Figure 4.6, the angle α was determined to be $11.5^\circ \pm 1.9^\circ$. Further investigations of this phenomenon will be presented later.

4.1.1.5 Stability of the FZ

The shape of the free melt surface is defined by the equilibrium of the acting forces as mentioned above. The question is, however, whether the zone is stable or unstable and where the (metastable) transition is.

It is necessary but not sufficient that the zone is in static equilibrium, i.e. its height does not exceed a certain limit which depends on diameter, gravity, surface tension and some other material constants. Additionally, the zone must be dynamically stable. A small mechanical disturbance, or any other type of disturbance, must not lead to self-amplifying shape changes which would lead to spilling out of the melt and an interruption of the zone.

The Laplace–Young equation (4.4) (see Chapter 1 for the details) describes the pressure balance for a stable molten zone:

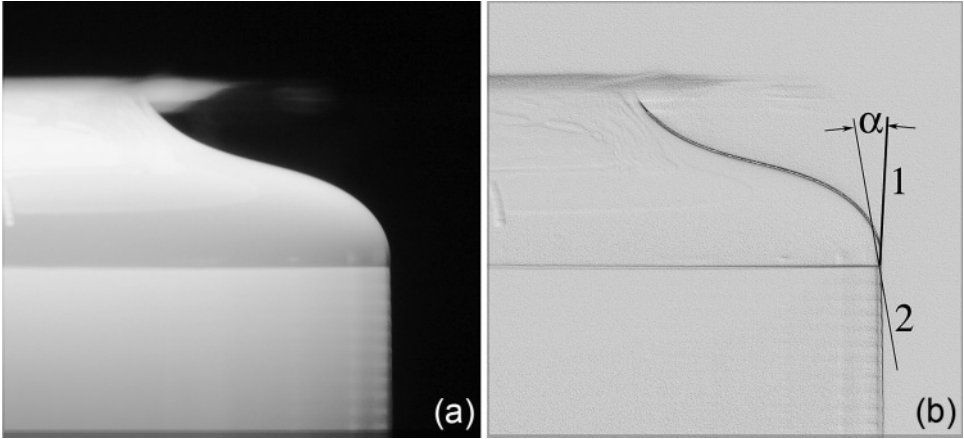


Figure 4.6 (a) Photograph of the growth angle during the FZ process of a 2'' Si single crystal; (b) growth angle α between the tangents 1 and 2; from this photograph, a value of $\alpha = 11.2^\circ$ can be derived.

$$\gamma_{lv}\kappa = p_0 - \rho_l g z + F_n \quad (4.4)$$

where κ is the curvature, z the coordinate for the height of the melt, $\gamma_{lv}\kappa$ the capillary pressure, $\rho_l g z$ the hydrostatic pressure, F_n the EM pressure and p_0 the isostatic pressure in the melt at $z = 0$. Generally, the value of p_0 is computed from the specific configuration of the molten zone: see Chapter 8 for examples of the computation of p_0 for different crystal growth processes. In the case of FZ, there is no simple way to compute p_0 which is controlled by the shape and volume of the molten zone. If it is too big, the angle at the svl triple-phase line is forced to exceed its steady-state value until the melt flows out over the svl line. On the other hand, if p_0 is too small, which means there is not enough melt in the zone, the melt neck will narrow and the surface tension force, rising with surface curvature, will strangle the neck with the result of zone separation and the end of the process.

Considered in more detail, the growing FZ crystal is not a perfect cylinder, mainly because of the inherent crystal anisotropy. The undercooling of the melt which is needed for the crystal to grow depends on the crystallographic orientation. Therefore, the crystallization interface is not absolutely equivalent to a distinct isothermal face. In particular, positions where the $\langle 111 \rangle$ direction crosses the svl line are exceptional, because the crystallization rate is slowest in the $\langle 111 \rangle$ direction and fastest perpendicular to $\langle 111 \rangle$. The svl line therefore moves downwards in a groove, with the consequence that the melt leans outwards a little more there and the crystal surface does, too. This effect stops if the crystal periphery comes close to a $\langle 111 \rangle$ face at that position and results in a mirror-like outer facet. There, the increased surface of the generated bulge causes an enhanced heat loss which locally lowers the temperature, lets the position of the svl line rise; both melt meniscus and crystal periphery retract back towards the initial position and the cycle can start again. Such bulges are well known for $\langle 111 \rangle$ FZ crystals, whereas for the $\langle 100 \rangle$ growth direction, because of the steeper angle of the $\langle 111 \rangle$ faces, this effect becomes steady-state with the result of straight ridges along the growth direction. Figure 4.7 shows

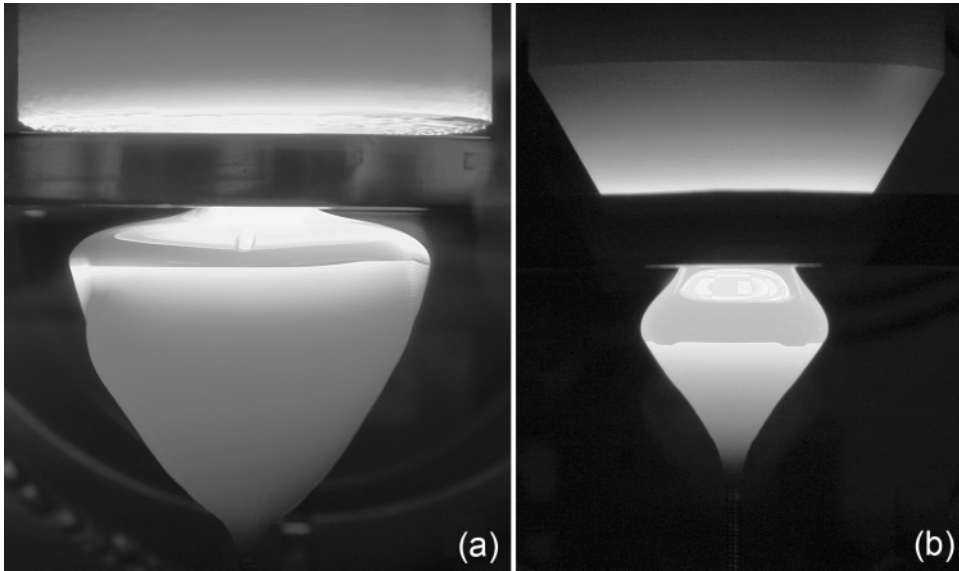


Figure 4.7 Pulling the cone of FZ crystals in (a) $\langle 111 \rangle$, (b) $\langle 100 \rangle$ growth direction.

two crystals, one growing in the $\langle 111 \rangle$ direction (Figure 4.7a), the other in the $\langle 100 \rangle$ direction (Figure 4.7b). The different shapes of the cones as well as the occurrence of bulges for the $\langle 111 \rangle$ crystal are obvious.

Of course, the crystal diameter strongly influences the stability of the zone. With increasing diameter, up to about 20 mm, the maximum zone height also rises and approximates a limiting value for large diameters, which is 16 mm for Si (see Table 4.1 and Equation 4.1). The needle-eye technique enables us to generate such zones for large diameters. Therefore, in principle, the maximum diameter of FZ crystals is not limited by capillary effects. The problems when increasing the diameter arise from the design of the RF inductor and will be described in the next section.

4.1.1.6 Melting the Feed Rod

The RF induction coil (Figure 4.3) has to ensure two different functions in the FZ process for Si: under it, the FZ has to be established with the thermal and capillary conditions for crystal growth; above it, the feed rod must be molten so that a slightly conical and smooth open melting front is formed. If there were hillocks or spikes of solid Si remaining at the melting front, they would be less heated by the RF field and touch the coil surface sooner. In other words, a large temperature gradient is necessary at the open melting front which can be achieved by the RF skin layer δ , in which, for high frequencies, the current flows mainly at the outer surface:

$$\delta = \frac{1}{\sqrt{\frac{1}{2} \omega \mu_0 \mu_r \sigma_{el}}} \quad (4.5)$$

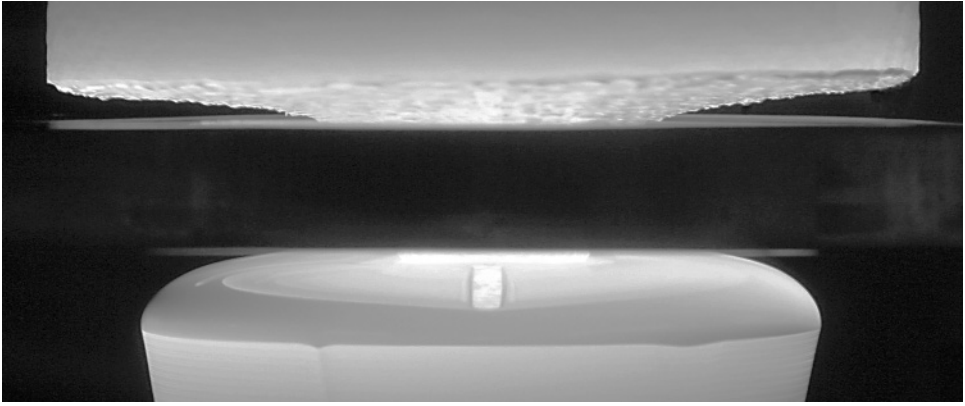


Figure 4.8 FZ process for Si; the inhomogeneous melting front at the feed rod on top is nicely visible.

where δ is the skin depth, ω the angular frequency, μ_0 and μ_r the absolute and the relative permeabilities and σ_{el} the electrical conductivity of the melt. The skin depth δ must be small enough so that the surface of the rod is predominantly heated. This condition is fulfilled if the RF frequency is higher than 2.5–3.0 MHz, which yields a skin depth of 0.27–0.29 mm for Si with $\sigma_{el} = 1.2 \times 10^6$ S/m.

Especially for the needle-eye case, the open melting front is laterally inhomogeneous and consists of small solid islands 1–2 mm in size which are surrounded by the melt because the Si melt does not perfectly wet the solid Si. This circumstance has to be borne in mind particularly for the numerical calculation of the shape of the melting front. Figure 4.8 shows the conical melting front in a FZ growth process. It can be seen that the melt front consists of solid islands and liquid puddles.

For larger diameters, it gets technically more and more difficult to design a suitable flat inductor which is able to melt large rods and to achieve crystal diameters of 200 mm or even more.

4.1.1.7 Pedestal Growth

In the reverse of the FZ process, the pedestal method delivers Si crystals pulled from an inductively heated melt reservoir on top of a cylindrical feed rod. Because of the high surface tension of molten Si, the melt can be held securely on the Si pedestal. For crystals less than 10–15 mm in diameter, a pedestal of the same diameter or slightly bigger is sufficient. For larger crystals, the diameter of the pedestal must be considerably larger. This is a disadvantage compared to the FZ method, where the crystal can be up to 20% thicker than the feed rod. However, the growing crystal hangs on the seed and is therefore mechanically stable. The maximum crystal diameter is defined by the inductor hole. Very long Si crystals with diameters up to 50 mm (Figure 4.9 shows a growing crystal of 40 mm diameter) or polycrystalline slim rods 5–8 mm in diameter and several metres in length can be pulled by the pedestal growth. Industrially these slim rods are pulled by pedestal growth as starting material for the Siemens process for producing polycrystalline Si feed rods for the FZ and Cz methods.

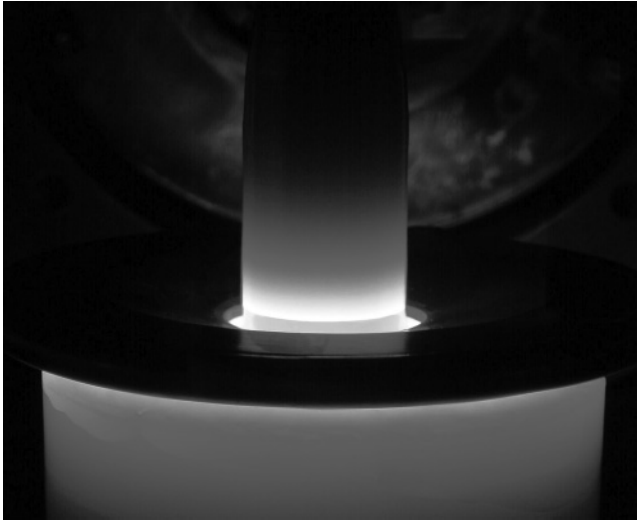


Figure 4.9 Pedestal growth of a 40-mm diameter Si crystal; the diameter of the pedestal is 135 mm.

In addition, monocrystalline Si fibres less than 1 mm thick can be grown by this method, as demonstrated by the present authors [Riemann 1996].

4.1.1.8 Growth of FZ Crystals with Quasi-Square Cross-Section

As already mentioned, and contrary to general opinion, a growing FZ crystal does not have to rotate. It is clear that, in this case, the temperature field is no longer rotationally averaged and the cross-section of the crystal can differ from a circular one. The cross-section of such a crystal is formed by the temperature field caused by the geometry of the heating coil and the anisotropy of the surface tension.

Figure 4.10 shows a FZ crystal growing without rotation. To reach this state, the FZ growth started in the usual way up to the steady-state diameter of the crystal. After that, the RF power and the feed rate were slightly decreased in order to reduce the volume of the molten zone according to the size of the square to be grown, then the crystal rotation was stopped, and, from then on, this crystal grew dislocation-free and square until the end. The inductor applied for this experiment has four diagonal slits and generates a temperature field of almost square symmetry. The main slit in the inductor, which has to form the current loop is not completely equivalent to the other three slits, however, as shown in Figure 4.11b. Furthermore, the surface tension rounds off the corners, minimizing the melt surface. This effect is undesirable because the practical goal of this project is square wafers cut directly from the crystal. On the other hand, on the straight sides, where the curvature is almost zero, growth instabilities can occur. For applications in the solar power industry, it is essential to get a stable cross-section approximating a square as effectively as possible, to save material losses and costs in cutting a round crystal into a square one.

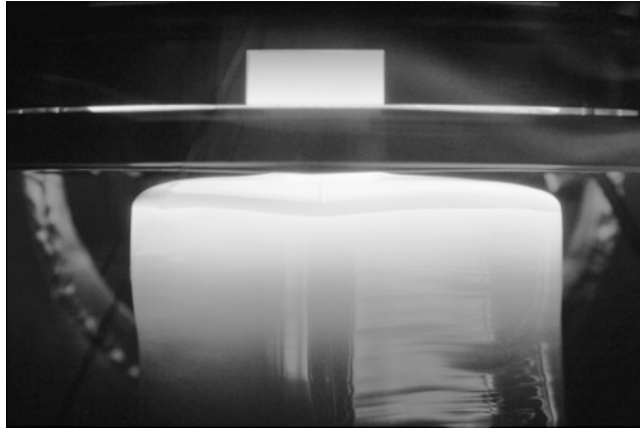


Figure 4.10 Growing a single-crystalline Si FZ crystal with a quasi-square shape (the feed rod on top of the dark coil is mostly covered by a heat shield).

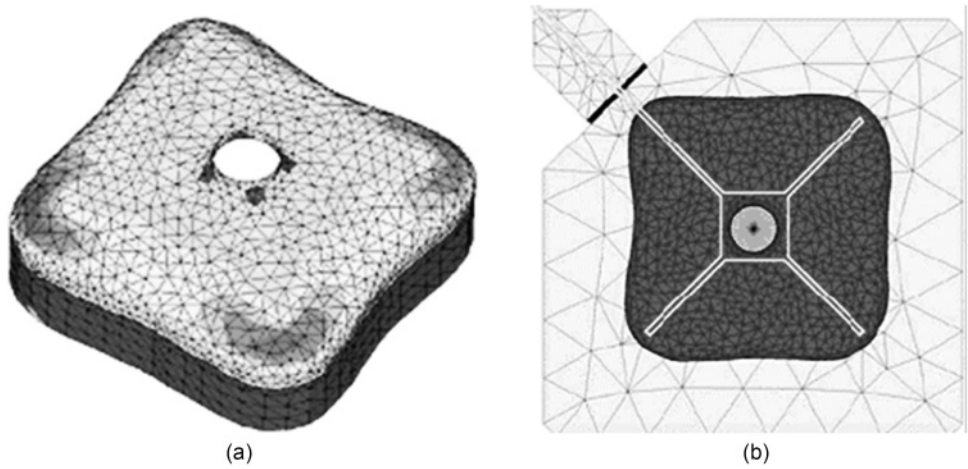


Figure 4.11 Numerical modelling for crystals grown without rotation: (a) molten zone; (b) inductor and calculated shape of the cross-section [Muiznieks 2006].

Later in this section, it will be shown how numerical modelling can support process development. Also for this application, calculations were done [Muiznieks 2006] in order to find out whether a symmetrical square cross-section is possible. Even with a rather simple inductor, the numerical calculation shows that it should be possible to form a useful crystal shape (Figure 4.11).

4.1.1.9 Comparison between Experiment and Numerical Results

As will be seen in section 4.3 below, numerical modelling of the FZ process can include almost the complete set of physical phenomena involved in the FZ process, partly in three dimensions, and deliver amazingly detailed results. The question is how to compare those numerical results with the experimental reality.

Because of the good view of the FZ process through the large windows of the growth chamber (Figure 4.12), the free melt surface can conveniently be photographed. The free surface can therefore be compared with the solution given by solving the Young–Laplace equation (see equation 4.4 and Chapter 1 for details). This equation is parameterized through the arc length s , which leads to a system of three differential equations [Lie 1990]. In our program, we use the dimensionless form of the equation:

$$\begin{cases} \frac{d\tilde{r}}{ds} = \sin(\beta) \\ \frac{d\tilde{z}}{ds} = \cos(\beta) \\ \frac{d\beta}{ds} = \frac{\cos(\beta)}{\tilde{r}} + \tilde{z} \cdot Bo + \frac{1}{4} Bo_{em} \tilde{J}(\tilde{z})^2 + La \end{cases} \quad (4.6)$$

where the coordinates r and z are reduced to the dimensionless form through the crystal radius r_c : $\tilde{r} = r / r_c$ and $\tilde{z} = z / r_c$, Bo is the Bond number $Bo = \rho_l g r_c^2 / \gamma_{lv}$ with ρ_l the density of liquid Si, γ_{lv} the surface tension of liquid Si, \tilde{J} the dimensionless surface current density, La the dimensionless isostatic pressure (Laplace number) $La = p_0 (r_c / \gamma_{lv})$ with p_0 the isostatic pressure and Bo_{em} the EM Bond number $Bo_{em} = V_0^2 / \mu \gamma_{lv} \omega^2 r_c^3$ with μ permeability, ω angular frequency of the RF field and V_0 the applied voltage. The angle β is measured clockwise starting from the direction of the z -axis.

The white curve in Figure 4.13a, which is overlaid with the picture taken from the process, was calculated without considering the electrodynamic forces and shows devia-



Figure 4.12 FZ machine in operation (pedestal experiment); large windows for process observation are available at the front and on both sides.

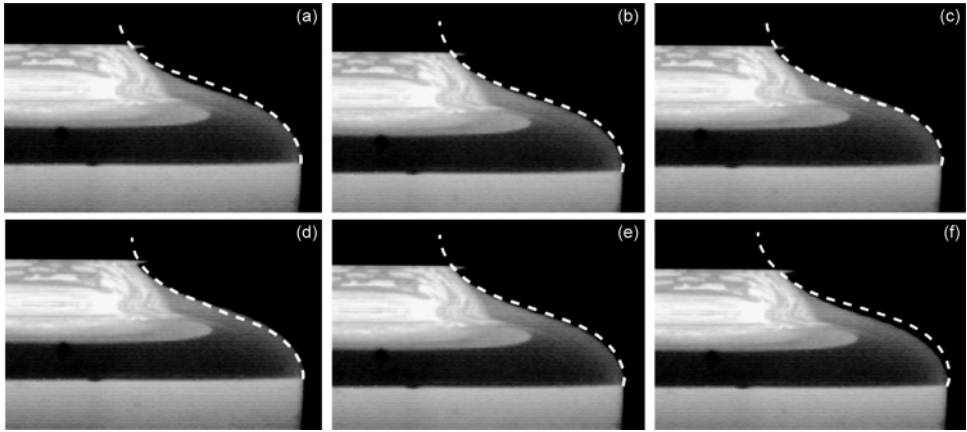


Figure 4.13 FZ process photograph (diameter 52mm) with overlaid calculated free surface curves: for different voltages (at 11°): (a) 0V, (b) 500V, (c) 650V and starting angles (at 500V): (d) 0° , (e) 11° (growth angle α for Si), (f) 20° , all fitting the same second point taken from the photo: $Bo = 21.43$; La , Bo_e (a) 7.68, 0; (b) 9.16, 40.69; (c) 10.06, 68.76; (d) 8.45, 40.69; (e) 9.16, 40.69; (f) 9.68, 40.69.

tions to the free surface in the photograph. Therefore, the additional EM forces caused by the RF heating have to be taken into account by calculating the surface current density \vec{J} in Equation (4.6) according to [Lie 1990]. The system of equations (4.6) is solved by a Runge–Kutta procedure. The initial conditions are $\tilde{r} = 1$ and $s = 0$. The initial angle corresponds to the growth angle α , see section 4.1.1.4. The first parameter, the Bond number, can be calculated from the material constants. For determining the second parameter, the Laplace number, a second point must be chosen from the photograph of the free surface. Normally one would choose the inner triple point, but this point, seen in Figure 4.13, is covered by the induction coil. So, a good viewable point at about 95% of the visible melt height is taken instead. Newton's algorithm is used to fit that second point by starting not too far from the solution and calculating the height for the radius of the second point by fitting the pressure La .

An example program to calculate the free surface shape of an axisymmetric zone without EM forces is given in the Appendix to the chapter. For this initial free surface, the white line in Figure 4.13a, the surface current density is calculated and iterated between fitting the Laplace number and calculating the surface current density, until the Laplace number does not change within a certain numerical precision. The third parameter, the electrical Bond number, is chosen to fit the free surface for a starting angle of about 11° , the value of the growth angle, see section 4.1.1.4.

Figure 4.13 shows the same photograph of the free surface throughout. In the upper row, the white curves are the solutions for three different inductor voltages V_0 (at a starting angle of 11°): (a) 0V, (b) 500V, (c) 600V. In the lower row are the solutions for three different starting angles (for $V_0 = 500$ V): (d) 0° , (e) 11° , (f) 20° . Without the EM forces, the calculated free surface could not be fit to the one in the photograph for a starting angle of 11° (Figure 4.13a). With increasing EM forces, the calculated free surface decreases and reaches a good agreement with the photograph for a value of 500V, as seen

in Figure 4.13b. For a higher voltage V_0 , the starting part of the calculated curve goes below the real free surface as seen in Figure 4.13c. The changes are only seen in the starting part of this curve because the end of the curve is fixed by the algorithm. The solution with a fixed voltage of 500 V and a starting angle of 0° lies below the real free melt surface (Figure 4.13d), and for 20° it lies above it (Figure 4.13f).

For further comparison, the interior of the molten zone and growing crystal as well as the shape of the solid–liquid interface are not visible *in situ*. Lateral photovoltage scanning (LPS) [Lüdge 1997] is one method that can visualize how the crystal grew inside on an axial sample cut from the crystal. A focused light spot is scanned over the rectangular sample. The voltage between two contacts at opposite edges is a measure of the resistivity gradient at the focus position and visualizes the dopant striation pattern. Striations are generated by a fluctuating incorporation of dopant at the crystallization interface due to changes of the local temperature and melt convection flow in the liquid boundary layer.

A sample prepared for LPS needs a smooth surface, preferably a polished one, in order to get the highest possible signals. Figure 4.14 shows the LPS plot of an axial section from a 2" FZ crystal. To extract a representative striation line from the measurement, all pairs of adjacent axial LPS line scans are correlated and their shift is determined. The experimental interface shape derived in this manner can be compared to the numerically simulated one. The measured and calculated phase boundaries are plotted into the LPS scan of the 2" Si sample as shown in Figure 4.14. The simulated interface was computed by calculating the temperature field of the FZ process with the same parameters used for the growth of the 2" crystal from which the sample for LPS was prepared. For this computation, the commercial program FEMAG FZ [Bioul 2007] was used, where the convection in the melt was neglected. A detailed description of numerical analyses of the FZ process is given in section 4.3.

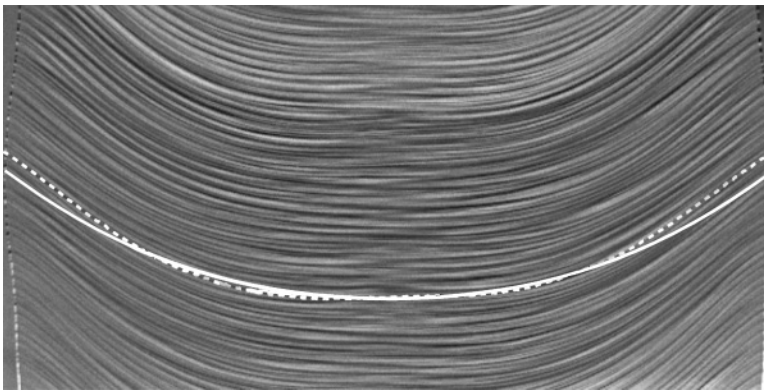


Figure 4.14 LPS plot of a 52 mm \times 20 mm single-crystalline Si sample grown at 3.2 mm/min. The solid white line is the calculated phase boundary deflection = 9.1 mm; the white dashed line is the phase boundary derived from the measurement, deflection = 11.0 mm.

Figure 4.14 shows that the measured and computed curves coincide well, but also that there are some small deviations. These can be caused by not taking the heat transport by melt convection into account in the computation. The melt flow has a small but noticeable influence on the temperature field, which can, when neglected, result in deviations to the measured phase boundary. For different melt zone dimensions and for different FZ process parameters, considerable changes take place in the interplay of the acting forces. Therefore, such a comparison between experiments and calculations must be done for changing process conditions in order to be sure that the computations fit reality.

4.1.2 FZ Growth for Metallic Melts

In the FZ crystal growth of intermetallics by RF heating, a cone-shaped single-turn or double-turn coil is usually applied as an external heat source (Figure 4.15). The alternating EM field couples directly to the material. This makes it easy to design different coil forms to obtain the correct shape of the growing interface so that a proper crystal is obtained.

Anisotropic interface energies can lead to facets on the surface of the growing crystal and to large deviations from the axisymmetric zone form [Mazilu 2007], as shown in Figure 4.16.

For the FZ growth of metallic melts, as for Si (section 4.1.1.6), a suitable frequency has to be used which allows the feed rods to melt. For a frequency of 250kHz, the skin depth δ is 0.47mm for Cu, 0.92mm for Ni, 0.9mm for Mb and 1.84mm for TiC. The heat diffuses from the outer heated zone to the centre of the rod. Above and below the radiated region, the isotherms of the rod become concave because of radiation and convection cooling by the ambient gas. The radial temperature distribution in the zone and the solid–liquid interface shape depend on the ratio δ/r . The interface shape is normally convex (towards the melt) in the central part of the zone. For large values of δ/r , there is a sizeable part of concave interface curvature near the rod surface (Figure 4.17). With increasing overheating of the zone (beyond the melting temperature), the radial heat flow

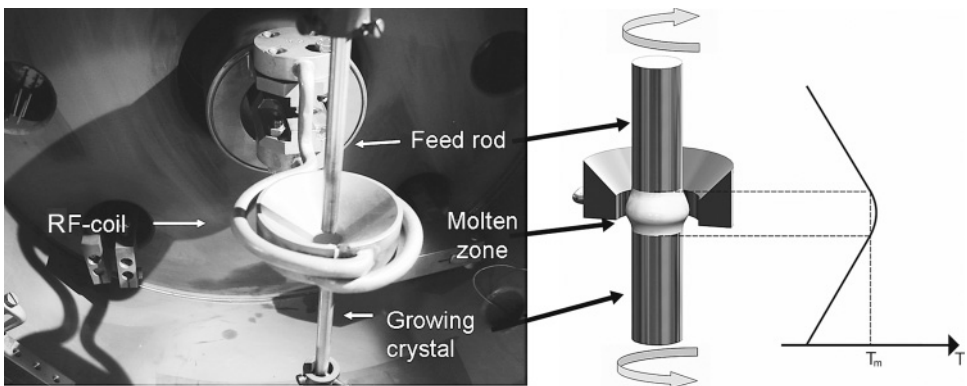


Figure 4.15 Vacuum chamber of a FZ melting apparatus with RF inductive heating. Right: sketch of the setup with schematic temperature profile (T_m , melting temperature) [Behr 2005-2].

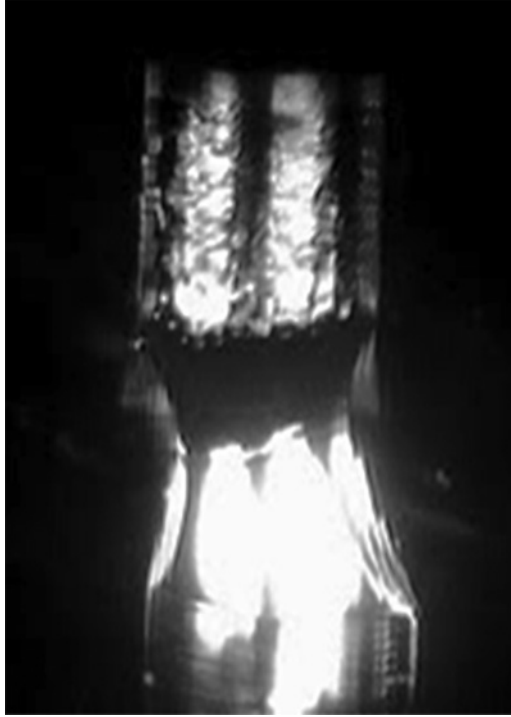


Figure 4.16 Facet (bottom) during the FZ growth of a Gd_2PdSi_3 crystal with upward motion (Reprinted with permission from [Mazilu 2007], copyright (2007) Uni-edition, Berlin).

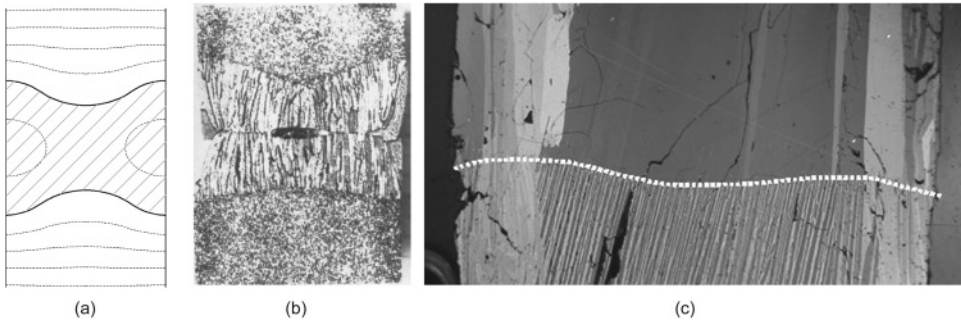


Figure 4.17 (a) Calculated temperature distribution in a Mo rod with melting temperature 2610°C . Isotherms are drawn at intervals of 100K . (b) Photograph of the longitudinal cross-section of the initial molten zone of the Mo rod. (c) Longitudinal cross-section of the molten zone of $Tb_{0.2}Y_{0.8}Ni_2B_2C$ (Reprinted with permission from [Otani 1984], copyright (1984) Elsevier Ltd).

increases until concave isotherms occur in the internal zone also, and the interface becomes concave [Kobayashi 1978, Otani 1984]. This is also the case for large zone lengths.

The slightly concave interface curvature in the outer part of the growing crystal is basically caused by the finite penetration depth of the RF EM field, but it can be intensified by the melt flow driven by EM fields, which transports the hot melt from the surface to the inner region. The concave interface regions may become one serious drawback with RF EM heating in comparison with other heating modes for FZ growth. As shown in Figure 4.17c for the FZ growth of $\text{Tb}_{0.2}\text{Y}_{0.8}\text{Ni}_2\text{B}_2\text{C}$ crystals, polycrystalline surface layers are formed and only the inner part is single-crystalline. This behaviour is typical in processes with slow growth velocities (1–2 mm/h), where nuclei formed on the zone surface can overgrow the seed crystal. In FZ growth with optical radiation (see section 4.2) or electron beam heating, the heat is generated immediately at the surface, and concave interface regions can be effectively circumvented at least for appropriate (short) zone lengths.

4.1.2.1 *Convective Flow in the FZ*

The crystal–melt interface shape and velocity are mainly governed by heat transport in the molten zone by diffusion and convection. The material-dependent Prandtl number $Pr = \nu/D_{th}$ characterizes the relation between convection-driven and diffusive heat transports. The kinematic viscosity ν is a measure of the convection damping, and D_{th} is the thermal diffusivity. The kinematic viscosity in oxide melts ($Pr > 1$) is of the same order of magnitude as for metallic melts, but the thermal diffusivity in metallic melts is two orders of magnitude larger, leading to typical Prandtl numbers of $Pr \approx 2\text{--}3 \times 10^{-2}$. Convection therefore has a sizeable effect in the FZ growth of oxides [Kitamura 1980] but it often plays a minor role in the heat transport for the FZ melting of metals and can only slightly modify the zone shape, which is basically determined by heat diffusion. On the other hand, the ratio between convective and diffusive solute transport is reflected by the Schmidt number $Sc = \nu/D$. Here, D is the diffusion coefficient of solute atoms in the melt. Because for metallic melts $Sc \gg 1$ (typically Sc is of the order 10^2 [Chang 1975]), convection has a much stronger effect on the solute transport than on heat transfer and may lead to composition inhomogeneities in crystals [Barthel 1979, Chang 1975].

Experimental investigations of mass and heat transfer in FZ are very complicated because of the high temperatures and high chemical activities of most of the melts. Computer simulations are one effective way to get a deeper insight into the interplay of heat flow and nonlinear phenomena. In order to simulate convection patterns, the steady state Navier–Stokes equations must be solved numerically [Chan 1992, Chang 1976, Kobayashi 1982, Lan 2003, Mühlbauer 1983]. Another efficient method for visualizing flows is model experiments with transparent fluids such as NaNO_3 [Schwabe 1978], $\text{Na}_{1-x}\text{Cs}_x\text{NO}_3$ or n-decane [Schwabe 2007]. However, since most of the transparent fluids have $Pr > 1$, transferring the results to FZ processes of metals requires care. Moreover, computer simulations are often restricted to two-dimensional axisymmetric problems. Though the potential of simulation has already reached a high level, as shown in section 4.3, a three-dimensional simulation of FZ growth considering all factors, particularly the zone shape, interfaces, and the morphology of the grown crystal, in a self-consistent

manner has not yet been reported. Therefore, only a complex consideration of computer simulations and model experiments, careful studies of temperature profiles, FZs and crystal–melt interface shapes during the FZ process [Hermann 2001] combined with investigations of grown crystals [Barthel 1979, Vaněk 1983] can provide a realistic view of the convection phenomena [Louchev 1996].

The melt convection in the zone is induced by different driving forces which result from the inherent temperature and concentration gradients within the zone and from external factors like crystal rotation and EM fields, as explored in numerous theoretical and experimental studies [Carruthers 1976, Jurisch 1990-2, Lan 2003, Vaněk 1983]. Typical flow patterns in the FZ originating from different driving forces – surface tension, buoyancy, centrifugal and EM forces – are illustrated in Figure 4.18 [Souptel 2005-2]. The resultant flow pattern in actual crystal growth processes is a superposition of forces of different kinds.

The thermocapillary (Marangoni) convection is caused by the temperature-dependent surface tension of the melt on the free surface of the zone (Figure 4.18a). The strength of the thermocapillary convection is governed by the Marangoni number [Chang 1975] which expresses the ratio of a characteristic time for Marangoni-driven flow and a characteristic heat dissipation time:

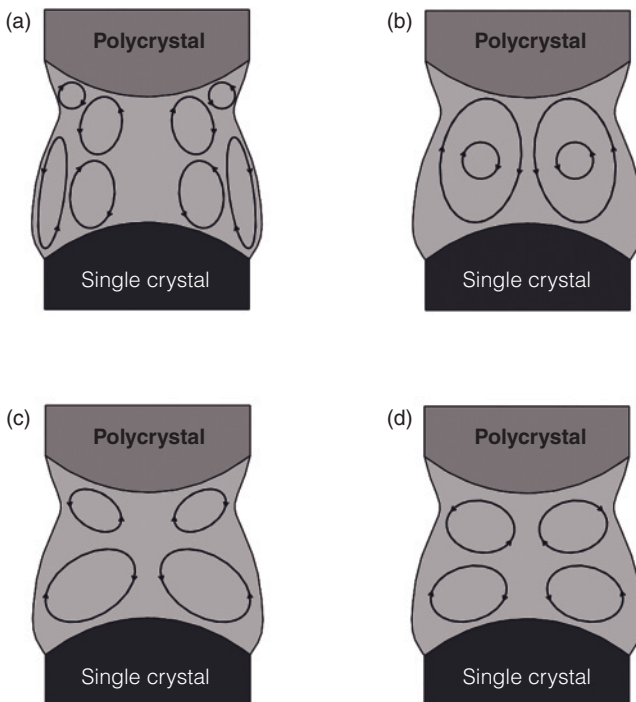


Figure 4.18 Schemes of convective flows in the molten zone: (a) Marangoni convection; (b) natural convection; (c) forced convection driven by crystal and feed rotation; (d) EM convection through RF induction heating.

$$Ma = \frac{|\partial\gamma_{lv}/\partial T| \cdot \Delta T \cdot L}{\rho_l \cdot \nu \cdot D \text{th; thermal diffusivity}}, \quad (4.7)$$

where ΔT is the temperature difference on the free surface of the zone, ρ_l is the melt density and L is a characteristic dimension of the molten zone (normally zone height or rod diameter). For almost all liquids, the temperature coefficient of the surface tension $\partial\gamma_{lv}/\partial T$ is negative and convection flows are directed from the middle of the zone to the solid interfaces along the free surface. The flows are commonly concentrated near the free melt surface and persist even in the presence of other forces, but they are much weaker in the bulk melt. A comprehensive survey of Marangoni convection in crystal growth from the melt is given in Chapter 8.

Because the melt density depends on the temperature, buoyancy forces cause the so-called natural convection, governed by the Grashof number:

$$Gr = \frac{\beta_T \cdot g \cdot \Delta T \cdot L^3}{\nu^2}, \quad (4.8)$$

where β_T is the thermal expansion coefficient and g the acceleration due to gravity. The Grashof number is a ratio between buoyancy force and viscous forces in the melt [Carruthers 1976]. The convectonal flows commonly consist of two large eddies in the bulk melt, which are caused by the up-streaming melt in the outer (heated) part of the zone and the back flow in the centre.

The relative strength of the natural convection in relation to the Marangoni convection is often measured by the dynamic Bond number [Barthel 1979, Schwabe 1978]:

$$Bo = \frac{\beta_T \cdot g \cdot \rho_l \cdot L^2}{|\partial\gamma_{lv}/\partial T|}. \quad (4.9)$$

Bo decreases very fast as the size of the molten zone diminishes. For $Bo < 1$, the Marangoni convection becomes the dominating driving force, which is typically achieved for zone heights less than 5–20 mm [Barthel 1979].

In crystal growth of alloys and compounds, where the melt consists of multiple components, additional driving forces for convection may arise from concentration gradients in the zone, which can generate density differences enhancing the natural convection as well as surface tension differences giving rise to solutal Marangoni flow [Schwabe 1978]. The radial concentration profile of crystals grown from an alloy melt is tightly connected with the local flow direction close to the melt–crystal interface [Barthel 1979, Chang 1975, Jurisch 1982, Lan 1993] and can lead to variations of the physical properties [Souptel 2005-1].

Centrifugal or rotation-driven flows in the FZ are generated by the rotation of crystal and feed rod, as shown in Figure 4.18c. The flow patterns depend on rotation rates, zone size and melt properties. The characteristic rotational Reynolds number is the ratio between inertia forces and viscous forces:

$$Re = \frac{\Omega_c \cdot D^2}{\nu}, \quad (4.10)$$

where Ω_c is a characteristic rotation rate of crystal and feed rod. Forced rotation is intended to homogenize both the temperature and the solute distribution of the FZ in order to improve crystal perfection. The actual flow pattern depends on the rotation method – single rotation, iso- or counter-rotation of crystal and feed rod – and is superimposed by buoyancy and Marangoni forces [Chun 1980, Kobayashi 1982]. The rotation-driven convection pattern is significantly changed in zones of high kinematic viscosity ν , such as zones of Al_2O_3 compared with those of Si. Therefore, in oxide melts, the direction of rotation plays a more important role than for metallic melts.

In FZ processes with induction heating, the RF EM field of a coil generates a radial EM force component. RF-induced EM fields with a maximum flux in the middle plane induce a flow in the opposite direction to Marangoni convection (Figure 4.18d), which can lead to a dramatic change of solute distributions in the grown crystals [Vaněk 1983]. The maximum velocity can reach 10–100 cm/s, which is more than one order of magnitude higher than the Marangoni convection in the molten zone [Lauder 1975]. Sometimes, due to very strong EM forces and high corresponding Reynolds numbers, the convection becomes turbulent. Convection pattern and strength are strongly affected by the design of the RF coil, frequency, electrical melt parameters, and crystal–melt and melt–feed interface shapes [Hermann 2001]. A wider inner diameter and a greater height of the coil reduce the gradient of the EM field and the undesired melt flow towards the centre of the solid–liquid interface.

Flow stability is one crucial problem not only for the mechanical stability of the FZ but also for the perfection of the grown crystals. Unsteady oscillatory flow in FZ processes arises for high driving forces, i.e. if the characteristic dimensionless numbers exceed critical values. For thermocapillary flow, oscillations occur in half-zone experiments with NaNO_3 ($Pr = 9$) beyond the critical value $Ma_c \approx 10^4$ [Schwabe 1978]. The period of oscillation increases with zone dimensions. The oscillatory mode was identified with an azimuthally travelling hydrothermal wave [Schwabe 2007]. In FZ experiments with fluids of low Prandtl number such as Nb [Jurisch 1990-1] and Mo ($Pr \approx 0.025$) [Jurisch 1990-2], critical Marangoni numbers of $Ma_c \approx 600$ –1600 were obtained for increasing zone lengths, which are one order of magnitude smaller than in high Prandtl number fluids. Characteristic frequencies were in the order of 1 Hz [Jurisch 1990-2]. See Chapter 7 for a detailed discussion of the various flow fields due to Marangoni convection.

Oscillatory flow beyond a critical zone length ($L_c = 3.5$ mm in FZ crystal growth of Mo) can lead to a drastic change of impurity distribution and the formation of impurity striations in the grown crystal [Barthel 1967, Barthel 1979, Jurisch 1990-2, Vaněk 1979]. For more vigorous flow, back-melting phenomena at the growing interface can detract from crystal perfection. The convective state in a FZ process must therefore be controlled by an appropriate zone length, melt overheating and other process parameters. The oscillatory Marangoni flow can be effectively suppressed by isorotation [Chun 1980].

According to Tiller's criterion, the morphological instability caused by constitutional supercooling ahead of the crystal–melt interface occurs beyond a critical value of G/ν , where G is the temperature gradient in the melt at the interface and ν is the growth rate [Wilke 1988-1]. Practical experience of FZ crystal growth reveals that melt convection is another important factor. RF EM heating causes vigorous flow and solute mixing in the molten zone, which has beneficial effects compared to optical or electron beam heating. It can suppress constitutional undercooling and cellular growth instability due to

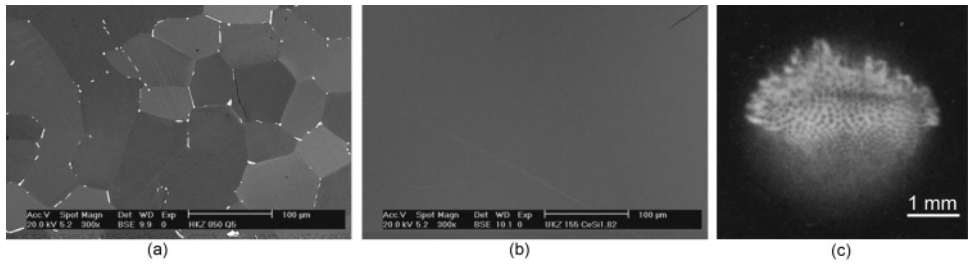


Figure 4.19 SEM images of cross-sections with cellular structure (a) and without cellular structure (b) of CeSi_{2-x} ($x = 0.19$) crystals grown with 10 mm/h FZ methods with optical and RF induction heating, respectively (Reprinted with permission from [Souptel 2004], copyright (2004) Elsevier Ltd). Bright phase: CeO_2 . (c) Cellular growth instability at core regions of the interface of a Mo-1 wt.% Ir crystal grown by FZ with electron beam heating (autoradiograph) [Barthel 1981].

trace elements. Figure 4.19 illustrates that a cellular instability is induced by the oxygen trace element in a $\text{CeSi}_{2-\delta}$ crystal grown at $v = 10$ mm/h by optically heated FZ, which contrasts with the stable interface for RF EM heating [Souptel 2004]. Therefore, RF EM heating allows higher growth rates in FZ processes. The actual form of the cellular instability often depends on convection peculiarities. For the FZ growth of a Mo 1 wt.%-Ir crystal, it was proved that the cellular instability first occurs at core regions of the interface (Figure 4.19c) near the stagnant points of the convection vortices where the diffusion boundary layer thickness increases [Barthel 1979, Barthel 1981].

4.1.2.2 The Travelling Solvent FZ Method

In crystal growth of incongruently melting compounds by the FZ technique, the molten zone has a different composition from the solidifying material. If, at the beginning, feed rod and initial molten zone have the stoichiometric composition of the incongruently melting compound, the melt composition changes continuously by primary phase crystallization until it approaches the primary crystallization field of the desired compound. This is illustrated in Figure 4.20 for the FZ crystal growth of the intermetallic compound $\text{TbNi}_2\text{B}_2\text{C}$, which melts incongruently at 1518°C with a peritectic phase TbB_2C_2 according to the reaction $\text{TbB}_2\text{C}_2 + \text{L} \leftrightarrow \text{TbNi}_2\text{B}_2\text{C}$.

Metallographic images of longitudinal sections of $\text{TbNi}_2\text{B}_2\text{C}$ crystals, grown from stoichiometric feed rods, show inclusions of the TbB_2C_2 primary phase (Figure 4.20b). These are periodically precipitated in the $\text{TbNi}_2\text{B}_2\text{C}$ matrix. This is accompanied by a shift of the FZ composition (Ni enrichment, C depletion) until the $\text{TbNi}_2\text{B}_2\text{C}$ primary crystallization region is reached. Unlike the fortunate case considered here, where the primary phase and the matrix grow practically independently, the primary phase can often generate new grains of the main phase. This can obstruct single-crystal growth or decrease the quality of crystals. Furthermore, the simple FZ method cannot be used for the crystal growth of incongruently melting compounds from an oriented seed, because the seed would decompose once in contact with the stoichiometric melt. For this reason it is better to use the travelling solvent FZ method (TSFZ), a modification of the FZ technique. Here, at the very beginning of the crystal growth process, an additional piece of material with a dif-

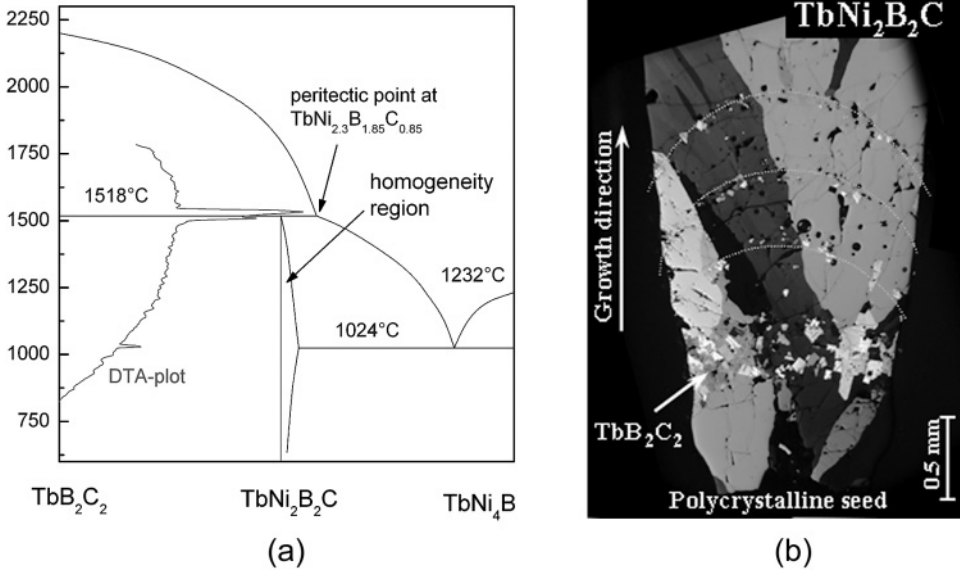


Figure 4.20 (a) *Tb-Ni-B-C* phase diagram. The section TbB_2C_2 - $TbNi_2B_2C$ - $TbNi_4B$ is relevant for $TbNi_2B_2C$ crystallization processes. Superimposed is a DTA heating plot [Behr 2005-2]. (b) Metallographic images of longitudinal sections of $TbNi_2B_2C$ crystals (grown by FZ with radiation heating) with inclusions of the primary phase TbB_2C_2 (Reproduced with permission from [Souptel 2005-1], copyright (2005) Elsevier Ltd).

ferent composition is placed between seed and feed rod, so that the initial molten zone has a composition in the primary solidification range of the incongruently melting phase. In this case, the incongruently melting phase crystallizes from the beginning of the crystal growth, without peritectic phase precipitation. During the rest of the process, the molten zone should maintain its composition, if the zone size is not changed and the compositions of melting feed rod and solidified crystal coincide. The TSFZ method has been successfully applied for the growth of various incongruently melting compounds [Kimura 1977]; in particular it has been extensively used for crystal growth of superconducting cuprates [Liang 2002, Takekawa 1988]. One unique application of TSFZ with RF heating is the crystal growth of WC, which does not coexist with the binary W-C melt at elevated temperature [Tanaka 1988]. The addition of B stabilizes the WC structure. Crystal growth has been accomplished with a ternary W-C-B FZ under pressurized He atmosphere at 2900 °C, leaving a WC crystal containing B only at an impurity level (100 ppm). More details of TSFZ growth for YNi_2B_2C are given in [Behr 1999]. The key role of the liquid-solid interface shape is of particular interest for the grain selection process mentioned above.

In the TSFZ method, crystal perfection crucially depends on the exact control of process parameters such as the zone travel rate. Because of the high concentration of solvent in the molten zone, the growth rate is normally much smaller than for congruently melting materials (typically ≤ 2 mm/h). Otherwise constitutional supercooling may occur in front of the solidifying interface, which is often accompanied by second-phase precipitation and generation of new grains [Souptel 2005-1]. The difference in composi-

tion between melt and crystal leads to solute boundary layers ahead of the crystallizing interface and requires intensive convective mixing of the zone either by the inherent RF EM stirring or by asymmetric counter-rotation of feed rod (10 rpm) and seed (20–50 rpm), which is commonly employed.

Because of the large concentration difference between the FZ and the adjacent crystal/feed rod in TSFZ, any fluctuation of the zone dimension will immediately result in a change of the melt composition and finally in local composition fluctuations in the crystal, depending on the solute partition coefficient of the element under consideration. In Figure 4.21a, the dependence of the element concentration on the length coordinate of a $\text{Ce}_2\text{Pd}_{0.3}\text{Co}_{0.7}\text{Si}_3$ crystal grown by TSFZ with RF inductive heating is shown [Mazilu 2005]. The variation of the Co/Pd ratio is caused by fluctuations of local growth conditions. For TSFZ with radiation heating of the same intermetallic compound the course of the Co/Pd ratio is smoother over the length coordinate because the temperature regime is more stable, resulting in smaller fluctuations of the zone length than for inductive heating. On the other hand, the radial composition differences turned out to increase slightly because of less intensive convective stirring of the melt [Mazilu 2005]. Therefore, in TSFZ, a proper choice of heating mode is decisive for the growth strategy of crystals of high quality.

The operating point of the growth process in TSFZ is primarily fixed by the average composition of the FZ. However, it may respond to temporal composition fluctuations and may also drift continuously by gradual accumulation of elements in the molten zone if the composition of the feed rod differs from that of the crystal. The temperature at the surface of the FZ measured by a pyrometer can point to changes in the growth process. As shown in Figure 4.21b for the TSFZ growth of the $\text{Tb}_{0.4}\text{Y}_{0.6}\text{Ni}_2\text{B}_2\text{C}$ compound, the zone temperature starts below the peritectic temperature of 1556°C . Apart from temperature fluctuations typical for TSFZ growth with RF heating, the average temperature decreases with processing time t , which is caused by a gradual drift of the melt composition towards a higher Tb/Y ratio. This leads to a slight gradient of the Tb fraction in the grown crystal [Bitterlich 2000]. Fluctuations in the local growth regime are often evident from small-diameter changes of the grown crystal. These surface ripples (Figure 4.22) are more marked in FZ growth with RF induction heating where the zone is less stable than for radiation heating.

4.1.2.3 *Effect of Ambient Atmosphere and Metal–Vapour Reactions*

The refining of materials [Pfann 1966] is still an important aspect in FZ crystal growth. The ambient atmosphere plays a crucial role. Normally, for metals and intermetallic compounds, high-purity protective gases like Ar or He are used to avoid reactions with the melt. Volatile elements and constituents with low melting and boiling points can evaporate from the FZ into the gas atmosphere and finally sublime at the cold container walls. This permits a low partial pressure of the impurity elements in the ambient atmosphere. Therefore, the growing crystal is constantly purified during the growth process and finally has a higher purity than the feed rod. This effect is utilized especially for growing ultrahigh-purity crystals of refractory metals [Berthel 1963] by the FZ method with electron beam heating in a high-vacuum environment. In the crystal growth of intermetallics, the selective evaporation of elements is normally an undesired phenomenon because it

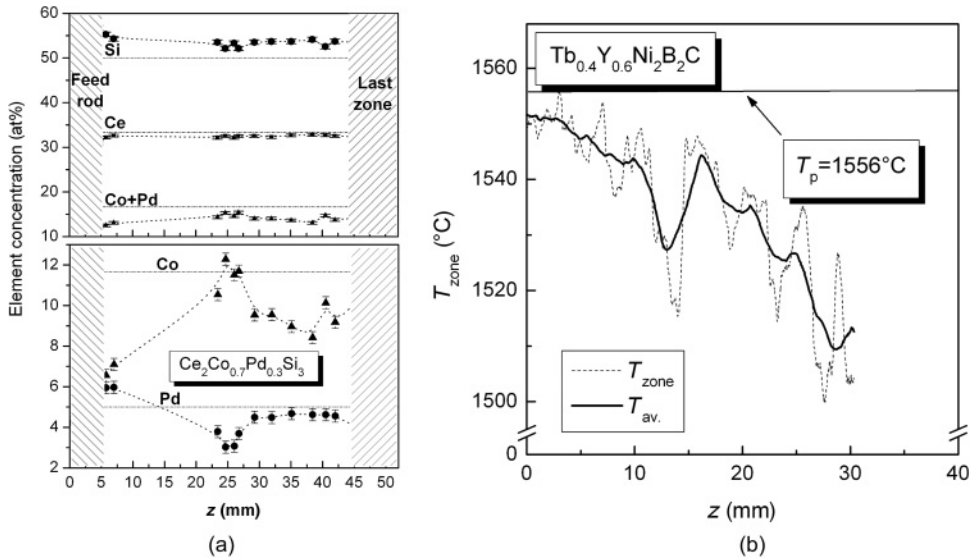


Figure 4.21 (a) Element segregation of Si, Ce, Co + Pd, and Co, Pd (bottom part) near the rod axis z in the $\text{Ce}_2\text{Pd}_{0.3}\text{Co}_{0.7}\text{Si}_3$ crystal grown with $v = 10$ mm/h for FZ growth with induction heating. Dotted lines serve as guides for the element concentrations. Thin horizontal lines show nominal composition (Reprinted with permission from [Mazilu 2005], copyright (2005) Elsevier Ltd). (b) Temperature of the FZ during the growth process of $\text{Tb}_{0.4}\text{Y}_{0.6}\text{Ni}_2\text{B}_2\text{C}$ with zone travelling velocity $v = 2$ mm/h. The axial coordinate of the crystal $z = tv$ is related to the processing time t . Dashed line, recorded temperature T_{zone} ; solid line, averaged temperature T_{av} . For comparison, peritectic temperature $T_p = 1556^\circ\text{C}$ (Reprinted with permission from [Bitterlich 2000], copyright (2000) Elsevier Ltd).

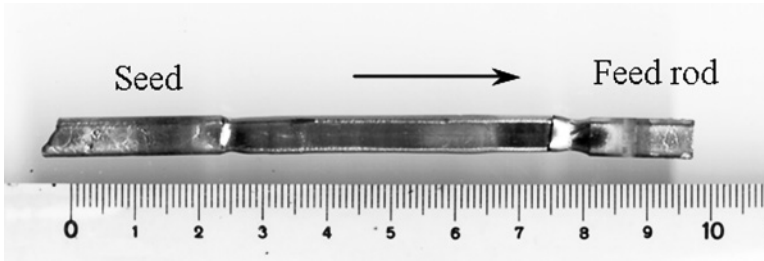
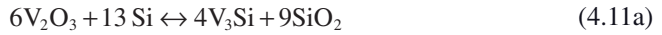


Figure 4.22 CeSi_2 single crystal grown by a FZ method with induction heating, showing typical growth facets and surface ripples (Reprinted with permission from [Souptel 2004], copyright (2004) Elsevier Ltd).

alters the stoichiometry of the melt and the growing crystal. However, under certain circumstances, the vaporization can be employed for melt refining during the growth process. In the FZ crystal growth of V_3Si and Cr_3Si it was shown that a silicothermic reaction of oxides proceeds for melting temperatures higher than 1500°C , leading to a marked depletion of the oxygen content [Behr 1985, Jurisch 1979]. The oxygen impurities in the form of transition metal oxides are reduced by Si, e.g.



The volatile SiO can evaporate from the molten zone into the ambient atmosphere (Ar) and sublimes at the cold coil or container walls. Surprisingly, this method of purification also works for the FZ crystal growth of rare earth (RE)–transition metal compounds. Although rare earth oxides are thermodynamically much more stable than SiO₂, they experience a similar reduction during the melting process. This has led to a reduction of the oxygen content by a factor of 2–3 in crystal growth of CeSi₂ [Souptel 2004]. This reaction also takes place in ternary melts of RE–transition metal silicides (RE₂PdSi₃, RE = Tb, Dy, Ho, Ce) and results in improved crystal quality [Behr 2005-2]. To compensate for the loss of Si caused by the silicothermic reaction during the FZ crystal growth, excess Si was added to the prepared feed rod.

In a similar way, borothermic or carbothermic reactions can proceed at elevated temperature (>1500 °C) in melts containing B or C [Souptel 2007-2]. In these reactions, the volatile boron oxides (BO) and carbon oxides (CO) are formed. The long exposure time of the melt under Ar gas flow in the growth chamber during the slow growth (~1 mm/h is typical for RENi₂B₂C crystals) boosts the extraction of BO and CO from the molten zone. This reduces the O₂ content in the melt and finally in the grown crystals.

In practice, in FZ crystal growth of intermetallic compounds with high melting temperatures containing volatile elements (Eu, Tm, Ce), one is often faced with the opposite situation. Evaporation of important constituents with low melting temperatures must be prevented during the FZ growth process. High growth velocities and small zone length can reduce the evaporation losses within narrow limits [Behr 2008]. Another more efficient means is to use an elevated pressure of the ambient gas. For FZ growth with RF induction heating, the enhancement of gas pressure is rather limited because of the large dimension of the growth chamber. In case of optical heating, the growth chamber can be more compact, enabling gas pressures of some MPa, depending on the set-up (see next section).

4.2 FZ Growth with Optical Heating

4.2.1 Introduction

Although RF heating is the main technique employed in FZ growth, especially for the industrial FZ growth of Si as described in section 4.1.1, optical heating with focused EM radiation in the visible and infrared part of the spectrum is used for instance to melt small-diameter semiconductors and oxides. This heating method allows excellent visual observation of the sample, very high temperatures, and operation in vacuum as well as in a gas atmosphere. The two main options for optical heating are the use of image furnaces and laser heating.

4.2.2 Image Furnaces

Image or mirror furnaces use a light source (e.g. the filament of a light bulb) as heat source and optical elements (mirrors, lenses) to focus it onto the sample. Additional

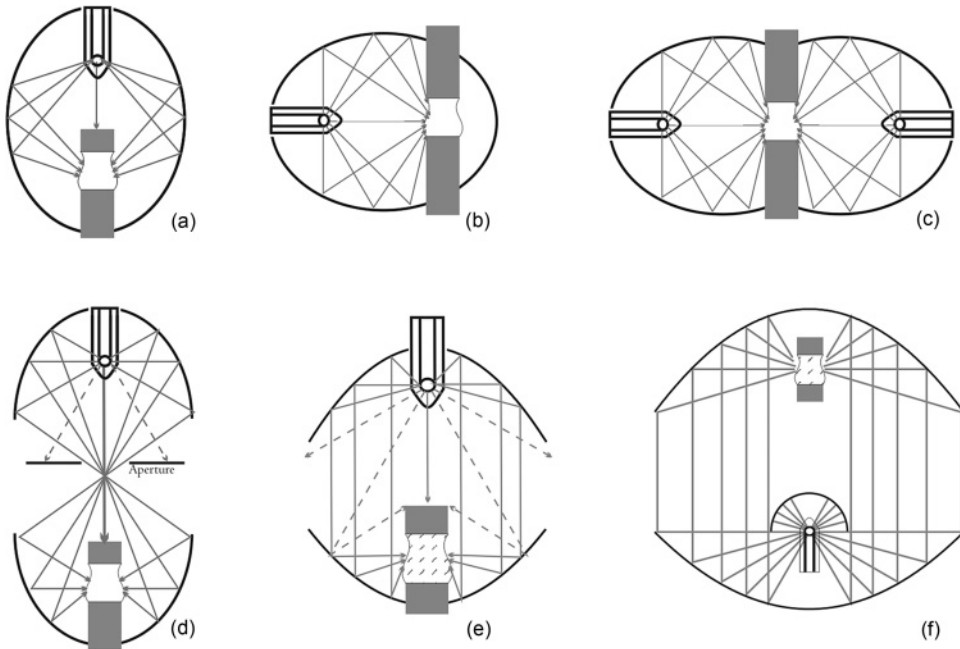


Figure 4.23 Mirror furnace set-ups. (a) and (b), closed monoellipsoid mirror furnaces; (c) double ellipsoid mirror furnace; (d) open ellipsoid mirror furnace with aperture; (e) parabolic mirror furnace; (f) parabolic mirror furnace with lamp below the sample and additional hemispherical mirror. Dashed lines indicate unfocused rays (copyright A. Cröll; reproduced with permission).

optical elements (apertures, baffles) may be used to influence the amount and the profile of the incoming radiation. Some basic configurations of such furnaces are shown in Figure 4.23.

Imaging furnaces can be very energy efficient, there is in principle no limit to processing temperatures, and the visual control of the zone and the crystal growth process is excellent. Starting in the 1950s and 1960s [Baum 1959, Field 1968, Kooy 1961, Weisberg 1956] different image furnaces have been developed over the years, especially for FZ growth of nonmetallic melts and the study of thermocapillary (Marangoni) convection in FZs, e.g. [Akashi 1969, Arsenjew 1973-1, Arsenjew 1973-2, Balakrishnan 1993, Balbashov 1981, Bednorz 1984, Carlberg 1984, Carlberg 1986, Cox 1972, Cröll 1994-2, Eyer 1979, Kitazawa 1977, Koochpayeh 2008, Lenski 1990, Matsumoto 1992, Mizutani 1974, Saurat 1971, Souptel 2002, Trivich 1970]. Commercial systems specifically designed for FZ growth have become available from several different companies over the years, e.g. Astrium-EADS, Crystal Systems Inc., GERO, LOT-Oriel, Moscow Power Engineering Institute, NEC. Many optical furnaces were also built in-house in research laboratories [Bednorz 1984, Eyer 1979]. Practically all optical furnaces employ reflective, not refractive elements because the geometric efficiency of lenses is quite limited and the heat exposure of the optical elements excludes most refractive materials except fused quartz or sapphire.

Either ellipsoidal or parabolic mirrors are used to focus the light from one or several lamps as shown in Figure 4.23. Closed monoellipsoidal mirrors as in Figure 4.23a, b are the most efficient because nearly all of the light is focused onto the sample; open ellipsoidal (Figure 4.23d) or parabolic mirrors (Figure 4.23e) do not use the radiation directly reflected by the mirror shell on the sample side. Improved efficiency of parabolic mirrors or of ellipsoidal reflectors using only partial ellipsoids [Arsenjew 1973-1, Arsenjew 1973-2, Ray 1988] is possible by the introduction of an additional hemispherical mirror as shown in Figure 4.23f. Parabolic mirrors have the advantage that the distance between the foci can be varied.

For a real point focus, there is in principle no limit for the separation of parabolic mirror shells. However, because of the finite dimensions of the lamp filaments or arcs, the resulting optical aberrations usually preclude large separations. A combination of ellipsoidal and parabolic geometries is also possible (Figure 4.24).

A distinction can be made between furnaces where the sample axis and the main axis of the furnace coincide, and furnaces where the main axis is at 90° to the main sample axis. The first concept, shown in Figure 4.23a, d–f, allows a very good rotational symmetry of the radiation field and thus the thermal field, but the accommodation of different translation mechanisms for the feed rod and the crystal is difficult (compare e.g. the construction in [Bednorz 1984]) and the maximum processing length is limited to a value less than the lamp focus–sample focus distance. In this type of furnace, an ampoule or similar construct is necessary to hold the feed rod and the growing crystal (compare Figure 4.24). With the second type of furnace (Figure 4.23b, c), the processing length is limited only by the translation mechanism and independent translation of the feed rod and crystal is possible, but the thermal symmetry is considerably degraded, making crystal rotation a necessity. Often several mirrors are combined to partially alleviate the thermal asymmetry, as in the double-ellipsoid mirror furnace shown in Figure 4.23c or the four-mirror furnace made by Crystal Systems in Japan; this allows also an increase in heating power [Crystal 1992]. The good efficiency of a closed single ellipsoid is reduced by combining several mirrors, because the radiation directly emitted from one lamp into a different ellipsoid is not focused and is lost. A furnace with toroidal geometry (Figure 4.25) can also be regarded as part of this group, or as a cross between a ring resistance heater and an image furnace. The rotational symmetry of such a furnace is quite good, but only a few types have been reported to date [Davidson 1978, Quon 1993]. The furnace described in [Quon 1993], used for the crystal growth of Ge and $\text{Bi}_{12}\text{GeO}_{20}$, used a Super Kanthal resistance heating element, not a lamp.

Mirrors are either made of glass [Crystal n.d.] or machined from metal, e.g. aluminium alloys, brass, or steel. The inner surface has to be polished and can either be used as is (aluminium alloy mirrors) or is coated with a highly reflective metal, usually gold (see Figure 4.26). Silver, although having the best reflectance, is avoided because of its unfavourable tarnishing properties when used as first surface mirror.

If processing in air is not possible, the processing atmosphere can be provided by the furnace volume itself in the case of closed mirror furnaces with vacuum-tight feedthroughs, or by additional transparent containers, e.g. ampoules or fused quartz tubes. Transparent vessels for pressures up to 10^7 Pa have been used [Balbashov 1981].

Although some of the first furnaces to be developed used carbon arcs [Kooy 1961], the light sources used today are either tungsten halogen lamps of the order of 0.5–1.5 kW

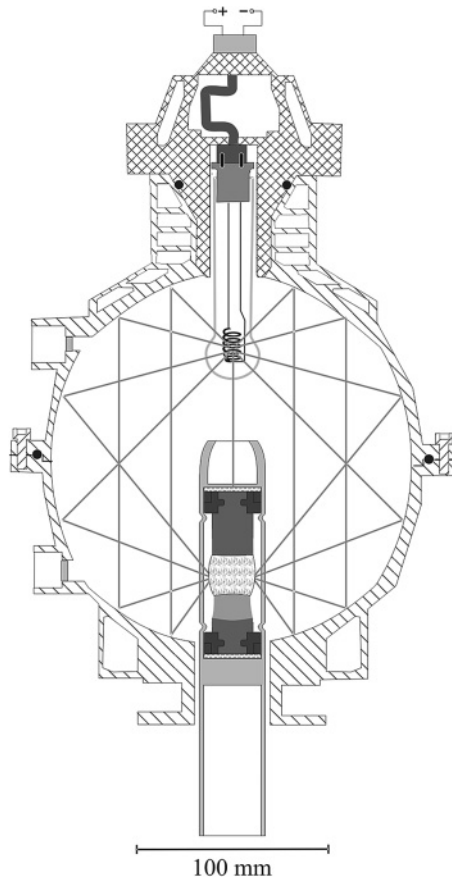


Figure 4.24 Paraboloid–ellipsoid mirror developed by Astrium-EADS (Reprinted with permission from [Lenski 1990], copyright (1990) Elsevier Ltd). The foci of the two outer paraboloids coincide with the foci of the centre ellipsoid. The lower focus is an annulus of 20 mm diameter. The sample is housed in a fused quartz ampoule (copyright A. Cröll; reproduced with permission).

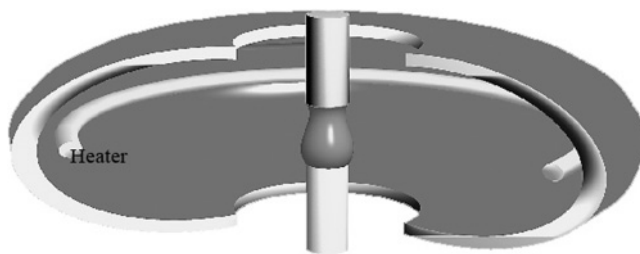


Figure 4.25 Schematic view of a FZ furnace with toroidal elliptic reflector, after [Quon 1993] (copyright A. Cröll; reproduced with permission).

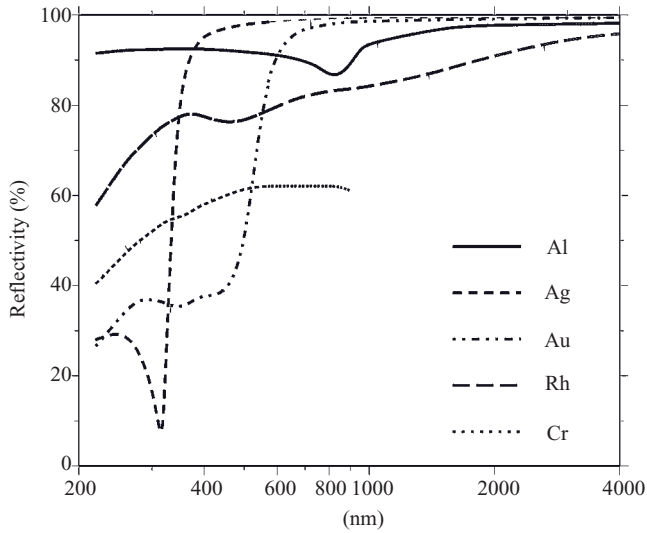


Figure 4.26 Reflectivity of several mirror materials from 200 to 4000 nm, using values from [Naumann 1987] (copyright A. Cröll; reproduced with permission).

maximum power or xenon arc lamps up to 10 kW for high power requirements [Balbashov 1981, Eyer 1979, Kitazawa 1977]. In the latter case, the spectral distribution of the radiation (important for simulations) has to be taken from the manufacturer's data. The spectral intensity of thermal radiators such as tungsten filaments is given by Planck's law for black body radiation and the emissivity of the emitting material. Note that in this case the maximum sample temperature is always below the filament temperature. In all cases where lamp bulbs are made of fused quartz, wavelengths shorter than $0.2\mu\text{m}$ or longer than $4\mu\text{m}$ are cut off. The lamp filaments or arcs should be as small and isometric as possible, as the focusing properties degrade rapidly for nonfocal/nonparaxial rays (Figure 4.27) because of the marked coma in parabolic and elliptic mirrors [Ray 1988].

Optical aberrations are more pronounced for strongly curved surfaces, i.e. for ellipsoids with an axis ratio much less than 1 [Eyer 1979] or paraboloids with large geometric coefficients (Figure 4.27). Furnaces based on point focus geometries, such as standard ellipsoid or parabolic optics, limit the maximum sample diameter to 10–15 mm. This can be partially counteracted by deviation from the ideal shape, introducing a so-called ring focus where the energy maximum is not a point but an annulus optimized for a given sample diameter [Danilewsky 1996, Kramer 1985, Lenski 1990]. The maximum sample size and the maximum temperature that can be achieved in a given image furnace depend heavily on the absorption and reflection coefficients of the solid and liquid material.

A disadvantage of mirror furnaces is the fact that temperature measurements during growth are often difficult. The temperature in the heating elements (i.e. the lamps) is only indirectly related to the sample temperature, and contactless measurement of the sample temperature by pyrometry is nearly impossible because of the much higher level of light reflected versus radiation emitted from the sample. Theoretically, pyrometric measurements can be made by using light sources emitting only a line spectrum, or by filtering.

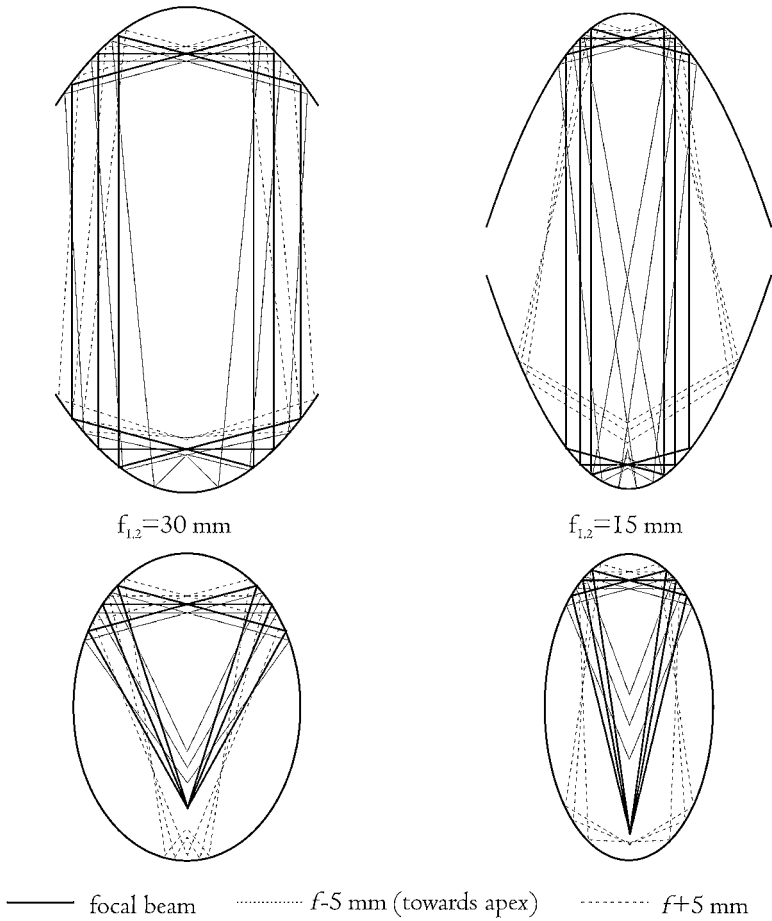


Figure 4.27 Focusing properties of differently shaped parabolic and ellipsoidal mirrors for focal rays and rays originating from axial positions $\pm 5 \text{ mm}$ from the focus; shown are three rays 15° apart on each side for each position. f is the distance from the focal point to the apex of the mirror. The progressive coma for strongly curved geometries is clearly visible (copyright A. Cröll; reproduced with permission).

Temperature field data can be obtained from special samples with incorporated temperature sensors, from numerical simulations, and from analytical computations [Dold 1994, Haya 1996, Lan 1997, Rivas 1992, Rivas 1999, Rivas 2001, Rivas 2002, Rivas 2004, Souptel 2007-1, Watson 1994]. Feedback control of image furnaces using the sample temperature is therefore uncommon; a feedback loop of the lamp brightness is useful, however. The zone height is often controlled just by visual observation of the sample and manual regulation of the power. If automatic processing must be used, an optimum parameter set (power/translation/rotation) is first established by simulations, measurement samples, and test runs, and then executed automatically. A control loop regulates either the lamp power or the light intensity measured by photodiodes pointing at the filament.

Light intensity control takes into account changes of the light output not only related to voltage fluctuations and filament resistance, but also other changes such as the discoloration of the lamp bulb or the higher light intensity during processing under microgravity, caused by the absence of convective gas cooling of the filament. Because of the nature of closed mirror furnaces, however, the photodiode signal can be quite susceptible to changes of the light reflected back from the sample towards the lamp, such as changes of the zone shape. Light intensity measurement devices employing diffusers and beam splitters between the mirror shells are possible in open mirror furnaces (Figure 4.23d–f), and are better suited for control [Balbashov 1981]. With modern image analysis techniques, a control loop using the zone shape or height determined by image analysers should be possible, although the many reflections and back-reflections in a mirror furnace make automatic detection of the interfaces difficult.

The power of incandescent lamps can be varied between zero and full power, but arc lamps allow changes of the light intensity only within a smaller power range (usually 3/4 to full power). In this case, or when a constant colour temperature is desired with incandescent lamps, the light flux can be controlled by an aperture in open geometries (Figure 4.23d–f, [Balbashov 1981]).

Temperature gradients in the sample are determined mainly by the geometry of the furnace, the filament and the sample, as well as by the optical and thermal coefficients of the solid and liquid sample material. As an example, the direct radiation of the lamp on to the sample top in monoellipsoid furnaces and the focusing properties lead to a considerable flattening of the temperature gradient at the upper interface. A small absorber or reflector mounted between the tips of the lamp and the sample, such as the hemispherical mirror in Figure 4.23f, can reduce this effect.

The absorber needs to be actively cooled, though, because, otherwise, it will heat up and emit radiation itself. A small (1–5 mm) defocusing of the lamp towards the apex of the ellipsoid also steepens the temperature profile between the focus and the centre of the ellipsoid in these furnaces, because it diminishes the amount of defocused rays coming from parts of the filament located nearer to the furnace centre in favour of rays coming from near the apex (Figure 4.27). The latter are better focused, but can lead to a second focus below the original focus for certain defocusing distances [Dold 1994]. It should be noted that the position of the temperature maximum in monoellipsoid mirror furnaces, sometimes called ‘thermal focus’, is usually not located at the geometric focus, but a few millimetres towards the centre of the ellipsoid. Paraboloidal mirrors with moderate curvature allow a more symmetric axial gradient than ellipsoidal ones, at the expense of efficiency. An example of combining both concepts is a closed mirror furnace using a combination of two paraboloids and an ellipsoid with common foci (Figure 4.24) built by Astrium-EADS [Lenski 1990]. It was successfully used on several space missions for samples up to 20 mm in diameter [Cröll 1994-1, Cröll 1998, Danilewsky 1994, Herrmann 1995, Lopez 1999, Maffei 1997].

The results of the FZ crystal growth of GaSb by optical heating in space and on Earth are shown in Figure 4.28. The two microgravity-size crystals were grown in the paraboloid–ellipsoid mirror furnace shown in Figure 4.24, the 1-g crystal in a double-ellipsoid mirror furnace. The 1-g crystal was grown with a zone height of 6.5–7.0 mm, close to the maximum possible zone height of 8.7 mm. Because of the interface curvature, the zone height limits the maximum diameter of GaSb to 5–6 mm on Earth. The microgravity



Figure 4.28 Two GaSb crystals of 16 mm diameter grown under microgravity (left and centre) during the Spacehab-4 mission [Tegetmeier 1996], and one 5-mm diameter GaSb crystal grown under gravity (right) (copyright A. Cröll and R. Geray; reproduced with permission).

crystal, however, was grown with a zone height of 13–14 mm, allowing a much larger crystal diameter. Even larger zone heights are possible for small crystal sizes, but aspect ratios much above 1 lead to the formation of concave interfaces.

During the German Spacehab mission D-2 in 1993, the GaAs crystal shown in Figure 4.29 was grown in space with a diameter of about 20 mm; on Earth GaAs only crystals of 6–8 mm diameter can be grown using the FZ method. For the GaSb crystal, the zone height of 20–24 mm was more than twice the terrestrial value. For details see [Herrmann 1995].

One important peculiarity of radiation heating is the feedback between the heating power absorbed and the change of absorption and reflection coefficients upon melting. For some materials, these coefficients change considerably at the melting point (Table 4.3). In Figure 4.30, the substantial increase in the reflectivity of Si and in the absorption coefficient (colour change) of GGG on melting can easily be seen. The first case, i.e. the increase in reflectivity of an opaque substance on melting, leads to the formation of a pattern of droplets and solid material on the surface at melting temperature [Celler



Figure 4.29 20-mm diameter GaAs FZ crystal grown under microgravity during the German Spacehab mission D-2 in 1993 (Reprinted with permission from [Herrmann 1995], copyright (1995) Elsevier Ltd).

Table 4.3 Optical material parameters in the solid (s) and liquid (l) state for several materials

Material	Wavelength	r_s	r_l	ϵ_s	ϵ_l	α_s	α_l	Reference
Si	VIS	0.38	0.72	0.60	0.28			[Celler 1985]
Ge	VIS	0.35	0.82	0.65	0.18			[Crouch 1982]
Fe	650 nm	0.65	0.63	0.35	0.37			[Weast 1981]
Au	650 nm	0.86	0.78	0.14	0.22			[Weast 1981]
Al ₂ O ₃	633 nm	0.04	0.06			0.01–0.1	0.5	[Nason 1990]
Y ₃ Al ₅ O ₁₂	633 nm	0.07–0.08	0.09			0.083–0.111	2	[Nason 1990]

r , reflectivity; ϵ , emissivity; α , absorption coefficient.

The ϵ_s and α_s values are for smooth surfaces. Value ranges indicate temperature-dependent measurements. Note that the absorption coefficient is used, not the absorptance, equivalent to the emittance (equals emissivity only for opaque materials with smooth surfaces).

1984, Celler 1985, Jackson 1985], adjusting the macroscopic average reflectivity such that the melting temperature is maintained despite the changes in absorption coefficient at the phase transition. In other words, between the point where the surface starts melting and the point where the whole surface is molten, a substantial increase in heating power

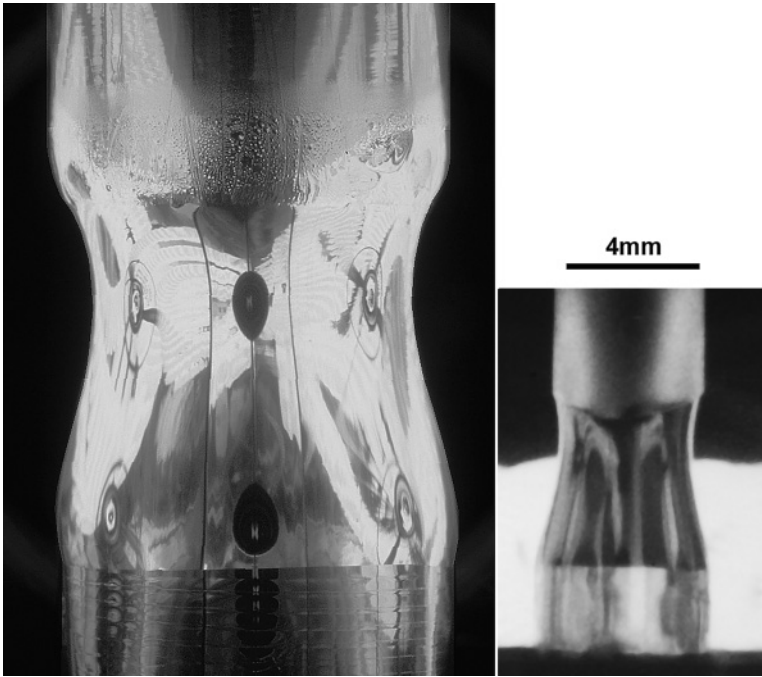


Figure 4.30 Floating zones in a double ellipsoid mirror furnace. Left: Si (T_m 1410°C), diameter 12 mm, power 850 W. Right: $Gd_3Ga_5O_{12}$ (GGG, T_m 1767°C), 4 mm diameter, with passive afterheater (visible at bottom), power 1200 W (from [Geray 1984]). Note the much higher reflectivity of the Si melt zone compared to the Si crystal and the darker colour of the garnet melt zone compared to the GGG crystal (adapted from [Cröll 1998], by permission from Elsevier).

is necessary to allow for the reduction of the absorptivity, in addition to the latent heat required. The droplets at the interface are not stable, but move and coalesce in the temperature gradient as a result of surface tension effects and gravity, and can introduce some irregular vibrations of the zone. These effects are enhanced for materials where superheating of the solid is possible, such as many semiconductors [Wenzl 1978]. Apart from the movements, this change of reflectivity is advantageous in general in that it leads to a self-stabilization of the system; it damps the effect of a perturbation or an asymmetry of the radiative flux, unavoidable in real systems, on the energy flux into the sample. Materials with a higher absorption coefficient of the melt than of the solid, such as many oxides, show the opposite effect (Figure 4.30). The power must be decreased immediately on the formation of the melt zone, and asymmetries in the external radiation/temperature field are amplified. Constant attention is necessary for the control of these melt zones.

The complex interplay between the different material parameters, temperatures, convective flows and geometry leads to difficulties in determining the temperature fields in mirror furnaces. Advances in computing power mean that numerical simulations by finite element methods can now predict some aspects of the process, if the energy flux on the

surface of the sample is calculated by other means such as a Monte Carlo simulation or an optics program; with some simplifications analytical methods are also possible [Haya 1996, Lan 1997, Rivas 1992, Rivas 1999, Rivas 2001, Rivas 2002, Rivas 2004, Souptel 2007-1]. Simulations have shown that the secondary radiation, i.e. the radiation emitted by the sample, cannot be neglected in calculating the temperature field in mirror [Dold 1994, Haya 1996, Kramer 1985, Lan 1997, Rivas 2002, Watson 1994].

4.2.3 Laser Heating

Laser heating shares many aspects with the image furnaces described above, including good visual control, unlimited temperature range (in principle), no general limitations for the processing atmosphere, and the effects associated with the change of reflectivity and absorption coefficient at the melting point. Because of its monochromatic nature, laser heating allows straightforward pyrometric temperature measurements. Secondary radiation does not influence the temperature profile greatly unless radiation shields are used. Automatic diameter control, e.g. with a second laser at a different wavelength [Fejer 1984], is also easier than in mirror furnaces. The energy efficiency of laser furnaces is not as good as that of mirror furnaces, starting with a low electro-optical conversion efficiency, e.g. 10% for a CO₂ laser [Carlberg 1991]. The available optical power is then further reduced in the optical system (beam expander, mirrors) by reflection and absorption losses. Typically, 4–10 optical surfaces are common in advanced systems. Additional pre- and afterheaters are sometimes used to reduce the necessary laser power. Although all types of lasers providing the power at an appropriate wavelength might be used, the continuous-wave CO₂ laser with a wavelength of 10.6 μm is a common type. This reason for this is that oxides, the material group where laser heating furnaces are most often applied, are opaque at this wavelength. The same reason, however, precludes the use of this laser when standard ampoule or tube materials (SiO₂, Al₂O₃) are used for sample containment. Therefore lasers with wavelength in the visible or near infrared, such as Nd:YAG lasers with $\lambda = 1.06 \mu\text{m}$, are also used.

The use of lasers for FZ growth started in 1969 with the growth of ruby crystals by Eickhoff and Gürs [Eickhoff 1969] and has continued over the years [Burrus 1977, Chen 1995, Chen 1996, Dreeben 1980, Elwell 1985, Gasson 1970, Gurtler 1978, Kim 1979, Sekijima 1998, Takagi 1977]. The main application has been for pulling optical single-crystal fibres by the pedestal method, e.g. [Feigelson 1986, Feigelson 1988, Fejer 1984, Imai 1995, Lai 2001, Nason 1990, Tang 1988, Tiller 1991, Yangyang 1991].

Early designs employed a single laser or several lasers directed at the zone (sometimes with beamsplitter and mirrors, see e.g. [Gasson 1970]), resulting in strongly asymmetric temperature profiles. For good rotational symmetry, axicon optics as shown in Figure 4.31 are employed [Carlberg 1991, Feigelson 1986]. A focusing system as in Figure 4.31a does not pose any difficulties for cooling the optical elements and, at the CO₂ laser wavelength, more materials than the ones listed in Figure 4.26 are available as mirrors (e.g. Mo has a reflectivity of 98% at this wavelength). Another possibility is the use of a catadioptric system as shown in Figure 4.31b.

Refractive elements can be made of GaAs, ZnSe (Irtran-4) for $\lambda = 10.6 \mu\text{m}$; Si or Ge are not suitable for high-power CO₂ lasers owing to absorption bands (Si) or thermal

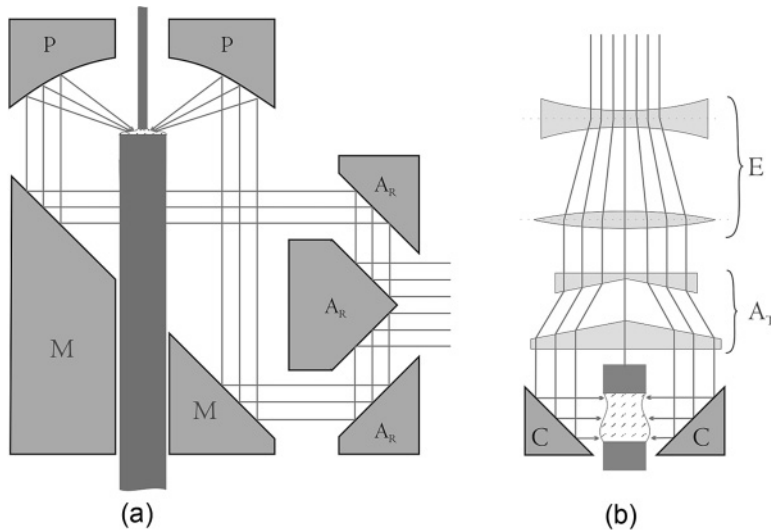


Figure 4.31 Axicon optics-based laser heating systems: (a) Catoptric pedestal growth system, after (Reprinted with permission from [Fejer 1984, Feigelson 1986], copyright (1986) Elsevier Ltd). (b) Catadioptric system for FZ growth, after (Reprinted with permission from [Carlberg 1991], copyright (1991) Springer Science + Business Media). A parabolic mirror may be used instead of the conical one (or vice versa), depending on the desired radiation distribution. AR, axicon mirror system; P, parabolic mirror; M, flat mirror; E, optional beam expander; AT, axicon lens system; C, conical mirror.

runaway (Ge) [Karow 1993]. The high refractive index of these materials (e.g. $n = 2.43$ for ZnSe, $n = 3.28$ for GaAs at $10.6\mu\text{m}$) leads to a considerable loss of power by reflection (17% for ZnSe) and makes antireflective coatings a necessity. An analysis by [Carlberg 1991] showed that in a typical setup only 50% of the power leaving the laser is absorbed by the sample (Al_2O_3), and, in another example, 900 W of electrical power (equivalent to 58 W laser power reaching the sample) was needed to form a FZ in 10 mm diameter LiNbO_3 rods (T_m 1260 °C). A possible advantage of laser heating systems is that tilting of optical elements might be used for translating a zone without mechanical movements of the sample [Bagdasarov 1986].

The axial temperature gradient in laser-heated FZs is usually rather high (up to 1000 K/cm [Feigelson 1988]) if the profile of the laser beam is maintained or focused by the optical system. This can be advantageous in terms of high possible growth rates [Feigelson 1986, Feigelson 1988], but also introduces higher thermal stress in the crystal and strong, time-dependent thermocapillary convection in the zone. If these disadvantages outweigh the benefits of a high pulling rate, the axial gradient (as well as the interface curvature) can be changed by additional pre- and afterheaters, thermal shields around the sample, defocusing of the beam profile by the optical system, the use of several coaxial laser/axicon systems for producing concentric ring beams [Carlberg 1991], or a combination of a laser heating system and image furnace [Geho 2004].

4.2.4 FZ Growth for Oxide Melts

4.2.4.1 General Growth Features for Various Classes of Oxides

The basic difference between the FZ crystal growth of metals and most oxides is the low electrical conductivity of the latter. With the exception of some special oxides like UO_2 , which exhibit semiconducting properties, RF heating cannot be applied to this class of materials. Single crystals of UO_2 were grown by FZ with RF heating by using an additional Mo preheating element [Chapman 1960]. Alternative heating methods for FZ crystal growth use resistive Ir heaters for YVO_4 [Muto 1969] or a hollow cathode gun for YAlO_3 and $\text{Y}_3\text{Al}_5\text{O}_{12}$ garnet materials [Class 1968]. The methods might lead to contamination of the melt by the heater materials.

Poplawsky was the first to use an arc image furnace for FZ melting of oxide crystals of various ferrites, Fe_3O_4 , MnFe_2O_4 and NiFe_2O_4 [Poplawsky 1962]. Optical heating with various modifications of image furnaces has become a well-established method for FZ growth of oxides (see section 4.2.2).

Oxides exhibit much smaller heat conductivities than metals and intermetallics. Temperature gradients in the crystal during the growth process are therefore greater and precautions, such as an additional resistance heater around the rod, are required to avoid cracks and other defects caused by inherent thermal stresses [Balbashov 1981].

Various oxide single crystals are used as optical materials. Large sapphire (Al_2O_3) crystals are commercially grown by the Czochralski or the Verneuil method [Wilke 1988-2] or the temperature gradient technique [Jianwei 1998]. These techniques of crystal growth are also useful for other oxides. In some cases hydrothermal growth, Czochralski pulling from a skull, solidification of a skull melt and flux methods can be used. FZ growth is employed if high-quality crystals cannot be prepared by other methods because of high thermal stresses or high temperatures and the high reactivity of the melt. This is illustrated by the following typical examples.

The FZ growth of Al_2O_3 is suitable if small quantities of crystals are required. An Al_2O_3 crystal of 6 mm diameter enriched with the ^{17}O isotope for electron spin resonance (ESR) studies was grown at 1.5 cm/h in an optical furnace, wasting only a minimum amount of material [Cox 1972].

Rutile (TiO_2) single crystals are important materials for polarizers in a variety of optical devices. Transparent and grain-boundary-free TiO_2 single crystals, to which a small amount of Al_2O_3 was added, were successfully grown by the FZ method with an infrared image furnace under an O_2 stream [Hatta 1996]. SrTiO_3 and SrZrO_3 single crystals are used for substrates in optical and many other scientific and technical applications. Their crystal growth using container methods is hampered by the high melting temperatures of about 2040 °C for SrTiO_3 and 2650 °C for SrZrO_3 . Internal stresses, subgrain boundaries and high dislocation densities are therefore common in these crystals. High-quality SrTiO_3 crystals with dimensions up to 20 mm in diameter and 60–80 mm in length were grown by the FZ method with optical heating [Nabokin 2003]. The maximum misorientations of subgrains were at most 100–300'' and dislocation densities of $1\text{--}5 \times 10^5 \text{ cm}^{-2}$ were determined. The influence of FZ growth conditions on the quality of SrZrO_3 crystals was studied [Souptel 2002]. Instability of the molten zone was observed at growth rates of 30 mm/h. Increasing the growth rate up to 40–60 mm/h resulted in colourless, transparent

and crack-free single crystals 5 mm in diameter and 40 mm long. The key factors for preparing high-quality crystals are low temperature gradients in the grown crystal achieved by an in-growth annealing furnace and the stoichiometry and purity of the initial materials. Changes composition of the molten zone during growth due to evaporation of SrO were minimized by high growth rates.

Compared to the single-crystal growth of garnets like $Y_3Fe_5O_{12}$ (YIG) or $Y_3Al_5O_{12}$ (YAG) by melt flux methods, the TSFZ method with radiation heating offers a higher growth rate of about 1 mm/h and avoids contamination with the flux [Kimura 1977, Kitamura 1980]. The method has also been applied to orthoferrites, ferrites and related oxide compounds [Balbashov 1981].

4.2.4.2 Control of Interface Shape

The control of the interface shape is one crucial point of the crystal growth of oxides. A concave interface is unfavourable for the growth of single crystals from the melt, because it enhances the concentration of inclusions and dislocations along the core of growing crystals. The tendency to form a concave interface is promoted for melts with small thermal conductivities. Although the exact material parameters are unknown unfortunately, a sequence of interface shapes (Figure 4.32) was predicted from the striations in crystals grown with the FZ method [Kitamura 1980].

Here, forsterite (Mg_2SiO_4) has a comparatively low thermal conductivity of $0.008 \text{ W cm}^{-1} \text{ K}^{-1}$ (Al_2O_3 $0.07 \text{ W cm}^{-1} \text{ K}^{-1}$) as extrapolated from sintered samples to the melting points. Obviously, it has the strongest tendency to form a concave interface. The growing interface of oxide materials, which absorb very little of the near-infrared radiation, tends to become concave towards the melt in FZ growth using an infrared radiation convergence-type heater [Kitamura 1982].

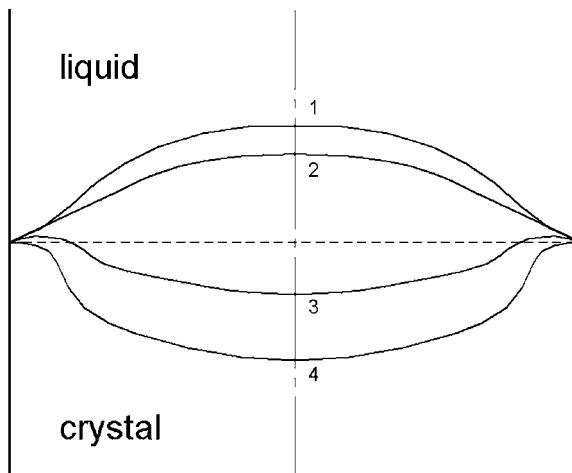


Figure 4.32 Interface shapes of growing oxide materials in FZ crystal growth with radiation heating: 1, $YFeO_3$; 2, YIG; 3, NdGG; 4, Mg_2SiO_4 (Reprinted with permission from [Kitamura 1980], copyright (1980) Elsevier Ltd).

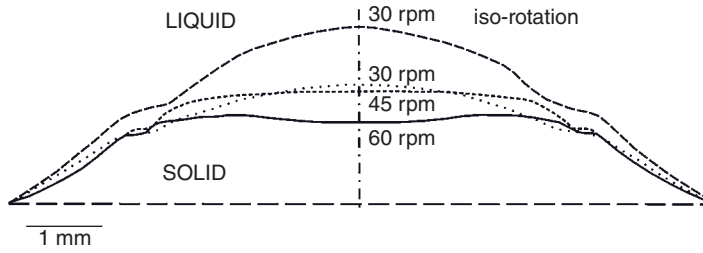


Figure 4.33 Influence of rotation rate on the growing interface (Reprinted with permission from [Kitamura 1979], copyright (1979) Elsevier Ltd).

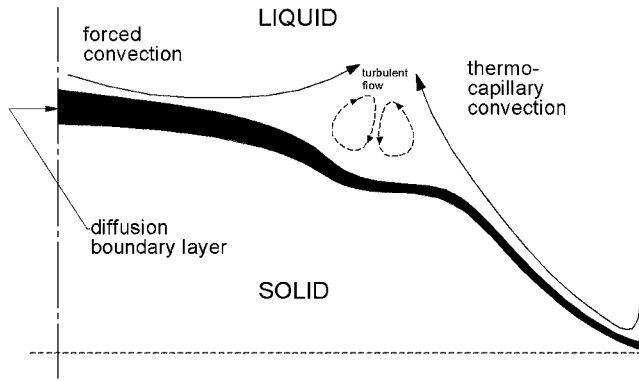


Figure 4.34 Schematic representation of flows in the molten zone near the growing interface and local variation of the diffusion boundary layer thickness at a rotation rate of 30 rpm (Reprinted with permission from [Kitamura 1979], copyright (1979) Elsevier Ltd).

A computer simulation showed the effect of fluid flow on the isotherms in the FZ during crystal growth for melts with low ($Pr = 0.01$) and high ($Pr = 1$) Prandtl numbers representing metals and oxides, respectively [Kobayashi 1984]. While the isotherms in the FZ of metallic melts remain virtually unaffected by the flow patterns of different rotation modes, for oxides a tendency towards concave isotherms near the interface was predicted for counter-rotation of seed and feed rod. This has been qualitatively confirmed by TSFZ experiments with YIG crystals [Kitamura 1979]. In this case, the interface was only stable for a growth rate less than 1 mm/h.

The interface shape tends to become more and more concave in the core region of the growing crystal with increasing strength of counter-rotation (Figure 4.33), whereas it becomes convex if crystal and feed rod are rotated in the same direction (iso-rotation). In this case, or in a situation where no rotation is applied, the interface becomes unstable. The choice of the optimum rotation mode is therefore a subtle balance of the growth parameters, which have to be adapted to the individual substance.

The schematic flow pattern close to the interface is illustrated in Figure 4.34. The convection in the outer region is dominated by thermocapillary flow. In the core region, the forced convection from the centre toward the periphery ahead the growing interface

is generated by crystal rotation. The different eddy flows can also produce radial segregation profiles in the YIG crystals doped with Al or Ga [Kitamura 1979].

When a heat reservoir is used in the form of an hollow alumina cylinder around the crystal heated by radiation from a lamp, the temperature distribution in the vicinity of the growing interface is altered. For YAG crystal growth, where the interface is concave without a heat reservoir, the interface can be changed into a convex form towards the crystal [Kitamura 1982].

Laser heating is now often used, e.g. for FZ crystal growth of sapphire or spinel (MgAl_2O_4) fibres [Dreeben 1980, Sigalovsky 1993]. FZ with CO_2 laser heating was used for crystal growth of small diameter (0.25–0.5 mm) sapphire crystals with high rates of 50–300 cm/h [Dreeben 1980]. A television viewing system allows the growth of fibres with a constant cross-section. Anisotropy of the growth angle α was measured in $\langle 10\bar{1}0 \rangle$ growth. A value of $\alpha = 35^\circ \pm 4^\circ$ is measured at the faceted trijunction, in contrast to $\alpha = 17^\circ \pm 4^\circ$ at the nonfaceted periphery of $\langle 0001 \rangle$ growth.

4.2.4.3 Effect of Ambient Atmosphere

Apart from the heating mode, the FZ crystal growth of oxides is distinguished from that of metals and intermetallics by the very different atmospheres needed. In the FZ growth of metals, high-purity protective gases (Ar, He) are utilized and traces of O_2 are largely removed to avoid any oxidation which could decrease crystal quality. Some oxide crystals can be grown in air, but for most of them a well-controlled O_2 partial pressure must be applied. The O_2 partial pressure depends strongly on the thermodynamic stability of valence states of the cationic components in the materials at melting temperature. For example, a valence state Fe^{2+} requires the use of purified H_2 or H_2/Ar mixtures [Chen 2005], the Mn^{2+} state is stable in pure Ar [Wizent 2009] and the Co^{2+} state is stable in a 1-bar O_2 atmosphere [Saint-Martin 2008]. The O_2 partial pressure can be further increased by applying high pressure, which is of striking importance in FZ crystal growth (up to 10 MPa [Balbashov 1981] or 15 MPa [Behr 2008]). Elevated gas pressure up to 10 MPa can be used to reduce evaporation losses from the molten zone and to maintain the stoichiometry [Balbashov 1981]. In FZ crystal growth of LiMnPO_4 , 4 MPa Ar pressure was applied to avoid Li_2O vaporization and the oxidation of Mn^{2+} to Mn^{3+} [Wizent 2009].

On the other hand, elevated O_2 pressure can directly affect the thermodynamic equilibrium and the solidification behavior. For example, CuO is an incongruently melting compound [Schramm 2005]. Elevated O_2 pressure brings CuO closer to the congruent melting behaviour (Figure 4.35). This has facilitated the FZ crystal growth of CuO under high O_2 pressure of 3.5–5.5 MPa, enabled higher growth rates up to 10 mm/h and improved crystal quality [Behr 2005-1].

Comparable behaviour is also observed for a wide class of ternary and quaternary cuprates, such as $\text{La}_4\text{Sr}_{10}\text{Cu}_{24}\text{O}_{41}$ (Notbohm 2007). In a similar way, the interval between the eutectic and the peritectic temperature is increased by applying high O_2 pressures for incongruently melting compounds like $\text{Y}_3\text{Fe}_5\text{O}_{12}$ and $\text{Gd}_3\text{Fe}_5\text{O}_{12}$. Therefore, these crystals grown by FZ with radiation heating under O_2 pressures of typically 2–5 MPa have a higher quality and fewer secondary-phase inclusions [Balbashov 1981]. Barium hexaferrite ($\text{BaFe}_{12}\text{O}_{19}$) melts incongruently in air. Congruent melting can be achieved at 4 MPa O_2

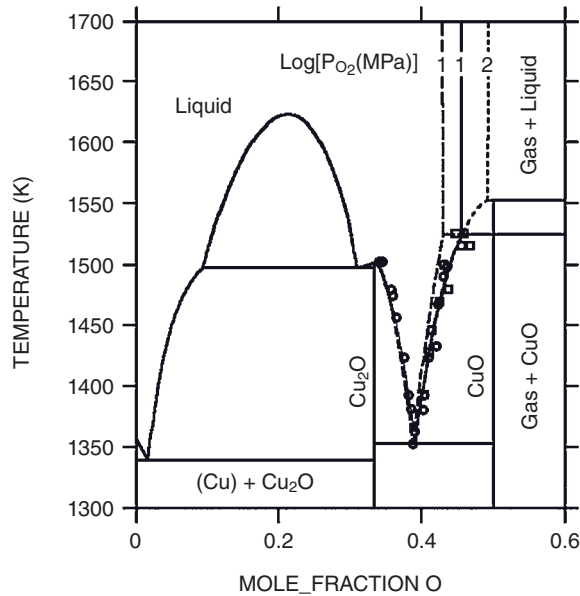


Figure 4.35 Calculated Cu–O phase diagram projection. Dashed line [Hallstedt 2003] at $P_{\text{O}_2} = 10$ MPa; solid line, calculated phase equilibria at $P_{\text{O}_2} = 10$ MPa; dotted line, calculated phase equilibria at $P_{\text{O}_2} = 10$ MPa. Circles and squares indicate experimental data for the CuO and Cu₂O liquidus (Reprinted with permission from [Schramm 2005], copyright (2005) Springer Science + Business Media).

pressure. BaFe₁₂O₁₉ crystals were grown by the FZ method under 7 MPa O₂ pressures where the content of the FeO phase is dramatically reduced [Balbashov 1981].

For incongruently melting oxides a vast difference in the oxygen content at the oxide/melt interface may arise because the metal ions may change their valence. The O₂ released must be removed from the interface and can lead to gas bubbles in the melt, which destabilize the FZ or become trapped in the growing crystal. Conversely, O₂ must be transported to the interface if the oxygen concentration in the melt is lower than in the solid phase. The latter case is illustrated by a SEM cross-section through the interface of the growing CuO crystal and the quenched last zone in FZ crystal growth experiments under 3 MPa O₂ pressure (Figure 4.36). The huge oxygen deficiency of the melt becomes clear from the high Cu₂O fraction in the microstructure of the quenched FZ. To grow a CuO crystal, the excess O₂ must be transported by diffusion and convection through the molten zone towards the interface. On the other hand, the O₂ released at the melting interface must be removed. Gas bubbles are formed if the solubility limit of oxygen in the melt is exceeded, which destabilize the FZ or are even trapped in the growing crystal. This naturally limits the growth velocity of oxide crystals.

The growth parameters can be optimized by adapting the oxygen partial pressure of the ambient atmosphere. The situation becomes more complex because O₂ exchange between the melt and the ambient atmosphere via the free surface of the travelling zone has to be taken into account. If the solubility of oxygen in the melt is high, the molten zone can take up O₂ from the ambient atmosphere which is released at the growing interface [Li 1979]. The oxygen content in the melt can be reduced by lowering the O₂ partial

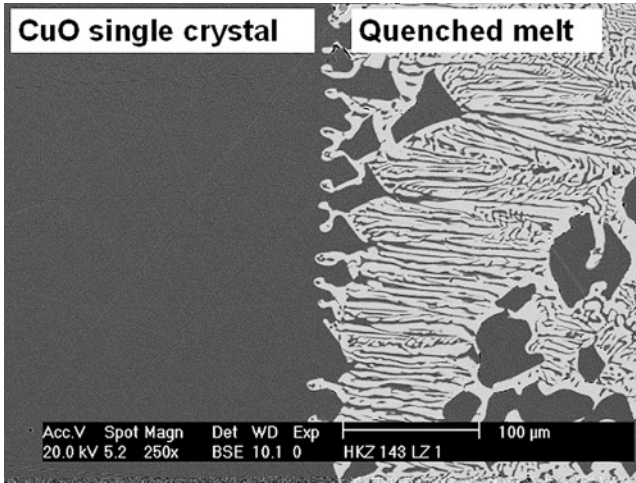


Figure 4.36 SEM image showing the interface between the grown CuO crystal (left) and the quenched molten zone (right) consisting of CuO (dark) and Cu₂O (bright) ($v = 10\text{ mm/h}$) (Reprinted with permission from [Behr 2005], copyright (2005) Wiley-VCH).

pressure in the growth chamber, limiting the O₂ uptake of the melt, or forcing oxygen to be transported from the melt into the atmosphere. For instance, bubble-free crystals of Ca₂MgSi₂O₇, and Ca₂Al₂SiO₇ produced by the FZ technique were achieved if the O₂ atmosphere was replaced by air, N₂ or Ar, the latter two delivering the better results [Ii 1979]. By diluting O₂ with Ar in an Ar/O₂ mixture the formation of gas bubbles at the melting interface was prevented in the FZ crystal growth of CaCu₂O₃ [Sekar 2005-1, Sekar 2005-2].

The O₂ partial pressure affects not only the solidification mode and the growth process of oxides but also the composition, homogeneity and properties of the oxide crystals themselves. Bi₂Sr₂CaCu₂O₈ (Bi-2212) oxides are an example showing high-temperature superconductivity [Takekawa 1988]. Underdoped Bi-2212 single crystals were successfully grown by the TSFZ technique under low O₂ pressures. A starting composition of Bi_{2.1}Sr_{1.9}CaCu₂O_{8+d} and a slow growth rate of 0.2 mm/h were employed [Liang 2002]. The growth habit was not sensitively influenced by decreasing P_{O_2} from 1 bar to 5×10^{-4} bar. However, the oxygen distribution in as-grown crystals became inhomogeneous as P_{O_2} decreased. The crystals do not show phase segregation until $P_{\text{O}_2} = 1 \times 10^{-3}$ bar. When P_{O_2} decreases from 1 bar to 1×10^{-3} bar the c-axis expands while T_c is reduced from 92 to 79 K and ΔT_c increases from 2 to 10 K. A further decrease of P_{O_2} leads to a broader superconducting transition range ΔT_c due to the oxygen inhomogeneity and phase decomposition.

4.3 Numerical Analysis of the Needle-Eye FZ Process

In the previous sections, several FZ processes which are strongly influenced by capillarity forces were described, and modelling results of different authors were shown and discussed. In the present section, as a more detailed example, the numerical modelling of

the FZ process for the industrial growth of large Si single crystals with the needle-eye technique using RF pancake inductors is described. This process has great relevance for the electronic and photovoltaic industry and the corresponding mathematical models, which have been described in great detail in the literature, have reached a high level of sophistication.

4.3.1 Literature Overview

We start with a brief literature review of the mathematical modelling of the FZ process mentioned above.

The first numerical calculations of the needle-eye configuration were made in a simplified way by Mühlbauer *et al.* in [Mühlbauer 1983]. They calculated the induced current distribution at the free melt surface and the only EM-driven fluid flow in the FZ with a presumed shape of the free surface. In the 1990s, Lie *et al.* in [Lie 1991] calculated the melt motion in the FZ under a strong axial magnetic field. The influence of the inductor slit on the distribution of the EM field in a FZ system was analysed in [Mühlbauer 1993] by means of three-dimensional calculations.

In a publication by Mühlbauer's international team [Mühlbauer 1995] and in the PhD thesis of Virbulis [Virbulis 1997], an axisymmetric model was presented for calculating the phase boundaries and the global heat transfer with melt convection in a needle-eye FZ process for the growth of 100-mm diameter crystals. Their model included most of the physical features that can be considered in a two-dimensional model, even including the large open part of the melting front, which is characteristic of the needle-eye process. Meanwhile, Riemann *et al.* [Riemann 1995] calculated interface shape and heat transfer by a more limited model without melt convection and open melting front calculation, and analysed the thermal stress inside the crystal.

Later, Mühlbauer, Muiznieks and Virbulis [Mühlbauer 1997, Mühlbauer 1999-1] completed their model with axisymmetric calculations of the time-dependent dopant transport in the melt, derived the resistivity variation in the grown crystal from the time-dependent dopant distribution and compared the theoretical results with resistivity measurements performed by Riemann and Lüdge. The calculated model showed a good agreement with the laboratory experiments concerning the shape of the crystallization interface and the radial profile of the resistivity. An overview of the full model is given in [Mühlbauer 1999-2]. Raming *et al.* used the above model to study the influence of different magnetic fields on the resistivity distribution of FZ crystals [Raming 1999] (see also Raming's PhD thesis [Raming 2000]).

Japanese researchers also developed axisymmetric calculation models of the needle-eye FZ process and compared the results to resistivity measurements of the crystal. Togawa *et al.* [Togawa 1998] calculated the global heat transfer and the liquid zone shape, the time-dependent melt flow and the dopant transport, and obtained the radial resistivity distribution in the crystal. The work of Togawa *et al.* is complemented by better radiation heat transfer models by Guo *et al.* in [Guo 1998]. The effect of the vertical magnetic field on the FZ growth process was investigated by Kimura *et al.* in [Kimura 1993, Kimura 1996]. Their calculations, however, assumed an oversimplified shape of the molten zone. The approximation of the radiation heat transfer is an important issue for modelling the

phase boundaries in the FZ growth of large crystals. Of the references mentioned above, only Guo *et al.* [Guo 1998] considered the view factors associated with the surface of the sample including crystal, melt and feed rod, with inductor and casing. They also studied the importance of modelling the specular properties of the crystal and melt surfaces instead of treating them all as diffuse. Guo *et al.* concluded that the specular property could be important.

The global Czochralski model developed from the work of Dupret and van den Bogaert [Dupret 1994] has been applied for modelling the FZ process [Assaker 1998]. Bioul [Bioul 2007] developed a new RF model of the magnetic field distribution, where the small but not negligible skin depth is taken into consideration. Their quasi-static FZ model is axisymmetric and considers heat transfer by conduction, convection and grey radiation; the open melting front has to be specified. These models are used in the program FEMAG-FZ.

The quasi-stationary model of the needle-eye FZ process for the growth of large Si single crystals as given in the PhD theses of Virbulis [Virbulis 1997] was essentially improved by Ratnieks, see [Ratnieks 2003] and his PhD work [Ratnieks 2008], and the model was implemented in the specialized program FZone [Ratnieks 2003]. After that, the nonstationary axisymmetric model was developed in the PhD theses of Rudevics [Rudevics 2008] and this model was implemented in the program FZoneT [Rudevics 2004]. A range of model and program components from the program FZone was used to create the nonstationary FZ model. For that reason, and because of the importance of quasi-stationary calculations for industrial practice, the quasi-stationary model will be described first here.

4.3.2 Quasi-Stationary Axisymmetric Mathematical Model of the Shape of the Molten Zone

In reality, the FZ crystal process is always nonstationary because the lengths of feed rod and crystal change over time during crystal growth. Nevertheless, the so-called laboratory reference system (LRS) can be introduced, in which the position of the RF inductor is fixed. In this reference system, the molten zone and the nearest parts of feed rod and crystal do not change their geometry and their temperature distributions if it is assumed that the crystal grows with a constant radius, the volume of melt does not change in time, and feed rod as well as crystal are cylinders of sizeable lengths moving with a constant speed. We call such a process 'quasi-stationary'. The corresponding quasi-stationary mathematical model allows calculation of the initially unknown phase boundaries and the corresponding distributions of temperature and EM fields for those processes. In this model, the algorithms used for calculating the quasi-stationary melting and crystallization interfaces are partially based on modelling the movement of interfaces in time. The model was implemented in the computer program FZone [Ratnieks 2003].

4.3.2.1 Key Assumptions and Approximations of the Quasi-Stationary Model

The elaboration of the final version of the quasi-stationary model for FZ processes with a needle-eye inductor [Ratnieks 2003] assume the FZ system to be axisymmetric (see Figure 4.37), except for the RF inductor (see Figure 4.38), which can have radial gaps.

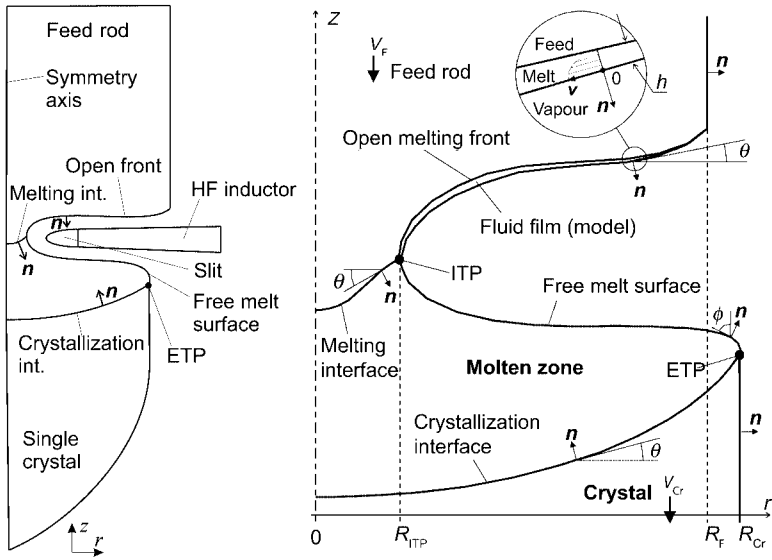


Figure 4.37 Vertical cross-section of the FZ system in axisymmetric approximation (Reprinted with permission from [Ratnieks 2003], copyright (2003) Elsevier Ltd).

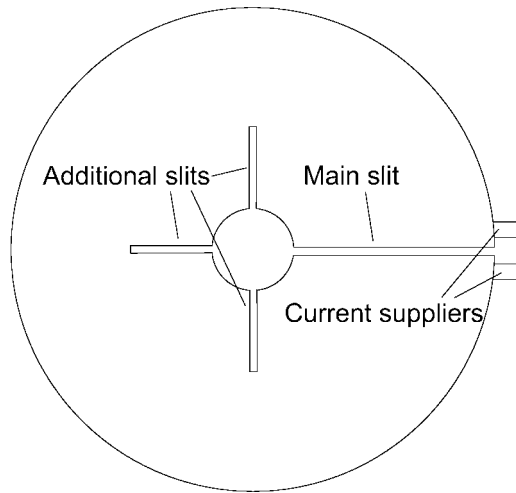


Figure 4.38 RF inductor with radial gaps, top view (Reprinted with permission from [Ratnieks 2003], copyright (2003) Elsevier Ltd).

Nevertheless, the influence of the gaps is approximated using the azimuthally averaged axisymmetric EM field and, thus, the mathematical treatment of the FZ process can be implemented in two dimensions in a vertical cross-section with a cylindrical coordinate system (r, z) .

The temperature field is calculated in crystal, feed rod and molten zone. As well as the heat diffusion in both feed rod and crystal, the convective heat transport due to the pull

velocity in the solid parts is considered. In this section, the influence of the flow on the temperature field in the molten zone is neglected because of the relatively low Prandtl number of molten Si ($Pr = 0.013$). This approximation has proved to be sufficiently accurate for many practical cases. The analysis of the influence of the melt flow on the zone shape can be found in the literature, e.g. in [Ratnieks 2008].

In the model, positions and shapes of the phase boundaries are initially unknown and must be calculated. Crystallization interface, melting interface and open melting front are determined by using the balance of the local heat flux density. The free melt surface is modelled by a simplified stationary model using the Young–Laplace equation (Equation 4.4). It is assumed that the exterior surfaces of feed rod and crystal are known.

As an AC current with a RF frequency of about 3 MHz is used in the FZ processes under consideration, the corresponding values of the skin depth δ (Equation 4.5) of the EM field in molten and solid Si are 0.27 mm and 1.30 mm, respectively. These values are several orders of magnitude less than the characteristic dimensions of the system, which are about 100 mm. Therefore, surface values such as linear surface current density, Joule's thermal source surface density and EM field pressure can be used for describing the EM processes in Si. For that reason, the boundary element method (BEM) is applied in the numerical calculations of the electromagnetic field; see [Ratnieks 2003].

4.3.2.2 Phase Boundary Models

In this section the models for calculating the phase boundaries are reviewed; see also [Ratnieks 2003]. First, the models for computing the melting interface, the crystallization interface, and the open melting front are given, which are based on the balance of the heat flux density. Later, the stationary model for modelling the free melt surface in the FZ system is considered.

Models of the Melting and Crystallization Interfaces. The melting and crystallization interfaces are modelled as nonstationary, i.e. to get the steady-state solution. The interface form is iteratively modified using its motion speed in the LRS with the given time step. The local speed of the phase boundary in the solid Si reference system (SRS) is calculated from the balance of the local heat flux density at the interface after the following equation:

$$\lambda_s \left(\frac{\partial T}{\partial n} \right)_s = \lambda_l \left(\frac{\partial T}{\partial n} \right)_l + \zeta V_n \quad (4.12)$$

where the indices s and l denote solid and molten Si, n denotes the local normal to the interface coordinate directed into the melt (see Figure 4.37), ζ is the latent heat of melting, V_n the local speed of the phase boundary in the direction of the local normal to the interface in the SRS, λ_s and λ_l the thermal conductivities in solid and liquid Si respectively and T the temperature field. The left-hand side of Equation (4.12), represents the local heat flux density directed from the interface into the solid Si; the right-hand side, the sum of the heat flux density supplied to the interface from the hot melt (first term) and the crystallization heat surface density due to the latent heat of crystallization (second term).

In the LRS, the crystal is pulled with a speed \bar{v}_c and the local interface speed \bar{v}_n is expressed as follows:

$$\bar{v}_n = \bar{v}_c + V_n \cdot \bar{n}, \quad (4.13)$$

where $V_n \cdot \bar{n}$ is the local speed of the interface in the SRS, expressed in vector form. The calculated speed of the interface \bar{v}_n and the chosen time step Δt are used to calculate changes of the position of the phase boundary in the LRS. In the numerical implementation, the interface form is approximated by a chain of line segments (boundary elements), where the speed \bar{v}_n in the LRS is calculated at the endpoints of the segments in compliance with Equations (4.12) and (4.13). Correspondingly, these points are shifted by $\bar{v}_n \cdot \Delta t$ in the LRS at each time step. When the speed \bar{v}_n reaches a value of zero for the whole interface, it is assumed that the stationary solution for the phase boundary has been obtained.

Model of the Open Melting Front. The open melting front is that part of the melting front of the feed rod which builds the interface with the vapour in the FZ process equipment. The heat flux density balance on this interface can be expressed as:

$$\lambda_s \left(\frac{\partial T}{\partial n} \right)_s = q^{\text{EM}} - q^{\text{rad}} + \zeta V_n \quad (4.14)$$

where q^{EM} is the surface density of the induced EM power (it is adjusted by applying the thin film model [Ratnieks 2003]), q^{rad} the emitted power density of the surface (for more about the radiation model see [Ratnieks 2003]) and $\zeta |V_n|$ the specific melting heat power surface density where V_n is the local speed of the phase boundary in the direction of the local normal to the interface in the SRS ($V_n < 0$ because in the calculations of the open melting front it is assumed that the direction of the normal vector \bar{n} is directed to the exterior of the solid Si). Thus, the right-hand side of Equation (4.14) describes the local heat flux density which penetrates into the solid Si. The value of V_n in Equation (4.14) is used to calculate the local interface speed in the LRS according to Equation (4.13), but instead of the crystal pull rate, the feed rod push rate is applied.

Stationary Model of the Free Melt Surface. Under stationary conditions, the pressure balance must be valid for each point (r, z) on the free melt surface, see Figure 4.39. The following equation is applied, which is derived from the Young–Laplace equation (4.4) adding the electrodynamic and centrifugal forces:

$$D^{\text{PI}} = 0 \text{ with } D^{\text{PI}} = p_0 - \rho_l g z + \frac{1}{2} \rho_l \Omega^2 r^2 - p^{\text{EM}} - \gamma_v \left(\frac{\cos \alpha_0}{r} + \frac{1}{R'} \right) \quad (4.15)$$

where D^{PI} is the pressure imbalance (must be zero at all surface points in the case of stationary solution); α_0 is the local angle of the surface with the vertical (Figure 4.37); γ_v the surface tension coefficient, R' the radius of curvature of the surface in the meridian plane; Ω the cyclic frequency of crystal rotation (it is assumed that the liquid rotates along with the crystal like a solid body), p_0 the interior gauge pressure in the melt at

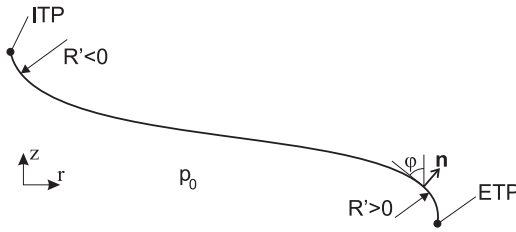


Figure 4.39 Free melt surface in vertical cross-section with endpoints – internal triple point (ITP) and external triple point (ETP).

$z = 0$ which determines the volume of the molten zone and p^{EM} the pressure caused by the EM field.

For the given endpoints of the free melt surface in a vertical cross-section, the internal triple point (ITP) and the external triple point (ETP) (see Figure 4.39), and a given interior gauge pressure p_0 , it is possible to compute the shape of the free melt surface unequivocal from Equation (4.15). To establishing the initially unknown value of the interior gauge pressure p_0 , an additional condition is necessary. It is known from the literature [Bardsley 1974] (also measured for a 50 mm FZ crystal in sections 4.1.1.4 and 4.1.1.9) that the free melt surface has a specific growth angle of $\alpha \approx 11^\circ$ with the vertical at the ETP of Si during stationary growth conditions and for a growing crystal of constant radius. Therefore for a given surface shape, an expression for p_0 can be derived from Equation (4.15) for a growing crystal with constant radius:

$$p_0 = \rho_l g z_{\text{ETP}} - \frac{1}{2} \rho_l \Omega^2 r_{\text{ETP}}^2 + p_{\text{ETP}}^{\text{EM}} + \gamma_{\text{lv}} \left(\frac{\cos \alpha}{r_{\text{ETP}}} + \frac{1}{R'_{\text{ETP}}} \right), \quad (4.16)$$

where the index ETP indicates that the corresponding values are taken at the ETP. In order to compute the free melt surface shape numerically, it is described with finite-length segments and a special iteration procedure is used, in which each of the segments is moved in the direction of decreasing the local imbalance D^{PI} . During the iteration steps, the interior gauge pressure p_0 is recalculated repeatedly by Equation (4.16) with regard to the actual surface shape. The output of the iteration procedure is the shape of the free melt surface with $D^{\text{PI}} = 0$ for the endpoint of each segment including the ETP (for more details see [Ratnieks 2003]).

Model for the Position of the Internal Triple Point. Unlike the ETP position, the ITP position needs a special modelling procedure. The ITP is defined as that point in the vertical cross-section where the three phase boundaries connect: melting interface, open melting front, and free melt surface (see Figure 4.40).

While modelling the FZ process, the position of the ITP is iteratively determined by a special procedure. First, along the common line of melting interface and open melting front, the position of the ITP is moved iteratively until the imbalance at the ITP reaches the value $D^{\text{PI}} = 0$; see Equation (4.15) and Figure 4.40a. Secondly, the ITP position is changed corresponding to the local interface speed, see Equation (4.13) and Figure 4.40b,

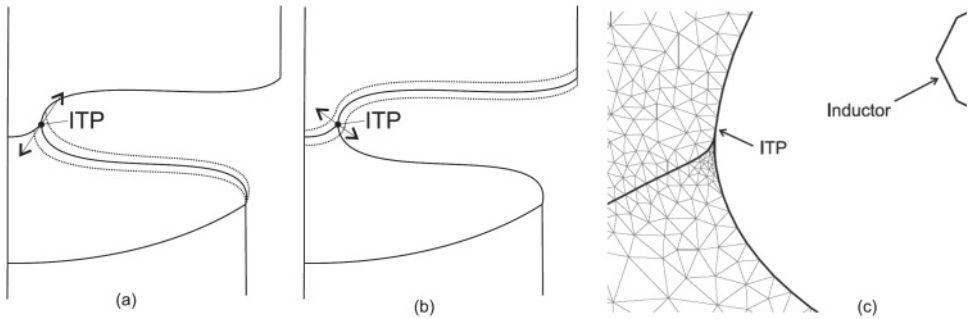


Figure 4.40 Internal triple point (ITP) model: (a) and (b), scenarios for changes of positions; (c) finite-element mesh used (Reprinted with permission from [Ratnieks 2003], copyright (2003) Elsevier Ltd).

which is determined by the melting process of the feed rod. For the interface speed at the ITP, a smooth connection is assumed between the melting interface and the open melting front. An example for this connection in the numerical calculation of a realistic FZ process is shown in Figure 4.40c. A more detailed description of the ITP model is given in [Ratnieks 2003].

4.3.2.3 Axisymmetric Modelling of the EM Field for an Inductor with Slits

In a typical FZ process at frequencies around 3 MHz, the EM skin depth is very thin (distinct skin effect), so the boundary elements method can be used to solve the EM problem numerically; see [Ratnieks 2003]. In a vertical cross-section of the system, the surfaces of Si and inductor are covered with line segments, i.e. boundary elements. In each boundary element, the initially unknown surface current density (linear current density), which is azimuthally directed, is defined. By using the Biot–Savart law, it is possible to obtain the relationship between the linear current densities in the boundary elements and the magnetic field at arbitrary points in the system. Because of the distinct skin-effect, the normal component of the magnetic field is zero on the surfaces of all Si parts and of the inductor. This is used to obtain the linear algebraic equation system for the values of the unknown linear current densities in the boundary elements. As an additional condition, the total current in the vertical cross-section of the inductor is used. The influence of narrow inductor slits (Figure 4.38) is modelled with a specific axisymmetric approximation; see the detailed description of this approximation in [Mühlbauer 1993, Ratnieks 2003]. Such approximation is justifiable, because the influence of the nonsymmetric three-dimensional EM field on the FZ process is averaged over time due to rotation of crystal and feed rod. In the model, the azimuthally directed linear current densities are calculated on all the outer surfaces of Si and inductor. These values are used to calculate the heat source surface densities on the outer surfaces of Si in the skin boundary layer approximation and the electromagnetic pressure on the free surface of the melt; see [Ratnieks 2003].

4.3.2.4 Heat Transfer Modelling

Radiation Modelling. In the radiation model, it is assumed that the surfaces to be considered are opaque (emission, absorption, and reflection occur on the surfaces of the

objects) and optically grey. Furthermore, radiation is considered to be diffusive. For the system of relevant radiation equations, the view factors are used in the axisymmetric approximation [Ratnieks 2003].

After solving the system of radiation equations, the distribution of the radiation power surface density q^{rad} falling on all exterior surfaces in the system is obtained. The value q^{rad} is used as a boundary condition for the temperature problem in the FZ system. Since q^{rad} itself depends on the temperature field, the models for calculating the radiation and temperature fields are iteratively connected:

$$\dots \rightarrow T_{(n)} \rightarrow q_{(n)}^{\text{rad}} \rightarrow T_{(n+1)} \rightarrow q_{(n+1)}^{\text{rad}} \rightarrow \dots, \quad (4.17)$$

where $T_{(n)}$ is the temperature field at the n th step of the system and $q_{(n)}^{\text{rad}}$ the corresponding distribution of the surface density of radiation power. Such iterations are continued until the changes in the temperature field become less than a given numerical precision.

Modelling the Temperature Field. The temperature field is solved separately in feed rod, melt, and crystal [Ratnieks 2003] according to the following equation:

$$\rho_1 c_p u_z \frac{\partial T}{\partial z} = \frac{1}{r} \frac{\partial}{\partial r} \left[r \lambda(T) \frac{\partial T}{\partial r} \right] + \frac{\partial}{\partial z} \left[\lambda(T) \frac{\partial T}{\partial z} \right] \quad (4.18)$$

where ρ_1 is the density, c_p the specific thermal capacity, $\lambda(T)$ the heat conductivity, temperature-dependent only in the solid, and u_z is the material convection speed due to the movement of feed rod and crystal. In the quasi-stationary model, the temperature field is calculated in the LRS. Therefore, in order to model the convective heat transfer of feed rod and crystal, their pull rates are used as the convective speed in the temperature equation. The convective heat transport is neglected in the liquid Si [Ratnieks 2003]. To solve the temperature problem, the following boundary conditions are applied: $\partial T / \partial r = 0$ at the symmetry axis, $T = T_0$ ($T_0 = 1420^\circ\text{C}$) at the crystallization and melting interfaces, $\lambda(T) \partial T / \partial n = q^{\text{EM}} - q^{\text{rad}}$ (the right-hand side of the equation expresses the difference between the induced surface densities of electromagnetic and radiation power) on all exterior surfaces of feed rod, melt and crystal. In order to solve the temperature problem numerically, the finite element method (FEM) is applied [Mühlbauer 1995, Ratnieks 2003].

4.3.2.5 General Calculation Algorithm

A simplified block scheme for the calculation algorithm of the quasi-stationary FZ process is shown in Figure 4.41 [Ratnieks 2003]. At the beginning of the calculation for the outer iteration step, all phase boundaries (except the free melt surface) are moved in compliance with their local speed at the current time step. Thereafter, the free melt surface and the EM field are iteratively calculated at a fixed ITP position; afterwards, the imbalance at the ITP $D_{\text{ITP}}^{\text{PI}}$ is calculated. If the obtained value of $D_{\text{ITP}}^{\text{PI}}$ is not zero, then the ITP point is moved in accordance with a special algorithm and the calculation of the free melt surface is repeated until $D_{\text{ITP}}^{\text{PI}} = 0$. Then, radiation and temperature distribution in the system are

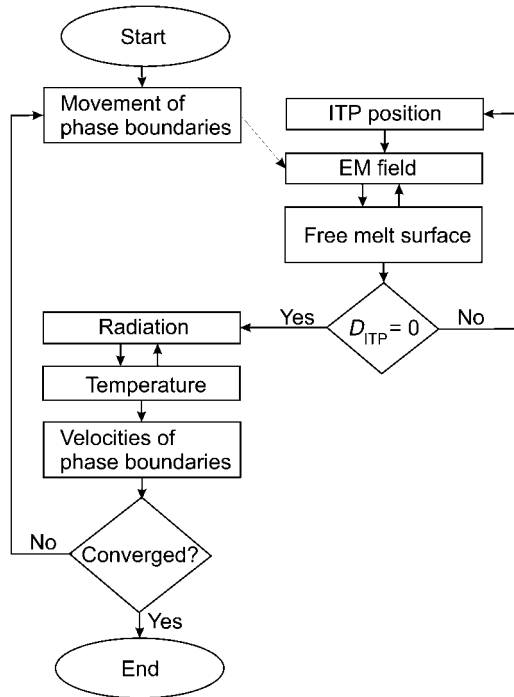


Figure 4.41 Simplified block scheme for the calculation algorithm in the quasi-stationary model of the FZ process (Reprinted with permission from [Ratnieks 2003], copyright (2003) Elsevier Ltd).

calculated iteratively until the stationary solution of the temperature field in all Si parts of the system is reached. With the temperature field in all Si parts known, the temperature gradients are calculated along the phase boundaries. The temperature gradients are then used to calculate the local normal speeds of the phase boundaries in the LRS. It is assumed that a quasi-stationary solution is obtained when the corresponding speeds of the phase boundaries tend to zero.

4.3.3 Numerical Investigation of the Influence of Growth Parameters on the Shape of the Molten Zone

In the 1990s, the industrial production of Si single crystals with diameters of up to 150 mm was possible. At the beginning of this century, Siltronic AG was the first company to produce FZ Si crystals of 200 mm (8") diameter [von Ammon 2004], a size that was not believed to be attainable a few years ago. In this section the modelling of the 8" Si crystal growth process is described in order to demonstrate the possibilities of mathematical modelling for supporting industrial process development.

Figures 4.42, 4.43 and 4.44 show typical examples of the shape of the molten zone for an 8" FZ process and its dependence on inductor current and feed rod diameter. The FEM

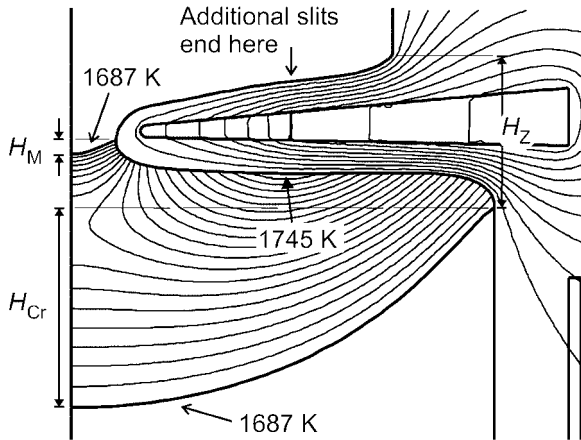


Figure 4.42 Temperature isolines in the melt ($\Delta T = 58\text{ K}$) and the magnetic field lines; H_Z is the zone height, H_{Cr} and H_M are the deflections of the crystallization and melting interfaces, respectively.

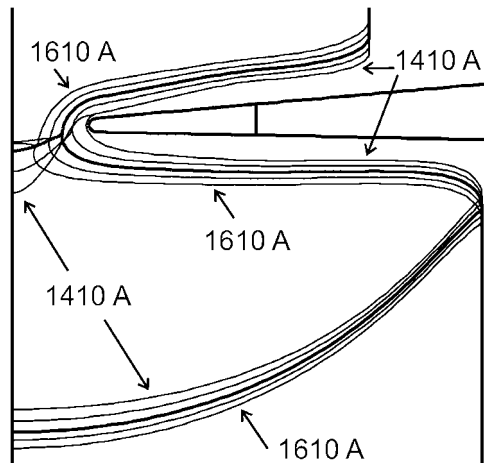


Figure 4.43 Phase boundaries with different zone heights corresponding to inductor current values of 1410–1610 A with steps of 50 A. The thick phase boundary lines correspond to the reference case with 1510 A and $H_Z = 37\text{ mm}$.

grid used is shown in Figure 4.45. For all cases, the crystal pull rate is 1.8 mm/min. In these calculations, the influence of the melt flow on the shape of the molten zone is neglected. More results of calculations and results including the influence of melt flow are given in [Ratnieks 2008].

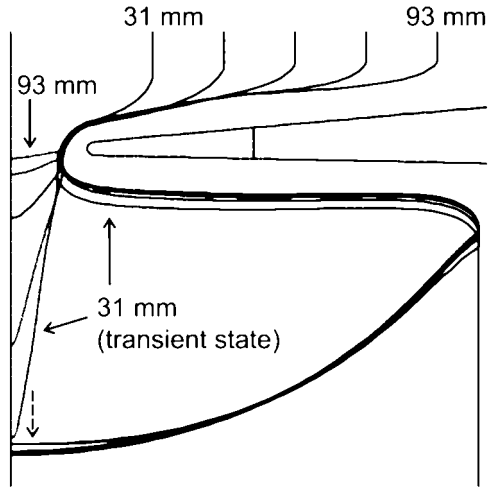


Figure 4.44 Phase boundaries with feed rod radii from 93 mm to 31 mm. A stable quasi-stationary solution does not exist for a feed rod radius of only 31 mm – the feed rod does not melt sufficiently and touches the crystal.

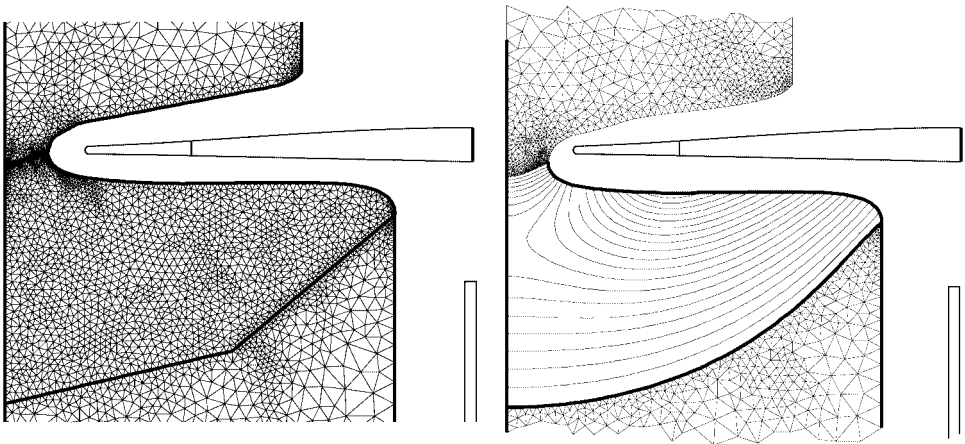


Figure 4.45 Finite-element grid as used in the calculations: left, starting grid; right, result of the calculated temperature field.

4.3.4 Nonstationary Axisymmetric Mathematical Model for Transient Crystal Growth Processes

A new nonstationary axisymmetric (two-dimensional) model of the FZ process, based on the components of the quasi-stationary model of the FZ crystal growth described in the previous section, was elaborated and validated [Rudevics 2004, Rudevics 2008]. By using

this model, it is possible to calculate the time-dependent shape of the molten zone. The model also provides the opportunity to study this process at the initial and final stages of the growth process (growing the start and end cones), where the phase boundaries in the LRS essentially change in time. In addition to that, this model makes it possible to examine the automated process control, which has an important role in the industrial growth of FZ crystals. This model was implemented in the computer program FZoneT [Rudevics 2004].

4.3.4.1 Mathematical Model and Numerical Implementation

Several components of the quasi-stationary model are taken over for the nonstationary model: the model of the open melting front, the RF EM field model, the ITP model and the models of temperature and radiation. The model of the free melt surface is also applied, with slight modifications.

The new and basic component of the nonstationary FZ model is the calculation of the actual value of the melt volume. The amounts of molten Si and of crystallized Si are calculated during the given time interval and used to compute the change in the melt volume, which is then applied to determine the actual free melt surface. Thereafter, depending on this shape, the formation of the crystal shape is modelled at the ETP by 'growing' the crystal along the free melt surface. A brief description of the most significant components of the nonstationary model is given below.

Calculation of Melt Volume. In order to find out the change ΔV_{melt} of the melt volume in a time interval $[t, t + \Delta t]$, it is necessary to calculate the volume of the liquid Si ΔV_{feed} , which originates by melting the feed rod at the melting interface and the open melting front, as well as to calculate the loss of liquid Si ΔV_{c} at the crystallization interface where the material crystallizes. Knowing both volumes, the change in the melt volume ΔV_{melt} can be calculated according to the following equation:

$$\Delta V_{\text{melt}} = \Delta V_{\text{feed}} - \Delta V_{\text{c}}. \quad (4.19)$$

To describe the feed rod melting, the axial coordinate $Z_{\text{F}}(r, t)$ is introduced in the LRS for the melting interface and the open melting front at a time t (see Figure 4.46). As a result of melting, after a time interval Δt the surface can be moved to a condition $Z_{\text{F}}(r, t + \Delta t)$. Taking into consideration that the feed rod itself is moved downwards at a specific rate $v_{\text{F}}(t)$ in the LRS, the amount of molten Si coming from the feed rod can be calculated for a time interval Δt according to the following equation:

$$\Delta V_{\text{feed}} = \frac{\rho_{\text{s}}}{\rho_{\text{l}}} \left(v_{\text{F}}(t) \pi r_{\text{F}}^2 \Delta t + \int_0^{r_{\text{F}}} [Z_{\text{F}}(r, t + \Delta t) - Z_{\text{F}}(r, t)] 2\pi r dr \right), \quad (4.20)$$

where ρ_{s} is the density of solid Si and ρ_{l} the density of molten Si. The amount of liquid Si which crystallizes at the crystallization interface $Z_{\text{cr}}(r, t)$ is calculated analogously:

$$\Delta V_{\text{c}} = \frac{\rho_{\text{s}}}{\rho_{\text{l}}} \left(v_{\text{cr}}(t) \pi r_{\text{c}}^2 \Delta t + \int_0^{r_{\text{c}}(t)} [Z_{\text{cr}}(r, t + \Delta t) - Z_{\text{cr}}(r, t)] 2\pi r dr \right). \quad (4.21)$$

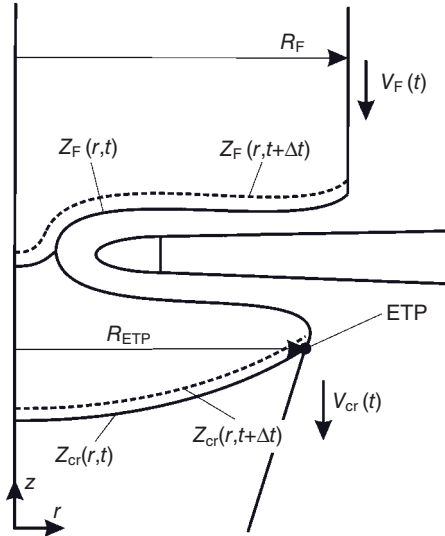


Figure 4.46 Surfaces used in the calculation of the actual melt volume value (Reprinted with permission from [Rudevics 2004], copyright (2004) Elsevier Ltd).

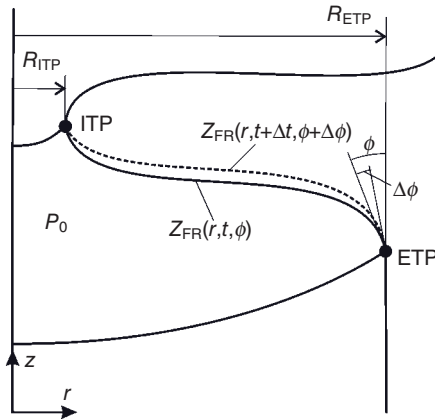


Figure 4.47 Calculation of the free melt surface (Reprinted with permission from [Rudevics 2004], copyright (2004) Elsevier Ltd).

Model of Free Melt Surface. During the short time interval Δt , the change of the melt volume ΔV_{melt} causes a corresponding change in the free melt surface. The shape of the free melt surface at a time t can be described by its axial coordinate $Z_{\text{FR}}(r, t, \phi_0)$ in the LRS, where the additional parameter ϕ_0 is the angle between the vertical z -axis and the tangent to the free surface at the ETP (Figure 4.47).

The surface shape after the time interval Δt is $Z_{\text{FR}}(r, t + \Delta t, \phi_0 + \Delta\phi_0)$; thus, the change of the actual melt volume has to be calculated by the following equation:

$$\Delta V_{\text{act}} = \left(\int_{R_{\text{ITP}}}^{R_{\text{ETP}}} [Z_{\text{FR}}(r, t + \Delta t, \phi_0 + \Delta\phi_0) - Z_{\text{FR}}(r, t, \phi_0)] 2\pi r dr \right), \quad (4.22)$$

where R_{ETP} is the radial coordinate of the external triple point and R_{ITP} is the radial coordinate of the internal triple point. Because of the conservation of the melt volume in the nonstationary model, it is necessary to ensure that

$$\Delta V_{\text{act}} = \Delta V_{\text{melt}}. \quad (4.23)$$

This is achieved by an iterative algorithm, where a change of the angle $\Delta\phi_0$ is sought, such that the change of the actual melt volume ΔV_{act} is equal to ΔV_{melt} , which is known from the analyses of the melting and crystallization fronts. In this algorithm, the shape of the free melt surface is calculated at the fixed extreme points (ITP and ETP), requiring that for each surface point the imbalance is zero, $D_{\text{ITP}}^{\text{PI}} = 0$; see Equation (4.15).

Modelling the Crystal Surface. The crystal shape that develops during the nonstationary FZ process is dependent on the angle ϕ_0 between the tangent to the free melt surface and the vertical direction at the ETP. In the numerical calculations, the free melt surface is described with line segments of finite length (see Figure 4.48). To enhance the precision of the calculation, the vertical cross-section of the melt surface at the ETP is approximately described by the circumference, which goes through the extreme points of the line segment at the ETP so that its tangent at the ETP creates the angle ϕ_0 , which is calculated from Equation (4.23). Thus, the tangent to the free melt surface at the ETP is the same as the corresponding tangent at the circumference. For a nonzero growth angle α , the direction of the tangent to the solid is correspondingly corrected. This tangent at time t is used to calculate the new position ETP' of the external triple point at the time $t + \Delta t$. For this, first, the crystallization interface at the time $t + \Delta t$ is obtained by moving the

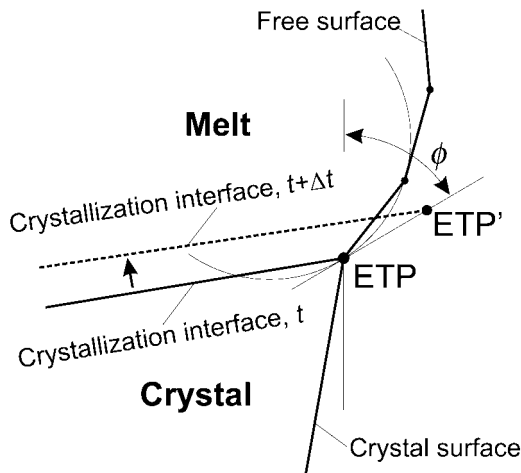


Figure 4.48 Modelling the crystal surface (Reprinted with permission from [Rudevics 2004], copyright (2004) Elsevier Ltd).

one at the time t in the normal direction to the growth speed in the LRS. Then, the point ETP' is obtained as the point of intersection between the new crystallization interface and the tangent of the free melt surface at the ETP (see Figure 4.48).

Modelling the Nonstationary Temperature Field. In the mathematical model for the nonstationary FZ process, the heat transfer is modelled similarly to the previously described quasi-stationary model (see section 4.3.2.4). In each FZ system sector, an unstable version of Equation (4.18) is solved with the corresponding boundary conditions. Moreover, in the nonstationary model, when solving the temperature equation in feed rod and crystal, it is assumed that the temperature field is calculated correspondingly in the reference systems connected with feed rod and crystal, i.e. the convective speed of the material is zero. The convective heat transfer is taken into account by moving the finite element grid in feed rod and crystal with the calculated temperature values in the grid nodes in the LRS.

Grid Processing Algorithms in the Nonstationary FZ Process. For the complete modelling of the nonstationary FZ process, it must be taken into account that the initial phase of the process starts with a small single crystal with a diameter of only a few millimetres and ends up with the final phase of the process, where the diameter of the crystal can reach as much as 200 mm. Thus, special grid processing algorithms are necessary for the numerical solution of the problem [Rudevics 2004, Rudevics 2008]. The generating algorithms of the boundary element grids were elaborated first, ensuring adaptation of the grid to the system dimensions, i.e. with the element number dependent on the system size. Moreover, in order to optimize the numerical implementation and decrease the total number of elements, while maintaining sufficient numerical precision for calculating the phase boundaries, an algorithm was developed that also changes the element size based on the assumption that the smallest elements are used for the melt. The crystal and feed rod are described with elements of size gradually increasing away from the molten zone. For instance, Figure 4.49 shows a grid of boundary elements on the feed rod surface. It can be seen that the element size, beginning with a minimum size a , increases gradually in the direction away from the molten zone.

Next, for the generation of the boundary elements on the crystal surface, a special auxiliary surface was used with many more points than in the boundary element grid. This auxiliary surface describes the precise crystal shape up to the current point in time. This is important especially in regions far away from the molten zone, where the boundary elements are very large. The left side of Figure 4.50 shows the numerical divisions of the crystal geometry during the modelling time when the auxiliary surface is not used (the auxiliary surface is shown only for comparison), the right side exhibits the crystal shape obtained using the auxiliary surface in the grid generation algorithm.

This grid generation algorithm is illustrated in Figure 4.51, where the initial modelling condition of the crystal cone and three consequential system conditions are shown. It can be observed that, at the initial stage of the modelling, the small crystal has a relatively fine grid compared with the one used for later phases of the nonstationary calculations, where the crystal dimensions have already significantly increased. In order to optimize the calculations, the size of the finite elements gradually increases in the direction away from the molten zone.

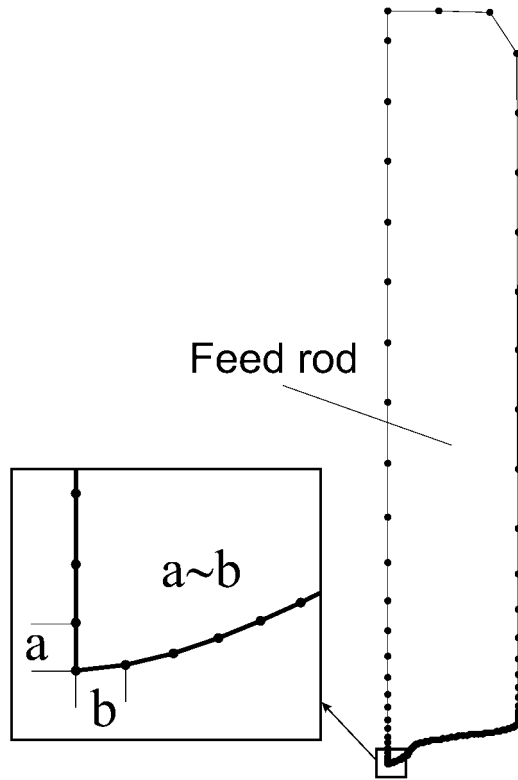


Figure 4.49 Grid sample of the boundary elements for the feed rod at a given time (Reprinted with permission from [Rudevics 2004], copyright (2005) Elsevier Ltd).

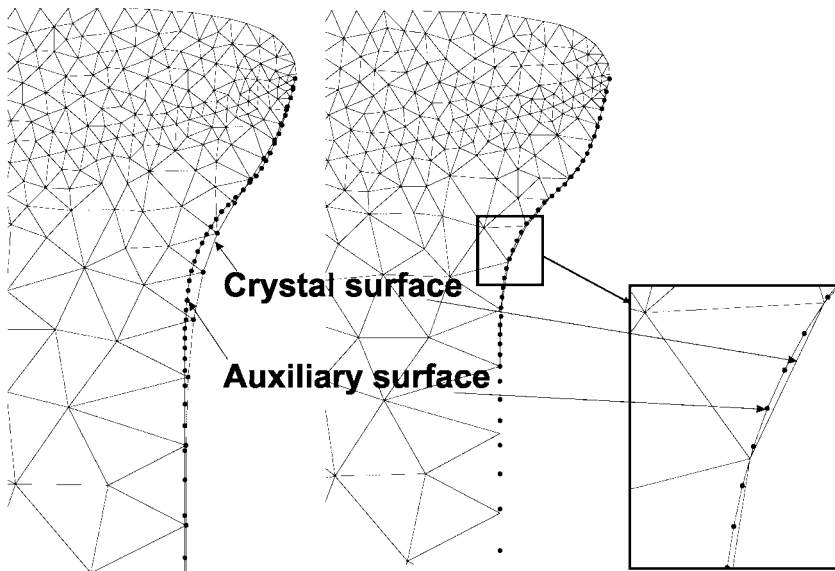


Figure 4.50 Modelling the crystal surface: left, without auxiliary surfaces; right, with auxiliary surfaces (Reprinted with permission from [Rudevics 2004], copyright (2005) Elsevier Ltd).

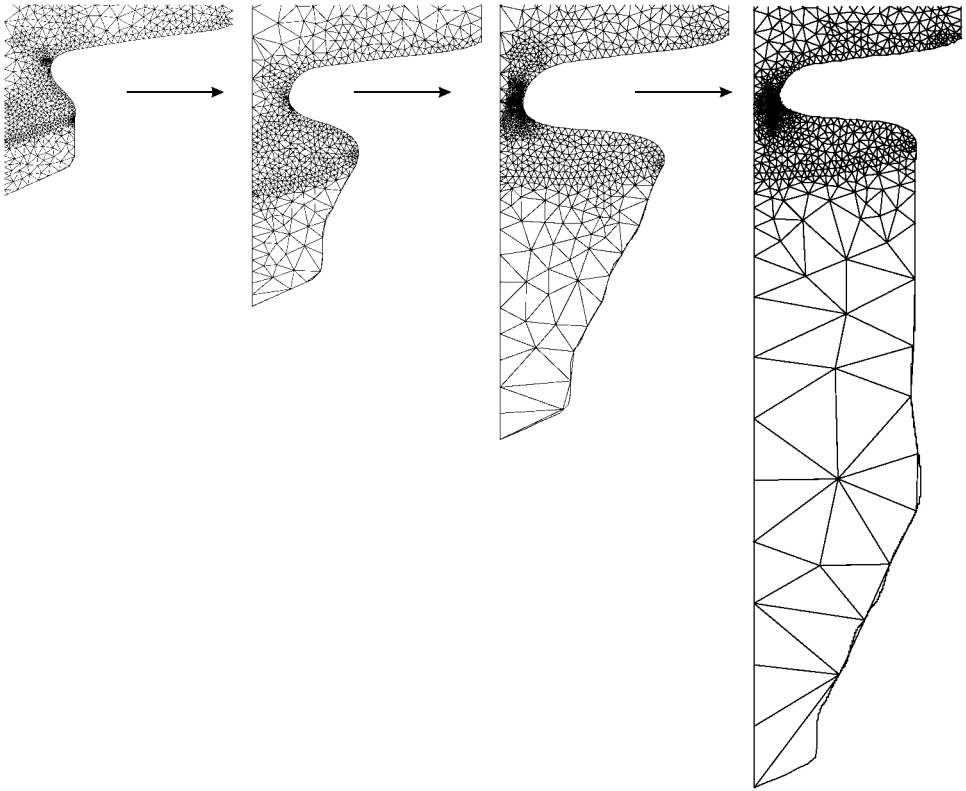


Figure 4.51 Finite-element grids for four different phases of the nonstationary FZ process starting from the cone.

4.3.4.2 Calculations for the Nonstationary FZ Process

Experimental Verification. At the Institute for Crystal Growth (ICG), Berlin, an experiment was performed to examine the reaction of the FZ system to changes of inductor power and feed rate. The impulse-type parameter changes were applied after the system reached an equilibrium state, i.e. the crystal was growing with constant radius. These data were used to carry out a corresponding nonstationary simulation with the mathematical FZ model implemented in the program FZoneT [Rudevics 2005-1].

The initial geometry used for the nonstationary calculation is shown in Figure 4.52 and corresponds to the experimental FZ system at the quasi-stationary process stage. During the crystal growth process, the inductor current I_0 and the feed rate v_F were changed as shown in Figure 4.53, which caused changes in the crystal radius r_c and zone height H_Z . A comparison of the results of the nonstationary FZ model with the experiment is given in Figure 4.54 and shows that the features of the calculated changes of crystal radius and zone height in time correspond well with the experiment. The visible differences can be

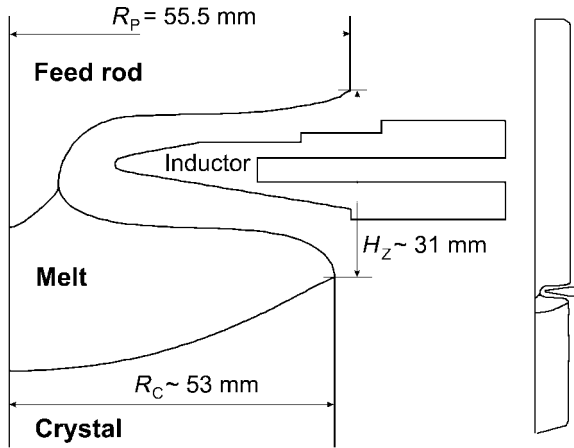


Figure 4.52 Phase boundary shapes and characteristic parameters for the FZ system at the beginning of the nonstationary calculation (Reprinted with permission from [Rudevics 2005-1], copyright (2005) Elsevier Ltd).

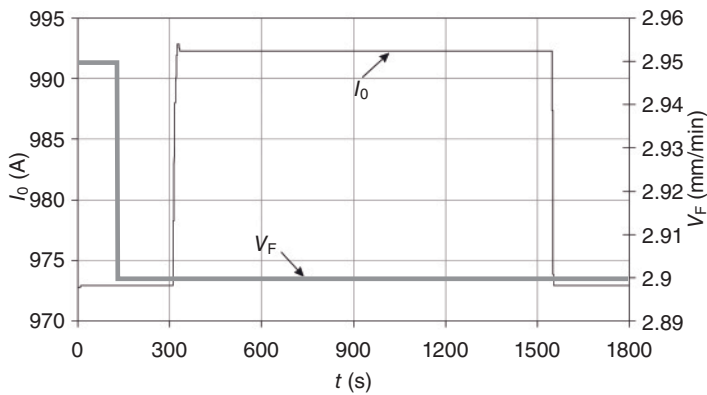


Figure 4.53 Impulse-type changes of inductor current and feed rod speed used in the experiment and in the calculations (Reprinted with permission from [Rudevics 2005-1], copyright (2005) Elsevier Ltd).

explained by the precision of the numerical approximation as well as measurement errors of zone height and crystal radius during the experiment. Figure 4.54 also shows that the characteristic transition time of the system response to parameter changes is about 15 min and is well described by the numerical model. The diameter response also shows decreasing oscillations; see [Rudevics 2005-1].

Further numerical nonstationary calculations [Rudevics 2005-1] for the end cone of crystal growth (crystal diameter is decreasing) have also shown that the angle between crystallization interface and crystal surface at the ETP is larger than during cylindrical growth. On the other hand, during the growth of the crystal cone (crystal diameter is

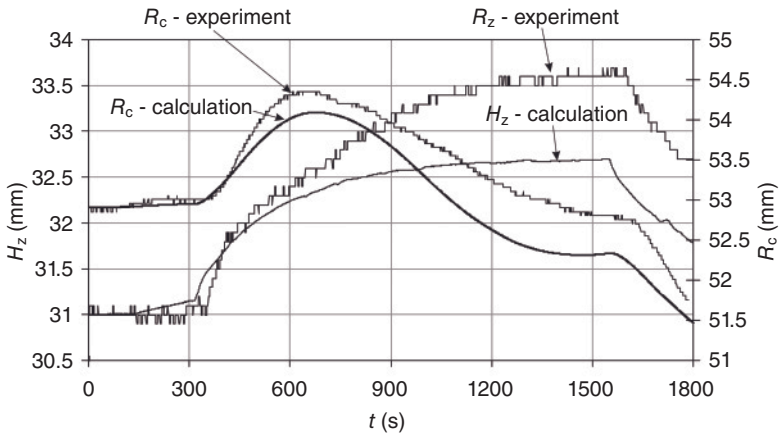


Figure 4.54 Reactions of crystal radius and zone height on the impulse-type changes (Reprinted with permission from [Rudevics 2005-1], copyright (2005) Elsevier Ltd).

increasing), this angle is smaller than during cylindrical growth. Such dependencies could be important for stability analyses of crystal growth.

Modelling the Transient FZ Crystal Growth Process with Control. One of the most significant tasks in practice is to ensure the growth of crystals with a definite shape, e.g. with a given slope of the crystal surface and with defined conditions, e.g. a given zone height. Control of the zone height ensures the stability of the process and precludes emergency interruption of the process, e.g. spilling of the melt or collision of the feed rod with the RF inductor. Therefore in practice, special automatic control algorithms are used, during which the previously unknown values of the process parameters, e.g. value of the inductor current, are found during the growth process.

For modelling the dynamics of crystal growth with automatic control, proportional–integral–differential (PID) controllers were implemented in a separate program module [Rudevics 2005-2] in the nonstationary program FZoneT. For PID control, the following control parameters were used: molten zone height H_z , inductor current I_0 , feed rate v_F , and angle ϕ_0 between the tangent to the crystal surface at the ETP and the vertical direction. Figure 4.55 shows a sample calculation in which a FZ system is modelled with a PID control during a time period of 4000s (from the beginning of the simulation) to ensure a specified crystal surface slope of 11° . It can be seen that the control algorithm ensures the desired shape of the crystal. It must be emphasized that the time dependencies of inductor current and feed rate during this calculation are not preplanned but obtained from the simulated PID control of the process.

In conclusion, it must be emphasized that the behaviour of the free melt surface strongly influences the whole process of FZ crystal growth. Capillary forces therefore play a crucial role in the system and must be modelled properly. The examples of mathematical modelling presented in this chapter show that, by using advanced mathematical models

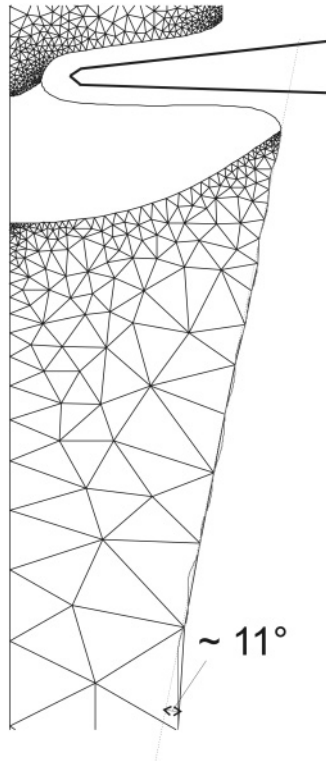


Figure 4.55 Result of modelling a nonstationary FZ crystal growth process with PID control to obtain 11° slope of the crystal surface.

together with increased computer performance, stationary and nonstationary crystal growth processes can be modelled with an acceptable approximation. Such modelling is a real help for optimizing the FZ process in industry [von Ammon 2004].

Appendix: Code for Calculating the Free Surface During a FZ Process in Python as used in 4.1.1.9

```
#!/usr/bin/env python
# -*- coding: utf-8 -*-
# Author: Michael Wünscher <wuenscher@ikz-berlin.de>
#
# You can freely use the code for whatever you want.
#
# Any comments are welcome.
from numpy import array, zeros, sin, cos, pi, double
from pylab import plot, show
```

```

class RungeKuttaFreeSurface:
    ``This is the class which implements the Runge-Kutta-
    Solver using
    the numpy array functions.``
    force = None
    def __init__(self, x, y, para, dx):
        ``Initialise the integrator with the given variables and
        parameter
        - x arc length
        - y variable array r, z and beta
        - para parameter
        - dx step length``
        self.x = double(x)
        self.y = array(double(y))
        self.para = array(double(para))
        self.dx = double(dx)
        print `RK4-FreeSurface-Init: `, x, y, para, dx
    def abl(self, x, y):
        ``Derivative which implement the Young- Laplace's
        -Equation``
        dydx = zeros(len(y))
        #eqn for the radius
        dydx[0] = sin(y[2])
        #eqn for the horizontal
        dydx[1] = cos(y[2])
        #eqn for the angle
        dydx[2] = cos(y[2])/y[0] + self.para[0] * y[1]
        - self.para[1]
        #Setting a electric force object
        if self.force:
            dydx[2]+ = self.force(x)
        return dydx
    def step(self):
        ``Calculates a rk4 step of the length dx``
        hdx = 0.5*self.dx
        hx = self.x+hdx
        dydx0 = self.abl(hx, self.y)
        dydx1 = self.abl(hx, self.y+hdx*dydx0)
        dydx2 = self.abl(hx, self.y+hdx*dydx1)
        dydx3 = self.abl(self.x+self.dx, self.y+self.dx*dydx2)
        self.y + = self.dx/6. * (dydx0 + 2. * (dydx1 + dydx2) +
        dydx3)
        self.x + = self.dx
    def GetData(self):
        return self.x, array(self.y)
    def GetAngle(self):

```

```

    return self.y[2]
def SetForceSpline(self, force):
    self.force = force
class FreeSurfaceFZSolver(RungeKuttaFreeSurface):
    ``It is used to initialize the solver and make the unit
    conversion``
def __init__(self, pressure = 232.5, radius = 0.0255,
beta_degree = 11.,
rho = 2530., gamma = 0.783, grav = 9.81, stepsize =
0.002):
    ``Initilize the integrator``
    #Intial Conditions
    self.radius = radius
    self.para_dim = (pressure, radius, beta_degree,
rho, gamma, grav)
    r = 1.
    z = 0.
    beta = beta_degree * pi / 180
    bondnr = rho * grav * radius*radius / gamma
    pzero = pressure * radius / gamma
    RungeKuttaFreeSurface.__init__(self, 0., [r, z, beta],
[bondnr, pzero], stepsize)
def solve(self, stop_angle = 0., integration_length =
(0.5, 2.), output_steps = 10):
    ``Solve the system and out put the result``
    minintegration = int(integration_length[0] / self.dx)
    maxintegration = int(integration_length[1]/ self.dx)
    stop_angle = stop_angle /180. * pi
    i = 0
    x, y = self.GetData()
    data = [[], [], [], []]
    #data[0] = []
    data[0].append(x)
for j in range(1, 3):
    #data[j] = []
    data[j].append(y[j-1])
while i < maxintegration:
    self.step()
    i+ = 1
if i % output_steps == 0 :
    x, y = self.GetData()
    data[0].append(x)
for j in range(1, 3):
    data[j].append(y[j-1])
if i > minintegration and self.GetAngle() > stop_angle :
break

```

```

data_scaled = []
for vari in data:
    data_scaled.append(array(vari)*self.radius)
return data_scaled, self.para_dim
def main_fsFZ():
    ``Sample solution for Si``
    fsFZ = FreeSurfaceFZSolver()
    data, parameter = fsFZ.solve()
    #Plot using matplotlib from pylab
    plot(data[1]*1000., data[2]*1000.)
    show()
if __name__ == '__main__':
    main_fsFZ()

```

References

- [Akashi 1969] Akashi T., Matsumi T., Okada T., Mizutani T., *IEEE Trans. Magn.* **5** (1969) 285.
- [Arsenjew 1973-1] Arsenjew P.A., Baranow M.N., Kustow E.F., Bienert K., *Exp. Tech. Phys.* **21** (1973) 289.
- [Arsenjew 1973-2] Arsenjew P.A., Baranow M.N., Bienert K., Kustov E.F., *Krist. Tech.* **8** (1973) 1113.
- [Assaker 1998] Magneto hydrodynamics in Crystal Growth, PhD thesis, Université Catholique de Louvain, Belgium (1998).
- [Bagdasarov 1986] Bagdasarov Kh.S., Dyachenko V.V., Kevorkov A.M., Kholov A., In: *Application of Laser Heating to Crystal Growth*, ed.E.I. Givargizov, Plenum Press, New York (1986), p. 364.
- [Balakrishnan 1993] Balakrishnan G., Paul D.McK., Lees M.R., Boothroyd A.T., *Physica C* **206** (1993) 148.
- [Balbashov 1981] Balbashov A.M., Egorov S. K., *J. Cryst. Growth* **52** (1981) 498.
- [Bardsley 1974] Bardsley W., Frank F.C., Green G.W., Hurle D.T.J., *J. Cryst. Growth* **23** (1974) 341.
- [Barthel 1967] Barthel J., Eichler K., *Krist. Tech.* **2** (1967) 205–215.
- [Barthel 1979] Bartel J., Eichler K. Jurisch M., Löser W., *Krist. Tech.* **14** (1979) 637–644.
- [Barthel 1981] Barthel J., Göbel R., Jurisch M., Ovsienko D.E., Sosina E.I, Urunbaev S.M., *J. Cryst. Growth* **52** (1981) 369–375.
- [Baum 1959] Baum F.J., *Rev. Sci. Instr.* **30** (1959) 1064.
- [Bednorz 1984] Bednorz J.G., Arend H., *J. Cryst. Growth* **67** (1984) 660.
- [Behr 1985] Behr G., Bartsch K., Jurisch M., Schönherr M., Wolf E., *Cryst. Res. Technol.* **20** (1985) K93–K95.
- [Behr 1999] Behr G., Löser W., Graw G., Bitterlich H., Freudenberger J., Fink J., Schultz L., *J. Cryst. Growth* **198–199** (1999) 642–648.
- [Behr 2000] Behr G., Löser W., Graw G., Bitterlich H., Fink J., Schultz L., *Cryst. Res. Technol.* **35** (2000) 461–72.
- [Behr 2002] Behr G., Löser W., Bitterlich H., Graw G., Souptel D., Sampathkumaran E.V., *J. Cryst. Growth* **237–239** (2002) 1976–80.
- [Behr 2005-1] Behr G., Löser W., Apostu M.-O., Gruner W., Hücker M., Schramm L., Souptel D., Teresiak A., Werner J., *Cryst. Res. Technol.* **40** (2005) 21–25.
- [Behr 2005-2] Behr G., Löser W., *Recent Research and Development in Crystal Growth 4*, Transworld Research Network, Trivandrum, India (2005), pp. 129–165.
- [Behr 2008] Behr G., Löser W., Souptel D., Fuchs G., Mazilu I., Cao C., Köhler A., Schultz L., Büchner B., *J. Cryst. Growth* **310** (2008) 2268–2276.

- [Berthel 1963] Berthel K.-H., Longo H.-E., Schlaubitz K., In: *Reinststoffe in Wissenschaft und Technik*, ed. Rexer E., Witzmann H., Lange W. Akademieverlag, Berlin (1963), pp. 293–300.
- [Bioul 2007] Bioul, F. Use of mathematical expansions to model crystal growth from the melt under the effect of magnetic fields, PhD thesis Université Catholique de Louvain 2007.
- [Bitterlich 2000] Bitterlich H., Löser W., Behr G., Graw G., Yang-Bitterlich W., Krämer U., Schultz L., *J. Cryst. Growth* **213** (2000) 319–327.
- [Bohm 1994] Bohm J., Lüdge A., Schröder W., In: *Handbook of Crystal Growth. Volume 2a, Bulk Crystal Growth*, ed. D.T.J. Hurler, Elsevier Science, Amsterdam (1994).
- [Burrus 1977] Burrus C.A., Stone J., *Appl. Phys. Lett.* **31** (1977) 383.
- [Carlberg 1984] Carlberg T., *Proc. 5th European Symp. Materials Sciences and Microgravity*, Schloß Elmau (1984), p. 367.
- [Carlberg 1986] Carlberg T., *Acta Astronaut.* **13** (1986) 639.
- [Carlberg 1991] Carlberg T., Levenstam M., *Microgravity Sci. Technol.* **IV**(4) (1991) 254.
- [Carruthers 1976] Carruthers J.R., *J. Cryst. Growth* **32** (1976) 13–26.
- [Celler 1984] Celler G.K., Jackson K.A., Trimble L.E., Robinson McD., Lischner D.J., *Proc. Energy Beam–Solid Interactions and Transient Thermal Processing Symp.*, Boston, 1983 (1984), p. 409.
- [Celler 1985] Celler G.K., Trimble L.E., Wilson L.O., *Proc. Energy Beam–Solid Interactions and Transient Thermal Processing Symp.*, Boston, 1984 (1985), p. 635.
- [Chan 1992] Chan Y.T., Choi S.K., *J. Appl. Phys.* **72** (1992) 3741–3749.
- [Chang 1975] Chang C.E., Wilcox W.R., *J. Cryst. Growth* **28** (1975) 8–12.
- [Chang 1976] Chang C.E., Wilcox W.R., *Int. J. Heat Mass Transfer* **19** (1976) 355–366.
- [Chapman 1960] Chapman A.T., Clark G.W., *J. Am. Ceram. Soc.* **48** (1960) 494.
- [Chen 1995] Chen J.-C., Hu C., *J. Cryst. Growth* **149** (1995) 87.
- [Chen 1996] Chen J.-C., Hu C., *J. Cryst. Growth* **158** (1996) 289.
- [Chen 2005] Chen D.P., Maljuk A., Lin C.T., *J. Cryst. Growth* **284** (2005) 86.
- [Chun 1980] Chun Ch.-H., *J. Cryst. Growth* **48** (1980) 600–610.
- [Class 1968] Class W., *J. Cryst. Growth* **3** (1968) 241.
- [Cox 1972] Cox R.T., Revcolevschi A., Collongues R., *J. Cryst. Growth* **15** (1972) 301.
- [Cröll 1994-1] Cröll A., Tegetmeier A., Nagel G., Benz K.W., *Cryst. Res. Technol.* **29** (1994) 335.
- [Cröll 1994-2] Cröll A., Dold P., and Benz K.W., *J. Cryst. Growth* **137** (1994) 95.
- [Cröll 1998] Cröll A., Kaiser Th., Schweizer M., Danilewsky A.N., Lauer S., Tegetmeier A., Benz K.W., *J. Cryst. Growth* **191** (1998) 365.
- [Crouch 1982] Crouch R.K., Fripp A.L., Debnam W.J., In: *Thermophysical properties of germanium for thermal analysis of growth from the melt*, ed. G.E. Rindone, Elsevier, Amsterdam (1982), p. 657.
- [Crystal 1992] Crystal Systems Inc., *Four mirror type optical FZ furnace*, Technical Report FZ-E-002.
- [Danilewsky 1994] Danilewsky A.N., Nagel G., Benz K.W., *Cryst. Res. Technol.* **29** (1994) 171.
- [Danilewsky 1996] Danilewsky A.N., Lauer S., Bischofink G., Benz K.W., *Cryst. Res. Technol.* **31** (1996) 11.
- [Dash 1958] Dash W.C., *J. Appl. Phys.* **29** (1958) 705.
- [Dash 1960] Dash W.C., *J. Appl. Phys.* **31** (1960) 736.
- [Davidson 1978] Davidson M.C., Holland L.R., *Rev. Sci. Instrum.* **49** (1978) 1156.
- [Dold 1994] Dold P., PhD thesis, University of Freiburg, Germany (1994).
- [Dreeben 1980] Dreeben V., Kim K.M., Schujko A., *J. Cryst. Growth* **50** (1980) 126.
- [Dupret 1994] Dupret F., Van den Bogaert N., In: *Handbook of Crystal Growth Vol. 2b, Bulk Crystal Growth*, ed. D.T.J. Hurler, Elsevier Science, Amsterdam (1994), p. 875.
- [Eickhoff 1969] Eickhoff K., Gürs K., *J. Cryst. Growth* **6** (1969) 21.
- [Elwell 1985] Elwell D., Kway W.L., Feigelson R.S., *J. Cryst. Growth* **71** (1985) 237.
- [Essmann 1995] Essmann U., Henes R., Holzwarth U., Klopper F., Büchler E., *Phys. Stat. Sol. A*, **160** (1977) 487–497.
- [Eyer 1979] Eyer A., Zimmermann H., Nitsche R., *J. Cryst. Growth* **47** (1979) 219.
- [Feigelson 1986] Feigelson R.S., *J. Cryst. Growth* **79** (1986) 669.
- [Feigelson 1988] Feigelson R.S., *MRS Bulletin XIII*(10) (1988) 47.

- [Fejer 1984] Fejer M.M., Nightingale J.L., Magel G.A., Byer R.L., *Rev. Sci. Instrum.* **55** (1984) 1791.
- [Field 1968] Field W.G., Wagner R.W., *J. Cryst. Growth* **3–4** (1968) 799.
- [Gasson 1970] Gasson D.B., Cockayne B., *J. Mater. Sci.* **5** (1970) 100.
- [Geho 2004] Geho M., Sekijima T., Fujii T., *J. Cryst. Growth* **267** (2004) 188.
- [Geray 1984] Geray R., Master's thesis, University of Freiburg, Germany (1984).
- [Guo 1998] Guo Z., Maruyama S., Togawa S., *J. Cryst. Growth* **194** (1998) 321.
- [Gurtler 1978] Gurtler R.W., Baghdadi A., Ellis R.J., Lesk J.A., *J. Electron. Mater.* **7** (1978) 441.
- [Hallstedt 2003] Hallstedt B., Gaukler L., *Calphad* **27** (2003) 177–191.
- [Hatta 1996] Hatta K., Higuchi M., Takahashi J., Kodaira K., *J. Cryst. Growth* **163** (1996) 279–284.
- [Haya 1996] Haya R., Rivas D., Sanz J., *Int. J. Heat Mass Transfer* **40** (1996) 323.
- [Hermann 2001] Hermann R., Priede J., Behr G., Gerbeth G., Schultz L., *J. Cryst. Growth* **223** (2001) 577–587.
- [Hermann 1995] Hermann F.M., Müller G., *J. Cryst. Growth* **156** (1995) 350.
- [Hermann 2008] Hermann R., Vinzelberg H., Behr G., Woll K., Mücklich F., Büchner B., *J. Cryst. Growth* **310** (2008) 4286–4289.
- [Heywang 1954] Heywang W., *Z. Naturforschung* **11a** (1956) 238.
- [Ii 1979] Ii N., Shindo I., *J. Cryst. Growth* **46** (1979) 569–574.
- [Iida 1993] Iida T., Guthrie R.I.L., *The Physical Properties of Liquid Metals*. Clarendon Press, Oxford (1993).
- [Imai 1995] Imai T., Yagi S., Sugiyama Y., Hatakeyama I., *J. Cryst. Growth* **147** (1995) 350.
- [Jackson 1985] Jackson K.A., Kurtze D. A., *J. Cryst. Growth* **71** (1985) 385.
- [Jianwei 1998] Jianwei X., Yongzong Z., Guoqing Z., Ke X., Peizhen D., Jun X., *J. Cryst. Growth* **193** (1998) 123–126.
- [Jurisch 1977] Jurisch M., Berthel K.-H., Ullrich H.-J., *Phys. Stat. Sol. A*, **44** (1977) 277–284.
- [Jurisch 1979] Jurisch M., Behr G., *Acta Phys. Acad. Sci. Hungar* **47** (1979) 201–207.
- [Jurisch 1982] Jurisch M., Löser W., Lyumkis E., Martuzāne E., Martuzāns B., *Cryst. Res. Technol.* **17** (1982) 963–971.
- [Jurisch 1990-1] Jurisch M., *J. Cryst. Growth* **41** (1990) 223–232.
- [Jurisch 1990-2] Jurisch M., Löser W., *J. Cryst. Growth* **102** (1990) 214–222.
- [Kadečková 1963] Kadečková S., Šesták B., *Br. J. Appl. Phys.* **14** (1963) 927.
- [Karow 1993] Karow H.H., *Fabrication Methods for Precision Optics*. John Wiley & Sons, Ltd, New York (1993).
- [Keck 1953] Keck P.H., Golay M.J.E., *Phys. Rev.* **89** (1953) 1297.
- [Kim 1979] Kim K.M., Dreeben A.B., Schujko A., *J. Appl. Phys.* **50** (1979) 4472.
- [Kimura 1977] Kimura S., Shindo I., *J. Cryst. Growth* **41** (1977) 192–198.
- [Kimura 1993] Kimura M., Arai H., Mori T., Yamagishi H., *J. Cryst. Growth* **128** (1993) 282.
- [Kimura 1996] Kimura M., Yoshizawa K., Yamagishi H., *Proc. 4th Int Symp High Purity Silicon*, 96–13 (1996), p. 58.
- [Kitamura 1979] Kitamura K., Ii N., Shindo I., Kimura S., *J. Cryst. Growth* **46** (1979) 277–285.
- [Kitamura 1980] Kitamura K., Kimura S., Hosoya S., *J. Cryst. Growth* **48** (1980) 469–472.
- [Kitamura 1982] Kitamura K., Kimura S., Watanabe K., *J. Cryst. Growth* **57** (1982) 475–481.
- [Kitazawa 1977] Kitazawa K., Nagashima N., Mizutani T., Fueki K., Mukaibo T., *J. Cryst. Growth* **39** (1977) 211.
- [Kobayashi 1978] Kobayashi N., *J. Cryst. Growth* **43** (1978) 417–424.
- [Kobayashi 1982] Kobayashi N., Wilcox W.R., *J. Cryst. Growth* **59** (1982) 616–624.
- [Kobayashi 1984] Kobayashi N., *J. Cryst. Growth* **66** (1984) 63–72.
- [Koohpayeh 2008] Koohpayeh S.M., Fort D., Abell J.S., *Progr. Cryst. Growth Charact. Mater.* **54** (2008) 121–137.
- [Kooy 1961] Kooy C., Couwenberg H.J.M., *Philips Techn. Rundschau* **23** (1961/62) 143.
- [Kramer 1985] Kramer I., Langbein D., Harr M., ESA Contract Report, Contract No. 6065/84/NL/PR(SC), Battelle, Frankfurt, Germany (1985).
- [Lai 2001] Lai Y.J., Chen J.C., *J. Cryst. Growth* **231**(2001) 222.
- [Lan 1993] Lan C.W., Kou S., *J. Cryst. Growth* **132** (1993) 578–591.

- [Lan 1997] Lan C.W., Tsai C.H., *J. Cryst. Growth* **173** (1997) 561.
- [Lan 2003] Lan C.W., *J. Cryst. Growth* **247** (2003) 597–612.
- [Lauder 1975] Launder B.E. (ed.), *Studies in Convection: Theory, Measurement, and Applications*, Academic Press, London (1975).
- [Lanski 1990] Lenski H., *Microgravity Q* **1** (1990) 47.
- [Liang 2002] Liang B., Lin C.T., *J. Cryst. Growth* **237–239** (2002) 756–761.
- [Lie 1990] Lie K.H., Walker J.S., Riahi D.N., *J. Cryst. Growth* **100** (1990) 450.
- [Lie 1991] Lie K.H., Walker J.S., Riahi D.N., *J. Cryst. Growth* **109** (1991) 167.
- [Lopez 1999] López C.R., Mileham J.R., Abbaschian R., *J. Cryst. Growth* **200** (1999) 1.
- [Louchev 1996] Louchev O.A., Otani S., Ishizawa Y., *J. Appl. Phys.* **80** (1996) 518–528.
- [Lüdge 1997] Lüdge A., Riemann H., *Inst. Phys. Conf. Ser. No 160* (1997) 145–148.
- [Maffei 1997] Maffei N., Quon D.H.H., Aota J., Kuriakose A.K., Saghir M.Z., *J. Cryst. Growth* **180** (1997) 105.
- [Matsumoto 1992] Matsumoto K., Fujimori Y., Shimizu M., Usami R., Kusunose T., Kimura H., Ohya M., Ishikura S., Nishida H., Negishi N., Kawabata S., *Acta Astronaut.* **27** (1992) 167
- [Mazilu 2005] Mazilu I., Löser W., Behr G., Werner J., Eckert J., Schultz L., *J. Cryst. Growth* **275** (2005) e109–e114.
- [Mazilu 2007] Mazilu I., Thesis, TU Darmstadt, Germany (2007).
- [Mizutani 1974] Mizutani T., Matsumi K., Makino H., Yamamoto T., Kato T., *NEC Res. Dev.* **33** (1974) 86.
- [Mühlbauer 1983] Muehlbauer A., Erdmann W., Keller W., *J. Cryst. Growth* **64** (1983) 529.
- [Mühlbauer 1993] Muehlbauer A., Muiznieks A., Jakowitsch A., Virbulis J., *Arch. Elektrotech.* **76**, 161 (1993).
- [Mühlbauer 1995] Muehlbauer A., Muiznieks A., Virbulis J., Luedge A., Riemann H., *J. Cryst. Growth* **151** (1995) 66.
- [Mühlbauer 1997] Muehlbauer A., Muiznieks A., Virbulis J., *J. Cryst. Growth* **180** (1997) 372.
- [Mühlbauer 1999-1] Muehlbauer A., Muiznieks A., Raming G., Riemann H., Luedge A. *J. Cryst. Growth* **198–199** (1999) 107.
- [Mühlbauer 1999-2] Muehlbauer A., Muiznieks A., Raming G., *Cryst. Res. Technol.* **34** (1999) 217.
- [Muiznieks 2006] Muiznieks A., Rudevics A., Lacis K., Riemann H., Lüdge A., Schulze F.W., Nacke B., *Proc. Int. Colloq. Modelling of Material Processing*, Riga (2006).
- [Muto 1969] Muto K., Awazu K., *Jpn. J. Appl. Phys.* **8** (1969) 1360.
- [Nabokin 2003] Nabokin P.I., Souptel D., Balbashov A.M., *J. Cryst. Growth* **250** (2003) 397–404.
- [Nason 1990] Nason D.O., Yen C.T., Tiller W.A., *J. Cryst. Growth* **106** (1990) 221.
- [Naumann 1987] Naumann H., Schröder G., *Bauelemente der Optik*, 5th ed. Hanser, Munich (1987).
- [Niemyski 1968] Niemyski T., Kierzek-Pecold E., *J. Cryst. Growth* **3** (1968) 162–165.
- [Notbohm 2007] Notbohm S., Ribeiro P., Lake B., Tennant D.A., Schmidt K.P., Uhrig G.S., Hess C., Klingeler R., Behr G., Büchner B., Reehuis M., Bewley R.I., Frost C.D., Manue P., Eccleston R.S., *Phys. Rev. Lett.* **98** (2007) 027403.
- [Otani 1984] Otani S., Tanaka T., Ishizawa Y., *J. Cryst. Growth* **66** (1984) 419–425.
- [Otani 1990] Otani S., Tanaka T., Ishizawa Y., *J. Cryst. Growth* **106** (1990) 498–502.
- [Otani 1998] Otani S., *J. Cryst. Growth* **192** (1998) 346–349.
- [Otani 1999] Otani S., Ohsawa T., *J. Cryst. Growth* **200** (1999) 472–475.
- [Otani 2000] Otani S., Korsukova M.M., Mitsunashi T., Kieda N., *J. Cryst. Growth* **217** (2000) 378–382.
- [Pfann 1966] Pfann W.G., *Zone Melting*, 2nd ed., Wiley, New York (1966).
- [Poplawsky 1960] Poplawsky R., Thomas J.E., *Rev. Sci. Instrum.* **31** (1960) 1303.
- [Poplawsky 1962] Poplawsky P.R., *J. Appl. Phys.* **33** (1962) 1616–1617.
- [Quon 1993] Quon D.H.H., Chehab S., Aota J., Kuriakose A.K., Wang S.S.B., Saghir M.Z., Chen H.L., *Microgravity Q.* **3** (1993) 135.
- [Raming 1999] Raming G., Muiznieks A., Muehlbauer A., *Proc. Int. Colloq. Modelling of Material Processing*, Riga (1999), pp. 24–29.

- [Raming 2000] Raming G., PhD Thesis, Institut für Elektrowärme, Universität Hannover, Germany (2000).
- [Ratnieks 2003] Ratnieks G., Muiznieks A., Mühlbauer A., *J. Cryst. Growth* **255** (2003) 227–240.
- [Ratnieks 2008] Ratnieks G., PhD thesis, Faculty of Physics and Mathematics, University of Latvia, Riga (2008).
- [Ray 1988] Ray S.F., *Applied Photographic Optics*, Focal Press, London (1988).
- [Riemann 1995] Riemann H., Lüdge A., Boettcher K., Rost H.-J., Hallmann B., Schroeder W., Hensel W., Schleusener B., *J. Electrochem. Soc.* **142**(3) (1995) 1007.
- [Riemann 1996] Riemann H., Hallmann B., Lüdge A., *Meeting of the ACCG-10*, Vail (1996).
- [Rivas 1992] Rivas D., Sanz J., Vázquez C., *J. Cryst. Growth* **116** (1992) 127.
- [Rivas 1999] Rivas D., Haya R., *J. Cryst. Growth* **206** (1999) 230.
- [Rivas 2001] Rivas D., Vázquez-Espi C., *J. Cryst. Growth* **223** (2001) 433.
- [Rivas 2002] Rivas D., Haya R., *J. Cryst. Growth* **241** (2002) 249.
- [Rivas 2004] Rivas D., *J. Cryst. Growth* **262** (2004) 48.
- [Rudevics 2004] Rudevics A., Muiznieks A., Ratnieks G., Mühlbauer A., Wetzel Th., *J. Cryst. Growth* **266** (2004) 54–59.
- [Rudevics 2005-1] Rudevics A., Muiznieks A., Riemann H., Luedge A., Ratnieks G., von Ammon W., *J. Cryst. Growth* **275** (2005) 561–565.
- [Rudevics 2005-2] Rudevics A., Muiznieks A., Ratnieks G., *Proc. Joint 15th Riga and 6th PAMIR Int. Conf. Fundamental and Applied MHD*, Rigas Jurmala, Vol. II (2005), pp. 229–232.
- [Rudevics 2008] Rudevics A., PhD thesis, Faculty of Physics and Mathematics, University of Latvia, Riga (2008).
- [Saint-Martin 2008] Saint-Martin R., Franger S., *J. Cryst. Growth* **310** (2008) 861.
- [Saurat 1971] Saurat M., Revcolevschi A., *Rev. Internat. Hautes Temp. Refract.* **8** (1971) 291.
- [Schramm 2005] Schramm L., Behr G., Löser W., Wetzig K., *J. Phase Equilib. Diff.* **26** (2005) 605–612.
- [Schwabe 1978] Schwabe D., Scharmann A., Preisser F., Oeder R., *J. Cryst. Growth* **43** (1978) 305–312.
- [Schwabe 2007] Schwabe D., Mizev A.I., Udhayasankar M., Tanaka S., *Phys. Fluids* **19** (2007) 072102.
- [Sekar 2005-1] Sekar C., Krabbes G., Teresiak A., *J. Cryst. Growth* **273** (2005) 403–411.
- [Sekar 2005-2] Sekar C., Krabbes G., Teresiak A., Wolf M., Eckert D., Mueller K.-H., *J. Cryst. Growth* **275** (2005), e1961–e1965.
- [Sekijima 1998] Sekijima T., Satoh H., Tahara K., Fujii T., Wakino K., Okada M., *J. Cryst. Growth* **193** (1998) 446.
- [Shimizu 1975] Shimizu R., Kataoka Y., Kawai S., Tanaka T., *Appl. Phys. Lett.* **27** (1975) 113–114.
- [Sigalovsky 1993] Sigalovsky J., Haggerty J.S., Sheehan J.E., *J. Cryst. Growth* **134** (1993) 313–324.
- [Souptel 2002] Souptel D., Behr G., Balbashov A.M., *J. Cryst. Growth* **236** (2002) 583.
- [Souptel 2004] Souptel D., Behr G., Löser W., Teresiak A., Drotziger S., Pfeleiderer C., *J. Cryst. Growth* **269** (2004) 606–616.
- [Souptel 2005-1] Souptel D., Behr G., Kreyszig A., Löser W., *J. Cryst. Growth* **276** (2005) 652–662.
- [Souptel 2005-2] Souptel D., Thesis, TU Dresden, Germany (2005).
- [Souptel 2007-1] Souptel D., Löser W., Behr G., *J. Cryst. Growth* **300** (2007) 538.
- [Souptel 2007-2] Souptel D., Löser W., Gruner W., Behr G., *J. Cryst. Growth* **307** (2007) 410–420.
- [Surek 1975] Surek T., Chalmers B., *J. Cryst. Growth* **42** (1975) 1.
- [Takagi 1977] Takagi K., Ishii M., *J. Cryst. Growth* **40** (1977) 1.
- [Takekawa 1988] Takekawa S., Nozaki H., Umezono A., Kosuda K., Kobayashi M., *J. Cryst. Growth* **92** (1988) 687–690.
- [Tanaka 1975] Tanaka T., Bannai E., Kawai S., Yamane T., *J. Cryst. Growth* **30** (1975) 193–197.

- [Tanaka 1980] Tanaka T., Nishitani R., Oshima C. Bannai E., Kawai S., *J. Appl. Phys.* **51** (1980) 3877–3883.
- [Tanaka 1988] Tanaka T., Otani S., Ishizawa Y., *J. Mater. Sci.* **23** (1988) 665–669.
- [Tang 1988] Tang D.Y., Route R.K., *J. Cryst. Growth* **91** (1988) 81.
- [Tegetmeier 1995] Tegetmeier A., PhD thesis, University of Freiburg, Germany (1995).
- [Tegetmeier 1996] Tegetmeier A., Cröll A., Danilewsky A., Benz K.W., *J. Cryst. Growth* **166** (1996) 651.
- [Theuerer 1952] Theuerer H.C., Method of processing semiconductive materials, US Patent No. 3060123, 17 December 1952.
- [Tiller 1991] Tiller W.A., Yen C.T., *J. Cryst. Growth* **109** (1991) 120.
- [Togawa 1998] Togawa S., Nishi Y., Kobayashi M., *Electrochem. Soc. Proc.* **98**(13) (1998) 67.
- [Trivich 1970] Trivich D., Pollack G.P., *J. Electrochem. Soc.* **117** (1970) 344.
- [Vaněk 1979] Vaněk P., Kadečková S., *J. Cryst. Growth* **47** (1979) 458.
- [Vaněk 1983] Vaněk P., Kadečková S., Jurisch M., Löser W., *J. Cryst. Growth* **63** (1983) 191–196.
- [Virbulis 1997] Virbulis J., Numerische Simulation der Phasengrenzen und Schmelzenströmung bei der Züchtung von Siliziumeinkristall Mit dem Floating-Zone Verfahren, PhD thesis. University of Latvia, Riga (1997).
- [von Ammon 2004] von Ammon W., In: *Crystal Growth – From Fundamentals to Technology*, ed. G. Müller, J.-J. Metois, P. Rudolph, Elsevier, Amsterdam (2004).
- [Voronkov 1963] Voronkov V.V., *Fizika Tverdogo Tela* **5**(2) (1963) 571 (in Russian; English translation *Sov. Phys. Solid State* **5**(2) (1963) 415).
- [Voronkov 1974] Voronkov V.V., *Kristallografiya* **19** (1974) 475 (in Russian; English translation *Sov. Phys. Crystallogr.* **19** (1974) 296).
- [Voronkov 1978] Voronkov V.V., *Kristallografiya* **23** (1978) 249 (in Russian; English translation *Sov. Phys. Crystallogr.* **23** (1976) 137–141).
- [Watson 1994] Watson T., Master's thesis, University of Freiburg, Germany (1994).
- [Weast 1981] Weast R.C., Astle M.J. (eds), *CRC Handbook of Chemistry and Physics*, 62nd ed., CRC Press, Boca Raton, FL (1981).
- [Weisberg 1956] Weisberg L.R., Gunther-Mohr G.R., *Rev. Sci. Instrum.* **26** (1956) 896.
- [Wenzl 1978] Wenzl H., Fattah A., Gustin D., Mihelcic M., Uelhoff W., *J. Cryst. Growth* **43** (1978) 607.
- [Wilke 1988-1] Wilke K.Th., In: *Kristallzüchtung*, ed. J. Bohm, VEB Deutscher Verlag der Wissenschaften, Berlin (1988), p. 816 ff.
- [Wilke 1988-2] Wilke K.Th., In: *Kristallzüchtung* (ed. J. Bohm, VEB Deutscher Verlag der Wissenschaften, Berlin (1988), p. 854 ff.
- [Wizent 2009] Wizent N., Behr G., Lipps F., Hellmann I., Klingeler R., Kataev V., Löser W., Sato N., Büchner B., *J. Cryst. Growth* **311** 1273–1277.
- [Yangyang 1991] Yangyang J., Shuqing Z., Yijing H., Hangwu Z., Ming L., Chaoen H., *J. Cryst. Growth* **112** (1991) 283.
- [Zulehner 2000] Zulehner W., *Mater. Sci. Eng. B* **73** (2000) 7–15.

5

Shaped Crystal Growth

Vladimir N. Kurlov and Sergei N. Rossolenko
Institute of Solid State Physics RAS

Nikolai V. Abrosimov
Leibniz-Institut für Kristallzüchtung, Berlin

Kheirreddine Lebbou
Université de Lyon I

5.1 Introduction

Although metallic crystals were grown through a hole in a floating mica disc as early as the 1920s [Gomperz 1922, Linder 1927, Mark 1923], primarily to prevent the oxidation of the melt surface, A.V. Stepanov of the Ioffe Physico-Technical Institute, Leningrad, in the 1960s was the first to formulate a concept of crystal shaping:

the shape or an element of shape to be produced is created in the liquid state by means of various effects enabling the liquid to retain that shape, and then the shape or element is converted to the solid state by the use of appropriate crystallization conditions [Stepanov 1963].

For the growth of shaped crystals and material structures, he suggested forming a melt column of a defined shape with the aid of a special *shaper* (i.e. a *die*), and subsequently crystallizing the melt column outside the vessel walls. Liquid melt columns can be made in a variety of shapes by the application of a suitable high-frequency electromagnetic (EM) field or by the use of the hydromagnetic effect, among others.

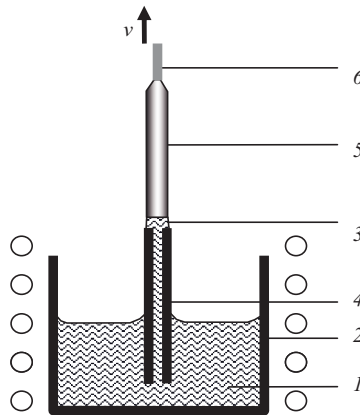


Figure 5.1 The principle of the EFG technique. 1, melt; 2, crucible; 3, meniscus; 4, die; 5, crystal; 6, seed.

In fact, the main idea of this concept was to limit the area of the liquid-free surface and its perturbations. Then there are only two possibilities that can be used for shaping: the edges or the walls of shaper (die) [Tatartchenko 1969]. This means that in the theoretical analyses two different boundary conditions have to be used: fixing a line on the surface of the meniscus by the edges of the shaper (die) or fixing the wetting angle between the melt and the wall of the shaper. The details of the theoretical analysis of shaping processes are discussed in Chapter 2 of this book.

Since any desired sectional shape can be obtained – ribbons, tubes, rods and others – cutting processes can be eliminated, allowing for a reduction in cost in comparison with bulk crystals grown by other techniques. Various profiles were grown by Stepanov and his coworkers [Koptev 1967, Shach-Budagov 1959, Stepanov 1959, Stepanov 1963, Tsivinskii 1965, Tsivinskii 1966]. The Stepanov group mainly studied systems in which the die material is not wetted by the melt.

A very important step in shaped crystal growth was the discovery and development of the edge-defined film-fed growth (EFG) technique [LaBelle 1971-1, LaBelle 1971-2], based on Stepanov's concept. The die is drilled with capillary channels so that, when it is held in contact with the melt, the liquid rises by capillary action to the top of the wettable die, where crystal growth proceeds at or slightly above the top of the die, where thermal gradients are controlled as in any crystal pulling processes (Figure 5.1).

Intensive research has been devoted to designing and optimizing this process and investigations of shaped crystal growth can be found in numerous original papers. The proceedings of Soviet and Russian conferences on shaped crystal growth were published in [Bull. Acad. Sci., Proc. Stepanov Conf. 1969–2004]. A special issue on shaped crystal growth was published in the *Journal of Crystal Growth* [Cullen 1980] after the appearance of numerous papers in this area. The first and second international symposiums on shaped crystal growth (SSCG-1 and SSCG-2) were held in Budapest (Hungary) in 1986 and 1989. The proceedings were published in [Proc. SSCG-1 1986, Proc. SSCG-2 1990]. Several monographs on shaped crystal growth have also been published [Antonov 1981, Rudolph 1982, Dobrovinskaya 2002, Fukuda 2003, Tatartchenko 1993, Tatartchenko 1994] as well as reviews [Abrosimov 2003, Antonov 1988, Antonov 1990, Antonov 2002-1, Antonov

Table 5.1 Some materials for which the EFG/Stepanov technique has been applied

$\text{Al}_2\text{O}_3\text{-Y}_3\text{Al}_5\text{O}_{12}$	[Pollock 1974-2, Starostin 1994]
$\text{Al}_2\text{O}_3\text{-Zr}_2\text{O}_3(\text{Y}_2\text{O}_3)$	[Borodin 1988, Bates 1992]
$\text{Ca}_3(\text{Nb,Ga})_2\text{Ga}_3\text{O}_{12}$	[Voronkov 1988]
$\text{Ca}_3\text{VO}_4, \text{Bi}_{12}\text{SiO}_{20}, \text{Bi}_{12}\text{GeO}_{20},$ $\text{Bi}_4\text{Ge}_3\text{O}_{12}, \text{Nd}_3\text{Ga}_5\text{O}_{12}$	[Ivleva 1987]
$\text{Ga}_3\text{Gd}_5\text{O}_{12}$	[Swartz 1974]
GaAs	[Egorov 1976]
$\text{Gd}_2(\text{MoO}_4)_3$	[Kurlov 1994]
Ge	[Antonov 1980, Kuznetsov 1980, Levinson 1980]
Heavy metal halides	[Dmitruk 1985, Dmitruk 1988]
InSb	[Nosov 1969]
LiF, CaF_2	[Antonov 1988, Nicolov 2000, Tsivinskii 1966]
LiF-NaCl, LiF- CaF_2	[Pollock 1974-1]
LiNbO ₃	[Matsumura 1976, Red'kin 1987]
LiTaO ₃	[Red'kin 1986]
$\text{LiTa}_x\text{Nb}_{1-x}\text{O}_3$ solid solution	[Fukuda 1976]
$\text{Lu}_x(\text{RE}^{3+})_{1-x}\text{AlO}_3$	[Mareš 2002]
MgAl_2O_4	[Hurley 1975]
Mn_2SiO_4	[Finch 1975]
NaNO_2	[Antonov 1990]
NaNO_3	[Lin 1993]
PbTe	[Klimakow 1984]
Rare earth orthovanadates	[Epelbaum 1998, Kochurikhin 2006, Zhang 2002]
$\text{Sr}_x\text{Ba}_{1-x}\text{Nb}_2\text{O}_6$	[Ivleva 1995]
TiO ₂	[Machida 1993]
$\text{Y}_3\text{Al}_5\text{O}_{12}$	[Kravetskii 1980]
$\text{Y}_3\text{Al}_5\text{O}_{12}:\text{RE}^{3+}$	[Kurlov 2005]

2002-2, Buzynin 1977, Ciszek 1984, Dobrovinskaya 1979, Dobrovinskaya 1988, Kalejs 1987, Kurlov 2001, LaBelle 1980, Nikanorov 1987, Rudolph 1999, Shikunova 2007, Tatartchenko 2005, Taylor 1983].

The concept of the EFG/Stepanov technique and the research and engineering efforts have focused on the application and optimization of the process for a wide variety of materials (Table 5.1). Single crystals and eutectics have been grown by the EFG/Stepanov technique or by the micro pulling down (μ -PD) technique. However, the industrial processes have been developed primarily for the manufacture of shaped crystals of sapphire and Si. These shaped crystals are now produced commercially throughout the world and have many industrial uses.

The development of various techniques for the growth of sapphire and Si shaped crystals is described in this chapter. Also special attention is devoted to the μ -PD technique, which has been developed on the basis of the Stepanov concept.

5.2 Shaped Si

Because photovoltaic energy conversion constitutes a form of electricity production that is environmentally clean and structurally very modular it is becoming more and more important in replacing fossil fuels and preserving the environment from global warming.

Crystalline Si technology is clearly dominant in solar cell production today, with about 90% of the market, and will remain dominant for at least the next decade.

Photovoltaics (PV) was and is the driving force for shaped Si crystal growth. Starting just before the oil crises in the early 1970s, the development of shaped Si growth over 30 years has played an important role in world production of Si substrates for solar cells. Market share changes continually, because of the expanding production of PV products; at the turn of the millennium the proportion of shaped Si was about 10% [Kalejs 2003].

The goal of research and development activities in PV is cost reduction of the electricity produced, to compete with other energy sources. One of the main expenses incurred is in fabrication of Si wafers, which makes up about one-third of the cost of the finished PV module. Some 30–50% of Si crystallized in the form of ingots (from the Czochralski process, casting etc.), which has to be cut into slices to produce Si wafers, is wasted as kerf loss during the cutting process. In addition to wasting material, wafering suffers from surface damage which leads to further use etching and polishing techniques. Moreover, it is difficult to produce a thin wafer (100 μm). An alternative approach is to grow shaped Si by pulling from the melt. In this case the as-grown crystal is in form of the end substrate for solar cell production and nearly all the starting material from the crucible is crystallized. This reduces the use of Si feedstock, which is a critical parameter for the long-term success of the PV industry because of the need to lower costs.

Shaped crystal growth of Si began in the early 1960s with the dendritic web growth technique [Dermatis 1963], in which the ribbon shape of the crystal was controlled by crystallography and surface tension of the melt, followed by the Stepanov method [Boatman 1967], in which the crystal shape was defined by a nonwetting slot at the top of an inductively melted Si rod. Quite soon, a dendritic web-grown ribbon 30 mm wide and 100 μm thick was reported [Barrett 1971]. Though Stepanov-grown shaped crystals were dislocation free, the growth of ribbons wider than 12 mm was difficult.

The situation changed after introduction of wetted dies for the growth of shaped crystals, applied for the first time in the growth of sapphire [LaBelle 1971-1]. This technique was called edge-defined film-fed growth (EFG), because crystal grows from the melt acted on by capillary force and spread as a thin film on the top of the die. The cross-section of the growing crystal in EFG is defined by the form of the die, as in the Stepanov method, which makes both methods similar. In 1972, EFG was applied to Si ribbon growth [Ciszek 1972] and 3 years later to the growth of Si tubes [Ciszek 1975]. Some years after that Russian scientists published the first results dealing with the Stepanov growth of Si ribbons [Tatartchenko 1978], Si tubes [Abrosimov 1983] and hexahedral crystals [Abrosimov 1985] (more detailed information on this development can be found in Chapter 2).

The golden age of Si shaped crystal growth began in the mid 1970s. T.F. Ciszek in his review [Ciszek 1984] described 15 sheet growth methods that were under development at that time, and in the next few years more than a dozen techniques appeared. He proposed a classification of Si sheet growth methods based on the shape of meniscus that forms between the melt and the growing shaped crystal (sheet) (Figure 5.2). M_1 and M_2 menisci are typical for the vertical ribbon (tube) growth methods and differ in height: the height of the M_1 meniscus is of the order of the profiled crystal thickness (e.g. EFG) and the M_2 meniscus rises from the free melt surface to the solid–liquid interface and typically has a height of the order of 6–7 mm (e.g. dendritic web growth, String Ribbon™). The

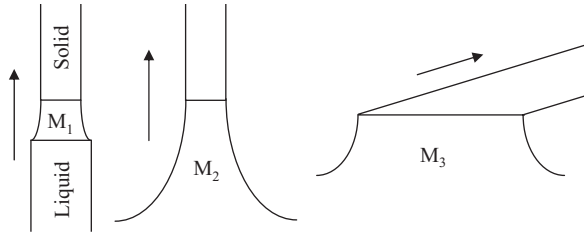


Figure 5.2 Classification of Si ribbon technologies according to the shape of the meniscus at the solid–liquid interface (Reprinted with permission from [Hahn 2004], copyright (2004) Institute of Physics).

M_3 meniscus is characterized by a large solid–liquid interface that typically occurs for the horizontal growth techniques either with a free melt surface (e.g. horizontal ribbon growth (HRG)) or with a supporting substrate (e.g. ribbon growth on substrate (SGR) or Silicon Film™).

Of the 30 or more shaped crystal growth techniques that have been developed since the 1960s, only a few have been commercialized or are in the pilot production phase [Kalejs 2003]. Some techniques (e.g. EFG, String Ribbon) can up to now compete with traditional Si wafer production from bulk materials. The application of apparently well-developed techniques like dendritic web growth depends on the willingness of the method's owners to invest in the R&D and take it from pilot stage to production. In what follows, the leading shaped crystal growth techniques and technologies will be discussed, including historical aspects of their development.

5.2.1 EFG Method

The EFG method was the first one to be used for commercial PV Si substrate production. Because solar cell substrates are flat, the process development was concentrated on the growth of Si ribbons from the very beginning. A critical parameter for the cost reduction of the grown crystals is the productivity of the process (or productivity per furnace). So, in 1975, Mobil Tyco Solar Energy Corporation reported the continuous growth of Si ribbons 25 mm wide and 25 m long [Ravi 1975]. Another important value for productivity is the growth rate. The maximum growth rate for melt-grown ribbon-shaped crystals was derived in [Ciszek 1976]:

$$v_{\max} = \frac{1}{\zeta \rho_1} \left(\frac{\sigma \varepsilon (W + t) \lambda_s T_m^5}{Wt} \right)^{1/2} \quad (5.1)$$

where ζ is the latent heat of fusion, ρ_1 is the density of the crystal at the melting temperature T_m , σ is the Stefan–Boltzmann constant, ε is the surface emissivity of the crystal, λ_s is the thermal conductivity of the solid crystal at the melting temperature, W is the ribbon width and t is the ribbon thickness. If the width-to-thickness ratio of the growing ribbon is large ($W/t \gg 1$), v_{\max} is essentially independent of width and varies as $t^{-1/2}$. The

maximum growth rate for shaped Si crystals (the formula is also valid for the growth of Si tubes) with a thickness of about 300 μm could be predicted to be about 6–7 cm/min. But in practice the pulling rate is limited to 1–2 cm/min because of thermal stresses that produce both a high level of dislocations and residual stresses that cause ribbon splitting or bucking, leading to low yield during further solar cell processing.

Fundamental barriers for Si ribbon growth, such as growth stability or residual stresses, were not recognized in the early stage of process development and the main goals were to grow wider ribbons with higher pulling rates. The peak level was reached with the growth of Si ribbon up to 7.5 cm wide at a growth rate of 7.5 cm/min [Kalejs 1980]. This was achieved by the construction of high-speed cartridges including forced cooling elements to remove the latent heat of crystallization from the growth interface and afterheater systems with linear cooling plate to minimize the residual stresses in the grown ribbon. As a result, a steep temperature gradient (up to 2500 $^{\circ}\text{C}/\text{cm}$) in the solid near the growth interface was obtained through combined action of the die heaters, the die-top radiation shields, and the heat removal elements, making possible a growth rate of up to 7.5 cm/min. To minimize the high level of residual stresses that undoubtedly accompany such severe growth conditions, the ribbon was reheated to temperatures $\geq 1200^{\circ}\text{C}$ and cooled in a linear temperature profile to room temperature, passing through linear cooling plates.

Another fundamental problem of ribbon growth – the stability of the ribbon width caused by control of the ribbon edges (see Chapter 2 for more details) – was investigated by using the die end heaters to heat each end of the die independently from its central part. The end heaters were used mainly to supply enough power to control the ribbon edge isotherms. In spite of all the technical solutions used, the residual stress and buckling problems still remained and the process did not attain the expected productivity. Also, because of the complexity of the high-speed cartridge for ribbon growth, the process was too complicated to be adapted for mass production, which requires simplicity of technology.

The physical cause of ribbon edge instability is that, for steady-state growth, the meniscus height must be lower on the edges than on the ribbon face [Tatartchenko 1993]. This problem does not exist for the growth of shaped crystals with a closed shape, e.g. Si tubes first reported in [Ciszek 1975]. The next idea was to use Si tubes for production of Si solar cells used in photovoltaic–solar thermal energy systems, combining solar cells with a light concentrator and with an internal working fluid to obtain low-grade heat [Eriss 1980]. Because of the small diameter (9.5 mm) it was possible to grow crystalline Si tubes at pulling rates up to 12 cm/min, ~ 140 cm in length and with wall thicknesses in the range 0.05–1.0 mm. An important result concerns the effect of the growth rate on the wall thickness variation: the observed smaller thickness variation at higher pulling rates is because the latent heat of crystallization terms begins to dominate as the temperature gradient in the meniscus approaches zero. The process stability in Si tube growth is an advantage in comparison to the edge-caused instability during ribbon growth, but the tubular substrate is unusual for solar cell technology and this prevented further development, in spite of the reported simultaneous growth of several tubes [Abrosimov 1983].

The essential step for EFG Si growth and further process development was based on the idea of combining the advantage of a closed crystal shape with plane ribbon geometry. This is possible when the cross-section of the shaped crystal is polygonal. Initially, decagons were grown with 2.5-cm wide faces, and nonagons with 5-cm faces [Taylor 1981],



Figure 5.3 EFG growth furnace at RWE SCHOTT Solar with growing thin-walled octagonal Si tube (Reprinted with permission from [Behnken 2005], copyright (2005) Elsevier Ltd).

but the commercialization of EFG Si shaped growth was on the basis of an octagon with 10-cm wide faces, equivalent to simultaneous growth of eight 10-cm wide ribbons from a single furnace [Kalejs 2002]. The octagonal tubes have average wall thickness of $300\ \mu\text{m}$ and can be grown to a height of 5.4 m with continuous melt replenishment. Although the graphite crucible with an integrated capillary die contains only about 1 kg of Si, continuous melt replenishment makes possible to grow up to 200 kg of shaped Si during a growth run (Figure 5.3).

Market pressures and the standards of the PV industry are directing EFG technology development to increase the EFG furnace productivity and the width of the polygons in steps from 10 cm to 12.5 cm and 15.6 cm (Figure 5.4) [Mackintosh 2006]. The same furnace used for the 12.5-cm faced octagon growth can be used for the growth of 15-cm faced hexagon, or the 50-cm EFG cylinder furnace can accommodate either a 12.5-cm faced dodecagon or a 15-cm faced decagon.

The common feature of all polygonal hollow Si tubes is the tendency to buckling with the reduced wall thickness and increased in face width and growth rate. Together, the larger faces of polygons and larger furnace diameters required to grow such crystals force furnace designers to maintain uniform temperatures of the order of 1°C across each individual face width with a tolerance acceptable for solar cell production. In comparison, the growth of large-diameter EFG cylindrical tubes can offer the possibility of increasing

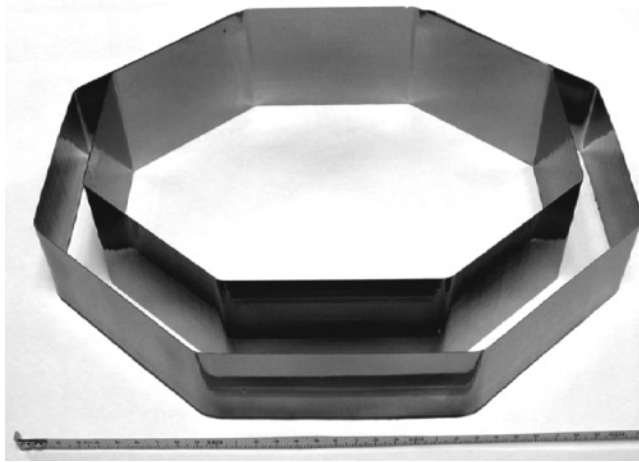


Figure 5.4 10-cm and 12.5-cm face octagons grown by EFG (Reprinted with permission from [Mackintosh 2006], copyright (2006) Elsevier Ltd).

productivity per furnace and ensure temperature uniformity around the perimeter of the growing tube. The axial symmetry of the growing system reduces thermoplastic stress, which is the main limitation for pulling rate, and makes thin wafer growth more practical. Using this approach EFG cylindrical tubes with a diameter of 50 cm and wall thickness 75–80 μm have been grown up to a length of 1.2 m [Garcia 2001]. In addition, tube rotation can be used to minimize the circumferential temperature variations that make growth of EFG polygons with wall thickness less than 200 μm difficult. The PV industry has to balance the advantages and the drawbacks of a curved substrate.

Modelling plays an important role in the understanding and improvement of crystal growth processes. Various modelling approaches have been used to study meniscus dynamics, heat and mass transport, melt flow and impurity distribution, stress, and deformation behaviour for both Si ribbon and thin-wall cylinder (polygons) [Kalejs 2001]. With the development of better computing systems and physical and mathematical models of the process, modelling has been extended to three-dimensional computation because the growth system of polygonal symmetry cannot be adequately described in an axially symmetrical model. Figure 5.5 shows the schematic and geometry of an EFG Si tube growth system commonly used for modelling [Sun 2004].

Recently three-dimensional models have been used:

- for evaluation of stress development and bucking deformation during the growth of octagonal thin-walled tubes [Behnken 2005];
- for coupled electromagnetic and thermal modelling of three-dimensional temperature fields to analyse the temperature profiles along and across the growing Si tubes (octagonal with 125-mm face) and to investigate the thermally induced stress and strain in different cases [Kasjanow 2007];
- for three-dimensional unsteady analysis of melt flow and Ga segregation during the growth of a dodecahedral EFG Si tube 0.5 m in diameter and 3 m in grown length [Smirnova 2008].

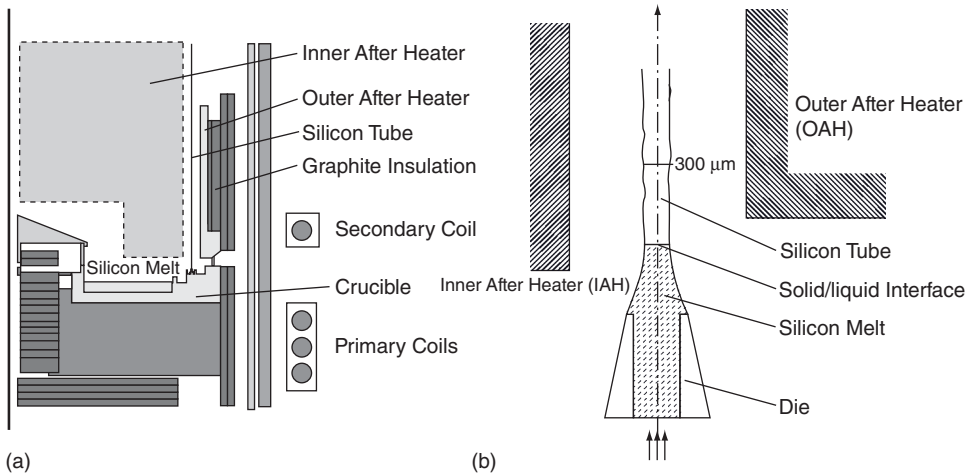


Figure 5.5 Schematic and geometry of a commonly used EFG Si tube growth system: (a) general view, (b) die top and meniscus geometry (Reprinted with permission from [Sun 2004], copyright (2004) Elsevier Ltd).

Based on these achievements, the current owner of the EFG technology, Wacker SCHOTT Solar, introduced the growth of a 12.5-cm faced dodecagon (12 sides) as the standard process for EFG ribbon growth, and the growth of a 15-cm faced decagon (10 sides) is under development.

As mentioned earlier, the advantage of shaped crystal growth is better use of the feedstock. Taking into account all steps from crystal growth to wafer preparation, about 90% of feedstock can be transformed into usable wafer for solar cell production [Kalejs 2003]. Furthermore, some the losses, including transient parts just after seeding, pot scrap and EFG tube corners (arising from cutting the polygonal crystal to wafers using a Nd:YAG laser) can be recycled.

From the crystal quality point of view, the EFG Si ribbon is similar to other multicrystalline materials obtained by directional solidification. In spite of the long history of Si shaped crystal growth for solar cell applications, not all the factors that limit the electronic properties of as-grown EFG substrates have as yet been identified. Carbon crucibles and dies and higher pulling rates are the main causes of defects. Independently of the seed orientation, ribbons grown by the EFG process achieve quasi-equilibrium defect structure after sustained growth [Garone 1976, Rao 1980]. The predominant surface orientation is close to the $\{011\}$ plane (within about $\pm 15^\circ$) and the preferred growth direction is $\langle 211 \rangle$. The structure consists of crystallographic defects parallel to each other, and also parallel to the growth direction. Arrays of dislocations and twin boundaries dominate the macroscopic defects, although a few grain boundaries can be found, too. The defects generally extend through the thickness of the shaped crystal. SiC formation and its incorporation into the crystal is another factor influencing the crystal quality.

During the growth of Si crystals with a closed shape, e.g. Si tubes, there are some peculiarities in the defect structure formation because of the curved crystal surface [Abrosimov 1985]. The predominant surface orientation with the planar defects

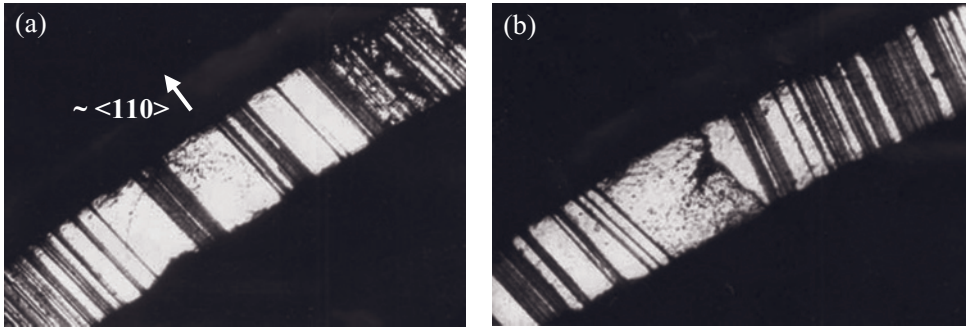


Figure 5.6 Defect structures of Si tubes (cross-sectional fragments), a pattern of selective chemical etching (wall thickness of the tube 400 μm): (a) quasi-equilibrium defect structure (twins perpendicular to the tube surface); (b) defect area providing rotation of the system of twin-boundary planes.

perpendicular to the crystal surface can be achieved only within the segments where the surface orientation is close to $\{011\}$ (Figure 5.6a). Whenever the deflection of the surface from $\{011\}$ reaches $\sim 15^\circ$, the surface orientation changes abruptly because of a ‘severely defective spot’ that causes an unavoidable rotation of the crystal surface orientation in such a way that the system of planar defects becomes again approximately perpendicular to the crystal surface. Either large-angle grain boundaries or dislocation pile-ups can act as such defect areas (Figure 5.6b). It was observed that 11–12 ‘severely defective spots’ are needed to form the quasi-equilibrium defect structure of Si tubes with diameter up to 20 mm.

Electrical activity of the dislocations and grain boundaries contributes to a relatively short lifetime for the as-grown EFG wafer; however, the specific solar cell processes developed for EFG materials improve it to levels comparable with those of other multi-crystalline solar cells. Starting with 11–12% solar cell efficiency [Ravi 1977], EFG-grown Si substrates have since been improved to a quality level sufficient to produce solar cell efficiencies of 14–15% in large-scale manufacturing [Kalejs 2004].

5.2.2 Dendritic Web Growth

Historically, dendritic web growth was the first method applied for Si shaped crystal growth by the Westinghouse Corporation [Dermatis 1963]. Unlike EFG growth using a shape-defining die, the ribbon form of dendritic web Si is controlled by crystallography and surface tension forces. Because the web ribbon growth is carried out from the free surface of the melt, this method can be classified as an M_2 meniscus form (Figure 5.2). Figure 5.7 shows the principle of dendritic web growth [Seidensticker 1977]. The growth process starts by dipping a dendrite seed crystal into a supercooled Si melt, which leads first to lateral growth in the $\langle 110 \rangle$ direction to form a button at the melt surface. The button is then pulled from the melt and two needle-like dendrites, aligned in the $\langle 112 \rangle$ growth direction, propagate from each end of the button into the melt. The solidification of the liquid film, supported initially by the button and the bounding dendrites, results in

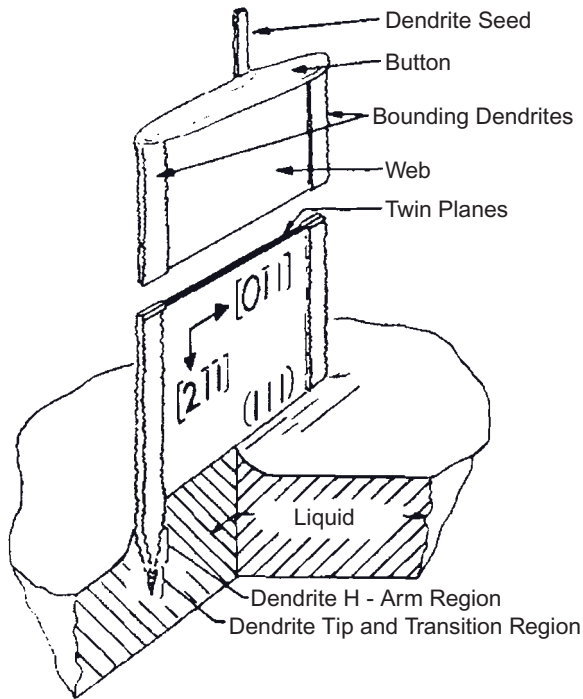


Figure 5.7 Schematic geometry of dendritic web growth (Reprinted with permission from [Seidensticker 1977], copyright (1977) Elsevier Ltd).

ribbon growth with a $\{111\}$ surface. The ribbon thickness is typically $\sim 100\mu\text{m}$, depending on the pulling rate and melt temperature profile. The odd number of twin planes introduced from the seed (extending from one dendrite to the other) provides re-entrant corners for dendrite growth and allows a high growth rate of the crystal.

The goal of any process development for the PV industry is to achieve low-cost solar cells. For ribbon crystal growth this means increasing the output rate – the product of ribbon width and growth rate. The process should be carried out continuously in steady state mode, which requires a melt replenishment system to keep the thermal field in the furnace constant. The growth of a wide ribbon by the dendritic web growth method is difficult because of the initial button growth stage and the difficulty in obtaining widely spaced bounding dendrites. It requires very precise control of the temperature distribution in the melt and on the melt surface, which should be essentially isothermal over a distance of the order of the ribbon width. The temperature control requirements in dendritic web growth are typically of the order of $\pm 0.1^\circ\text{C}$.

The basic replenishment system used in dendritic web growth is a multichambered crucible in which the melting of granular feedstock is separated from the growth process by a perforated barrier [Seidensticker 1982]. The melt level controller uses a laser melt level detector [Hopkins 1987] and keeps the level constant to within a few tenths of a millimetre. Another closed-loop system controls the melt temperature and the melt thermal symmetry, to keep both bounding dendrites at the optimal growth temperature. Because

the dendrite thickness is sensitive to melt temperature changes, dendrite size is also used as a regular parameter in the automatic control system. But in spite of the high level of automation, dendritic web growth demands great skill.

As in EFG Si ribbon growth, the attempts to grow a wide, thin web with a high growth rate lead to elastic buckling and plastic deformation generated by thermally induced stresses. As result of this limitation, ribbons 5–8 cm wide can be grown with pulling rate 1–2 cm/min, which provides a throughput of 5–16 cm²/min [Kalejs 2002]. That is why full commercialization of dendritic web growth is difficult, in spite of the reported maximal solar cell efficiencies of 17.3%. The pilot production by EBARA Solar Inc. was closed down in 2003.

5.2.3 String Ribbon

Another vertical silicon ribbon growth technique is String Ribbon™. This technique, earlier called ‘edge supported ribbon’ or ‘edge stabilized ribbon’ was developed in the 1980s at the National Renewable Energy Laboratory [Ciszek 1982] and at Arthur D Little [Sachs 1987] and commercialized by Evergreen Solar Inc. in 1994. Geometrically, String Ribbon growth is analogous to dendritic web growth where the edge-stabilized bounding dendrites are replaced by two wetted strings which are resistant to Si (the material of the strings is not described in the relevant papers). It makes the technique easier because the temperature control requirements are not so tight as in dendritic web growth and temperature excursions of $\pm 5^\circ\text{C}$ can be tolerated. As a result, the process is simple and robust and has excellent stability and reliability.

The general schema of String Ribbon growth is shown in Figure 5.8 [Hanoka 2001]. High-temperature strings pass up through a crucible with a shallow Si melt. The edge of the growing ribbon is determined and stabilized by capillary attachment to the wetted strings. Because the ribbon grows directly from the surface of the melt like in dendritic web growth, this method can be classified as an M_2 meniscus type (Figure 5.2) and the typical meniscus height is equal to 7 mm. The growth process begins with the dipping of the seed into the melt; after that the process is conducted by the furnace controller. After steady-state growth has been achieved, Si is continuously fed into the crucible. The primary process controls on the growth furnaces are temperature, pulling rate and Si feed rate. The growth runs continuously for many hour; the operator cut strips without interrupting the growth when the given length of 2 m is achieved, and makes process adjustments. In the conventional String ribbon method, a single Si ribbon is 8 cm wide with thickness of about 250 μm . The String Ribbon growth process called Gemini (dual ribbon growth) allows production of two Si ribbons simultaneously from a single crucible [Wallace 2003].

Another concept in String Ribbon growth – the Mesa Crucible concept – offers new possibilities of reducing the process costs. The Mesa Crucible is a narrow piece of graphite, 2 cm wide by 65 cm long, upon which molten silicon rests [Sachs 2004]. The melt is contained by capillary attachment to the edges of the crucible, not by walls (Figure 5.9). The free melt surface has a concave downward shape. The edges of the Mesa stabilize the melt if the melt height does not exceed about 6 mm above the mesa plane. The

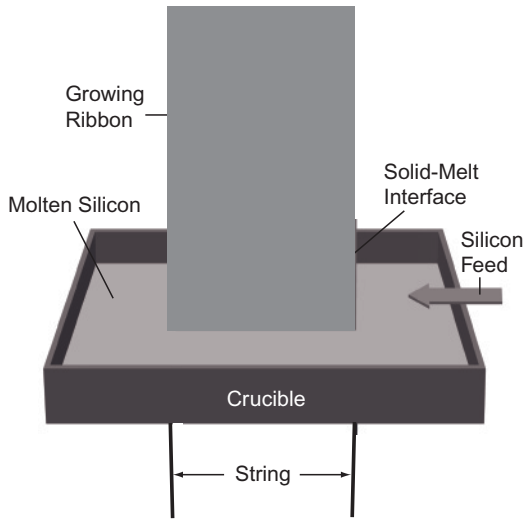


Figure 5.8 Schematic of String Ribbon growth (Reprinted with permission from [Hanoka 2001], copyright (2001) Elsevier Ltd).

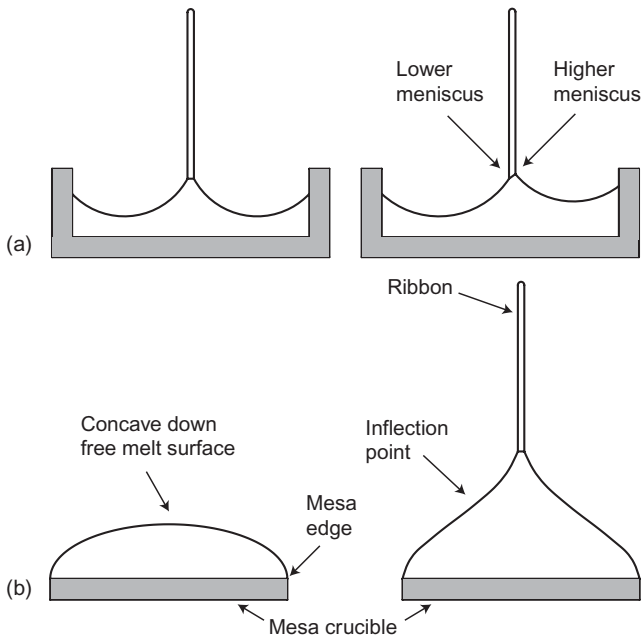


Figure 5.9 (a) A schematic conventional ‘walled’ crucible: the left image shows a centred ribbon, the right image shows a ribbon displaced to the right of centre. (b) A schematic cross-section through a mesa crucible: the left image shows the melt with no ribbon present, the right image shows a ribbon growing. (Reprinted with permission from [Sachs 2004], copyright (2004) WIP-Renewable Energies, <http://www.wip-munich.de/>).

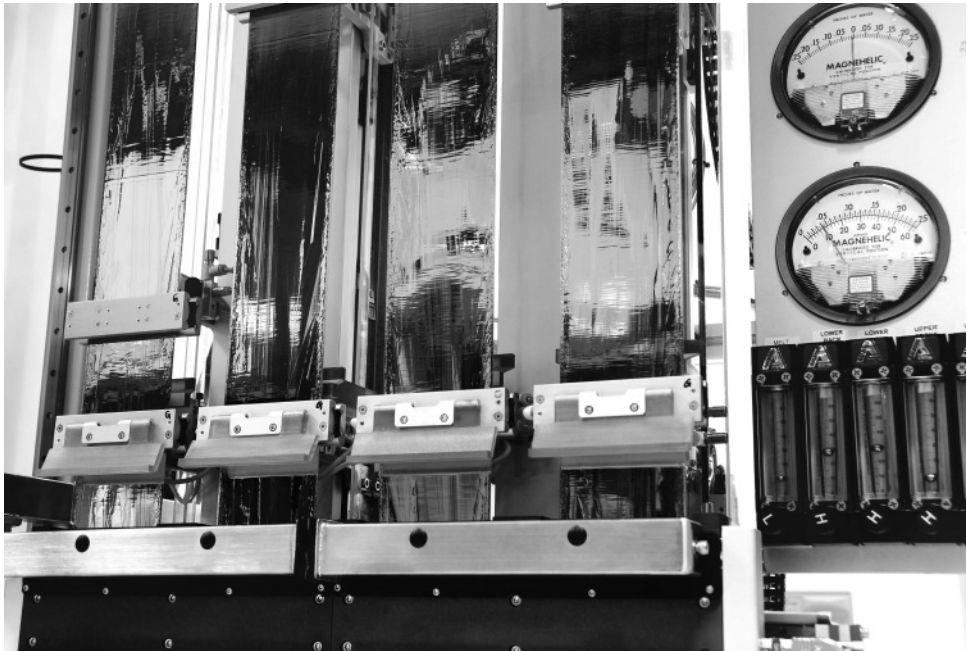


Figure 5.10 Growth of four 80mm-wide ribbons at pulling rate of about 25mm/min using Mesa Crucible concept (reproduced with the permission of Evergreen Solar).

meniscus shape that forms during the growth leads to an inherently stable flatness for the string ribbon. Mesa Crucible concept allows four ribbons to grow in a furnace (Figure 5.10) [Sachs 2004].

The common challenge for all ribbon technologies is to overcome stress-related issues like buckling caused by high cooling rates. It limits the pulling rates of String Ribbon to 1–2cm/min. The use of an active afterheater to linearize the cooling profile allows an increase of the growth rate and a decrease in the ribbon thickness to 100 μm .

From the point of view of crystal quality, String Ribbons are identical to EFG: many twin boundaries and some high-angle grain boundaries caused by contact of strings with Si₃N₄ melt. For String Ribbon the twinned regions (bands) can be as much as 1 cm wide and the minority carrier lifetime can be as high as 10–15 μs resulting in a solar cell efficiency of over 16% (laboratory process) [Hanoka 2001].

5.2.4 Ribbon Growth on Substrate (RGS)

There are two methods – RGS and Silicon Film™ – that belong to the M₃ meniscus type (Figure 5.2). Both of them utilize a substrate to assist in the process of crystallization. The difference is that the substrate for the Silicon Film process becomes incorporated

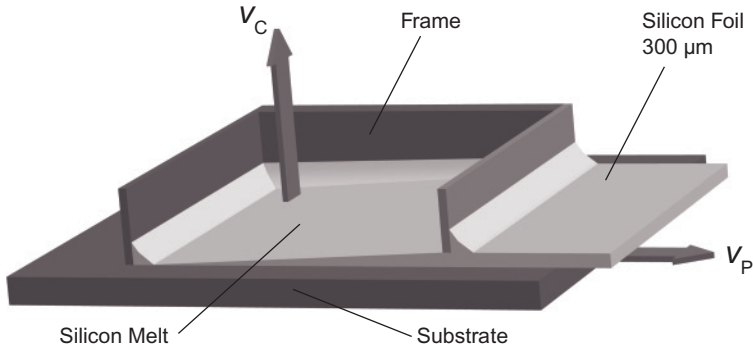


Figure 5.11 Principle of the RGS process (Reprinted with permission from [Burgers 2006], copyright (2006) WIP-Renewable Energies, <http://www.wip-munich.de/>).

into the solar cell while the RGS ribbon is separated from the substrate after the growth and the substrate can then be reused. Because of the lack of information concerning the Silicon Film growth process commercialized by AstroPower [Kalejs 2003], only the RGS process will be analysed here.

The RGS method was originally developed by Bayer AG in the 1990s. Figure 5.11 shows a schematic view of the technique. Substrates move under a crucible containing Si melt at a pulling rate v . The Si layer crystallizes with crystallization rate v_c in a direction perpendicular to the moving direction of the substrate. The frame acts as a melt container, as well as a shaper which determines the width of the ribbon and the thickness of the wetted melt layer and solidified Si foil on the graphite substrate. During cooling, the difference in thermal expansion coefficient between the substrate material and the Si layer causes the separation of the Si ribbon from the substrate and allows re-use of the substrate [Hahn 2004]. In the RGS process the substrate is used for cooling the bottom surface of the Si layer and the solid–liquid interface length is greater than the ribbon thickness. The directions of pulling and crystallization are almost perpendicular to one another, depending on the temperature conditions during growth. This allows for the decoupling of the crystallization rate and the pulling rate, and leads to high productivity of the growth process.

The maximum ribbon growth rate for horizontal growth techniques with wafer transport almost perpendicular to the crystal growth direction can be estimated using one-dimensional considerations of the thermal fluxes during ribbon growth [Lange 1990]:

$$v_{\max} = \frac{4\alpha\lambda_s s}{(2\lambda_s - \alpha t)\zeta\rho_1} \Delta T, \quad (5.2)$$

where α is the effective coefficient of heat transfer, λ_s is the thermal conductivity of the solid crystal at the melting temperature, s is the length of the solid–liquid interface (in the pulling direction), t is the ribbon thickness, ζ is the latent heat of fusion, ρ_1 is the density of the crystal at the melting temperature T_m , and ΔT is the temperature difference between melt and substrate. This equation predicts a 600 cm/min pulling rate for $\Delta T = 160^\circ\text{C}$.

In general, high crystal pulling rates influence the crystal structure. In comparison to the horizontal ribbon growth (HRG) process [Bleil 1969] which used crystallization from the free surface of the Si melt, RGS has the advantage of a substrate, which leads to heterogeneous nucleation and columnar crystallization with grain size of the order of the ribbon thickness. In this way the instabilities that occurred at the tip of the crystallization front in the HRG process, leading to dendritic growth with 10 K undercooling, can be avoided. The heterogeneous nucleation process on the substrate limits the supercooling of the liquid Si near the ribbon tip to the nucleation supercooling [Steinbach 1997].

The RGS process is now under development at the Energy Research Centre of the Netherlands (ECN). The R&D growth equipment now used by ECN allows a very high production rate of one wafer per second. Silicon wafers are 10 cm wide and 300 μm thick, but the growth of RGS ribbon with a thickness of about 100 μm is possible too. In spite of the high carbon concentration and small grains, nearly 13% efficiency shunt-free solar cells was achieved on RGS Si wafers [Burgers 2006].

In conclusion, the ribbon growth techniques remain a promising cost-effective alternative to multicrystalline wafers sliced from ingots as there are no kerf losses [Hahn 2006]. Although some techniques, e.g. dendritic web growth are no longer in development, other techniques, e.g. Ribbon on a Sacrificial Template (RST), formerly called Ribbon Against Drop (RAD) [Belouet 1987] are again in development at Solarforce. This technique is characterized by a vertical growth direction combined with the use of a substrate.

5.3 Sapphire Shaped Crystal Growth

Sapphire has been recognized for a long time as a material with important properties. It has a high refractive index and a broad transmission band spanning the ultraviolet, visible and infrared bands, a high hardness, melting point, very good thermal conductivity, tensile strength and thermal shock resistance. The favourable combination of excellent optical and mechanical properties, along with high chemical durability, makes sapphire an attractive structural material for high-technology applications. Sapphire crystals are used in medicine and blood chemistry as they are resistant to human blood and body fluids, are totally impervious to moisture, and are chemically inert. Frequently it is the combination of two or more of its properties that makes sapphire the only material available to solve complex engineering design problems [Klassen-Neklyudova 1974].

However, sapphire is difficult to shape because of its high hardness, and its physical properties are anisotropic since it possesses a hexagonal crystal structure. Nevertheless, there is a high demand for sapphire and it has been grown for a variety of applications by a number of techniques. Techniques for growing sapphire crystals of any predetermined cross-section, constant along the crystal length (rods of various cross-sections, ribbons, tubes, fibres, capillaries), and crystals with discretely changing cross-sectional configurations (crucibles, boats, near-net-shaped domes, etc.) have been developed.

Sapphire has been produced commercially for many years and its unique properties make it an ideal material for hundreds of applications. The main applications of shaped sapphire crystals are scanner windows, windows for high-temperature and high-pressure applications, chemical vapour deposition (CVD) reactors, arc envelopes for vapour lamps,

thermocouple sleeves, wear-resistant nozzles, substrates, watch windows, transparent armour, optical systems for high-power laser optics, insulators, high-pressure reactors, high-vacuum equipment, moving pieces for friction welding, guides for textile machinery, precision bearings, heat and water impeller meters, chromatograph pistons, engines, domes for high-speed missiles, light guides, acoustic rods, reinforcing elements for composite materials, sensors, nuclear components, research and technological equipment, medicine (implants, scalpels, needles for laser therapy, medical power delivery systems), jewels, etc.

Although sapphire has been used for many years, it is still in a development stage. The optimization of standard crystal growth technologies and development of new techniques are actively pursued in order to increase the dimensions of crystals, improve the quality, reduce the cost of material, and grow complex shapes. There are good reasons to believe that sapphire will not only strengthen its position in traditional markets, but will also be used in a number of new applications.

5.3.1 EFG

This sapphire shaping technique has been described, discussed and reviewed in numerous publications [Abrosimov 2003, Antonov 2002-1, Dobrovinskaya 1980, Kravetskii 1980, Krymov 1999, Kurlov 1997-1, Kurlov 1997-2, Kurlov 1997-3, 1998-3, Kurlov 1999-1, Kurlov 2001, LaBelle 1967, LaBelle 1971-1, LaBelle 1971-2, LaBelle 1980, Locher 1992, Nicoara 1987, Novak 1980, Perov 1979, Tatartchenko 2005, Théodore 1999-2, Wada 1980, Zatulovskii 1983] and only a summary is presented here.

In 1967 LaBelle and Mlavsky [LaBelle 1967] reported on the growth of sapphire filament from the melt using a wetted die made of molybdenum. In the first instance they used the Gomperz principle [Gomperz 1922] where the crystal was pulled through a disk-like die located on the surface of the melt. The floating orifice technique proved to be a reliable experimental approach for producing sapphire filaments. But although the technique was used as an excellent research tool, it was difficult to conceive of it as a reliable manufacturing process. A principal concern was the continual change in temperature at the orifice as the melt was consumed and the disk moved lower in the crucible. In addition, there were always occasions where mechanical instability would cause the disc to become submerged in the melt [LaBelle 1980]. LaBelle and Mlavsky subsequently improved the technique by using a die with capillary channels attached to the bottom of the crucible [LaBelle 1971-1, LaBelle 1971-2]. Crystals are grown from a melt film formed on the top of the capillary die. The melt rises to the crystallization front within the capillary channel. This is ideal for producing crystals with small square cross-section.

It was clear that the EFG technique offered major advantages as a crystal growth process. Since the die is rigidly fixed in the crucible, its top surface and, therefore the growing interface remain essentially fixed with respect to the crucible, heat shields, and heating source. It solved the problem of mechanical instability and eliminated the variability of melt temperature at the die top with the decreasing melt level in the crucible. Molybdenum is considered to have good chemical compatibility with molten alumina: sapphire crystals grown using molybdenum crucibles and dies contain only 5 parts per million of molybdenum, and molten alumina is able to wet the molybdenum.

Several outstanding results have been achieved in sapphire shaped crystal growth by the EFG technique. Sapphire fibres have been produced at Saphikon, Inc. and at the former parent company, Tyco Laboratories, since the early 1970s. The method was used to produce sapphire fibres for reinforcement of ceramic and metal matrix composites for high-temperature use in aircraft engines. Saphikon has worked extensively since 1987 to advance the production capability further, and by 1994 they produced structural grade fibre at volumes over 10 000 m per week through cooperation with several companies. The process allows for the continuous growth of multiple fibre strands from a single machine; in structural fibre production, 75 strands have been grown simultaneously. Continuous growth of lengths exceeding 300 m has been demonstrated [Fitzgibbon 1998].

Production of optical-grade sapphire fibre for use in high-temperature fibre optics is has also been developed. Sapphire fibres grown using the Saphikon EFG technique have proved to be effective converging systems for Er:YAG and Er:YSGG lasers for medical applications. In a summary report by Fitzgibbon *et al.*, relating to sapphire fibre performance, experimental results were detailed: fibre losses as low as 0.2 dB/m with an average of 1.5 dB m^{-1} ; laser damage threshold 1245 J cm^{-2} ; laboratory lifetime testing of 1-m fibre samples (325 μm diameter) demonstrated 150 000 pulses at a delivered energy of 275 mJ/pulse [Fitzgibbon 1996].

Sapphire fibres can be used for infrared spectroscopy, as well as for very high-temperature sensing (2000 °C). Sapphire has replaced quartz (silica) fibres in many of these applications, as the wavelength extends beyond the transmission limit of quartz. With a usable temperature range up to 2000 °C, sapphire exceeds the usable range for quartz, which devitrifies in the 1100–1200 °C range. Quartz also degrades in moist or chemically aggressive environments, while sapphire can be used in extremely harsh conditions. Sapphire fibres are now routinely used in the aggressive environment of fluorine (NF_3 , CF_4) plasma etching chambers used in the manufacture of semiconductor wafers. Bare sapphire fibres are prime candidates for evanescent wave sensing because of their chemical inertness and low bending losses [Fitzgibbon 1998].

In 2005, J. Locher and others (Saphikon) reported EFG sapphire sheets measuring $305 \times 510 \text{ mm}$ and $225 \times 660 \text{ mm}$ [Locher 2005]. That was a great step in technology, which provided the aerospace industry with sapphire of the required size. The EFG method seems to be the best choice for producing large-area sapphire crystals. The large crystal size requires not only appropriate dimensions of the growth machine but also the creation of a uniform temperature along the very long top face of the die. These sapphire plates were high quality. The average optical transmission of 6.15-mm thick uncoated polished panels is $84.0\% \pm 0.5\%$ at 700 nm. This value assures good transmission throughout the 500–5000 nm spectral range. Effective absorption coefficients for this spectral range and thickness are calculated and reported. An average index inhomogeneity of $6 \text{ ppm} \pm 2 \text{ ppm}$ has been measured and is the requirement for panels polished to 0.1λ at this thickness ($\sim 633 \text{ nm}$) [Bates 2005].

The EFG method initiated the development of other growth techniques for shaped sapphire crystals which fulfilled the requirements for practical use. Some versions are described here in more detail for shaped sapphire single crystals because in this area the problems of obtaining crystals of preset shape, control of single crystal structure quality, defectiveness, and optical and mechanical properties can be solved.

5.3.2 Variable Shaping Technique (VST)

The development of modern science and technology requires sapphire crystals of complex forms, i.e. shaped crystals with variable cross-section. The variable shaping technique (VST) makes it possible to vary the dimension and configuration of the crystal cross-section during pulling. This method allows a gradual transition from one preset configuration of the crystal cross-section to another during the same crystal growth process.

It is well known that in the process of crystal growth by the EFG technique, the shape of the cross-section profile is controlled mainly by the die design, and its cross-sectional dimensions can vary only within very narrow limits restricted by the meniscus-existence zone, with the melt meniscus catching on the free edge of the die (see Chapter 2). Hence, the first attempt to increase the possibility of varying pulled profile cross-sectional dimensions in the process of growth was to displace movable die elements [Mlavsky 1975]. The cross-section was varied by using complex external and internal dies. The first die was used for tubular crystal growth; the second one was connected to a rod that could be shifted in the axial direction so as to move the top surface of the two dies in and out of horizontal alignment with each other. When the internal die moved into alignment with external one, the crystal grew as a circular rod.

Other techniques of varying the inner tube diameter are based on melt spreading from a circular capillary channel on the top surface of the die [LaBelle 1975]. Initially, the melt film covers only part of the top surface in the vicinity of the circular capillary channel, and a tubular crystal grows. Then the pulling velocity and the melt temperature are adjusted so that the surface tension causes the film to spread toward the centre of the top surface. As a result, the cross-section of the crystal is changed. Both techniques allow transition from a tubular crystal to a circular rod in one process.

The next technique for discrete variation of the dimensions and geometry of the crystal cross-section during growth was based on the relative displacement of the elements of the thermal zone in a horizontal or vertical plane. This technique was proposed by Kravetskii *et al.* [Kravetskii 1980, Zatulovskii 1983] and later developed by Borodin *et al.* [Borodin 1983, Borodin 1985-1, Borodin 1999].

In order to change the preset crystal shape during crystallization and to preserve the altered cross-sectional configuration during further growth, it is necessary to alter the geometry of the liquid meniscus. This technique consists of a sequence of steady state growth steps with different transition crystallization modes. During the transition the base of the meniscus moves across the top surface of the die assembly from one edge to the other, and the meniscus volume and shape are changed. A VST schemes with a changeable crucible position is illustrated in Figure 5.12 [Borodin 1999]. The sequence of operations to alter the crystal cross-sectional configuration is shown from left to right. The set of dies is not connected with the crucible, so the crucible can be translated along the vertical axis relative to a fixed position of the die assembly. The dies should be of different lengths to allow their lower parts to be dipped into the melt separately. In shape transition mode, the lateral surfaces of the neighbouring dies are separated by narrow gaps which can serve as capillary feeding channels for the melt. When the crucible is raised so that the next die is dipped into the melt, the capillary gap supplies an additional mass of melt to the top of the die assembly. This portion of the melt contacts the already existing meniscus with the edge of the die just dipped into the melt. As a result, a new type

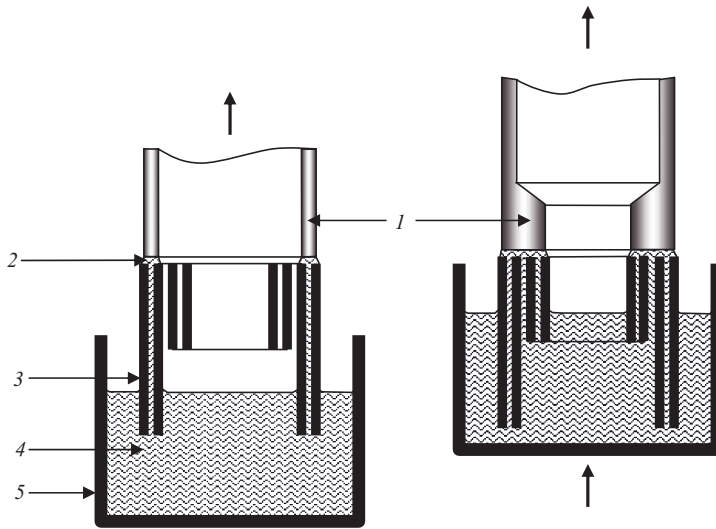


Figure 5.12 Principle of the VST using displacement of the crucible: 1, crystal; 2, meniscus; 3, die; 4, melt; 5, crucible.



Figure 5.13 Sapphire shaped crystals grown by the VST.

of meniscus forms and the growing crystal alters its shape which is controlled by the dies dipped into the liquid. If the crucible is lowered so that one of the dies is withdrawn from the melt, the pulled crystal will suck the rest of the melt out of the die capillary channel and out of the capillary gap between the neighbouring dies. In this case the base of the meniscus will move to the top surface edges of the die which is still dipped in the melt. This causes alteration and reduction of the crystal cross-section.

Sapphire shaped crystals grown by the VST are shown in Figure 5.13. Sapphire crucibles, boats, caps for thermocouples, crystals with change from rectangular cross-section

to tube, tubes with predetermined inside and outside diameters, tubes with attachment of side ribs and envelopes for high-pressure sodium lamps were grown by VST.

5.3.3 Noncapillary Shaping (NCS)

One of the basic defects in crystals grown from the melt is gas bubbles, which appear at some critical supersaturation of the melt with a gas impurity whose distribution coefficient is usually less than unity. In this case the homogeneous nucleation and growth of a gas bubble can take place in the impurity-enriched zone ahead of the crystallization front [Geguzin 1981, Tiller 1953]. Distribution of the gas-forming impurity ahead of the crystallization front in Czochralski growth depends on the pattern of the forced melt convection. This is mainly defined by the crystal rotation [Miyazawa 1980]. Melt stirring close to the crystallization front sweeps away the impurity-enriched zone and decreases the amount of impurities at the crystallization front. Therefore, melt stirring decreases the probability of gas-forming impurities in the crystal.

The growth of shaped crystals by the EFG method with a die wetted by the melt and with a capillary feeding system does not allow impurities to be removed from the crystallization front. In this case the distribution of gas bubbles is determined by the hydrodynamic flow of the melt in the neighbourhood of the crystallization front and thus the die design plays an important role. The dependence of the gas bubbles and dopant distribution on the geometry of the capillary channels in the dies has been observed earlier when growing shaped Si and sapphire crystals [Andreev 1986, Borodin 1985-2, Kalejs 1978, Kurlov 1994, Kurlov 1997-1, LaBelle 1980].

Figure 5.14 shows the cross-section of a sapphire rod 40 mm in diameter grown from a die with four ring capillary channels. Comparison of the sapphire crystal cross-section with the top surface of the die shows that the gas bubbles in the disk are located at the places where melt flows moving from the capillary channels meet each other. An analogous situation has been observed when growing sapphire rods of 12 mm diameter from a die with a ring capillary channel or from one made from sections of a molybdenum wire placed in a cylindrical tube [Borodin 1985-2]. The authors [Andreev 1986, Borodin 1985-2] showed analytically that the regions with an enhanced concentration of gas impurities driven back by the interface surface are adjacent to those regions of the crystallization front under which the components of the velocity of the melt flow are minimum. These minimum-velocity regions are formed by intersecting melt flows which spread over the top surface of the die, and are the most likely sites for the generation and capture of gas inclusions. So, one of the main problems in high-quality shaped crystal growth is how to prevent the formation of gas bubbles and other inclusions, which are formed in the regions where the melt velocity ahead of the crystallization front is minimum.

The primary difference [LaBelle 1980] between LaBelle's EFG process and Stepanov's early work is that the EFG process must use a wettable die and the Stepanov technique generally used a nonwetted die. For melt-nonwetable materials, the melt column should be surrounded externally, providing additional pressure on the liquid to make the melt-die contact point touch the sharp edge of the die [Tatartchenko 1994] (Figure 5.15a). For melt-wetable materials, the melt column has negative pressure using the capillary die (Figure 5.15b).

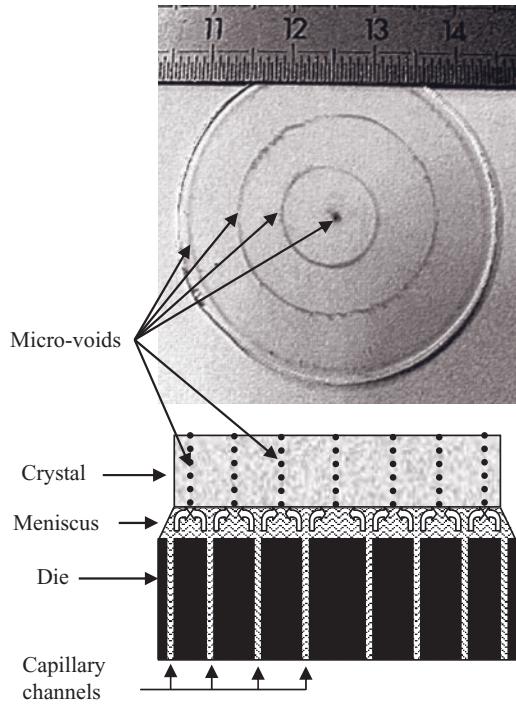


Figure 5.14 Distribution of gas bubbles in the cross-section of a 40-mm diameter sapphire rod, grown using a die with four ring-shaped capillary channels.

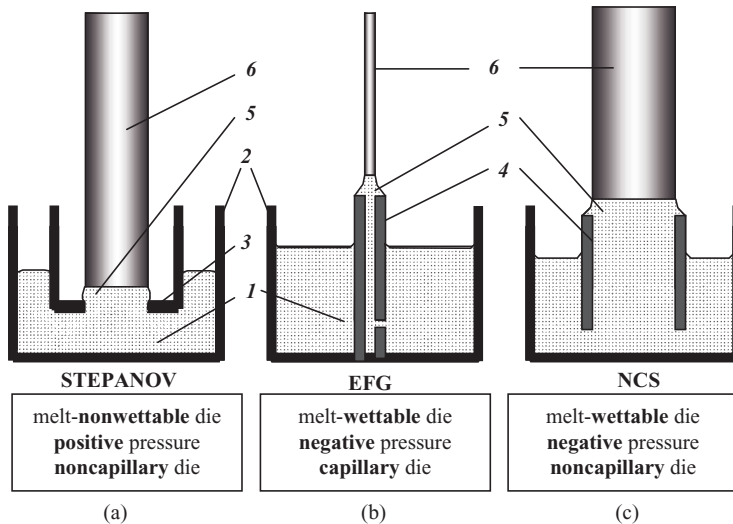


Figure 5.15 Principle of Stepanov (a), EFG (b) and NCS (c) methods: 1, melt; 2, crucible; 3, nonwetted die; 4, wettable die; 5, meniscus; 6, crystal (Reprinted with permission from [Antonov 2002-1], copyright (2002) Elsevier Ltd).

The NCS method, unlike the traditional capillary feed technique, ensures the absence of micro-voids and gaseous and solid inclusions, which are formed in the regions with minimum components of melt velocity ahead of the crystallization front. The dominant flow always moves from the centre to the periphery irrespective of crystal cross-section, thus enabling the growth of large sapphire crystals free of bulk inhomogeneities. The formation of the optimal interface surface and the hydrodynamic flows of melt ahead of the crystallization front are determined by the shape of the top surface of the die, the growth velocity, and the size of the noncapillary channel (the word ‘noncapillary’ means that the diameter of the channel is greater than the value of the capillary constant).

The NCS method was developed for the growth of high-quality shaped sapphire crystals with large cross-section. This method uses a wettable die. However, in contrast to the EFG method the NCS technique does not use the lifting of the melt from the crucible to the die-top through a capillary channel. But nevertheless the melt column has a negative pressure, as for the EFG method. The main feature of the NCS technique consists of the delivery of the melt to the growth interface through a noncapillary channel via a wettable die (Figure 5.15c).

But why does the melt rise to the crystallization front through a noncapillary channel via a wettable die? Figure 5.16 shows the sequence of bulk crystal growth stages by the NCS method using different seed shapes. At the beginning of the process the die top is at the level of the melt in the crucible. By using a small seed (Figure 5.16a), the crystal

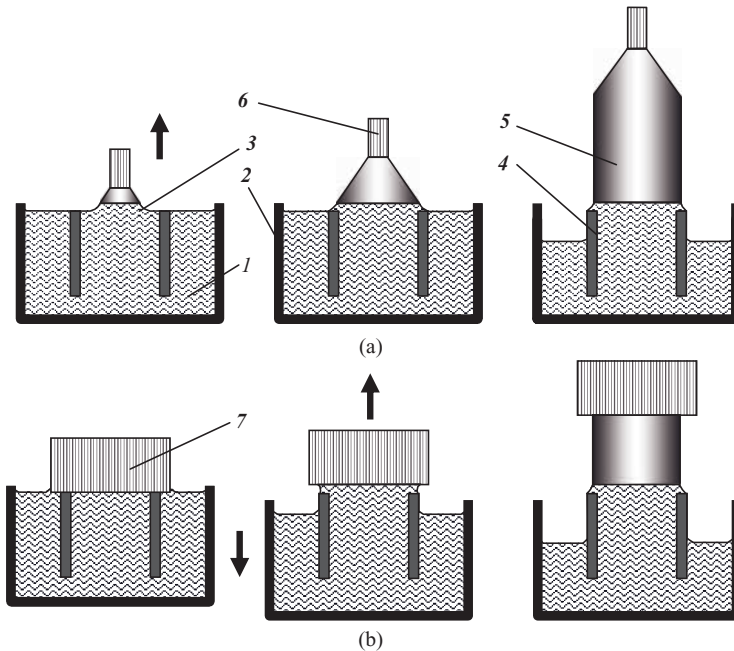


Figure 5.16 The sequence of bulk crystal growth stages by NCS method using different seed shapes: (a) with the use of a point seed; (b) with the use of a bulk seed. 1, melt; 2, crucible; 3, meniscus; 4, die; 5, crystal; 6, point seed; 7, bulk seed.

grows up to the edges of the die during the initial stage. After that the melt level in the crucible can be lowered relative to the level of the die top. The melt rises to the crystallization front through the central noncapillary channel because it is pumped up by the crystal, which acts as a piston. A wettable rod can also be used as a seed (Figure 5.16b). The melt level in the crucible can be lowered after the seeding process.

The special case of seeding using both capillary and noncapillary channels is described in [Kurlov 1997-1]. The lifting of the melt to the crystallization front inside a noncapillary channel is achieved by the pressure difference between the growth chamber and the internal closed volume under the seeding plate. The melt arriving through the noncapillary section of the die joins the melt meniscus coming through the ring capillary channel, which results in the growth of a crystal in the shape of a solid rod (Figure 5.17). To create the closed volume, the seeding is performed over the entire perimeter of a ring capillary channel (Figure 5.17a). In the initial stage, when the melt approaches the crystallization front only through the capillary feed, a hollow crystal grows. The closed volume below the seed begins to increase and the pressure decreases according to the Boyle–Mariotte law. The resulting difference in pressures forces the melt to rise inside the noncapillary section of the die (Figure 5.17b). On further pulling, the melt arriving through the noncapillary section of the die joins the melt meniscus coming through the ring capillary channel, which results in the growth of a crystal in the shape of a solid rod (Figure 5.17c).

The distance l between the seeding point and the beginning of the solid rod depends substantially on the pressure p in the growth chamber. The distance l , assuming that the crystallization of the melt arriving from both capillary and noncapillary sections occurs at the same level from the die top, is:

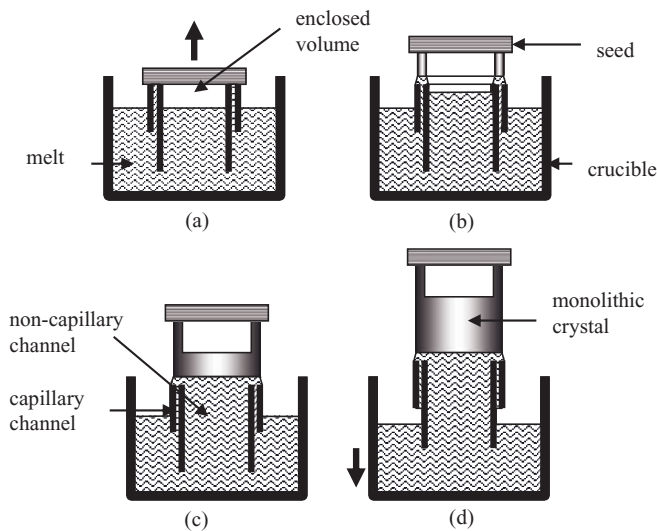


Figure 5.17 Principle of monolithic crystal growth by the NCS method using the pressure difference in the growth chamber and inside a closed volume under the seeding plate: (a) seeding, (b) growing a hollow closed shape, (c, d) growing a monolithic crystal (Reprinted with permission from [Kurlov 1997-1], copyright (1997) Elsevier Ltd).

$$l = \frac{H}{1 - (H_f \rho_l g / p)} - H + H_f, \quad (5.3)$$

where H is the distance between the level of melt in the crucible and the top of the die, H_f the distance between the melt level in crucible and the crystallization front, ρ_l the melt density and g the gravitational constant.

5.3.3.1 Growth of Crystals with a Predetermined Cross-Section

The formation of the optimum interface surface and the hydrodynamic flows of melt in the neighbourhood of the crystallization front are determined by the shape of the top surface of the die, and by the relationship between the crystal cross-section, velocity of growth and size of the central noncapillary channel.

When the solid rod starts growing, the crystallization front is fed with melt through the ring capillary and central noncapillary channels (Figure 5.17b). The regions in which these flows join are characterized by a minimum in the resulting velocity. In these areas homogeneous nucleation, growth and capture of gas bubbles by the crystallization front is likely to occur (Figure 5.14). Figure 5.18 (on the left) shows the characteristic ring-shaped porous regions in the cross-section of solid sapphire rods grown under simultaneous melt feeding from the capillary and noncapillary channels of dies with different geometries. The distribution of gas bubbles (width of the ring, its location, etc.) depends on the position of the capillary channel and on the velocity components of melt flows below the crystallization front.

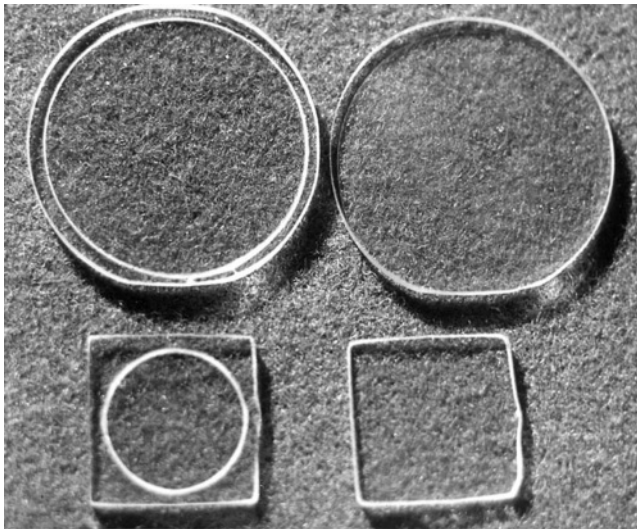


Figure 5.18 Cross-sections of sapphire crystals grown by the NCS method: crystals grown with simultaneous feed from capillary and noncapillary channels (on the left) and using feed provided only from the noncapillary channel (on the right) (Reprinted with permission from [Kulov 1997-1], copyright (1997) Elsevier Ltd).

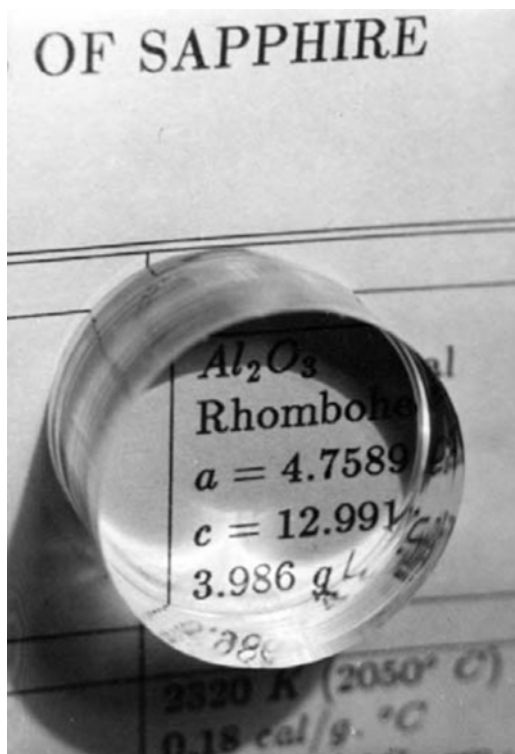


Figure 5.19 Sapphire bulk crystal of 35 mm diameter grown by the NCS method using feed provided only from a noncapillary channel (Reprinted with permission from [Kurlov 1997-1], copyright (1997) Elsevier Ltd).

However, the most important aspect of this method is that it allows the production of crystals completely free of gas bubbles whose origin is connected with the presence of regions characterized by a minimum in the melt flow velocities. This is achieved either by the suppression of the capillary flow from the noncapillary channel, or by shutting off the capillary feed; then the crystal grows only from the melt fed from the noncapillary channel (Figure 5.17d). The melt moves only from the centre to the periphery; in this case the free surface of the meniscus is a sink for gaseous impurities, which results in the absence of bubbles both in the centre of the growing crystal, and near its surface (Figure 5.18, right).

Sapphire cylindrical rods up to 40 mm in diameter for use in optics (Figure 5.19) and rods of other shapes for various applications have been grown by the NCS technique. Investigation of the grain structure of sapphire crystals grown by the NCS method has shown a misorientation of less than 1° between the grain boundaries over a finite length of the grown rods (150–300 mm).

The method based on noncapillary feed is also applicable to the growth of thick-walled tubes and plates free of gas bubbles. The noncapillary channel is arranged between the two capillary channels, or other channels with more complicated profiles, which can be ‘switched off’ or ‘switched on’ to act as capillary or noncapillary channels.

5.3.3.2 Growth of Crystals with a Variable Cross-Section

The NCS technique also allows changing the growing crystal from one shape to another, e.g. from a solid crystal to a hollow one (where the feed of melt proceeds only from the ring capillary) and vice versa [Kurlov 1994, Kurlov 1997-1] (Figure 5.20). Like the VST, the NCS method produces a wide range of sapphire crystals [Borodin 1985-1, Kravetskii 1980] and it has vastly increased the dimensions of grown crystals. The essential difference between the crystals grown by the NCS method and those produced by the VST is the absence of gas bubbles in the crystal volume.

Figure 5.21 shows sapphire crucibles grown by the VST (on the left) and by the NCS method (on the right). The arrow indicates a typical column of gas bubbles in the bottom part of the crucible grown by the VST. Bubbles of this type are absent in the same section of the sapphire crucible grown by the NCS method. Consequently, this method is good

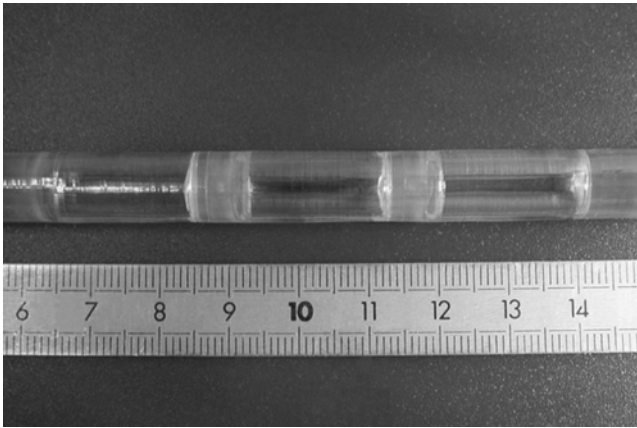


Figure 5.20 The transformation from sapphire rod to tube and vice versa.

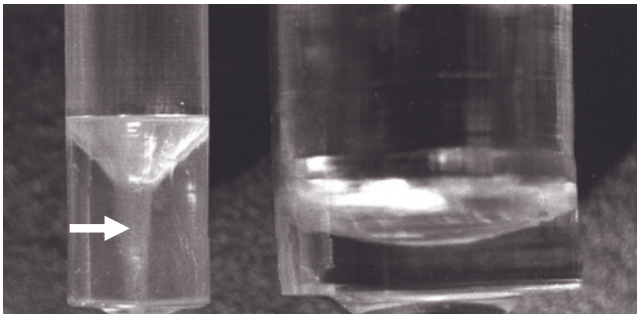


Figure 5.21 Sapphire crucibles grown by the VST: external diameter 13 mm and the arrow indicates a column of gas bubbles (on the left); and one grown by the NCS method, external diameter of crucible 34 mm (on the right) (Reprinted with permission from [Kurlov 1997-1], copyright (1997) Elsevier Ltd).



Figure 5.22 Sapphire crucibles of 65 mm in diameter grown by the NCS technique.

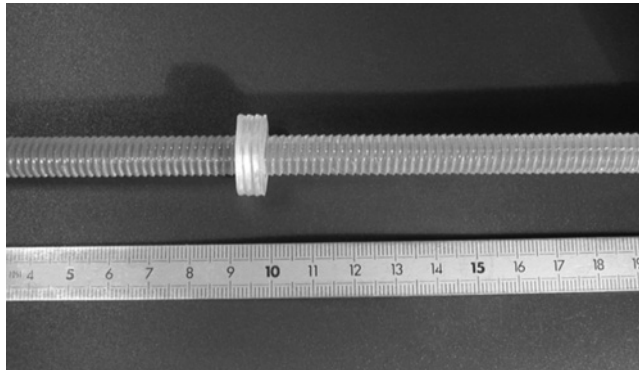


Figure 5.23 Sapphire crystals with internal and external threads grown by the NCS method.

for growing sapphire crucibles with transparent bottoms (free of gas bubbles) and crystals of variable cross-section of other shapes without gaseous inclusions. Figure 5.22 shows sapphire crucibles 65 mm in diameter.

The NCS method was used to grow sapphire rods and tubes with internal and external threads (Figure 5.23). This method allows a change in the pitch of thread during the growth process.

Besides controlling the lateral form of the crystal, it is also possible to control the formation of the junction between the hollow part of the crystal and its solid region, and

vice versa. Combination of this control with the possibility of producing crystals without gas inclusions in their volume by the NCS method enables the growth of near-net-shaped domes [Kurlov 1997-2].

Sapphire is the most durable commercially available mid-infrared window material. One of the most important applications is domes for relatively high-speed missiles. Here, the main problem is to obtain transparent materials that have good high-temperature properties and good resistance to rain and other sources of damage. A new approach to producing sapphire at reduced cost is to grow a near-net-shaped crystal. Methods for the preparation of near-net shapes directly in the course of the growth process by the heat exchange method (HEM) [Khattak 1989, Khattak 1992], the gradient solidification method (GSM) [Horowitz 1993, Horowitz 1996] and the modified EFG method [Locher 1990, Locher 1992] have been reported. NCS is another technique that can be used to produce sapphire domes.

The main design feature of the die is a hemispherical top for the inner thick-wall liner with a noncapillary channel (Figure 5.24). The die is also provided with a capillary channel along its perimeter. The height of the hollow spherical segment h is $h = \sqrt{d(2R - d)}$, where R is the radius of the spherical segment and d the required thickness of the blank wall. At the initial stage, after the formation of a ring meniscus between the seed plate and the die (Figure 5.24a), the melt approaches the crystallization front only through the capillary feed, and the crystal grows in a tubular shape (Figure 5.24b). As the enclosed volume increases, the difference between the gas pressure in the enclosed volume and that in the growth

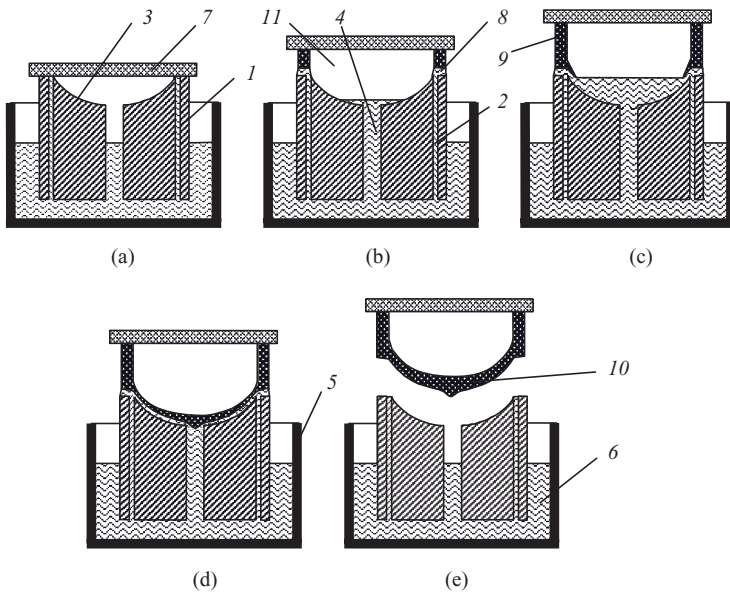


Figure 5.24 The sequence of individual near-net-shaped dome growth stages. 1, die; 2, ring capillary channel; 3, liner cavity; 4, noncapillary channel; 5, crucible; 6, melt; 7, seed plate; 8, ring meniscus; 9, tubular crystal; 10, near-net-shaped dome; 11, enclosed volume (Reprinted with permission from [Kurlov 1997-2], copyright (1997) Elsevier Ltd).

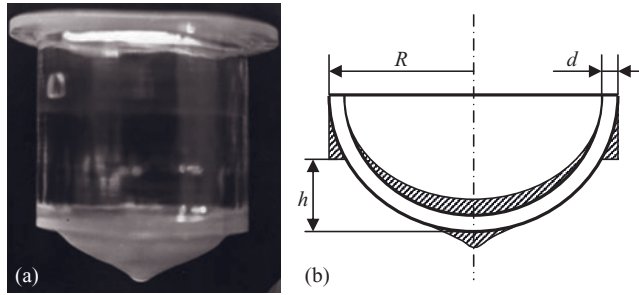


Figure 5.25 The as-grown near-net-shaped sapphire dome grown by the NCS method (a). Near-net-shaped dome cross-section (b) (Reprinted with permission from [Kurlov 1997-2], copyright (1997) Elsevier Ltd).

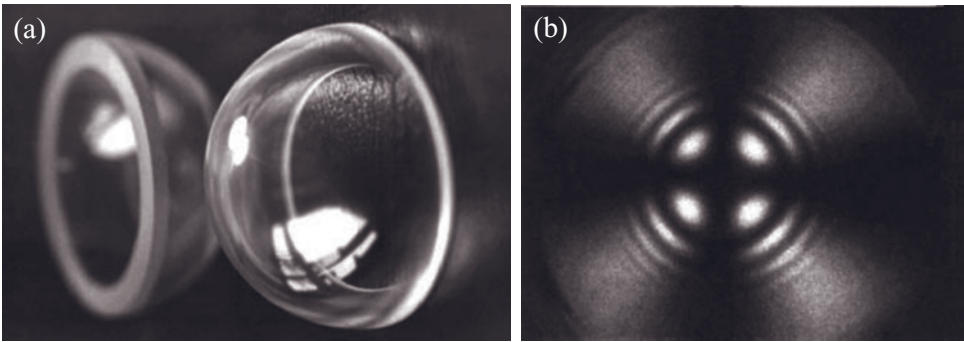


Figure 5.26 (a) Mechanically finished hemispheres produced by the NCS method. (b) Conoscopic figure from sapphire dome grown along the c-axis (photograph taken with dome between crossed polarizers) (Reprinted with permission from [Kurlov 1997-2], copyright (1997) Elsevier Ltd).

chamber also grows. because of this pressure difference, the melt rises in the hole and then in the liner cavity. When the melt in the cavity reaches the edges and meets the meniscus, the hemispherical part of the blank (Figure 5.24c) begins to crystallize. The shape of the inner surface of the blank depends on the rate of pulling and the radial temperature gradient. Under proper thermal conditions this shape may resemble that of the crystallization front. The front surface reflects the hemispherical configuration of the liner top (Figure 5.24d). As soon as the stage c begins, the crystal is pulled to a length equal to the height h of the spherical segment. The hemispherical sapphire blank is then abruptly broken from the die top (Figure 5.24e) at high pulling velocity.

Figure 5.25a shows the as-grown near-net-shaped hemispherical sapphire blank with the seed plate. Figure 5.25b shows the cross-section of a near-net-shaped dome grown by the NCS method. The surface sections to be removed mechanically for fabricating a final-shaped dome are shaded. This shows that the surfaces can be controlled accurately so that minimum grinding and polishing is necessary to produce the finished domes. Final-shaped sapphire domes fabricated from near-net-shaped blanks and a conoscopic figure from the sapphire dome are shown in Figure 5.26. High-quality near-net-shaped sapphire domes were grown by the NCS method.

Experiments were also carried out to obtain a set of near-net-shaped domes during one growth cycle for additional cost saving in crystal growth. The NCS method allows the passage from a solid crystal to a hollow one (where the feed of the melt proceeds only from the ring capillary) and vice versa [Kurlov 1997-2].

5.3.4 Growth from an Element of Shape (GES)

Stepanov's concept [Stepanov 1963] indicates that two modes of capillary shaping can be used in pulling a crystal from the liquid on a seed: producing a meniscus whose shape completely coincides with that of the grown crystal and producing a meniscus representing a small element in the crystal shape.

The growth from an element of shape (GES) method was developed on the basis of the Stepanov concept and its main principles were described by Antonov *et al.* [Antonov 1985]. It consists of pulling a shaped crystal from a melt meniscus, which is only a small element of the whole transverse cross-section configuration of the growing crystal (Figure 5.27). The crystal grows layer by layer and the period l is determined by the ratio v/ω , where v is the pulling rate and ω is the rotation frequency.

The first experiments involved the growth of lithium fluoride single tubular crystals [Antonov 1985]. Between the surface of the seed and the shaper there is a column of liquid, which is a small element of the tubular form of the future crystal. When the seed is rotated, its horizontal surface contacts the meniscus in the column, and a thin layer of liquid is formed.

The most important development of the GES method was the growth of complicated sapphire crystals with continuous variation of the lateral surface profile. The authors of the GES method report that small liquid volumes can be continuously solidified after

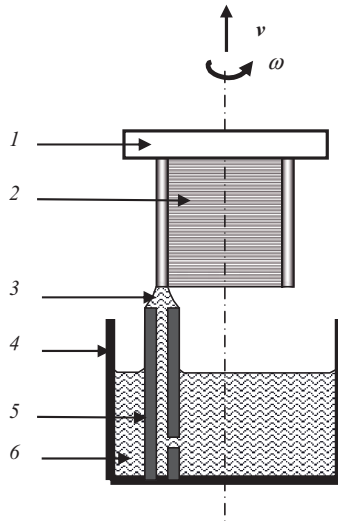


Figure 5.27 Principle of the GES method. 1, seed plate; 2, tubular crystal; 3, meniscus; 4, crucible; 5, die; 6, melt.

combined displacements of the seed relative to the die, in order to produce crystals with complicated shapes. During growth, the displacement may be applied to the seed or the die, or to both simultaneously [Nikiforov 1988].

Sapphire tubes and other hollow revolving bodies were first grown by Borodin *et al.* [Borodin 1990], who used the term ‘local shaping technique’ (LST) rather than the GES. To alter the profile of the lateral surface according to a preset program they used horizontal die displacement relative to the crystal rotation axis [Borodin 1999]. Following variation of the horizontal die coordinate the inner and the outer radii of the sapphire tube change, and the profile of the lateral surface changes accordingly.

The alternative is to use horizontal displacement of the seed during the growth process. A specially designed apparatus with horizontal translation of the pulling shaft, in addition to the usual vertical and rotating movements, was used to produce sapphire crystals of complicated shapes [Kurlov 1999-1]. Hollow sapphire crystals of complex shapes were grown by the GES technique using horizontal translation of the pulling shaft (Figure 5.28).

The following results were achieved for the preparation of high-quality sapphire hemispheres for use in high-temperature optics: (i) growth of GES crystals free of gas bubbles and solid inclusions in their volume; (ii) growth of near-net-shaped blanks close to dome shape; (iii) growth of crack-free sapphire hemispheres.

GES crystals grew layer by layer, with the thickness of each layer being determined by the ratio of pulling rate to rotation rate: v/ω . As a consequence, GES sapphire crystals



Figure 5.28 *Sapphire hollow crystal grown by the GES technique.*

contained regular striations and a band-like distribution of voids described [Borodin 1990] as gas bubbles, solid inclusions and inhomogeneous doping impurities. On the one hand, argon, nitrogen, carbon oxides, molybdenum oxides and products of alumina dissociation may contribute to striation forming. On the other hand, the striations may also be caused by structural imperfections; a configuration of void pile-ups is often followed by striations. The regular striations and band-like distribution of voids observed in the longitudinal sections of the sapphire tubes display a spiral distribution in the bulk of the crystal, with the angle of the spiral line slope given by $\alpha = \arctan(v/2\pi R\omega)$, where R is the distance from the rotation axis of the seed holder to the axis of the die. The arrangement and dimension of voids in the crystal are determined by the morphology of the solid-liquid interface, the period v/ω , and the linear growth rate $v_\omega = 2\pi R\omega$.

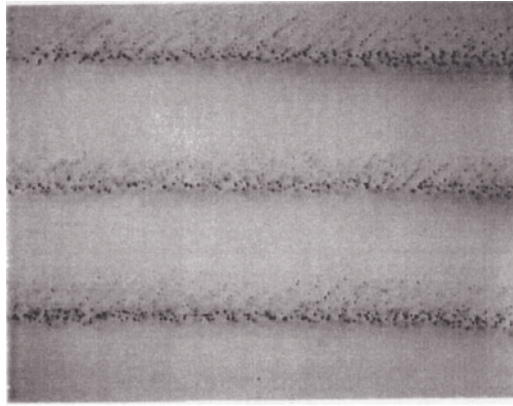
These defects greatly decrease the optical and mechanical properties [Gurjiyants 1999] of the material. In broken GES crystals, steps were observed on the fracture surface. The height of the step is correlated with the height of the layer, so the crack propagates in several jumps from one level to another. The failure originates in a zone where there is a high concentration of voids. The location of these zones coincides with the bubbles distributed along each new crystallized layer. Partial removal of stress is observed in GES crystals before destructive failure. This occurs as a result a crack interacting with defective layers, resulting in the partial loss of energy of the crack.

It is therefore very important to find the optimum regimes that lead to GES sapphire growth without striations. It was found that a marked decrease in the linear growth rate and period v/ω leads to improved GES crystal quality. Figure 5.29 shows a longitudinal cross-section of a sapphire GES crystal which was grown using a low rotation rate (1 rpm) [Kurlov 1999-1]. The ratio v/ω was reduced from $130\mu\text{m}$ (Figure 5.29a) to $4\mu\text{m}$ (Figure 5.29b) to obtain GES crystals completely free of voids.

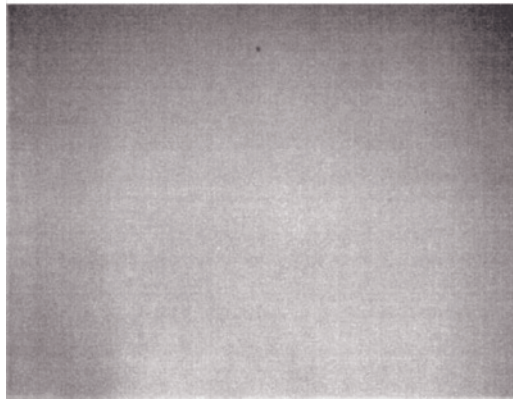
Light transmittance measurements along the c -axis are compared for GES samples with $4\mu\text{m}$ and $130\mu\text{m}$ layer thicknesses [Kurlov 1999-1]. When the crystallized layer is small enough, the light transmittance for GES crystals become comparable with Gentilman's reference data [Gentilman 1986].

An interesting application of the GES is the pulling of hemispherical hollow crystals. The most difficult part of this application is the initial stage of hemisphere formation after seeding, when pulling is carried out practically only in a horizontal direction. The size of the crystal cross-section d_c depends on the size of the die-top cross section d_d and the angle φ between the pulling direction and vertical axis; it is determined by a simple ratio $d_c = d_d \cos\varphi$ for a horizontal die-top surface (Figure 5.30a). In the initial stage of growth the thickness of the hemisphere wall approaches zero and growth is impossible because of the absence of attachment of the melt column to the die edge. One way to solve this problem is to design the die with a tilted top surface [Théodore 1999-1], as shown in Figure 5.30b, in order to make the process available for any crystal shape by rotation of the seed together with a combination of vertical and horizontal translations. A 45° tilted angle for the molybdenum die is optimum for use with a factor $d_c/d_d = \sqrt{2}$ for pulling crystals over a wide range of angles. The thickness of the growth layer for each turn of a die angle of 45° is:

$$h_c = \frac{v_x \cos\theta + v_z \sin\theta}{\omega}, \quad (5.4)$$



(a)



(b)

Figure 5.29 Longitudinal cross-sections of GES sapphire crystals using a 1 rpm rotation rate at a ratio v/ω equal to: (a) $130\ \mu\text{m}$; (b) $4\ \mu\text{m}$ (Reprinted with permission from [Kurlov 1999-1], copyright (1999) Wiley-VCH).

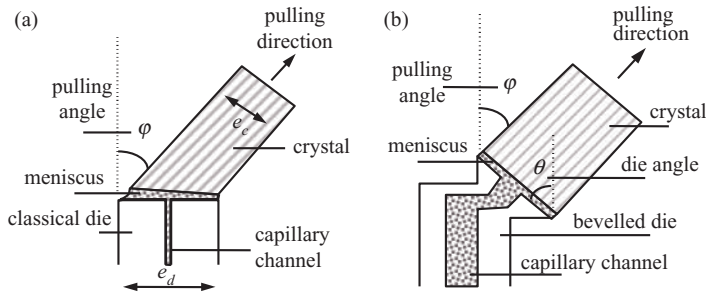


Figure 5.30 Scheme showing the dependence between size of the die-top and crystal cross-sections for: (a) horizontal die-top surface, (b) tilted die surface.

where v_z and v_x are the corresponding vertical and horizontal translation rates, and ω is the rotation rate.

A failure mechanism has been proposed in order to explain the generation and propagation of cracks during the growth of sapphire domes from an element of shape [Théodore 1999-2]. According to this model, expansion of 10- μm gas bubbles is induced by glide dislocations (Orowan's model), up to a critical size at which the crack is initiated. Numerical simulation of stresses during growth explains how cracks propagate first vertically (V-type cracks) then horizontally (H-type cracks). The calculations were done on the basis of *in situ* temperature measurements [Krymov 1999]. In order to avoid crack initiation, it is necessary to keep the plastic strain rate, which relaxes the stresses and at the same time lengthens the initial defect, below a critical value. One solution consists of relaxing the opening hoop stress at the same rate as that which is lengthening the defect.

A criterion based on plastic strain relaxation is defined in order to determine the growth parameters (pulling and rotation rates) as a function of the measured thermal gradients in the crystal. The time derivative of the crystal base radius is the same as the horizontal translation rate of the seed, v_x ; a no-failure criterion is obtained:

$$\omega(r) \leq \frac{2\dot{\epsilon}_{\text{pl}}^{\text{max}} - |v_x| \cdot \nabla_r T}{2\pi r \cdot \nabla_s T}, \quad (5.5)$$

where $\nabla_s T$ represents the curvilinear thermal gradient, $\nabla_r T$ represents the radial thermal gradient, $\dot{\epsilon}_{\text{pl}}^{\text{max}}$ is the maximum strain rate and α_{th} is the thermal expansion coefficient. The vertical translation v_z is combined with the other displacements to grow sapphire domes in the way presented in Figure 5.31a.

According to the equation, ω reaches its lowest value, ω_c , at the end of the growth, where the crystal radius is maximum. This defines the linear growth rate that is kept

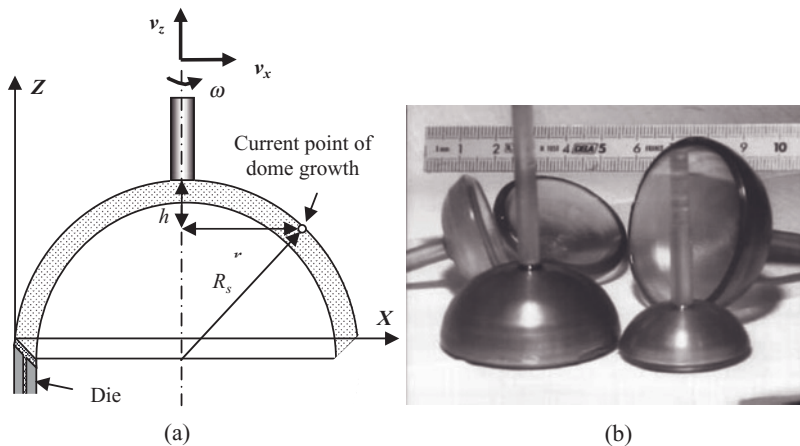


Figure 5.31 Principle of the growth of a dome from an element of shape (a) and crack-free sapphire hemispheres (b) (Reprinted with permission from [Théodore 1999-2], copyright (1999) Elsevier Ltd).

constant all through the process in order to keep a constant liquid flow rate in the die. In practice, crack-free crystals were obtained for linear pulling rates of about twice the latter critical value, a result consistent with the fact that the $\sigma_{\theta\theta}$ stress component reaches its maximum when the crystal horizontal radius is close to half the ultimate base radius [Théodore 1999-2].

The other parameters (v_x, v_z) are derived from the Pythagorean relation and from crystallized layers of constant thickness. In practice, (v_x, v_z, ω) are calculated at each time step, connected with latitude increments that describe the hemispherical dome from its top to its base. These increments (0.5°) are small enough to get a roughness lower than the surface defect between successive growth layers.

This led to the growth of GES crack-free sapphire hemispheres (Figure 5.31b) that can be used for infrared dome blanks.

5.3.5 Modulation-Doped Shaped Crystal Growth Techniques

A current problem in the field of optoelectronics is the development of new materials that can combine several different functions simultaneously. One way to do this is to grow bulk crystals with regularly doped structures. In particular, the presence of spatial resonance structures (periodic structures of variable composition) in crystals of $\text{Al}_2\text{O}_3:\text{Ti}^{3+}$ sharply reduces the threshold for laser oscillation and makes it almost independent of the external cavity characteristics [Kaminsky 1986]. The characteristics of the laser medium are also influenced by the contrast of the spatial resonance structures in terms of a parameter a , e.g. refractive index. The contrast is determined as in Equation (5.6), and is a function of many variable quantities at the same time (activator concentration, growth conditions, etc.).

$$K = \frac{a_{\max} - a_{\min}}{a_{\max} + a_{\min}}. \quad (5.6)$$

5.3.5.1 Periodically Doped Structures

In the first approach to the *in situ* production of crystals with regularly doped structures, crystals were grown by the EFG technique in the shape of ribbons, rods, and tubes. Changing the crystallization rate leads to a periodic disturbance of temperature conditions at the crystal–liquid interface and hence to periodic capture of the dopant by the crystal. The frequency of the temperature fluctuations can be varied by changing the pulling rates, periodically displacing the die, and varying the power supply. The periodic change of pulling rate was achieved in two different ways: either the rate was periodically increased and decreased, or the pulling mechanism was periodically switched on and off. The duration of the periodic structures produced in this way ranged from 5 to 100 μm . The periodic structure in a longitudinal section of a sapphire is shown in Figure 5.32a [Kurlov 1998-1]. The dopant modulation in the grown crystals was observed using cathodoluminescence (scanning electron microscope DSN-960 ('Opton')), the image contrast being dependent on the contents of the luminescent impurity in the matrix–activator couple. This approach also made it possible to change the period of the spatially doped structures during the process of growth and to go from a periodically doped structure to a homogeneously doped one [Kurlov 1998-2] (Figure 5.32b).

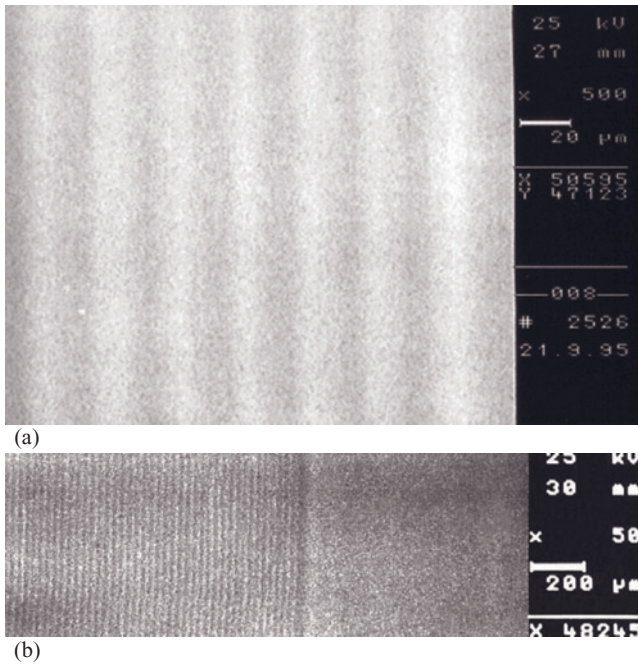


Figure 5.32 The periodic structure $\text{Al}_2\text{O}_3:\text{Ti}^{3+}$ in the longitudinal section of a sapphire rod grown by the EFG method. The structures were prepared by changing the pulling rate.

The contrast in the stripes produced in the structures is not great because it is limited by the redistribution of the impurity in advance of the crystallization front in only a small volume of melt – in the meniscus. The activator concentration varies by no more than one order of magnitude. The thickness of the transition layer between ‘doped’ and ‘undoped’ regions is comparable to the striation period. The contrast decreases with decreasing striation period and virtually vanishes for periods less than $5\mu\text{m}$. Somewhat thinner transition layers were observed by periodically stopping the pulling.

Antonov and his coworkers [Antonov 1985, Nikiforov 1988] developed the GES concept with the simultaneous operation of two (or more) dies. The dies were placed at some distance from the rotation axis and the menisci form from small elements of the melt (Figure 5.33). These authors used layered single crystals having the composition LiF-LiF:Mg^{2+} as a model for the investigation of mechanical parameters and dislocations in composite structures.

Later, the applicability of the GES method for high-temperature multicomponent oxide crystal growth was investigated. Sapphire [Kurlov 1998-1, Kurlov 1998-2, Kurlov 1998-3], calcium–niobium–gallium garnet (CNGG) and yttrium orthovanadate (YVO) [Epelbaum 1998-2] were chosen as representative test materials. Shaped crystals in the form of rods and tubes were grown at a pulling rate of 3–25 mm/h and at a rotation rate 0.5–20 rpm. Grown crystals included regularly doped structures $\text{Al}_2\text{O}_3\text{-Al}_2\text{O}_3:\text{Ti}^{3+}$ with periods of 5–100 μm [Kurlov 1998-3] (Figure 5.34a). The impurity concentration in the undoped parts of the crystal was less than 10^{-4} wt.% and in the doped parts of crystal it

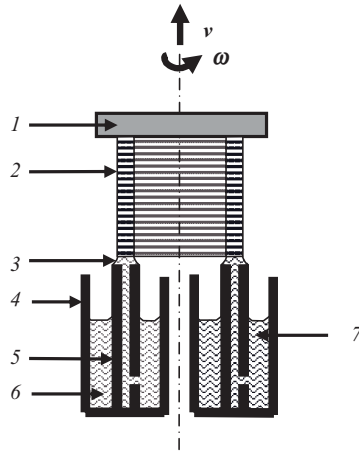


Figure 5.33 Principle of layered crystal growth by the GES method using two crucibles: 1, seed plate; 2, layered crystal; 3, meniscus; 4, crucible; 5, die; 6, undoped melt; 7, doped melt.

was up to 0.2 wt%. The doped and undoped layers constitute spirals with the angle of the spiral line slope given by $\alpha = \arctan(v/2\pi R\omega)$ where R is the distance from the rotation axis of the seed holder to the axes of the dies (when dies are located at equal distance from the axis of rotation of the seed holder). The volume of the transition region between layers is defined mainly by the width of partial melting of the initially crystallized layer as a result of contact of the layer with the meniscus. The width of the partially melted zone and the pattern of the impurity distribution in the transition region depend on the thermal conditions in the crystallization zone, the frequency of rotation and the pulling rate of the crystal. In particular, high-contrast structures with small periodicity were produced under conditions close to supercooling on the crystallization front, i.e. with a small meniscus height.

Application of the GES method allows *in situ* production of various types of spatially periodic structures:

- A change of period during the growth process can be realized by varying the ratio v/ω (Figure 5.34b) [Kurlov 1998-3].
- Application of this method allows predetermining the required ratio of layer heights within a period and also allows this ratio to be varied during the growth process (Figure 5.34c) [Kurlov 1998-1]. Change of doped–undoped layer width ratio can be achieved in one of two ways, either by variation of the top surface level of one of the dies or by variation of the relative location of the dies if the top surface levels are constant.
- Transition from the periodic structures to uniformly doped or undoped crystal was carried out by disconnecting melt feeding in one die during the growth process.
- Location of dies having various areas of work surface and/or various distances of dies from the rotation axis and/or combinations of the die arrangements makes it possible to obtain various types of doping structures in crystals [Kurlov 1998-3].

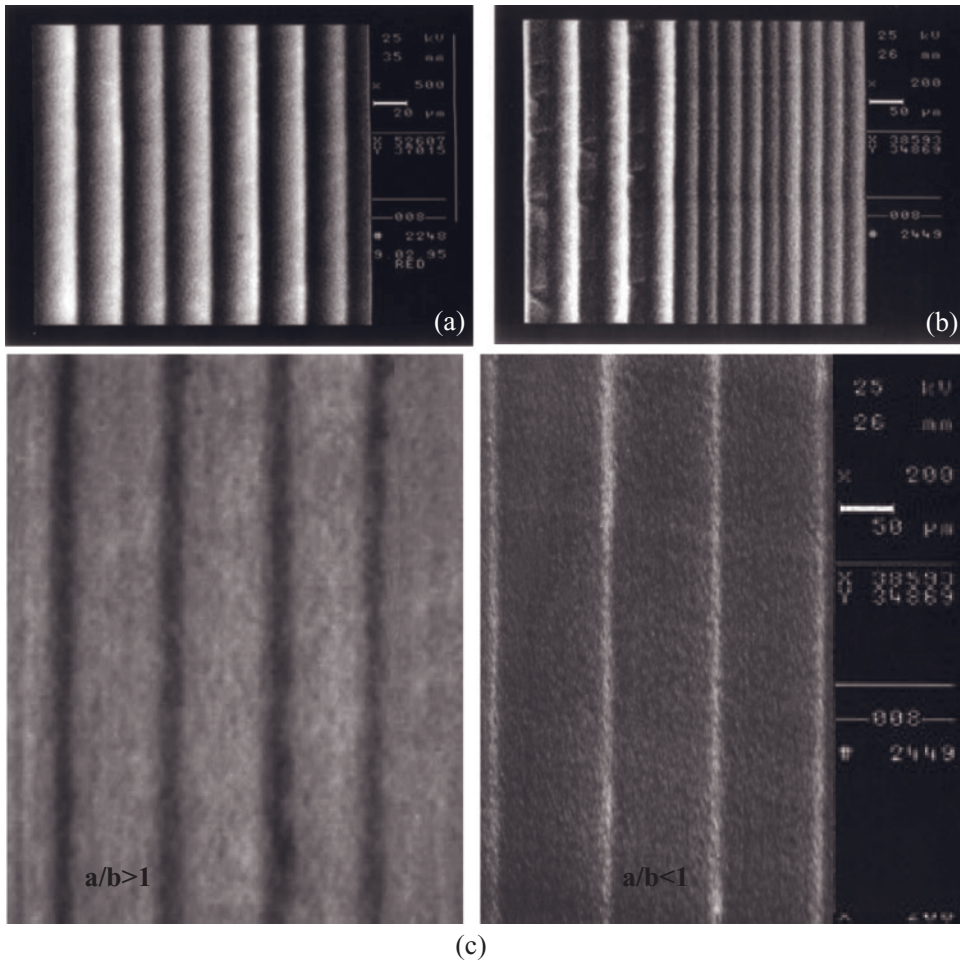


Figure 5.34 Periodical structures of $\text{Al}_2\text{O}_3\text{-Al}_2\text{O}_3\text{:Ti}^{3+}$ grown by the GES method: (a) structure with constant period; (b) structure with a variable period; (c) structure with different ratios of width of doped and undoped regions in one period (Reprinted with permission from [Kurlov 1998-1], copyright (1998) Wiley-VCH).

- The GES technique make it possible to control not only the contrast, period, and ratio of heights of doped regions in one period, but also the pattern of dopant distribution within the period (Figure 5.35).

The two techniques of *in situ* preparation of modulated structures described here can be used universally in the growth of crystals of other compositions from the melt. The structures in bulk crystals outlined above amount to a new class of materials. The authors believe that these structures will find applications in the development and fabrication of various devices.

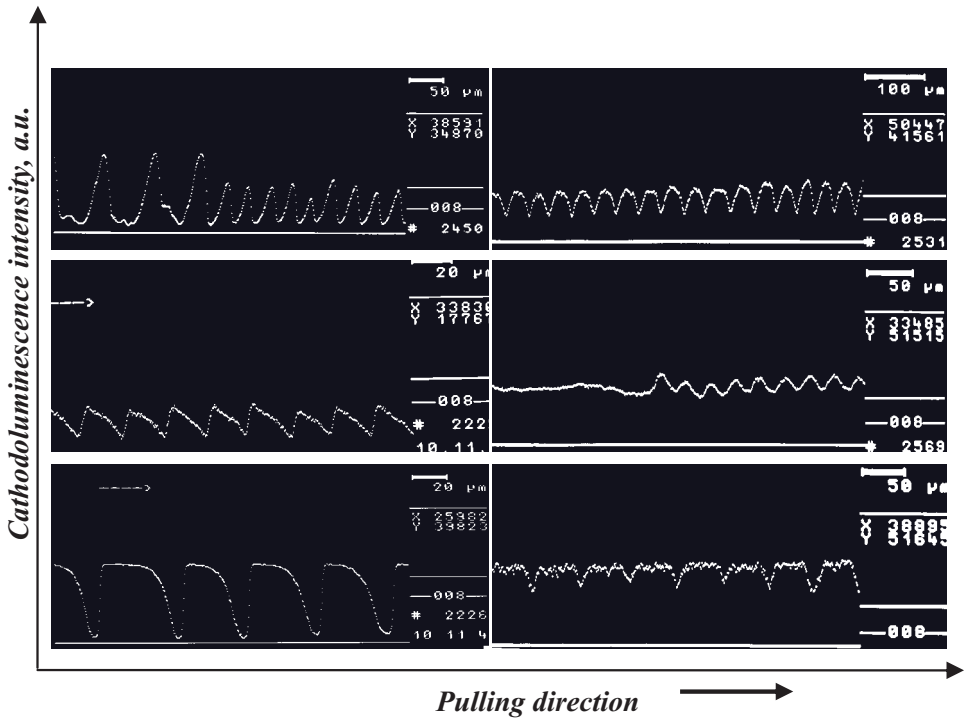


Figure 5.35 The distribution of cathodoluminescence intensity (a.u.) along the $\text{Al}_2\text{O}_3\text{-Al}_2\text{O}_3\text{:Ti}^{3+}$ samples (Reprinted with permission from [Kurlov 1998-3], copyright (1998) Elsevier Ltd).

5.3.5.2 Core-Doped Fibres

The availability of high-quality fibre crystals doped with active laser ions only in a sharply separated inner core region [Burrus 1977, Rudolph 1994] is of special interest. Because of the step-like change of the radial doping profile of nonlinear optical core-doped fibres, the pumping energy is absorbed only by the central part and an efficient laser mode translation takes place.

For the first time Burrus and Stone [Burrus 1977] grew a thin ruby laser as a quasi-cladded core-doped fibre with a diameter of $40\ \mu\text{m}$ by a two-step laser melting technique. Homogeneously doped ruby fibres were first grown by a floating zone technique from small source rods, and these fibres were then carefully surface melted in the same CO_2 laser apparatus to outdiffuse the Cr into a region near the fibre surface. Such a structure had a modulated radial refractive index with improved waveguide properties, i.e. transmission efficiency.

Core-doped fibres were grown directly from the melt for the first time by Dmitruk [Dmitruk 1985]. Two crucibles were combined with an outer and inner die for differently doped melts (Figure 5.36). While the melt of the outer crucible rises only in a small central bore, the melt of the inner crucible goes up within a ring-like aperture surrounding the central bore. A meniscus forms at the front consisting of two essentially different melt

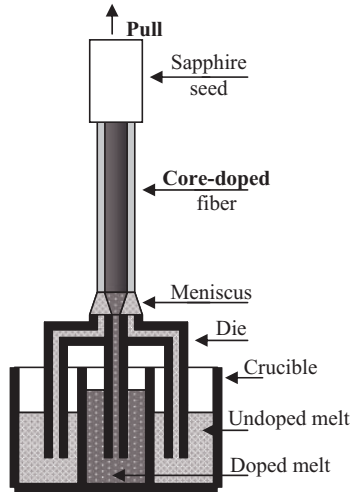


Figure 5.36 Principle of core-doped fibre growth using two crucibles (Reprinted with permission from [Kurlov 1998-4], copyright (1998) Elsevier Ltd).

columns – an inner doped core and an outer undoped wrapping. Core-doped fibres of CsBr(AgBr)–CsBr and TlBr–TlBr_xCl_{1-x} compositions were grown.

Later, the same approach was used [Shimamura 1994] for LiNbO₃ rods with a length of ~10 mm having an outer diameter of 5 mm consisting of a sharply separated inner Cr- or Nd-doped core region. Crystals with diameters ~1.5 and 4 mm were successfully grown at pulling rates up to 60 mm h⁻¹. This technique was also used for preparing *in situ* sapphire core-doped fibres (Al₂O₃–Al₂O₃:Ti³⁺) with automated weight control [Kurlov 1998-4].

To grow high-performance shaped crystals with different compositions in their cross-section it was necessary to solve the problem of forced mass transfer across the meniscus between melts of various composition and to control the introduction of gas bubbles and solid inclusions in the volume of the crystal. In order to solve the first problem it is necessary to form and maintain a preset spatial component distribution in the meniscus and in the region of crystallization during the growth process, which is determined by thermal convection, mass exchange by diffusion and convection induced by the gradient of surface tension at the meniscus surface. The main parameters that determine the extent of mixing between the different melt compositions in the meniscus are the pulling rate, the meniscus height which is dependent on the thermal gradient, the geometric sizes of the capillary channels of the dies and the form of the die top. Calculations were carried out to estimate the spreading region of the core-doped part of the meniscus as a function of the pulling rate and the meniscus height with regard to diffusion in the meniscus:

$$d_c = d_i + 2\sqrt{\frac{h_m D}{v}},$$

where d_c is the core diameter, d_i the diameter of the inner die bore, D the diffusion coefficient of the dopant in the melt, h_m the meniscus height and v the pulling velocity

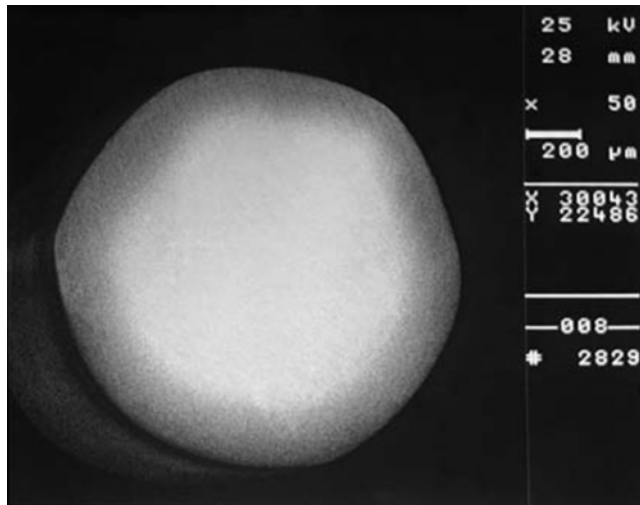


Figure 5.37 The cross-section of core-doped $\text{Al}_2\text{O}_3\text{-Al}_2\text{O}_3:\text{Ti}^{3+}$ fibre grown under optimal conditions.

[Rudolph 1994]. To grow a crystal with a small mixing zone between the doped and undoped parts it was necessary to achieve a small meniscus height and large pulling rate simultaneously. This displaces the growth conditions at the crystallization front to the supercooling region. Supercooling is followed by the appearance of cellular structure and facets on the growth surface, which results in the mass capture of bubbles and solid phase inclusions.

In order to control the growth conditions at the crystallization front and prevent the formation of related defects, an automated control system using a crystal weight sensor was applied to the process of shaped crystal growth. The meniscus height and the conditions at the melt–crystal interface, including supercooling and superheating, are controlled. Figure 5.37 shows the cross-section of a high quality core-doped fibre $\text{Al}_2\text{O}_3\text{-Al}_2\text{O}_3:\text{Ti}^{3+}$ grown under optimal conditions.

Supercooling at the crystallization front in the process of growing variable composition crystals can be nonuniform because of constitutional supercooling in the zone of the more refractory melt, which results in the appearance of solid-phase inclusions in the doped crystal part. To obtain the optimal temperature distribution in the crystallization zone, the heights of the edge for the inside and outside parts of the die were varied.

The modified EFG method involving two (or more) crucibles was also used to grow large composition-modulated $\text{Al}_2\text{O}_3\text{-Al}_2\text{O}_3:\text{Cr}^{3+}$ [Kurlov 1998-5] as ribbons, tubes, and rods. The modified NCS technique was also used for the growth of sapphire crystals of large cross-section with a controlled dopant distribution. Figure 5.38 [Kurlov 1998-5] illustrates the transition from a core-doped rod (B) to a uniformly doped rod (C), which was achieved by switching off the melt supply through the capillary channel. The state of the crystallization front was controlled in such a way as to prevent the entrapment of solid and gaseous inclusions. The automated control system was similar to that used in the EFG technique. The modified NCS method permits the growth of rods with various

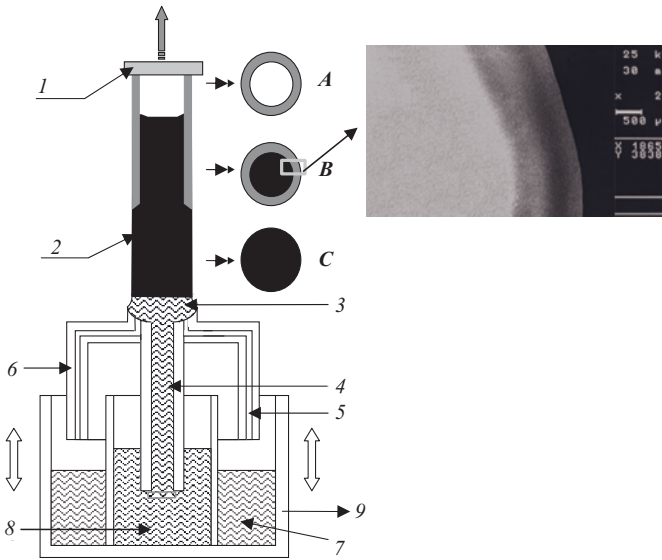


Figure 5.38 Principle for pulling a composition-modulated rod by the modified NCS technique: 1, seed plate; 2, crystal ingot with hollow part A, core-doped part B, and uniformly doped part C; 3, meniscus; 4, noncapillary channel; 5, capillary channel; 6, die; 7, doped melt; 8, undoped melt; 9, crucible with two compartments. The inset shows part of the cross-section of a 16-mm diameter $\text{Al}_2\text{O}_3\text{-Al}_2\text{O}_3\text{:Ti}^{3+}$ core-doped rod.

cross-sectional shapes and various transverse dopant distributions, thick tubes, and crystals of intricate external shape and doping patterns.

5.3.6 Automated Control of Shaped Crystal Growth

The growth of sapphire crystals of various shapes is now well developed. Currently, the most urgent problem in shaped crystal growth is to increase the crystal quality.

The most abundant defects in shaped crystals are gaseous and solid inclusions, as well as block boundaries. Their most probable origin is crystal supercooling (thermal or constitutional) and hence loss of the crystallization front stability [Dobrovinskaya 1980, Nicoara 1987, Novak 1980, Tatartchenko 1980, Wada 1980]. In order to control the growth conditions at the crystallization front and prevent the formation of related defects, an automated control system using a crystal weight sensor was applied to the process of shaped crystal growth. Automated computer systems provide *in situ* quality control as well as shape control, permitting an increase in the yield of high-quality crystals and an expansion of the areas of application of sapphire crystals as building and optical material.

Direct application of automated control systems such as that developed for the Czochralski technique is unacceptable for shaped crystal growth because of the anchoring of the meniscus to the edge of the die. This additional constraint for the growth of shaped crystals is the essential difference from the Czochralski technique.

The principles of automated control of shaped crystal growth with use of a crystal weighing technique have now been developed [Kurlov 1997-3] for all stages of the pulling process (seeding, crystal enlargement, stationary growth, *in situ* change of cross-section). Regulation of the crystal cross-section has been achieved by controlling the deviation δM of the real mass M_r from the programmed mass M_p by variation of the heating power P . The real mass M_r is calculated from the measured weight signal W .

The meniscus height and the conditions at the melt–crystal interface, including supercooling and superheating, are closely related to the amplitude of oscillations of the deviation of the mass rate $\delta \dot{M}$. Together with analysis of mass deviation δM and its first and second derivatives ($\delta \dot{M}$ and $\delta \ddot{M}$, respectively) the program also processes the amplitude of $\delta \dot{M}$ oscillations. The measured parameter $\delta \dot{M}$ is a characteristic of the oscillatory mass rate deviation, which always exists in any real growth process. The oscillation period is controlled by the time characteristics of the actual process and of the regulator. The oscillation amplitude is controlled by the heat transfer and the response rate of the mechanical system.

The amplitude of the oscillations $\delta \dot{M}$ is related implicitly to the meniscus height and the position of the melt–crystal interface. One should choose an amplitude range and maintain the amplitude within this range during growth. A relatively small amplitude indicates superheating of the melt–crystal zone and a rather large meniscus height. This may result in the appearance of facets on the lateral surface of the growing crystal with a decrease of cross-sectional area and, as a further consequence, a rupture of the meniscus. The upper boundary of the amplitude is the most important parameter for automated growth of high-quality shaped crystals. A large $\delta \dot{M}$ corresponds to supercooling in the melt–crystal zone, i.e. the meniscus height is correspondingly small. In this case a cellular structure can form on the melt–crystal interface, which leads to the formation of defects in the growing crystal. A further increase of $\delta \dot{M}$ can lead to the partial freezing of the crystal to the die and an undesirable change of crystal shape. The meniscus becomes so small that the crystallization front ‘sits down’ on the working surface of the die.

5.3.6.1 *Automated Crystal Seeding Process*

Crystal seeding is an important stage of the growth process. The further stages of crystal growth depend on successful seeding, so the seeding process has found its own place in the general problem of automation of shaped sapphire crystal growth.

There are two main versions of the seeding procedure [Kurlov 1997-3]. In the first case the seed crystal partially melts, which results in a slow increase of the weight signal W . The value of the weight signal change is proportional to the area of seeding. The weight signal increase can be explained by the influence of the surface tension force on the weight signal. The surface tension force appears when the seed starts to melt, and this results in the formation of a melt meniscus between the seed and the shaper. Too extensive seed melting can result in the rupture of the meniscus and a sharp decrease of the weight signal. When meniscus rupture occurs the heating power is decreased automatically by a certain amount, and the seeding process has to be repeated. This ‘calculation–technological’ cycle is repeated until the weight signal increases slowly or decreases (after its slow increase because of meniscus formation) to a value which is not less than that before the seeding cycle.

In the second case ‘cold’ contact of the seed crystal and shaper occurs (without meniscus formation) and the weight signal W decreases sharply. After that the heating power is increased gradually until meniscus formation starts.

The automatic crystal seeding process is tuned by a specific set of software parameters to get a stable ‘calculation–technological’ iteration process. The most important parameters that influence the stability of the crystal seeding process are as follows:

- maximum rates of seed crystal lowering and lifting;
- minimum time interval for the evaluation of the weight data change;
- minimum time interval for melt exposure for a specific value of heating power;
- minimum step in the heating power change.

Crystal pulling starts when the controlling computer has obtained a correct crystal seeding. Crystal enlargement proceeds if the weight signal W increases gradually with a sufficiently small amplitude $\delta\dot{M}$. The absence of a gradual increase of the weight signal or a too large $\delta\dot{M}$ amplitude during the first moments of crystal pulling indicate supercooling in the melt–crystal zone. In this case the computer will automatically increase the heating power until the weight signal starts to grow gradually with a sufficiently small $\delta\dot{M}$ amplitude, and then the process of crystal expansion will begin.

5.3.6.2 Calculation of Programmed Mass Change for Stationary Growth of Crystal Rods and Tubes with Arbitrary Cross-Sections

It is necessary to know the programmed mass at each time moment that it can be compared with real mass in the automated system with crystal weight control. This programmed mass is the sum of the crystal mass and meniscus mass including influence of the surface tension of the meniscus surface and influence of the external static pressure. External static pressure is calculated as the difference between the level of melt in the crucible and the level of the working surface of the die. In the most usable processes (for wetting melts) this pressure is negative, i.e. the melt surface in the crucible is lower than the working surface of the die.

The programmed mass of the meniscus is determined from integrating the Young–Laplace equation for each cross-section of the growing crystal. As found in [Rossolenko 2001], the program meniscus mass M_m for a crystal rod of arbitrary cross-section can be written as:

$$M_m = \rho_l h A_c + \frac{1}{2} \rho_l a_l^2 (\Gamma_c \cos \alpha - \Gamma_d \sin \theta_d) - \rho_l H_d A_d, \quad (5.7)$$

Here ρ_l is melt density, h is meniscus height, A_c is the area of crystal cross-section, A_d is the area of the die cross-section, a_l is the capillary constant, Γ_c is the length of the contour of the crystal cross-section, Γ_d is the length of the contour of the die cross-section, α is the growth angle, θ_d is the angle of contact of the meniscus profile curve with the die and H_d is the external hydrostatic pressure (in our case it is negative).

For a tubular crystal, the shape of the cross-section of the die is described in a cylindrical coordinate system with functions $r_{d,1}(\varphi)$ and $r_{d,2}(\varphi)$ of the outer and inner contours of the die cross-section, respectively. The shape of the cross-section of the growing crystal

is similar to the shape of the die cross-section and is described by the functions $r_{d,1}(\varphi)$ and $r_{d,2}(\varphi)$, respectively. Cross-sections of the die and crystal have their own lengths Γ and squares A . The length of the outer contour of the die is $\Gamma_{d,1}$, its inner contour length is $\Gamma_{d,2}$ and its cross-sectional area A_d . The length of the outer contour of the crystal is $\Gamma_{c,1}$, its inner contour length is $\Gamma_{c,2}$ and its cross-sectional area is A_c . The outer and inner meniscus profiles may have different meniscus heights h_1 and h_2 at their contours, respectively, assuming a planar interface boundary. The expression for the full mass M_m in this case can be written as:

$$M_m = \rho_1 \frac{h_1 + h_2}{2} A_c + \frac{1}{2} \rho_1 a_1^2 [(\Gamma_{c,1} + \Gamma_{c,2}) \cos \alpha - \Gamma_{d,1} \sin \theta_{d,1} - \Gamma_{d,2} \sin \theta_{d,2}] - \rho_1 H_d A_d. \quad (5.8)$$

5.3.6.3 Calculation of Programmed Mass Change for Tube Enlargement

We now consider the case of movement of the crucible according to the change in melt level. In this case the distance between the working surface of the die and the melt level should be constant. Enlargement of the crystal tube up to the die size was found to be the critical factor for high-quality crystal growth.

Calculation of the programmed mass for various profiles can be determined by integrating the preset crystal shape. For single point seeding (Figure 5.39) the shape of the

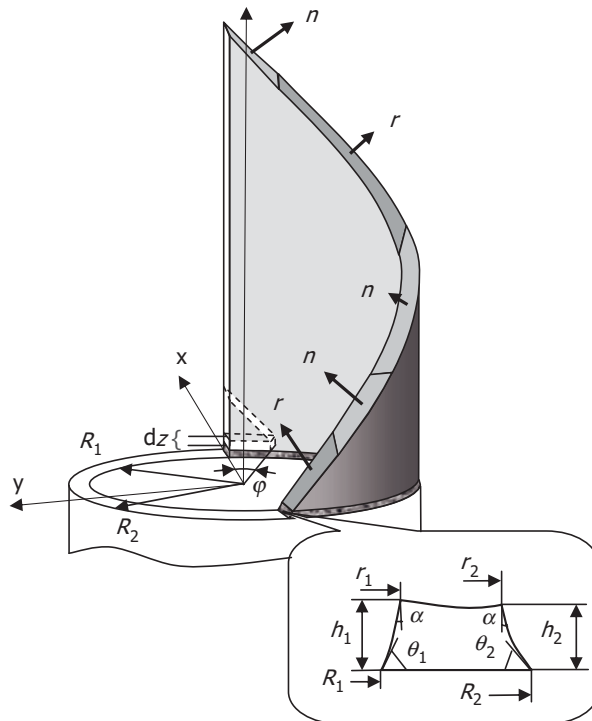


Figure 5.39 Tube growth drawing for calculation of the programmed mass with one seeding point (Reprinted with permission from [Abrosimov 2003], copyright (2003) Elsevier Ltd).

growing crystal is defined by the function of the angle $\beta(z)$ of the slope of the crystal unwrapping curve $\check{l}(z)$ to the crystal pulling axis z .

The mass M_d that is weighed with the weight sensor is the sum of the mass M_s of the solidified fraction of the melt and the mass M_1 of the meniscus (with consideration of the surface tension force) [Bardsley 1977]:

$$M_d = M_s + M_1. \quad (5.9)$$

The crystal mass change dM_s during a small time interval dt is:

$$dM_s = \rho_s r^\circ \delta_T \varphi(z) v_c(z) dt, \quad (5.10)$$

where ρ_s is crystal density, $r^\circ = 0.5 \cdot (r_1 + r_2)$ is the mean tube radius, r_1 and r_2 are inner and outer crystal radii, respectively, $\varphi(z)$ is the angular coordinate of the boundary segment of crystal enlargement in the cylindrical system of coordinates (r, φ, z) , δ_T is the tube thickness and $v_c(z)$ is the crystallization rate (which is not generally constant). Using Equation (5.10) one can obtain the rate \dot{M}_s of crystal mass change:

$$\dot{M}_s = \rho_s r^\circ \delta_T \varphi(z) v_c(z). \quad (5.11)$$

The mass M_s of growing crystal may be obtained by integrating Equation (5.11):

$$M_s = \rho_s r^\circ \delta_T \int_{t_0}^t \varphi(z(\tau)) v_c(z(\tau)) d\tau, \quad (5.12)$$

where $z(t) = \int_{t_0}^t v_c d\tau$.

The length of the crystal unwrapping curve $\check{l}(z)$ is defined as $\check{l}(z) = r\varphi(z)$. Then, $\tan\beta(z) = d\check{l}(z)/dz$, $\beta(z) = \arctan\varphi'(z)$ (where $\varphi'(z)$ is the derivative of $\varphi(z)$), and the angular coordinate φ may be determined as follows:

$$\varphi = \frac{1}{r} \int_{t_0}^t \tan\beta(z(\tau)) v_c(z(\tau)) d\tau. \quad (5.13)$$

Expressions (5.12) and (5.13) define the crystal mass M_s at each moment of time for the preset shape of crystal.

The meniscus mass, taking into consideration the surface tension force on the edges of the die and the lateral crystal surfaces (but without consideration of surface tension in boundary segments of the cross-section) is determined from the approximate expression:

$$M_1 = 2\rho_1 \varphi (r^\circ \delta_T h_m + a_1^2 r \cos\alpha - a_1^2 r \sin\Theta) - 2\rho_1 H_d \phi R \delta_D, \quad (5.14)$$

where ρ_l is the density of the melt, $h_m = (h_1 + h_2)/2$ is the mean meniscus height, h_1 and h_2 are the heights of meniscus on the inner and outer surfaces of the crystal, respectively, α is the growth angle, $R = (R_1 + R_2)/2$ is the mean radius of the die, R_1 and R_2 are the radii of inner and outer edges of the die, respectively, and $\Theta = (\theta_1 + \theta_2)/2$ is the mean angle between the meniscus and the working surface of the die, with θ_1 and θ_2 the contact angles between meniscus and the working surface of the shaper at inner and outer shaper edges, respectively, and δ_0 the thickness of the working edge of the die.

The shape of the melt–crystal interface, the values of the meniscus heights h_1 , h_2 , and contact angles θ_1 , θ_2 can be determined from the coupled numerical solution of the capillary and Stefan problems. These problems are not considered for arbitrary profiles in the controlling software. Instead of the exact values of the above parameters, approximate estimations are used. The expressions (5.12)–(5.14) define the programmed mass change for a preset crystal shape.

For sapphire tubes of large diameter grown along the c -axis, the most remarkable occurrence at this stage was the appearance of inclined facets at the end surface [Kurlov 1998-6]. This surface was defined by the sequential appearance of positive rhombohedral planes r ($\{10\bar{1}1\}$, $\{0\bar{1}11\}$, $\{\bar{1}101\}$) and the dipyramidal planes n ($\{4\bar{2}\bar{2}3\}$, $\{2\bar{4}23\}$, $\{2\bar{2}43\}$, $\{4\bar{2}23\}$, $\{2\bar{4}\bar{2}3\}$, $\{22\bar{4}3\}$) (Figure 5.39). During the enlargement of the tube, up to the die size, the transition from one plane to another may be of three types: $n \rightarrow r$, $r \rightarrow n$ or $n \rightarrow n$. The angle between the perpendicular to r -planes and the c -axis is 57.6° and the angle between the perpendicular to n -planes and the c -axis is 61.2° [Klassen-Neklyudova 1974].

To optimize the enlargement of the sapphire tube, the angle of the unwrapping curve should be changed according to r - and n -planes (Figure 5.40).

Let $\{\varphi_i\}$ be a sequence of azimuthal angles between centres of rhombohedral and dipyramidal planes having the declination angles $\{\beta_i\}$ to the vertical. Obviously, if $\{\beta_i\}$ is kept constant, then the current crystal length l is defined by the sequence $\{\varphi_i\}$. In particular, if a discrete transition from one plane to another is assumed, neglecting smooth plane transition, then the current length l_c is defined by:

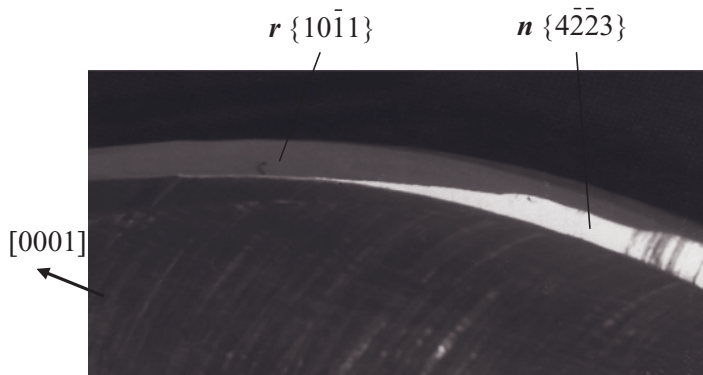


Figure 5.40 Faceting of 85-mm diameter sapphire tubular crystal: the r - and n -planes at the end surface (Reprinted with permission from [Abrosimov 2003], copyright (2003) Elsevier Ltd).

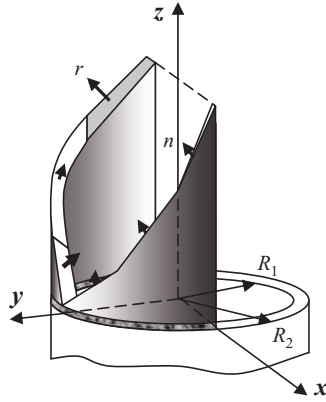


Figure 5.41 Tube growth drawing for calculation of the programmed mass with two seeding points (Reprinted with permission from [Abrosimov 2003], copyright (2003) Elsevier Ltd).

$$l_c = r^\circ \sum_{i=1}^k \text{ctg} \beta_i (\varphi_{i+1} - \varphi_i) + r^\circ \text{ctg} \beta_{k+1} (\varphi - \varphi_{k+1}), \quad \varphi > \varphi_{k+1}, \quad (5.15)$$

where k is the number of planes already grown and $k + 1$ is the number of the growing plane.

The current length is known, since it is the integral of the pulling velocity. Therefore, Equation (5.15) can be used to find the current angular coordinate of the profile φ depending on the sequence $\{\beta_i\}$ to calculate the programmed mass.

The length of enlargement depends on the tube radius $r^\circ = (r_1 + r_2)/2$ and the averaged declination angle β , given by the equation $l = \pi r^\circ / \tan \beta$. Obviously, the value of the crystal expansion angle that needs to be maintained in the course of the enlargement stage is in the range of 28.8° ($90 - 61.2^\circ$) to 32.4° ($90 - 57.6^\circ$). In this case, the optimum length is in the range $l = (4.96 - 5.72)r^\circ$. In practice, the enlargement from two opposite die points (with two-point seeding) is of interest (Figure 5.41).

For a pair of growing profiles, two current azimuthal angles φ_1 and φ_2 are calculated to depend on different sequences $\{\varphi_{ij}\}$ and $\{\beta_{ij}\}$ ($j = 1, 2$) of azimuthal and vertical angles of rhombohedral and dipyrimal planes. For different sequences $\{\beta_{i,1}\}$ and $\{\beta_{i,2}\}$, defined by seed orientations, the junction point is shifted relatively to the horizontal symmetry axis of the seeding points, which is perpendicular to the line connecting them. The shift of the seeding point f relative to the symmetry axis is written as:

$$f = r^\circ \sin |(\varphi_1 - \varphi_2)/2|, \quad (5.16)$$

where φ_1 and φ_2 are taken at the junction of the two profiles.

5.3.6.4 Calculation of Programmed Mass Change for Plate Enlargement

The case of the constant distance between the working surface of the die and the melt level is considered. The grown profile for the plate is defined by the angle $\beta(z)$ of the

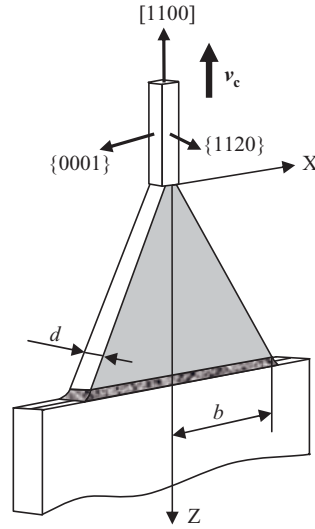


Figure 5.42 Schematic illustration of plate growth by the EFG technique (Reprinted with permission from [Abrosimov 2003], copyright (2003) Elsevier Ltd).

plate lateral profile to the crystal pulling axis [Kurlov 1999-4] (Figure 5.42). The mass M_d measured by the weight sensor is composed of crystallized melt and meniscus masses M_s and M_1 . The crystal mass rate \dot{M}_s is given by:

$$\dot{M}_s = b_s(z) d_s \rho_s v_c(z), \quad (5.17)$$

where b_s and d_s are the plate width and thickness, respectively, ρ_s is the crystal density, and v_c is the crystallization rate. The meniscus mass M_1 is:

$$M_1 \approx b_s d_s h \rho_1, \quad (5.18)$$

where ρ_1 is the melt density and h is the meniscus height. The rate of mass increase of the growing meniscus is approximately written as:

$$\dot{M}_1 = 2d_s h \rho_1 v_c(z) \tan \beta(z). \quad (5.19)$$

The crystallization front shape and meniscus height can be found by simultaneous solution of the capillary problem and the Stefan thermal problem. In the control system this problem is not solved and estimations are used instead of exact values.

5.3.6.5 In Situ Correction of Programmed Mass Change

Since the meniscus parameters cannot be calculated exactly during the growth process, especially for complicated crystal cross-sections and multicrystal processes, Equations (5.12)–(5.14), (5.17) and (5.18) cannot exactly describe the programmed mass change. To compensate for the error of this calculation, one parameter of the meniscus is corrected

from the measured weight signal, other ‘doubtful’ parameters of meniscus and crystal being constant. Therefore one parameter involved in Equations (5.12)–(5.14), (5.17) and (5.18) is adjusted so as to compensate for the estimation errors of the other parameters. For this selected parameter an equation must be solved, the left-hand side of which has an expression similar to Equation (5.9) and the right-hand side the measured mass data.

In the case of sapphire tube growth the tube thickness is selected as the tuning parameter, and it is determined from the equation:

$$\dot{M}_s(\delta_T^r(t)) + \dot{M}_l(\delta_T^r(t)) = \dot{M}_r(t), \quad (5.20)$$

where $\dot{M}_r(t)$ is the measured real mass rate data depending on time, and $\delta_T^r(t)$ is the ‘real’ tube thickness calculated from Equation (5.20). For the case of constant melt level and using Equation (5.20) we can find the tube thickness:

$$\delta_T^r(t) = \frac{\frac{1}{2} \dot{M}_r(t) - \rho_l a_l^2 \left(\cos \alpha - \frac{R}{r^o} \sin \Theta \right) v_c \tan \beta}{\rho_s r^o \varphi v_c + \rho_l h v_c \tan \beta}. \quad (5.21)$$

In the case of enlargement of a plate, the plate thickness d is used as a free variable. During the process, the equation

$$\dot{M}_s(d^r(t)) + \dot{M}_l(d^r(t)) = \dot{M}_d^r(t), \quad (5.22)$$

where $\dot{M}_d^r(t)$ is the measured real mass rate data depending on time, is used to find the ‘real’ profile thickness $d^r(t)$ of the plate:

$$d^r(t) = \frac{\dot{M}_d^r(t)}{\rho_s b_s v_c + 2 \rho_l h v_c \tan \beta}. \quad (5.23)$$

Note that the tube and plate thickness as calculated from Equations (5.21) and (5.23) can differ considerably from the real thickness of the tube or plate, depending on the accuracy of values of other ‘weakly known’ parameters of the crystal and meniscus that are involved in Equations (5.21) and (5.23).

At the first moments of crystal expansion the control parameters of the software provide ‘mild’ automated control based mainly on manual regulation. At this stage it is necessary to observe the state of the melting zone, i.e. to analyse the excessive overheating or overcooling of the crystal, and to observe the behaviour of the deviation $\delta \dot{M}$ and calculated thickness $\delta_T^r(t)$ for tube growth and $d^r(t)$ for plate growth. The user then makes corrections to the programmed mass rate \dot{M} by adjusting the programmed thickness d_s or δ_T and after that crystal regulation is totally performed by the computer.

Crucible translation is also necessary for shape and quality control. The rate of crucible translation is calculated according to the change of melt level during the crystal growth process. It is important to maintain a constant distance between the working edges of the shaper and the level of the melt in the crucible, to keep a sufficiently constant thermal gradient in the shaper and constant hydrostatic pressure in the meniscus. Additional changes to the crucible translation rate can be used for control of the crystal shape and quality.

5.3.6.6 *Steady State Growth*

At the steady state growth stage the programmed rate \dot{M} of mass increase is constant and controlled by the cross-section of the crystal. As shown above, the grower can correct \dot{M} to improve growth conditions by changing the programmed tube thickness (δ_r) or plate thickness (d_s) (or another geometrical parameter in the case of an arbitrary shape). The behaviour of the deviation $\delta\dot{M}$ can be observed and analysed on the computer display without visual inspection of the state of the molten zone.

In the case of plate growth the required plate thickness is estimated by Equation (5.23) simplified to:

$$d^r(t) = \frac{\dot{M}_r(t)}{\rho_s b_s v_c} \quad (5.24)$$

for the steady state growth stage.

Optimum seed orientation is extremely important to produce a large-scale, high-quality sapphire plate. Growth experiments with plates of various orientations have shown that plate growth perpendicular to the c -axis is preferred to prevent small-angle grain boundary formation. The plates are pulled in the direction of the hexagonal prism m $[1\bar{1}00]$, the plate plane coincides with the plane a $\{11\bar{2}0\}$, and the basis plane c $\{0001\}$ is the lateral face of the plate (Figure 5.42). Because of the singular minimum of the specific free surface energy, the outer crystal surface has an energetically favourable orientation as the angle between meniscus and face (or the meniscus height) is varied, i.e. a mirror face is formed at the outer surface of the growing crystal [Voronkov 1983].

If the lateral faces of the plate comprise the singular face $\{0001\}$, this significantly increases the temperature range during crystal growth because of the high stability of the face adherent to the die edges. A steady state growth shift toward higher temperatures elevates the meniscus (increases the angle between meniscus and face) with no substantial change in the plate cross-section. A wide temperature range is extremely important when growing several plates in multirun growth processes and wide plates with a nonuniform thermal field in the die or dies.

Along with power control, crucible movement is also effectively controlled. First, the rate of crucible translation is calculated according to the change of melt level during the crystal growth process. It is important to maintain a constant distance between the working edges of the die and the level of the melt in the crucible. This distance should maintain a sufficiently constant thermal gradient in the die and constant hydrostatic pressure in the meniscus to improve the crystal quality. Secondly, a fixed displacement of the crucible in combination with weight control is used for the control of the crystal shape and quality.

Sapphire tubes with diameter up to 85 mm (Figure 5.43a) [Kurlov 1999-2] and other various shapes [Kurlov 1999-3] have been grown using the automated control system. A multicrystal pulling process with *in situ* quality control provided an increase in growth productivity. Sapphire crystals in the shape of rods and tubes with up to 50 crystals per pulling process were grown by a multicrystal system [Kurlov 1997-3] (Figure 5.43b).

For crystal growth by the EFG technique using an automated control system based on the application of the crystal weight sensor, estimating the real current melt level in the

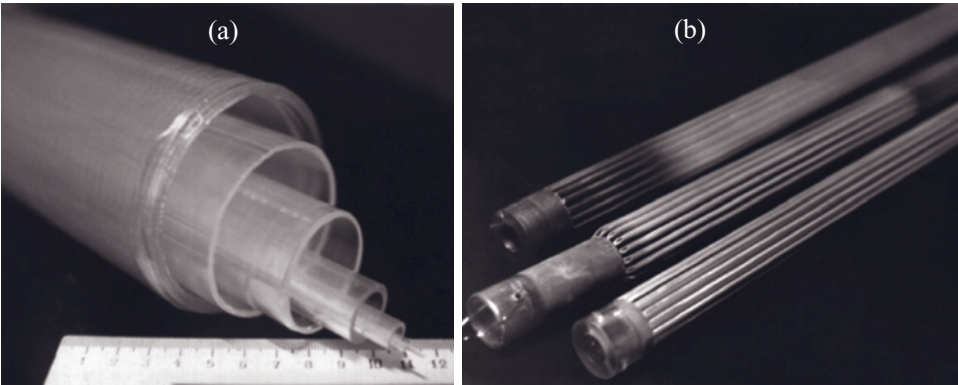


Figure 5.43 Sapphire crystals grown by the Stepanov/EFG technique with automated control: (a) tubes with diameter up to 85 mm; (b) rods 3.0 mm in diameter and tubes 3.5 mm in outer diameter grown by the multirun pulling process (Reprinted with permission from [Abrsimov 2003], copyright (2003) Elsevier Ltd).

crucible during the pulling process is a problem. Information about the changing melt level is necessary to define the crucible movement rate in order to maintain the melt level at one preset value or to change the melt level due to some growth strategy. The problem is to determine the melt level on the basis of the meniscus shape, crystal shape and measured weight.

The EFG technique is characterized by the presence of the die, which influences the weight signal. As well as the weight of the growing crystals and the weight of the menisci, the sensor also measures the influence of the external hydrostatic pressure resulting from the difference between the heights of the melt level in the crucible and the working edges of the die. The weight sensor also measures the capillary force of the meniscus.

The mass conservation law gives an approximate expression for the rate of the melt level change based on the measured weight signal rate \dot{M}_d :

$$\dot{H}_m = \frac{(A_d - A_{d,c})v_T - \frac{\dot{M}_d}{\rho_l} + A_c \dot{h}}{\pi r_T^2 - (A_d - A_{d,c})}. \quad (5.25)$$

Here A_d is the area of the lower part of the die dipped in the melt in the crucible, $A_{d,c}$ is the area of the working surface of the die contacting with the meniscus, A_c is the surface of the crystal cross-section, r_T is the inner radius of the cylindrical crucible, ρ_l is the melt density, v_T is the rate of crucible translation and \dot{h} is the derivative of the meniscus height change, which can be neglected in steady state growth conditions.

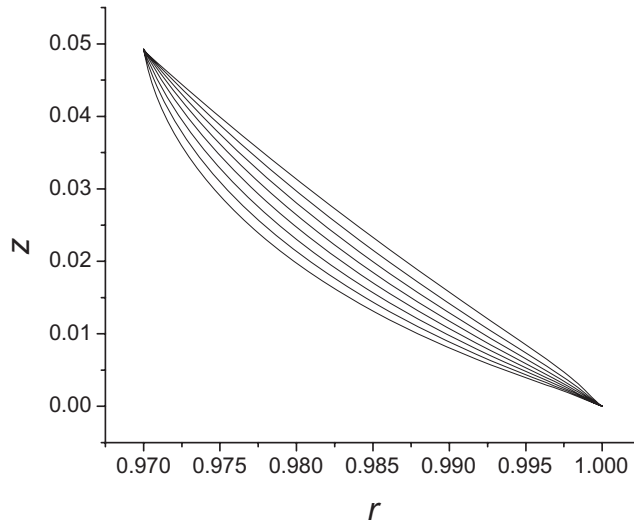


Figure 5.44 Meniscus profile curves calculated for the single meniscus height and for various values of the external hydrostatic pressure H_d .

As mentioned above, it is necessary to distinguish two types of crucible movements. First, a slow crucible translation relative to the pulling rate. In this case, the crucible translation acts as an additional factor to the slow heating or cooling of the crystallization zone and slow external pressure change. Secondly, a fast (small, almost stepwise, short-term) crucible movement which is, in fact, an additional method of crystal profile control, acting almost without inertia, on the heating or cooling of the crystallization zone and giving a stepwise change of external pressure in the meniscus, with subsequent influence on the profile of the growing crystal.

In order to understand this effect, first the capillary Young–Laplace equation was solved for the preset meniscus height which is approximately equal to 0.05 in capillary constants, i.e. for sapphire it is 0.3 mm. The external pressure H_d changes during the calculations. For each value of the external pressure the meniscus angle near the die changes so that the profile curve reaches the preset meniscus height at the preset crystal radius. The calculated set of profile curves is shown in Figure 5.44.

The minimal external pressure ($H_d = -8$ in capillary constants) corresponds to the lower curve in Figure 5.44 and the maximal external pressure ($H_d = -1$ in capillary constants) to the upper curve. Thus, fast short-term stepwise crucible translation, and, correspondingly, decrease of the absolute value of the external pressure, result in an increased convexity of the meniscus. As consequence, the meniscus angles near the crystal and the die will change. The value of the meniscus angle near the crystal increases with decrease of the absolute value of the external pressure (Figure 5.44). Thus, fast short-time stepwise crucible translation is a factor that widens the crystal (besides acting the thermal factor).

The dependence of the meniscus angle near the die on the external pressure has the opposite behaviour, but the same result: amplifying the convexity of the meniscus profile curve.

5.3.6.7 Automated Growth of Capillary Crystal Tubes

Automated crystal growth of capillary (small) crystal tubes has some specific difficulties relating to the small dimensions of the meniscus. The oscillations of the weight signal of the meniscus and crystal variations are very small. Secondly, the shapes of the inner and outer menisci of the capillary are different. Figure 5.45 shows typical shapes of the inner and outer menisci for capillary crystal growth.

As shown in Figure 5.45, the convexity of the inner and outer menisci of the capillary is different. This can be explained by the different signs of the azimuthal curvatures involved in the Young–Laplace equation. In addition, the weight of the capillary menisci is sufficiently small to have an influence on the menisci shape.

The convexity of the inner meniscus of the crystal capillary directed toward the centre of the crystal is a negative factor for growth stability, because it is difficult to maintain a meniscus with such a convex shape. Such a meniscus can be mechanically destroyed at any moment of the growth run.

During the crystal growth process of the capillary crystals the automated system also analyses the behaviour of the mass rate deviation $\delta\dot{M}$. During the growth process the control is based on the maintenance of the amplitude of the $\delta\dot{M}$ oscillation in a certain, very narrow, range of values to maintain the melt–crystal interface close to the supercooling condition.

A proportional–integral–differential (PID) procedure was used in the closed loop of the automated system. The change of heating power resulting from PID processing of the deviation $\delta\dot{M}$ was limited to a certain value $|\delta P|_{\max}$. A geometrical parameter r of

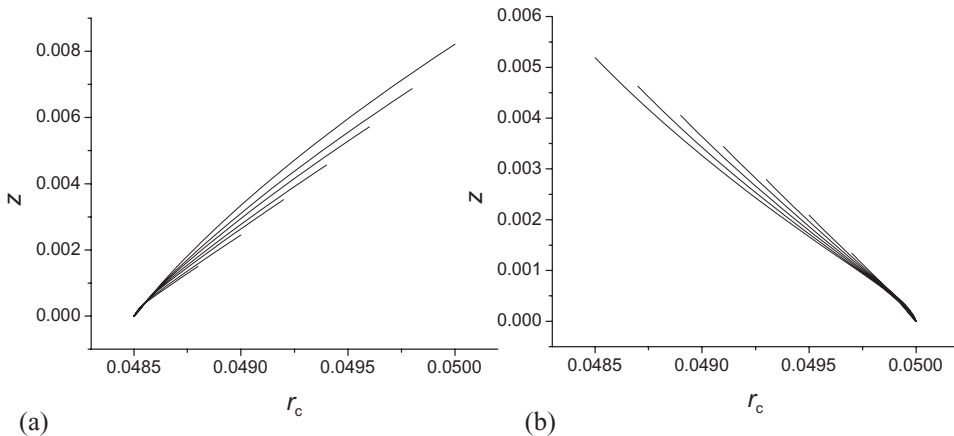


Figure 5.45 Meniscus profile curves of capillary tubes calculated for various values of the radius of the working edges of the die: (a) inner menisci, (b) outer menisci.

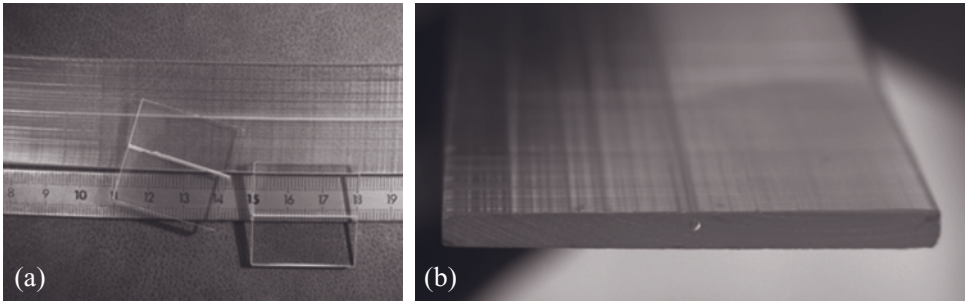


Figure 5.46 Sapphire ribbons with a channel 0.5 mm in diameter: (a) general view; (b) cross-section.

the crystal (e.g. middle radius of the capillary tube) is involved in the calculation of the programmed mass and thus in the evaluation of the deviation $\delta\dot{M}$ as well as in the heating power limitation $|\delta PI|_{\max}$. The geometrical parameter r is evaluated from the weight signal in the controlling software during growth run [Kurlov 1997-3]. So, the user has the possibility of taking into account the evaluation of the parameter r and changing its programmed value r_p without interrupting the process control. The geometrical parameter r is the main parameter for changing the $\delta\dot{M}$ amplitude to the necessary range. Varying r modifies the middle value of the $\delta\dot{M}$ oscillations and thus changes the slope of the heating power curve. This results in overheating or overcooling of the meniscus and melt–crystal interface, and the $\delta\dot{M}$ amplitude decreases or increases, respectively.

The variation of r is done automatically. For this, the amplitude of the oscillations $|\delta\dot{M}|_{\max}$ is calculated at each period of its wave. Then this value is compared with necessary optimal value $|\delta\dot{M}|_0$ which should be found experimentally. The change δr of the programmed radius is proportional to the difference between these two amplitudes of oscillation:

$$\delta r = -k_r (|\delta\dot{M}|_{\max} - |\delta\dot{M}|_0), \quad (5.26)$$

where k_r is proportional coefficient which should be determined experimentally.

The value of the heating power limitation $|\delta PI|_{\max}$ also influences the heating power curve. Small $|\delta PI|_{\max}$ results in an increase of auto-oscillations of the heating power (in our case a permanent increase during the growth run) and, consequently, in larger oscillations of $\delta\dot{M}$, i.e. an overcooling regime. Large $|\delta PI|_{\max}$ leads to more freedom in the closed loop and more accurate increments of power change at each step of control, and to smaller $\delta\dot{M}$ amplitude. Therefore, variation of $|\delta PI|_{\max}$ during the growth process was also used for changing the $\delta\dot{M}$ amplitude under constant and optimal parameters of the PID controller.

Various shaped crystals with capillary channels in their volume have been grown using an automated control system. Sapphire ribbons comprising a channel 0.5 mm in diameter are shown in Figure 5.46, and Figure 5.47 show sapphire rods with channels.

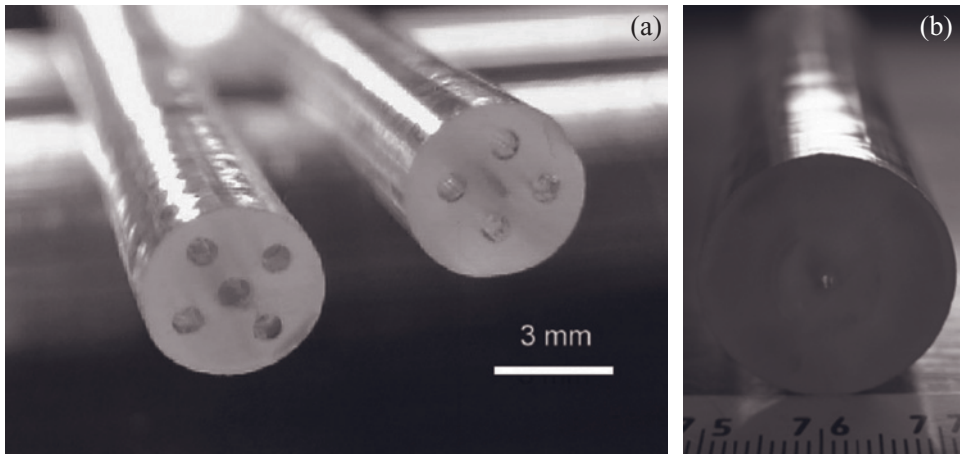


Figure 5.47 Sapphire rods with capillary channels: (a) 4.5-mm diameter rods with five and four 0.6–0.7-mm diameter channels; (b) 22-mm diameter rod with one 0.9-mm channel.

5.4 Shaped Crystals Grown by the Micro-Pulling Down Technique (μ -PD)

The pulling down technology as a growth process (also based on the Stepanov concept) has been available since 1976. Ricard *et al.* [Ricard 1980, Duffar 1991] originated this technology and used the process to grow sapphire plates, Si sheets [Duffar 1982] and NaCl fibres. Rudolph and Fukuda provide an overview of the μ -PD story [Rudolph 1999]. But it is important to identify the early 1990s as an important time of increasing research relating to μ -PD technology. During this period, many projects were developed in Fukuda's laboratory at Tohoku University (Japan) using μ -PD technology for fibre pulling. Resistive μ -PD has been used for the growth of LiNbO_3 [Yoon 1994-1] and $\text{K}_3\text{Li}_2\text{Nb}_5\text{O}_{15}$ [Yoon 1994-2, Yoon 1994-3] and a radiofrequency (RF) inductive μ -PD machine was built to grow high-melting materials (melting temperature $>1500^\circ\text{C}$). Different material families have been grown in the framework of national and international collaborative projects between research laboratories and private companies. As a result of this research effort, high-quality fibres have been pulled under stationary stable growth conditions using the μ -PD method. Chani [Chani 2004], Epelbaum [Epelbaum 2004], Yoshikawa [Yoshikawa 2004], Lebbou *et al.* [Lebbou 2004] and Lee *et al.* [Lee 2001] have developed a large range of single-crystalline and polycrystalline fibres from congruent and noncongruent melts. These researchers had worked together under the umbrella of a fundamental and applied research programme in Fukuda's laboratory in Japan. Table 5.2 summarizes some crystal fibres grown by the μ -PD technique using resistive and radiofrequency μ -PD equipment. Since 2000, the μ -PD technique has been introduced to other countries throughout the world: Brazil, France, Germany, Italy, Korea,

Table 5.2 A selection of crystals grown by the μ -PD technique. Most crystals are fibres

Crystals	Machine	Crucible	Melt behaviour	Pulling rate (mm/min)	Shape	Quality problem	Ref
Si	RF	Mo C	Congruent	0.02–0.5	Fibre Plate	Problem Impurities	[Shimamura 1996]
LiNbO ₃	RF RES	Pt	Congruent Limit eutectic Li ₂ O losses	0.1–0.9	Fibre	Transparent Colouration	[Yoon 1994–1]
KNbO ₃	RES	Pt	Incongruent K ₂ O losses	0.09–0.4	Fibre	Cracks Colouration	[Chani 1999–2]
K ₃ Li ₂ Nb ₅ O ₁₂	RES	Pt	Noncongruent K ₂ O losses	0.1–2	Fibre Plate	Transparent Acceptable	[Yoon 1994–2] [Yoon 1994–2]
Ba ₂ NaNb ₅ O ₁₅	RES	Pt	Nearly congruent	0.1–0.5	Fibre	Transparent Acceptable	[Lebbou 2000]
Sr _{1-x} Ba _x Nb ₂ O ₆	RES	Pt	Congruent	0.1–0.5	Fibre	Transparent brown	[Hassouni 2003]
Bi ₂ Sr ₂ CaCu ₂ O _x	RES	Pt	Noncongruent	0.01–0.2	Fibre	Textured grains	[Lebbou 2000]
Bi ₄ Ge ₃ O ₁₂	RES RF	Pt	Congruent Bi ₂ O ₃ losses	0.2–0.8	Fibre	Transparent	[Chani 2006]
Sr ₃ Nb _{1-x} Ga _{3+(5/3)x} Si ₂ O ₁₄	RES	Pt	Congruent	0.1–0.5	Fibre	Transparent	[Jung 2001]
Al ₂ O ₃ /YAG eutectic	RF	Ir	Noncongruent	0.1–10	Fibre Plate	Opaque High strength stress	[Yoshikawa 1999] [Lee 2001]
YAG (Nd, Yb)	RF	Ir	Congruent	0.1–5	Fibre	Transparent Comparable to bulk Laser power (10W)	[Chani 1999–1] [Shimamura 1996] [Chani 1999–2] [Lebbou 2000] [Hassouni 2003] [Lebbou 2000] [Chani 2006] [Jung 2001] [Yoshikawa 1999] [Lee 2001] [Chani 2000–2]

Tb ₃ Ga ₅ O ₁₂	RF	Ir	Ga ₂ O ₃ evaporation	0.4–1	Fibre	Transparent	[Chani 2000]
(Tb,Lu) ₃ Al ₅ O ₁₂	RF	Ir	Congruent	1.2	Fibre	Transparent Quality depends on composition	[Chani 2000–1]
Ca ₈ La ₂ (PO ₄) ₆ O ₂ :Yb	RF	Ir	Congruent	0.1–0.8	Fibre	Transparent Acceptable	[Boulon 2001]
(Lu,Yb) ₃ Al ₅ O ₁₂	RF	Ir	Congruent	0.1–1	Fibre	Transparent Acceptable	[Yoshikawa 2002]
MgAl ₂ O ₄ :Ti, Mn	RF	Ir	Congruent	0.05–0.5	Fibre Square	Transparent	[Jouini 2006]
Lu ₂ SiO ₅ :Pr	RF	Ir	Congruent SiO ₂ losses		Rod	Transparent	[Novoselov 2006]
LYSO:Ce	RF	Ir	Congruent SiO ₂ losses		Rod	Transparent	[Hautefeuille 2006]
Al ₂ O ₃	RF	Ir	Congruent	0.5–2	Fibre Rod Square	Transparent	[Sato 2007]
YAIO ₃ (Ce)	RF	Ir	Congruent	0.02–0.1	Fibre	Transparent	[Alshourbagy 2007]
Gd _{1-x} Yb _x F ₃	RF	C	Congruent	0.05–0.5	Fibre	Transparent	[Simura 2006]
LiF	RES	Pt	Congruent	0.6–1.5	Fibre	Transparent	[Santo 2004]

RES, resistive; RF, radiofrequency.

Poland and the USA. There may also exist other laboratories we do not know of. The total number of μ -PD machines around the world is approximately 40. Several master's and PhD theses have been defended on crystals grown by the μ -PD technique for lasers and scintillating applications. The numbers of researchers involved in μ -PD techniques is increasing and there is much effort by the scientific and industrial communities to improve this technique and its industrialization. As a consequence, a small μ -PD community has been created, centred on Fukuda's laboratory, and various exchange programmes have been supported.

Today μ -PD technology is an attractive process, especially for research laboratories. The simplicity of this technique, the small quantity of starting raw materials required, and the crucible design and cost compared to crucibles used in the case of bulk crystals grown by the Czochralski and Bridgman techniques makes it possible to carry out fundamental research on phase diagram equilibrium, crystallization kinetics of complex multicomponent materials, crystal growth dynamic, modelling and simulation of specified crystal growth process. The μ -PD technique could be a great help in the development of large new crystal growth compositions for use in the Czochralski technique, for example. By testing with a low-cost technique, such as the μ -PD technique, which saves material and time, it is possible to estimate the possibility of growing high-quality bulk crystals that have been rejected for Czochralski or other comparable complex techniques. There are many materials that are unavailable in single-crystal form and that are difficult to grow using the classical standard growth methods because of their unknown equilibrium phase diagrams or incongruent melting behaviours.

Much effort, time and financial support are required to develop crystal growth technology resulting in good quality and high performance. Most optical, laser and scintillating crystals are RE^{3+} doped, such as Nd^{3+} in YAG [Belt 1972], Ce^{3+} in LSO [Melcher 1993] and $Al_2O_3:Ti^{3+}$ [Moulton 1986]. Segregation problems are observed, but because of the high pulling rate (1–20 mm/min), it is possible to overcome the segregation difficulties and to introduce higher dopant concentrations [Chani 1999-1]. It is also possible to grow incongruently melting materials from melts where the composition is slightly different from that of the crystal. In such a situation, the segregation problem can be studied precisely depending on the starting composition in the equilibrium diagram. It is clearly important to take advantage of the μ -PD technique for the growth of particular materials based on a phase diagram corresponding to complex compositions (eutectic, peritectic, volatile compounds, etc.).

The μ -PD technology is based on pulling fibres or shaped crystal bodies from a crucible with a hole of a predetermined shape. Numerous variations in crucible design have been developed by research laboratories and companies involved in shaped crystal growth. The basic concept of this technology is the melting of a mixture of the starting raw materials to a temperature slightly above its melting temperature in a specified crucible (Pt, Ir, Mo, W, etc.) depending on the raw material melting point and on the required crystal geometry. A pendant drop forms at the lower part of the capillary die at the bottom of the crucible by the action of gravity, an appropriately oriented seed crystal is connected to the drop, and then the crystal is pulled down from the opening of the crucible (Figure 5.48). The quantity of crystal-forming material fed per unit of time is equal to the quantity of solidified single crystal. The flow quantity Q of liquid passing through a capillary die is given by:

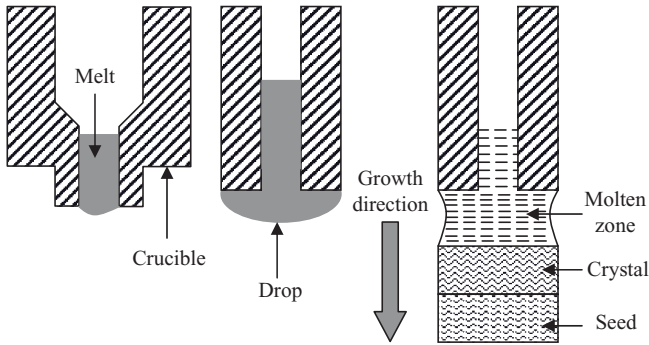


Figure 5.48 Schematic illustration of the μ -PD technique.

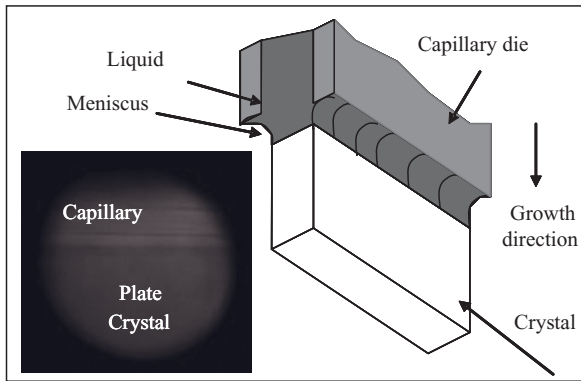


Figure 5.49 Plate pulling down by the μ -PD technique.

$$Q = (\pi R^4 / 8 \mu l) (p_1 - p_2), \quad (5.26)$$

where R is the radius of the capillary die, l is the length of the capillary die, μ is the dynamic viscosity of the liquid and $(p_1 - p_2)$ is the pressure difference between the ends of the capillary die.

Drops continue to fall until the liquid height in the crucible reaches a value h fixed by the capillary forces. The length H is determined by the following equation for a capillary die of circular section:

$$H = \frac{2 \gamma_{lv} \cos \theta}{R \rho_l g} \quad (5.27)$$

where γ_{lv} is the surface tension of the liquid at the given temperature, ρ_l is the liquid density at the given temperature, g is the acceleration due to gravity, R is the internal radius of the capillary die and θ is the wetting angle of the melt on the crucible.

For the growth of plate crystals using a capillary die with a rectangular section (Figure 5.49), the length H is given by:

$$H = \frac{2\gamma_{lv} \cos \theta}{e\rho_1 g} \quad (5.28)$$

where e is the capillary channel rectangular width.

Unfortunately, so far there is a limit to μ -PD plate crystal growth. Pulling plate-shaped crystals using a planar seed crystal geometry generates some defects such as cracks near the interface connection between the seed crystal and the die body. This is why plate crystals are preferably grown by the EFG technique. Nevertheless, some plate crystals have already been grown by μ -PD such as sapphire, Si, LiNbO₃, KLN and YAG.

The starting raw materials for growing the crystals (the charge) can be fed in any appropriate form such as fine, granular, sponge or spheroidal powders. Fine powders are better compacted, otherwise they will flow through the capillary hole. The crystal growth process can be carried out under an appropriate atmosphere depending on the chemical composition, the melt behaviour and the crucible material. Depending on the machine type, it is possible to grow crystals under an inert gas or oxygen-free gas such as nitrogen or argon, or in air. Quite often, the use of a controlled atmosphere necessitates a primary vacuum to eliminate the impurities inside the chamber. The pressure can varied over a wide range. In the case of fluoride fibre crystal growth, it is possible to use CF₄ as the gas. The temperature of the crucible is chosen so that the material is entirely molten. Thus, in the case of YAG ($T_{\text{melt}} \approx 1980^\circ\text{C}$), a temperature of 2010°C would be used, for sapphire ($T_{\text{melt}} \approx 2050^\circ\text{C}$), a temperature of 2080°C would be used. For high-melting materials such as LSO ($T_{\text{melt}} \approx 2150^\circ\text{C}$), this poses problems, especially with an Ir crucible. It is important to optimize the thermal insulation and control the thermal gradient, otherwise the crucible will be damaged.

The μ -PD crucible and the growth process with RF heating are shown in Figure 5.50. The heating system was specially set up for fibres and shaped crystal growth (plates, tubes, rods). The crucible (~ 30 – 70 mm in height \times 15 – 20 mm in diameter) is placed on an alumina pedestal inside a quartz chamber and is heated using a RF generator. The

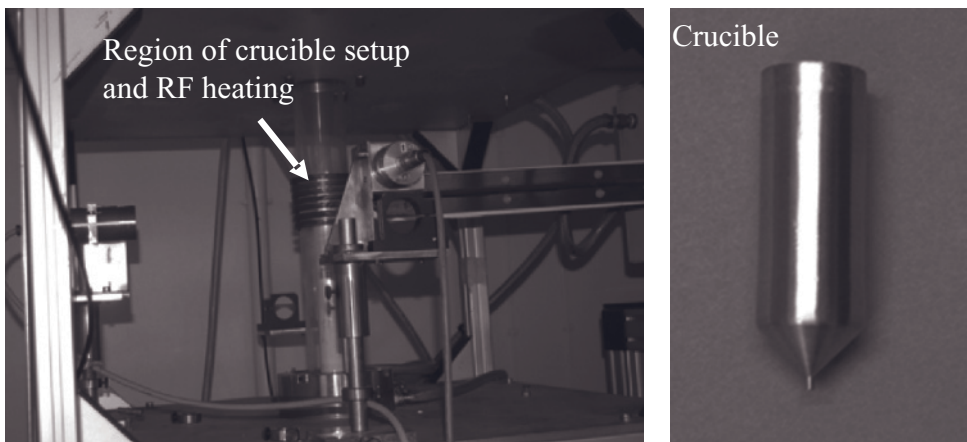


Figure 5.50 RF μ -PD machine and crucible used for heating and melting the feed.

meniscus region, the solid–liquid interface and the crystals are visually observed by a CCD camera and monitor. The calibrated hole in the capillary die is drilled at the crucible bottom to allow the melt to flow in the direction of the liquid–solid interface. An after-heater is used to adjust and control the temperature gradient under the crucible and therefore allow the regulation of the position of the solid–liquid interface in the vicinity of the crucible tip.

Shaped pulling down of crystals by the μ -PD technique, like other crystal growth techniques, must be set up in good conditions without any perturbation during the growth operation. It is very important to pull down fibres at stable rate and with a constant heater power, especially with a RF heating source. The important parameters for fibre crystal growth are:

- *Mass conservation.* If the density difference between the liquid and the crystal is neglected:

$$(r_{\text{cry}})^2 / (r_{\text{cap}})^2 = v_{\text{cap}} / v_{\text{cry}} \quad (5.29)$$

where r_{cry} and r_{cap} are the radius of the pulled crystal and capillary die, respectively, v_{cry} is the growth rate and v_{cap} is the mean flow rate in the capillary die.

- *Stationary state.* This behaviour corresponds to a given meniscus height that requires solving the Young–Laplace equation:

$$\left(\frac{1}{R_1} + \frac{1}{R_2} \right) = - \frac{p_O - p_v - \rho_l g z}{\gamma_{lv}} \quad (5.30)$$

with boundary condition:

$$\alpha = \alpha_0 \quad (5.31)$$

and

$$2r = D_{\text{cap}} \quad (5.32)$$

on the die, where α is the growth angle of the crystal (Figure 5.51a), a constant for a given crystal (see Chapter 1).

It is clear that the fundamental parameters involved in pulling down crystals by the μ -PD technique are the crucible diameter capillary die, the fibre diameter and the meniscus length (H) of the molten zone. These parameters fix the stationary stable state growth conditions and there is a theoretical relationship between these parameters (Equation 5.30).

5.4.1 Crucible–Melt Relation During Crystal Growth by the μ -PD Technique

In spite of the simplicity of the μ -PD technique, some problems exist during the growth of high-quality crystals with controlled sizes (diameter, section). Depending on the viscosity of the liquid, each melt has its own behaviour as a function of the crucible shape.

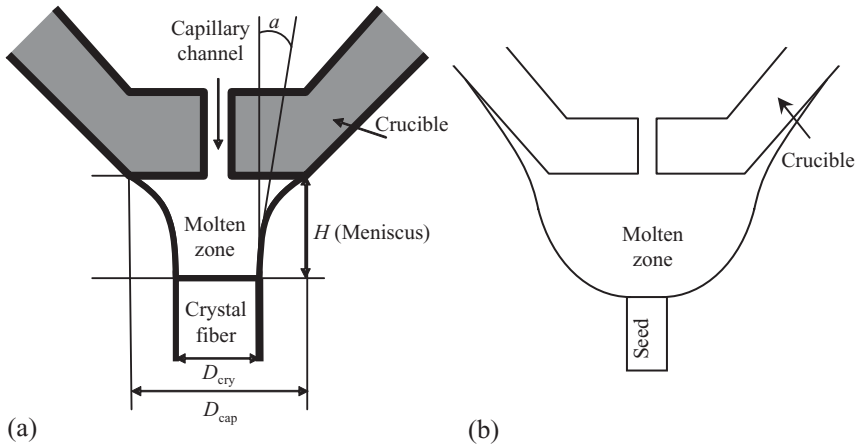


Figure 5.51 Meniscus representation during μ -PD fibre pulling: (a) nonwetting melt; (b) wetting melt.

Some melts, such as $Y_3Al_5O_{12}$ (YAG) garnet, are nonwetttable; in this case, it is possible to grow crystal fibres under stationary stable state conditions with a controlled diameter. The fibre diameter can be adjusted by the RF power control. Quite often, an increase (decrease) of the crucible temperature, resulting in an increase (decrease) in the heat supplied to the liquid, affects the variation of the fibre diameter, a behaviour comparable to that the Czochralski growth technique. But if the melt wets the crucible, it is difficult to control the fibre diameter. The $LiNbO_3$ fibre is a good example of such behaviour. The control of the position of the solid–liquid interface is quite different from that of a nonwetting melt (e.g. YAG) and it is difficult to control the seeding and the growth process (Figure 5.51b). Overheating of the melt will be accompanied by its overflow through the crucible lip and spreading on the wall surface. Under these conditions, Chani *et al.* [Chani 2000] proposed growing a fibre with minimal possible overheating of the crucible, which allows the minimization of the liquid width between the crystal and the crucible. But technically, it is very difficult to accurately control the power (melt temperature) for a slightly overheated melt. To overcome this type of problem, the tendency is to focus on the crucible shape design.

5.4.2 Examples of Crystals Grown by the μ -PD Technique

5.4.2.1 $Y_3Al_5O_{12}$ (YAG) Garnet Crystals

Garnet crystals are of great interest because of the wide variety of their compositions [Geller 1967]. The YAG crystals belong to the Y_2O_3 – Al_2O_3 pseudo-binary equilibrium diagram. Their cubic structure ($a = 12.01 \text{ \AA}$) is stable from room temperature to melting temperature and they melts congruently at 1980°C [Monchamps 1971]. Because of their good properties, YAG crystals are a popular material for a large range of applications, especially optics and lasers. The available commercialized YAG- RE^{3+} crystals are grown

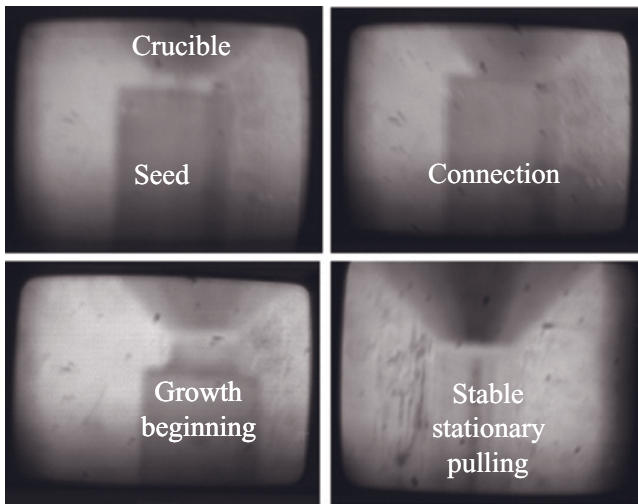


Figure 5.52 The different intermediary steps for μ -PD YAG fibre growth.

by the Czochralski technique, but they can be also grown by Bridgman and other conventional techniques. In YAG crystals, it is possible to substitute Y^{3+} sites (doping) by RE^{3+} (Lu^{3+} , Yb^{3+} , Tm^{3+} , Er^{3+} , ... , Nd^{3+} , Ce^{3+}). The dopant concentrations depend on the RE^{3+} ionic radius (Vegard's law). If the radius difference is more than 10%, some segregation problems might be observed in melt crystal growth, and the crystal quality is strongly affected by the fluctuations in composition parallel and perpendicular to the growth direction.

Demonstration of the growth of undoped and RE^{3+} -doped YAG crystals by μ -PD has stimulated the scientific community to develop homogeneous fibres for laser and scintillation applications. The first paper on YAG fibre crystals grown by μ -PD was published in 1999 [Chani 1999-1]. Undoped and doped YAG crystals can be grown by μ -PD under stationary stable conditions. Figure 5.52 shows the different steps of YAG fibre growth by μ -PD. The fibre crystals can be grown at a pulling rate in the range 0.1–10 mm/min and diameter 0.3–3.0 mm. The meniscus length is about 100 μ m. In the μ -PD technique, growing YAG crystals under stationary stable conditions corresponds to a flat crystallization interface. In this case, it is possible to grow undoped and RE^{3+} -doped YAG crystals whose length can easily reach 1 m, depending on the quantity of starting raw material in the crucible. The temperature distribution in the lower part of the crucible and the melt in the capillary die can be measured with an optical pyrometer. Several measurements always gave the same results, which allows for process control. If the crucible is stationary, heat is transferred through the melt mainly by conduction and there is little natural convection. The absence of a rotating seed minimizes the transfer of additional heat by forced convection. Whatever the dopant type (Yb^{3+} , Nd^{3+} , Ce^{3+}), no difference was observed in the behaviour of the melt. Figure 5.53 shows some examples of YAG garnet fibres and plates grown by the μ -PD technology. By using Ir wire or dense YAG ceramic seed, the grown YAG fibres were faceted with hexagonal cross-section along the $\langle 111 \rangle$ direction, which is typically the easy growth direction of garnet materials [Yu 1997]. The

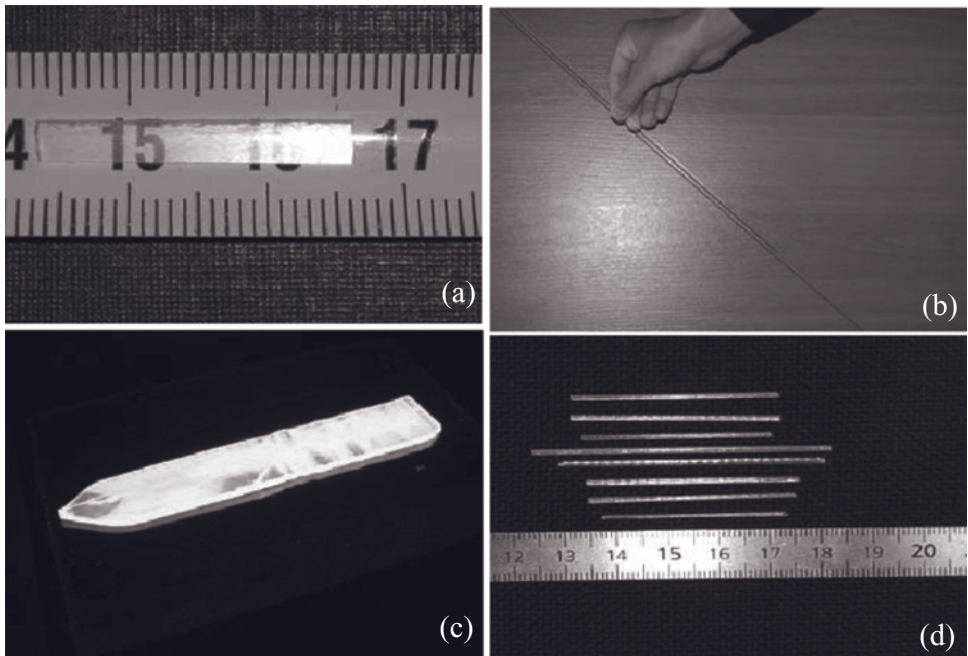


Figure 5.53 YAG crystals grown by the μ -PD technique: (a) undoped YAG plate (width 3 mm); (b) Nd^{3+} -doped YAG fibres (length up to 1 m); (c) Ce^{3+} :YAG plate (width 10 mm); (d) Ce^{3+} :YAG fibres.

grown fibre crystals are reproducible; the diameter and the cross-section are uniform. The crystals are transparent and their coloration depends on the added dopant (yellow for Ce^{3+} , for example). Growing large YAG crystals (diameter > 2 mm) by μ -PD is possible, but the crystal quality is decreased. This problem is related to the difficulties of controlling the shape of the molten zone because of the nonwetting properties of YAG melts. In addition, other macroscopic defects are observed such as scattering particles and constitutional supercooling in Nd:YAG [Zhang 1990]. There are also microscopic defects such as dislocations which can strongly affect the YAG optical quality. Up to now, the presence of dislocations has been the principal source leading to optical inhomogeneity of the crystals. Compared to others technologies, the segregation problem can be more easily controlled in the case of fibre crystals grown by the μ -PD technique. The average segregation coefficient of crystals grown by the Czochralski method is 0.15 [Nishimura 1975]. The segregation coefficient can be raised to 0.8 by growing fibres under high pulling rate (5 mm/min), but this value is still less than 1 [Chani 1999-1]. The Nd^{3+} dopant substitution in YAG crystals increases when the pulling rate is increased [Chani 1999-1]. But in order to attain the best performance, such as laser generation, it is necessary to find a compromise between pulling rate and crystal quality. Yb:YAG and Nd:YAG fibres of high quality have been grown by the μ -PD technique [Lebbou 2006, Lebbou 2007, Yoshikawa 2003]. Lasers have been made from Nd:YAG single crystal fibres grown by μ -PD; a laser power of 10 W at 1064 nm for an incident pump power of 60 W at 808 nm and

360 kW peak power for 12-ns pulses at 1 kHz in the Q -switched regime has been achieved [Didierjean 2006]. In the past, the μ -PD technique has been known as a powerful laboratory-scale method, but the encouraging results on Nd:YAG fibres shows the possibility of using this technique to manufacture fibres for laser devices.

5.4.2.2 $\text{Bi}_4\text{Ge}_3\text{O}_{12}$ (BGO) Fibre Crystals

Because of its remarkable properties such as fast luminescence and highly efficient scintillation in gamma-ray spectroscopy and high-energy physics, bismuth orthogermanate (BGO) is an important strategic material [Hubner 1969]. In the scintillating crystal market, BGO represents 70% of the crystals produced. BGO crystals, as potential scintillating material and high-quality bulk crystals, can be grown by the industrial Czochralki technique [Borovlev 2001, Vasiliev 2005].

BGO crystal was chosen as a candidate for μ -PD because it combines both congruent melting [Kaplun 1996] and a relatively high rate of evaporation of one of the constituents, namely Bi_2O_3 [Shim 2002]. The resistive μ -PD technique has been used to grow BGO fibres [Chani 2006]. Crystal growth of BGO fibres using a stoichiometric melt composition was performed in an air atmosphere using a Pt crucible directly heated by electrical current (Figure 5.54). Evaporation of the Bi_2O_3 was observed even by visual observation of the surfaces of the parts forming the μ -PD system. It has not proved possible to avoid the evaporation or decrease it greatly by modifying the set-up and temperature parameters (gradients) acting in the vicinity of the crucible and the solid–liquid interface. As a result, the problem of stability of the melt composition has not generally been solved. However, by controlling the temperature gradient, the melt composition, and power to the crucible, it was possible to grow high-quality fibres (Figure 5.55). BGO fibre crystal growth is very promising and has yielded original results. In spite of the volatility of Bi_2O_3 , homogeneous BGO fibres of constant diameter were grown. But it is necessary to improve the process and control the different growth parameters.

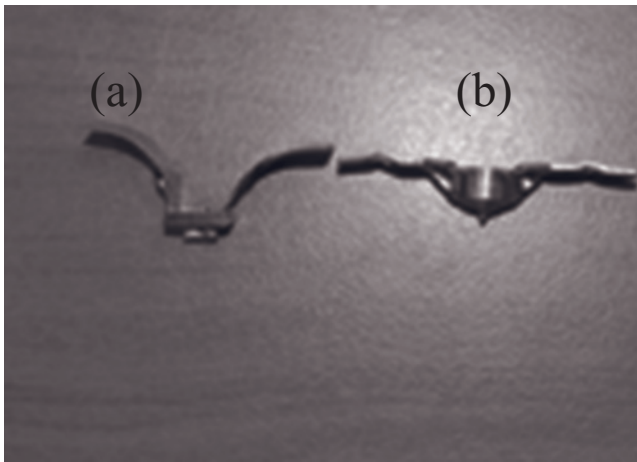


Figure 5.54 Crucible types that can be used for resistive heating: (a) crucible for BGO crystal growth; (b) crucible causing wetting problems in the case of BGO.

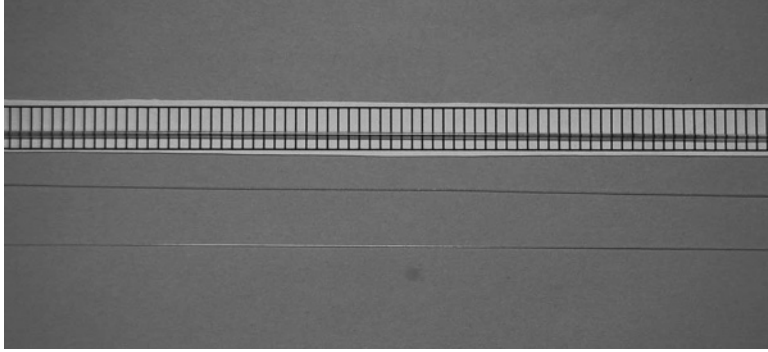


Figure 5.55 BGO fibres grown by the μ -PD technique. The starting melt contains an excess of Bi_2O_3 (5%).

5.4.2.3 LiNbO_3 (LN) Fibres

Lithium niobate (LiNbO_3 , LN) is an attractive material for a wide range of applications because of its properties [Nassau 1966]. It is used for different devices in optics and opto-electronics [De La Rue 1990, Voges 1986]. In addition, LN is a standard model for fundamental research that uses electro-optic, birefringent, acousto-optic, or piezoelectric properties, making it a preferred material for applications in surface acoustic waves and integrated optics. It has a complex structure and crystal growth technology which has led to a promising technology for device processing, although its thermal instability led to problems of waveguide fabrication which have now been overcome [Dierolf 1999]. Crystal growth by the Czochralski technique was reported almost simultaneously in 1965 by Ballman [Ballman 1965] and Fedulov *et al.* [Fedulov 1965]. Its total production now amounts to about 50–150 tonnes/year.

Yoon and Fukuda have studied the quality of LiNbO_3 crystalline fibres grown by the μ -PD technique [Yoon 1994-1, Yoon 1994-2]. Epelbaum has studied the relationships between faceting and LiNbO_3 crystalline qualities as a function of growth conditions by the μ -PD technique [Epelbaum 2004]. Even though this material has been well known for long time and much progress has been made on the technology of its crystal growth, there remain many problems that are observed during the crystal growth process and the composition problem remains unresolved, especially with regard to the need for stoichiometric single crystals.

Oriented LiNbO_3 single crystal fibres were grown using μ -PD. The fibres were oriented along the c -axis or a -axis as a function of initial seeding. The fibres were grown using pulling rates in the range of 0.1–0.7 mm/min in air. The fibres are transparent and crack-free and have a homogeneous diameter. The loss of Li_2O causes a displacement of the composition in the Li_2O – Nb_2O_5 binary equilibrium diagram and the crystal quality decreases; in particular, the interface crystallization geometry becomes unstable. On the other hand, the use of an excess of Li_2O with controlled temperature gradient around the melting zone region makes it possible to obtain stable growth conditions and a high level crystal quality even during an extended period of crystal growth operation. The fibres

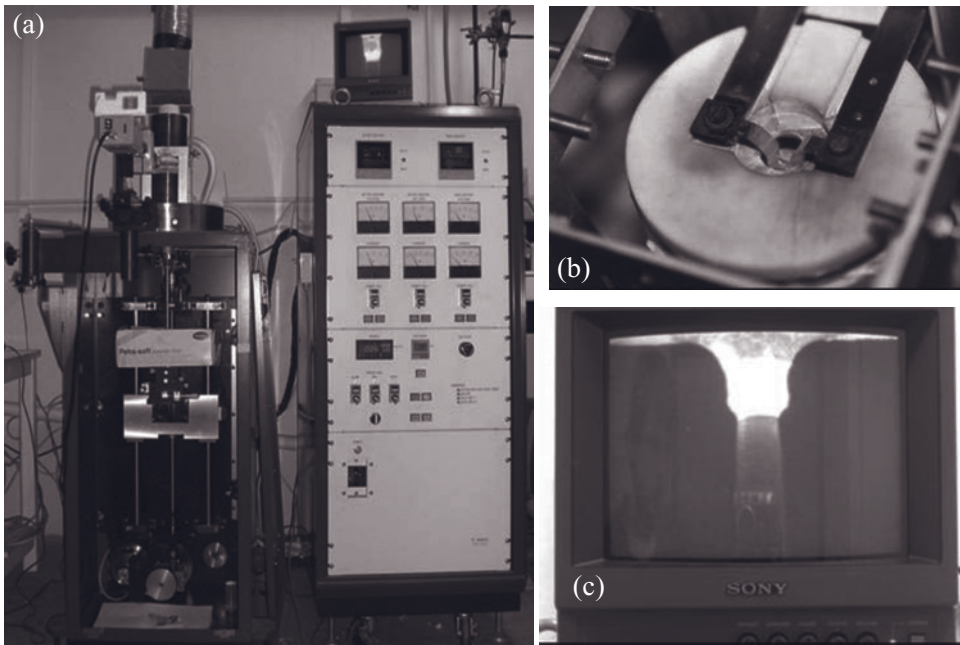


Figure 5.56 LiNbO_3 crystal growth: (a) resistive μ -PD machine; (b) resistive crucible heating step and melting charge; (c) connection and pulling.

obtained work as light guides and the losses are rather low. Figure 5.56a shows the resistive μ -PD used for the LiNbO_3 fibre crystal and Figure 5.56b shows the heating of the crucible up to the melting temperature of LiNbO_3 . Figure 5.56c shows the connection stage of the seed to the melt and the growth process. Table 5.3 gives the lattice parameters and the Curie temperature of the grown fibres as a function of the starting composition. It is clear that in order to grow homogeneous reproducible congruent LiNbO_3 (CLN) by μ -PD it is necessary to start from a rich Li_2O melt to compensate the Li_2O losses. The Curie temperature of stoichiometric LN is about 1200°C , in good agreement with the results obtained by Kitamura *et al.* [Kitamura 1992]. Figure 5.57 shows some LiNbO_3 fibres grown in the authors' laboratory.

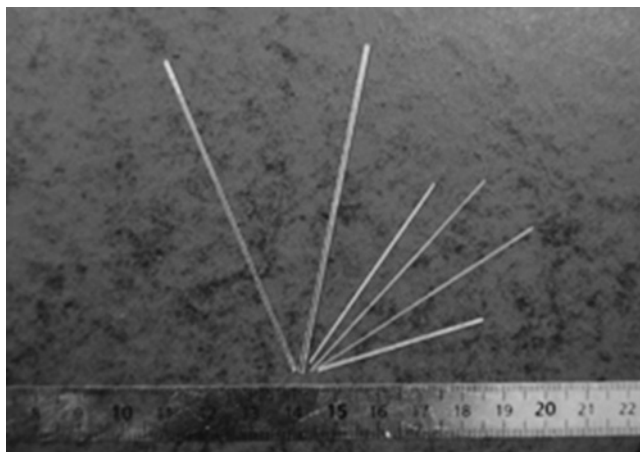
Even though different fibre crystal materials have been grown by the μ -PD technique, growing high-quality reproducible fibres by this method is a challenge to. It is a fast and inexpensive way to grow optical crystals for test evaluation. There are many opportunities for the use of this technology in crystal growth science, materials studies, determination of phase equilibrium diagrams, studies of melt behaviours such as convection, turbulence, viscosity and validation of simulation and modelling programs to be used for bulk crystals. The μ -PD technology can also be used in the evaluation of fibre crystals for laser applications as passive elements. Small-diameter fibres contain small defects in comparison to bulk crystals. In this case, single-crystal fibres can be used for applications requiring high optical energy. However, there remain many technological problems relating to

Table 5.3 *Lithium niobate fibres single crystal grown by the μ -PD technique, and their properties*

Starting composition (%Li ₂ O)	Pulling rate (mm/min)	Materials obtained	Lattice parameters (Å)	Curie temperature (°C)	Fibre qualities
47	0.6	LN ^a	a = 5.1460 c = 13.8638	1134	Cracks, defect
48	0.6	LN ^a	a = 5.1462 c = 13.8641	1132	Cracks, defect
49.5	0.5	CLN	a = 5.1492 c = 13.8649	1140	Transparent, good quality
50	0.5	CLN	a = 5.1495 c = 13.8651	1142	Transparent, good quality
51	0.4	CLN	a = 5.1499 c = 13.8652	1141	Transparent, good quality
52	0.5	SLN	a = 5.1479 c = 13.8566	1201	Transparent, good quality
54	0.5	SLN	a = 5.1476 c = 13.8568	1202	Transparent, good quality

CLN, congruent lithium niobate, composition analysed by ICP; SLN, stoichiometric lithium niobate, composition analysed by ICP.

^aLiNb₃O₈ secondary phase is observed by X-ray powder diffraction on cracked fibre.

**Figure 5.57** *High-quality LiNbO₃ fibres grown by the μ -PD technique.*

μ -PD technology. It is difficult to grow reproducible thin fibres (100 μ m) with high crystal quality and homogeneous diameter. The laser heated pedestal growth (LHPG) technique is a serious competitor to μ -PD growth of thin fibres and can be a good candidate for thin single-crystal fibres. Nonetheless, different research programmes on the μ -PD technique are in progress and the number of published papers shows the dynamic activity in this area.

5.5 Conclusions

The development of shaped crystal growth was a great technological advance, which has provided several types of applications. Although shaped crystals have been produced commercially and used for many years, the technology is still in a developmental stage. The optimization of standard crystal growth technologies and the development of new techniques are actively pursued in order to increase the dimensions of crystals, improve the quality, reduce the cost of material, and grow complex shapes. There is good reason to believe that shaped crystals will not only strengthen their position in traditional markets, but will also be used in a number of new applications.

References

- [Abrosimov 1983] Abrosimov N.V., Brantov S.K., Tatartchenko V.A., *Fiz. Khim. Obrab. Mat.* **2** (1983) 79 (in Russian).
- [Abrosimov 1985] Abrosimov N.V., Erofeeva S.A., Tatartchenko V.A., *Bull. Acad. Sci. USSR Phys. Ser.* **49** (1985) 2361–2363.
- [Abrosimov 2003] Abrosimov N.V., Kurlov V.N., Rossolenko S.N., *Progr Cryst. Growth Charact. Mater.* **46** (2003) 1–57.
- [Alshourbagy 2007] Alshourbagy M., Bigotta S., Herbert D., Del Guerra A., Toncelli A., Tonelli M., *J. Cryst. Growth* **303** (2007) 500.
- [Andreev 1986] Andreev E.P., Litvinov L.A., Pischik V.V., *Proc. All-Union Conf. Production of Shaped Crystals and Products by the Stepanov Method and their Applications in the National Economy*, LIYaF, Leningrad (1986), p. 87 (in Russian).
- [Antonov 1980] Antonov P.I., Galaktionov E.V., Krymov V.M., Yuferev V.S., *Bull. Acad. Sci. USSR Phys. Ser.* **44** (1980) 21–25.
- [Antonov 1981] Antonov P.I., Zatulovskii L.M., Kostigov A.S., Levinzon D.I., Nikanorov S.P., Peller V.V., Tatartchenko V.A., Yuferev V.S. (eds): In: *The Growth of Shaped Single Crystals and Industrial Articles by Stepanov Method*, ed. V.R. Regel, S.P. Nikanorov, Nauka, Leningrad (1981), p. 280 (in Russian).
- [Antonov 1985] Antonov P.I., Nosov Yu.G., Nikanorov S.P., *Bull. Acad. Sci. USSR Phys. Ser.* **49** (1985) 6–8.
- [Antonov 1988] Antonov P.I., Bakholdin S.I., Nikanorov S.P., *Progr. Cryst. Growth Charact. Mater.* **16** (1988) 19.
- [Antonov 1988] Antonov P.I., Bakholdin S.I., Vasil'ev M.G., Krymov V.M., Yuferev V.S. *Bull. Acad. Sci. Phys.* **52** (1988) 108–113.
- [Antonov 1990] Antonov P.I., *J. Cryst. Growth* **104** (1990) 39–46.
- [Antonov 2002-1] Antonov P.I., Kurlov V.N., *Progr. Cryst. Growth Charact. Mater.* **44** (2002) 63–122.
- [Antonov 2002-2] Antonov P.I., Kurlov V.N. *Crystallogr. Rep.* **47** (2002) S43–S52.
- [Ballman 1965] Ballman A.A., *J. Am. Ceram. Soc.* **48** (1965) 112.
- [Bardsley 1977] Bardsley W., Hurlle D.T.J., Joyce G.C., *J. Cryst. Growth* **40** (1977) 13.
- [Barrett 1971] Barrett D.L., Myers E.H., Hamilton S.H., Bennett A.I., *J. Electrochem. Soc.* **118** (1971) 952.
- [Bates 1992] Bates H.E., *Proc. 16th Conf. Composites and Advanced Ceramic Materials. Part 1. Ceram. Eng. Sci. Proc.* **13** (1992) 190–197.
- [Bates 2005] Bates H.E., Jones C.D., Locher J.W., *Window and Dome Technologies and Materials IX. SPIE Proc.* **5786** (2005) 165–174.
- [Behnken 2005] Behnken H., Seidl A., Franke D., *J. Cryst. Growth* **275** (2005) e375.

- [Belouet 1987] Belouet C., *J. Cryst. Growth* **82** (1987) 110.
- [Belt 1972] Belt R.F., Puttback R.C., Lepore D.A., *J. Cryst. Growth* **13–14** (1972) 268.
- [Bleil 1969] Bleil C.E., *J. Cryst. Growth* **5** (1969) 49.
- [Boatman 1967] Boatman J., Goundry P., *Electrochem. Technol.* **5** (1967) 98.
- [Borodin 1983] Borodin V.A., Steriopolu T.A., Tatartchenko V.A., Yalovets T.N., *Bull. Acad. Sci. USSR Phys. Ser.* **47** (1983) 151.
- [Borodin 1985-1] Borodin V.A., Steriopolu T.A., Tatartchenko V.A., *Cryst. Res. Technol.* **20** (1985) 833.
- [Borodin 1985-2] Borodin V.A., Steriopolu T.A., Tatartchenko V.A., Yalovets T.N., *Cryst. Res. Technol.* **20** (1985) 301.
- [Borodin 1988] Borodin V.A., Starostin M.Yu., Yalovets T.N., *Bull. Acad. Sci. Phys. Ser.* **52** (1988) 138–141.
- [Borodin 1990] Borodin V.A., Sidorov V.V., Rossolenko S.N., Steriopolu T.A., Tatartchenko V.A., *J. Cryst. Growth* **104** (1990) 69–76.
- [Borodin 1999] Borodin V.A., Sidorov V.V., Rossolenko S.N., Steriopolu T.A., Yalovets T.N., *J. Cryst. Growth* **198–199** (1999) 201.
- [Borovlev 2001] Borovlev Yu.A., Ivannikova N.V., Shlegel V.N., Vasiliev Ya.V., Gusev V A., *J. Cryst. Growth* **229** (2001) 305.
- [Boulon 2001] Boulon G., Collombet A., Brenier A., Cohen-Adad M., Yoshikawa A., Lebbou K., Lee J.H., Fukuda T., *Adv. Funct. Mater.* **11**(4) (2001) 243.
- [Bull. Acad. Sci.] *Bull. Acad. Sci. USSR Phys. Ser.*: **33**(12) (1969); **35**(3) (1971); **36**(3) (1972); **37**(11) (1975); **40**(7) (1976); **42**(9) (1980); **44**(2) (1980); **47**(2) (1983); **49**(12) (1985); **52**(10) (1988); **58**(9) (1994); **63**(9) (1999); **68**(6) (2004).
- [Burgers 2006] Burgers A., Gutjahr A., Laas L., Schönecker A., Seren S., Hahn G., *Proc. 4th World Conf. Photovoltaic Energy Conversion* (2006), p. 1183.
- [Burrus 1977] Burrus C.A., Coldren L.A., *Appl. Phys. Lett.* **31** (1977) 383.
- [Buzynin 1977] Buzynin Yu.N., Buzynin A.N., Bletskan N.I., Malinin A.Yu., Sokolov E.B., *Elektron. The. Ser. Mater.* **10** (1977) 3 (in Russian).
- [Chani 1999-1] Chani V.I., Yoshikawa A., Kuwano Y., Hasegawa K., Fukuda T., *J. Cryst. Growth* **204** (1999) 155.
- [Chani 1999-2] Chani V.I., Shimamura K., Fukuda T., *Cryst. Res. Technol.* **34** (1999) 519.
- [Chani 2000] Chani V.I., Yoshikawa A., Machida H., Fukuda T., *J. Cryst. Growth* **212** (2000) 469.
- [Chani 2004] Chani V.I., In: *Fiber Crystal Growth from the Melt*, ed. T. Fukuda P. Rudolph, S. Uda, Springer-Verlag, Berlin (2004).
- [Chani 2006] Chani V., Lebbou K., Hautefeuille B., Tillement O., Fourmigué J.M., *Cryst. Res. Technol.* **41** (2006) 972.
- [Ciszek 1972] Ciszek T.F., *Mater. Res. Bull.* **7** (1972) 731.
- [Ciszek 1975] Ciszek T.F., *Phys. Stat. Sol. A* **32** (1975) 231.
- [Ciszek 1976] Ciszek T.F., *J. Appl. Phys.* **47** (1976) 440.
- [Ciszek 1982] Ciszek T.F., Hurd J.L., Schitzelt M., *J. Electrochem. Soc.* **129** (1982) 2838.
- [Ciszek 1984] Ciszek T.F., *J. Cryst. Growth* **66** (1984) 655.
- [Cullen 1980] Cullen G.W., Surek T., Antonov P.I. (eds.) Shaped crystal growth. *J. Cryst. Growth* **50** (1980) 1–396.
- [De La Rue 1990] De La Rue R.M., In: *Materials for Waveguide Optoelectronics*, ed. J.H. Marsh, R.M. DeLaRue, Proc. Nato Advanced Study Institute on Waveguide Optoelectronics, 30 July–10 August 1990, Glasgow, Scotland.
- [Dermatis 1963] Dermatis S.N., Faust J.W., *IEEE Trans. Commun. Electron.* **82** (1963) 94.
- [Didierjean 2006] Didierjean J., Castaing M., Balembos F., Georges P., Perrodin D., Fourmigué J.M., Lebbou K., Brenier A., Tillement O., *Opt. Lett.* **31**(23) (2006) 3468.
- [Dierolf 1999] Dierolf V., Kutsenko A.B., Sandmann C., Tallian F., Von der Osten W., *Appl. Phys. B* **68** (1999) 767.
- [Dmitruk 1985] Dmitruk L.N., *Bull. Acad. Sci. USSR Phys. Ser.* **49** (1985) 130–131.
- [Dmitruk 1988] Dmitruk L.N., Perminova V.N., *Bull. Acad. Sci. USSR Phys. Ser.* **52** (1988) 125–127.

- [Dobrovinskaya 1979] Dobrovinskaya E.R., *Control of Structural Perfection of Single Crystals of a Corundum*, NIITEHIM, Moscow (1979) (in Russian).
- [Dobrovinskaya 1980] Dobrovinskaya E.R., Litvinov L.A., Pishchik V.V., *J. Cryst. Growth* **50** (1980) 341.
- [Dobrovinskaya 1988] Dobrovinskaya E.R., Pishchik V.V. *Single Crystals of a Corundum: Problems of Obtaining and Quality*, NIITEHIM, Moscow (1988) (in Russian).
- [Dobrovinskaya 2002] Dobrovinskaya E., Litvinov L., Pishchik V., *Sapphire & Other Corundum Crystals*, Kharkiv, Ukraine (2002)
- [Duffar 1982] Duffar T., PhD thesis, INP-Grenoble, France (1982) (in French).
- [Duffar 1991] Duffar T., Harter I., *Ann. Chim.* **16** (1991) 123–131.
- [Egorov 1976] Egorov L.P., Milvidskii M.G., Zatulovskii L.M. *et al.*, *Bull. Acad. Sci. USSR Phys. Ser.* **40** (1976) 1359.
- [Epelbaum 1998-1] Epelbaum B.M., Shimamura K., Inaba K., Satoshi U., Kochurikhin V.V., Machida H., Terada Y., Fukuda T., *J. Cryst. Growth* **186** (1998) 607–611.
- [Epelbaum 1998-2] Epelbaum B.M., Shimamura K., Kochurikhin V.V., Fukuda T., *Cryst. Res. Technol.* **33** (1998) 787–792.
- [Epelbaum 2004] Epelbaum B.M., In: *Fibre Crystal Growth from the Melt*, ed. T. Fukuda, P. Rudolph, S. Uda, = Springer Verlag, Berlin (2004), pp. 103–127.
- [Eriss 1980] Eriss L., Stormont R.W., Surek T., Taylor A.S., *J. Cryst. Growth* **50** (1980) 200.
- [Fedulov 1965] Fedulov S.A., Shapiro Z.I., Ladyzhenskii P.B., *Kristallografiya* **10** (1965) 268.
- [Finch 1975] Finch C.B., Clark G.W., Kopp O.C., *J. Cryst. Growth* **29** (1975) 269–272.
- [Fitzgibbon 1996] Fitzgibbon J.J., Pryshlak A.P., Dugan J.R., *SPIE Proc.* **2677** (1996) 35–42.
- [Fitzgibbon 1998] Fitzgibbon J.J., Collins J.M., *Surgical-Assist Systems, SPIE Proc.* **3262** (1998) 135–141.
- [Fukuda 1976] Fukuda T., Hirano H., *J. Cryst. Growth* **35** (1976) 127–132.
- [Fukuda 2003] Fukuda T., Rudolph P., Uda S. (eds.), *Fiber Crystal Growth from the Melt*, Springer-Verlag, Berlin (2003).
- [Garcia 2001] Garcia D., Ouelette M., Mackintosh B., Kalejs J., *J. Cryst. Growth* **225** (2001) 566.
- [Garone 1976] Garone L.C., Hari Rao C.V., Morrison A.D., Surek T., Ravi K.V., *Appl. Phys. Lett.* **29** (1976) 511–513.
- [Geguzin 1981] Geguzin Ya.E., Dzyuba A.S., Kononenko N.V., *Kristallografiya* **26** (1981) 571.
- [Geller 1967] Geller S., *Z. Kristallogr.* **125** (1967) 1.
- [Gentilman 1986] Gentilman R.L., *Infrared and Optical Transmitting Materials, SPIE Proc.* **683** (1986) 2–11.
- [Gomperz 1922] Gomperz V.E., *Z. Phys.* **8** (1922) 184.
- [Gurjijants 1999] Gurjijants P.A., Starostin M.Yu., Kurlov V.N., Théodore F., Delepine J., *J. Cryst. Growth* **198–199** (1999) 227–231.
- [Hahn 2004] Hahn G., Schönecker A., *J. Phys. Condens. Mat.* **16** (2004) R1615.
- [Hahn 2006] Hahn G., Seren S., Kaes M., Schönecker A., Kalejs J.P., Dube C., Grenko A., Belouet C., *Proc. 4th World Conf. Photovoltaic Energy Conversion* (2006), p. 972.
- [Hanoka 2001] Hanoka J.I., *Sol. Energ. Mat. Sol. C* **65** (2001) 231.
- [Hassouni 2003] Hassouni A.E., Lebbou K., Goutaudier C., Boulon G., Yoshikawa A., Fukuda T. *Opt. Mater.* **24** (2003) 419.
- [Hautefeuille 2006] Hautefeuille B., Lebbou K., Dujardin C., Fourmigue J.M., Grosvalet L., Tillement O., Pédrini C., *J. Cryst. Growth* **289** (2006) 172.
- [Hopkins 1987] Hopkins R.H., Easoz J., McHugh J.P., Piotrowski P., Hundal R., Przywarty F., Seidensticker R.G., Sprecace R., Meier D.L., Campbell R.B., *J. Cryst. Growth* **82** (1987) 142.
- [Horowitz 1993] Horowitz A., Biderman S., Gazit D., Einav Y., Ben-Amar G., Weiss M., *J. Cryst. Growth* **128** (1993) 824–828.
- [Horowitz 1996] Horowitz A., Biderman S., Einav Y., Ben-Amar G., Gazit D., *J. Cryst. Growth* **167** (1996) 183–189.
- [Hubner 1969] Hubner K.H., *Neues Jb. Miner. Monat.* **335** (1969).
- [Hurley 1975] Hurley G.F., Meusse D.J., Morrison A.D., Smith S.M., *Am. Ceram. Soc. Bull.* **54** (1975) 510–513.

- [Ivleva 1987] Ivleva L.I., Bogodaev N.V., Polozkov N.M., Osiko V.V., *J. Cryst. Growth* **82** (1987) 168–176.
- [Ivleva 1995] Ivleva L.I., Bogodaev N.V., Polozkov N.M., Osiko V.V., *Opt. Mater.* **4** (1995) 168–173.
- [Jouini 2006] Jouini A., Sato H., Yoshikawa A., Fukuda T., Boulon G., Kato K., Hanamura E., *J. Cryst. Growth* **287** (2006) 313.
- [Kalejs 1980] Kalejs J., Mackintosh B.H., Surek T., *J. Cryst. Growth* **50** (1980) 175.
- [Kalejs 1987] Kalejs J., In: *Silicon Ribbon Production for Photovoltaic Applications*, Elsevier Science (1987).
- [Kalejs 2001] Kalejs J., *J. Cryst. Growth* **230** (2001) 10.
- [Kalejs 2002] Kalejs J., *Sol. Energ. Mater. Sol. C.* **72** (2002) 139.
- [Kalejs 2003] Kalejs J., *Proc. 3rd World Conference on Photovoltaic Energy Conversion* (2003), p. 903.
- [Kalejs 2004] Kalejs J., *Solid State Phenom.* **95–96** (2004) 159.
- [Kaplun 1996] Kaplun A.B., Meshalkin A.B., *J. Cryst. Growth* **167** (1996) 171.
- [Kasjanow 2007] Kasjanow H., Nikanorov A., Nacke B., Behnken H., Franke D., Seidl A., *J. Cryst. Growth* **303** (2007) 175.
- [Kalejs 1978] Kalejs J.P., *J. Cryst. Growth* **44** (1978) 329.
- [Kaminsky 1986] Kaminsky A.A., Kaminov L.K. *et al.* In: *Physics and Spectroscopy of Laser Crystals*, ed. Kaminsky A.A. Nauka, Moscow (1986) (in Russian).
- [Khattak 1989] Khattak C.P., Schmid F., *Mater. Lett.* **7** (1989) 318–321.
- [Khattak 1992] Khattak C.P., Schmid F., *Window and Dome Technologies and Materials III, SPIE Proc.* **1760** (1992) 41–47.
- [Kitamura 1992] Kitamura K., Yamamoto J.K., Iyi N., Kimura S., *J. Cryst. Growth* **116** (1992) 327.
- [Klassen-Neklyudova 1974] Klassen-Neklyudova M.V., Bagdasarov Kh.S. (Eds.), *Ruby and Sapphire*, Nauka, Moscow (1974) (in Russian).
- [Klimakow 1984] Klimakow A.M., Hoefer C., *Cryst. Res. Technol.* **19** (1984) 1433.
- [Kochurikhin 2006] Kochurikhin V.V., Klassen A.V., Kvyat E.V., Ivanov M.A., *J. Cryst. Growth* **292** (2006) 248–251.
- [Koptev 1967] Koptev Yu.I., Stepanov A.V., *Fiz. Tverd. Tela* **9** (1967) 3007 (in Russian).
- [Kravetskii 1980] Kravetskii D.Ya., Egorov L.P., Zatulovskii L.M. *et al.*, *Bull. Acad. Sci. USSR Phys. Ser.* **44** (1980) 126–130.
- [Krymov 1999] Krymov V.M., Kurlov V.N., Antonov P.I., Théodore F., Delepine J., *J. Cryst. Growth* **198/199** (1999) 210–214.
- [Kurlov 1994] Kurlov V.N., *Bull. Russ. Acad. Sci. Phys.* **58** (1994) 1498–1502.
- [Kurlov 1997-1] Kurlov V.N., *J. Cryst. Growth* **179** (1997) 168.
- [Kurlov 1997-2] Kurlov V.N., Epelbaum B.M., *J. Cryst. Growth* **179** (1997) 175–180.
- [Kurlov 1997-3] Kurlov V.N., Rossolenko S.N., *J. Cryst. Growth* **173** (1997) 417–426.
- [Kurlov 1998-1] Kurlov V.N., Belenko S.V., *Adv. Mater.* **10** (1998), p. 539–541.
- [Kurlov 1998-2] Kurlov V.N., Belenko S.V., *Inorg. Mater.* **34** (1998) 571.
- [Kurlov 1998-3] Kurlov V.N., Belenko S.V., *J. Cryst. Growth* **191/4** (1998) 779–782.
- [Kurlov 1998-4] Kurlov V.N., Rossolenko S.N., Belenko S.V., *J. Cryst. Growth* **191** (1998) 520–524.
- [Kurlov 1998-5] Kurlov V.N., Belenko S.V., *Inorgan. Mater.* **34** (1998) 1233–1237.
- [Kurlov 1998-6] Kurlov V.N., Epelbaum B.M., *J. Cryst. Growth* **187** (1998) 107.
- [Kurlov 1999-1] Kurlov V.N., Théodore F., *Cryst. Res. Technol.* **34** (1999) 293.
- [Kurlov 1999-2] Kurlov V.N., Epelbaum B.M., Rossolenko S.N., *Bull. Rus. Acad. Sci. Phys.* **63** (1999) 1705.
- [Kurlov 1999-3] Kurlov V.N., Rossolenko S.N., *Bull. Rus. Acad. Sci. Phys.* **63** (1999) 1711.
- [Kurlov 1999-4] Kurlov V.N., Rossolenko S.N., *Bull. Rus. Acad. Sci., Phys.* **63** (1999) 1339.
- [Kurlov 2001] Kurlov V.N., In: *Encyclopedia of Materials: Science and Technology*. Elsevier Science, Oxford (2001), pp. 8259–8265.
- [Kurlov 2005] Kurlov V.N., Klassen N.V., Dodonov A.M., Shmurak S.Z., Strukova G.K., Shmyt'ko I.M., Derenzo S.E., Weber M.J., *Nucl. Instrum. Methods A* **537** (2005) 197–199.

- [Kuznetsov 1980] Kuznetsov A.S., Levinson D.I., Sidorenko N.V., Peller V.V., Vorob'ev M.A., *Bull. Acad. Sci. USSR Phys. Ser.* **44** (1980) 79–85.
- [LaBelle 1967] LaBelle H.E., Mlavsky A.I., *Nature* **216** (1967) 574.
- [LaBelle 1971-1] LaBelle H.E., Mlavsky A.I., *Mater. Res. Bull.* **6** (1971) 571–580.
- [LaBelle 1971-2] LaBelle H.E., *Mater. Res. Bull.* **6** (1971) 581–590.
- [LaBelle 1975] LaBelle H.E., Cronan C., US Patent No. 3915662 (1975).
- [LaBelle 1980] LaBelle H.E., *J. Cryst. Growth* **50** (1980) 8–17.
- [Lange 1990] Lange H., Schwirtlich I.A., *J. Cryst. Growth* **104** (1990) 108.
- [Lebbou 2000-1] Lebbou K., Yoshikawa A., Fukuda T., Cohen Adad M.Th., Boulon G., *Mater. Res. Bull.* **35V8** (2000) 1277.
- [Lebbou 2000-2] Lebbou K., Yoshikawa A., Kikuchi M., Fukuda T., Cohen-Adad M.T., Boulon G., *Physica C* **336** (2000) 254.
- [Lebbou 2004] Lebbou K., Boulon G., In: *Fiber Crystal Growth from the Melt*, ed. T. Fukuda, P. Rudolph, S. Uda, Springer Verlag., Berlin (2004), p. 219–254.
- [Lebbou 2006] Lebbou K., Perrodin D., Chani V.I., Brenier A., Tillement O., Aloui O., Fourmigue J.M., Didierjean J., Balembois F., Gorges P., *J. Am. Ceram. Soc.* **89** (2006) 75.
- [Lebbou 2007] Lebbou K., Brenier A., Tillement O., Didierjean J., Balembois F., Georges P., Perrodin D., Fourmigue J.M., *Opt. Mater.* **30**(1) (2007) 82.
- [Lee 2001-1] Lee J.H., Yoshikawa A., Fukuda T., Waku Y., *J. Cryst. Growth* **231** (2001) 115.
- [Lee 2001-2] Lee J.H., Yoshikawa A., Lebbou K., Kaiden H., Fukuda T., Yoon D.H., Waku Y., *J. Cryst. Growth* **231** (2001) 179.
- [Levinson 1980] Levinson D.I., Nefedov V.N., Rykin E.P., *Bull. Acad. Sci. Phys* **44** (1980) 14–15.
- [Lin 1993] Lin M.-H., Kou S., *J. Cryst. Growth* **132** (1993) 467–470.
- [Linder 1927] Linder E.G., *Phys. Rev.* **29** (1927) 554.
- [Locher 1990] Locher J.W., Bennet H.E., Archibald P.C., Newmyer C.T., *Window and Dome Technologies and Materials II, SPIE Proc.* **1326** (1990) 2–6.
- [Locher 1992] Locher J.W., Bates H.E., Severn W.C., Pazol B.G., DeFranzo A.C., *Window and Dome Technologies and Materials III, SPIE Proc.* **1760** (1992) 48–54.
- [Locher 2005] Locher J.W., Bates H.E., Jones C.D., Zanella S.A., *Window and Dome Technologies and Materials IX, SPIE Proc.* **5786** (2005) 147–153.
- [Jung 2001] Jung I.H., Yoshikawa A., Lebbou K., Fukuda T., Auh K.H., *J. Cryst. Growth* **226** (2001) 101.
- [Machida 1993] Machida H., Hoshikawa K., Fukuda T., *J. Cryst. Growth* **128** (1993) 829–833.
- [Mackintosh 2006] Mackintosh B., Seidl A., Ouelette M., Bathey B., Yates D., Kaleski J., *J. Cryst. Growth* **287** (2006) 428.
- [Mareš 2002] Mareš J.A., Nikl M., Bartoš K., Nejezchleb K., Blazek K., de Notaristefani F., D'Ambrosio C., Puertolas D., Rosso E., *Opt. Mater.* **19** (2002) 117–122.
- [Mark 1923] Mark H., Polanyi M., Schmid E., *Z. Phys.* **12** (1923) 58.
- [Matsumura 1976] Matsumura S., Fukuda T., *J. Cryst. Growth* **34** (1976) 350–352.
- [Melcher 1993] Melcher C.L., Manente R.A., Peterson C.A., Schweitzer J.S., *J. Cryst. Growth* **128** (1993) 1001.
- [Miyazawa 1980] Miyazawa S., *J. Cryst. Growth* **49** (1980) 515.
- [Mlavsky 1975] Mlavsky A., Panidscic N.A., US Patent No. 3868228 (1975).
- [Monchamps 1971] Monchamps R.R., *J. Cryst. Growth* **11** (1971) 310.
- [Moulton 1986] Moulton P.F., *J. Opt. Soc. Am. B* **3** (1986) 125.
- [Nassau 1966] Nassau K., Levinstein H.J., *J. Phys. Chem. Solids* **27** (1966) 983.
- [Nicoara 1987] Nicoara D., Nicoara I., *J. Cryst. Growth* **82** (1987) 95.
- [Nicoara 2005] Nicoara I., Bunoiu M., Santailier J.L., Duffar T., *J. Cryst. Growth* **275** (2005) e799–e805.
- [Nicolov 2000] Nicolov M., *J. Cryst. Growth* **35** (1976) 127–132.
- [Nikanorov 1987] Nikanorov S.P., Antonov P.I., *J. Cryst. Growth* **82** (1987) 242–249.
- [Nikiforov 1988] Nikiforov A.V., Nosov Yu.G., Kljavin O.V., Antonov P.I., Mikhamedzhanova M.B., *Bull. Acad. Sci. USSR Phys. Ser.* **52** (1988) 131–133.
- [Nishimura 1975] Nishimura T., Omi T., *J. Appl. Phys.* **14** (1975) 1011.

- [Nosov 1969] Nosov Yu.G., Antonov P.I., Stepanov A.V., *Bull. Acad. Sci. USSR Phys. Ser.* **33** (1969) 2008.
- [Novak 1980] Novak R.E., Metzl R., Dreeben A., Berkman S., Patterson D.L., *J. Cryst. Growth* **50** (1980) 143.
- [Novoselov 2006] Novoselov A., Ogino H., Yoshikawa A., Nikl M., Pejchal J., Mares J.A., Beitlerova A., D'Ambrosio C., Fukuda T., *J. Cryst. Growth* **287** (2006) 309.
- [Perov 1979] Perov V.F., Papkov V.S., Ivanov I.A., *Bull. Acad. Sci. USSR Phys. Ser.* **43** (1979) 1977.
- [Pollock 1974-1] Pollock J.T.A., Stormont R., *J. Mater. Sci.* **9** (1974) 508–510.
- [Pollock 1974-2] Pollock J.T.A., Bailey J.S., *J. Mater. Sci.* **9** (1974) 323.
- [Proc. SSCG-1 1986] Proceedings of SSCG-1. *J. Cryst. Growth* **82** (1986).
- [Proc. SSCG-2 1990] Proceedings of SSCG-2. *J. Cryst. Growth* **104** (1990).
- [Proc. Stepanov Conf. 1968] *Proc. Stepanov Conf.*, Physico-Technical Institute, Leningrad (1968) (in Russian).
- [Proc. Stepanov Conf. 1989] *Proc. Stepanov Conf.*, Physico-Technical Institute, Leningrad (1989) (in Russian).
- [Rao 1980] Rao C.V.H.N., Cretella M.C., Wald F.V., Ravi K.V., *J. Cryst. Growth* **50** (1980) 311–319.
- [Ravi 1975] Ravi K.V., Serreze H.B., Bates H.E., Morrison A.D., Jewett D.N., Ho J.C.T., *Proc. 11th IEEE Photovoltaic Spec. Conf.* (1975), p. 280.
- [Ravi 1977] Ravi K.V., *J. Cryst. Growth* **39** (1977) 1–16.
- [Red'kin 1987] Red'kin B.S., Kurlov V.N., Tatartchenko V.A., *J. Cryst. Growth* **82** (1987) 106–109.
- [Red'kin 1986] Red'kin B.S., Satunkin G.A., Kurlov V.N., Tatartchenko V.A., In: *Crystal Growth XV*, Nauka, Moscow (1986), pp. 210–216.
- [Ricard 1980] Ricard J., Excoffon C., US Patent 4,233,338, 11 November 1980.
- [Rossolenko 2001] Rossolenko S.N., *J. Cryst. Growth* **231** (2001) 306.
- [Rudolph 1982] Rudolph P., *Profizüchtung von Einkristallen*, Akademie Verlag, Berlin (1982) (in German).
- [Rudolph 1994] Rudolph P., Shimamura K., Fukuda T., *Cryst. Res. Technol.* **29** (1994) 801–807.
- [Rudolph 1999] Rudolph P., Fukuda T., *Cryst. Res. Technol.* **34** (1999) 3–40.
- [Rudolph 2004] Rudolph P., In: *Fiber Crystal Growth from the Melt*, ed. T. Fukuda, P. Rudolph, S. Uda, Springer Verlag, Berlin (2004), pp. 1–46.
- [Sachs 1987] Sachs E., Ely D., Serdy D., *J. Cryst. Growth* **82** (1987) 117.
- [Sachs 2004] Sachs E., Harvey D., Janoch R., Anselmo A., Miller D., Hanoka J.I., *Proc. 19th European Photovoltaic Solar Energy Conf.* (2004), p. 552.
- [Santo 2004] Santo A.M.E., Epelbaum B.M., Morato S.P., Vieira N.D. Jr., Baldochi S.L., *J. Cryst. Growth* **270** (2004) 121.
- [Sato 2007] Sato H. In: *Shaped crystals. Growth by Micro-Pulling Down Technique*, ed. T. Fukuda, V.I. Chani, Springer Verlag, Berlin (2007), pp. 239–249.
- [Seidensticker 1977] Seidensticker R.G., *J. Cryst. Growth* **39** (1977) 17.
- [Seidensticker 1982] Seidensticker R.G., In: *Crystals: Growth, Properties and Application, Vol. 8*, ed. J. Grabmaier, Springer, Berlin (1982), p.145.
- [Shach-Budagov 1959] Shach-Budagov A.L., Stepanov A.V., *Zh. Tech. Fiz.* **29** (1959) 394 (in Russian).
- [Shikunova 2007] Shikunova I.A., Kurlov V.N., Klassen N.V., *Mater. Sci.* **10** (2007) 43–55 (in Russian).
- [Shim 2002] Shim J.B., Lee J.H., Yoshikawa A., Nikl M., Yoon D.H., Fukuda T., *J. Cryst. Growth* **243** (2002) 157.
- [Shimamura 1994] Shimamura K., Kodama N., Fukuda T., *J. Cryst. Growth* **142** (1994) 400–402.
- [Shimamura 1996] Shimamura K., Uda S., Yamada T., Sakaguchi S., Fukuda T., *Jpn J. Appl. Phys.* **35** (1996) L793.
- [Simura 2006] Simura R., Jouini A., Kamada K., Yoshikawa A., Aoki K., Guyot Y., Boulon G., Fukuda T., *J. Cryst. Growth* **291** (2006) 309.

- [Smirnova 2008] Smirnova O.V., Kalaev V.V., Seidl A., Birkmann B., *J. Cryst. Growth* **310** (2008) 2209–2214.
- [Starostin 1994] Starostin M.Yu., *Bull. Russ. Acad. Sci. Phys.* **58** (1994) 1508–1510.
- [Steinbach 1997] Steinbach I., Höfs H.-U., *Proc. 26th IEEE Photovolt. Spec. Conf.*, (1997), p. 91.
- [Stepanov 1959] Stepanov A.V., *Zh. Tech. Fiz.* **29** (1959) 382 (in Russian).
- [Stepanov 1963] Stepanov A.V., *The Future of Metalworking*, Lenizdat, Leningrad (1963) (in Russian).
- [Swartz 1974] Swartz J.C., Siegel B., Morrison A.D., Lingertat H., *J. Electron. Mater.* **3** (1974) 309–326.
- [Sun 2004] Sun D., Wang C., Zhang H., Mackintosh B., Yates D., Kalejs J. *J. Cryst. Growth* **266** (2004) 167.
- [Tatartchenko 1969] Tatartchenko V.A., Saet A.I., Stepanov A.V. *Bull. Acad. Sci. USSR Phys. Ser.* **33** (1969) 1954–1959.
- [Tatartchenko 1978] Tatartchenko V.A., Brantov S.K., Abrosimov N.V., *Fiz. Khim. Obrab. Mat.* **1** (1978) 79 (in Russian).
- [Tatartchenko 1980] Tatartchenko V.A., Yalovets T.N., Satunkin G.A., Zatulovsky L.M., Egorov L.P., Kravetsky D.Ya., *J. Cryst. Growth* **50** (1980) 335.
- [Tatartchenko 1988] Tatartchenko V.A. *Stable Crystal Growth*, Nauka, Moscow (1988) (in Russian).
- [Tatartchenko 1993] Tatartchenko Y.A., *Shaped Crystal Growth*, Kluwer Academic Publishers, Dordrecht (1993).
- [Tatartchenko 1994] Tatartchenko V.A., In: *Handbook of Crystal Growth 2*, ed. D.T.J. Hurle, Elsevier, Amsterdam (1994), pp. 1011–1110.
- [Tatartchenko 2005] Tatartchenko V.A., In: *Bulk Crystal Growth of Electronic, Optical and Optoelectronic Materials*, ed. P. Capper, John Wiley & Sons, Ltd, Chichester (2005), pp. 299–328.
- [Taylor 1981] Taylor A.S., Stormont R.W., Chao C.C., Henderson E.J., *Proc. 15th IEEE Photovoltaic Spec. Conf.* (1981), p. 589.
- [Taylor 1983] Taylor A.S., *J. Cryst. Growth* **65** (1983) 314.
- [Théodore 1999-1] Théodore F., Duffar T., Sentailler J.L., Pesenti J., Keller M., Dusserre P., Louchet F., Kurlov V.N., *Bull. Rus. Acad. Sci. Phys.* **63** (1999) 1686–1693.
- [Théodore 1999-2] Théodore F., Duffar T., Sentailler J.L., Pesenti J., Keller M., Dusserre P., Louchet F., Kurlov V.N., *J. Cryst. Growth* **198–199** (1999) 317–324.
- [Tiller 1953] Tiller W.A., Jackson K.A., Rutter J.W., Chalmers B., *Acta Metall.* **1** (1953) 428.
- [Tsvinskii 1965] Tsvinskii S.V., Stepanov A.V., *Zh. Tech. Fiz.* **7** (1965) 194 (in Russian).
- [Tsvinskii 1966] Tsvinskii S.V., Koptev Yu.I., Stepanov A.V., *Fiz. Tverd. Tela* **8** (1966) 449 (in Russian).
- [Vasiliev 2005] Vasiliev M.G., Budenkova O.N., Yuferev V.S., Kalaev V.V., Shlegel V.N., Ivannikova N.V., Vasiliev Ya.V., Mamedov V.M., *J. Cryst. Growth* **275** (2005) 745.
- [Voges 1986] Voges E., *Electro-Optics and Photorefractive Materials, Proceedings in Physics* **18**, ed. P. Gunter, Springer Verlag, Berlin (1986).
- [Voronkov 1983] Voronkov V.V., *Bull. Acad. Sci. USSR Phys. Ser.* **47** (1983) 1.
- [Voronkov 1988] Voronkov V.V., Lavrishchev S.V., Myzina V.A., Osiko V.V., Polozkov N.M., *Bull. Acad. Sci., Phys. Ser.* **52** (1988) 104–107.
- [Wada 1980] Wada K., Hoshikawa K., *J. Cryst. Growth* **50** (1980) 151.
- [Wallace 2003] Wallace R.L., Sachs E., Hanoka J.I., *Proc. 3rd World Conf. Photovoltaic Energy Conversion* (2003), p. 1297.
- [Yoon 1994-1] Yoon H.D., Fukuda T., *J. Cryst. Growth* **144** (1994) 201.
- [Yoon 1994-2] Yoon H.D., Fukuda T., *J. Korean Assoc. Cryst. Growth* **4** (1994) 405.
- [Yoon 1994-3] Yoon H.D., Hashimoto M., Fukuda T., *Jpn. J. Appl. Phys.* **33** (1994) 3510.
- [Yoshikawa 1999] Yoshikawa A., Epelbaum B.M., Hasegawa K., Durbin S.D., Fukuda T., *J. Cryst. Growth* **205** (1999) 305.
- [Yoshikawa 2002] Yoshikawa A., Akagi T., Nikl M., Solovieva N., Lebbou K., Dujardin C., Pedrini C., Fukuda T., *Nucl. Instrum. Meth. A* **486** (2002) 79.
- [Yoshikawa 2003] Yoshikawa A., Ogino H., Lee J.H., Nikl M., Solovieva N., Garnier N., Dujardin C., Lebbou K., Pedrini C., Fukuda T., *Opt. Mater.* **24** (2003) 275.

- [Yoshikawa 2004] Yoshikawa A., In: *Fiber Crystal Growth from the Melt*, ed. T. Fukuda, P. Rudolph, S. Uda, Springer Verlag, Berlin (2004), pp. 185–217.
- [Yu 1997] Yu Y.M., Chani V.I., Shimamura K., Fukuda T., *J. Cryst. Growth* **171** (1997) 463.
- [Zatulovskii 1983] Zatulovskii L.M., Kravetskii D.Ya., Egorov L.P., *et al. Bull. Acad. Sci. USSR Phys. Ser.* **47** (1983) 157.
- [Zhang 1990] Zhang Q., Deng P., Gan F., *Crystal Res. Technol.* **25** (1990) 385.
- [Zhang 2002] Zhang H., Liu J., Wang J., Wang C., Zhu L., Shao Z., Meng X., Hu X., Jiang M., Chow Y.T., *J. Opt. Soc. Am. B* **19** (2002) 18–27.

6

Vertical Bridgman Technique and Dewetting

Thierry Duffar
SIMaP-EPM

Lamine Sylla

Freiburger Materialforschungszentrum FMF, Albert-Ludwigs-Universität Freiburg, Germany

This chapter deals with the vertical Bridgman (VB) technique of crystal growth and its variants. In these processes, the material is introduced in a crucible placed in a furnace. By heating the furnace and controlling a vertical thermal gradient, the material is melted, possibly with a remaining unmelted single-crystal seed placed at the bottom of the crucible. The controlled solidification is obtained by cooling down the furnace (vertical gradient freeze growth, VGF), or by pulling down the crucible (VB) or both (Figure 6.1). The Stockbarger variant uses a specific furnace made up of two heating elements separated by an adiabatic zone. These techniques are commonly used for the growth of III–V and II–VI semiconductors, halide and chalcogenide crystals, and a number of oxides for scintillation or laser applications.

Compared to capillary-based techniques, these processes have advantages:

- The shape of the crystal is a direct result of the shape of the crucible; there is no concern with control of the crystal shape. As both diameters are equal, the furnace is generally smaller than for other techniques.
- In the other crystal growth methods studied in this book, it is necessary to apply relatively high thermal gradients in order to control the crystal shape. This is detrimental to crystal quality because high thermal gradients generate thermal stresses in the hot crystal, above the elasticity limit, and dislocations are then generated in the crystal. In Bridgman-type methods, the thermal gradient can be as small as necessary: thermal gradients as low as 3 or 4 K cm⁻¹ have been used for the growth of GaAs [Asahi, Buhrig].

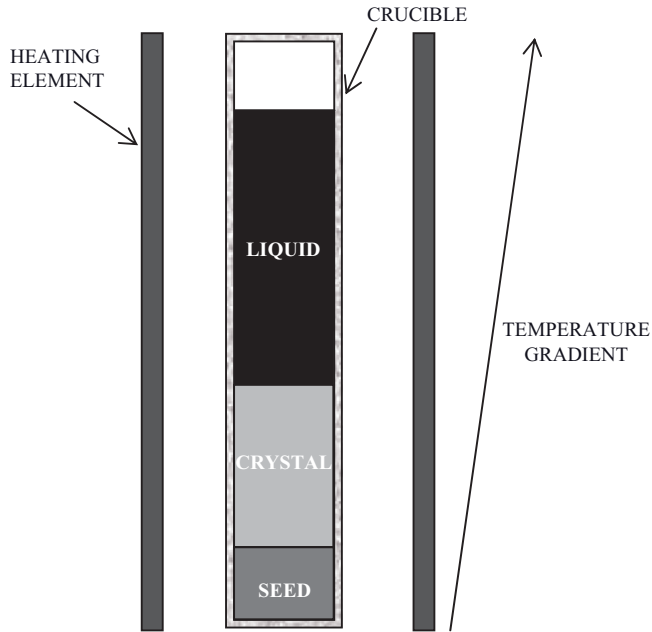


Figure 6.1 *General sketch of a Bridgman set-up.*

- Once the process is established, reproducibility is good and growth is easily controlled automatically, without human intervention.
- The result is relatively simple, small and cheap growth equipment, especially for processes where the growth is controlled by simply cooling down the furnace, without any moving parts in the furnace.

Clearly the drawbacks of these methods are linked to the use of a crucible in intimate contact with the crystal. This has thermal, thermodynamic and mechanical adverse consequences. In itself the technique does not involve capillarity, but in order to solve these problems some variants based on capillarity aspects have been proposed, such as full encapsulation or dewetting. Other important points linked to interfacial energy are the adhesion of the solid to the crucible and the crystal–liquid–crucible contact angle, which have consequences for crystal quality.

6.1 Peculiarities and Drawbacks of the Bridgman Processes

6.1.1 Thermal Interface Curvature

During crystal growth from the melt in a crucible, thermal transfer in the furnace–crucible–sample system leads to curvature of the isotherms and especially of the solid–liquid interface. This has many well-known effects on the grown crystal, such as spurious

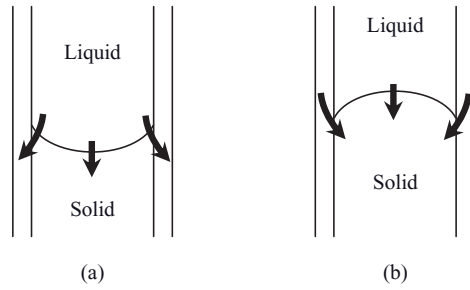


Figure 6.2 Local heat fluxes at the liquid–solid interface: (a) a solid with lower thermal conductivity than the liquid; (b) a solid with higher thermal conductivity than the liquid.

grain nucleation [Feigelson, Pfeiffer] or radial solute segregation [Coriell 1979, Coriell 1981, Möller]. Global heat transfer in the furnace, related for instance to the design of the heating and cooling elements, has a major effect in terms of interface shape [Chang, Naumann 1982]. Various strategies have been proposed to limit the curvature of the solid–liquid front [Feigelson, Huang, Jasinski], since it is often detrimental to crystal quality.

The local heat transfer between the crucible, the solid and the liquid is also of major importance in terms of interface shape (see Figure 6.2). This so-called ‘crucible effect’ has been widely studied in the past [El Mahallawy, Jasinski, Naumann 1983], Naumann being the first author to show that it is controlled by the difference between the thermal conductivities of the material in the liquid and solid states. In an interesting paper, Jasinski and Witt [Jasinski] analytically estimated the crucible effect from a model of the heat fluxes in an ideal Bridgman configuration. They obtained a rather complex solution for the temperature field within the furnace, and performed a parametric study, featuring the various thermal conductivities, the thermal gradient and the geometry of the problem.

[Barat] studied the problem experimentally, numerically and by simple considerations of the heat flux transfer between the liquid, the solid and the crucible. The geometry of the system is shown in Figure 6.3. The crucible is long enough that end effects on the interface are negligible. The sample radius is r_s , the thickness of the crucible is d and the interface curvature, defined as the difference in height between the center and the crucible wall, is f . The thermal conductivities of the crucible, liquid and solid sample are respectively λ_c , λ_l and λ_s .

In order to study only the crucible effect the external wall of the crucible was taken as adiabatic, so that heat conservation requires:

$$\Phi_l + \Phi_c^{\text{hot}} = \Phi_s + \Phi_c^{\text{cold}}. \quad (6.1)$$

The thermal fluxes can be locally expressed as:

$$\Phi = \lambda \cdot G \cdot A, \quad (6.2)$$

with G the thermal gradient and A the surface through which the flux is flowing. Using these expressions, with the hypothesis that the interface has a parabolic shape, Barat finally obtained for the interface curvature:

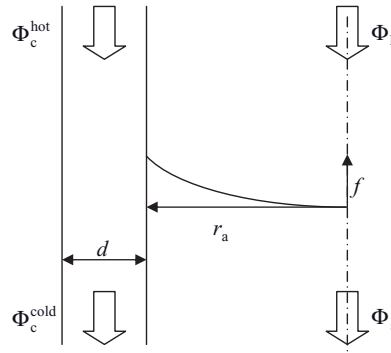


Figure 6.3 Geometry and principal parameters of the ‘crucible effect’ problem (see text for details) (Reprinted with permission from [Barat 1998], copyright (1998) Elsevier Ltd).

$$f = \frac{r_a}{2} \left[\frac{\lambda_l \left(\lambda_s r_a^2 + \lambda_c (2r_a + d) d \right)}{\lambda_s \left(\lambda_l r_a^2 + \lambda_c (2r_a + d) d \right)} - 1 \right]. \quad (6.3)$$

Such a simple treatment gives only an approximate value of the interface deflection, but comparisons with experimental measurements and numerical simulation have shown that the expression gives the appropriate variation with the parameters of the problem. Useful values are obtained provided that the amount of heat carried by the crucible is small compared to the overall heat flux, which is generally the case.

It can be seen that this expression is indeed independent of the magnitude of the temperature gradients G_l and G_s and of the temperature difference imposed on the crucible. The reason is that, in the simple case studied, only the repartition of the heat flux is of importance, not the absolute values of the fluxes. This is no longer the case if the latent heat of solidification, released at the interface, is taken into account. [Stelian 2001] studied this problem in the same way as above and found an additional term due to the latent heat, where G_l is the thermal gradient in the liquid, v_i the interface velocity and H the latent heat of fusion:

$$f = \frac{r_a}{2} \left[\frac{\lambda_l \left(\lambda_s r_a^2 + \lambda_c (2r_a + d) d \right)}{\lambda_s \left(\lambda_l r_a^2 + \lambda_c (2r_a + d) d \right)} - 1 \right] + \frac{r_a}{2} \cdot \frac{\lambda_c (2r_a + d) d}{\lambda_s r_a^2 + \lambda_c (2r_a + d) d} \cdot \frac{v_c H}{k_l G_l - v_c H}. \quad (6.4)$$

This expression also gives values that compare well with numerical and experimental results.

In order to decrease the solid–liquid interface curvature, and the associated drawbacks for crystal quality, it is advisable to have an insulating layer between the crucible and the crystal. Techniques such as full encapsulation (section 6.2) and dewetting (section 6.3) can, to a certain extent, provide such a layer.

6.1.2 Melt–Crystal–Crucible Contact Angle

As shown in Figure 6.4, the equilibrium of interfacial energies at the liquid–solid–crucible triple line defines a contact angle θ which is characteristic of the sample–wall system. In

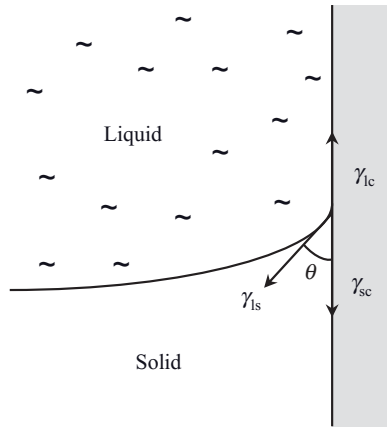


Figure 6.4 Interfacial energies at the solid–liquid–crucible triple line.

Table 6.1 Liquid–crystal–crucible contact angles for GaSb and Ge in various crucibles

	Crucible material	θ (°)
GaSb	SiO ₂	85–100
	BN	25–60
Ge	SiO ₂	110–120
	C and C-coated BN	90–100
	BN	60–70

order to find and measure this angle, specific experiments were performed in order to mark the solid–liquid interface in GaSb and Ge samples [Duffar 1999]. The samples were doped with Te for GaSb and Ga for Ge in order to get observable interfaces after etching. The marks were obtained by interruption of pulling for 2 h then pulling at high speed (40 mm/h). The samples were then cut along their axis, polished and etched. Figure 6.5 shows several examples of the contact angle for Ge. Figure 6.6 shows two examples of the shape of the GaSb liquid–solid interface close to the crucible wall for pyrolytic boron nitride (p-BN) and silica crucibles. Table 6.1 summarizes the results obtained for these crystals. The large uncertainty of these values is due to the difficulty of getting a good polish very close to the border of the sample and because the actual angle seems to be sensitive to the local roughness of the crucible (orientation towards the vertical), which is difficult to estimate on the pictures.

Note that one of the Ge crucibles was made of BN but with a pyrolytic carbon layer a few micrometres thick. It is believed that such a thin layer does not change the thermal curvature of the interface, as studied in section 6.1.1 (compare Figures 6.5c and 6.5d) and the contact angle is found to be the same as for bulk pyrolytic graphite (compare Figures 6.5b and 6.5c). This shows that the contact angle is related to the chemical nature of the wall rather than to its thermal properties. It is then expected that this measured angle corresponds to the contact angle as defined by Volmer in his classic work on heterogeneous nucleation [Volmer] because, as discussed in section 6.1.1, a change in the thermal field changes the overall interface shape but not the local angle, which changes the interface shape for a distance of about 100 μm .

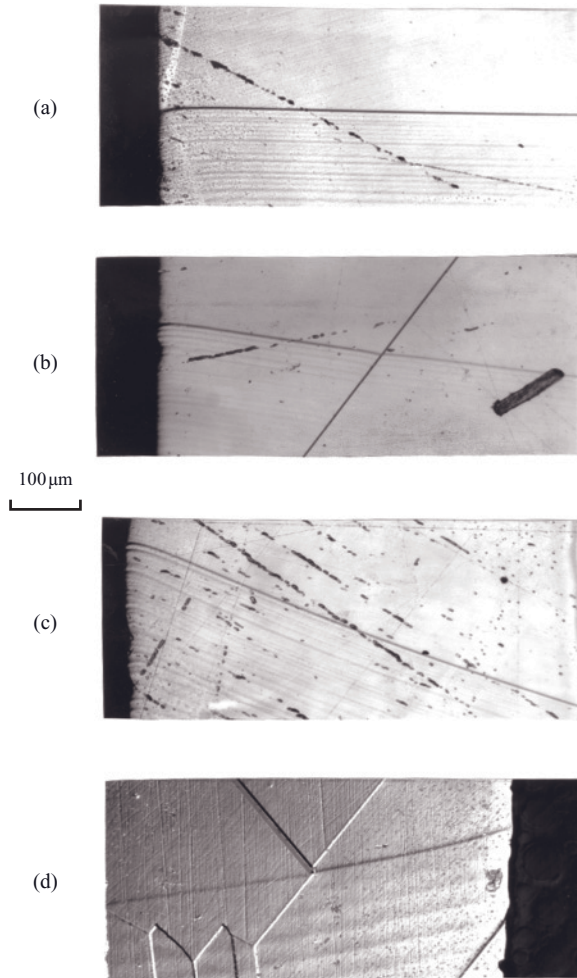


Figure 6.5 Metallographic pictures of marked Ge solid–liquid interfaces, in contact with the crucible wall: (a) silica ($\theta = 100^\circ$); (b) vitreous carbon ($\theta = 90^\circ$); (c) BN with carbon coating ($\theta = 90^\circ$); (d) BN ($\theta = 40^\circ$, crucible wall was on the right) (Reprinted with permission from [Duffar 1999], copyright (1999) Elsevier Ltd).

According to Figure 6.4, a low value of the angle shows that there is a noticeable difference between the crucible–liquid and crucible–crystal interfacial energies.

6.1.3 Crystal–Crucible Adhesion and Thermomechanical Detachment

During solidification, the crystal usually sticks to the crucible because of the solid–solid interfacial energy. In the general case, as discussed in Chapter 1 (section 1.3) it is difficult to measure and even to give an order of magnitude of this energy because it takes into account not only the chemical interaction between the crystal and the crucible, but also other parameters:

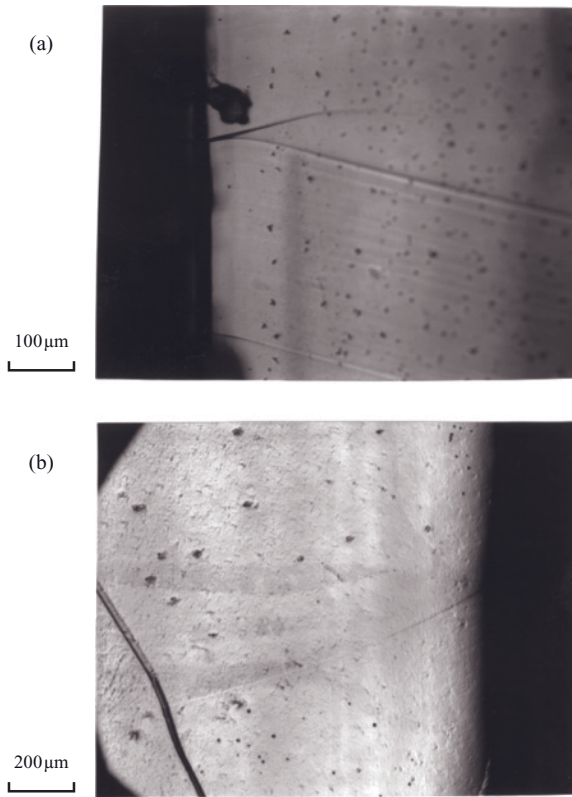


Figure 6.6 GaSb solid–liquid interfaces at the vicinity of the crucible wall for silica (a) and p-BN (b). The solidification proceeds from the bottom to the top and the crucible wall was on the left of (a) and on the right of (b) (Reprinted with permission from [Duffar 1999], copyright (1999) Elsevier Ltd).

- the crucible roughness, which increases or decreases the area of interaction depending whether or not composite wetting is obtained;
- the elastic energy due to the stresses created by the solid–solid interaction during cooling down and likely to evolve with time.

However, in the vicinity of the solid–liquid interface, close to the melting temperature, only the chemical interaction is active. It is after this, during cooling down, that thermal stresses are created in the crystal. For a general discussion of thermal stresses in crystal growth, see [Völkl].

When they are larger than the critical resolved shear stress, these stresses produce dislocations. Furthermore the dislocations, if numerous enough ($>5 \times 10^5 \text{ cm}^{-2}$), may align in subgrain boundaries and, ultimately, give grains (Figure 6.7). Such mechanism of grain generation in Bridgman growth has been reported for GaAs growth [Althaus] under high thermal stresses and for CdTe [Shetty 1995-1] and GaSb [Boiton] where sticking of the crystal to the crucible occurred.

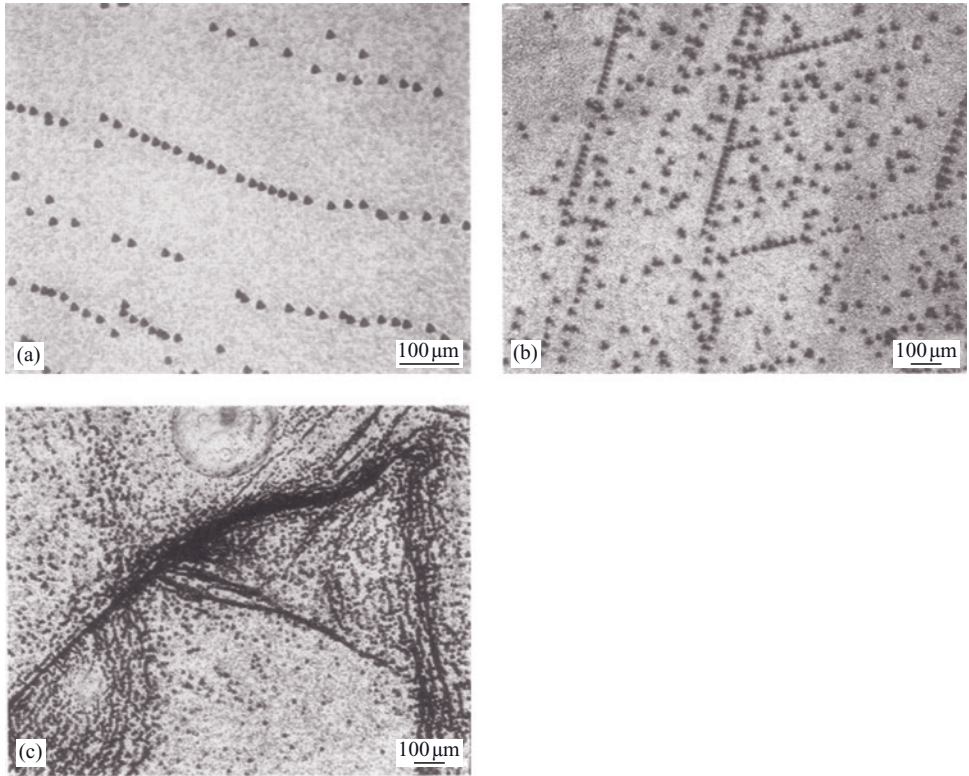


Figure 6.7 Etch pits of dislocations revealed at three successive locations (a, b, c) along the growth direction in a GaSb $\langle 111 \rangle$ crystal (Reprinted with permission from [Boiton], copyright (1999) Elsevier Ltd).

During cooling, the cylindrical crucible retracts towards its neutral cylinder and the crystal also retracts; consequently, whatever the relative magnitude of both dilatation coefficients, there is always a tensile strength tending to detach the crucible from the crystal. Numerical simulations for GaSb in a silica crucible have shown that the resulting stress reaches some 150 MPa, a value which is much higher than the critical resolved shear stress of the material [Santallier].

However, on opening the furnace and removing the crucible, the crystal is often found to be detached from the crucible. The phenomenon has been studied by [Boiton] for GaSb in silica crucibles. [Harter] gives the work of adhesion, for liquid GaSb, on silica, BN and C. It is generally accepted that the work of adhesion of a solid metal on a ceramic substrate is close to the liquid one [Pilliar], with a difference less than 20%. It will be supposed in the following that this is also true for GaSb, which has been shown to have a wetting behavior comparable to that of metals [Harter].

Considering a cylindrical layer of crystal, height dz and radius r , stuck to the crucible, detachment will occur if the elastic energy stored in the crystal, W_{el} , is greater than the energy of adhesion acting at the periphery:

$$W_{el}\pi r^2 dz > W_{adh} 2\pi r dz \quad (6.5)$$

or

$$W_{el} > 2W_{adh}/r. \quad (6.6)$$

Considering that the elastic energy is composed of energy of volume variation (at constant shape), W_s , and energy of shape variation (at constant volume), W_d , from classical elastic theory we get:

$$W_{el} = W_s + W_d = \frac{1-2\nu}{6E} \sigma_{VM}^2 + \frac{1+\nu}{3E} \sigma_{VM}^2. \quad (6.7)$$

Considering that the Von Mises stress, σ_{VM} , is limited by plasticity to the critical resolved shear stress, σ_{CRSS} , the criterion for detachment, Equation (6.6), is now written:

$$\sigma_{CRSS} > \sqrt{\frac{12EW_{adh}}{R(5-4\nu)}}. \quad (6.8)$$

Mezhennyi *et al.* [Mezhennyi] have measured the variation with temperature of the stress at which ‘the dislocation density is multiplied by a factor 1.5 to 3’ in GaSb. Interpolation from a value of $\sigma_{CRSS} = 0.5 \text{ MPa}$ at T_m gives:

$$\log_{10}(\sigma_{CRSS}/4) = -3.79 + 2833/T. \quad (6.9)$$

Substituting Equation (6.9) into (6.8) gives the temperature at which the crystal detaches from the crucible. It was found that detachment is likely to occur, as experimentally observed, between 750 K and 900 K, for all crucibles, and also in the seed well. The large divergence from the melting temperature (983 K) explains why, for a silica crucible, many dislocations are found in the samples, leading to grain boundaries.

This thermomechanical phenomenon has also been observed by [Sylla 2008-2] for GaSb, 11 mm in diameter, by taking video recordings through the transparent silica crucible during solidification. Optical interference, due to the small gap between the crystal and the crucible, appears suddenly from time to time all along the growing crystal (Figure 6.8). Subsequent surface analysis of the crystals has shown periodical striations on their external surface.

As can be seen in Table 6.2, the detachment temperature is expected to be 760 K, which is 220 K lower than the melting temperature. However, from Figure 6.8, the thermomechanical detachment occurs after a maximum of a few millimetres and considering the thermal gradient in the furnace during the experiment, 10 K mm^{-1} , the experimental temperature decrease needed for detachment to occur is in all cases less than 50 K. Thus the proposed model probably reflects the physics of the detachment but still needs to be improved in order to better fit the experimental results. Better knowledge of the critical resolved shear stress and of the energy of adhesion is also needed.

6.1.4 Spurious Nucleation on Crucible Walls

During crystal growth from the melt in a crucible, nucleation of grains on the walls often occurs and leads to polycrystalline material. Because of the energy associated with the

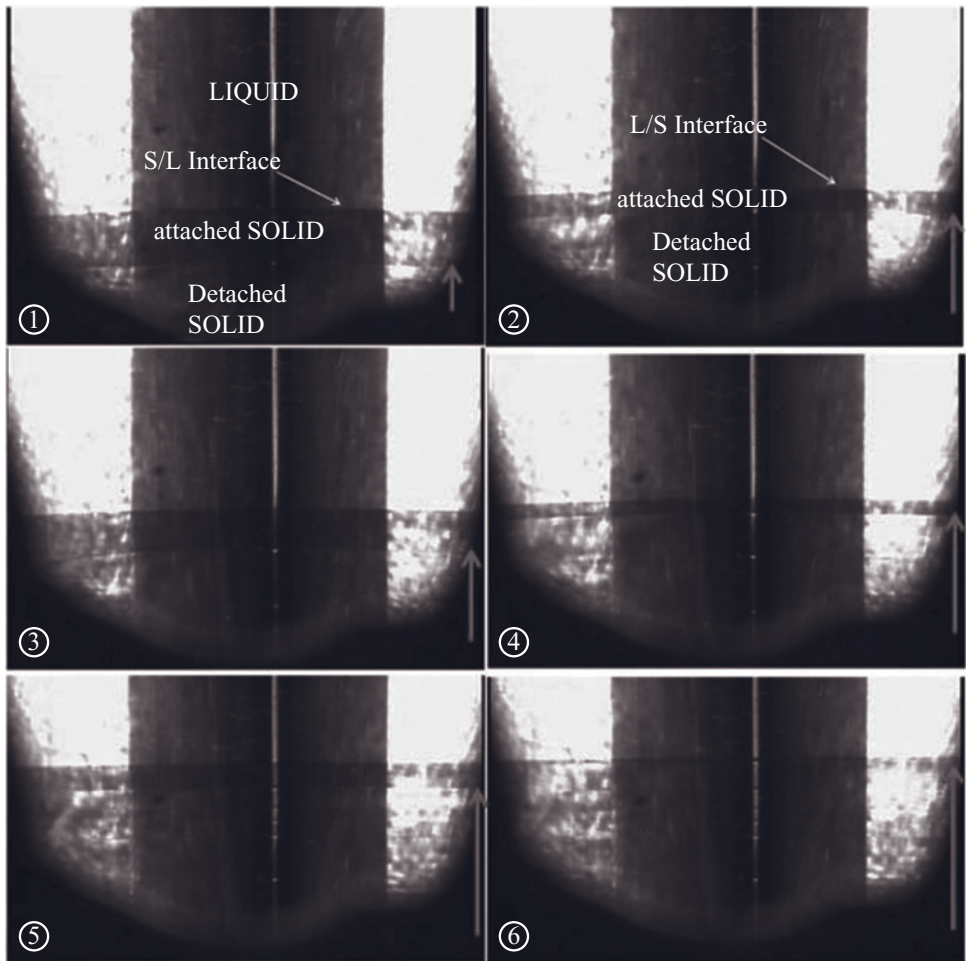


Figure 6.8 Video snapshots showing the thermomechanical detachment of GaSb in a silica crucible. The large dark central band is an optical artefact. The solid–liquid interface is the line separating the white upper side (liquid) from the darker lower side (solid). The red arrows show the line that separates the attached solid (darker) from the detached solid (clearer, the coloured interferences cannot be seen on this black and white figure). Window size: 9 mm.

Table 6.2 Detachment temperature of a GaSb crystal from various crucibles during cooling down

Crucible	SiO ₂	BN	Carbon
W_{adh} [Harter]	0.22 J m ⁻²	0.15 J m ⁻²	0.07 J m ⁻²
Diameter 10 mm	$T < 760 \text{ K}$	$T < 777 \text{ K}$	$T < 815 \text{ K}$
Diameter 44 mm	$T < 832 \text{ K}$	$T < 852 \text{ K}$	$T < 897 \text{ K}$

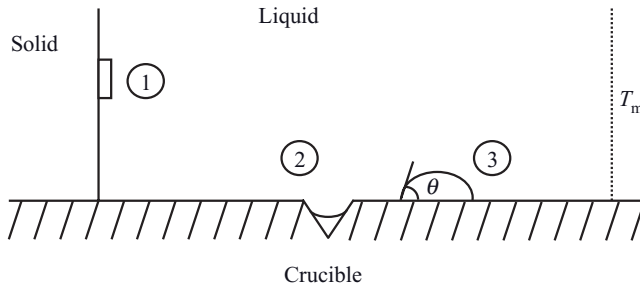


Figure 6.9 Nucleation of solid seeds above the solid–liquid interface (T_m shows the melting isotherm position): 1, on the interface; 2, in a hole in a rough crucible; 3, spurious nucleation on the crucible wall.

grain boundary, the nucleation of a randomly disoriented seed directly on the growing interface is not possible. It is considered that grain nucleation then occurs on the crucible wall, ahead of the solid–liquid interface which is undercooled by an amount depending on the growth mode (rough or faceted interface). Obviously, due to the temperature gradient applied to the system, the wall in contact with the liquid is at a temperature higher than the growing solid and, at first sight, nucleation on the wall is not likely to happen. In fact, there is competition between nucleation on the growing crystal and nucleation on the crucible wall ahead of the solid–liquid interface.

As shown in Figure 6.9, two configurations may lead to grain nucleation in the layer of undercooled melt ahead of the interface: nucleation on a smooth crucible wall or in the pores of a rough crucible.

From the classical nucleation theory, there is a critical radius for nucleation of a two-dimensional nucleus on a faceted interface (case 1 in Figure 6.9) and the associated energy is given by:

$$\Delta G_1 = \frac{\pi a \gamma_{sl}^2}{\Delta S_m \Delta T}, \quad (6.10)$$

where a is the height of an atomic row, ΔT the solid–liquid interface undercooling, ΔS the entropy of fusion and γ_{sl} the liquid–solid interfacial energy. On the smooth crucible wall (case 3 in Figure 6.9), the critical seed has a similar radius, but the energy is decreased by a factor depending on the contact angle of the seed on the wall [Volmer]:

$$\Delta G_w = \frac{16\pi \gamma_{sl}^3}{3\Delta S_m^2 \Delta T_{het}^2} \frac{(2 + \cos \theta)(1 - \cos \theta)^2}{4}, \quad (6.11)$$

with ΔT_{het} the undercooling of the seed depending on the seed radius of curvature R :

$$\Delta T_{het} = \frac{\gamma_{sl}}{\Delta S_m R}. \quad (6.12)$$

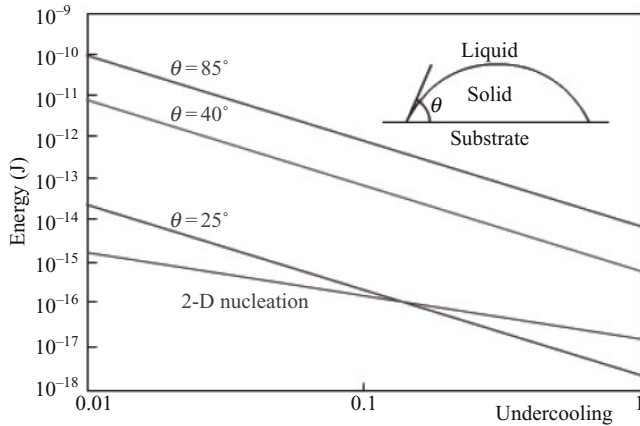


Figure 6.10 Nucleation energy of a two-dimensional nucleus on the interface and on a smooth wall with various contact angles, plotted as function of the undercooling (Reprinted with permission from [Duffar 1999], copyright (1999) Elsevier Ltd).

Figure 6.10 shows the variation of the energy of nucleation of a GaSb critical nucleus as a function of the undercooling for both cases (Equations 6.10 and 6.11) and for various θ , computed with $\sigma_{sl} = 0.166 \text{ Jm}^{-2}$ [Dashevskii]. From these results, it appears that the nucleation on the crucible is possible for faceted growth (undercooling of a few kelvin) and even for the growth of a semiconductor crystal with a nonfaceted interface (i.e. undercooling of a few tenths of kelvin, as given by [Brice]) but this necessitates low values of the contact angle θ . Statistics concerning spurious grain nucleation during semiconductor growth in various crucibles is in good agreement with this analysis [Duffar 1999].

When the crucible wall is rough, for example for nucleation in a pore, it can be seen for Figure 6.9 (2) that the sign of the curvature of the seed is changed (the centre of curvature is in the liquid in this case and R is negative). According to Equation (6.12) it follows that the undercooling of the solid seed is negative, and for low enough values of the contact angle, the nucleation temperature can be higher than the melting point, due to the curvature effect. The probability of spurious nucleation therefore becomes very high. Nevertheless, experiments show that parasitic grain nucleation is a very rare phenomenon, compared to the number of atomic layers that are piled up to make a crystal. Further theoretical and experimental work is still needed before we can gain complete knowledge of the phenomenon.

6.2 Full Encapsulation

6.2.1 Introduction

Liquid encapsulation by B_2O_3 was initially proposed in order to prevent evaporation of components from high vapour pressure melts during Czochralski growth of PbTe and

Table 6.3 Crystals grown by the liquid encapsulation Bridgman technique

Crystal	Encapsulant	Crucible	Reference
GaP	B ₂ O ₃	p-BN	[Blum]
CdTe	B ₂ O ₃	SiO ₂	[Carlsson]
InP	B ₂ O ₃	SiO ₂	[Ciszek]
CuAgInSe ₂	B ₂ O ₃	SiO ₂	[Ciszek]
Si	CaCl ₂	SiO ₂	[Ravishankar]
<111> InP	B ₂ O ₃	p-BN	[Monberg]
<100> InP			[Matsumoto]
GaAs	B ₂ O ₃	p-BN	[Swiggard] [Hoshikawa]
GaAs	B ₂ O ₃	SiO ₂	[Althaus]
GaSe	B ₂ O ₃ (?)	SiO ₂	[Singh]
ZnSe	B ₂ O ₃	p-BN	[Okada]
Si	CaCl ₂ -SiO ₂ (0.95-0.05)	Graphite	[Lay]
Si-Ge	CaCl ₂	SiO ₂	[Bliss, Kadokura]
GaSb	LiCl-KCl eutectic	SiO ₂	[Garandet]
InSb	LiCl-KCl eutectic	SiO ₂	[Potard]
AlSb	LiCl-KCl eutectic	SiO ₂	[Pino]
CdZnTe	B ₂ O ₃	SiO ₂	[Zappettini]

PbSe [Metz] and of InAs and GaAs [Mullin]. The technique was later introduced by [Blum] as an improvement of the gradient freeze growth of GaP in p-BN crucibles in order to prevent phosphorus evaporation. Since that time the method has been used for numerous materials. Table 6.3 lists all the crystals grown under encapsulation. Some of these processes are in common industrial use (growth of GaP, InP or GaAs).

Two simultaneous papers first reported the observation of full encapsulation of the crystal by the encapsulant. [Hoshikawa], after encapsulated growth of GaAs in p-BN, found a B₂O₃ layer between the crucible and the crystal all along the pulling length. In some places where this layer was absent, grain nucleation occurred as a consequence of crystal-crucible interaction. [Garandet] also obtained a continuous layer of salt between the crystal and the crucible after the growth of GaSb in silica crucibles with the LiCl-KCl eutectic as encapsulant; the dislocation density in these crystals was practically zero. Full encapsulation of the crystal was also reported in the InP-B₂O₃-BN [Matsumoto], Si-CaF₂-C [Lay 1987 and personal communication] and Ge:Si-CaCl₂-SiO₂ [Kadokura] systems.

[Bourret] studied the full encapsulation of GaAs by B₂O₃ in p-BN which effectively prevents the occurrence of grain nucleation. It was found that, in order to get a homogeneous oxide layer, the B₂O₃ lumps must be mixed with the GaAs or that the crucible inner wall must be oxidized, prior to the growth experiment, by heating at 1100 °C under oxygen flow; the effect of the water content of the B₂O₃ is also discussed. The chemistry of the GaAs-B₂O₃ system in the presence of small amounts of water (B₂O₃ is highly hygroscopic) has been studied by [Nishio] and the general agreement is that a water content of about 100 ppm in the encapsulant is optimal in order to get the best crystal quality. Fully encapsulated GaAs Bridgman growth was also used by [Althaus] in p-BN and silica crucibles but did not work when a pyrolytic carbon layer was deposited on the silica. [Amon] has extensively employed pre-oxidized p-BN crucibles for the growth of GaAs.

All papers report on the great advantage associated with full encapsulation: the encapsulant layer which remains liquid far below the solidification point of the semiconductor prevents any contact with the crucible, dramatically decreasing dislocation density and grain nucleation. It was also reported that the encapsulant prevents twinning and further solid state allotropic reactions [Okada] and can purify the liquid from some impurities [Bourret]. Of course all the cited examples have verified that the pollution of the crystal by the encapsulant is negligible.

It is therefore highly desirable that the encapsulant not only prevents vaporization of the crystallized species but also that the sample–crucible–encapsulant system presents the full encapsulation phenomenon. [Duffar 1997-1] and co-workers carried out an experimental and theoretical research programme with the aim of better understanding how the full encapsulation phenomenon works when using halides or B_2O_3 .

6.2.2 LiCl–KCl Encapsulant for Antimonides

The fact that solid salt is found between the crystal and the crucible, when cold, is not in itself evidence that a liquid salt layer was present when the semiconductor was liquid or even when it solidified. It could be thought, for example, that the salt is all located above the liquid semiconductor during the process and subsequently flows down into the gap that is created during cooling down between the crucible and the sample because of the great difference between the expansion coefficients of silica and GaSb. In order to answer this question, it was first observed visually that, above the melting point, a LiCl–KCl film exists between the GaSb and the silica crucible. These observations confirmed that the liquid salt, when it melts, flows down between the crucible and the solid sample and stays as a stable liquid layer when the semiconductor is molten.

A further step has been to measure the thickness of the layer between the cold crystal and the silica after fully encapsulated crystal growth. Measurements of the layer thickness vs GaSb depth have been performed on crucibles 10 and 14 mm in diameter. Results are plotted in Figure 6.11; the error for the thickness was estimated to be $\pm 9\mu\text{m}$ in the worse cases. From 0 to 60 mm, the thickness decreases. Beyond 60 mm from the top of the GaSb, the thickness is constant and equal to the differential contraction between silica and GaSb from the melting point of GaSb to ambient, which depends on the diameter of the tube.

These observations and measurements suggest that a liquid film exists between the semiconductor and the crucible and that, after solidification of the semiconductor, the gap between the crucible and the crystal increases due to differential contraction and is continuously filled by liquid salt from the top. For depths greater than 60 mm, the original thickness is negligible compared to the differential contraction.

In order to understand why this layer exists, the energies associated with the two configurations shown in Figure 6.12 are compared. If A_{cyl} is the inner lateral area of the cylinder along the GaSb depth and A_{bot} the area of the bottom of the crucible, then:

$$E_a + E_b = (A_{\text{cyl}} + A_{\text{bot}})(\gamma_{\text{sc}} - \gamma_{\text{Ec}} - \gamma_{\text{Es}}), \quad (6.13)$$

with γ_{sc} , γ_{Ec} and γ_{Es} the liquid–semiconductor–crucible, encapsulant–crucible and encapsulant–liquid–semiconductor surface energies, respectively. This can also be written, taking into account the Young–Dupré equation (see Chapter 1), as:

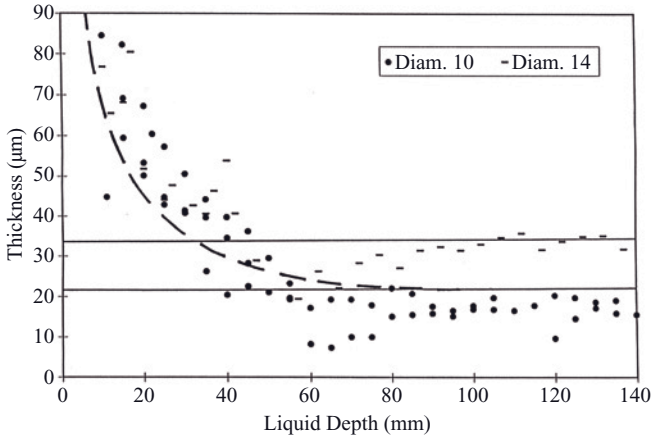


Figure 6.11 Thickness of the salt layer vs depth of GaSb melt, for several 10-mm and 14-mm diameter tubes. Lines correspond to the differential contraction, from 706 °C to ambient, of GaSb vs silica for both diameters. The broken line corresponds to Equation (6.18) for a diameter of 10 mm and a growth angle of 20° (Reprinted with permission from [Duffar 1997], copyright (1997) Elsevier Ltd).

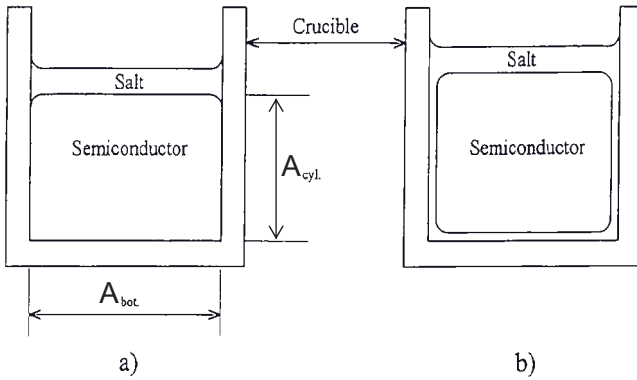


Figure 6.12 The two configurations discussed in the text: (a) regular encapsulation; (b) full encapsulation (Reprinted with permission from [Duffar 1997], copyright (1997) Elsevier Ltd).

$$E_a - E_b = (A_{cyl} + A_{bot})(\gamma_E \cos \theta_E - \gamma_s \cos \theta_s - \gamma_{Es}), \tag{6.14}$$

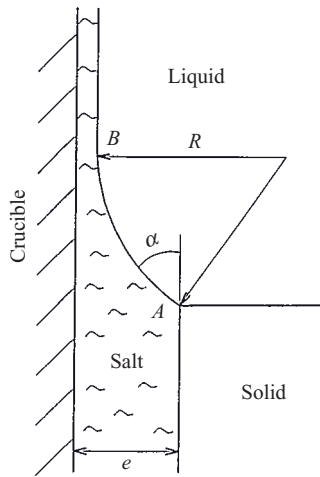
where θ_E and θ_s are the contact angles of the encapsulant and of the semiconductor on the crucible and γ_E and γ_s the surface tensions of the encapsulant and semiconductor. With the values of Table 6.4, for the system GaSb/LiCl-KCl/SiO₂:

$$\Delta\gamma = E_a - E_b / (A_{cyl} + A_{bot}) = 0.13 \pm 0.11 \text{ J m}^{-2}. \tag{6.15}$$

Then, configuration (a) has a greater energy than configuration (b) and the stable state of the system corresponds to the presence of a layer of salt between the molten semiconductor and the crucible.

Table 6.4 *Surface and wetting properties of the semiconductor/salt/crucible systems at the melting temperature of the semiconductor*

	Contact angle (°)	Reference		Surface tension (J m^{-2})	Reference
GaSb/SiO ₂	122 ± 2	[Harter]	GaSb	0.45 ± 0.03	[Harter]
LiCl–KCl/SiO ₂	0–10	[Duffar 1997-1]	LiCl–KCl	0.21 ± 0.05	[Ubbelohde]
GaAs/SiO ₂	120 ± 5	[Shetty 1990]	GaAs	0.4 ± 0.06	[Rupp]
B ₂ O ₃ /SiO ₂	10 ± 2	[Duffar 1997-1]	B ₂ O ₃	0.1	[Shipil'rain]
GaAs/BN	155 ± 5	[Shetty 1990]	GaSb/LiCl–KCl	0.31 ± 0.03	[Duffar 1997-1]
B ₂ O ₃ /BN	59 ± 2	[Duffar 1997-1]	GaAs/B ₂ O ₃	0.5	[Amashukeli]
GaAs/C	120 ± 5	[Shetty 1990]			
B ₂ O ₃ /C	79 ± 2	[Duffar 1997-1]			

**Figure 6.13** *Detail of the solid–liquid–salt triple line region during growth of a fully encapsulated semiconductor (Reprinted with permission from [Duffar 1997], copyright (1997) Elsevier Ltd).*

In order to estimate the thickness of the layer, e , as observed after growth, the following mechanism is suggested. As a consequence of the very good wetting of the salt on both GaSb and SiO₂, a thin wetting film of salt exists between the molten semiconductor and the crucible. During solidification, due to the growth angle α typical of semiconductors, the lateral surface of the crystal grows at an increased distance from the wall (see Figure 6.13) and, during cooling down, this gap increases again because of the differential contraction between the crucible and the sample.

[Joanny] and de Gennes studied the thickness of wetting films and found values less than 1 μm , even for strong Van der Waals or ionic interactions. The thickness of the initial layer is then supposed to be negligible. In order to estimate the gap generated by the solidification process, we will refer to Figure 6.13. For a first approximation, it will be supposed that the hydrostatic pressure does not change significantly along the little

meniscus created between the solid–liquid–salt triple line A and the point B where the liquid semiconductor is parallel to the crucible. In this case the meniscus is an arc of a circle and the Laplace equation gives:

$$R = \gamma_{\text{Es}} / \Delta\rho gh, \quad (6.16)$$

with R the radius of curvature (the second radius of curvature has the order of magnitude of the radius of the crucible and is negligible), $\Delta\rho$ the difference of density between GaSb and the salt ($6100 - 1600 = 4500 \text{ kg m}^{-3}$), g the acceleration due to gravity and h the GaSb depth. From Figure 6.13 we have:

$$e = R(1 - \cos \alpha) \quad (6.17)$$

or

$$e = \gamma_{\text{Es}}(1 - \cos \alpha) / \Delta\rho gh. \quad (6.18)$$

Taking into account the differential contraction between silica and GaSb from the melting point, T_m , to ambient, T_a , the thickness of the gap becomes

$$e = r_a(\beta_{\text{GaSb}} - \beta_{\text{SiO}_2})(T_m - T_a) + \gamma_{\text{Es}}(1 - \cos \alpha) / \Delta\rho gh, \quad (6.19)$$

with r_a the radius of the crucible. This result is shown by the dotted line on Figure 6.11. Of course the growth angle of GaSb immersed in the molten eutectic is not known and the value of 20° , typical of antimonides under inert gas, has been chosen for the calculations. Despite the approximations on which it is based, this rough expression gives a good estimate of the variation of the thickness of the layer.

6.2.3 B₂O₃ Encapsulant

For the growth of CdZnTe encapsulated by B₂O₃ in a silica crucible, [Zha] measured an encapsulant thickness of 100–200 μm . For GaAs in p-BN, [Bourret] reported an initial B₂O₃ layer 50 μm thick, but no value was measured after the growth experiment.

If Equation (6.15) is applied to the case of GaAs with B₂O₃, taking the numerical data from Table 6.4, the following results are obtained:

$$\Delta\gamma = -0.09 \pm 0.08 \text{ J m}^{-2}, \text{ for p-BN};$$

$$\Delta\gamma = -0.20 \pm 0.10 \text{ J m}^{-2}, \text{ for silica};$$

$$\Delta\gamma = -0.28 \pm 0.08 \text{ J m}^{-2}, \text{ for pyrolytic carbon on silica.}$$

These negative values indicate that a layer of B₂O₃ is not likely to exist between GaAs and any kind of crucible. Nevertheless, except in the case of carbon [Althaus], full encapsulation was observed. Despite the fact that the water content of the B₂O₃ [Bourret] or the stoichiometry of GaAs [Rupp] might have an effect on the surface properties and then increase the chance of full encapsulation, another explanation must be found.

The viscosity of B_2O_3 at the melting point of GaAs is 3.6 Pa s [Sabhapathy] (compare that of LiCl–KCl at 700 °C: 9.6×10^{-3} Pa s). The flow of a liquid under a pressure gradient between two plates gives the mean value of the velocity [Duffar 1997-1]:

$$\bar{v} = \frac{\rho_S - 2\rho_E}{12\mu_E} e^2. \quad (6.20)$$

For a layer 10 μm thick, this gives a mean velocity of 22.5 $\mu\text{m h}^{-1}$ (0.2 $\mu\text{m h}^{-1}$ for 1 μm , 2.2 mm h^{-1} for 100 μm). Then, for a typical growth process (~ 100 h), the encapsulation phenomenon must be as follows: the B_2O_3 melts before GaAs and wets the walls of the crucible. For silica the wetting is good, but for p-BN it is necessary to help it either by mixing the GaAs and B_2O_3 lumps or, better, by pre-oxidation of the crucible, as reported by several authors [Althaus, Amon, Bourret]. Then the GaAs melts and its hydrostatic pressure pushes the B_2O_3 layer upwards in order to get the configuration shown in Figure 6.12a. Because of the high viscosity of the layer, the steady state cannot be reached at the time scale of the growth process. For the case of pyrolytic carbon, the poor wetting of B_2O_3 prevents obtaining a homogeneous layer before melting the GaAs. During growth, increase of the gap thickness by the mechanism described for LiCl–KCl occurs but it is difficult to estimate the thickness of the initial layer of encapsulant.

[Zha] performed the same calculations for the CdZnTe– B_2O_3 – SiO_2 system and also obtained the result that the energy of the configuration in Figure 6.12a is lower than the energy of configuration in Figure 6.12b, and then the full encapsulation of CdTe by B_2O_3 cannot be spontaneous. Computing the maximum velocity for the encapsulant thickness of 100 μm that they measured, they found a value of 12 mm h^{-1} which is 10 times higher than the growth rate [Zappettini]. They conclude that some other mechanism must act in the case of B_2O_3 encapsulant in a silica crucible. They measured the chemical composition across the crucible–encapsulant interface and found a layer, presumably of borosilicate complexes, where the Si/O ratio decreases from the crucible to the encapsulant along the 200 μm of layer thickness (see Figure 6.14). It is therefore supposed that, in this case, the encapsulant reacts with the silica in order to form a borosilicate glass, the viscosity of which is higher than that of pure B_2O_3 .

6.2.4 Conclusion

The full encapsulation phenomenon occurring during encapsulated Bridgman growth of semiconductors can be explained as follows. For GaSb/LiCl–KCl, and presumably also the other halide encapsulants, the salt layer which prevents contact between the sample and the crucible corresponds to a stable energetic configuration due to the very good wetting of both the silica crucible and the semiconductor by the salt (contact angles practically zero). For B_2O_3 in silica or p-BN, with poorer wetting behaviour, an initial film of B_2O_3 or borosilicate must be established before the melting of the semiconductor and it is the high viscosity of this layer which prevents it from flowing upwards at the time scale of the growth process. During solidification, a mechanism specific to semiconductors increases the thickness of the encapsulant layer.

For the case of InP and GaP encapsulated by B_2O_3 , and for the other halide encapsulants, the lack of physical data prevents us from drawing a firm conclusion; surface

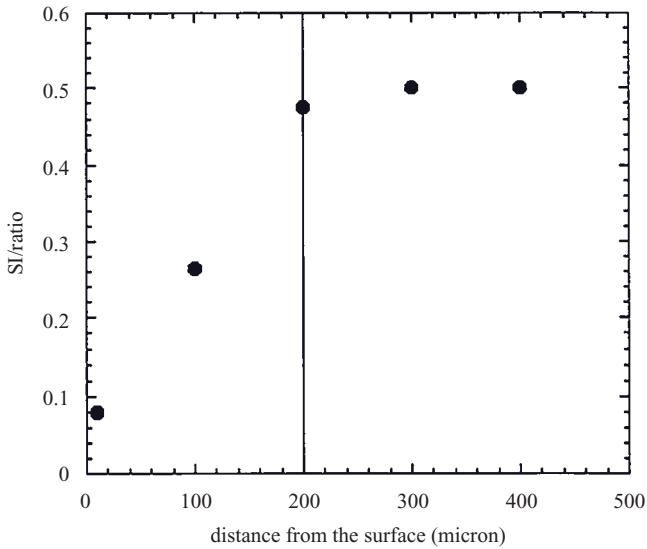


Figure 6.14 Chemical composition across the B_2O_3 - SiO_2 interface, after [Zha] (Reprinted with permission from [Duffar 1997-1], copyright (1997) Elsevier Ltd).

tension measurements would be of interest, as well as determination of layer thicknesses.

In their original paper, [Metz] and co-workers listed the properties necessary in order to select a good encapsulant for Czochralski growth:

- The vapour pressure of the encapsulant must be low at the melting point of the pulled material.
- The encapsulant must be less dense than the melt.
- The encapsulant must be insoluble in the liquid.
- The liquid must not contaminate and react with the encapsulant.

Considering the Bridgman techniques and the analysis of the phenomenon of full encapsulation, some more properties should be taken into account:

- The melting temperature and solid expansion coefficient of the encapsulant must be lower than for the crystal.
- The encapsulant must be chemically inert toward the crucible.
- The encapsulant must wet the crucible and the semiconductor as much as possible.
- A high viscosity of the encapsulant helps the full encapsulation.

6.3 The Dewetting Process: a Modified VB Technique

6.3.1 Introduction

Until the development of the dewetted Bridgman method [Duffar 1997-2], suppression of crystal–crucible contact during VB growth was ensured only by the encapsulated

Bridgman growth of semiconductors (section 6.2). In 1973, a peculiar phenomenon was observed by [Witt 1975] on the surface of InSb crystals grown from the melt in space, characterized by the absence of contact between the crystal and the inner walls of the container. The surface appearance of the detached parts was markedly different from that of the inner crucible walls. Obviously this phenomenon resulted from the appearance of a gap between the growing crystal and the crucible walls, which could not be explained by thermal contraction only. Removal of the crystal–crucible contact allows elimination of the adverse consequences resulting from the use of a crucible, such as thermal interface curvature, crystal–crucible adhesion and spurious nucleation on the walls. Hence, the major interest of this phenomenon is the drastic reduction of dislocations and other structural defects within the detached parts. The interpretation of this result by [Duffar 1997-2] is based on the assumed existence of a liquid meniscus separating the crystal from the crucible. Figure 6.15 shows a dewetted VB configuration involving the simultaneous presence of a liquid meniscus and a gap.

In normal terrestrial gravity, the dewetting has been achieved by counterbalancing the melt column hydrostatic pressure with the help of gas pressures applied at the hot (p_h) and cold (p_c) parts of the sample. This method almost reproduces the effects of microgravity. According to the macro-roughness or smoothness of the crucible walls, Duffar and co-workers have developed different methods to obtain effective dewetting in normal gravity [Duffar 2000, Duffar 2001-1].

The dewetted VB method offers an excellent compromise because it combines the advantages of the classical VB method with those of the capillary techniques (such as the Czochralski and floating zone techniques) without suffering from their main drawbacks. Hence, a low temperature gradient (a few degrees per centimetre) can be applied and both the shape and the size of the crystal can be controlled. Several III–V and II–VI crystals have been grown by this technique with a crystalline quality comparable to that of other capillary techniques (section 6.3.3).

Our approach in this review is to carry out a comprehensive analysis of the published experimental results that demonstrate the occurrence of dewetting and compare them to the proposed theoretical models. Strictly speaking, the terms ‘detached solidification’, ‘dewetted growth’, ‘detachment’ or ‘dewetting’ refer to a common and identical physical phenomenon that is defined and applied according to the following criteria:

- The materials studied are semiconductors: pure, doped or compounds.
- The growth technique is VB and its related techniques such as the Bridgman–Stockbarger and the Gradient Freeze.
- There must be a narrow and constant gap a few to tens of micrometres wide and several millimetres or centimetres long.
- The crystal surface morphology must differ from that of the crucible walls.

These criteria mean that this work does not include the study of voids, bubbles or other specific contactless morphologies, or other materials such as metals.

6.3.2 Dewetting in Microgravity

An exhaustive review of detached solidification in microgravity was published by [Wilcox 1998]. A large number of experimental results are listed and classified with respect to the

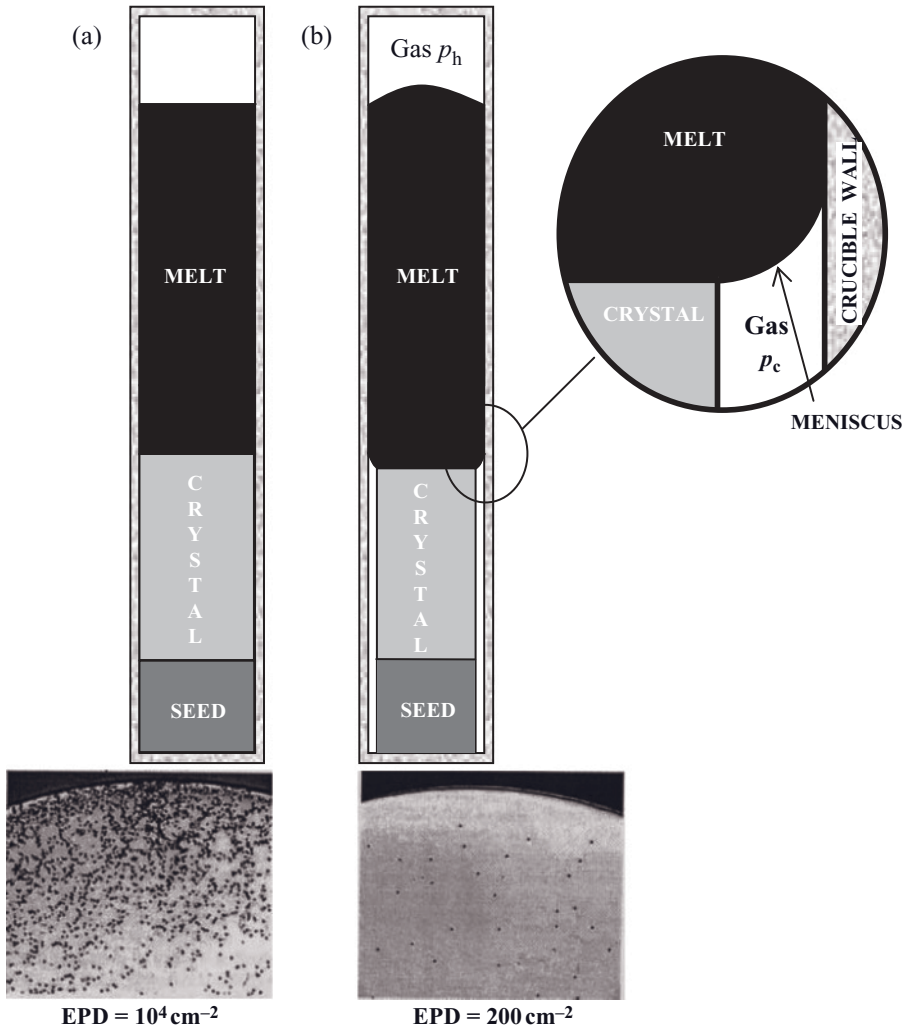


Figure 6.15 Comparison between a classical VB configuration (a) and one based on dewetting (b) requiring the coexistence of a liquid meniscus and a gap. Etched Ge slices show the dramatic decrease of the dislocation density by two orders of magnitude in a detached crystal [Schweizer 2002-1].

observation of reduced contact with ampoule wall (under its various surface shapes: voids, bubbles, necking, dewetting, growth morphology, gap width, etc.) and the influence of the detachment on crystallographic perfection and compositional homogeneity. [Duffar 2004-2] also published a general review that includes the study of the crystal–crucible adhesion, the dewetting of III–V and II–VI materials and transport and segregation phenomena under microgravity.

When dewetting has occurred, the existence of the gap is clearly proved after solidification by the easy removal of the crystals from the crucible. Unlike the corresponding

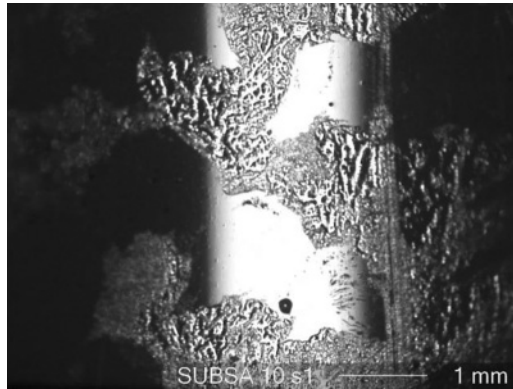


Figure 6.16 Surface of an InSb:Te ingot solidified on board the International Space Station during the SUBSA mission: the ridge pattern is easily identifiable by the valleys formed on the surface, indicating local detachment. In contrast, the shiny smooth surface indicates places where the crystal was in contact with the crucible wall [Ostrogorsky].

terrestrial samples, the removal of the microgravity solidified material was easy. Even a gap thickness of a few micrometres can provide this result. Unfortunately, there is a lack of quantitative measurements of surface roughness for microgravity crystals. As the matter stands, the occurrence of dewetting is validated by the observation of a constant gap width and the decrease of crystal defects (dislocation density).

Most of the semiconductor crystals grown under microgravity conditions were characterized by the presence of microscopic irregularities, known as ridges, when they grew partially detached from rough or smooth crucibles. According to [Witt 1975], the phenomenon of ridge formation was first observed on the surface of crystals grown under a confined geometry on board Skylab III. From the analysis of crystals grown on board Skylab IV [Witt 1978] they concluded that ridges are not the result of anomalous solidification. Surface ridges appear when the crystal diameter increases and approaches the value of the internal diameter of the ampoule. Their dimensions are typically tens of micrometres in width to hundreds in length. This surface feature might be formed on the melt prior to solidification, and reflects the morphological characteristics of the melt surface in the vicinity of the growth interface. Yet the explanation of ridge formation is still unclear. A direct consequence of a network of ridges on crystal surfaces is a definite rough aspect. Figure 6.16 shows a typical ridge pattern on a crystal surface.

Furthermore, peripheral faceting has also been observed on the surface of space-grown crystals (Figure 6.17) and, commonly, in nonconfined growth conditions such as in the Czochralski technique. Faceted free surfaces changed the crystal shape, and result from anisotropy effects due to the polycrystalline structure of these samples. The presence of ridges and facets is obviously an indication of contactless growth conditions. It is considered that the ridges result from a ‘partial’ dewetting because in this case the detachment is local.

[Duhanian] and co-workers have studied the effect of the crystal–crucible interactions leading to dewetting during the LMS-AGHF-ESA8 mission on board Spacelab. A pseudo-binary GaSb–InSb semiconductor crystal was grown in a crucible consisting of two

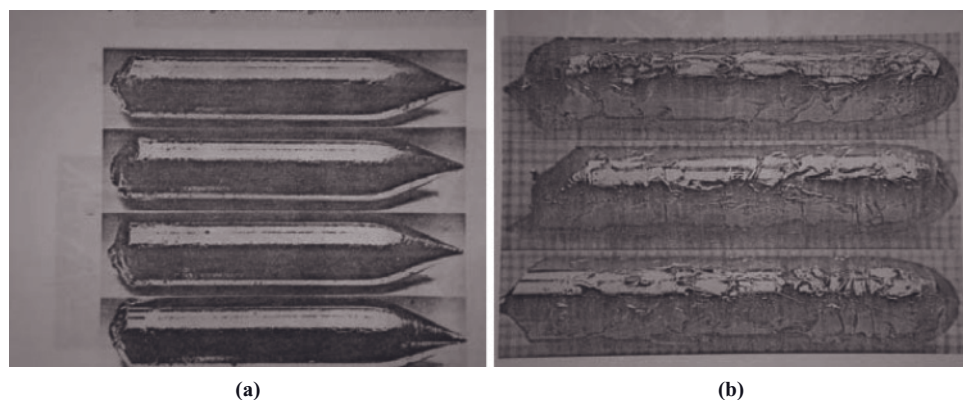


Figure 6.17 The growth of GaSb under microgravity conditions: (a) ground samples; (b) space samples (Reprinted with permission from [Lendvay], copyright (1985) Elsevier Ltd). The surface of the space samples shows ridges, proving the occurrence of local detachment.

different parts, one made from silica and the other from BN. The crystal surface shows ridges and facets on the BN side (Figure 6.18). The points to be emphasized here are the influence of the melt contact angle and the first quantification of a gap value that is constant for a length of several centimetres due to the dewetting in microgravity. The 70- μm gap is remarkably constant in the BN part. The contact angle of the GaSb–InSb melt is higher on BN than on silica, respectively 135° and 120° [Harter]. Dewetting occurred obviously only within the BN crucible. Therefore, a higher value of the melt contact angle enhances the occurrence of dewetting. The dewetting is said to be total, in contrast to the previous partial dewetting, when a constant gap is measured along several centimetres. The final value of the gap has to be corrected by the differential thermal expansion between the solidifying melt and the crucible.

Duffar and co-workers have widely studied the effect of a macro-roughness crucible. They obtained remarkable results for three microgravity experiments on the solidification of GaInSb alloys in machined rough crucibles on board the TEXUS 31 and 32, Spacelab D2 and EURECA missions [Duffar 1995, Duffar 1996, Duffar 1998]. The profile of the inner wall has a sawtooth shape, leading to a wavy profile of the crystal surface. Figure 6.19 shows that sharp roughness leads to the dewetting of two GaSb samples. The structure of both samples is initially polycrystalline and they end up as single crystals. The decrease in number of grains can be explained by avoiding stresses and nucleation in the peripheral regions of the growing crystal. Partial wall contact, at the end of growth, led to the nucleation of secondary grains or twins at the contact region.

In many microgravity experiments, the crystal surfaces are characterized by a dark and dull layer that is assumed to be oxide. Indeed, the usual long storage period of the ampoule before the flight and its subsequent outgassing can cause the formation of oxides. Hence, chemical pollution in the growth environment is suspected to participate in microgravity dewetting.

Dewetting never occurs if the melt undergoes overpressure by a spring within a closed crucible. Neither the pressure difference nor the magnitude of the growth rate has an effect on the dewetting phenomenon in microgravity [Duffar 2001-2].

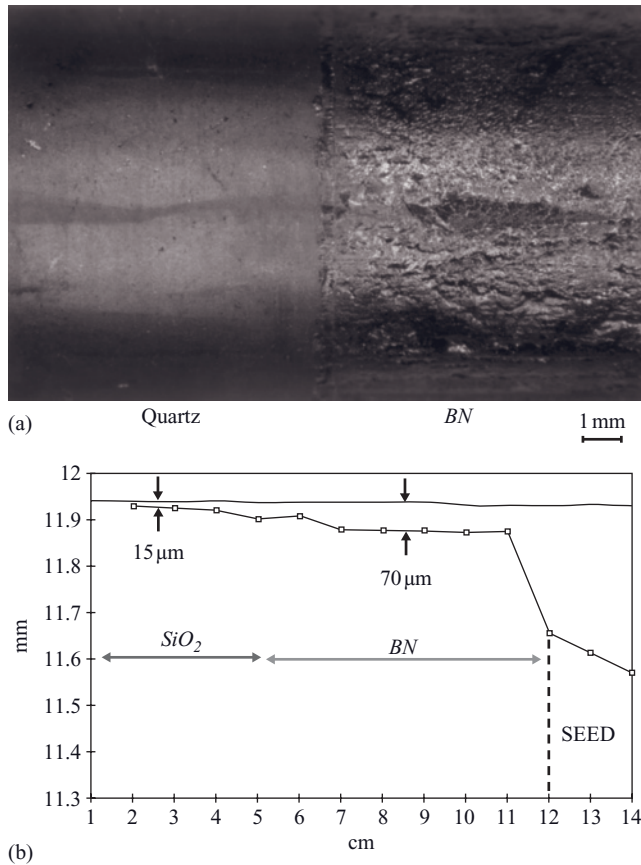


Figure 6.18 (a) Surface morphology of a GaSb–InSb polycrystal grown during the LMS-AGHF-ESAB mission (Reprinted with permission from [Duhanian], copyright (1997) Springer Science + Business Media). The crucible is made up of two parts: SiO₂ and BN. (b) Corresponding measurement of the surface profile: a constant gap 70 μm thick runs for 4 cm in the BN part of the crucible.

To conclude, the main identified parameters that lead to dewetting under microgravity conditions are crucible roughness, the crucible material, the wetting properties of the melt and chemical pollution. Apparently the roughness profile should be sharp, the crucible material nonadherent and the contact angle of the melt on the crucible high. As dewetting was unambiguously observed only for semiconductor growth, it is also expected that the growth angle, which is large for these materials, participates in the phenomenon. It is also important to underline that the dewetting is intrinsically stable, with the formation of a constant gap several centimetres long.

6.3.3 Dewetting in Normal Gravity

Even though the first observations under microgravity were made in 1973, effective reproduction of the dewetted growth on the Earth's surface started more recently, in the

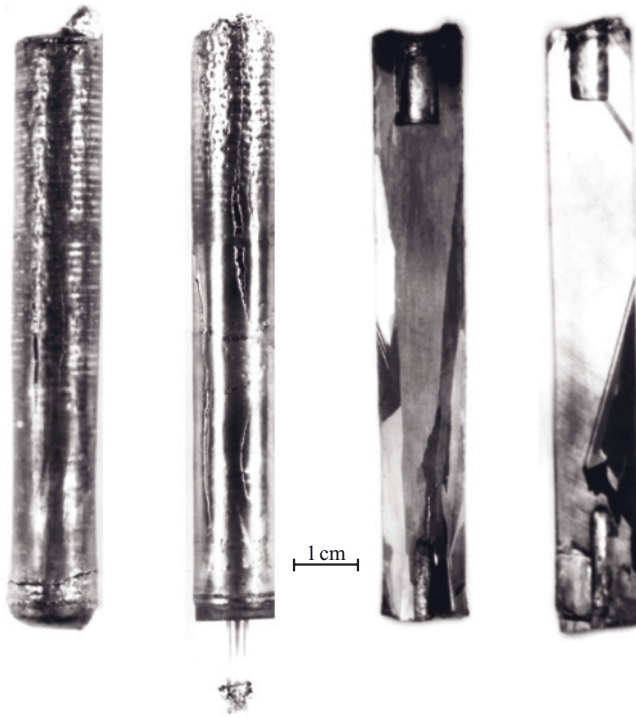


Figure 6.19 View of two GaSb EURECA samples (left) and corresponding metallographic analysis (right) (Reprinted with permission from [Duffar 1995], copyright (1995) Elsevier Ltd).

early 1990s. Tables 6.5–6.8 summarize the results of the published ground experiments. These tables are set out in accordance with the different operating parameters.

On the ground, the aim is to counterbalance the hydrostatic pressure due to the melt column in order to artificially reproduce the microgravity condition. This hinders the liquid–crucible contact at the level of the solid–liquid interface and favours dewetting.

The first method consists of applying a pressure difference with the help of an accurate external controller that is connected to the two closed gas volumes at the ends of the sample (Figure 6.20). The second method is similar, but has a more sophisticated external differential pressure system consisting of differential and absolute pressure gauges with a vacuum/backfilling gas system. The third method aims to manipulate the thermal field within the furnace and the ampoule in order to modify the pressure in one closed gas volume according to the ideal gas law. The liquid is pushed away from the wall when the temperature is decreased in the hotter part or increased in the colder part. Controlling the pressure difference across the meniscus is a very effective way to produce the dewetting under terrestrial gravity.

The existence of the liquid meniscus remained hypothetical till the dedicated experiments performed by Sylla. Closed ampoules containing antimonide samples and argon gas were introduced into a mirror furnace and dewetting was controlled by an additional furnace that increased the pressure at the cold part (see Figure 6.20c). A viewing window

Table 6.5 Dewetted crystal growth experiments in normal gravity for Ge and Ge-rich alloys

Feed material Seed crystal	Crucible Fill atmosphere	Crystal and feed dimensions	Method and growth rate Thermal conditions	Furnace	Results: dewetted length (<i>l</i>), gap thickness (<i>e</i>) and surface morphology	Crystallinity and relevant observations	Reference
Ge:Ga			VB	Monoellipsoid mirror furnace Bulb moved toward the ellipse center	<i>l</i> = 27 mm <i>e</i> = 30 μm Separated narrow ridges in contact with wall (~10 μm wide)	Dewetting obtained with 0T Rapid motion of particles on the top and wave-like motion of free surface during growth (3T)	[Szofran]
Ge:Ga 8.2 × 10 ¹⁸ at/cm ³ <111> Ge	Silica glass ampoule 600mbar Ar	Ø = 9 mm <i>L</i> = 41 mm	VB 0.5 mm/min <i>G</i> ≈ 100K/cm	Monoellipsoid mirror furnace Bulb moved 2 mm out of focus	After 7 mm attached growth: <i>l</i> = 27 mm 10 ≤ <i>e</i> < 80 μm Small bridges in contact with wall (tens of μm in width and hundreds in length)	No influence of dewetting on axial macrosegregation EPD in dewetted area is 10 times lower compared to attached areas	[Dold]
Ge:Ga ≈ 8 × 10 ¹⁸ at/cm ³ (111) Ge	Closed-bottom and open p-BN sealed in silica glass ampoule Ar containing 2% H ₂ or vacuum	<i>L</i> = 45–60 mm <i>L</i> _{seed} ≈ 20 mm Ø _{seed} = 12 mm	VB translation-free 5 mm/h <i>G</i> = 20–25 K/cm	Universal multizone crystallizator (UMC)	<i>e</i> ≈ 10 μm Small isolated islands 200 μm grew attached to the wall Attached growth for open-bottom ampoules	No influence of dewetting on axial macrosegregation EPD is reduced by more than two orders of magnitude in dewetted areas	[Schweizer 2002-1]
(111) Ge	Closed and open-bottom p-BN containers sealed in silica glass ampoule Ar containing 2% H ₂ or vacuum (2 × 10 ⁻⁶ mbar)	Ø = 12 mm <i>L</i> = 45–60 mm <i>L</i> _{seed} ≈ 20 mm	Translating 5 mm/h <i>G</i> = 30 K/cm	Seven zone vacuum (VF)	A few μm < <i>e</i> < 50 μm Observation of <i>e</i> fluctuations on one completely dewetted ingot Strong surface striations.	Axial spacing of striations and their amplitude increase along the dewetted part: 0.4 mm up to 3 mm and from 1–2 μm to 7–8 μm respectively.	[Schweizer 2002-2]
(111) Ge:Ga ≈ 7 × 10 ¹⁸ at. cm ³	Ar containing 2% H ₂ or vacuum (2 × 10 ⁻⁶ mbar)		Translation-free 5 mm/h <i>G</i> = 20 K/cm	24-zone UMC	A few μm < <i>e</i> < 50 μm Dewetted regions up to 100–200 μm on attached-grown crystals in open- bottom p-BN tubes		

Ge:Sb up to $1.5 \times 10^{20} \text{cm}^{-3}$	Porous graphite with treated surfaces: turned, polished and oxidized Flowing Ar: slow and fast rates (0.095 and 1.90l/min) 1.35 atm Ar pressure	$\varnothing = 38.1 \text{ mm}$ $L = 58 \text{ mm}$ Two seed geometries: $5 \times 5 \times 15 \text{ mm}^3$ prismatic, and cylindrical with the same \varnothing as crystal	VB modified: Use of a baffle heater to supply heat axially over the growth interface (AHP) 3–20mm/h $G = ?$	Three heating zones. Axial Heat Processing technique (AHP).	Conical geometry: all crystals grew attached Cylindrical: Fast Ar flow rates: all crystals grew attached Slow flow rates and Ar pressure: complete detached growth whenever GeO_2 film is formed on Ge melt. Gap size is constant	$\Delta P = 0$ because of graphite porosity GeO_2 film is off-white and deposited inside crucibles Higher growth velocity leads to detached growth (narrower gap) Melt/crucible interaction: formation of Ge–C mechanical bonding on roughened graphite surfaces for attached growth	[Balicki]
Single crystal Ge:Ga	Smooth or sandblasted silica: uncoated, graphite or BN coated p-BN tube fitted inside silica Annealed at 800–900°C under dynamic vacuum Backfilled with ~100mbar of 4% H_2 and 96% Ar	$\varnothing = 12 \text{ mm}$ $L = 75 \text{ mm}$	VB. Use of two chambers separated by melt height. Outer chamber connected to a ΔP gauge and a vacuum/ backfilling gas system. Inner (crucible) to ΔP and absolute pressure gauge 5 mm/h (solidification rate 7.5 mm/h) $G = 15^\circ\text{C}/\text{cm}$ at 950°C	Two heating zones with active control pressure.	Silica: occasionally partly dewetted for $\Delta P =$ a negative few to -0 mbar with $e = 0$ up to $60 \mu\text{m}$ Graphitized: attached for $\Delta P \sim 0$ – 30 mbar and $e = 0$ BN coating: attached for $\Delta P \sim 0$ – 45 mbar and $e = 0$ p-BN: Attached for $\Delta P < -(40$ – $50)$ mbar and $e = 0$ Dewetted for $\Delta P < -(30$ – $40)$ to a few mbar and e up to $15 \mu\text{m}$ Mostly dewetted for $\Delta P < -(15$ – $1)$ mbar and $e = 0$ to 10 – $60 \mu\text{m}$ Smooth and shiny surface with presence of microfacets for dewetted portions	Dewetting is successful in a wide range of negative ΔP with p-BN crucibles Melt run-down is observed at the growth beginning in ampoules with $\theta + \alpha < 180^\circ$ and initial e between 60 and $100 \mu\text{m}$ Dewetted growth is possible with an appropriate growth procedure for BN-coated silica crucibles BN coating is not optimized Good agreement between experimental results and stability analysis based on Duffar <i>et al.</i> model.	[Palosz]

Table 6.5 (continued)

Feed material Seed crystal	Crucible Fill atmosphere	Crystal and feed dimensions	Method and growth rate Thermal conditions	Furnace	Results: dewetted length (l), gap thickness (e) and surface morphology	Crystallinity and relevant observations	Reference
Polycrystalline Ge:Ga 10^{18} cm^{-3} Undoped (111) Ge	Open-top p-BN crucibles sealed in silica ampoule Conical geometry transition from round seed to cylindrical feed Ar: $3 \times 10^4 \text{ Pa}$ and $1 \times 10^4 \text{ Pa}$	$\text{Ø} = 2 \text{ in}$ $L = 45\text{--}60 \text{ mm}$	VGF. Three different temperature profiles to obtain small positive ΔP values 2.8 mm/h G ?	Seven heater	Slight overpressure in the gap (T_{top} decreased): Partial dewetting on the seed Oval-shaped areas caused by formation of bubbles. Almost the whole conical part grew dewetted Large dewetted areas of several cm^2 in the cylindrical part with $e \sim 10\text{--}80 \mu\text{m}$ separated by elevated islands Initial $\Delta P \geq P_{\text{hyd}}$ (T_{bottom} increased): dewetting occurs on seed with e of up to $300 \mu\text{m}$. Gap vanishing after a few mm.	s/l interface deflection is lower in case of dewetted growth leading to a decrease of thermal shear stress Dewetting is unstable in the region of changing crystal shape	[Pätzold]
$\text{Ge}_{1-x}\text{Si}_x$ ($0 < x < 12$) Ge	Closed-bottom and open p-BN sealed in silica glass ampoule 600 mbar Ar containing 2% H_2	$\text{Ø} = 12 \text{ mm}$ $L = 65\text{--}80 \text{ mm}$ $L_{\text{seed}} \approx 20 \text{ mm}$	VB with pressure difference (ΔP) controlled by decreasing T above the melt 0.2 and $0.3 \mu\text{m/s}$ $G \approx 35 \text{ K/cm}$	Resistively heated furnace with seven zone heaters	One sample is considered completely dewetted ($l \sim 70 \mu\text{m}$) Shininess and partial roughness of dewetted surface A few areas ($< 1 \text{ mm}^2$) with attachment Dewetting occurs at the end of growth for open-bottom ampoules	Effectiveness of ΔP control All dewetted or partially dewetted crystals slid out of the p-BN ampoules	[Volz]

EPD, etch pit density; VB, vertical Bridgman.

Table 6.6 Dewetted crystal growth experiments on the ground for antimonides

Feed material Seed crystal	Crucible Fill atmosphere	Crystal and feed dimensions	Method and growth rate Thermal conditions	Furnace	Results: dewetted length (l), gap thickness (e) and surface morphology	Crystallinity and relevant observations	Reference
InSb	Silica	$\text{Ø} = 14 \text{ mm}$	Bridgman Stockbarger 8 mm/h G between 5 °C/cm and ~100 °C/cm	Two heating zones	$e = ?$; $l = 10 \text{ mm}$ Ridges, roughness	Oxygen contamination has been identified.	[Duffar 2000]
GaSb Single crystal seed	Pure silica ampoule filled with 10–30 kPa Ar	$L = 100 \text{ mm}$ $\text{Ø} = 14 \text{ mm}$ $L_{\text{seed}} \sim 30\text{--}40 \text{ mm}$	VB with a third furnace heating an inert gas volume at the bottom: 150–200 °C 3 $\mu\text{m/s}$ 10 °C/h	Three heating zones with external pressure controller	$e \leq 10 \mu\text{m}$ $l = 40 \text{ mm}$ Dewetted surfaces are shiny	Neither twins nor grains observed (single crystals) Dislocation density of grown crystals is equal to that of seed. $= 10^4 \text{ cm}^{-2}$ Grain nucleation for melt run- down and air introduction	[Duffar 2001-1]

Table 6.6 (continued)

Feed material Seed crystal	Crucible Fill atmosphere	Crystal and feed dimensions	Method and growth rate Thermal conditions	Furnace	Results: dewetted length (<i>l</i>), gap thickness (<i>e</i>) and surface morphology	Crystallinity and relevant observations	Reference
Polycrystalline InSb:Ga 16 g containing 1 ppm C and O, and 0.1% Ga.	Fused silica Coated with hexagonal BN Uncoated Filled with 10, 20, 40 or 80 kPa of Ar + 10% H ₂ .	Ø = 9 mm with conical bottom <i>L</i> = 4–6 cm	VB 5 and 10 mm/h <i>G</i> ~20–30 K/cm depending on temperature settings	Two-zone VB furnace Temperature profile resulting from variations of spacing between heating wire turns	Uncoated: completely attached. Surfaces smooth and shiny with gas bubble indentations Coated: <i>e</i> = 8 µm, 20% of surface totally dewetted. Dull areas dewetted with some tiny facets and steps, no bubble indentations Neither small attached areas nor striations have been observed	Attached ingots partially or entirely covered with rough brown or black surface (presumably oxide, Ga ₂ O ₃) Best results with 20 kPa of fill atm. and convex freezing interface Freezing rates induced a small difference	[Wang 2004]

Table 6.7 Dewetted crystal growth experiments on the ground for cadmium telluride.

Feed material Seed crystal	Crucible Fill atmosphere	Crystal and feed dimensions	Method and growth rate Thermal conditions	Furnace	Results: dewetted length (l), gap thickness (e) and surface morphology	Crystallinity and relevant observations	References
CdTe Polycrystalline	Piece of pure Cd as a vapor counter-pressure to P_{hyd} of melt.	$\varnothing =$ 14 mm $L = ?$	VB with a third furnace 1.8 to 3 mm/h 2 °C/h during 37 h	Three heating zones with active control pressure	Dewetting is successful in the first phase of growth process.	Single crystals have been grown on polycrystalline or twinned seeds. Interface shape is convex during dewetted growth. Concave curvature initiates its interruption.	[Duffar, 2004-1] [Fiederle, 2004-2]
CdTe:Ge Single crystal			Idem 0.7 °C/h, then 5 °C/h and finally 100 °C/h: 47 h		Non constant gap from 10 to 60 μm (maximum in the beginning). Gap disappears at 25–30 mm from the seed.	Better crystallinity and high resistivity are obtained in dewetted areas. Absence of deposition on the ampoule walls.	
CdTe 80g single crystal with twins			0.7 °C/h and 5 °C/h: total 173 h		Twins and large-scale inclusions on attached areas.		

Table 6.8 Dewetted crystal growth experiments on the ground for nonsemiconductor materials

Feed material Seed crystal	Crucible Fill atmosphere	Crystal and feed dimensions	Method and growth rate Thermal conditions	Furnace	Results: dewetted length (<i>l</i>), gap thickness (<i>e</i>) and surface morphology	Miscellaneous and relevant observations	Reference
Water Deionized or Doubly distilled or HPLC	Uncoated and clean Pyrex ($\theta=0^\circ$) Coated with silicone oil ($\theta=80^\circ$), or Teflon ($\theta = 121^\circ$) or Teflon with powder ($\theta = 146^\circ$) All bottom sides are closed Air or CO ₂ is bubbled through the water	$\varnothing = 5, 10$ and 20mm $L = 12$ cm Bottom immersed 5–10 cm into cold bath	VB apparatus From 0.4 to 100mm/h Sometimes ampoule rotated slowly up to 10 rpm $G \sim 0.5^\circ\text{C}/\text{mm}$	Nichrome- wire around a silica tube and a refrigerated bath at the bottom	3 kinds of regular bubbles formed on the wall: Isolated gas bubbles uniformly distributed along the ampoule wall Long, narrow cylindrical gas tubes periodically formed around the periphery. Fraction of detached $\sim 60\%$ (air) Wider gas tubes with CO ₂ saturated water at 1 atm.: detachment is $\sim 85\%$ Wide gas tubes with a rough nonwetting coating. 95% detachment achieved	Gas bubbles and tubes do not propagate around the periphery of the freezing interface. They grow on the ampoule wall and not in the interior Freezing rate influences the interface shape and the convection Slow rotation decreases the transformation of gas bubbles to tubes	[Wang 2002-2]

HPLC, high-pressure liquid-chromatography.

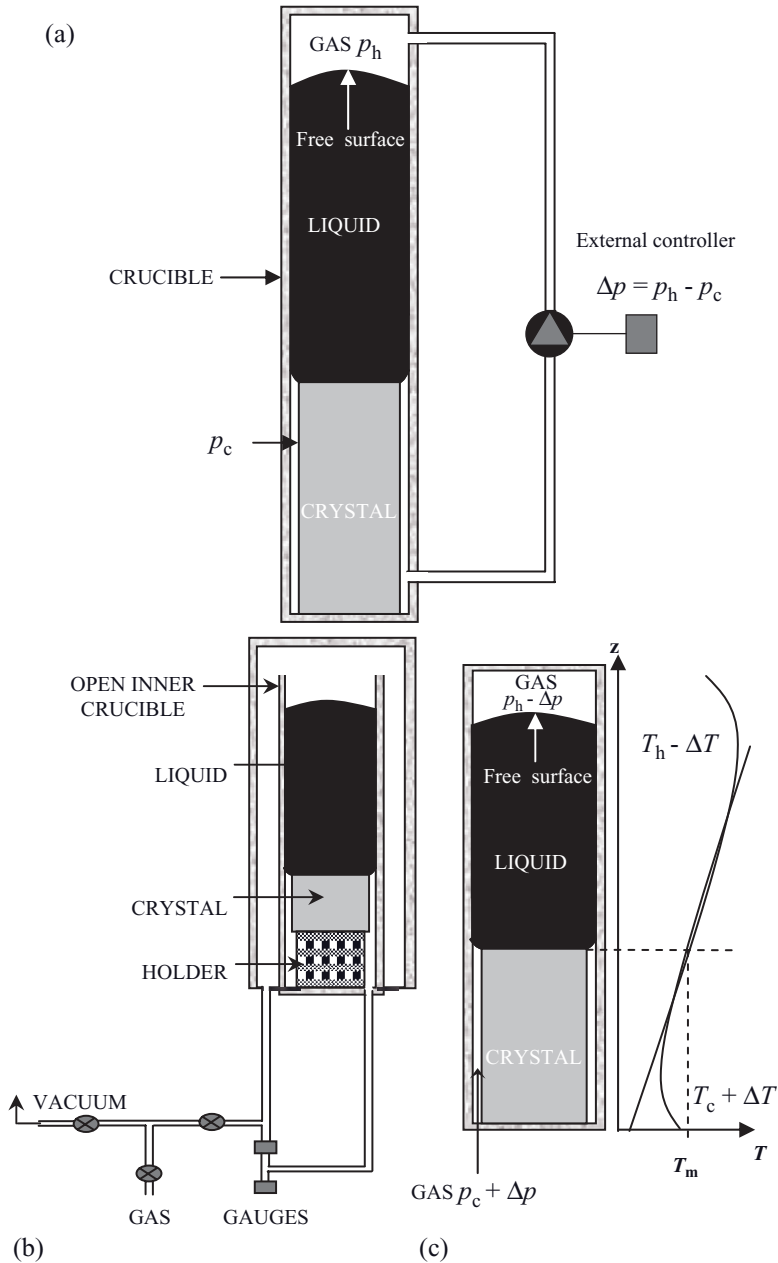


Figure 6.20 (a) VB configuration on the ground with different methods of controlling the pressure difference across the meniscus: (a) use of an external pressure controller [Duffar 2000]; (b) differential and absolute pressure gauges with a vacuum/backfilling gas system connected to both closed gas volumes separated by the melt [Palosz]; (c) manipulating the thermal field inside the furnace or the closed ampoule to decrease the hot pressure or increase the cold pressure [Duffar 2001-3].

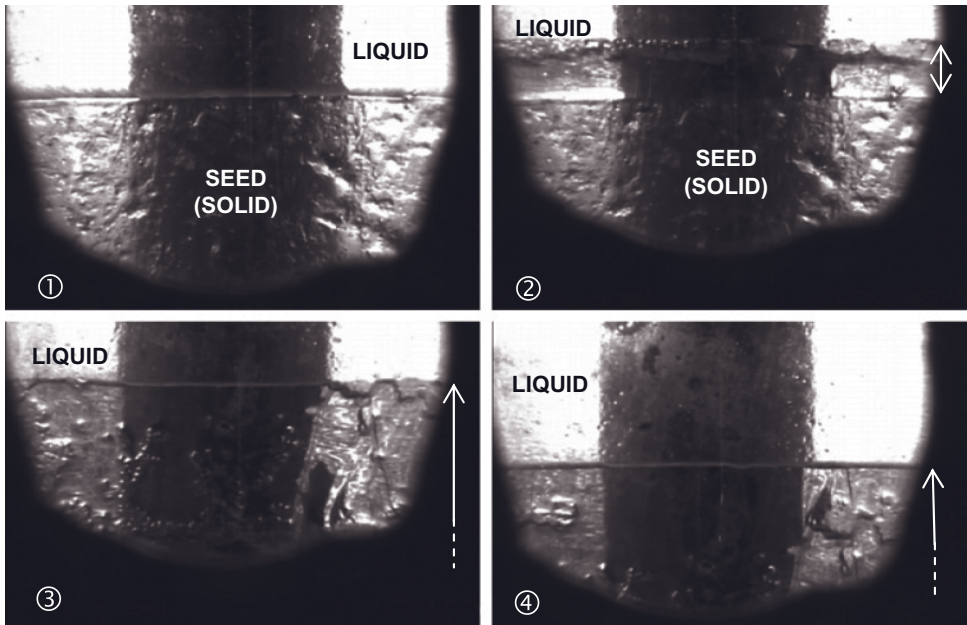


Figure 6.21 Video snapshots of the solid–liquid interface region during dewetted growth of GaSb in an ampoule filled with air [Sylla 2008-2]. 1, meniscus stabilization at the end of melting by an increase of the gas pressure at the cold side; 2, beginning of dewetted growth; 3 and 4, dewetted growth with a stable meniscus. White arrows show the dewetted solid surface of the ingot.

and video equipment enabled the solid–liquid interface region to be viewed throughout the melting and solidification phases [Sylla 2008-2]. This series of experiments made it possible to validate a number of hypotheses, including the existence of the liquid meniscus, as can be seen in Figure 6.21, and its control by manipulating the gas pressure in the ampoule.

A very important peculiarity of terrestrial dewetting is the self-stabilizing pressure difference: it was observed that, once the process has begun, it is no longer necessary to adjust the pressure difference. It appears that, as the hydrostatic pressure decreases when growth proceeds, the pressure at the bottom decreases, or the pressure at the top increases, in such a way that the liquid meniscus remains unchanged throughout growth. The mechanism is not yet totally understood, but rarely gas was observed passing upwards between the liquid and the crucible. Surprisingly, it looked like a thin gas layer rather than a gas bubble.

The main parameters that have been identified to enhance the occurrence of dewetting are described in the following sections.

6.3.3.1 Crucible Material and Wetting Properties of the Melt

It is well known from sessile drop measurements [Harter] that the values of the contact angle of the III–V, II–VI and Ge materials increase respectively with the following

crucible materials: SiO₂, C, BN and p-BN. Consequently most of the experiments carried out on the ground with the use of p-BN crucible material led to dewetting. Values of the apparent contact angle, θ_{app} , around 180° were measured by [Palosz] for Ge on p-BN. Single crystals of CdTe, Ge, Ge_{1-x}Si_x, GaSb and InSb were grown thanks to a total dewetting. It is therefore recommended to use a liquid/crucible material couple with a weak work of adhesion (W_a).

Another critical wetting parameter is the growth angle that corresponds to the contact angle of a melt on its own solid under dynamic growth conditions (see Chapter 1). The same conclusions can be drawn for the effect of the growth angle α , which must be larger than 0° (a condition satisfied by all semiconductor materials).

6.3.3.2 Value of the Applied Pressure Difference Across the Meniscus

[Palosz] and co-workers have successfully obtained dewetting by the method described in Figure 6.20b. Their results are impressive because they demonstrate in practice how the values of the pressure difference across the meniscus, Δp_m , influence the formation of a constant gap. These values are defined by the following expression:

$$\Delta p_m = p_h + \rho_l g H_m - p_c$$

with p_h and p_c the gas pressures in the hot and cold volumes, ρ_l the liquid density, g the acceleration due to gravity and H_m the height of the melt column. It seems that Δp_m should be of the order of a few millibars to stabilize the dewetted growth.

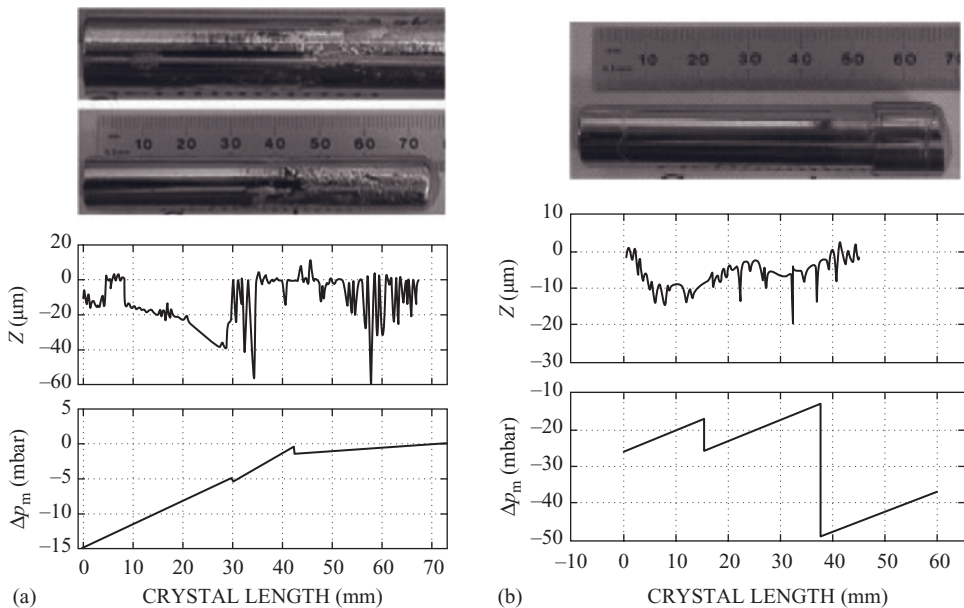


Figure 6.22 Ge:Ga crystals grown in a BN-coated silica crucible (a) and in p-BN sleeves (b). The corresponding measured surface profiles and applied pressure differences during growth are plotted (Reprinted with permission from [Palosz], copyright (2005) Elsevier Ltd).

6.3.3.3 *Sample and Growth Procedure*

Grown crystals vary in diameter from 9 mm to 50 mm. The successful dewetted growth of large single crystals proves its real potential for producing high-quality crystals [Pätzold]. Although larger crystal dimensions seem to be feasible, the geometrical shape of the seed and grown crystal is another factor influencing the steady state of dewetted growth. For the detached growth of 2" Ge crystals [Pätzold], a classical Bridgman crucible with seed well was used. The feed material consisted of an upper part, 2" in diameter, joined to the seed by a conical part. Large dewetted areas of several square centimetres were observed in the upper cylindrical part separated by elevated islands, whereas the seed was partially dewetted. As already mentioned, according to the authors the process seemed to be self-controlled. Dewetting was reported to be unstable in the region of changing crystal shape. In a similar way, for Sb-doped Ge [Balikci] studied the effect of conical and cylindrical geometry on the dewetting. All crystals grew attached to the conical crucibles, but the use of a cylindrical crucible led to completely dewetted growth with a specific growth atmosphere.

The growth procedure also determines the occurrence of dewetting. It has been shown that the seeding process is an essential step to start dewetting [Sylla 2008-2]. However, for the crystal growth of Ge:Ga dewetted growth was obtained when the seed was completely molten, whereas crystals grew attached if growth started on the seed/feed region [Palosz]. Melt run-down is also a problem to be overcome at the beginning, because it can hinder the dewetting from starting. Seed diameter is always less than crucible diameter and the initial gap should not be too large to avoid melt run-down. It is recommended not to exceed a 60 μm gap width [Sylla 2008-2].

Lastly Wang, Wilcox and Regel performed experiments on the freezing of water and studied the role of propagation of gas bubbles as a starting event in detached solidification [Wang 2002-2]. However, the observed gas bubbles and gas tubes did not propagate around the periphery of the freezing interface, so this phenomenon must be excluded as a likely mechanism for the initiation of detached solidification (especially for experiments without seeding procedure). In the case of a crystal initially stuck to the crucible it is believed rather that spontaneous detachment due to the stress caused by thermal contraction (see section 6.1.3) is at the origin of subsequent dewetting.

Finally, it seems that the dewetting does not require a seed. However, the use of a seed makes it easier to control the stability of the meniscus and the start of contactless growth.

6.3.3.4 *Growth Atmosphere and Pollution*

The growth atmosphere is a critical factor in the crystal growth process since its interaction with the solid and liquid phases influences the melt properties (wetting angle) and melt–crucible interactions, and the stoichiometry of grown crystals. All experiments require an inert growth atmosphere (except those involving stoichiometry control due to a volatile element for a compound semiconductor). Argon (Ar) with low hydrogen content (2–10%) is the gas commonly used to fill the quartz-glass ampoule just before sealing. The pressure level seems to be an important factor: the Ar pressure range is 10–80 kPa.

An interesting experimental study was performed by [Wang 2004]. The influence of operating conditions was determined to achieve detached solidification of InSb in their experimental set-up. The pressure of the forming gas (Ar-10% H₂) varied from 10 to

80 kPa. At under 10 kPa the ingot grew attached and had a totally rough surface. From 40 to 80 kPa, detachment was not conspicuous although some partially detached sections were observed. The best results were obtained at 20 kPa.

Purity of the growth atmosphere is another critical parameter. A number of terrestrial experiments have proved the involvement of oxygen activity in enhancing the dewetting process [Balikci, Duffar 2000, Sylla 2008-1]. Balikci *et al.* have grown Ge in graphite crucibles under various Ar atmosphere and gas flows. The gap width was about $10\mu\text{m}$ along the entire surface and can be attributed to nonadhesion phenomena, so that dewetting is not ascertained for these experiments. Anyhow they clearly reported nonadhesion (or dewetting) under oxidizing conditions and attachment under high Ar flow rate, when oxidation was unlikely to occur.

Sylla performed dedicated experiments on antimonide growth in order to study the effect of the gas on dewetting, with a series of atmospheres including air, regular polluted Ar, pure Ar, Ar + H_2 , purifying getters and vacuum [Sylla 2008-2]. It was unambiguously shown that any occurrence of dewetting is impossible under vacuum. The use of a reducing or very pure atmosphere always prevented dewetting in the GaSb– SiO_2 system. On the contrary, presence of small or important amounts of oxygen promoted dewetting. Surprisingly this was not the case for InSb– SiO_2 , for which dewetting was never obtained, whatever the conditions. In the same publication, a thermodynamic equilibrium analysis of the chemical compounds likely to exist in the quaternary Ga–Sb–Si–O and In–Sb–Si–O systems led to the conclusion that the Ga_2O_3 is stable above the melting point, whereas In_2O_3 is less stable and is likely to decompose a few degrees above the melting point. It is then argued that the Ga_2O_3 acts as a layer on the liquid meniscus with the effect of increasing the apparent growth angle and promoting dewetting, which cannot be the case for InSb (Figure 6.23). In this latter case, the quantity of dissolved oxygen X_{O} in the liquid

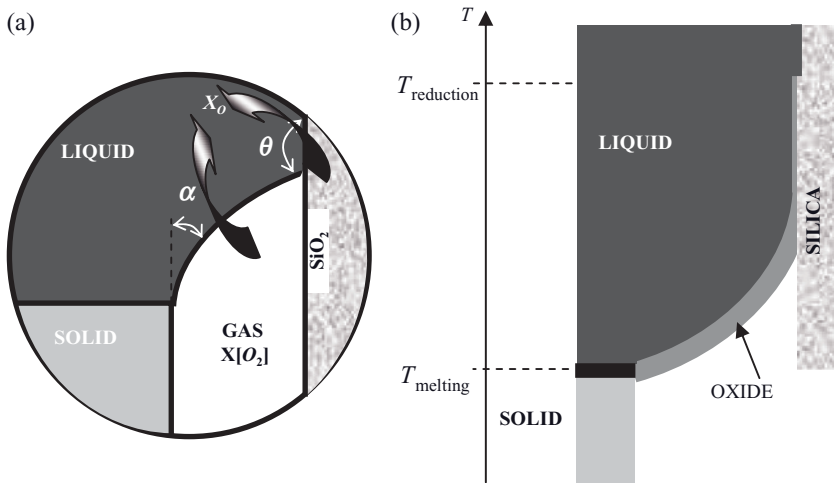


Figure 6.23 Schematic view of (a) the case of InSb where the In_2O_3 oxide is less stable above the melting point and oxygen is essentially dissolved in InSb and (b) the case of GaSb where the Ga_2O_3 oxide layer is more stable.

from the gas or from the silica crucible can increase the wettability of the liquid at the liquid/SiO₂ interface.

6.3.3.5 *Growth Velocity*

[Schweizer 2002-2] studied the stability of detached-grown Ge single crystals. One completely detached ingot was obtained. The measured profiles showed fluctuations of gap thickness, giving strong surface striations. These fluctuations can be explained by assuming different translation rates of the crucible–melt–gas and crystal–melt–gas tri-junctions. According to the authors, constant gap thickness and stable growth might be reached when the two velocities are equal.

However, [Sylla 2008-1] demonstrates by *in situ* observation that the growth velocity does not affect the occurrence of dewetting. Furthermore, a space experiment [Fiederle 2004-1] has also shown that a high growth velocity (almost quenching) leads to dewetting as well.

6.3.3.6 *Surface Morphology*

The surface morphology of Earth-grown crystals is similar to that of space-grown crystals. When detached growth occurs, the surface shows ridges and facets testifying the free growth of the melt. Figures 6.21 and 6.22 show facets and small bridges (equivalent to ridges) on dewetted surfaces.

6.3.3.7 *Interface Shape*

Dewetted parts of ingots have shown a convex interface (seen from the liquid) whereas the attached growth part is characterized by a concave interface on the ground [Chang, Fiederle 2004-2, Pätzold].

Dewetted growth of high-resistivity CdTe showed that dewetting was successful in the first phase of the growth process with a convex solid–liquid interface [Fiederle 2004-2]. Photoluminescence mapping revealed instability of the interface shape during growth. According to the authors, the concave curvature initiates the dewetting interruption.

The effect of dewetting on the deflection of the solid–liquid interface and the thermal shear stress has been studied for detached growth of 2" Ge crystals [Pätzold]. The interface in the attached-grown reference crystal is concave with a maximum deflection of 7.5% with respect to the radius of the seed. Detached seeding gave a flat or even slightly convex interface. For the grown crystals, the maximum deflection was 9.0% under attached conditions and 7.6% under detached conditions. The author performed a numerical simulation of these experiments with an ideal gap extending along the crystal–crucible boundary, the width of which was modelled with a value of 200 μm in the seed and 50 μm in the cylinder, in agreement with the experimental results. The numerical results were in good qualitative agreement with the experiments. Attached growth is characterized by a concave interface with relatively strong deflection. For dewetted growth, this deflection is lowered and at the edge of the seed, a transition to a convex-shaped interface occurs (an S shape).

On the basis of the analysis presented in section 6.1.1, [Epure 2008] performed a systematic study of the effect of the gap on the interface curvature. The dependence of the

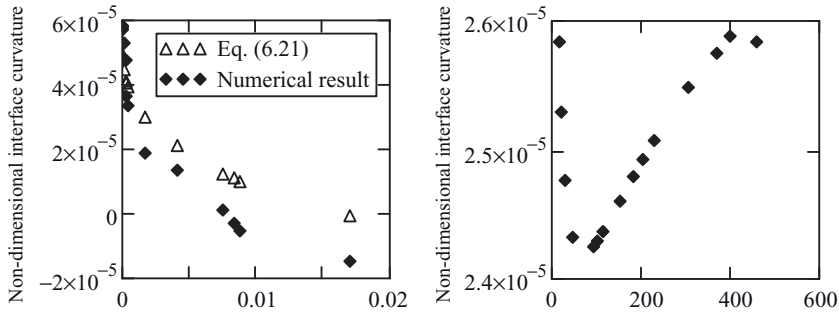


Figure 6.24 Nondimensional curvature of the solid–liquid interface α as function of the ratio of the surfaces of the gap and crystal (a) or of the ratio of thermal conductivities of the liquid and vapour (b) (Reprinted with permission from [Epure 2008], copyright (2008) Elsevier Ltd).

interface curvature on the gap thickness, crucible thickness, and on the liquid, solid and crucible thermal conductivities is studied analytically and compared with results obtained from numerical simulations using the finite element method. For the analytical study, the thermal conductivity of the gas in the gap is considered negligible compared to the other conductivities. The interface deflection varies as follows:

$$f = \frac{r_a}{5} \left[\frac{\lambda_l}{\lambda_s} \left(\frac{\lambda_s A_s + \lambda_c A_c}{\lambda_l (A_s + A_g) + \lambda_c A_c} \right) - 1 \right], \tag{6.21}$$

with A_s , A_g and A_c the surfaces of the solid, gap and crucible respectively. This formula is similar to Equation (6.3); the only difference is that now the surfaces of the liquid and the gap appear because the surface of the liquid is different from the surface of the solid, because of the existence of the crystal–crucible gap. The numerical analysis is in agreement with this simple expression and shows that the shape of the interface depends on the width of the gap (Figure 6.24a), the thickness of the crucible, and on the thermal conductivities of the liquid, solid, gas (Figure 6.24b) and crucible. As expected, the curvature of the interface decreases when the crystal–crucible gap increases. An interesting result is that, for a large enough gap, the curvature of the interface may be reversed.

If the latent heat release is taken into account, the interface curvature can be estimated by [Epure 2010]:

$$f = \frac{r_a}{5} \left[\frac{\lambda_l (\lambda_s A_s + \lambda_c A_c) - \lambda_s [\lambda_l (A_s + A_g) + \lambda_c A_c]}{\lambda_s [\lambda_l (A_s + A_g) + \lambda_c A_c] + \frac{\nu_c H}{G_1} (\lambda_s A_s + \lambda_c A_c)} \right]. \tag{6.22}$$

Recently, numerical simulations have been performed in order to investigate the shape of the melting isotherm close to the meniscus [Stelian 2009-1, Stelian 2009-2]. The authors demonstrated that depending on the heat transfer configuration in the furnace and

ampoule wall, the meniscus may in fact be undercooled; it is then likely to solidify and thus prevent dewetting from occurring. This might also be an explanation of the ridges and of the partial dewetting observed on the sample.

6.3.4 Theoretical Models of Dewetting

Figure 6.25 schematizes the different configurations leading to dewetting for which a theoretical explanation has been proposed. This classification is based first on the nature of the crucible: crucibles that are macroscopically rough, and smooth crucibles. This latter group is subdivided into two groups that are differentiated by the sum of the Young or apparent contact angle, θ_Y or θ_{app} , and the growth angle, α , of the liquid semiconductor. The notations 1g and $g = 0$ mean, respectively, presence and absence of gravitational acceleration (i.e. experiments on Earth or in space). All these models are based on an idea from Zemskov who postulated the existence of a liquid meniscus between the

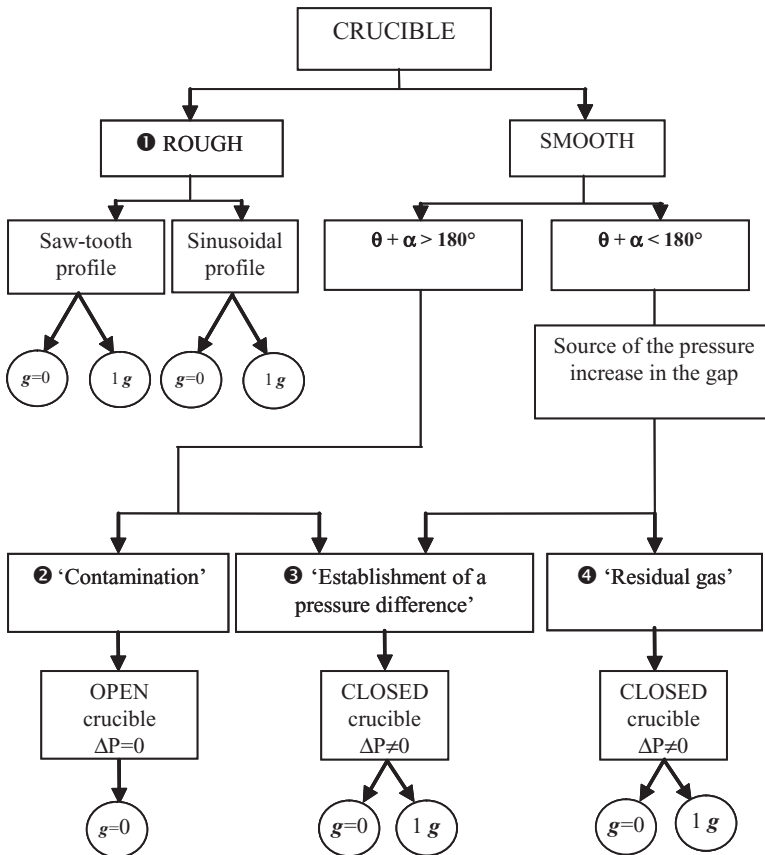


Figure 6.25 Overview of the different configurations leading to the dewetted Bridgman process.

solid–liquid interface and the crucible in order to explain the decrease of crystal diameter that he observed after a space experiment [Zemskov]. However, he never considered the case of a stable gap between a crystal with constant diameter and the crucible.

6.3.4.1 Rough Crucibles (Model 1)

The explanation of dewetting with rough crucibles was developed mainly by [Duffar 1990]. Dewetting is possible when the liquid does not penetrate into the cavities of the rough crucible surface, i.e. when the necessary condition of composite wetting is satisfied between the melt and the crucible roughness. Figure 6.26 illustrates composite wetting where the roughness is simulated by a sawtooth curve (sharp peaks). The radius of the liquid surface curvature, R , is given by the Laplace equation:

$$\Delta p = \gamma/R, \tag{6.23}$$

where Δp and γ are respectively the pressure difference and the surface tension.

On the ground, the hydrostatic pressure gives:

$$R = \gamma/\rho_l g h, \tag{6.24}$$

where ρ_l and h are respectively the specific mass and the height of the liquid. Under microgravity conditions, this pressure is negligible and a very large radius of curvature will be assumed compared to the characteristic roughness dimensions ($R \gg l$). The liquid surface is then assumed to be flat. The condition of composite wetting is satisfied by:

$$l/R \leq -2 \cos(\theta - \beta) \text{ (see Figure 6.26),} \tag{6.25}$$

where l is the distance separating the liquid–crucible punctual contacts.

In microgravity, it is easier to obtain composite wetting thanks to the relatively large value of R . The condition becomes:

$$\beta \leq \theta - \pi/2. \tag{6.26}$$

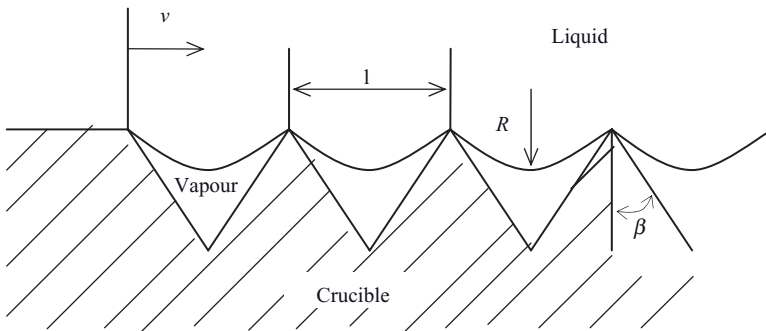


Figure 6.26 Composite wetting for sharp roughness (Reprinted with permission from [Duffar 1990], copyright (1990) Elsevier Ltd).

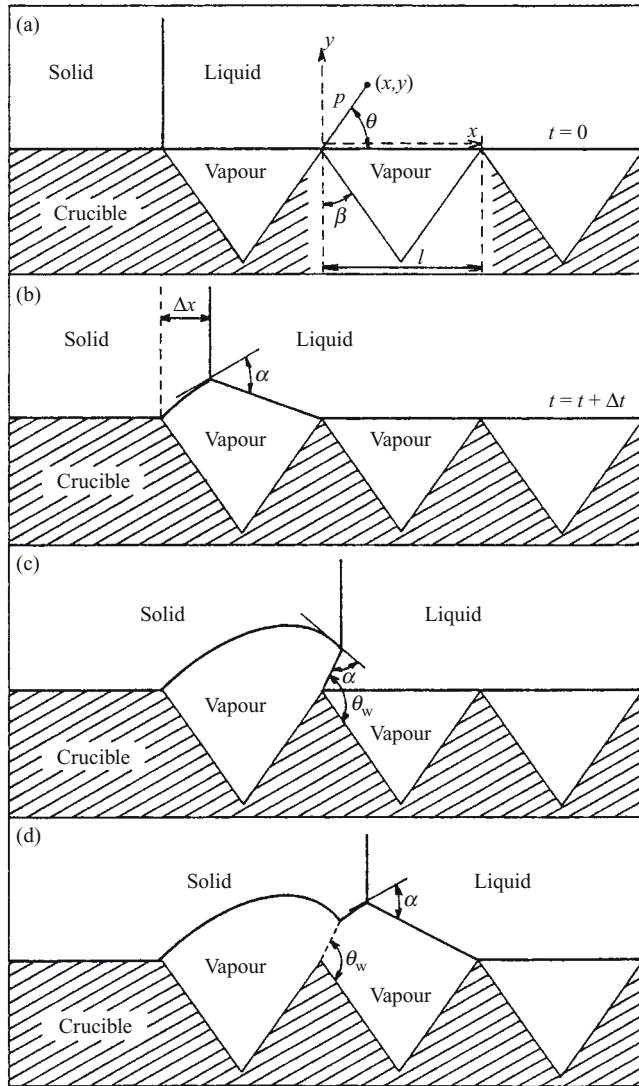


Figure 6.27 Solidification trajectory under microgravity conditions for a crucible with sharp roughness at four successive times, a, b, c, and d (Reprinted with permission from [Duffar 1990], copyright (1990) Elsevier Ltd).

Analytical solutions were developed for both sharp and rounded (sinusoidal) peaks in microgravity and on the ground. Assuming a planar front solidification and a constant growth angle between the solid and the liquid, the calculated solidification trajectory corresponds to the equation of an infinite spiral for sharp peaks in polar coordinates under microgravity conditions (Figure 6.27):

$$\rho = l \exp[(\theta - \pi) / \tan \alpha]. \quad (6.27)$$

On the ground, the solution also corresponds to the equation of an infinite spiral:

$$\rho = 2R \exp[(\theta + k)/\tan \alpha]. \quad (6.28)$$

These solutions were obtained with the initial conditions $d = l$ and $\theta = \pi$.

It was concluded that, as soon as composite wetting conditions are satisfied, detachment of the liquid takes place regardless of the growth angle value. This configuration was not widely used on Earth because the hydrostatic pressure forces the liquid into the crucible wall cavities.

There is a good agreement between the theoretical prediction of model 1 and the results of the space experiments TEXUS 31 and 32, Spacelab D2 and EURECA [Duffar 1995, Duffar 1996, Duffar 1998] because the measured profile corresponds to the computed one.

6.3.4.2 Contamination in a Smooth Crucible with $\theta + \alpha > 180^\circ$ Under Microgravity (Model 2)

Under microgravity conditions, the free surface of the melt adopts a concave curvature viewed from the liquid because the melt contact angle is higher than 90° . This curvature fixes the pressure inside the liquid and the same curvature of the liquid meniscus joining the crystal–melt–vapour and the crucible–melt–vapour triple lines. Because of the negligible hydrostatic pressure, the meniscus is then concave (viewed from the liquid).

Figure 6.29 shows the configuration of the melt, the solid, the vapour and the meniscus in an axisymmetric system. It is obvious that a concave meniscus must satisfy the geometrical condition $\theta + \alpha > 180^\circ$. However, no semiconductor has a Young contact angle higher than 150° at equilibrium when these values are obtained with the sessile drop measurement method. Moreover, except for InP, the growth angles of semiconductor melts are less than 30° . It is therefore impossible to satisfy this geometrical configuration if the equilibrium wetting parameters are considered. The concept of this second model relies on this inconsistency. [Duffar 1997-2] suggested a possible chemical contamination effect that modifies the contact angle by increasing it artificially. Indeed, the lengthy storage of the cartridges before the spacecraft launch could give rise to feed material contamination, e.g. by the outgassing of residual gases in a silica ampoule.

[Harter] and co-workers have performed several sessile drop experiments with III–V semiconductor materials on different kinds of substrates (ionocovalent oxides, graphite and BN). They observed reproducibly that the initial shape of the drop has a high contact angle value on oxide substrates. After applying some mechanical vibrations, the contact triple line moves to reach an equilibrium position which is considered as the Young contact angle with an ideal substrate (Figure 6.28).

This observation indicates that the droplet spreading kinetics could be hindered by the formation of a thin oxide layer on its liquid surface. Such a thin layer might modify the surface energies and artificially increase the contact angle, which then no longer corresponds to a Young contact angle. In most of the crystal growth experiments, it is therefore assumed that the contact angle of the melt on the crucible wall is an apparent contact angle because the mandatory conditions of an ideal substrate (nondeformable, smooth, clean and homogeneous) are not all fulfilled, especially under microgravity.

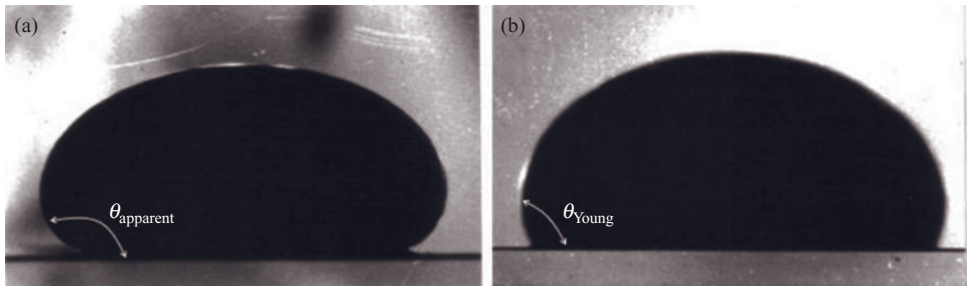


Figure 6.28 Observation of a GaSb sessile drop on an Al_2O_3 substrate. The residual oxygen in the vapour is supposed to change the melt/substrate interaction and the value of the contact angle: (a) measurement of a metastable apparent contact angle $\theta_{app} \cong 160^\circ$ just after melting; (b) measurement of an equilibrium contact angle after applying mechanical vibration $\theta_v = 112^\circ$ (Reprinted with permission from [Harter], copyright (1993) Elsevier Ltd).

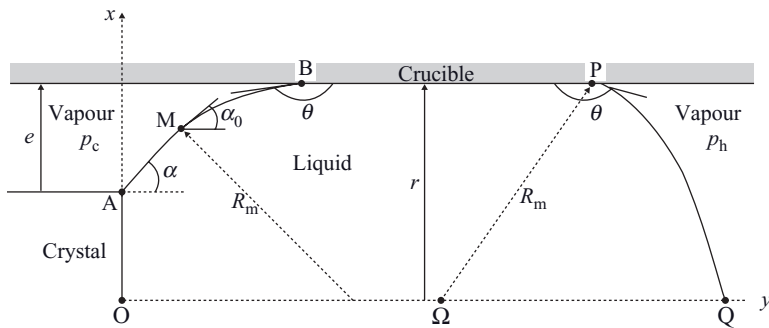


Figure 6.29 Growth configuration under microgravity conditions with $\theta + \alpha > 180^\circ$.

After analysing the space experimental results under microgravity conditions, Duffar and co-workers have proposed a theoretical explanation for dewetting in smooth crucibles [Duffar 1997-2]. The major assumptions about the model are: (i) the dewetting results from the common formation of a constant gap thickness, e , and a liquid meniscus joining the two triple lines (crucible–liquid–vapour and crystal–liquid–vapour); (ii) both triple lines move at the same velocity during the contactless growth. This model aims to predict the gap thickness e as a function of the different geometrical and physical parameters.

The configuration is schematized in Figure 6.29 with a constant gap and a concave meniscus. The free surfaces are represented by two arcs AB (meniscus) and PQ, which are sectors of a sphere. In this model, either both gas volumes are connected, or the crucible is opened, such that $p_h = p_c$. According to the Figure 6.29, the gap thickness is given by:

$$e = r_a \left(\frac{\cos \alpha + \cos \theta}{\cos \theta} \right). \tag{6.29}$$

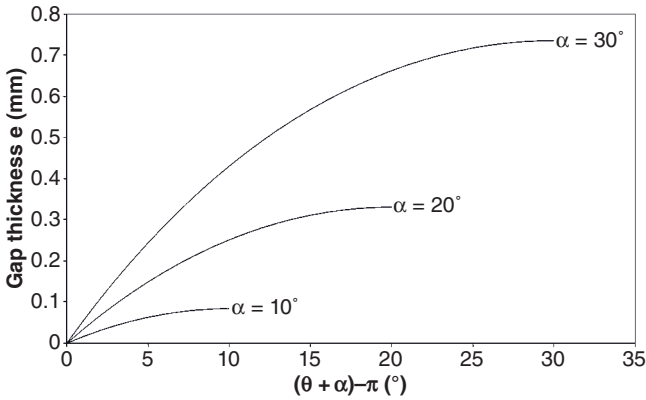


Figure 6.30 Variation of the gap thickness as a function of $(\theta + \alpha) - \pi$ for a GaSb crystal 11 mm in diameter, $g = 0$, $\theta + \alpha > 180^\circ$.

Figure 6.30 shows the variation of e as a function of the wetting parameters θ and α for a GaSb crystal in a crucible with an internal diameter of 11 mm. The calculated values of e are consistent only up to a few hundreds of micrometres ($200\mu\text{m}$ maximum). It appears that the gap thickness value is proportional to the crystal diameter.

The contact angle θ may vary from 178 to 152° for α varying from 10 to 30° and a maximum gap thickness of $100\mu\text{m}$. These values are much higher than the reported Young contact angle values. The authors assumed that the dewetting of a crystal in space and in an open crucible is possible only when the contact angle is artificially increased. They suggested that the chemical pollution is the source of increased θ , in order to explain the occurrence of dewetting under these specific conditions.

6.3.4.3 Pressure Difference in a Smooth Crucible with $\theta + \alpha > 180^\circ$ or $\theta + \alpha < 180^\circ$ (Model 3)

Microgravity. Consider first the system in Figure 6.29 where the two free gas volumes are disconnected. Experimentally, this corresponds to the use of a sealed silica ampoule where the liquid column acts as plug between both gas volumes so that $p_h \neq p_c$, where p_h is the gas pressure at the hot side and p_c the gas pressure at the cold (crystal) side. The expression of the gap thickness is in this case [Duffar 1997-2]:

$$e = \frac{r_a \frac{p_h - p_c}{\gamma_{lv}} - 2 \cos \theta - \cos \alpha + \sqrt{\Delta}}{\frac{p_h - p_c}{\gamma_{lv}} - \frac{2 \cos \theta}{r_a}}, \quad (6.30)$$

with

$$\Delta = \cos^2 \alpha + 2r_a \frac{p_h - p_c}{\gamma_{lv}} \left(r_a \frac{p_h - p_c}{\gamma_{lv}} - \cos \theta \right)$$

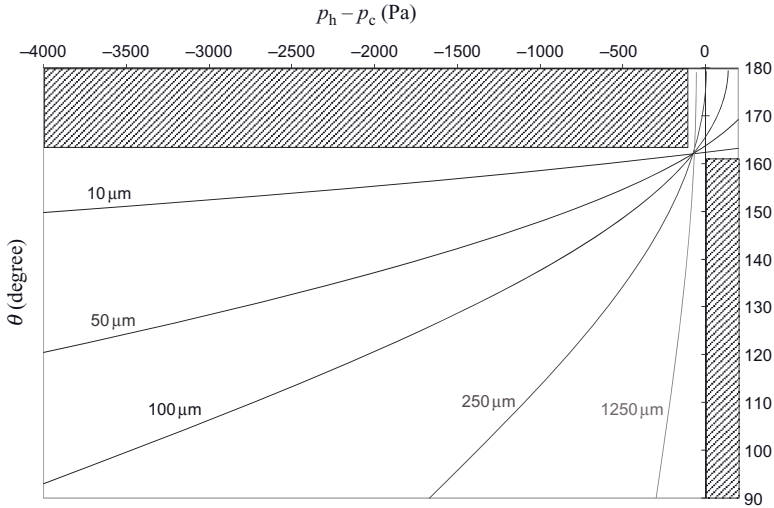


Figure 6.31 Values of $(p_h - p_c)$ recalculated from [Duffar 1997-2] to obtain a gap thickness e as function of θ for the growth of a GaSb crystal under microgravity ($2r_c = 11\text{ mm}$, $\gamma_v = 0,45\text{ J m}^{-2}$, $\alpha = 18^\circ$).

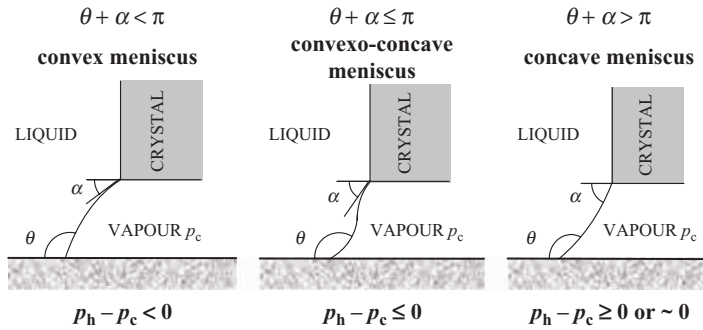


Figure 6.32 Various meniscus shapes during dewetting with different values of $(p_h - p_c)$ and $\theta + \alpha$ in a smooth crucible.

Figure 6.31 shows the variation of the pressure difference $(p_h - p_c)$ for a given gap thickness for an 11 mm diameter GaSb crystal under microgravity. Figure 6.32 illustrates the different meniscus shapes for various sets of both parameters values: $\theta + \alpha$ and $(p_h - p_c)$.

When the values of $(p_h - p_c)$ are negative (-4000 to -100 Pa) and θ is fixed, e increases when the pressure p_c decreases. The meniscus is convex viewed from the liquid (Figure 6.32) and the sum $\theta + \alpha$ is less than 180° . The values of e corresponding to the experimental results ($e < 100\text{ }\mu\text{m}$) correspond to negative values of $(p_h - p_c)$. If $\theta > 162^\circ$, there is no geometrical solution (horizontal hatched area in Figure 6.31).

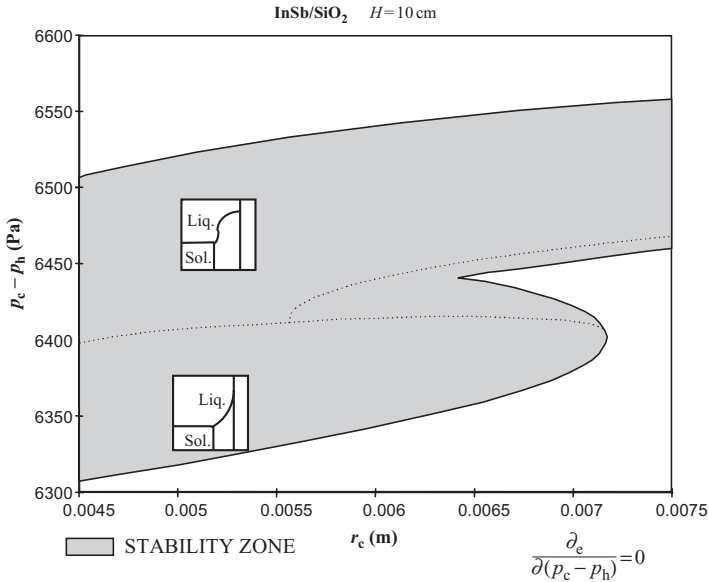


Figure 6.33 Stability diagram for the growth of InSb in a silica crucible. The grey area corresponds to stable growth condition for given radius a_c of the crystal and pressure difference $(p_h - p_c)$ (in the simulation, the hydrostatic pressure was 6327 Pa). The dotted lines represent the most stable condition, where e does not change with $(p_h - p_c)$ (Reprinted with permission from [Duffar 2000], copyright (2000) Elsevier Ltd).

When the value of $(p_h - p_c)$ is positive (0–200 Pa) and θ is fixed, the gap thickness increases with increasing $(p_h - p_c)$. The meniscus is concave and the sum $\theta + \alpha$ is greater than 180° . If $\theta < 162^\circ$, there is no geometrical solution (vertical hatched area in Figure 6.31).

The region of intermediate values of $(p_h - p_c)$ (–80 to 0 Pa) is characteristic of a convex-concave meniscus. The meniscus shape adopts an S shape (Figure 6.32). For a given θ , the value of e decreases drastically with increasing $(p_h - p_c)$.

Finally, the dewetting of a ‘clean’ crystal for which the contact angle is θ_Y (and so for $\theta + \alpha < 180^\circ$) requires increasing the gas pressure at the cold side p_c (negative values of $(p_h - p_c)$) in order to obtain values of e comparable to those measured experimentally ($e < 100 \mu\text{m}$). When $\theta + \alpha > 180^\circ$ (contamination model 2), the pressure difference must be zero or slightly positive. Therefore dewetting occurs more easily, with a high contact angle, when the pressure difference is not controlled. It appears from Figure 6.31 that the dewetting is possible for materials with a zero growth angle and $\theta = 180^\circ$. This case would correspond to metal solidification. However, so far no microgravity result has clearly shown dewetting of a metal.

Normal Gravity. On Earth, the hydrostatic pressure due to the liquid height has to be taken into account. Different methods have been used experimentally in order to counterbalance the hydrostatic pressure and create a stable meniscus (section 6.3.2).

[Duffar 2000] calculated the shape of the meniscus by solving the Laplace differential equations representative of the phenomenon on Earth. These calculations made it possible to plot a diagram giving the pressure difference values as a function of the crucible radius, which furthermore fulfill the capillarity stability criteria of the meniscus (see discussion of stability in section 6.3.5 below). For an InSb crystal, the absolute calculated pressure difference ($p_h - p_c$) is very close to the value of the hydrostatic pressure. The difference is of the order of a few hundred Pa, due to the curvature of the meniscus.

Palosz and co-authors have also used this model in order to explain the dewetting of Ge in SiO₂, BN and p-BN crucibles [Palosz]. There is a good agreement between the experimental results and the model.

To conclude, the value of the applied pressure difference should be very close to the hydrostatic pressure.

6.3.4.4 Residual Gases: ‘Detached’ Growth (Model 4)

This model was introduced by Wilcox and co-workers and is basically similar to the previous model, as gas pressures are also involved. It further assumes that the excess pressure comes from the residual gases present in the ampoule [Wilcox 1995]. This explanation is based on the release of gas between the crucible and the sample at the level of the solid–liquid interface (the segregation coefficient $k_{\text{gas}} < 1$). The gas, previously dissolved in the sample, is expelled from the liquid at the level of the solidification front, then transported towards the periphery by diffusion and capillary convection and finally released in the gap between the growing crystal and the crucible where it generates a pressure. Hence, a steady state with a constant gap width can be reached.

Steady state analysis has been studied by numerical solution of the hydrodynamic equations (Marangoni convection along the meniscus) and chemical species conservation. The numerical model is known as the ‘moving meniscus model’ for detached solidification [Popov 1997-1] (Figure 6.34). According to Wilcox *et al.*:

a steady-state gap width is reached when the transport of volatile species across the meniscus equals that required to maintain a gas pressure satisfying the condition of mechanical equilibrium across the meniscus.

The authors obtain the following expression for the stationary gap:

$$e_{\text{es}} = \left[\frac{RT_{\text{avg}}}{v_c} j_{\text{mol}} - 2\gamma_{\text{lv}} \cos\left(\frac{\alpha - \theta}{2}\right) \cos\left(\frac{\alpha + \theta}{2}\right) \right] / p_m. \quad (6.31)$$



Figure 6.34 Principle of the ‘detached solidification’ model: dissolved gases are rejected at the solidification interface and transported towards the meniscus where they feed the gap.

where T_{avg} is the mean temperature in the gap, v_c the growth rate, p_m the gas pressure at the hot side and j_{mol} the molar flux of gas through the meniscus. The leading parameters of the problem are the diffusion length D/v_c , the gas pressure p_m , the segregation and Henry coefficients of the volatile species, k and H , and the capillary parameters α , θ and γ_v . The main conclusions are as follows:

- The calculated gap thickness is ~ 1 mm.
- A low growth rate favours detachment and a high growth rate decreases the diffusion length and enhances backdiffusion in the bulk liquid.
- A high vapour pressure of the dissolved species favours detachment. When it is too small, a stationary state cannot be reached. It is recommended to maintain the liquid at high temperature in order to enhance the dissolution of gas before growth.
- The effect of Marangoni convection on the gap thickness is low.
- The gap thickness increases for large values of θ and α because the meniscus is longer and more gas can feed the gap.

In another study [Popov 1997-3], the authors include the liquid buoyancy convection in the model and show that the curvature of the solid–liquid interface is likely to significantly affect the transport of expelled gas toward the meniscus. Applied to InSb, the analysis gives reasonable conclusions, except for too large a gap thickness [Wang 2000]. Applied to the freezing of water, the model predicts that detached growth is not likely to occur [Wang 2001], in agreement with the experimental results of [Wang 2002-2].

The same authors studied the same problem in a different way, based on an approximate balance of the gas species in the vicinity of the solidification interface [Wang 2002-1]. This very elegant approach gave the same results as above, on a more physical basis.

6.3.4.5 Conclusions Concerning the Theoretical Models

The first point to note is that all models involve a liquid meniscus joining the solid liquid interface to a liquid–crucible triple line, with both triple lines having equal velocity. This meniscus remained hypothetical until the experimental results presented in Figure 6.21, but it is now universally accepted that dewetting is linked to the existence of the meniscus. On this basis, all models give a formula for the calculation of the gap thickness. Obviously large contact and growth angles enhance dewetting, which is in agreement with all the experimental results (see Figure 6.18).

For rough crucibles, model 1 above is in very good agreement with experiments [Duffar 1990, Duffar 1995, Duffar 1998]. For smooth crucibles, it has also been clearly shown that contamination of the melt surface increases the contact angle (and maybe the growth angle) and enhances dewetting (model 2); this is likely to have occurred in most of the microgravity experiments. In practice, dewetting in normal gravity can be controlled by monitoring the gas pressure in the ampoule and the pressure difference should be of the order of the hydrostatic pressure. The theoretical predictions of model 3 are in very good agreement with the experimental results of [Palosz]. This model gives gap thicknesses of the same order as the experimental ones, which is not the case with model 4.

This last model has the drawback of being based on physical parameters (segregation, diffusion and Henry coefficients of gases in semiconductors) that are unknown. Whatever

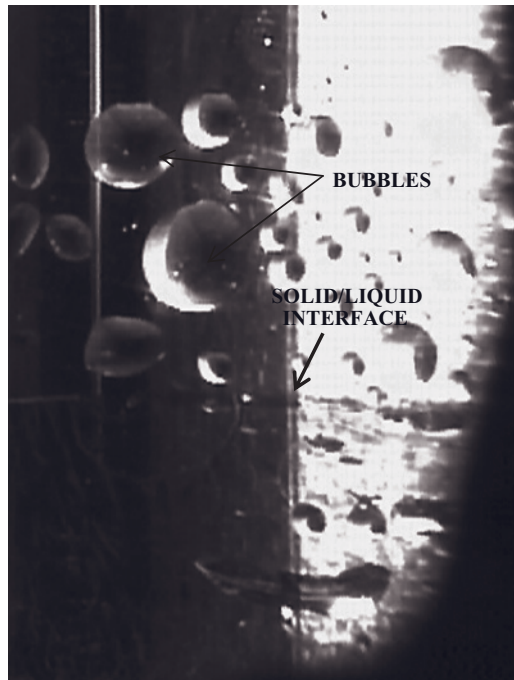


Figure 6.35 Bubbles nucleating on the crucible wall during the growth of GaSb under $\text{Ar} + 10\% \text{H}_2$ atmosphere [Sylla 2008-2].

the value chosen for these parameters, the model always gives gap thicknesses that are too large and a dependence on the growth rate that has never been observed experimentally. Furthermore, it can be applied only to closed ampoules and cannot explain the results obtained in open crucibles, where the pressures are equal on both sides of the sample. The main argument against the model 4 surely comes from the recent experiment of Sylla who grew GaSb under an $\text{Ar} + 10\% \text{H}_2$ atmosphere [Sylla 2008-2]. The H_2 dissolved into the melt and was expelled at the solid–liquid interface. However, instead of feeding a stationary gap, numerous bubbles nucleated on the crucible walls and were entrapped at the surface of the crystal (Figure 6.35). Only a very small part of the surface of the sample was dewetted. It therefore appears that this last model may occur under certain conditions but cannot explain most of the experimental results.

6.3.5 Stability Analysis

As mentioned earlier, the dewetting process is a very stable one; see Figure 6.18b where a constant gap of $70\mu\text{m}$ was observed along 5 cm of growth, without any external monitoring. This intrinsic stability is one of the most striking peculiarities of dewetting. The basis of the stability analysis of dewetting, as for all other capillary-based growth processes, is based on Tatartchenko's work which is explained in detail in Chapter 2 of this book and developed in his own book [Tatartchenko]. The objective of the analysis is to

find out the necessary conditions in order to get a stable dewetting, i.e. a stable crystal diameter or gap thickness.

Following the analysis presented in Chapter 2, it appears that under microgravity conditions there is only one variable parameter, the gap thickness, because the heat transfer cannot change the pressure in the meniscus (or only very marginally through modification of capillary parameters γ_{lv} and θ) and thus has no effect on the meniscus shape or on the gap. Therefore only one equation is needed, which is the Laplace equation.

For experiments performed on Earth, on the other hand, melting or solidification changes the height of liquid, then the hydrostatic pressure acting on the meniscus, and then the gap thickness. In this case the gap thickness and the solid–liquid interface position are variables of the problem and two equations are needed: the Laplace equation and the heat balance at the interface. Furthermore, in cases where gas pressures are likely to fluctuate, they also have an effect on the meniscus shape and the perfect gas law should be added to the initial set of equations.

In the microgravity case, only the capillary effects are taken into account. If the growth angle is considered to be constant, which is an important hypothesis throughout this book, the only point to take into account is the concavity of the meniscus at the triple line with the solid–liquid interface. If r_0 is the stable crystal radius ($r_0 = r_a - e$ with r_a the inner crucible radius) and α_0 the angle formed by the tangent to the meniscus with the vertical axis, we obtain (Figure 6.36):

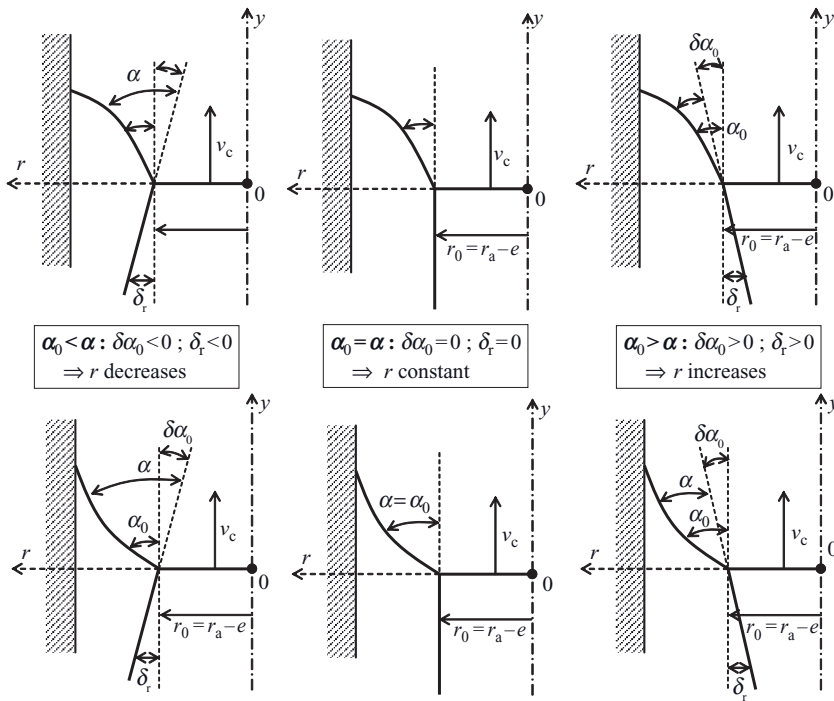


Figure 6.36 Effect of perturbation of the α_0 angle on variations of r_0 for a convex (top) and concave (bottom) meniscus.

$$\frac{d}{dt}(\delta r) = v_c \tan \delta \alpha_0(r), \quad (6.32)$$

where v_c is the the growth rate.

A Lyapunov analysis restricted to one parameter gives the stability criterion:

$$v_c \left(\frac{\partial \alpha_0}{\partial r} \right)_n < 0. \quad (6.33)$$

Stability is therefore linked to the concavity of the meniscus at the triple line: with a concave meniscus (as seen from the liquid, i.e. the centre of curvature is in the liquid), the growth is stable and with a convex meniscus it is unstable. Then, as is obvious from Figure 6.29, the growth is stable only if the condition $\theta + \alpha > 180^\circ$ applies, which is the necessary condition for a concave meniscus. This result is in perfect agreement with the experimental observations: dewetting only occurs with very large contact angles, either because the wetting angle is naturally large (e.g. for a BN crucible [Shetty 1995-2]) or because it has been artificially increased, e.g. by pollution (see Figure 6.23).

When a pressure difference is introduced under microgravity conditions, the problem has been solved in [Duffar 1997-2]:

$$\left(\frac{\partial \alpha_0}{\partial r} \right)_{r=r_a-e} = \frac{1}{2 \sin \alpha} \left[\frac{2 \cos \theta}{r_a} - \frac{p_h - p_c}{\gamma_{lv}} \left(1 + \frac{r_a}{(r_a - e)^2} \right) \right] \quad (6.34)$$

and the stability criterion is also (6.32):

$$\left(\frac{\partial \alpha_0}{\partial r} \right)_{r=r_a-e} < 0$$

Three cases should be considered:

- If e is very small ($r - e \approx r$), stability occurs if:

$$p_h - p_c > -\frac{2\gamma_{lv} \cos \theta}{r_a}, \text{ equivalent to } p_h - p_c > p_l - p_h \quad (6.35)$$

as $\theta \in [\pi/2; \pi]$ stability is obtained for all positive values of $(p_h - p_c)$.

- If e is not negligible, $(p_h - p_c)$ should be positive and increased (compared to the case above) by a factor $((1 + r_a^2)/(r_a - e)^2)$.
- If $(p_h - p_c) = 0$, growth is intrinsically stable (see above).

The capillary problem with terrestrial gravity has been partly studied numerically in [Duffar 2000], by solving the Laplace equation when changing the parameters of the problem. The numerical scheme (fourth-order Runge–Kutta) followed the recommendations of [Hartland] and stability diagrams have be plotted, such as the one shown in Figure 6.33. As the stability criterion is still the concavity of the meniscus, only concave and concavo-convex interfaces should be considered, as plotted on the figure. The most interesting dewetting conditions in this figure, plotted as dotted lines, are such that a small variation of pressure has no effect on the gap thickness:

$$\frac{\partial e}{\partial (p_c - p_h)} = 0. \quad (6.36)$$

In the paper [Duffar 1997-2], the authors discuss the effect of pressure fluctuations, based on Tatartchenko's approach. It follows that such fluctuations are not likely to destabilize stable dewetting; however, the analysis is simplified and further studies are necessary to ascertain this point.

As already mentioned, thermal transfer has no effect on a freely moving meniscus in microgravity, which is subject only to capillary stability. The two-equation problem (capillarity and heat transfer) has been studied under microgravity conditions, with the hypothesis that the liquid–crucible triple line of the meniscus is anchored by some hysteresis wetting [Bizet]. These authors studied several heat transfer cases and concluded that, in all the configurations studied, the dewetting remains stable provided that the concavity criterion is satisfied.

Popov *et al.* studied the stability of model 4 described above [Popov 1997-2]. This is a problem with three degrees of freedom, where capillarity, heat transfer and gas flux should be taken into account. The conclusions are as follows:

- Gas flux perturbations do not disturb the stability of the stationary growth.
- Fluctuations of growth rate have a great effect on the gas flux through the meniscus, more than fluctuations of gap or pressure, but do not destabilize growth.
- Pressure fluctuations have a destabilizing effect, more so if the gap is thin.
- There is a critical gap thickness above which the system is no longer stable, whatever the other conditions.

It follows from these analyses that a high wetting angle is definitely the main parameter for stability. Considering the existing literature on this subject, and the complexity of the many possible cases, further studies are needed in order to solve the problem fully, especially on Earth where it is of practical interest, and to find which are the stable conditions for dewetting for all configurations.

6.4 Conclusion and Outlook

Because it uses a crucible, the Bridgman crystal growth technique has advantages and drawbacks which have been discussed in details in this chapter. The main drawback is certainly the contact between the crucible and the crystal, which generates first-order defects (stress, grain nucleation, and twinning) and secondary problems through the curvature of the interface. However, the associated advantages – simplicity and consequent low cost, small thermal gradients, shaping of the crystal – are tempting. Two variants of the process, involving capillarity, have been devised in order to keep the advantages without the drawbacks.

Full encapsulation is used in industrial plants for production of GaAs and InP. Thanks to the work of Zappettini's team, it is likely that it will soon be used for CdTe and related compounds as well. However, this technique is restricted by the necessity to find an appropriate encapsulant, which in practice, for semiconductors, appears to be only B_2O_3 . It is not clear if other encapsulants could be found for other materials that have too low a melting point or for which B is unacceptable (such as photovoltaic Si).

Dewetting is probably the unique case of a phenomenon discovered as a result of microgravity experiments that has given birth to a promising terrestrial technology. Thanks to recent experiments and theoretical developments, the situation is clear from the theoretical point of view; only stability analysis needs some further developments. Our understanding of the phenomenon and associated process seems mature enough for us to think about a potential candidate for mass production. This next step will decide the usefulness of this technique.

References

- [Althaus] Althaus M., Sonnenberg K., Küssel E., Naeven R., *J. Cryst. Growth* **166** (1996) 566–571.
- [Amashukeli] Amashukeli M.D., Karataev V.V., Kekua M.G., Mil'vidskii M.G., Khantadze D.V., *Neorgan. Mater.* **17** (1982) 2126.
- [Amon] Amon J., Auer W., Zemke D., Müller G., *J. Cryst. Growth* **166** (1996) 646–650.
- [Asahi] Asahi T., Kainosho K., Kohiro K., Noda A., Sato K., Oda A., Chapter 15 in: *Crystal Growth Technology*, ed. H. Scheel, T. Fukuda, John Wiley & Sons, Ltd, Chichester (2003).
- [Barat] Barat C., Duffar T., Garandet J.P., *J. Cryst. Growth* **194** (1998) 149–155.
- [Balicki] Balicki E., Deal A., Abbaschian R., *J. Cryst. Growth* **271** (2004) 37–45.
- [Bizet] Bizet L., Duffar T., *Cryst. Res. Technol.* **39**(6) (2004) 491–500.
- [Bliss] Bliss D., Demczyk B., Anselmo A., Bailey J.J., *J. Cryst. Growth* **174** (1997) 187–193.
- [Blum] Blum S.E., Chicotka R.J., *J. Electrochem. Soc.* **120**(4) (1973) 588–589.
- [Boiton] Boiton P., Giacometti N., Duffar T., Santailler J.L., Dusserre P., Nabot J.P., *J. Cryst. Growth* **206** (1999) 159–165.
- [Bouret] Bouret E.D., Merk E.C., *J. Cryst. Growth* **110** (1991) 395–404.
- [Brice] Brice J.C., In: *The Growth of Crystals from Liquids*, ed. E.P. Wohlfarth, North-Holland/American Elsevier, New York (1973).
- [Buhrig] Buhrig E., Frank C., Hannig C., Hoffmann B., *Mater. Sci. Eng. B* **44** (1997) 248–251.
- [Carlsson] Carlsson L., Ahlquist C.N., *J. Appl. Phys.* **43** (1972) 2529–2536.
- [Chang] Chang C.E., Wilcox W.R., *J. Cryst. Growth* **21** (1974) 135–140.
- [Ciszek] Ciszek T.F., Evans C.D., *J. Cryst. Growth* **91** (1988) 533–537.
- [Coriell 1979] Coriell S.R., Sekerka R.F., *J. Cryst. Growth* **46** (1979) 479–482.
- [Coriell 1981] Coriell S.R., Boisvert R.F., Rehm R.G., Sekerka R.F., *J. Cryst. Growth* **54** (1981) 167–175.
- [Dashevskii] Dashevskii M.Y., Poterukhin A.N., *Neorg. Mater.* **5**(11) (1969) 2012.
- [Dold] Dold P., Szofran F.R., Benz K.W., *J. Cryst. Growth* **234** (2002) 91–98.
- [Duffar, 1990] Duffar T., Harter I., Dusserre P., *J. Cryst. Growth* **100** (1990) 171–184.
- [Duffar 1995] Duffar T., Dusserre P., Abadie J., *Adv. Space Res.* **16**(8) (1995) 199.
- [Duffar 1996] Duffar T., Abadie J., *Microgravity Sci. Technol.* **IX**(1) (1996) 35.
- [Duffar 1997-1] Duffar T., Gourbil J.M., Boiton P., Dusserre P., Eustathopoulos N., *J. Cryst. Growth* **179** (1997) 356–362.
- [Duffar 1997-2] Duffar T., Boiton P., Dusserre P., Abadie J., *J. Cryst. Growth* **179** (1997) 397–409.
- [Duffar 1998] Duffar T., Serrano M.D., Moore C.D., Camassel J., Contreras S., Dusserre P., Rivoallant A., Tanner B.K., *J. Cryst. Growth* **192** (1998) 63–72.
- [Duffar, 1999] Duffar T., Dusserre P., Giacometti N., Boiton P., Nabot J.P., Eustathopoulos N., *J. Cryst. Growth* **198–199** (1999) 374–378.
- [Duffar 2000] Duffar T., Dusserre P., Picca F., Lacroix S., Giacometti N., *J. Cryst. Growth* **211** (2000) 434–440.

- [Duffar 2001-1] Duffar T., Dusserre P., Giacometti N., *J. Cryst. Growth* **223** (2001) 69–72.
- [Duffar 2001-2] Duffar T., Dusserre P., Giacometti N., Benz K.W., Fiederle M., Launay J.C., Dieguez E., Roosen G., *Acta Astronaut.* **48**(2–3) (2001) 157–161.
- [Duffar 2001-3] Duffar T., Dusserre P., Giacometti N., *Crystal Growth Apparatus and Method*. PCT Int. Appl., WO 0168956 (2001).
- [Duffar 2004-1] Duffar T., Chevalier N., Dusserre P., Garandet J.-P., *J. Cryst. Growth* **261** (2004) 590–594.
- [Duffar, 2004-2] Duffar T. Chapter 17 in: *Bulk Crystal Growth of Electronic, Optical and Optoelectronic Materials*, ed. P. Capper, John Wiley and Sons, Ltd, Chichester (2004), pp. 477–524.
- [Duhanian] Duhanian N., Marin C., Duffar T., Abadie J., Chaudet M., Dieguez E., *Microgravity Sci. Technol.*, **XI**(4) (1997) 187–193.
- [El Mahallawy] El Mahallawy N.A., Farag M.M., *J. Cryst. Growth* **44** (1978) 251–258.
- [Epure 2008] Epure S., Duffar T., Braescu L., *J. Cryst. Growth* **310** (2008) 1559–1563.
- [Epure 2010] Epure S., PhD thesis, Grenoble Institute of Technology, France and West University of Timisoara, Romania (2010).
- [Feigelson] Feigelson R.S., Route R.K., *J. Cryst. Growth* **49** (1980) 261–273.
- [Fiederle 2004-1] Fiederle M., Duffar T., Babentsov V., Benz K.W., Dusserre P., Corregidor V., Dieguez E., Delaye P., Roosen G., Chevrier V., Launay J.C., *Cryst. Res. Technol.* **39**(6) (2004) 481–490.
- [Fiederle 2004-2] Fiederle M., Duffar T., Garandet J.P., Babentsov V., Fauler A., Benz K.W., Dusserre P., Corregidor V., Dieguez E., Delaye P., Roosen G., Chevrier V., Launay J.C., *J. Cryst. Growth* **267** (2004) 429–435.
- [Garandet] Garandet J.P., Duffar T., Favier J.J., *J. Cryst. Growth* **96** (1989) 888–898.
- [Harter] Harter I., Dusserre P., Duffar T., Nabot J.P., Eustathopoulos N., *J. Cryst. Growth* **131** (1993) 157–164.
- [Hartland] Hartland S., Hartley R., *Axi-Symmetric Fluid-Liquid Interfaces*, Elsevier, Amsterdam (1976).
- [Hoshikawa] Hoshikawa K., Nakanishi H., Kohda H., Sasaura M., *J. Cryst. Growth* **94** (1989) 643–650.
- [Huang] Huang C.E., Elwell D., Feigelson R.S., *J. Cryst. Growth* **64** (1983) 441–447.
- [Jasinski] Jasinski T., Witt A.F., Rohsenow W. M., *J. Cryst. Growth* **67** (1984) 173–184.
- [Joanny] Joanny F., de Gennes P.G., *C. R. Acad. Sc. Paris* **299** (1984) 279–283.
- [Kadokura] Kadokura K., Takano Y., *J. Cryst. Growth* **171** (1997) 56–60.
- [Lay 1987] Lay P., PhD thesis, Université de Caen, France (1987) (in French).
- [Lendvay] Lendvay E., Harsy M., Görög T., Gyuro I., Pozsgai I., Koltai F., Gyulai J., Lohner T., Mezey G., Kotai E., Paszti F., Hrijapov V.T., Kultchisky N.A., Regel L.L., *J. Cryst. Growth* **71** (1985) 538–550.
- [Matsumoto] Matsumoto F., Okano Y., Yonenaga I., Hoshikawa K., Fukuda T., *J. Cryst. Growth* **132** (1993) 348–350.
- [Monberg] Monberg E.M., Brown H., Bonner C.E., *J. Cryst. Growth* **94** (1989) 109–114.
- [Metz] Metz E.P.A., Miller R.C., Mazelsky R., *J. Appl. Phys.*, **33** (1962) 2016–2017.
- [Mezhennyi] Mezhennyi M.V., Osvenskii V.B., Mil'vidskaya A.G., *Sov. Phys. Crystallogr.* **35**(5) (1990) 695.
- [Möller] Möller U., Hildman B.O., Bahr G., *J. Cryst. Growth* **131** (1993) 165–175.
- [Mullin] Mullin J.B., Straughan B.W., Brickell W.S., *J. Phys. Chem. Sol.* **26** (1965) 782–784.
- [Naumann 1982] Naumann R.J., *J. Cryst. Growth* **58** (1982) 569–584.
- [Naumann 1983] Naumann R.J., Lehocsky S.K., *J. Cryst. Growth* **61** (1983) 707–710.
- [Nishio] Nishio J., Terashima K., *J. Cryst. Growth* **96** (1989) 605–608.
- [Okada] Okada H., Kawanaka T., Ohmoto S., *J. Cryst. Growth* **172** (1997) 361–369.
- [Ostrogorsky] Ostrogorsky A.G., Marin C., Volz M., Duffar T., *J. Cryst. Growth* **311** (2009) 3243–3248.
- [Palosz] Palosz W., Volz M.P., Cobb S., Motakef S., Szofran F.R., *J. Cryst. Growth* **277** (2005) 124–132.

- [Pätzold] Pätzold O., Jenkner K., Scholz S., Cröll A., *J. Cryst. Growth* **277** (2005) 37–43.
- [Pfeiffer] Pfeiffer M., Muhlberg M., *J. Cryst. Growth* **118** (1992) 269–276.
- [Pilliar] Pilliar R.M., Nuthiny J., *Phil. Mag.* **16** (1967) 181.
- [Pino] Pino R., Ko Y., Dutta P.S., *J. Cryst. Growth* **290** (2006) 29–34.
- [Popov 1997-1] Popov D.I., Regel L.L., Wilcox W.R., *J. Mater. Synth. Proces.* **5** (1997) 283.
- [Popov 1997-2] Popov D.I., Regel L.L., Wilcox W.R., *J. Mater. Synth. Proces.* **5** (1997) 299.
- [Popov 1997-3] Popov D.I., Regel L.L., Wilcox W.R., *J. Mater. Synth. Proces.* **5** (1997) 313.
- [Potard] Potard C., Dusserre P., Duffar T., *Cryst. Res. Technol.*, **32** (1997) 925–929.
- [Ravishankar] Ravishankar P.S., *J. Cryst. Growth* **94** (1989) 62–68.
- [Rupp] Rupp R., Müller G., *J. Cryst. Growth* **113** (1991) 131–139.
- [Sabhpathy] Sabhpathy P., Salcudean M.E., *J. Cryst. Growth* **113** (1991) 164–180.
- [Santailier] Santailier J.L., Duffar T., Théodore F., Boiton P., Barat C., Angelier B., Giacometti N., Dusserre P., Nabot J.P., *J. Cryst. Growth* **180** (1997) 698–710.
- [Schweizer 2002-1] Schweizer M., Cobb S.D., Volz M.P., Szoke J., Szofran F.R., *J. Cryst. Growth* **235** (2002) 161–166.
- [Schweizer 2002-2] Schweizer M., Volz M.P., Cobb S.D., Vujisic L., Motakef S., Szoke J., Szofran F.R., *J. Cryst. Growth* **237–239** (2002) 2107–2111.
- [Shetty 1990] Shetty R., Balasubramanian R., Wilcox W.R., *J. Cryst. Growth* **100** (1990) 58–62.
- [Shetty 1995-1] Shetty R., Wilcox W. R., Regel L.L., *J. Cryst. Growth* **153** (1995) 103–109.
- [Shetty 1995-2] Shetty R., Wilcox W.R., *J. Cryst. Growth* **153** (1995) 97–102.
- [Shipil'rain] Shipil'rain E.E., Yakimovitch K.A., Tsitsarkin A.F., Kagan D.N., Barkhatov L.S., Fomin V.A., Tsignkhagen Y., *Fluid Mech. Sov. Res.*, **3–4** (1974) 29.
- [Singh] Singh N.B., Narayanan R., Zhao A.X., Balakrishna V., Hopkins R.H., Suhre D.R., Fernelius N.C., Hopkins F.K., Zelmon D.E., *Mater. Sci. Eng. B* **49** (1997) 243–246.
- [Stelian 2001] Stelian C., Duffar T., Santailier J.L., Barvinschi F., Nicoara I., *Cryst. Res. Technol.*, **36(7)** (2001) 663–674.
- [Stelian 2009-1] Stelian C., Yeckel A., Derby J., *J. Cryst. Growth* **311** (2009) 2572–2579.
- [Stelian 2009-2] Stelian C., Volz M.P., Derby J., *J. Cryst. Growth* **311** (2009) 3337–3346.
- [Sylla 2008-1] Sylla L., Duffar T., *Mater. Sci. Eng. A* **495** (2008) 208–214.
- [Sylla 2008-2] Sylla L., PhD thesis, INP-Grenoble, France (2008) (in French).
- [Swiggard] Swiggard E.M., *J. Cryst. Growth* **94** (1989) 556–558.
- [Szofran] Szofran F.R., Benz K.W., Cröll A., Dold P., Cobb S.D., Lehoczy S.L., Volz P., Watring D.A., Motakef S., Proc. NASA Microgravity Mat. Sci. Conf., Huntsville, 10–11 June 1996, NASA Conf. Publ. **3342**, pp. 499–504.
- [Tatartchenko] Tatartchenko Y.A., *Shaped Crystal Growth*, Kluwer, Dordrecht (1993).
- [Ubbelohde] Ubbelohde A.R., *The Molten State of Matter*, J. Wiley & Sons, Ltd, New York (1978).
- [Völkl] Völkl J., In: *Handbook of Crystal Growth*, Vol. **2b**, ed. D.T.J. Hurle, North Holland, Amsterdam, pp 821–874.
- [Volmer] Volmer M., *Z. Elektrochem.* **35** (1929) 555.
- [Volz] Volz M.P., Schweizer M., Kaiser N., Cobb S.D., Vujisic L., Motakef S., Szofran F.R., *J. Cryst. Growth* **237–239** (2002) 1844–1848.
- [Wang 2000] Wang Y., Regel L.L., Wilcox W.R., *J. Cryst. Growth* **209** (2000) 175–180.
- [Wang 2001] Wang Y., Regel L.L., Wilcox W.R., *J. Cryst. Growth* **226** (2001) 430–435.
- [Wang 2002-1] Wang Y., Regel L.L., Wilcox W.R., *J. Cryst. Growth* **243** (2002) 546–560.
- [Wang 2002-2] Wang Y., Regel L.L., Wilcox W.R., *Cryst. Growth Des.* **2(5)** (2002) 453–461.
- [Wang 2004] Wang J., Regel L.L., Wilcox W.R., *J. Cryst. Growth* **260** (2004) 590–599.
- [Wilcox 1995] Wilcox W.R., Regel L.L., *Microgravity Sci. Technol.* **VIII(1)** (1995) 56.
- [Wilcox 1998] Wilcox W.R., Regel L.L., *Microgravity Sci. Technol.* **XI(4)** (1998) 152.
- [Witt 1975] Witt A.F., Gatos H.C., Lichtensteiger M., Lavine M.C., Herman C.J., *J. Electrochem. Soc.* **122** (1975) 276–283.
- [Witt 1978] Witt A.F., Gatos H.C., Lichtensteiger M., Lavine M.C., Herman C.J., *J. Electrochem. Soc.* **125** (1978) 1832–1840.

- [Zappettini] Zappettini A., Zha M., Pavesi M., Zanotti L., *J. Cryst. Growth* **307** (2007) 273–288.
- [Zemskov] Zemskov V.S., Raukhan M.R., Barmin I.V., Senchenkov A.S., Shul'pina I.L., Sorokin L.M., *Fiz. Khim. Obrab. Mat.* **17**(5) (1983) 56.
- [Zha] Zha M., Zappettini A., Calestani D., Marchini L., Zanotti L., Paorici C., *J. Cryst. Growth* **310** (2008) 2072–2075.

7

Marangoni Convection in Crystal Growth

Arne Cröll
University of Freiburg

Taketoshi Hibiya and Suguru Shiratori
Tokyo Metropolitan Institute of Technology

Koichi Kakimoto and Lijun Liu
Kyushu University

Marangoni convection is a capillary flow, named after the Italian physicist Carlo Giuseppe Matteo Marangoni (1840–1925). It is driven by the gradient of the surface tension at a free surface, which in turn results from temperature or concentration gradients. It can occur in every crystal growth set-up with a free liquid surface, i.e. in floating zone (FZ) growth, Czochralski (Cz) growth, horizontal Bridgman growth, and even vertical Bridgman (VB) growth and related methods such as vertical gradient freeze (VGF). Marangoni convection also occurs due to a gradient of interfacial tension at a liquid–liquid interface, e.g. in the case of liquid encapsulation. In this case a flow is observed in both liquids, with the flow velocities being determined by the more viscous liquid with respect to the continuity of shear stress through the interface.

The direction of a Marangoni flow is from areas of low surface tension to those of higher surface tension. Note that, strictly speaking, ‘Marangoni convection’ has historically been used in fluid science for an arrangement with a temperature gradient perpendicular to the surface of the liquid, the so-called Bénard configuration. In crystal growth arrangements, the temperature gradient nearly always has a component parallel to the

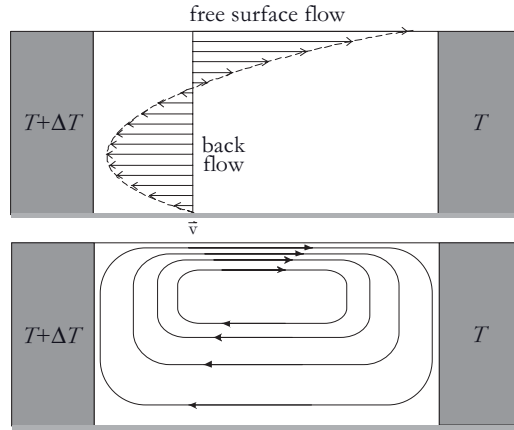


Figure 7.1 Schematic representation of thermocapillary flow velocities (top) and streamlines (bottom) in a rectangular cavity due to a temperature gradient parallel to the free surface (copyright A. Cröll; reproduced with permission).

liquid surface and this ‘thermocapillary’ convection is the one of interest here (Figure 7.1); very often it is also just called Marangoni convection in a more general use of the term. A good description of Marangoni effects in general can be found in [Scriven 1960]. In addition to the surface tension gradient arising from temperature gradients as in thermocapillary convection, concentration gradients will lead to chemo- or solutocapillary convection – ‘solutal Marangoni’ convection. This also needs to be taken into account for some systems, especially for the growth of mixed crystals. The most important effect, however, is Marangoni convection driven by thermal gradients. For most materials, the surface tension decreases with increasing temperature, leading to a flow from hot to cold areas of the surface. Thermocapillary convection is characterized by the Marangoni (or Péclet–Marangoni) number:

$$Ma = -\frac{\partial\gamma_{lv}}{\partial T} \cdot \frac{\Delta T \cdot L}{v \cdot \rho_l \cdot D_{th}}, \quad (7.1)$$

where $\partial\gamma_{lv}/\partial T$ is the temperature dependence of surface tension, ΔT is the temperature difference, v is kinematic viscosity, ρ_l is density, D_{th} is thermal diffusivity and L is the characteristic length.

Sometimes the related Reynolds–Marangoni number Re_M is used instead of Ma :

$$Re_M = \frac{Ma}{Pr} = -\frac{\partial\gamma_{lv}}{\partial T} \cdot \frac{\Delta T \cdot L}{v^2 \cdot \rho_l}, \quad (7.2)$$

where $Pr = \nu/D_{th}$ is the Prandtl number.

Similar to Ma , a solutal Marangoni number Ma_{sol} can be defined for solutocapillary convection:

$$Ma_{\text{Sol}} = -\frac{\partial\gamma_{\text{lv}}}{\partial C} \cdot \frac{\Delta C \cdot L}{v \cdot \rho_1 \cdot D}, \quad (7.3)$$

where $\partial\gamma_{\text{lv}}/\partial C$ is the concentration dependence of surface tension, ΔC is the concentration difference and D is the diffusion coefficient.

A good measure of the relative strength of thermal buoyancy and thermocapillary convection is the dynamic Bond number:

$$Bo_{\text{dyn}} = \frac{\rho_1 \cdot \beta \cdot g \cdot L^2}{\partial\gamma_{\text{lv}}/\partial T}, \quad (7.4)$$

where β is the expansion coefficient.

Fluid flow within a defined geometry exhibits transitions when its velocity exceeds a certain threshold value [Drazin 1981]. This is also true for Marangoni convection. The corresponding value of the control parameter, which is represented by the Marangoni or the Reynolds–Marangoni number (Equations (7.1) and (7.2)), is defined as the critical condition. For the classical Marangoni–Bénard configuration, where the temperature gradient is perpendicular to the interface, the critical condition for the onset of the flow is $Ma_c \approx 80$ [Pearson 1958]. For thermocapillary flow, where the gradient of surface tension is parallel to the free surface, there is no threshold for the flow to start. For a liquid bridge, when its size is finite, the Marangoni flow exhibits a stationary transition from axisymmetric steady flow to three-dimensional steady flow because of the existence of a solid end. The critical Marangoni number for this transition is defined as Ma_{c1} . This is the first bifurcation for a low- Pr liquid bridge geometry. A further increase in the Marangoni number results in an oscillatory transition, which occurs through a Hopf bifurcation [Wanschura 1995]. The critical Marangoni number for this transition is defined as Ma_{c2} . Above Ma_{c2} , velocity, pressure, and temperature fields become time dependent. As a result, the incorporation of impurities or dopants during crystal growth also shows time dependency, i.e. the spatially inhomogeneous distribution of impurities or dopants, also known as growth striations. At the critical condition Ma_{c2} , only a single pair of disturbance modes becomes unstable, thus the frequency of the oscillation is single. Another pair of disturbance modes becomes unstable and a multiperiodic oscillation of the flow occurs when the Marangoni number exceeds the critical Marangoni number Ma_{c3} . From stability analysis, the critical value can be determined as a condition where the growth rate of a disturbance becomes zero. However, the experimentally observed multiple oscillations appear to have larger Marangoni numbers (see below). This is attributed to the fact that the growth rate of the disturbance must be large enough that its amplitude becomes large enough to be detected in finite time.

The mechanism for the instability is different for low and high Pr -number fluids; for low Pr -number fluids, it is a mechanical instability and for high Pr -number fluids, a hydrothermal instability coupled with the temperature field. The hydromechanical feature of the Marangoni flow is reviewed in [Kuhlmann 1999].

Marangoni convection has been known to crystal growers for a long time, but used to be viewed as more of a curiosity with no real impact on crystal growth until the early 1980s; to quote from the book *Floating-Zone Silicon* [Keller 1981], p.42: ‘Marangoni

flow has not yet been observed experimentally in Si float zones although calculations of Chang and Wilcox render very high driving forces for this case'. Chang's articles [Chang 1975, Chang 1976] were the first numerical simulations elucidating the importance of thermocapillary convection, and were followed by a large number of other simulations and studies using transparent model materials [Chang 1979, Chun 1978, Chun 1979, Chun 1980, Chun 1982, Clark 1980, Schwabe 1978, Schwabe 1979, Schwabe 1981, Schwabe 1982, Kamotani 1984]. Triggered by the development of microgravity experiments in the late 1970s and 1980s, intensive studies of Marangoni flow have been stimulated both for low *Pr*-number fluids (opaque metallic melts) and high *Pr*-number fluids (transparent organic fluids), because Marangoni flow is a typical gravity-independent phenomenon but is often obscured by buoyancy convection on the ground.

The importance of thermocapillary convection for the crystal growth of semiconductors such as Si was demonstrated shortly thereafter with the first FZ experiments under microgravity [Carlberg 1984, Carlberg 1986-1, Cröll 1986, Cröll 1994-1, Eyer 1984, Eyer 1985-1]. Today thermocapillary convection has to be taken into account for all important crystal growth processes and nearly all numerical simulations of crystal growth melts with free surfaces.

Unfortunately, the values of $\partial\gamma_v/\partial T$, necessary for numerical simulations and for calculating *Ma* or *Re_M* values in order-of-magnitude analyses, are not always precisely known, or not known at all for a variety of important crystal growth materials. Surface tension values and $\partial\gamma_v/\partial T$ can also be quite sensitive to small amounts of impurities. This is the case for Si and O, as discussed in section 7.1.3. Table 7.1 shows the $\partial\gamma_v/\partial T$ values for a few common semiconductors.

Even less known than $\partial\gamma_v/\partial T$ is $\partial\gamma_v/\partial C$ for mixed crystals. The relationship between composition and surface tension can be linear, such as in the Ge–Si system with a value of $\partial\gamma_v/\partial C = +2.2 \times 10^{-3} \text{ N/m}\cdot x$ (*x* = mole fraction of Si content) [Cröll 2002-2], but this is not always the case. An example is shown for the Ga–Sb system in Figure 7.2 [Tegetmeier 1995], where the value of γ_v deviates from a linear relationship at both ends of the compositional range. For surface active components, there might be even larger deviations. A few systems, e.g. Sn–Bi [Tison 1992], or NaNO₃–C₂H₅COOK [Schwabe 1996], have been reported where $\partial\gamma_v/\partial T$ has a maximum as a function of composition.

Table 7.1 *Temperature dependence of the surface tension for several semiconductors. The surface tension of molten Si and its temperature coefficient have been found to show a marked oxygen partial pressure dependence; see 7.1.3*

	$\partial\gamma_v/\partial T$ (10^{-3} N/m K)	Reference
Si (for $P_{\text{O}_2} = 10^{-19} \text{ Pa}$)	–0.74	[Mukai 2000]
Si (for $P_{\text{O}_2} = 10^{-14} \text{ Pa}$)	–0.37	[Mukai 2000]
Ge	–0.08	[Kaiser 2001]
GaAs	–0.18	[Rupp 1991]
GaSb	–0.10	[Tegetmeier 1996]

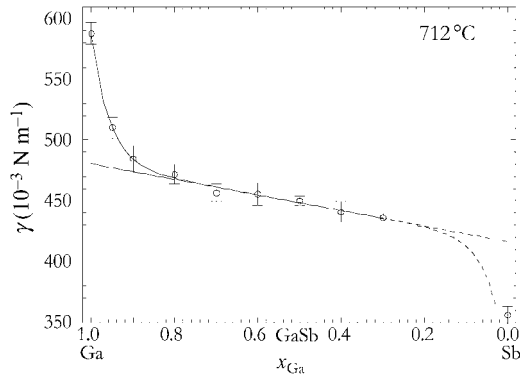


Figure 7.2 Surface tension vs composition for the system Ga–Sb, after (Reprinted with permission from [Tegetmeier 1995], copyright (1995) A. Tegetmeier).

7.1 Thermocapillary Convection in Float Zones

7.1.1 Model Materials

Since it has the highest surface/volume ratio of the common melt growth methods, FZ growth is affected the most by Marangoni flows. Thermocapillary convection in FZ set-ups was first investigated using transparent melts or model materials, since it is possible to visualize the flow in these systems. These materials, such as silicone oil or NaNO_3 , have a rather high Prandtl number ($Pr = 1\text{--}100$) compared to metallic melts such as semiconductors ($Pr = 10^{-2} - 10^{-1}$). Thermocapillary convection in these transparent systems usually shows two convection rolls as depicted in Figure 7.3, the standard pattern in a float zone. Note that in addition, many ‘half-zone’ model experiments were performed. A half-zone consists of a set-up with a solid hot end and a solid cold end, usually a material different from the melt material (Figure 7.3). Crystal growth is of course not possible, or is reduced to crystallizing the zone, but it is much easier to have a well-defined temperature gradient and thus Marangoni number in this set-up.

Stream velocities in the high Pr systems are usually of the order of mm/s. The transition to a time-dependent regime occurs at comparatively high Marangoni numbers, with $Ma_{c2} \approx 10^4$ [Kamotani 1984, Schwabe 1988]. The transition to time-dependency involves a reduction of the symmetry, i.e. a transition from a two-dimensional to a three-dimensional flow pattern, together with azimuthal running waves of the convection roll [Schwabe 1988]. There are other possibilities for instabilities in half-zones, such as surface waves, that have been studied in numerical simulations [Kazarinoff 1989]; a summary for earlier half-zone experiments can be found in [Levenstam 1995].

7.1.2 Semiconductors and Metals

Initially, thermocapillary convection for low Pr number melts such as metals and semiconductors was experimentally accessible only indirectly from the segregation of

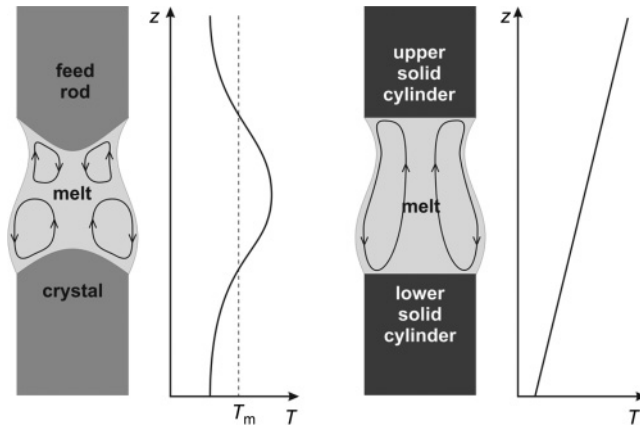


Figure 7.3 Schematic drawing of Marangoni flow in a full float zone (left) and in a model ‘half-zone’ (right), with corresponding temperature profiles. The half-zone usually uses a different material than the melt for the top and bottom solid cylinders, although the lower one can be crystallized melt material. The dotted line indicates the melting temperature (copyright A. Cröll; reproduced with permission).

crystals. The first experimental indications that thermocapillary convection is important were the results of [Barthel 1979] and [Jurisch 1982] on the formation of striations in FZ refractory metal crystals. Starting in 1983, several semiconductor FZ experiments were performed under microgravity conditions on sounding rockets and Spacelab flights, to separate the influences of buoyancy and thermocapillary convection in float zones of Si and Ge [Carlberg 1984, Carlberg 1986-1, Carlberg 1986-2, Cröll 1986, Cröll 1991, Cröll 1994-1, Eyer 1984, Eyer 1985-1, Kölker 1984, Kölker 1986]. Radiation heating (mirror furnaces, see Chapter 4.2) was always employed to avoid RF-induced convective flows. Comparison of the microgravity crystals and their terrestrial counterparts showed that similar striation patterns, although with slightly less variation in dopant concentration, were formed under microgravity (Figure 7.4, top and centre). These results lead to the conclusion that thermocapillary convection is a dominant source of striations in radiatively heated Si FZ zones.

Those findings were corroborated by later experiments with confined melt zones, where the Si melt zone was coated by a 5- μm thin film of SiO_2 to suppress thermocapillary convection [Cröll 1986, Eyer 1985-2]. Such crystals show no dopant striations at all (Figure 7.4, bottom), indicating that time-dependent thermocapillary convection is the only source for the formation of dopant striations in FZ-Si, at least with radiation heating and the zone dimensions (8–10 mm diameter, 10–15 mm length) and temperature gradients (30–100 K/cm) employed in these experiments. Similar results were found for Ge [Carlberg 1984, Carlberg 1986-1, Carlberg 1987, Levenstam 1996].

Other FZ experiments under microgravity with low Pr materials, using GaAs [Cröll 1994-2, Herrmann 1995, Müller 1991] and GaSb [Cröll 1998-1, Tegetmeier 1996], also pointed to time-dependent thermocapillary convection in these materials, as do the normal gravity results of the FZ growth of Mo and Nb [Barthel 1979, Jurisch 1982, Jurisch 1990-1, Jurisch 1990-2], and the half-zone results for Hg [Han 1996] and Sn [Yang 2001].

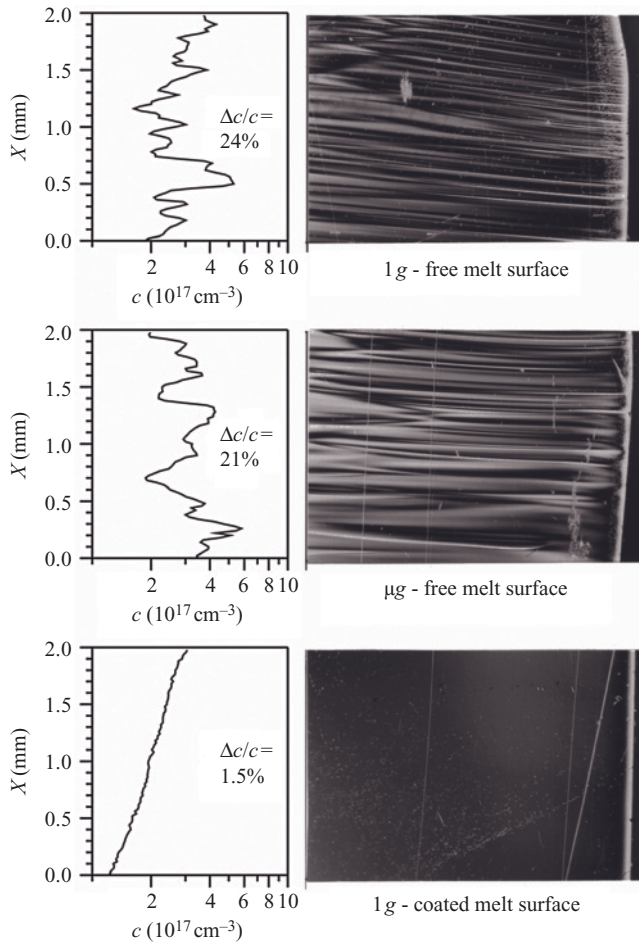


Figure 7.4 Micrographs of parts of Si:Sb crystals (growth direction bottom to top of each micrograph) and corresponding axial concentration profiles determined by spreading resistance measurements. Top: Crystal grown under normal gravity with dopant striations; centre, crystal grown under microgravity with dopant striations; bottom, crystal grown under normal gravity with surface coating, showing no dopant striations. Compare [Cröll 1986, Cröll 1991, Cröll 1994-1, Eyer 1985-2].

7.1.3 Effect of Oxygen Partial Pressure on Thermocapillary Flow in Si

One of the most important factors for the Marangoni flow of metallic melts including semiconductor melts is the effect of oxygen or sulphur. For example, in the welding process of steel, there is Marangoni flow due to temperature differences between the centre and the periphery of the weld pool, where flow direction depends on the oxygen partial pressure P_{O_2} of an ambient atmosphere. Normally, the flow direction is from the centre (hot) to the periphery (cold) because of the negative temperature coefficient of

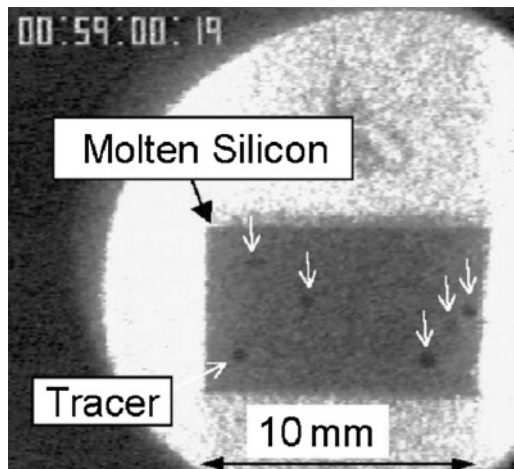


Figure 7.5 X-ray radiograph of tracer particles in a liquid bridge (half-zone) of Si under microgravity during parabolic flight (Reprinted with permission from [Azami 2001-2], copyright (2001) Electrochemical Society).

surface tension. However, in an ambient atmosphere with high P_{O_2} , the flow direction is the reverse, from the periphery (cold) to the centre (hot), because of a positive temperature coefficient of the surface tension [Heiple 1982]. For molten steel, the value of the temperature coefficient of surface tension, $|\partial\gamma_v/\partial T|$, has been reported to decrease with increasing P_{O_2} , to become zero at a certain P_{O_2} value, and then to turn positive [Takiuchi 1991]. This suggests that the direction and velocity of thermocapillary flow can be controlled by changing P_{O_2} values.

The thermocapillary flow of molten Si was observed for the first time *in situ* by X-ray radiography under microgravity using the parabolic flight of a jet aircraft, as shown in Figure 7.5 [Azami 2001-2, Nakamura 1999-3]. Figure 7.6 shows the tracer velocity in a liquid bridge with an aspect ratio As of 1.0 as a function of the oxygen partial pressure. In this experiment, P_{O_2} was defined at the pressure where the silica ampoule was evacuated and sealed. This oxygen partial pressure corresponds to that defined at $P_{O_2}^{\text{inlet}}$ by Ratto *et al.* [Ratto 2000]. The velocity was measured as the displacement of a tracer particle parallel to the axial direction of the liquid bridge per unit time and was of the order of 10 mm/s. This tracer particle velocity would not be the real flow velocity. The real surface velocity is expected to be one order of magnitude higher than that observed, as predicted by Lan and Kou [Lan 1991-5]. Nevertheless, it clearly depends on P_{O_2} .

The P_{O_2} dependence of the thermocapillary flow is explained by the fact that the Marangoni number, Ma , which shows the magnitude of the Marangoni flow, is a function of the temperature coefficient of surface tension, as given in Equation (7.1). Figure 7.7 shows the P_{O_2} dependence of the temperature coefficient of surface tension of molten Si [Mukai 2000]. The larger P_{O_2} becomes, the smaller the absolute value of the temperature coefficient, $|\partial\gamma_v/\partial T|$, becomes. The saturation oxygen partial pressure $P_{O_2}^{\text{sat}}$ is 1.32×10^{-14} Pa at 1693 K and 2.75×10^{-19} Pa at 1773 K. Above $P_{O_2}^{\text{sat}}$ the surface of molten Si is coated

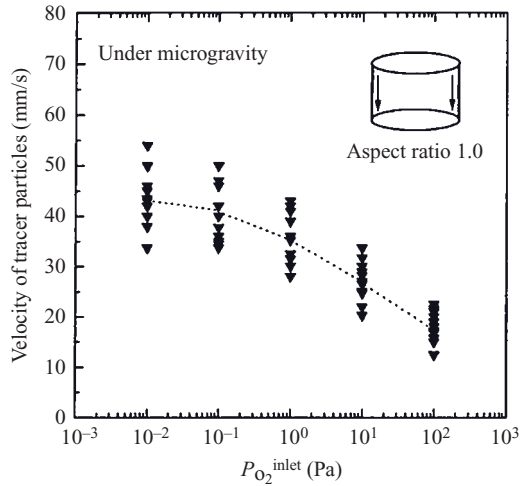


Figure 7.6 Tracer velocity due to thermocapillary convection vs oxygen partial pressure in a Si liquid bridge (aspect ratio $As = 1.0$) under microgravity (Reprinted with permission from [Azami 2001-2], copyright (2001) Electrochemical Society).

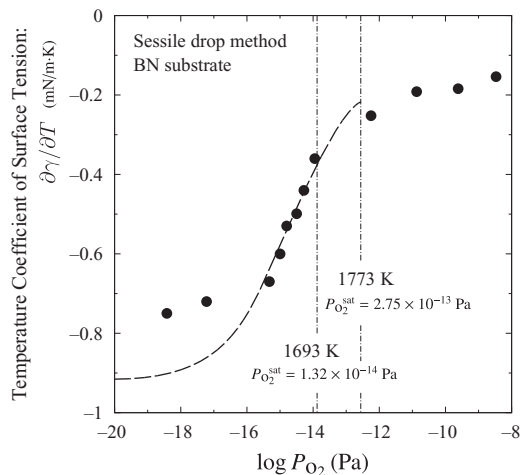


Figure 7.7 Temperature coefficient of surface tension for molten Si as a function of oxygen partial pressure of an ambient atmosphere (Reprinted with permission from [Mukai 2000], copyright (2000) ISIJ).

with a thin film of SiO_2 ; there is no Marangoni flow. In Figure 7.7, however, the temperature coefficient of the surface tension is plotted even in such a range. This strange behaviour of the temperature coefficient is due to the measurement method, i.e. the sessile drop method. The specimen behaves as if it were a single-phase liquid, although the melt surface is coated with a solid film of SiO_2 . This is why the temperature coefficient was measured over the $P_{O_2}^{\text{sat}}$ value.

Note that there is a large difference in P_{O_2} value in the abscissa between Figures 7.6 and 7.7. This difference depends on where P_{O_2} was measured; i.e. at the inlet or the outlet of the gas flow system. The idea was theoretically derived by [Ratto 2000] and experimentally validated by [Azami 2001-4]. The oxygen partial pressure at the Si melt surface, $P_{O_2}^{\text{surface}}$, can be estimated regardless of measurement position. From the practical point of view, controlling P_{O_2} at the inlet is convenient.

In order to check the possibility of controlling the thermocapillary flow during crystal growth by adjusting P_{O_2} , single crystals of Si were grown in an atmosphere with various oxygen partial pressures ranging from $P_{O_2}^{\text{surface}} = 5.3 \times 10^{-24}$ to 3.6×10^{-14} Pa at the melt surface [Hibiya 2003-1]. At $P_{O_2}^{\text{surface}} = 1.3 \times 10^{-14}$ Pa, which corresponds to the equilibrium oxygen partial pressure for SiO_2 formation, precipitation of SiO_2 was observed during the seeding process. At $P_{O_2}^{\text{surface}} = 3.6 \times 10^{-14}$ Pa, a thick SiO_2 powder layer was formed. Growth striations, which are evidence of oscillatory flow, were observed for all crystals except for those grown at $P_{O_2}^{\text{surface}} = 1.3 \times 10^{-14}$ and 3.6×10^{-14} Pa. This suggests that thermocapillary flow was not fully suppressed by increasing P_{O_2} , whereas above $P_{O_2}^{\text{surface}} = 1.3 \times 10^{-14}$ Pa thermocapillary flow was not possible because the melt surface was coated with SiO_2 . This shows that the thermocapillary flow of molten Si cannot be controlled by oxygen; for molten steel the velocity can be decreased gradually with P_{O_2} and finally the flow direction can be changed. Crystal growth experiments suggest that only turbulent Marangoni flow exists at the Si melt surface; the smallest estimate for the Marangoni number in this system is ~ 900 . This unique behaviour for molten Si can be attributed to the poor solubility of oxygen in the Si melt; the solubility of oxygen in molten Si is small (ppm range) compared with that in molten Fe (0.1%).

7.1.4 Fluid Dynamics of Thermocapillary Flow in Half-Zones

7.1.4.1 Introduction

As mentioned in section 7.1.1, the so-called ‘half-zone’ liquid bridge (see Figure 7.8) has been widely used to understand the fundamental features of thermocapillary flow in FZ

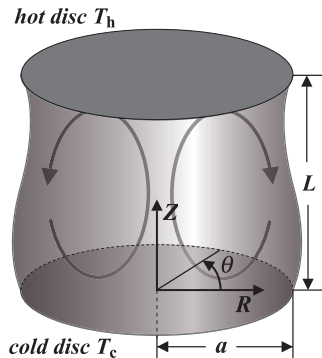


Figure 7.8 Half-zone configuration (Reprinted with permission from [Shiratori 2007-2], copyright (2007) S. Shiratori).

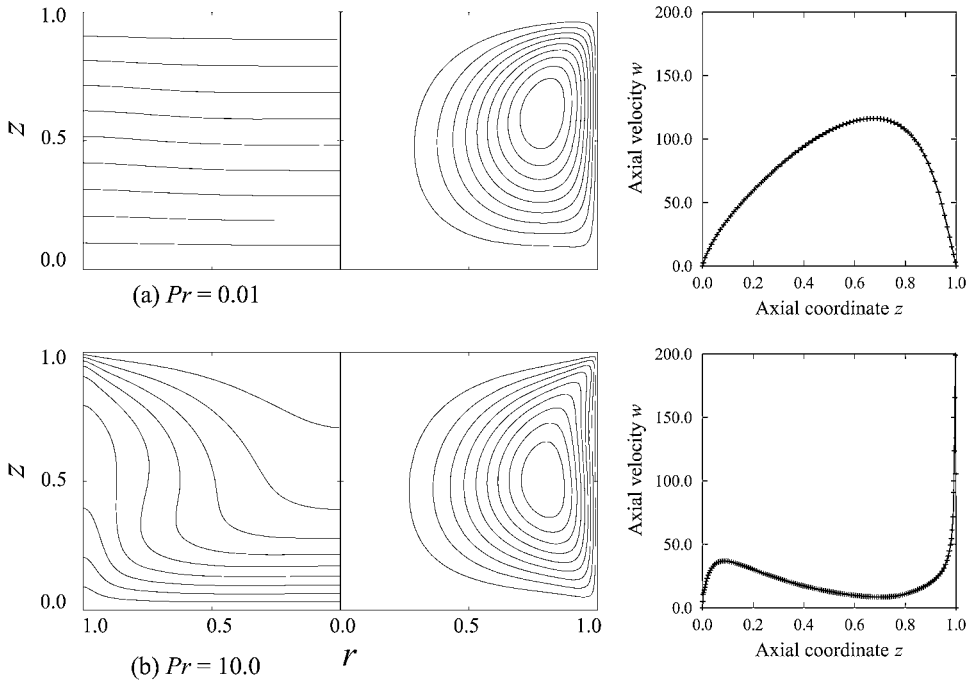


Figure 7.9 Isothermal lines, streamlines, and axial velocities along the free surface for two different Prandtl numbers at $Re_M = 1000$, $As = 1.0$; $Pr = 0.01$ (a); $Pr = 10.0$ (b). The step sizes between neighbouring contour lines are 0.1 for isothermal lines, and 0.9 ($Pr = 0.01$) and 0.41 ($Pr = 10.0$) for streamlines. Note that the lower disc is heated. Radial and axial coordinates are scaled by disc radius and bridge height respectively, and velocity w is scaled by kinetic viscosity over the disc radius (Reprinted with permission from [Shiratori 2007-2], copyright (2007) S. Shiratori).

crystal growth. Because of its simple configuration, thermocapillary flow in a half-zone can be discussed using well-defined parameters; this configuration is therefore more suitable for an investigation than a full zone from the viewpoint of fluid dynamics.

In the half-zone configuration, a liquid is sustained by surface tension between two parallel, coaxial and differently heated disks. The induced flow and temperature fields are strongly dependent on the Prandtl number (Pr) of the fluid. Figures 7.9a and 7.9b show the flow and temperature fields of the axisymmetric steady flow in a liquid bridge with an aspect ratio (the liquid height L over the radius a) of $As = 1.0$ at the Reynolds number $Re_M = 1000$ for two different Prandtl numbers: $Pr = 0.01$, 10.0. In the low Prandtl number case ($Pr = 0.01$), the temperature field is dominated by thermal conduction, and thus a nearly linear temperature distribution causes nearly homogeneous Marangoni effects all along the free surface. In contrast, for high Prandtl number ($Pr = 10.0$), the heat transfer due to convection is dominant in the temperature field. The isothermal lines are strongly deformed and concentrated into rigid boundaries, especially in the cold corner where the locally strong Marangoni effect causes a sharp peak in the velocity distribution. Because of these characteristics, the behaviour of the flow transitions and their instabilities differ

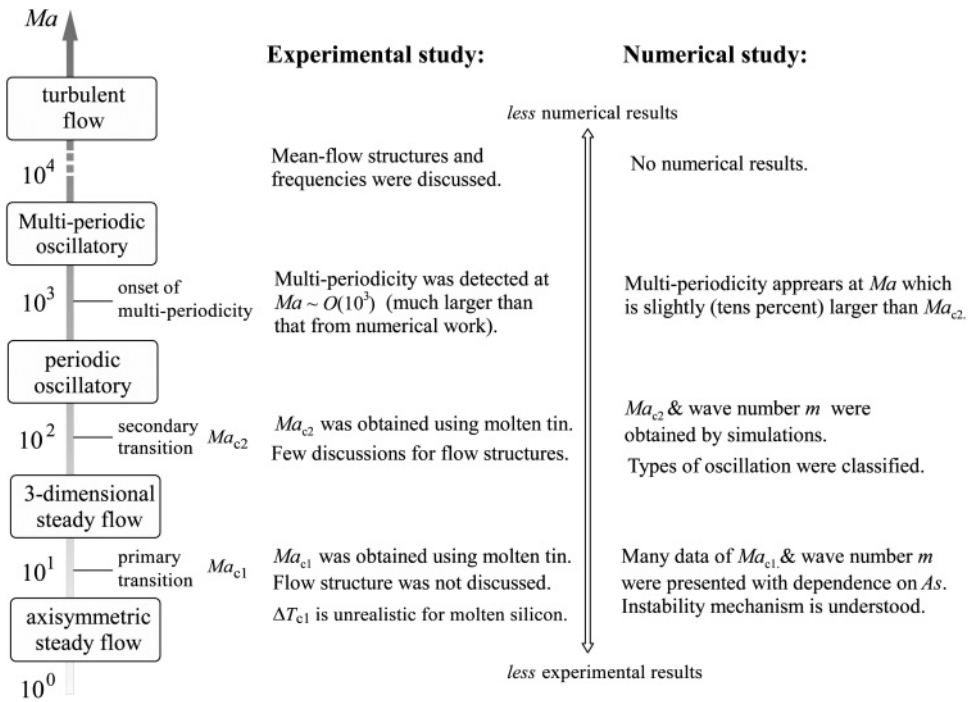


Figure 7.10 Outline of the current state of the research on thermocapillary half-zones of low Prandtl numbers.

significantly. The discussion here will be confined to low Prandtl numbers. An overview for high Prandtl numbers can be found e.g. in [Ueno 2003].

An outline of the current state of research on thermocapillary half-zones of low Prandtl numbers is shown schematically in Figure 7.10. Generally speaking, for the small Ma case, there are fewer results from experiments than from numerical work; for the large Ma case, the opposite holds true. Thus, there has been a long-standing problem of the mutual understanding between experimental and numerical work. Since low- Pr fluids usually have high melting points, opacity, and chemical reactivity, experiments become much more difficult than in transparent high- Pr systems. Especially for experiments using molten Si, a flow with small Ma below Ma_{c2} has not been achieved, because the temperature differences between the upper and lower edge of the liquid bridge corresponding to the critical conditions would be unrealistically small in the usual experimental set-up. Some experimental data for Ma_{c1} have been obtained using molten Sn [Matsumoto 2004].

Important tasks in the study of fluid dynamics are to determine the critical conditions for flow transitions (e.g. stationary to oscillatory), to clarify the mechanisms of the instabilities which cause the transitions and to give simple descriptions of flow structures. In the following sections, results for the above tasks are summarized. Theoretical and numerical aspects of the thermocapillary flow were reviewed by [Kuhlmann 1999]. Experimental studies using molten Si were overviewed in part by [Hibiya 2003-2].

7.1.4.2 Experimental Approach

In a typical experiment, small liquid bridges (radius <5 mm) are sustained between upper and lower carbon rods, as shown in Figure 7.11a, and they are heated from the top in order to suppress buoyancy flow on the ground. Heating is achieved by a mono-ellipsoidal infrared mirror furnace (Figure 7.12). In order to avoid oxidation of the melt surface, the ambient atmosphere must be replaced with pure Ar gas of 6N purity. Since the temperature coefficient of the surface tension depends strongly on the oxygen partial pressure P_{O_2} of an ambient atmosphere (see e.g. [Mukai 2000]), the control of the atmosphere is an important issue.

Because of the opacity of molten Si, the flow can only be visualized by X-ray radiography. X-ray visualization with tracer particles (zirconia, $450\ \mu\text{m}$ in diameter coated with silica glass to an outer diameter of 1 mm) has been done by [Nakamura 1996, Nakamura 1999-1, Nakamura 1999-3], but the size of the tracers might be too large to sufficiently follow the flow; i.e. the tracer diameter is larger than the velocity boundary layer thickness for a thermocapillary flow of 0.1 mm. Other experimental approaches have been employed based on temperature fluctuation measurements using multiple thermocouples located near the cold disc, as shown in Figure 7.11b, [Hibiya 1996, Hibiya 2005, Nakamura 1998, Yamane 2005], and observations of the liquid–solid interface position fluctuations using a laser microscope [Sumiji 2001, Sumiji 2002].

For noncontact measurement, the optical pyrometer [Cheng 2000] and the brightness of the recorded image have been employed to detect the frequencies of the temperature fluctuations [Azami 2001-3]. Sumiji *et al.* have optically observed the fluctuations of a solid–liquid interface position, and have confirmed that the frequencies and azimuthal distribution of solid–liquid interface fluctuations show similar features to that investigated by temperature observations [Sumiji 2001, Sumiji 2002]. Since the time-dependent hydrodynamic pressure causes dynamic surface deformations, surface oscillation is expected to be synchronized with that of an oscillatory flow field. Using a phase shift interferometry system, as shown in Figure 7.13, the free surface oscillation has been measured on a very small scale by [Okubo 2005, Onuma 1999, Sumiji 2000].

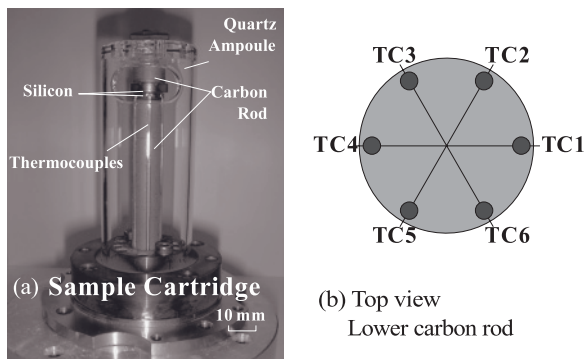


Figure 7.11 Configuration of sample: (a) sample cartridge; (b) layout of thermocouples (top view) (Reprinted with permission from [Hibiya 2005], copyright (2005) Springer Science + Business Media).

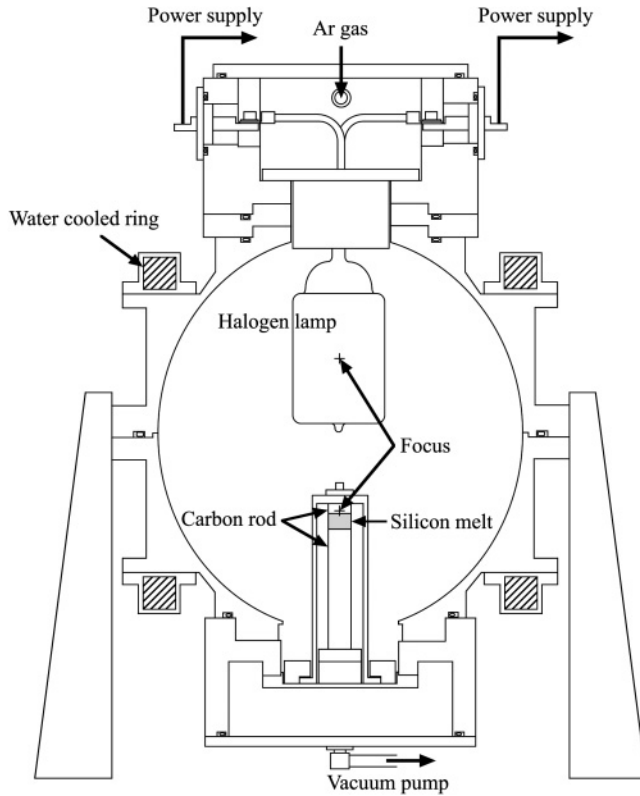


Figure 7.12 Mirror furnace for Marangoni flow study.

7.1.4.3 Flow Transitions

When the driving force of the flow exceeds a certain threshold in half-zones, the steady axisymmetric flow bifurcates to three-dimensional flows. In low- Pr fluids, it was suggested that the stationary transition takes place before the onset of oscillation, from the three-dimensional numerical simulations by [Rupp 1989]. After their suggestion, important information from linear stability analysis was given by [Kuhlmann 1993, Neitzel 1993, Shen 1990, Wanschura 1995]. From these investigations, the primary instability for the low- Pr fluids is understood to be stationary. The Marangoni number corresponding to this threshold is defined as Ma_{c1} . The critical Reynolds number (Re_M , as shown in section 7.1.1) which has been obtained from numerical studies, was summarized in [Shevtsova 2005].

In FZ configurations, the onset of the oscillatory Marangoni flow was experimentally detected for the first time by [Cröll 1989], as explained in section 7.1.6. In half-zones, the second critical Reynolds number Re_{Mc2} was calculated for the first time by [Levenstam 1995]. [Leyboldt 2000] provided the values of Re_{Mc2} and the first explanation of the instability of the second transition. [Imaishi 2001] conducted a number of numerical simulations, and provided the first and second critical Reynolds numbers as a function of the widely varied aspect ratio.

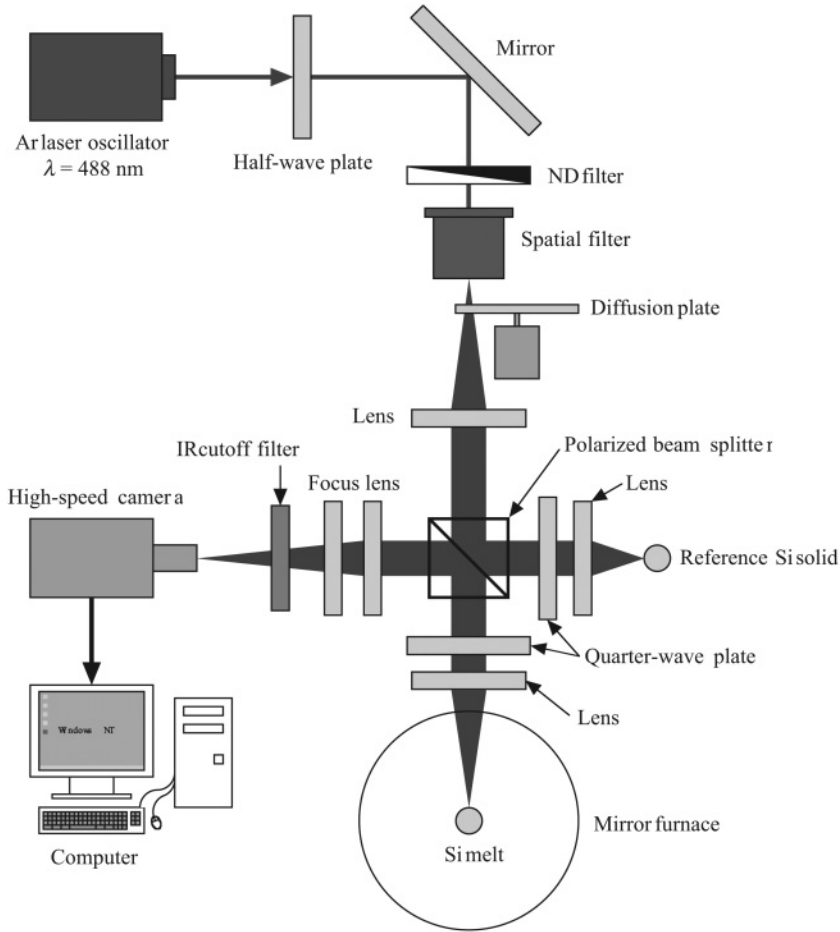


Figure 7.13 Schematic diagram for phase-shift interferometry for observing molten Si surface oscillations [Okubo 2005, Sumiji 2000] (Reprinted with permission from [Okubo 2005], copyright (2005) Springer Science + Business Media).

The first transition of the flow was observed experimentally for the first time, using molten Sn with Fe rods, by [Matsumoto 2004]. Numerical simulations that model the experiments of [Matsumoto 2004] have been carried out by [Li 2005, Yasuhiro 2004]. The experimentally estimated values of $Ma_{c1} = 10\text{--}20$ by [Matsumoto 2004] agreed well with those reported in numerical studies.

The critical Reynolds numbers Re_{Mc1} , Re_{Mc2} for the low- Pr half-zones are summarized in Figure 7.14, as a function of the aspect ratio. The second critical conditions is rather dependent on the geometry, compared to that of the first transition. Ma_{c2} has been determined experimentally for molten Sn by [Takagi 2001], as $Ma_{c2} = 43.3$ for the case $As = 2.02$.

In many of the numerical investigations mentioned, the static and dynamic deformations of the free surface were not taken into account, i.e. the liquid bridge was assumed

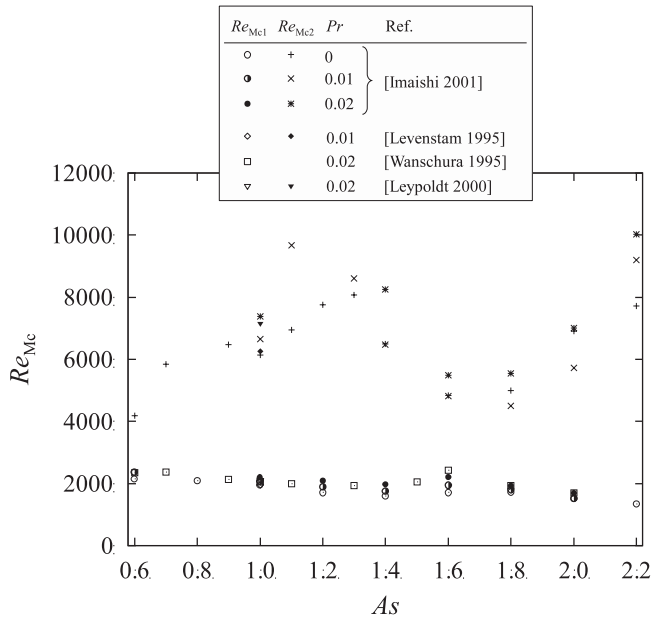


Figure 7.14 Critical Reynolds numbers Re_M as a function of the aspect ratio for the pure thermocapillary flows in cylindrical liquid bridges of low- Pr fluids [Imaishi 2001, Levenstam 1995, Leyboldt 2000, Wanschura 1995].

to be cylindrical. This corresponds only to a liquid bridge with large surface tension, or the case of zero gravity, whereas under gravity the liquid bridge deforms under its own weight, as shown in Figure 7.8. By use of the body fitted coordinate (BFC), the effect of the free surface deformation can be investigated. Chen *et al.* carried out the linear stability analysis for the case that the liquid volume is different from that of the cylinder [Chen 1998, Chen 1999]. [Nienhüser 2002] investigated the detailed linear stability analysis with consideration of the static deformation due to the liquid’s own weight. These results coincide qualitatively, and the first critical Reynolds number Re_{Mc1} has a local minimum near the condition that the volume ratio (normalized by 1 for the cylinder) becomes 0.9, for low- Pr cases.

When the Reynolds number of the flow increases beyond the second critical condition $Re_M > Re_{Mc2}$, the oscillation of the flow shows multiperiodicity. From the experiments by Nakamura *et al.* and Azami *et al.*, the Ma values at which the multiperiodic oscillatory flows take place can be roughly determined to be of the order of 10^3 [Azami 2001-1, Nakamura 1999-1]. On the other hand, from the numerical work, the onset of the multiperiodicity seems to be much lower than that observed by experiment [Imaishi 1999]. One of the reasons for this discrepancy may be the difficulty in experimental detection of the onset of multiperiodicity in small Marangoni number conditions.

The three-dimensional flow has azimuthally periodic structures which are represented by an azimuthal wave number m , which is an integer because of the cylindrical domain. The geometrical dependence of the azimuthal wave numbers has been investigated by

numerical analysis or by experimental observation of the transparent high- Pr fluids. A typical empirical relation is provided by [Preisser 1983] for the high- Pr fluids as

$$As \cdot m \approx 2.2. \quad (7.5)$$

This relationship also holds true for the low- Pr case, as reported by [Wanschura 1995].

7.1.4.4 Instability Mechanisms

The instability mechanisms for the first transitions (at Re_{Mc1}) were explained for the first time by [Wanschura 1995] for both low and high Prandtl numbers. For low Prandtl numbers, the instability is solely caused by inertia effects: in the three-dimensional steady flow obtained by the numerical simulation, there exists an azimuthal flow directed against the Marangoni effect, and the same three-dimensional structures arise in the case of the pure conduction limit $Pr \rightarrow 0$ (see e.g. [Imaishi 2001]). In the stability analysis by [Xu 1984], who treated an infinitely long cylinder, the instabilities of axisymmetric flows were oscillatory, even for the low- Pr cases. This suggests that the existence of the upper and lower discs is necessary for the appearance of a three-dimensional steady flow.

According to [Levenstam 1995] and [Wanschura 1995], the instability mechanism for the first transition can be understood in terms of strain acting on the basic vortex core. This mechanism is analogous to that in vortex rings, which suffer instabilities due to a self-induced strain field caused by the natural curvature of the vortex ring [Fukumoto 2005, Widnall 1974]. As a result of the instability, Kelvin waves are resonantly amplified. Both the instability explained by [Wanschura 1995] and that of vortex ring belong to the same type of vortex instability, which is now termed ‘elliptic instability’ [Bayly 1986, Kerswell 2002]. In addition, [Nienhüser 2002] reported that a ‘centrifugal instability’ mechanism also contributes to the instability for the first transition at Re_{Mc1} .

For low- Pr half-zones the elliptic and centrifugal mechanisms reinforce each other mutually. The balance of these two mechanisms may change due to geometrical conditions. This balance change has been investigated numerically, using the configuration of a liquid bridge in which the free surface is partially confined by solid walls, as shown in Figure 7.15a [Shiratori 2004, Shiratori 2007-1, Shiratori 2007-2]. The balance of the elliptic and centrifugal mechanisms was found to determine the variety of the resulting instability, and it may cause the direct transition from axisymmetric steady flow to oscillatory flow. This configuration is quite effective in reducing the Reynolds number of the flow and in keeping the temperature difference across the whole liquid bridge at realistic values. This idea was first applied to experimental FZ crystal growth by [Cröll 1991], as explained in Section 7.1.6.

In this partially confined half-zone (PCHZ) configuration, the ratio of the free surface length L_w to the whole liquid height L is defined as $\xi = L_w/L$. The driving force is represented by the Reynolds number using L_w and the temperature difference along the free surface: $Re^w = -\partial\gamma_s/\partial T \Delta T_w L_w / (\rho v^2)$, where $\partial\gamma_s/\partial T$ is the temperature coefficient of the surface tension, ρ is density, and v is kinematic viscosity. In addition, the axial position of the free surface is indicated using angle brackets, e.g. <hot> for the case that the free surface is located adjacent to the hot disc. In PCHZ, the structure of axisymmetric steady flow depends on the fraction ξ and the axial position of the free surface, as shown in Figure 7.16. In particular, in the case <hot>, the shape of the vortex core becomes circular

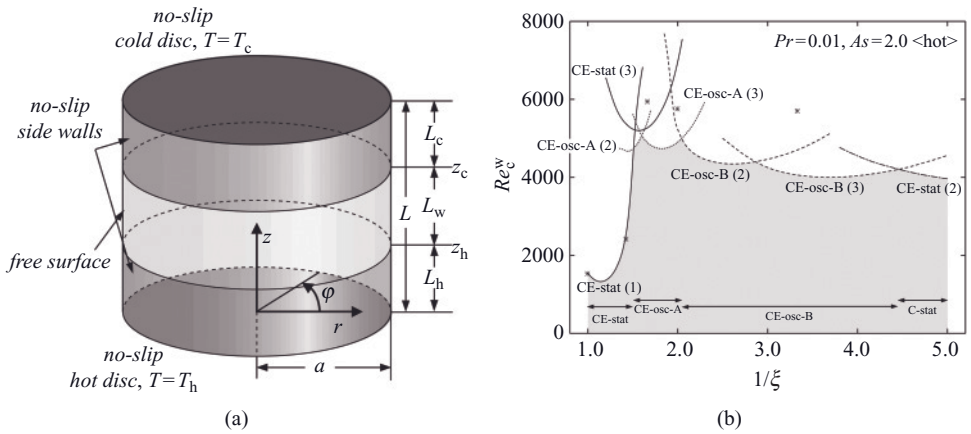


Figure 7.15 (a) Configuration of partially confined half-zones (PCHZ), in which the free surface is partially covered by solid side walls leaving the length L_w . Free surface fraction ξ is defined as L_w/L (Reprinted with permission from [Shiratori 2004], copyright (2004) Elsevier Ltd). (b) Critical Reynolds number Re_c^w as a function of the inverse free surface fraction for the case where the free surface is located adjacent to the hot disc (Reprinted with permission from [Shiratori 2007-1, Shiratori 2007-2], copyright (2007) American Institute of Physics). Line styles and labels indicate different instability mechanisms, and the azimuthal wave number is given in brackets. Axisymmetric steady flow is linearly stable in the shaded region. Asterisks indicate critical data taken from time-dependent simulations.

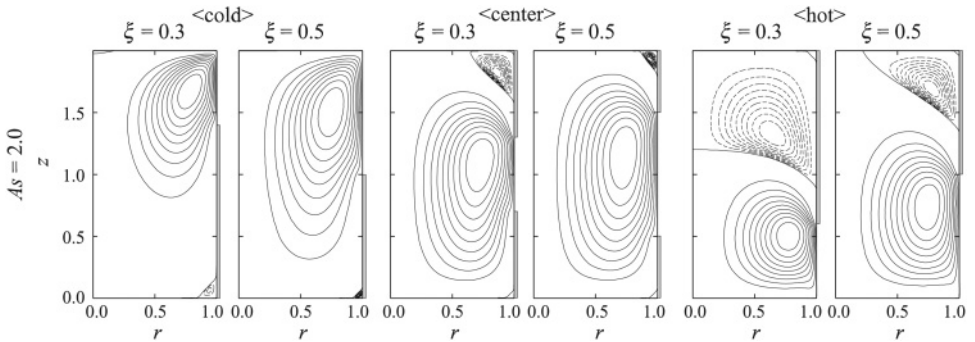


Figure 7.16 Streamlines of the basic axisymmetric steady flow for $Pr = 0.01$, $As = 2.0$ and $Re_0^w = 1000$. Solid lines indicate positive values of the Stokes stream function and dotted lines indicate negative values. The step size between neighbouring contour lines is constant with $\Delta(r\psi_0) = r\psi_0^{\max}/10$ for positive values, and $\Delta(r\psi_0) = r\psi_0^{\min}/10$ for negative values. The term in angle brackets defines the location of the free surface (Reprinted with permission from [Shiratori 2007-1], copyright (2007) American Institute of Physics).

for small ξ . Because the elliptic instability is due to the elliptical shape of the streamlines of axisymmetric steady flow, the configuration <hot> affects the balance of elliptic and centrifugal instabilities. Figure 7.15b shows the critical Reynolds numbers Re_c^w in PCHZ of $As = 2.0$ for the case <hot>. From the analysis of the energy transfer, four qualitatively

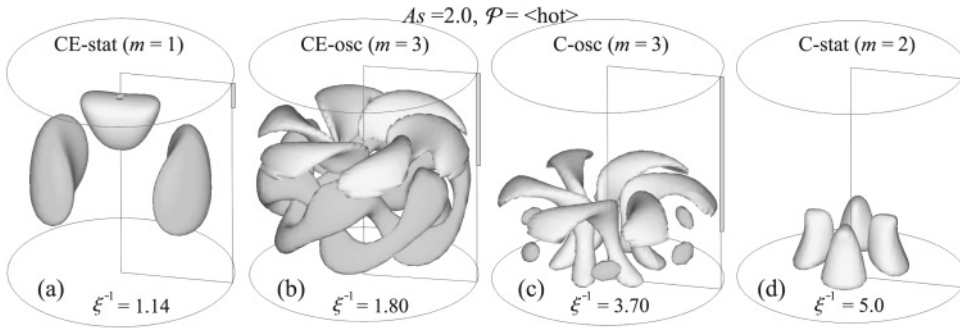


Figure 7.17 Iso-surfaces of local energy production. The free surfaces are located adjacent to the hot disc, and the aspect ratio for whole liquid bridge is $As = 2.0$. The light grey and dark grey regions indicate the centrifugal and elliptic mechanisms, respectively (Reprinted with permission from [Shiratori 2007-2], copyright (2007) American Institute of Physics).

different types of instability mechanisms are classified, depending on the geometry [Shiratori 2007-1]. Two of them are oscillatory instabilities, i.e. the axisymmetric steady flow exhibits a direct transition to oscillatory flow in these geometrical conditions [Shiratori 2004]. Figure 7.17 shows the regions where the energy production of the disturbance flow is strong. The light grey regions indicate the centrifugal mechanism and dark grey regions the elliptic mechanism. Decreasing the free surface fraction ξ reduces the ellipticity of the streamlines near the basic vortex core. This leads to a reduction of the contribution of the elliptic mechanism and results in the balance with the centrifugal mechanism on the instability [Shiratori 2007-1].

7.1.4.5 Flow Structures at Supercritical Marangoni Numbers

When the Marangoni number exceeds the second critical condition, the flow shows an oscillatory behaviour both in the temperature and flow fields. At near the critical condition ($Ma \approx Ma_{c2}$), only a few modes are unstable so that the behaviour of oscillatory flow is described rather simply [Imaishi 2001, Li 2007]. For conditions with a higher Ma , many modes become unstable, thus the description of the flow is typically represented by mean-flow structures.

From the synchronized temperature oscillation data obtained by six thermocouples, information on the temperature fluctuation T , time t , and space (azimuth φ) could be obtained. The T - φ relationship at each moment was interpolated using a periodic cubic spline function and plotted in a circular format, so that the azimuthal wave number and its motion can be visualized, as shown in Figure 7.18. Note that, in this method, the spatial resolution with respect to the azimuth is limited by the number of thermocouples; i.e. with only six thermocouples, an azimuthal wave number of 4 or more cannot be observed. As can be seen from the figures, the azimuthal structure of the temperature field is time-dependent. Some typical structures can be observed. For $As = 2.0$ (Figure 7.18a), the global rotating motion of the $m = 1$ structure can be recognized. By the same token, the twisting motion of the $m = 2$ structure is seen in the $As = 1.0$ case (e.g. in the range $0 < t < 8$ s in Figure 7.18b), and the pulsating motion of the $m = 3$ structure in the $As = 0.8$ case (Figure 7.18c) as well. The $m = 3$ type structure was experimentally confirmed for

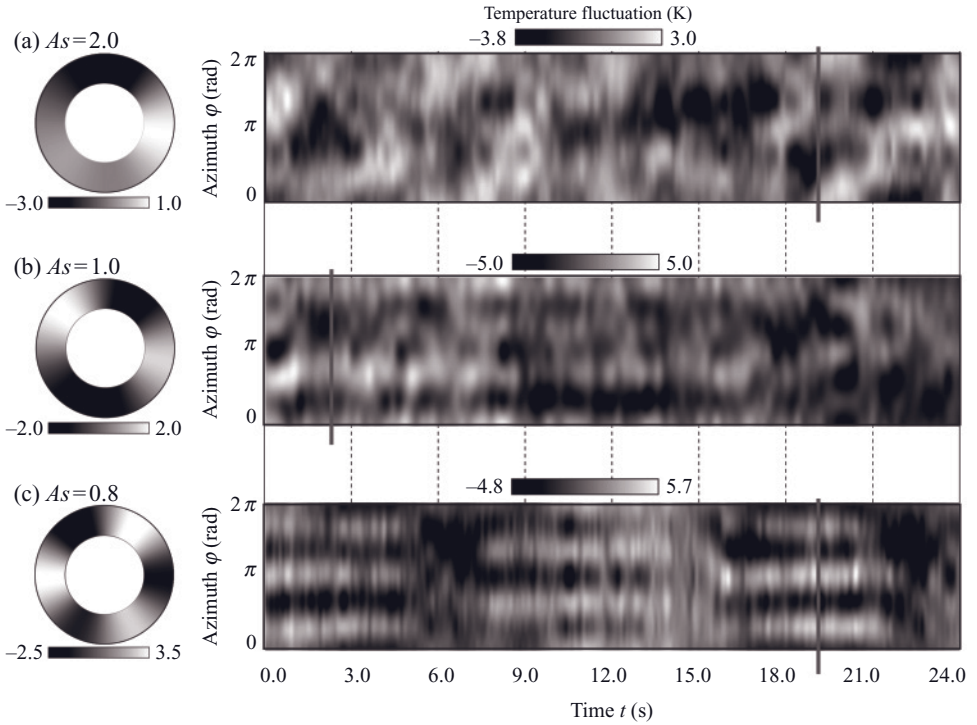


Figure 7.18 Time evolution of azimuthal temperature distribution interpolated from six thermocouples (Reprinted with permission from [Yamane 2005], copyright (2005) Springer Science + Business Media). The circular figures on the left are snapshots which indicate typical wave numbers at the time indicated as grey bars in the figures on the right. (a): $As = 2.0$; (b): $As = 1.0$; (c): $As = 0.8$.

the first time for a molten Si bridge by [Hibiya 2005, Yamane 2005]. In order to quantify the time-dependent motion of the temperature field presented above, the spatial Fourier expansion and time averaging are introduced as follows [Yamane 2005].

An azimuthal temperature distribution can be expressed by the superposition of some wave numbers:

$$T(\varphi, i) = a_{0,i} + \sum_{m=1}^n a_{m,i} \cos(m\varphi) + b_{m,i} \sin(m\varphi), \quad (7.6)$$

where $a_{m,i}$ and $b_{m,i}$ are the coefficients corresponding to wave number m . Based on this viewpoint, we attempted to quantify the azimuthal temperature distribution by the mode appearance coefficient (MAC) defined as follows:

$$\phi_{m,i} = \sqrt{a_{m,i}^2 + b_{m,i}^2}, \quad (7.7a)$$

$$\phi_m = \frac{1}{N} \sum_{i=1}^N \phi_{m,i}, \quad (7.7b)$$

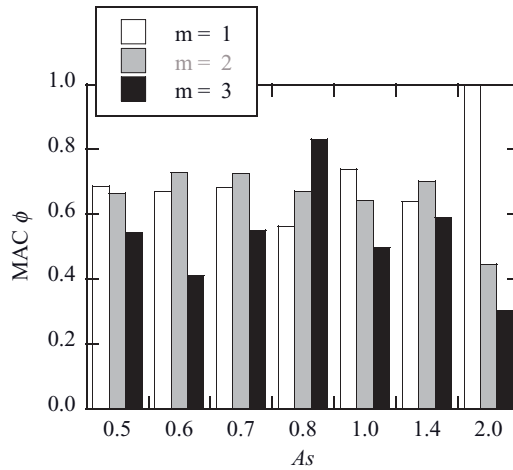


Figure 7.19 Mode appearance coefficient ϕ_m as a function of the aspect ratio As . The values are normalized with respect to the largest one (Reprinted with permission from [Yamane 2005], copyright (2005) Springer Science + Business Media).

where N is the number of the sampled data. In the present experiment, the detectable wave number is limited to values up to $m = 3$. ϕ_m is the MAC for the wave number m , which may represent the intensity of the m -fold symmetry of the mean flow structure. The coefficient for $m = 0$ measures an axisymmetric component. For all aspect ratios considered here, the MAC ϕ_m is calculated.

Figure 7.19 shows the calculated MAC as a function of the aspect ratio As . In the figure, the values of MAC are normalized by the strongest of all the As . It should be noted that the effect of the wave numbers higher than $m = 3$ may appear in these coefficients as a result of the aliasing error due to the spatial resolution of six thermocouples. For examples, the $m = 4$ structure is identified as $m = 2$, and $m = 5$ as $m = 1$. The $m = 1$ mode seems to appear preferentially at the aspect ratio $As = 2.0$, and the $m = 3$ mode at $As = 0.8$. Although the other distinctive relations are not observed, we can suggest that the mean flow structures indicate the empirical relation $As \cdot m = 2.0$ – 2.4 , as reported from the numerical investigations (see e.g. [Levenstam 1995, Preisser 1983, Wanschura 1995]). The aliasing error from higher wave numbers may appear in small As cases. In conclusion, it is suggested that even under conditions of high Marangoni number, such as 10^3 – 10^4 , the unstable flow sustains the mean flow structure which takes place at the condition of low Marangoni number.

The frequency is an important characteristic as a quantitative measure for the complicated oscillatory flow, in addition to the wave numbers discussed above. The frequency of the oscillatory flow has been investigated using free surface oscillation measured by phase-shift interferometry [Okubo 2005]. Figure 7.20a shows a time evolution of the frequency of dynamic radial displacement for the case $As = 1.2$, $Ma = 8200$ – 14000 . This time–frequency plane (called the signal plane) is obtained by wavelet analysis in which the Gabor function is used as a mother wavelet [Mallet 1999]. When a strong black contrast appears in the signal plane, this suggests that the amplitude of oscillation is strong.

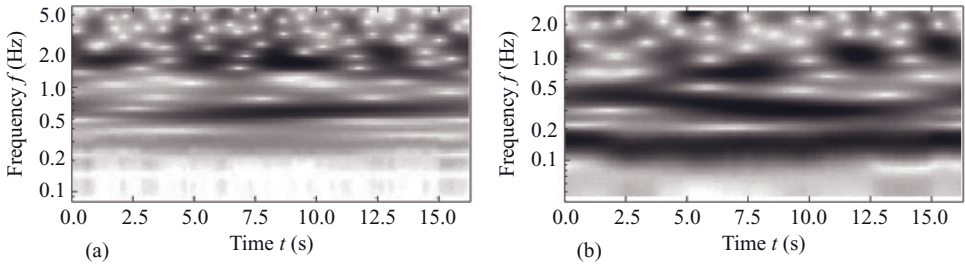


Figure 7.20 The signal plane for radial displacement oscillations obtained by wavelet analysis. (a): $As = 1.2$ and $Ma = 8200\text{--}14000$; (b): $As = 0.6$, $Ma = 2800\text{--}4800$ (Reprinted with permission from [Okubo 2005], copyright (2005) Springer Science + Business Media).

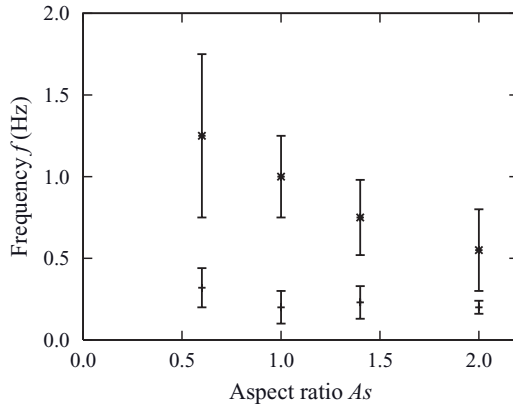


Figure 7.21 The ranges of the frequency bands as a function of the aspect ratio. The lower bands appear time-independently, whereas the higher bands appear intermittently (Reprinted with permission from [Okubo 2005], copyright (2005) Springer Science + Business Media).

As shown in Figure 7.20a, a band whose central frequency is about 0.5 Hz probably exists continuously from $t = 3.0$ s on. There is an unsteady frequency band whose central frequency appears at $f = 1.2$ Hz and above. This indicates that the oscillation takes place intermittently. This frequency band, whose peak was 0.5 Hz or less, shows an agreement to that of the simple oscillatory flows near the second threshold (see e.g. [Imaishi 2001, Leyboldt 2000]). The frequency which appeared at 1.5 Hz and higher could be generated due to strong instability caused by a high Marangoni number. A similar tendency was observed regardless of aspect ratio As and sampling rate.

Figure 7.20b shows the signal plane obtained under a relatively low Marangoni number condition. This condition was attained by employing a lower rod with a hybrid structure, alumina with a carbon attachment. For this configuration, the Marangoni number was estimated to be 20% smaller than that for the conventional set-up, which utilizes carbon for both the upper and lower rods. In Figure 7.20b, it is clear that the frequency bands were observed more clearly compared to those for the higher Ma case. The intermittent appearance of the frequency is also seen in the range $0.6 < f < 2.0$ Hz. Figure 7.21 shows

the relationship between the frequency of surface oscillation and aspect ratio As [Okubo 2005]. This tendency agrees with that observed for high- Pr fluid reported by [Preisser 1983].

7.1.5 Full Float Zones

In the case of full float zones, direct measurements can not be as precise as in the case of the half-zone set-up described above, because the interfaces are not flat and the temperature gradient along the surface cannot be determined as precisely. Some measurements are possible, however.

Spatially resolved pyrometric measurements of electron beam-heated Mo and Nb zones have been made by [Jurisch 1990-2], showing oscillations in the 0.25–2 Hz range as well as transitions from single mode oscillatory to multimode oscillatory to chaotic behaviour upon increasing the zone height and temperature difference, i.e. the Ma number. For a full Si float zone, optical fibre thermometry has been used both on the ground and under microgravity to measure the temperature fluctuations [Cröll 2002-1, Dold 2002, Schweizer 1999]. A typical result is shown in Figure 7.22 for pure thermocapillary convection. Temperature fluctuations over 1 K amplitude with the main frequencies around 0.3 Hz could be found, which is in good agreement with other results.

Temperature fluctuations and dopant striations are of course coupled through the growth rate. That growth rate fluctuations in semiconductor melt growth due to time-dependent convection can have considerable amplitudes has been shown by, for instance, [Kim 1972, Kim 1978, Murgai 1976, Witt 1973]. A direct measurement of the microscopic growth rate is thus useful to identify the effect of time-dependent thermocapillary convection in FZ growth. Figure 7.23 shows a series of single frames from a video sequence of the microscopic observation of the interface in Si FZ growth, and Figure 7.24 shows the growth rate measured by analysing the video images. As can be seen in Figure 7.24, strong fluctuations of the growth rate occurred, with rates up to 17 mm/min and down to 0 mm/min at a translation rate of 1 mm/min. With no translation, occasional back-melting of the crystal could be detected. The main frequencies fit well with the ones measured for the temperature fluctuations and the distance of the dopant striations [Schweizer 1999].

7.1.6 The Critical Marangoni Number Ma_{c2}

Since time-dependent thermocapillary convection is the predominant factor in the formation of dopant striations in low- Pr float zones, a determination of the critical number for the onset of time-dependent convection, Ma_{c2} , in a full zone, is of particular interest. The easiest way is a simple reduction of the zone length L until the striations vanish; this method changes L and ΔT in Equation (7.1) at the same time. This approach has been used to determine Ma_{c2} values for Mo and Nb [Jurisch 1990-1, Jurisch 1990-2], GaAs [Müller 1991, Rupp 1990], and GaSb [Cröll 1998-1]. Figure 7.25 shows periodic striations in a GaSb crystal grown under microgravity (compare Figure 4.29) that vanish slowly with a reduction in zone height, resulting in a value of $Ma_{c2} = 375 \pm 125$ [Cröll 1998-1]. This method is, however, limited by the minimum zone height as determined

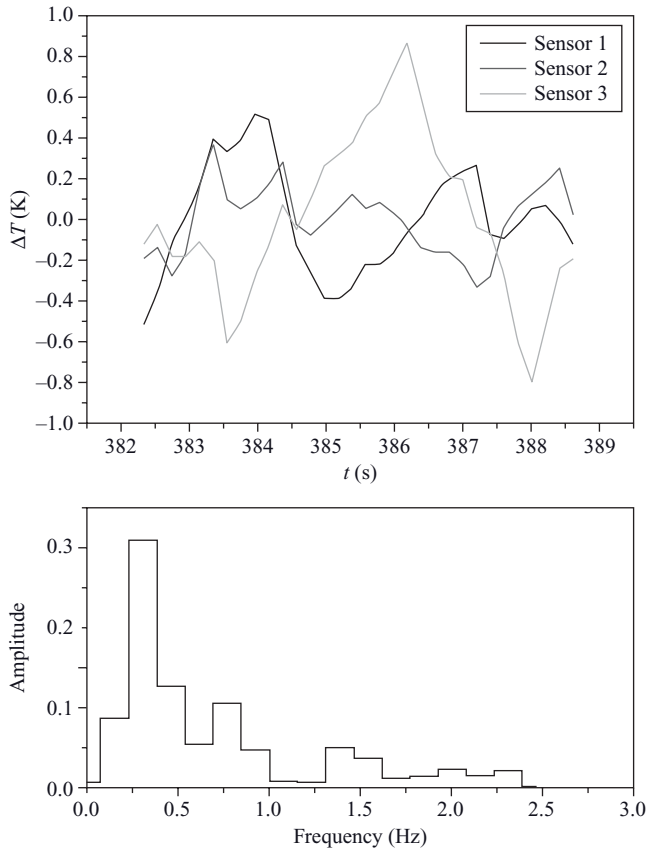


Figure 7.22 Temperature fluctuations (top) and corresponding FFT frequency distribution of the temperature fluctuations in a Si float zone under microgravity during the MAXUS 6 sounding rocket flight. Three temperature sensors were used: sensor 1 was close to the growing interface, sensor 2 several mm above it near the centre of the zone, and sensor 3 120° away from sensor 1. A cross-correlation analysis of the signals of sensors 1 and 3 pointed to a lag of 2 s (copyright A. Cröll; reproduced with permission).

by the interface curvature and therefore not applicable to all systems. In the case of Si and Ge, striations can be found even in material grown from very small zones such as thin necks. Ma_{c2} for Si was determined by decoupling L and ΔT in Equation (7.1) by coating the crystals, but removing a ring-shaped part to obtain a partially confined melt zone with an annular free surface of constant height (Figure 7.26). Free surface heights ≤ 1 mm resulted in striation-free crystals, similar to totally coated ones, and surface heights ≤ 3 mm produced a continuously striated area below the free surface. Crystals grown with intermediate heights of the free surface exhibit a succession of striated and nonstriated parts below the free surface (Figure 7.27). This can be explained by the change of ΔT along the free surface during the movement of the zone, depicted schematically in Figure 7.28. Initially, when the melt zone is fully covered by the SiO_2 coating, the crystal grows

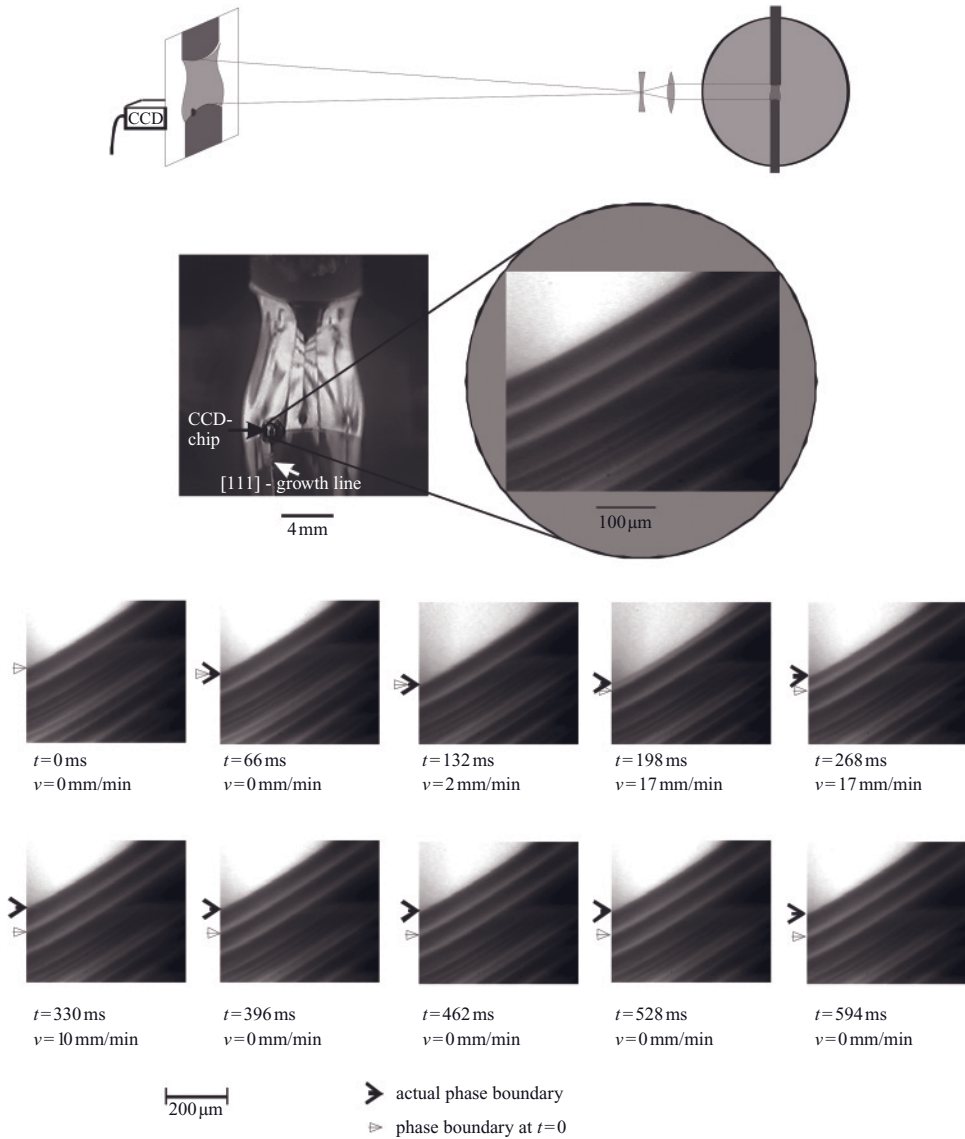


Figure 7.23 Top: basic set-up to obtain microscopic video images of the crystal–melt interface. An enlarged image of the zone is projected onto a screen, where a video CCD chip is placed at the position of the interface. Bottom: evolution of a crystal–melt interface over a time of 0.6 s in a Si float zone. The translation rate was 1 mm/min. The dark arrow indicates the actual interface; the light-coloured area above it is the melt, the darker area the outside of the grown crystal. The grey arrow indicates the initial interface position. (Reprinted with permission from [Dold 1994], copyright (1994) P. Dold).

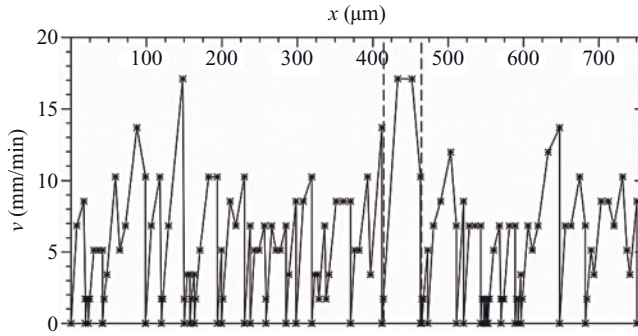


Figure 7.24 Growth rate fluctuations determined by the analysis of the melt-crystal interface position through video images. The translation rate was 1 mm/min. After [Cröll 1997, Dold 1994].

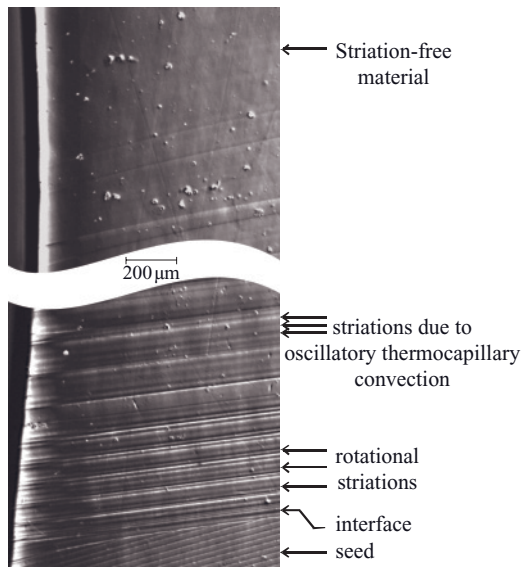


Figure 7.25 Dopant striations in a FZ GaSb crystal grown on the Spacehab-4 mission under microgravity (compare Figure 4.29). In the first part of the crystal, striations due to thermocapillary convection are visible in addition to rotational striations. When the zone height was reduced later on, the striations vanish (upper part of the image). The critical Marangoni number Ma_{c2} was determined to be 375 ± 125 ; (Reprinted with permission from [Cröll 1998-1], copyright (1998) Elsevier Ltd).

striation-free because thermocapillary convection is completely suppressed (Figure 7.28a). When the zone reaches the opening, a free melt surface is formed. Since ΔT is large in this position, Ma_{c2} is surpassed and striations are generated (Figure 7.28b). Now ΔT decreases until the free surface reaches the centre of the zone where ΔT is small. In this phase, no striations are generated, implying $Ma < Ma_{c2}$ (Figure 7.28c). Then ΔT

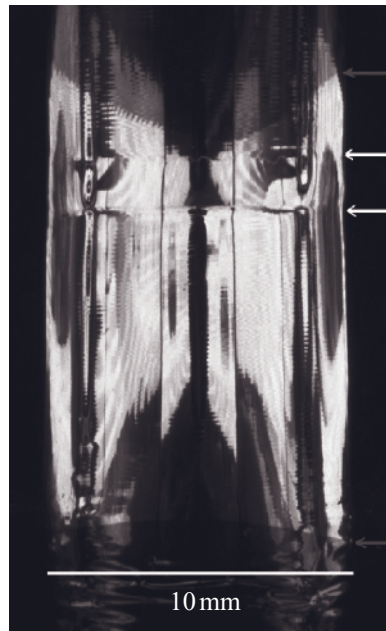


Figure 7.26 Si melt zone with a partially free surface in a double ellipsoid mirror furnace. The free surface is located between the inner white arrows; the solid–liquid interfaces are marked by the outer grey arrows. The feed rod was coated by a 5- μm thick SiO_2 coating which was partially removed by machining to achieve the annular free surface (copyright A. Cröll; reproduced with permission).

increases again until $Ma > Ma_{c2}$ and striations reappear (Figure 7.28d). In the last phase, when the zone is again totally covered, Marangoni convection stops and the crystal grows striation free (Figure 7.28e). If the axial temperature distribution at the zone surface is known, Ma_{c2} can be calculated from the relative sizes of the striated and unstriated parts, resulting in a value of 150 ± 50 [Cröll 1989, Cröll 1991].

With numerical simulations, it is also possible to determine critical Marangoni numbers and at the same time gain insight into the paths leading to time-dependency. Early simulations like those of [Chang 1975, Chang 1976] for Si zones chose a two-dimensional approach, because of the constraints of computing power and time. However, the critical numbers predicted were two orders of magnitude higher ($Ma_{c2} \approx 10^4$) than the ones later determined experimentally for low- Pr materials. Simulations using a three-dimensional approach gave a very different result for the low- Pr materials [Herrmann 1994, Kaiser 1993, Kaiser 1998, Levenstam 1996, Müller 1991, Rupp 1990], as shown in Figure 7.29. The classic two-roll pattern of the full float zone is only present at very small Marangoni numbers; even before a transition to time-dependency, the symmetry is broken, similar to the half-zone results discussed above. The two rolls unite and form a large diagonally oriented roll plus small secondary rolls in the zone. These structures can rotate or pulsate leading to dopant striations. For Si float zones of 10 mm diameter and 12 mm length, the three-dimensional simulations resulted in Ma_{c2} values of 115 [Rupp 1990] and 150 [Kaiser

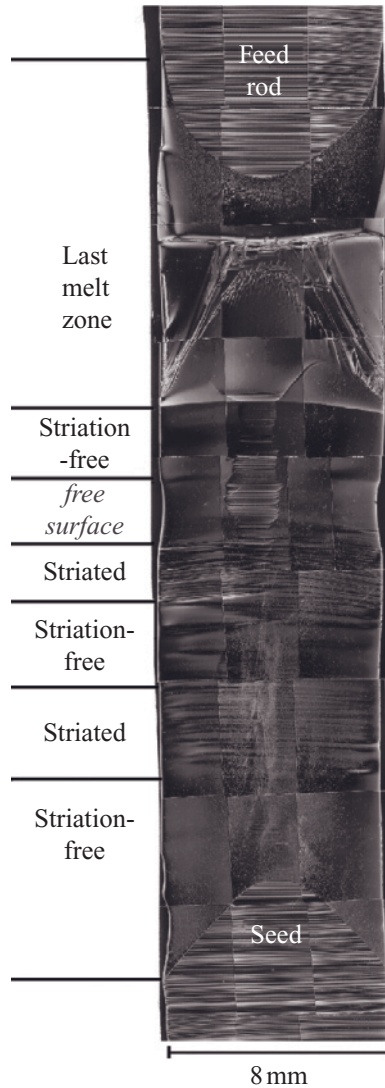


Figure 7.27 Composite NDIC micrographs of a Si:Sb crystal ($[111]$, $2 \times 10^{18} \text{ cm}^{-3}$, translation rate 5 mm/min), grown in a monoellipsoid mirror furnace with a partially free melt surface. A succession of striated and nonstriated areas is visible one zone length below the ring-shaped opening in the SiO_2 coating (copyright A. Cröll; reproduced with permission).

1993], close to the experimentally determined values. Three-dimensional simulations are therefore often a necessity for simulations of low- Pr materials. A simulation of a half-zone [Rupp 1990] gave $Ma_{c2} = 290$, about 2.5 times higher than his full-zone result; this is easily explained by the additional no-slip condition and reduced degrees of freedom compared to the full zone set-up. Changes in the zone geometry (e.g. cylindrical to barrel-

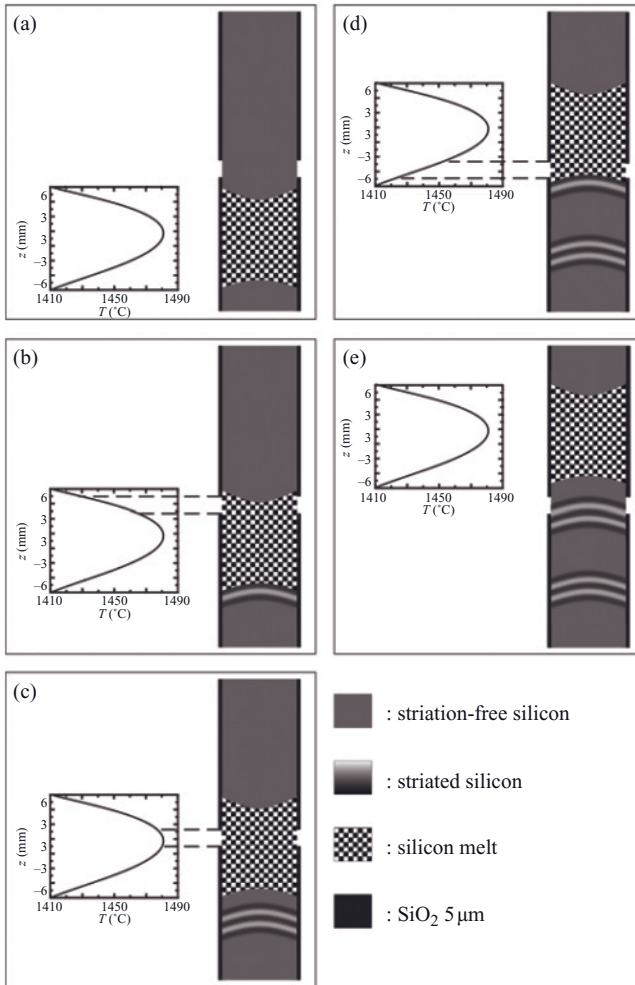


Figure 7.28 Schematic sequence of striation formation during FZ growth of Si with a partially free melt surface. The diagram on the left shows a measured axial temperature distribution in a double-ellipsoid mirror furnace. See text for details (copyright A. Cröll; reproduced with permission).

shaped under microgravity, bottle-shaped under normal gravity) influence the flow field and thus the critical numbers [Herrmann 1994, Kaiser 1993, Kozhoukarova 1986]. A bottle-shaped zone stabilizes the flow, as shown by an increase of Ma_{c2} from 112 to 145 when going from a cylindrical (microgravity) zone to a bottle-shaped one [Kaiser 1993]; see Figure 7.29.

Several empirical formulas have been suggested for the dependence of Ma_{c2} on Pr over the years; for the large range of $Pr = 0.01-100$, a relationship of $Ma_{c2} = 2000 \cdot Pr^{0.6}$ [Yang 2001] has been proposed (Figure 7.30).

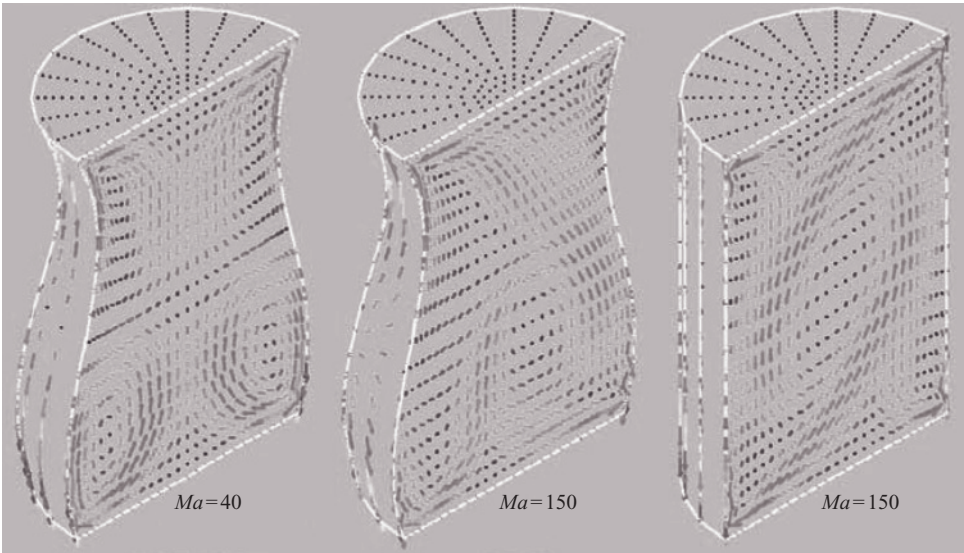


Figure 7.29 Three-dimensional numerical simulations of Marangoni convection in a full Si float zone for different Ma numbers and geometries. $Ma = 40$ (top) is below the critical number and shows the classic two-roll pattern of Figure 7.3. $Ma = 150$ (centre and bottom) shows the breaking of the radial symmetry at the transition to time-dependency. Buoyancy convection was not considered; however, the upper two simulations used the normal gravity shape of the zone whereas the bottom simulation used a microgravity shape. The transition to time-dependency happens at $Ma = 145$ for the normal gravity shape and earlier, at $Ma = 112$, for the microgravity shape. (Reprinted with permission from [Kaiser 1993], copyright (1993) T. Kaiser).

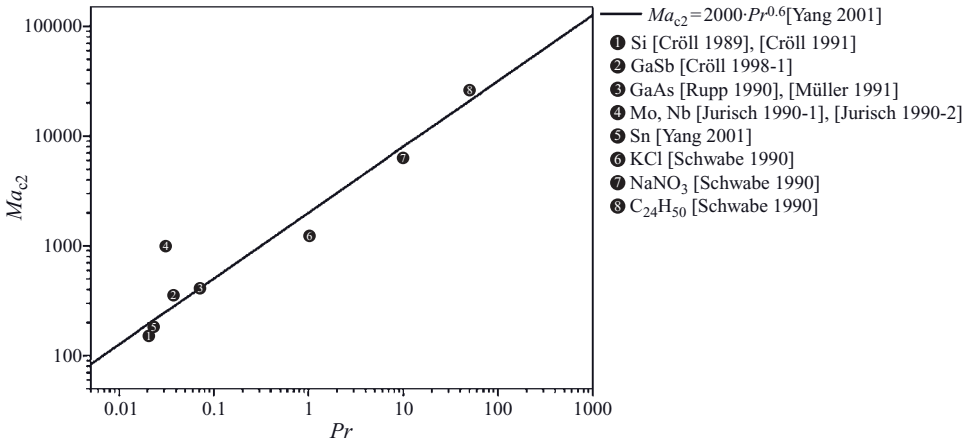


Figure 7.30 The critical Marangoni number Ma_{c2} vs the Prandtl number. Some experimental results are shown (nos. 1–8) as well as one empirical relationship (solid line). Note that Ma_{c2} is dependent on the aspect ratio of the zone and the zone shape; this will account for some variation in the numbers (copyright A. Cröll; reproduced with permission).

7.1.7 Controlling Thermocapillary Convection in Float Zones

7.1.7.1 Introduction

The experimental results and the three-dimensional simulations show that Ma_{c2} is much lower for low- Pr melts than for high- Pr melts; the Ma_{c2} values of the low- Pr materials are often 1–2 orders of magnitude lower than actual Ma values of real float zone systems, e.g. $Ma = 3000$ – 4000 for a Si float zone of 8 mm diameter and 10 mm height in a typical mirror furnace [Cröll 1994-1], 20 times higher than Ma_{c2} . Typical flow velocities for a Si zone with $Ma = 3000$ are of the order of 10^{-1} m/s. It is obvious from these numbers that in this case it is impossible to avoid time-dependent Marangoni convection by reducing the temperature gradient or the zone height; in the above example an axial temperature gradient of less than 1 K cm^{-1} would be necessary for a zone height of 10 mm. Similar values have been reported by other authors [Levenstam 1995]. In addition to causing microsegregation, thermocapillary convection in float zones is of course also a strong influence on axial segregation, radial segregation and interface shape. As shown above, trying to change the temperature coefficient of the surface tension by introducing small amounts of oxygen works, but is not fully sufficient. Coating with SiO_2 leads to twinning and polycrystalline growth [Cröll 1989]. To reduce or suppress time-dependent Marangoni convection, other methods have to be used.

Because of the strong dependence of Ma_{c2} on Pr , the situation is not as bad for systems with somewhat higher Pr values and smaller $\partial\gamma_v/\partial T$ values than Si or Ge; using small zones and/or low temperature gradients, materials such as GaSb can be FZ-grown striation-free.

7.1.7.2 Static Magnetic Fields

The damping of any flow in an electrically conducting liquid by a static magnetic field is possible by the action of the Lorentz force on the flow components perpendicular to the magnetic field lines. An important implication is that sufficient damping will result in suppression of time-dependent flows and can therefore eliminate dopant striations. The characteristic dimensionless number to quantify the influence of the magnetic field is the Hartmann number Ha , given by:

$$Ha = B \cdot L \cdot \sqrt{\frac{\sigma_{el}}{\nu \cdot \rho_l}}, \quad (7.8)$$

where B is magnetic induction, L is the characteristic length, σ_{el} is electrical conductivity, ν is kinematic viscosity, and ρ_l is density.

Following the successful use of magnetic fields in Si-Cz growth, the first experimental investigations on the use of both transverse and axial static magnetic fields in Si FZ growth appeared in the 1980s [DeLeon 1981, Kimura 1983, Kimura 1993, Robertson 1986-1, Robertson 1986-2]. They all employed RF heating, so the strong additional influences of its electrodynamic forces led to difficulties with respect to experiment control and interpretation of the results. Typical inductions used were on the order of 100 mT, with 500–550 mT being the maximum inductions reported [Robertson 1986-1, Robertson

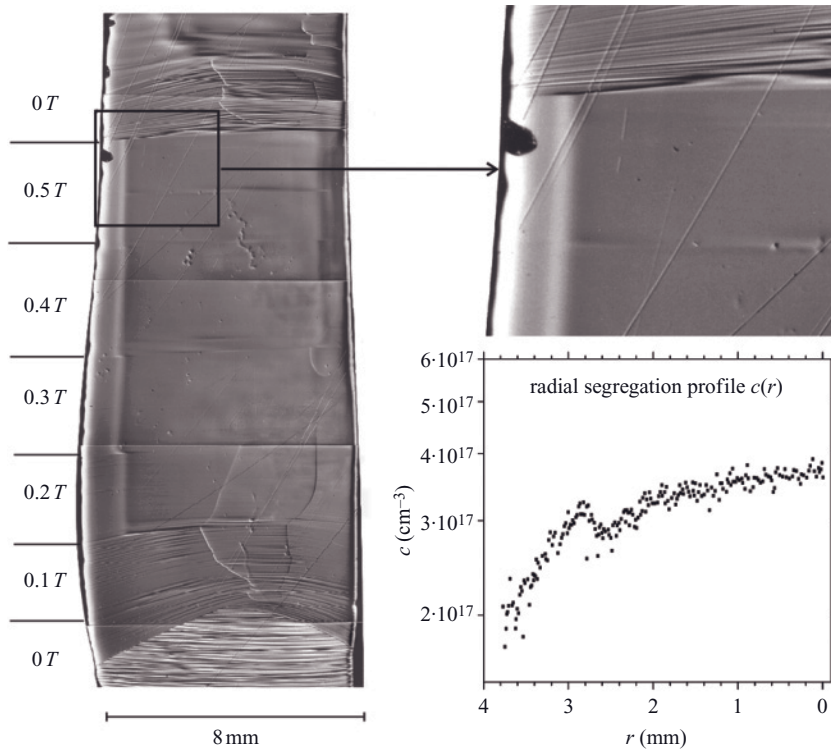


Figure 7.31 Composite NDIC micrograph of an etched axial section of a Si:P crystal, grown with different axial magnetic fields. The induction was increased in 100-mT steps. Right: Enlargement of the structure separating core and periphery and corresponding radial concentration profile from spreading resistance measurements. The dependence of the core width on the induction is clearly visible (copyright A. Cröll and P. Dold; reproduced with permission).

1986-2]. A reduction of striation intensity, but no complete suppression of striations, has been found in such experiments, especially with axial fields of 550 mT.

The use of static magnetic fields to specifically suppress thermocapillary convection in radiation-heated zones has been studied in detail by [Cröll 1994-1, Cröll 1998-2, Cröll 1999, Dold 1998, Dold 2003, Kaiser 1998]. For axial fields and a Ma number of the order of 10^3 , a reduction of the frequency spectrum and a transition to oscillatory behaviour could be found at about 60 mT, a transition to just one frequency at 200 mT ($Ha = 75$), and a disappearance of striations above 200 mT (Figure 7.31). At the same time, a core structure appears in the crystal, which is not identical with the (111) facet core, with the core diameter being a function of induction (Figure 7.31). The appearance of this radial inhomogeneity can be explained by two different flow regimes due to the damping of only radial and azimuthal components of the flow by the field: in the centre a quiescent regime close to diffusive conditions prevails, whereas in the periphery of the melt zone a regime with still vigorous thermocapillary flow dominates, and the boundary between

them leads to a build-up of solute concentration [Cröll 1998-2]. The structure finally disappears at inductions larger than 2T with strong enough damping [Cröll 1998-2]. Transverse fields break the symmetry of a float zone, which leads to problems in the RF heated zones [Robertson 1986-1], but was quite effective for radiation-heated zones. An induction of 40 mT was enough to facilitate a transition to a single oscillatory state, and 60–80 mT to achieve striation-free growth [Dold 2003]. No coring was observed, but both for transverse and for higher axial fields the occurrence of thermoelectromagnetic convection, caused by the interaction of the fields with thermoelectric currents generated by segregation at the interface, leads to other radial inhomogeneities and even a new type of dopant striations [Cröll 1998-2, Dold 2003]. These problems, as well as the comparatively high fields needed, reduce the usefulness of pure static fields for the FZ process.

7.1.7.3 Alternating Magnetic Fields

Alternating magnetic fields are rotating, travelling, or pulsating fields that induce a flow in an electrically conducting melt. For float zones, rotating magnetic fields have been used successfully to influence segregation due to thermocapillary convection [Dold 1999, Dold 2001, Dold 2003, Dold 2004, Knobel 2005]. The force that drives the convection due to the field is characterized by the magnetic Taylor number Ta :

$$Ta = \frac{B^2 \omega_B r^4 \sigma_{el}}{2\nu^2 \rho_l}, \quad (7.9)$$

where B is induction, ω_B is the angular velocity of the field, r is the radius, σ_{el} is electrical conductivity, ν is kinematic viscosity and ρ_l is density.

For pure thermocapillary convection, a significant change was found at inductions between 2.5 and 3.75 mT ($Ta = 1 \times 10^4$ – 2.3×10^4) with a shift to a new higher characteristic frequency. An induction of 7.5 mT at 50 Hz ($Ta = 3.9 \times 10^4$) proved to be enough to practically eliminate dopant striations due to time-dependent convection [Dold 2001]. The striation patterns in the crystals indicate a shift from low frequencies and high amplitudes to high frequencies and low amplitudes with increasing induction. This is corroborated by temperature measurements: Figure 7.32 shows the temperature signal of fibre-optic sensors in a Si float zone under microgravity with a field of 7 mT at 50 Hz. With the full field, the temperature fluctuations are essentially reduced to the sensor noise, whereas without field they reach over 1 K (Figure 7.22). Simulations show that the flow field in this case is dominated by the induced azimuthal flow and radial and axial components are reduced considerably [Dold 2001, Kaiser 1998], leading to a much more symmetrical flow pattern than in the pattern without field. Rotating magnetic fields are now used in the industrial FZ growth of Si [Knobel 2005].

7.1.7.4 Vibration

Vibrating a float zone to reduce time-dependent convection and dopant striations seems counterintuitive, but is a viable new and promising method to counterbalance thermocapillary convection. In a free zone that is subjected to axial vibrations, three mechanisms lead to convective flow: thermovibrational convection, the Schlichting effect, and a flow generated by surface waves which are damped by viscosity [Gershuni 1998, Lyubimov

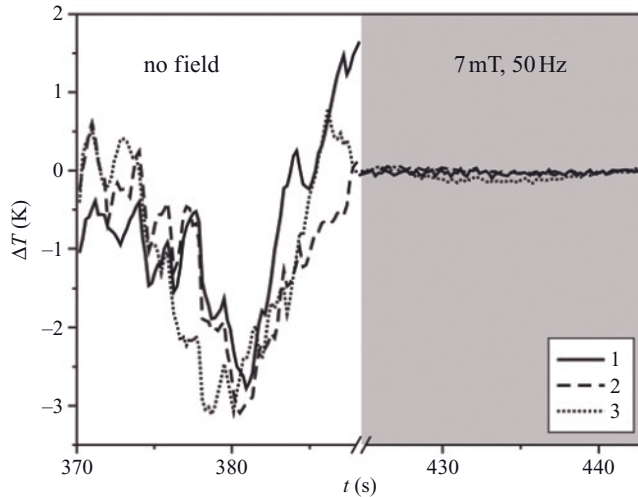


Figure 7.32 Temperature fluctuations in a Si float zone under microgravity during the MAXUS 6 flight without field (left) and using a rotating magnetic field at 50 Hz and $B = 7 \text{ mT}$ (right). Three temperature sensors were used: Sensor 1 was close to the growing interface, sensor 2 several mm above it near the centre of the zone, and sensor 3 120° away from sensor 1 (copyright A. Cröll; reproduced with permission).

1997]. This latter flow opposes thermocapillary convection. It has been shown by simulations [Lyubimov 2002, Lyubimova 2003] as well as experiments with half-zone model systems using silicone oil and NaNO_3 [Anilkumar 1993, Anilkumar 2005, Dold 2003, Shen 1996] that this is an effective method to control or even dominate thermocapillary convection. By adjusting the amplitude and/or frequency it is possible to slow or stop thermocapillary convection, or even reverse the flow roll. It should be noted that this method works independently of the electrical conductivity of the melt, whereas magnetic fields only work for conducting liquids. First results using this method with Si float zones show that it does indeed work. Experiments with high-frequency vibrations (4 kHz, $1 \mu\text{m}$ amplitude) showed a slight decrease of the dopant striations and a reduction of the interface curvature [Dold 2003]. Vibrations with higher amplitudes at a lower frequency (70 Hz, $100\text{--}375 \mu\text{m}$) showed a strong weakening of the dopant striations at $250 \mu\text{m}$ amplitude and a reappearance at higher amplitudes, this time probably due to a time-dependent reversed flow [Dold 2003]. Figure 7.33 shows micrographs of different striation pattern grown without and with vibration; the reduction in the part grown with vibration is quite apparent.

7.1.7.5 Other Methods

There have been at least two proposals to use a directional gas jet blown tangentially at the zone surface to reduce thermocapillary convection, with the flow direction opposite that of thermocapillary convection. This idea was investigated by numerical simulations [Li 2003] and by using a model system [Dressler 1988]. Both approaches showed the viability of the basic concept. The simulations predict a reduction of thermocapillary

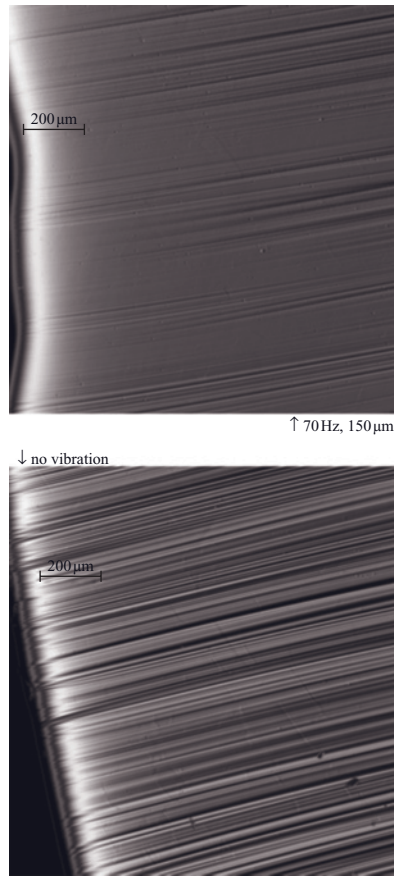


Figure 7.33 Micrographs of an etched axial slice of a Si:Sb crystal. The bottom image shows the usual dopant striations due to time-dependent thermocapillary convection, the upper image shows a part of the crystal grown under axial vibrations of $150\ \mu\text{m}$ at $70\ \text{Hz}$, with a marked reduction of the striation intensity (copyright A. Cröll; reproduced with permission).

convection up to 99% [Li 2003], and the model experiments using silicone oil showed a reduction of the flow velocity of up to 66%. However, this idea has not yet been tried for real crystal growth systems. The technical difficulties of blowing high-speed gas jets at a hot melt zone are likely to be severe; the gas would probably have at least to be pre-heated to the melt temperature to avoid a rapid cooling of the zone, and contamination problems might also occur.

Other methods that have been suggested include reduction of the free surface with heaters covering the surface [Lan 1991-1, Lan 1991-2, Lan 1991-3], although that method negates the main advantage of FZ growth, that the melt does not have contact with a crucible; and high-speed counterrotation of crystal and feed rod with rotation rates up to 400 rpm [Lan 1991-4]. Simulations and model experiments with NaNO_3 [Lan 1991-4]

showed the viability of the latter approach in principle, but it has not yet been used in other systems.

7.2 Thermocapillary Convection in Cz Crystal Growth of Si

7.2.1 Introduction

High-quality bulk crystals of Si have become a key material in the electronic industry owing to the development of large-scale integrated circuits (LSIs) and the increasing demand for large-diameter Si substrates for large memory chips. The Cz method is widely used to produce such crystals in industry. Accurate control of the melt–crystal interface shape and of the flow in the melt during Cz growth is essential to produce high-quality crystals, since the temperature distribution in the crystal affects crystal quality. Thermocapillary flow has been shown to affect interface shape and flow in crystal growth systems as discussed above. The effect of thermocapillary flow on the melt flow in this system is not so large compared with those of buoyancy convection and the rotation of the crystal and/or a crucible, especially in a large volume of the melt. However, the effect on impurity distributions, especially near the edge of the crystal, is significant. The effect is dependent on the materials and their thermophysical properties.

In the 1970s, several papers reported the so-called ‘spoke and wave’-like pattern on high- Pr melt surfaces in the Cz system [Brandle 1977, Takagi 1976, Whiffin 1976] which is partly based on thermocapillary flow. Miller [Miller 1981, Miller 1982] first carried out the experiments by using water as a melt of simulated garnet in a container. They reproduced the spoke pattern which was modified by the crystal rotation rate. They deduced that a thermocapillary instability was an indispensable factor in the formation of the spoke pattern. This inference was supported by Hurle [Hurle 1983], Shigematsu [Shigematsu 1987], and Morita [Morita 1993]. Jones carried out a lot of work on cold model experiments with a fluid of $Pr = 1$; he observed spoke patterns on the top of the melt and concluded that the spoke pattern was caused by a buoyancy instability [Jones 1983, Jones 1984, Jones 1985, Jones 1989].

Schwabe and coworkers [Schwabe 1981] performed several experiments regarding thermocapillary convection. They found that the flow and isotherms near the melt surface and the crystal are influenced by thermocapillary forces. Nikolov [Nikolov 1988] reported a numerical study on the influence of physical and geometrical parameters on Cz flow.

The application of magnetic fields in Cz growth has been shown to be an effective tool for controlling the melt flow in general [Hurle 1994, Kakimoto 2002, Krauze 2004-1, Krauze 2004-2, Ozoe 1994]. It is also important for the interaction of the thermocapillary flow in a Cz set-up, as will be shown below.

7.2.2 Surface Tension-Driven Flow in Cz Growth

[Jing 2000, Jing 2008] reported mechanisms of the formation of spoke patterns in oxide melts by using three-dimensional time-dependent numerical calculations. The spoke pattern was formed by both Rayleigh–Bénard (buoyancy) and thermocapillary instabili-

ties. They succeeded in reproducing spoke patterns visually by taking into account the temperature distribution at the top of the melt [Jing 2000] and the effect of thermocapillary flow. They also reported a three-dimensional global model which includes the calculation of three-dimensional flow and two-dimensional radiative heat and mass transfer in a Cz furnace [Jing 2008]. They studied how the three-dimensional flow patterns including the surface-tension flow affects the shape of the interface between the crystal and the melt. They concluded that the shape of the interface became more concave to the melt when a three-dimensional flow including thermocapillary flow was taken into account.

The hydrothermal wave is an interesting phenomenon in the Si Cz case [Nakamura 1999-2]. They reported that the azimuthal velocity of a thermal wave on top of the Si melt is smaller than that of the crucible rotation rate. Moreover, the wave number of the thermal wave increased when the crucible rotation rate increased. [Azami 2001-5] observed the spoke patterns on shallow Si melts and polygonal cellular patterns on the surface of the Cz Si melts by a CCD camera. The dark stripes of the spoke patterns indicated a lower temperature on the top of the melt. They found that the number of spokes depends on the depth of the Si melt. When the thermocapillary flow was dominant in an Si melt 3-mm deep, a spoke pattern was observed on top of the surface.

7.2.3 Numerical Model

Configurations and dimensions of the computation model of Cz growth are shown in Figures 7.34 and 7.35 [Liu 2005-1]. For any case with an axisymmetric magnetic field such as a vertical (VMCz) or cusp-shaped magnetic (CMCz) field, two-dimensional global modelling is done as shown in Figure 7.34. For the case of a transverse magnetic field (TMCz), three-dimensional global modelling is done as shown in Figure 7.35. The growth process is assumed to be quasi-steady. All the constituents of the furnace are subdivided into a set of block regions as shown in Figure 7.34. Each block region is covered by a structured grid. In order to perform three-dimensional global modelling with moderate requirements of computer memory and computation time for TMCz, a mixed two-dimensional/three-dimensional finite-volume scheme was developed [Liu 2005-1, Liu 2005-2]. The three-dimensional domain, as shown in Figure 7.35, includes the crystal, melt, crucible, and heater. The other regions in the furnace are included in the two-dimensional domain. The calculation of view factors in the radiation modelling is an important part of the model with such a space discretization scheme and is described in [Liu 2005-1].

Transverse magnetic fields influence interface shape and temperature distribution near the melt–crystal interface through the melt convection in a crucible by exerting a Lorentz force on the melt. The governing equations for melt convection under the influence of a transverse magnetic field with the assumptions of a quasi-steady process and incompressible laminar flow of the melt are as follows:

$$\nabla \cdot u = 0, \quad (7.10)$$

$$\rho_1 u \cdot \nabla u = -\nabla p + \nabla \cdot [\mu(\nabla u + \nabla v^T)] - \rho_1 g \beta_T (T - T_m) + \vec{J} \times \vec{B}, \quad (7.11)$$

$$\rho_1 c_p u \cdot \nabla T = \nabla \cdot (\lambda \nabla T), \quad (7.12)$$

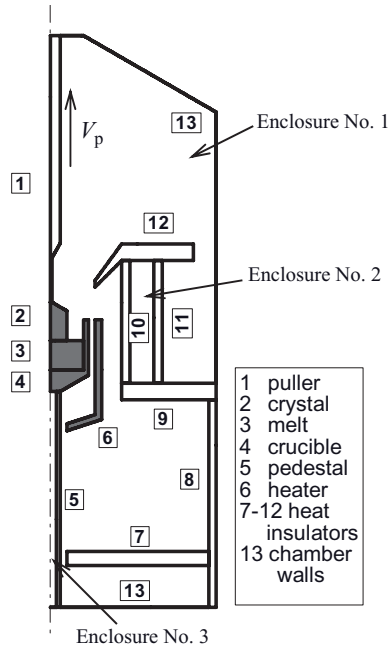


Figure 7.34 Configuration of the computation model for Cz growth (Reprinted with permission from [Lui 2005-1], copyright (2005) Elsevier Ltd).

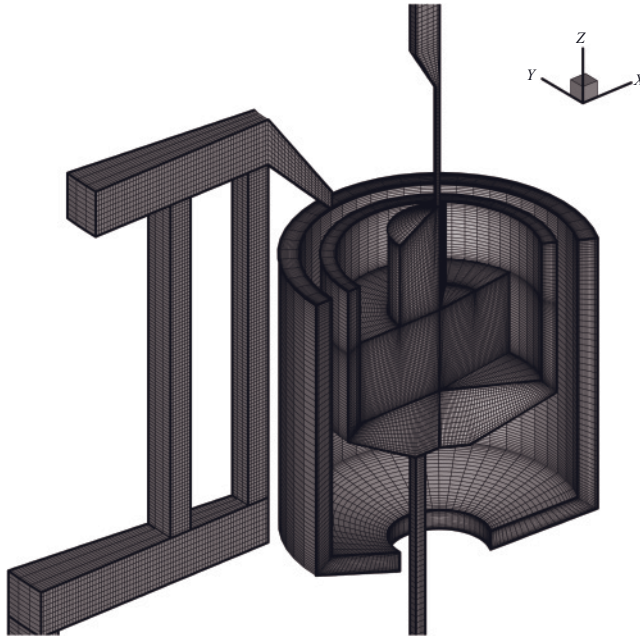


Figure 7.35 Configuration of the computational grid (Reprinted with permission from [Lui 2005-1], copyright (2005) Elsevier Ltd).

where u is the melt velocity, ρ_1 the melt density, p the melt pressure, μ the melt dynamic viscosity, g the acceleration due to gravity, β_T the thermal expansion coefficient, T_m the melting temperature, \vec{J} the electrical current density, \vec{B} the magnetic flux density, c_p the heat capacity and λ the thermal conductivity.

In order to obtain the Lorentz force exerted on the melt, it is necessary to solve the electrical field induced by the imposed magnetic field and governed by

$$\nabla \cdot \vec{J} = 0, \quad (7.13)$$

$$\vec{J} = \sigma_{\text{el}}(\vec{E} + u \times \vec{B}), \quad (7.14)$$

$$\vec{E} = -\nabla\Phi, \quad (7.15)$$

where σ_{el} is the electrical conductivity, \vec{E} the electric field and Φ the electric potential. The crucible, pulling rod and ambient gas are electrically insulated, while the Si crystal is an electrical conductor. Therefore, the calculation of electromagnetic field is limited to the melt–crystal domain. The melt flow is solved by a finite-volume method.

The thermocapillary flow was expressed by the following equations:

$$u \cdot n = 0, \quad (7.16)$$

$$\mu \frac{\partial u_t}{\partial n} = \frac{\partial \gamma_{lv}}{\partial T} \frac{\partial T}{\partial t}, \quad (7.17)$$

$$\mu \frac{\partial u_\varphi}{\partial n} = \frac{\partial \gamma_{lv}}{\partial T} \frac{\partial T}{r \partial \varphi}, \quad (7.18)$$

where u_t and u_φ are the velocities in tangential and azimuthal directions, n is the normal vector to the free surface of the melt, $\partial \gamma_{lv} / \partial T$ is the temperature gradient of surface tension, and r and φ the radius and azimuthal angle respectively, as shown in Figure 7.36.

The global solution is obtained by an iterative procedure that consists of a set of local iterations for all block regions, calculation of radiative heat transfer in the furnace and a global conjugated iteration among them. The input heater power and melt–crystal interface are unknown *a priori*. They are solved during the iterative procedure. Details of the model, including treatments of boundary conditions, have been published elsewhere [Liu 2005-1, Liu 2005-2].

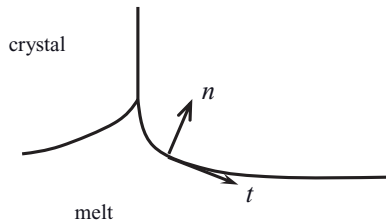


Figure 7.36 Coordination at the melt surface (Reprinted with permission from [Liu 2005-3], copyright (2005)).

Four cases of magnetic field arrangement are numerically investigated: without magnetic field, with a vertical magnetic field (VMCz), with a cusp-shaped magnetic field (CMCz) with its symmetric plane along the free surface of the melt, and with a transverse magnetic field (TMCz). VMCz is 0.1 T, which is distributed homogeneously. CMCz has a distribution with the symmetric plane of the magnetic field along the free surface of the melt. In this case the strength of magnetic flux density at the centre of the crucible bottom wall is 0.1 T.

7.2.4 Calculation Results

7.2.4.1 Without Magnetic Fields

Figure 7.37 shows results of the calculation of the distributions of temperature and velocity with and without thermocapillary flow [Liu 2005-3]. The results indicate that flow velocity near the point where melt, crystal and gas coexist becomes large due to thermocapillary flow as shown in Figure 7.37a, while the velocity becomes small at that point without thermocapillary flow as shown in Figure 7.37b. The maximum flow velocity with thermocapillary flow is about 6 cm/s, while that without thermocapillary flow is 1 cm/s. The effect can be recognized in the streamlines shown in the figure.

The results also indicate that temperature distributions along the crystal surface with and without thermocapillary flow are almost the same since such distributions were mainly determined by radiative heat transfer among the crystal surface, melt surface and crucible wall. The maximum temperature in the melt with thermocapillary flow is 1722 K, while the value without thermocapillary flow is 1726 K. This homogenization of temperature in the melt with thermocapillary flow is due to the enhancement of flow mixing in the melt.

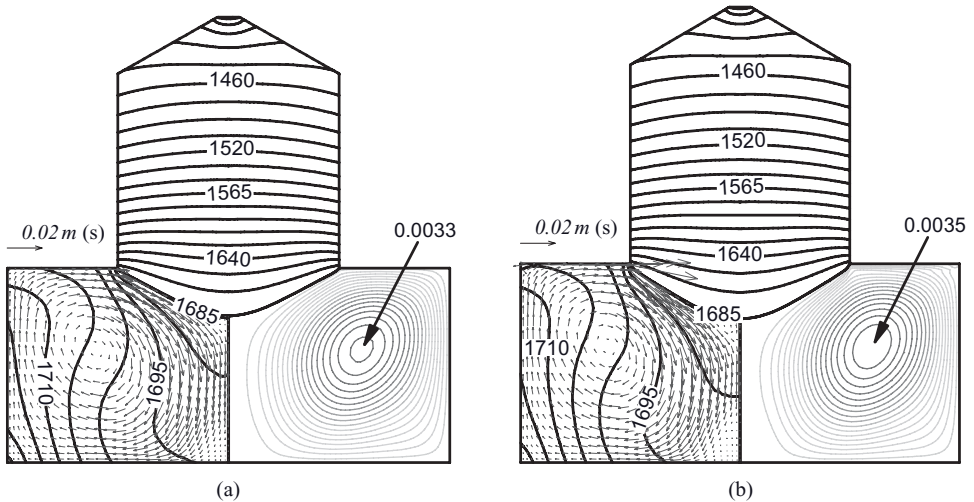


Figure 7.37 Temperature distribution of melt and crystal, velocity vectors (lower left) and streamlines (lower right) with (a) and without (b) surface tension-driven flow, without a magnetic field (Reprinted with permission from [Liu 2005-3], copyright (2005) Elsevier Ltd).

7.2.4.2 Vertical Magnetic Fields

Vertical magnetic field Cz crystal growth (VMCz) was one of the candidates for the control of melt flow. However, the radial distribution of oxygen concentration in Si crystals became inhomogeneous and consequently the VMCz method has not been used for the production of Si crystals.

Figure 7.38 shows velocity distributions in the melt with and without thermocapillary flow with vertical magnetic fields [Liu 2005-3]. The convective flow in the meridional plane is markedly decreased by applying a magnetic field, which has the effect of stabilizing the convective flow. The maximum velocity of the melt was 20 cm/s at the periphery of the crystal–melt interface in the case with thermocapillary flow, while that without thermocapillary flow was 0.5 cm/s in the bulk of the melt. The radial velocity in the bulk flow has been reported to be suppressed by vertical magnetic fields due to hydromagnetic dynamics when thermocapillary flow is ignored. However, the figure shows that the radial flow is not suppressed, especially at the surface. This discrepancy is based on the difference between bulk flow and surface flow. Force based on surface tension acts only at the surface of the melt; it is therefore difficult to suppress the flow because the breaking force due to the magnetic field acts in the whole volume of the melt.

Figure 7.39 shows temperature distributions in the melt with and without thermocapillary flow [Liu 2005-3]. The deflection of the interface between the crystal and melt with thermocapillary flow is larger than that without thermocapillary flow. This phenomenon is related to the flow described above. Radial flow at the top of the melt, in the same direction as natural convection, is large; therefore, the velocity of the descending flow at the centre of the melt becomes large. Consequently, the temperature at the centre of the interface between the crystal and melt becomes low. Thus, the position of the interface becomes lower with thermocapillary flow than without thermocapillary flow, as shown by the dashed line in Figure 7.39. The force of the surface tension acts at the top of the

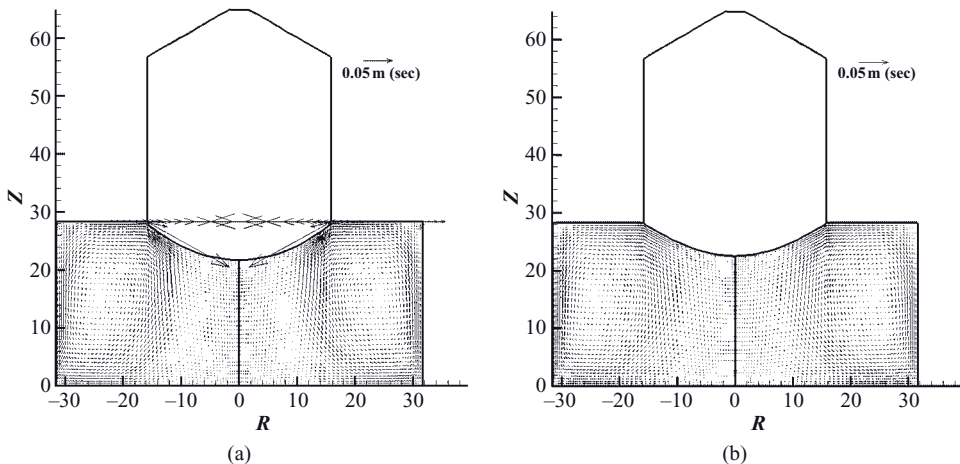


Figure 7.38 Velocity distributions in the melt with (a) and without (b) thermocapillary flow with vertical magnetic fields (Reprinted with permission from [Liu 2005-3], copyright (2005) Elsevier Ltd).

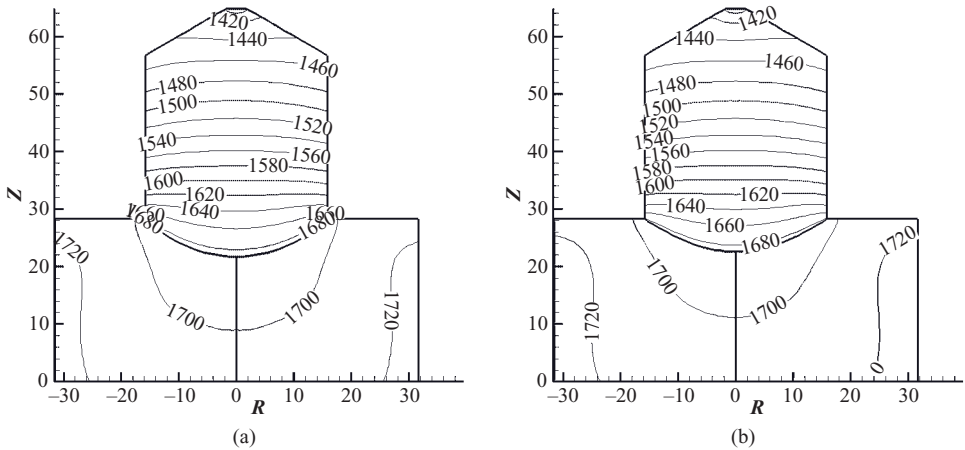


Figure 7.39 Temperature distribution in the melt with (a) and without (b) thermocapillary flow with vertical magnetic fields (Reprinted with permission from [Liu 2005-3], copyright (2005) Elsevier Ltd).

melt; however, it penetrates into the bulk melt through flow. Therefore, the melt is mixed even with vertical magnetic fields.

7.2.4.3 Cusp-Shaped Magnetic Fields

The cusp-shaped magnetic field Cz (CMCz) method has been reported to partly modify heat and mass transfer in the melt [Hurle 1994]. Magnetic fields in CMCz are distributed inhomogeneously, and the breaking force based on Lorenz force is therefore also distributed inhomogeneously.

Figure 7.40 shows velocity distributions in the melt with and without thermocapillary flow, with a cusp-shaped magnetic field with its symmetry plane along the free surface of the melt [Liu 2005-3]. The flow velocity in the melt is larger than in the VMCz case. This is because of the difference in the breaking force distribution between VMCz and CMCz. In VMCz the breaking force is distributed throughout the melt, while for CMCz it is distributed in only part of the melt. Therefore, in CMCz the motion of the melt is not as suppressed as it is in VMCz. The maximum velocity of the melt was 25 cm/s at the periphery of the crystal–melt interface in the case with thermocapillary flow, while that without thermocapillary flow was 0.6 cm/s in the bulk of the melt.

One interesting point is that the top of the melt near the crucible wall has a flow in an outward direction. This is due to the recirculation flow near the top at the edge of the melt. Such recirculation shifts the temperature distribution towards the outside of the melt; therefore, the outward flow is formed at the edge of the melt. Such outward flow sometimes enhances erosion of the fused quartz crucible. Therefore, controlling the recirculation flow is one of the key issues for maintaining a fused quartz crucible for a long time.

Figure 7.41 shows the temperature distributions in the melt with and without thermocapillary flow [Liu 2005-3]. The effect of the breaking force due to the cusp-shaped magnetic field is not as large as that in the case of VMCz shown in Figures 7.38 and 7.39,

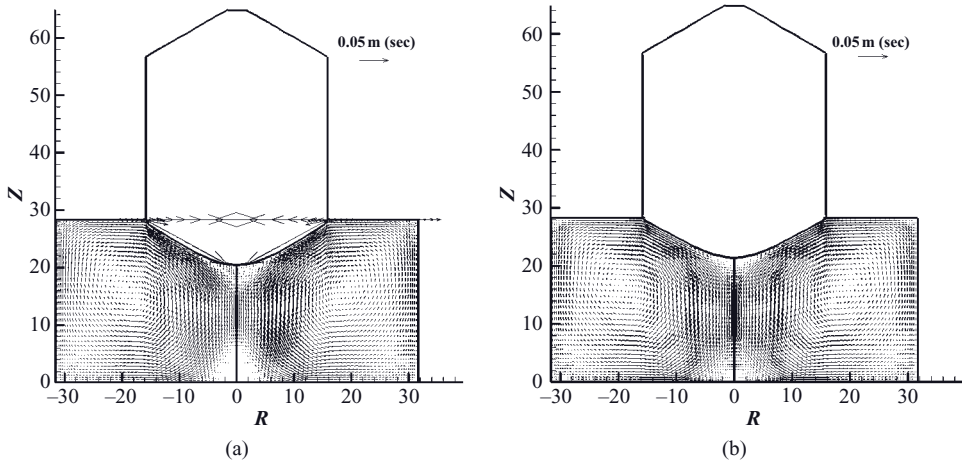


Figure 7.40 Velocity distributions in the melt with (a) and without (b) thermocapillary flow with cusp-shaped magnetic fields (Reprinted with permission from [Liu 2005-3], copyright (2005) Elsevier Ltd).

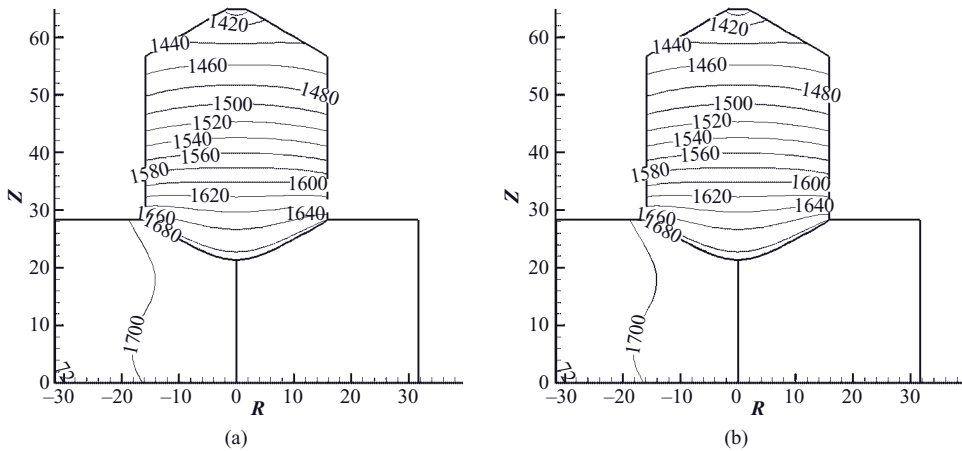


Figure 7.41 Temperature distributions in the melt with (a) and without (b) thermocapillary flow with cusp-shaped magnetic fields (Reprinted with permission from [Liu 2005-3], copyright (2005) Elsevier Ltd).

and the difference in temperature distributions between the cases with and without thermocapillary flow is therefore not so large even if a recirculation flow is formed as shown in Figure 7.40a. This is because of the large value of thermal conductivity of the melt, which homogenizes the temperature distribution.

7.2.4.4 Transverse Magnetic Fields

Figure 7.42 shows velocity distributions in the melt with and without thermocapillary flow, with transverse magnetic fields [Liu 2005-4]. The data were averaged along the

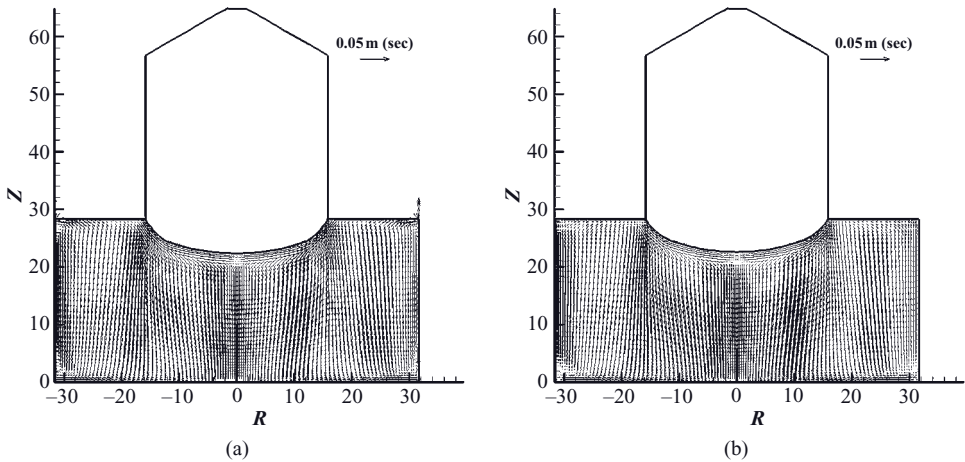


Figure 7.42 Velocity distributions in the melt with (a) and without (b) thermocapillary flow with transverse magnetic fields (Reprinted with permission from [Liu 2005-3], copyright (2005) Elsevier Ltd).

azimuthal direction because TMCz has an asymmetric configuration. The directions of the flow in the meridional plane with and without thermocapillary flow are opposite, due to surface tension force. Consequently, the interface shape, especially at the edge with thermocapillary flow, was different compared to that without thermocapillary flow. Such opposite types of flow modify the temperature distribution in the melt. The average velocity of this system is larger than in VMCz. This means that the flow was not suppressed as much as it is in VMCz.

7.2.5 Summary of Cz Results

Thermocapillary flow is one of the most important factors of the melt convection in the Cz method. The effect of thermocapillary flow on the bulk flow is not significant; however, thermocapillary flow modifies the temperature distribution in the melt, especially near the surface of the melt. Moreover, in the case of applied magnetic fields, the thermocapillary flow affects the interface shape between the melt and the crystal. The degree of the effect is dependent on the type of magnetic field, e.g. vertical, cusp-shaped, and transverse magnetic fields.

7.3 Thermocapillary Convection in EFG Set-Ups

Edge-defined film-fed growth (EFG) is described in detail in Chapter 5. It is used commercially for the production of multicrystalline solar Si tubes [Smirnova 2008] and for shaped sapphire crystals [Bunoiu 2005]. In EFG there are two areas with a free surface and thus thermocapillary flow to consider: one is the melt pool in the crucible, and the other the small meniscus connecting the shaping die with the growing crystal. The results of numerical simulations, validated by the results of the actual crystal growth processes,

have shown that thermocapillary convection plays a significant role in both. In the melt pool, the interaction of thermocapillary and natural convection determines a three-dimensional time-dependent flow structure which in turn has some influence on the segregation of impurities, e.g. for EFG Si [Bellmann 2007, Smirnova 2008].

The flow in the meniscus is almost entirely dominated by thermocapillary convection as shown in [Bellmann 2007, Braescu 2008]. The resulting flow velocity depends significantly, apart from the material and the temperature gradient, on the design of the shaping die, as shown by the simulations of [Buniou 2005] comparing a die with a central channel and an annular channel. These differences in turn lead to a different concentration field of solute in front of the interface. In the case of EFG sapphire growth, [Buniou 2005] showed that this effect determines the incorporation of bubbles into the crystals.

Three-dimensional simulations of the meniscus flow in the case of EFG Si compared the flow velocity with and without thermocapillary convection, resulting in values of 3.44 cm/s and 0.34 cm/s, respectively [Bellmann 2007]. It turned out that the pressure distribution caused by the thermocapillary convection rolls led to a reversion of the flow in some of the channels in the shaping die; this in turn altered the distribution of solute considerably. Due to this effect, the concentration of carbon (from the SiC-coated die) in front of the crystallization interface stays below the saturation point, whereas without thermocapillary convection the carbon concentration would reach the saturation point in the meniscus [Bellmann 2007].

7.4 Thermocapillary Convection in Bridgman and Related Set-Ups

Obviously, Marangoni convection will also play a significant role in horizontal Bridgman set-ups and must be considered by the crystal grower. Simulations can be found in [Kaddeche 1994-1, Kaddeche 1994-2].

What may not be immediately obvious is the fact that even for VB growth, or similar set-ups like VGF, thermocapillary convection can influence the mixing of the melt. The radial temperature gradient along the free top of the melt in a VB crucible can drive a sufficiently strong (laminar) thermocapillary convection to achieve even mixing of a dopant introduced from the gas phase into a Bridgman set-up. This has been proved by Ge:Zn growth experiments under microgravity [Pätzold 2002]. In the microgravity experiment, the top surface of an undoped Ge melt was in contact with the ampoule atmosphere which contained a Zn source. The resulting distribution of Zn did not follow a diffusive profile, but a profile suggesting good mixing of the melt, which could only be attributed to thermocapillary convection at the top of the melt. Subsequent numerical simulations proved that this was the case [Pätzold 2002].

7.5 Solutocapillary Convection

As mentioned in the main discussion of Marangoni convection above, solutocapillary or solutal Marangoni convection can exist in mixed growth systems, with the solutal Marangoni number given by Equation (7.3). For example, it plays a significant role in

welding [Nakajima 2003]. Considering both thermocapillary and solutocapillary convection, i.e. taking into account the contributions of both the temperature and the concentration gradient, an axial surface tension gradient at the interface of a growing crystal is given by:

$$\frac{\partial \gamma_{lv}}{\partial z} = \frac{\partial \gamma_{lv}}{\partial C} \cdot \frac{\partial C}{\partial z} + \frac{\partial \gamma_{lv}}{\partial T} \cdot \frac{\partial T}{\partial z}, \quad (7.19)$$

with z as the axial coordinate. If $\partial \gamma_{lv} / \partial C \neq 0$ and the segregation coefficient $k \neq 1$, which holds for the vast majority of all crystal growth cases, the actual growth process will cause a surface tension gradient close to the growing interface due to the segregation-induced concentration gradient in the boundary layer ahead of the interface. Both thermal and solutal Marangoni forces will inevitably persist as long as the crystal growth continues. An important difference between thermo- and solutocapillary convection is that thermocapillary convection will be constant as long as the temperature gradient is maintained, whereas solutocapillary convection will change during growth in accordance with the build-up (or reduction) of solute in front of the interface, in dependence on the growth rate. When the growth stops, e.g. by stopping translation during FZ or Cz growth, solutocapillary convection will also stop, while thermocapillary convection will continue as long as the temperature gradient and the free surface are kept constant.

An assessment of the configurations possible can be made [Tison 1992], assuming that

- the growth process is not in a transient stage, and;
- the growth rate is at the limit of constitutional supercooling, i.e. the concentration gradient $\partial C / \partial z$ can then be substituted by

$$\frac{dC_L}{dT} \cdot \frac{\partial T}{\partial z},$$

with dT/dC_L being the liquidus slope:

$$\frac{\partial \gamma_{lv}}{\partial z} = \left(\frac{dC_L}{dT} \cdot \frac{\partial \gamma_{lv}}{\partial C} + \frac{\partial \gamma_{lv}}{\partial T} \right) \cdot \frac{\partial T}{\partial z} \quad (7.20)$$

The sign and amount of surface tension-driven convection are in this case governed by the contribution of the thermally driven part versus that of

$$\frac{dC_L}{dT} \cdot \frac{\partial \gamma_{lv}}{\partial C}$$

for the solutally driven part. In principle, four different combinations are discernible, but since $\partial \gamma_{lv} / \partial T$ is usually negative, only two cases are of practical importance:

Case 1: Normal (towards the interface) thermocapillary and solutocapillary flow:

$$\frac{\partial \gamma_{lv}}{\partial T} < 0, \quad \frac{dC_L}{dT} \cdot \frac{\partial \gamma_{lv}}{\partial C} < 0.$$

Case 2: Normal thermocapillary flow and inverse (away from the interface) solutocapillary flow:

$$\frac{\partial \gamma_{lv}}{\partial T} < 0, \quad \frac{dC_L}{dT} \cdot \frac{\partial \gamma_{lv}}{\partial C} > 0.$$

For Case 2, an inverse solutocapillary driven flow in front of the interface will be observable if

$$\left| \frac{dC_L}{dT} \cdot \frac{\partial \gamma_{lv}}{\partial C} \right| > \left| \frac{\partial \gamma_{lv}}{\partial T} \right|. \tag{7.21}$$

Obviously, this will influence the segregation during crystal growth significantly. The effect has been shown experimentally for the metallic system Sn–Bi [Tison 1992, Camel 2002], for the system InSb–Sb [Arafune 1998], and for the system Ge–Si [Campbell 2001]. [Arafune 1999] measured the flow velocities for pure solutal convection in the

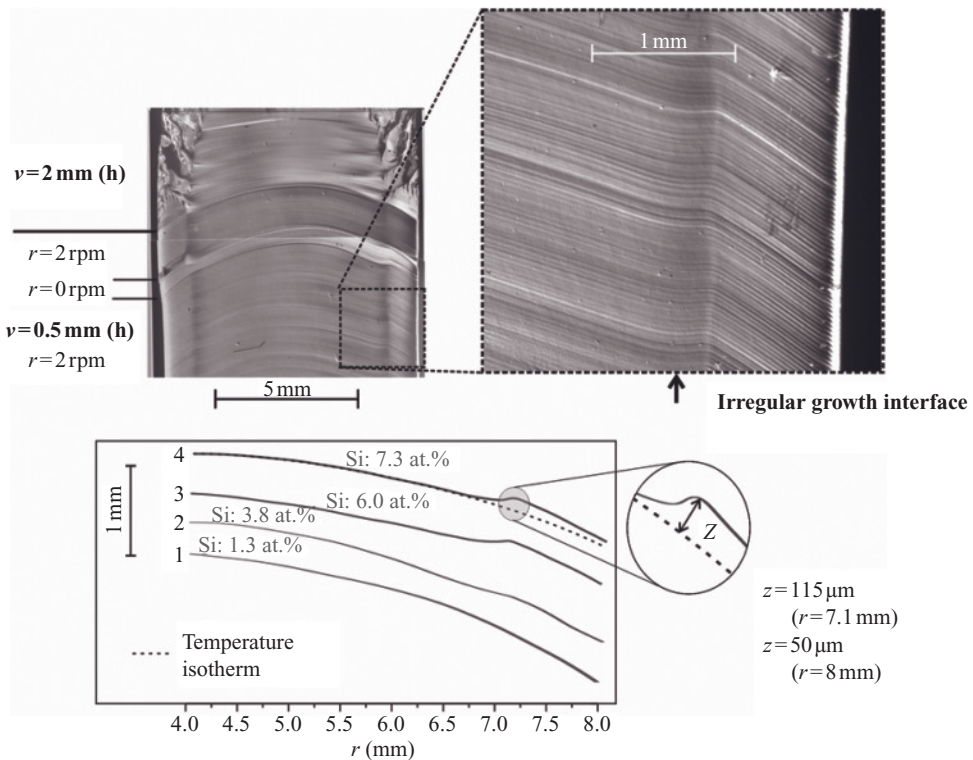


Figure 7.43 Change of the interface shape with the Si content in a FZ-grown Ge–Si crystal due to solutocapillary convection. With increasing Si content the outer part of the interface deviates from the convex isotherm for the composition. (Reprinted with permission from [Campbell 2001, Dold 2003], copyright (2001) Elsevier Ltd).

system In–Ga–Sb by adding a liquid of different composition to an initially isothermal melt. Velocities up to 200 mm/s were measured, about 5–10 times faster than the velocities of thermocapillary convection caused by temperature differences of 10–80 K in the same geometry. Numerical simulations of horizontal directional solidification by [Kaddeche 1994-2] in a differentially heated rectangular cavity found solutocapillary flow opposing thermocapillary convection, the size increasing with the build-up of solute, corroborating the experimental results. Results by [Campbell 2001] pointed to pronounced solutocapillary convection during the FZ growth of Ge–Si mixed crystals. A significant change of the interface shape with increasing Si content, shown in Figure 7.43, suggested the appearance of additional convective cells near the interface periphery. An order of magnitude analysis of solutocapillary convection in this configuration, as well as numerical simulations corroborated the existence of solutocapillary convection with an opposing flow in this system [Dold 2003]. Recent $\text{Ge}_{1-x}\text{Si}_x$ ($0.03 < x < 0.1$) crystallization experiments in a shallow rectangular cavity under microgravity showed tracer velocities up to 55 mm/s due to solutocapillary convection away from the interface at the onset of crystallization [Cröll 2009]. Since the tracers were comparatively large (1 mm), the real flow velocity can be assumed to be even higher. These results show that solutocapillary convection in crystal growth, although often neglected in experiments and simulations, can play as large a role as thermocapillary convection.

References

- [Anilkumar 1993] Anilkumar A.V., Grugel R.N., Shen X.F., Lee C.P., Wang T.G., *J. Appl. Phys.* **73** (1993) 4165.
- [Anilkumar 2005] Anilkumar A.V., Grugel R.N., Bhowmick J., Wang T.G., *J. Cryst. Growth* **276** (2005) 194.
- [Arafune 1998] Arafune K., Kamei T., Hirata A., *Proc. 49th IAF Congress*, Melbourne (1998).
- [Arafune 1999] Arafune K., Hirata A., *J. Cryst. Growth* **197** (1999) 811.
- [Azami 2001-1] Azami T., Nakamura S., Hibiya T., *J. Cryst. Growth* **223** (2001) 116.
- [Azami 2001-2] Azami T., Nakamura S., Hibiya T., *J. Electrochem. Soc.* **148** (2001) G185.
- [Azami 2001-3] Azami T., Nakamura S., Hibiya T., *J. Cryst. Growth* **231** (2001) 82.
- [Azami 2001-4] Azami T., Hibiya T., *J. Cryst. Growth* **233** (2001) 417.
- [Azami 2001-5] Azami T., Nakamura S., Eguchi M., Hibiya T., *J. Cryst. Growth* **233** (2001) 99.
- [Barthel 1979] Barthel J., Eichler K., Jurisch M., Löser M., *Krist. Tech.* **14** (1979) 637.
- [Bayly 1986] Bayly B.J., *Phys. Rev. Lett.* **57** (1986) 2160.
- [Bellmann 2007] Bellmann M., PhD thesis, Technical University of Freiberg, Germany (2007).
- [Braescu 2008] Braescu L., Duffar T., *J. Cryst. Growth* **310** (2008) 484–489.
- [Brandle 1977] Brandle C.D., *J. Cryst. Growth* **42** (1977) 400.
- [Buniou 2005] Buniou O., Nicoara I., Santailier J.L., Duffar T., *J. Cryst. Growth* **275** (2005) e799.
- [Camel 2002] Camel D., Tison P., Garandet J.P., *Eur. Phys. J. Appl. Phys.* **18** (2002) 201.
- [Campbell 2001] Campbell T.A., Schweizer M., Dold P., Cröll A., Benz K. W., *J. Cryst. Growth* **226** (2001) 231.
- [Carlberg 1984] Carlberg T., *Proc. 5th European Symp. Materials Sciences and Microgravity*, Schloß Elmau (1984) (ESA-SP222), p. 173.
- [Carlberg 1986-1] Carlberg T., *Acta Astronaut.* **13** (1986) 639.
- [Carlberg 1986-2] Carlberg T., *J. Cryst. Growth* **79** (1986) 71.
- [Carlberg 1987] Carlberg T., *J. Cryst. Growth* **85** (1987) 32.
- [Chang 1975] Chang C.E., Wilcox W.R., *J. Cryst. Growth* **28** (1975) 8.

- [Chang 1976] Chang C.E., Wilcox W.R., *Int. J. Heat Mass Transfer* **19** (1976) 355.
- [Chang 1979] Chang C.E., Wilcox W.R., Lefever R.A., *Mat. Res. Bull.* **14** (1979) 527.
- [Chen 1998] Chen Q.S., Hu W.R., *Int. J. Heat Mass Tran.* **41** (1998) 825.
- [Chen 1999] Chen Q.S., Hu W.R., Prasad V., *J. Cryst. Growth* **203** (1999) 261.
- [Cheng 2000] Cheng M., Kou S., *J. Cryst. Growth* **218** (2000) 132.
- [Chun 1978] Chun C.H., Wuest H., *Acta Astronaut.* **5** (1978) 681.
- [Chun 1979] Chun C.H., Wuest H., *Acta Astronaut.* **6** (1979) 1073.
- [Chun 1980] Chun C.H., *J. Cryst. Growth* **48** (1980) 600.
- [Chun 1982] Chun C.H., Wuest H., *Z. Flugwiss. Weltraumforsch.* **6** (1982) 316.
- [Clark 1980] Clark P.A., Wilcox W.R., *J. Cryst. Growth* **50** (1980) 461.
- [Cröll 1986] Cröll A., Müller W., Nitsche R., *J. Cryst. Growth* **79** (1986) 65.
- [Cröll 1989] Cröll A., Müller-Sebert W., Nitsche R., *Mater. Res. Bull.* **24** (1989) 995.
- [Cröll 1991] Cröll A., Müller-Sebert W., Benz K.W., Nitsche R., *Microgravity Sci. Technol.* **III** (1991) 204.
- [Cröll 1994-1] Cröll A., Dold P., Benz K.W., *J. Cryst. Growth* **137** (1994) 95.
- [Cröll 1994-2] Cröll A., Tegetmeier A., Nagel G., Benz K.W., *Cryst. Res. Technol.* **29** (1994) 335.
- [Cröll 1997] Cröll A., Habilitation thesis, University of Freiburg, Germany (1997).
- [Cröll 1998-1] Cröll A., Kaiser Th., Schweizer M., Danilewsky A.N., Lauer S., Tegetmeier A., Benz K.W., *J. Cryst. Growth* **191** (1998) 365.
- [Cröll 1998-2] Cröll A., Szofran F.R., Dold P., Benz K.W., Lehoczky S.L., *J. Cryst. Growth* **183** (1998) 555.
- [Cröll 1999] Cröll A., Dold P., Kaiser T., Szofran F.R., Benz K.W., *J. Electrochem. Soc.* **146** (1999) 2270.
- [Cröll 2002-1] Cröll A., Schweizer M., Dold P., Kaiser Th., Lichtensteiger M., Benz K.W., *Adv. Space Res.* **29** (2002) 527.
- [Cröll 2002-2] Cröll A., Salk N., Szofran F.R., Cobb S.D., Volz M.P., *J. Cryst. Growth* **242** (2002) 45.
- [Cröll 2009] Cröll A., Mitric A., Aniol O., Schütt S., *Cryst. Res. Technol.* **44** (2009) 1101.
- [DeLeon 1981] DeLeon N., Guldborg J., Salling J., *J. Cryst. Growth* **55** (1981) 406.
- [Dold 1994] Dold P., PhD thesis, University of Freiburg, Germany (1994).
- [Dold 1998] Dold P., Cröll A., Benz K.W., *J. Cryst. Growth* **183** (1998) 545.
- [Dold 1999] Dold P., Benz K.W., *Progr. Cryst. Growth Charact. Mater.* **38** (1999) 39.
- [Dold 2001] Dold P., Cröll A., Lichtensteiger M., Kaiser Th., Benz K.W., *J. Cryst. Growth* **231** (2001) 95.
- [Dold 2002] Dold P., Schweizer M., Cröll A., Benz K.W., *J. Cryst. Growth* **237–239** (2002) 671.
- [Dold 2003] Dold P., Habilitation thesis, University of Freiburg, Germany (2003).
- [Dold 2004] Dold P., *J. Cryst. Growth* **261** (2004) 1.
- [Drazin 1981] Drazin P.G., Reid W.H., *Hydrodynamic Stability*, Cambridge University Press, Cambridge (1981).
- [Dressler 1988] Dressler R.F., Sivakumaran N.S., *J. Cryst. Growth* **88** (1988) 148.
- [Eyer 1984] Eyer A., Leiste H., Nitsche R., *Proc. 5th European Symp. on Materials Sciences and Microgravity*, Schloß Elmau (1984) (ESA-SP222), p. 173.
- [Eyer 1985-1] Eyer A., Leiste H., Nitsche R., *J. Cryst. Growth* **71** (1985) 173.
- [Eyer 1985-2] Eyer A., Leiste H., Nitsche R., *J. Cryst. Growth* **71** (1985) 249.
- [Fukumoto 2005] Fukumoto Y., Hattori Y., *J. Fluid Mech.* **526** (2005) 77.
- [Gershuni 1998] Gershuni G.Z., Lyubimov D.V., *Thermal Vibrational Convection*, John Wiley & Sons, Ltd, New York (1998).
- [Han 1996] Han J.H., Sun Z.W., Dai L.R., Xie J.C., Hu W.R., *J. Cryst. Growth* **169** (1996) 129.
- [Heiple 1982] Heiple C.A., Roper J.R., *Welding J.* **61** (1982) 975.
- [Herrmann 1994] Herrmann F.M., PhD thesis, University of Erlangen-Nürnberg, Germany (1994).
- [Herrmann 1995] Herrmann F.M., Müller G., *J. Cryst. Growth* **156** (1995) 350.
- [Hibiya 1996] Hibiya T., Nakamura S., Kakimoto K., Imaishi N., Nishizawa S., Hirata A., Mukai K., Matsui K., Yokota T., Yoda S., Nakamura T., *Proc. Fluids in Space*, Naples (1996), p. 231.
- [Hibiya 2003-1] Hibiya T., Asai Y., Sumiji M., *Cryst. Res. Technol.* **38** (2003) 619.
- [Hibiya 2003-2] Hibiya T., Azami T., Sumiji M., Nakamura S., *Lect. Notes Phys.* **628** (2003), 131.

- [Hibiya 2005] Hibiya T., *J. Mater. Sci.* **40** (2005) 2417.
- [Hurle 1983] Hurle D.T.J., *J. Cryst. Growth* **65** (1983) 124.
- [Hurle 1994] Hurle D.T.J., Series R.W., In: *Handbook of Crystal Growth* Vol. 2a, ed. D.T.J. Hurle Elsevier, Amsterdam (1994), p. 261.
- [Imaishi 1999] Imaishi N., Yasuhiro S., Sato T., Yoda S., *Materials Research in Low Gravity II, SPIE Proc.* **3792** (1999) 344.
- [Imaishi 2001] Imaishi N., Yasuhiro S., Akiyama Y., Yoda S., *J. Cryst. Growth* **230** (2001) 164.
- [Jing 2000] Jing C.J., Imaishi N., Sato T., Miyazawa Y., *J. Cryst. Growth* **216** (2000) 372.
- [Jing 2008] Jing C.J., Ihara S., Sugioka K.-I., Tsukada T., Kobayashi M., *J. Cryst. Growth* **310** (2008) 204.
- [Jones 1983] Jones A. D.W., *J. Cryst. Growth* **63** (1983) 70.
- [Jones 1984] Jones A. D.W., *J. Cryst. Growth* **69** (1984) 165.
- [Jones 1985] Jones A. D.W., *Phys. Fluid* **28** (1985) 31.
- [Jones 1989] Jones A. D.W., *J. Cryst. Growth* **94** (1989) 421.
- [Jurisch 1982] Jurisch M., Löser W., Lyumkis E., Martuzane E., Martuzans B., *Cryst. Res. Technol.* **17** (1982) 963.
- [Jurisch 1990-1] Jurisch M., Löser W., *J. Cryst. Growth* **102** (1990) 214.
- [Jurisch 1990-2] Jurisch M., *J. Cryst. Growth* **102** (1990) 223.
- [Kaiser 1993] Kaiser T., PhD thesis, University of Freiburg, Germany (1993).
- [Kaiser 1998] Kaiser T., Benz K.W., *J. Cryst. Growth* **183** (1998) 564.
- [Kaiser 2001] Kaiser N., Cröll A., Szofran F.R., Cobb S.D., Benz K.W., *J. Cryst. Growth* **231** (2001) 448.
- [Kaddeche 1994-1] Kaddeche S., Ben Hadid H., Henry D., *J. Cryst. Growth* **135** (1994) 341.
- [Kaddeche 1994-2] Kaddeche S., Ben Hadid H., Henry D., *J. Cryst. Growth* **141** (1994) 279.
- [Kakimoto 2002] Kakimoto K., *J. Cryst. Growth* **237–239** (2002) 1785.
- [Kamotani 1984] Kamotani Y., Ostrach S., Vargas M., *J. Cryst. Growth* **66** (1984) 83.
- [Kerswell 2002] Kerswell R.R., *Annu. Rev. Fluid Mech.* **34** (2002) 83.
- [Kazarinoff 1989] Kazarinoff N.D., Wilkowski J.S., *Phys. Fluids A* **1** (1989) 625.
- [Keller 1981] Keller W., Mühlbauer A., *Preparations and Properties of Solid-State Materials, Vol. 5 Floating-Zone Silicon*, ed. W.R. Wilcox, Marcel Dekker, New York (1981).
- [Kim 1972] Kim K.M., Witt A.F., Gatos H.C., *J. Electrochem. Soc.* **119** (1972) 1218.
- [Kim 1978] Kim K.M., Witt A.F., Lichtensteiger M., Gatos H.C., *J. Electrochem. Soc.* **125** (1978) 475.
- [Kimura 1983] Kimura H., Harvey M.F., O'Connor D.J., Robertson G.D., Valley G.C., *J. Cryst. Growth* **62** (1983) 523.
- [Kimura 1993] Kimura M., Arai H., Mori T., Yamagishi H., *J. Cryst. Growth* **128** (1993) 282.
- [Knobel 2005] Knobel R., Ammon W., Virbulis J., Grundner M., German patent DE 10216609 B4 (2005).
- [Kölker 1984] Kölker H., *Proc. 5th European Symp. on Materials Sciences and Microgravity, Schloß Elmau* (1984) (ESA-SP222), p. 169.
- [Kölker 1986] Kölker H., *Proc. Norderney Symp. Scientific Results of the German Spacelab Mission D1*, Norderney (1986), p. 264.
- [Kozhoukarova 1986] Kozhoukarova Z., Slavchev S., *J. Cryst. Growth* **74** (1986) 236.
- [Krauze 2004-1] Krauze A., Muiznieks A., Mühlbauer A., Wetzels Th., Ammon W.v., *J. Cryst. Growth* **262** (2004) 157.
- [Krauze 2004-2] Krauze A., Muiznieks A., Mühlbauer A., Wetzels Th., Tomzig E., Gorbunov L., Pedchenko A. and Virbulis J., *J. Cryst. Growth* **265** (2004) 14.
- [Kuhlmann 1993] Kuhlmann H.C., Rath H.J., *J. Fluid Mech.* **247** (1993) 247.
- [Kuhlmann 1999] Kuhlmann H.C., *Thermocapillary Convection in Models of Crystal Growth*, Springer-Verlag, Berlin (1999).
- [Lan 1991-1] Lan C.W., Kou S., *J. Cryst. Growth* **108** (1991) 340.
- [Lan 1991-2] Lan C.W., Kou S., *J. Cryst. Growth* **108** (1991) 1.
- [Lan 1991-3] Lan C.W., Kou S., *J. Cryst. Growth* **108** (1991) 541.
- [Lan 1991-4] Lan C.W., Kou S., *J. Cryst. Growth* **114** (1991) 517.
- [Lan 1991-5] Lan C.W., Kou S., *J. Cryst. Growth* **104** (1991) 351.

- [Levenstam 1995] Levenstam M., Amberg G., *J. Fluid Mech.* **297** (1995) 357.
- [Levenstam 1996] Levenstam M., Amberg G., Carlberg T., Andersson M., *J. Cryst. Growth* **158** (1996) 224.
- [Leypoldt 2000] Leypoldt J., Kuhlmann H.C., Rath H.J., *J. Fluid Mech.* **414** (2000) 285.
- [Li 2003] Li J., Li M., Hu W., Zeng D., *Int. J. Heat Mass Trans.* **46** (2003) 4969.
- [Li 2005] Li K., Yasuhiro S., Imaishi N., Yoda S., *J. Cryst. Growth* **280** (2005) 620.
- [Li 2007] Li K., Imaishi N., Jing C.J., Yoda S., *J. Cryst. Growth* **307** (2007) 155.
- [Liu 2005-1] Liu L., Kakimoto K., *Int. J. Heat Mass Trans.* **48** (2005) 4481.
- [Liu 2005-2] Liu L., Kakimoto K., *Int. J. Heat Mass Trans.* **48** (2005) 4492.
- [Liu 2005-3] Liu L., Kitashima T., Kakimoto K., *J. Cryst. Growth* **275** (2005) e2135.
- [Liu 2005-4] Liu L., Kakimoto K., *J. Cryst. Growth* **275** (2005) e1521.
- [Lyubimov 1997] Lyubimov D., Lyubimova T., Roux B., *Int. J. Heat Mass Trans.* **40** (1997) 4031.
- [Lyubimov 2002] Lyubimov D.V., Lyubimova T.P., Skuridin R.V., Chen G., Roux B., *Comput. Fluids* **31** (2002) 663.
- [Lyubimova 2003] Lyubimova T.P., Scuridin R.V., Cröll A., Dold P. *Cryst. Res. Technol.* **38** (2003) 635.
- [Mallet 1999] Mallet S., *A Wavelet Tour of Signal Processing*, 2nd ed. Academic Press, London (1999).
- [Matsumoto 2004] Matsumoto S., Hayashida H., Yoda S., Komiya A., Natsui H., Imaishi N., *Thermal Sci. Eng.* **12** (2004) 21.
- [Miller 1981] Miller D.C., Pernell T.L., *J. Cryst. Growth* **53** (1981) 523.
- [Miller 1982] Miller D.C., Pernell T.L., *J. Cryst. Growth* **57** (1982) 253.
- [Morita 1993] Morita S., Sekima H., Toshima H., Miyazawa Y., *J. Ceram. Soc. Japan* **101** (1993) 108.
- [Mukai 2000] Mukai K., Yuan Z., Nogi K., Hibiya T., *ISIJ Int.* **40** suppl. (2000) 148.
- [Müller 1991] Müller G., Rupp R., *Cryst. Prop. Prep.* **35** (1991) 138.
- [Murgai 1976] Murgai A., Gatos H.C., Witt A.F., *J. Electrochem. Soc.* **123** (1976) 224.
- [Nakajima 2003] Nakajima K., Yasuhiro S., Mizoguchi S., Imaishi N., *Metall. Mater. Trans. B* **34** (2003) 37.
- [Nakamura 1996] Nakamura S., Kakimoto K., Hibiya T., *Lect. Notes Phys.* **464** (1996) 343.
- [Nakamura 1998] Nakamura S., Hibiya T., Kakimoto K., Imaishi N., Nishizawa S., Hirata A., Mukai K., Yoda S., Morita T.S., *J. Cryst. Growth* **186** (1998) 85.
- [Nakamura 1999-1] Nakamura S., Hibiya T., Imaishi N., *Microgravity Sci. Technol.* **12** (1999) 56.
- [Nakamura 1999-2] Nakamura S., Eguchi M., Azami T., Hibiya T., *J. Cryst. Growth* **207** (1999) 55.
- [Nakamura 1999-3] Nakamura S., Hibiya T., Imaishi N., Yoda T., *Adv. Space Res.* **24** (1999) 1417.
- [Neitzel 1993] Neitzel G.P., Chang K.-T., Jankowski D.F., Mittelmann H.D., *Phys. Fluids A* **5** (1993) 108.
- [Nienhüser 2002] Nienhüser C., Kuhlmann H.C., *J. Fluid Mech.* **458** (2002) 35.
- [Nikolov 1988] Nikolov V., Iliev K., Peshev P., *J. Cryst. Growth* **89** (1988) 313.
- [Okubo 2005] Okubo N., Jono R., Shiratori S., Goto S., Hibiya T., *J. Mater. Sci.* **40** (2005) 2245.
- [Onuma 1999] Onuma K., Sumiji M., Nakamura S., Hibiya T., *Appl. Phys. Lett.* **74** (1999) 3570.
- [Ozoe 1994] Ozoe H., Iwamoto M., *J. Cryst. Growth* **142** (1994) 236.
- [Pätzold 2002] Pätzold O., Fischer B., Cröll A., *Cryst. Res. Technol.* **37** (2002) 1058.
- [Pearson 1958] Pearson J.R.A., *J. Fluid Mech.* **4** (1958) 489.
- [Preisser 1983] Preisser F., Schwabe D., Scharmann A., *J. Fluid Mech.* **126** (1983) 545.
- [Ratto 2000] Ratto M., Ricci E., Arato E., *J. Cryst. Growth* **217** (2000) 233.
- [Robertson 1986-1] Robertson G.D., O'Connor D.J., *J. Cryst. Growth* **76** (1986) 100.
- [Robertson 1986-2] Robertson G.D., O'Connor D.J., *J. Cryst. Growth* **76** (1986) 111.
- [Rupp 1989] Rupp R., Mueller G., Neumann G., *J. Cryst. Growth* **97** (1989) 34.
- [Rupp 1990] Rupp R., PhD thesis, University of Erlangen-Nürnberg, Germany (1990).
- [Rupp 1991] Rupp R., Müller G., *J. Cryst. Growth* **113** (1991) 131.
- [Schwabe 1978] Schwabe D., Scharmann A., Preisser F., Oeder R., *J. Cryst. Growth* **43** (1978) 305.
- [Schwabe 1979] Schwabe D., Scharmann A., *J. Cryst. Growth* **46** (1979) 125.

- [Schwabe 1981] Schwabe D., *Physicochem. Hydrodyn.* **2** (1981) 263.
- [Schwabe 1982] Schwabe D., Scharmann A., Preisser F., *Acta Astronaut.* **9** (1982) 183.
- [Schwabe 1988] Schwabe D., In: *Crystals – Growth, Properties and Applications*, ed. H.C. Freyhardt. Springer, Berlin (1988), p. 75.
- [Schwabe 1990] Schwabe D., Velten R., Scharmann A., *J. Cryst. Growth* **99** (1990) 1258.
- [Schwabe 1996] Schwabe D., Da X., Scharmann A., *J. Cryst. Growth* **166** (1996) 483.
- [Schweizer 1999] Schweizer M., Cröll A., Dold P., Kaiser Th., Lichtensteiger M., Benz K.W., *J. Cryst. Growth* **203** (1999) 500.
- [Scriven 1960] Scriven L.E., Sterling C.V., *Nature* **187** (1960) 186.
- [Shen 1990] Shen Y., Neitzel G.P., Jankowski D.F., Mittelmann H.D., *J. Fluid Mech.* **217** (1990) 639.
- [Shen 1996] Shen X.F., Anilkumar A.V., Grugel R.N., Wang T.G., *J. Cryst. Growth* **165** (1996) 438.
- [Shevtsova 2005] Shevtsova V., *J. Cryst. Growth* **280** (2005) 632.
- [Shigematsu 1987] Shigematsu K., Anzai Y., Morita S., Yamada M. and Yokoyama H., *J. Appl. Phys.* **26** (1987) 1988.
- [Shiratori 2004] Shiratori S., Yasuhiro S., Hibiya T., *J. Cryst. Growth* **266** (2004) 145.
- [Shiratori 2007-1] Shiratori S., Kuhlmann H.C., Hibiya T., *Phys. Fluids* **19** (2007) 044103.
- [Shiratori 2007-2] Shiratori S., PhD thesis, Tokyo Metropolitan Institute of Technology, Japan (2007).
- [Smirnova 2008] Smirnova O.V., Kalaev V.V., Seidl A., Birkmann B., *J. Cryst. Growth* **310** (2008) 2209.
- [Sumiji 2000] Sumiji M., Nakamura S., Onuma K., Hibiya T., *Jpn. J. Appl. Phys* **39** (2000) 3688.
- [Sumiji 2001] Sumiji M., Nakamura S., Azami T., Hibiya T., *J. Cryst. Growth* **223** (2001) 503.
- [Sumiji 2002] Sumiji M., Nakamura S., Hibiya T., *J. Cryst. Growth* **235** (2002) 55.
- [Takagi 1976] Takagi K., Fukazawa T., Ishii M., *J. Cryst. Growth* **32** (1976) 89.
- [Takagi 2001] Takagi K., Otaka M., Natsui H., Arai T., Yoda S., Yuan Z., Mukai K., Yasuhiro S., Imaishi N., *J. Cryst. Growth* **233** (2001) 399.
- [Takiuchi 1991] Takiuchi N., Taniguchi T., Tanaka Y., Shinozaki N., Mukai K., *J. Jpn. Inst. Metals* **55** (1991) 180 (in Japanese).
- [Tegetmeier 1995] Tegetmeier A., PhD thesis, University of Freiburg, Germany (1995).
- [Tegetmeier 1996] Tegetmeier A., Cröll A., Danilewsky A., Benz K.W., *J. Cryst. Growth* **166** (1996) 651.
- [Tison 1992] Tison P., Camel D., Tosello I., Favier J.J., *Proc. Int. Symp Hydromechanics and Heat/Mass Transfer in Microgravity*, Perm–Moscow, 1991 (1992), p. 121.
- [Ueno 2003] Ueno I., Tanaka S., Kawamura H., *Phys. Fluids* **15** (2003) 408.
- [Wanschura 1995] Wanschura M., Shevtsova V.M., Kuhlmann H.C., Rath H.J., *Phys. Fluids* **7** (1995) 912.
- [Whiffin 1976] Whiffin P. A.C., Burton T.M., Brice J.C., *J. Cryst. Growth* **32** (1976) 205.
- [Widnall 1974] Widnall S.E., Bliss D.B., Tsai C.-Y., *J. Fluid Mech.* **66** (1974) 35.
- [Witt 1973] Witt A.F., Lichtensteiger M., Gatos H.C., *J. Electrochem. Soc.* **120** (1973) 1119.
- [Xu 1984] Xu J.-J., Davis S.H., *Phys. Fluids* **27** (1984) 1102.
- [Yamane 2005] Yamane N., Nagafuchi K., Shiratori S., Okubo H., Sato N., Hibiya T., *J. Mater. Sci.* **40** (2005) 2221.
- [Yang 2001] Yang Y.K., Kou S., *J. Cryst. Growth* **222** (2001) 135.
- [Yasuhiro 2004] Yasuhiro S., Imaishi N., Akiyama Y., Fujino S., Yoda S., *J. Cryst. Growth* **262** (2004) 631.

8

Mathematical and Numerical Analysis of Capillarity Problems and Processes

Liliana Braescu
West University of Timisoara

Simona Epure
SIMaP-EPM and West University of Timisoara

Thierry Duffar
SIMaP-EPM

One major problem confronting crystal growth researchers has been the development of techniques capable of monitoring and controlling the external shape of melt-grown crystals, and simultaneously improving the crystal structures. In the EFG, Cz, dewetted Bridgman and FZ processes, the shape and the dimensions of the crystal are determined by the liquid meniscus and by the heat transfer at the melt–crystal interface. In addition, the meniscus is also of great practical use for techniques of diameter control: in the weighing method ([Bardsley 1974, Bardsley 1977, Dijk 1974, Johansen 1992, Chapter 3]) the weight of the melt enclosed by the meniscus appears as an essential parameter; when using video observation ([Gartner 1972, Gartner 1973, O’Kane 1972, Sachs 1980]), the crystal diameter and the interface height have to be measured exactly.

Historically, the physical origin and the shape of a liquid meniscus were among the first phenomena to be studied in capillarity [Hauksbee 1709]. The first formal analytical expression was given by Laplace [Laplace 1806], after introduction of the *mean curvature* κ defined as the average (arithmetic mean) of the principal curvatures $\kappa = \frac{1}{2}(1/R_1 + 1/R_2)$

[Young 1805]. Laplace showed that the *mean curvature* of the free surface is proportional to the pressure change across the surface. The proportionality coefficient is the surface tension γ_{lv} . The pressure change across the surface contains p_v the pressure of the external gas on the melt; p_o , the internal pressure applied on the liquid, which can generally be defined at the origin; $\rho_l g z$, the hydrostatic pressure; $\frac{1}{2} \rho_l \Omega_l^2 (x^2 + y^2)$, the pressure determined by the centrifugal force due to a possible liquid rotation $\frac{1}{2} \rho_l \Omega_l^2 (x^2 + y^2)$ where Ω_l is the angular velocity of the liquid (around the Oz axis in crystal growth techniques), and, when magnetic fields are used, the Maxwell pressure which is proportional to the square of the magnetic induction $B^2(x, y) / 2\mu$ (μ -magnetic permeability). The following equality known as the Young–Laplace equation must hold:

$$\frac{1}{R_1} + \frac{1}{R_2} = \pm \frac{p_o - p_v - \rho_l g z + \frac{1}{2} \rho_l \Omega_l^2 (x^2 + y^2) - [B^2(x, y) / 2\mu]}{\gamma_{lv}}. \tag{8.1}$$

As quoted in [Landau 1971], the choice of the positive sign is a convention which generally follows the physical meaning. However, from the mathematical point of view, the positive or negative signs depend on the axis frame convention. Generally, the curvature is taken to be positive if the curve turns in the same direction as the surface’s chosen normal, and negative otherwise.

The result can be summarized as follows: the positive sign corresponds to the cases where the liquid has the shape of a sessile or pendant drop (Figure 8.1a), e.g. floating zone (FZ), dewetting or Verneuil configurations, and the negative sign corresponds to the cases where the liquid has the shape of an external meniscus (Figure 8.1b), e.g. EFG or Cz configurations [Hartland 1976].

Denoting the meniscus surface by $A: z(x, y)$, it is known from differential geometry, that the mean curvature is expressed as [Finn 1986]:

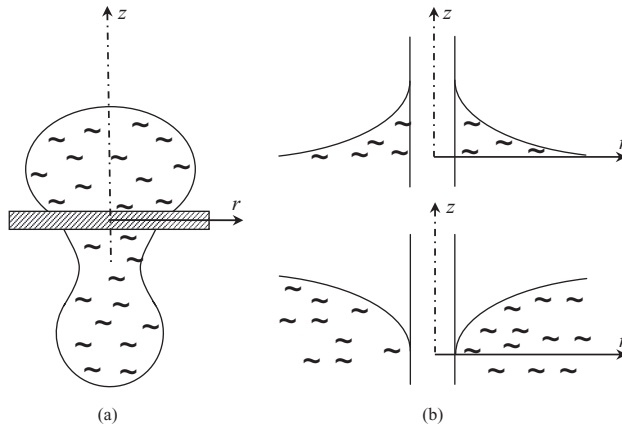


Figure 8.1 (a) Sessile or pendant drop: + positive sign in Young-Laplace equation. (b) External meniscus: – negative sign in Young-Laplace equation.

$$\kappa = \frac{E_I G_{II} - 2F_I F_{II} + G_I E_{II}}{2(E_I G_I - F_I^2)}, \tag{8.2}$$

where E_I, F_I, G_I represent the coefficients of the first fundamental form of the surface A and E_{II}, F_{II}, G_{II} represent the coefficients of the second fundamental form. According to Finn, for a surface given in explicit form $z = z(x, y)$, these coefficients are given by:

$$\begin{aligned} E_I &= 1 + \left(\frac{\partial z}{\partial x}\right)^2, & F_I &= \frac{\partial z}{\partial x} \cdot \frac{\partial z}{\partial y}, & G_I &= 1 + \left(\frac{\partial z}{\partial y}\right)^2, \\ E_{II} &= \frac{\partial^2 z / \partial x^2}{\sqrt{1 + (\partial z / \partial x)^2 + (\partial z / \partial y)^2}}, \\ F_{II} &= \frac{\partial^2 z / (\partial x \partial y)}{\sqrt{1 + (\partial z / \partial x)^2 + (\partial z / \partial y)^2}}, \\ G_{II} &= \frac{\partial^2 z / \partial y^2}{\sqrt{1 + (\partial z / \partial x)^2 + (\partial z / \partial y)^2}}, \end{aligned}$$

and hence the Young–Laplace equation (8.1) becomes:

$$\begin{aligned} & \frac{\left[1 + \left(\frac{\partial z}{\partial y}\right)^2\right] \cdot \frac{\partial^2 z}{\partial x^2} - 2 \cdot \frac{\partial z}{\partial x} \cdot \frac{\partial z}{\partial y} \cdot \frac{\partial^2 z}{\partial x \partial y} + \left[1 + \left(\frac{\partial z}{\partial x}\right)^2\right] \cdot \frac{\partial^2 z}{\partial y^2}}{\left[1 + \left(\frac{\partial z}{\partial x}\right)^2 + \left(\frac{\partial z}{\partial y}\right)^2\right]^{3/2}} \\ &= \pm \frac{p_0 - p_v - \rho_l g z + \frac{1}{2} \rho_l \Omega_l^2 (x^2 + y^2) - [B^2(x, y) / 2\mu]}{\gamma_{lv}}. \end{aligned} \tag{8.3}$$

This equation is a nonlinear partial differential equation (PDE) of second order, and the unknown function $z(x, y)$ represents the meniscus surface. Because of the nonlinearity of this equation, it is necessary to do qualitative analysis and to develop specific numerical tools for finding the meniscus surface, which, furthermore, should satisfy the boundary conditions depending on the chosen configuration.

Section 8.1 below contains a mathematical formulation of the capillary problem. The boundary value problem for the Young–Laplace equation in the three-dimensional and axisymmetric cases is presented, and the initial and boundary condition of the axisymmetric meniscus problem are given. The growth angle criterion and some approximated solutions of the axisymmetric meniscus problem are also included.

In sections 8.2–8.4 some analytical and numerical solutions for the meniscus equation in the Cz, EFG and dewetted Bridgman growth techniques are presented. The case of the FZ process is extensively described in Chapter 4 and is not treated here.

8.1 Mathematical Formulation of the Capillary Problem

8.1.1 Boundary Value Problems for the Young–Laplace Equation

8.1.1.1 Three-Dimensional Case

In order to find physically sound solutions of the Young–Laplace equation, it is generally necessary to formulate the model as a ‘well posed’ PDE problem. A PDE problem is said to be well posed if: (i) a solution to the problem exists; (ii) the solution is unique; and (iii) the solution depends continuously on the problem data. In practice, the question of whether a PDE problem is well posed can be difficult to settle.

The Young–Laplace equation (8.3) can be written as follows:

$$a(x, y) \cdot \frac{\partial^2 z}{\partial x^2} + 2 \cdot b(x, y) \cdot \frac{\partial^2 z}{\partial x \partial y} + c(x, y) \cdot \frac{\partial^2 z}{\partial y^2} + d(x, y) \cdot z = e(x, y), \quad (8.4)$$

where

$$a(x, y) = \frac{1 + \left(\frac{\partial z}{\partial y}\right)^2}{\left[1 + \left(\frac{\partial z}{\partial x}\right)^2 + \left(\frac{\partial z}{\partial y}\right)^2\right]^{3/2}}, \quad (8.5)$$

$$b(x, y) = \frac{-\frac{\partial z}{\partial x} \cdot \frac{\partial z}{\partial y}}{\left[1 + \left(\frac{\partial z}{\partial x}\right)^2 + \left(\frac{\partial z}{\partial y}\right)^2\right]^{3/2}}, \quad (8.6)$$

$$d(x, y) = \frac{\rho_l g}{\gamma_{lv}}, \quad (8.7)$$

$$c(x, y) = \frac{1 + \left(\frac{\partial z}{\partial x}\right)^2}{\left[1 + \left(\frac{\partial z}{\partial x}\right)^2 + \left(\frac{\partial z}{\partial y}\right)^2\right]^{3/2}}, \quad (8.8)$$

$$e(x, y) = \pm \frac{p_o - p_v + \frac{1}{2} \rho_l \Omega_i^2 (x^2 + y^2) - B^2(x, y) / 2\mu}{\gamma_{lv}}. \quad (8.9)$$

The inequality

$$a(x, y) \cdot c(x, y) - b^2(x, y) = \frac{1}{\sqrt{1 + (\partial z / \partial x)^2 + (\partial z / \partial y)^2}} > 0$$

looks like an elliptic type of any solution $z(x,y)$ [Finn 1986]. Unfortunately Equation (8.4) cannot be included in the general theory of the elliptic PDE from variational calculus because the functions $a, b, c, d, e: \Omega \subset \mathbb{R}^2 \rightarrow \mathbb{R}$ are unknown and strongly nonlinear. Moreover, a well-posed elliptic PDE problem usually takes the form of a boundary value problem (BVP) with the solution required to satisfy a single boundary condition (Dirichlet, Neumann or Robin boundary condition) at each point on the boundary $\partial\Omega$ of the region.

These circumstances have important consequences for the behaviour of the solutions, reasons for which each problem containing the Young–Laplace equation should be treated separately. The peculiarities of each problem will lead to a corresponding mathematical context capable of providing conditions that ensure the existence and uniqueness of the solution.

Because of the complexity of the BVP associated to the Young–Laplace equation, there is no general analytical solution and the problem must be addressed numerically [Clanet 2002]. In some particular domains Ω , e.g. those obtained from crystal growth configurations (Cz, EFG, dewetted Bridgman, FZ), certain approximations can be made in order to simplify the problem and hence the equation can be integrated. In the following, the approximations most commonly used in the literature are presented, i.e. the domain Ω is two-dimensional or axisymmetric. These two-dimensional models will then be developed for EFG, Cz and dewetted Bridgman growth techniques. In some particular conditions, analytical solutions will be given.

8.1.1.2 Axisymmetric Case

In the axisymmetric case, the Young–Laplace equation (8.3) can be written using cylindrical polar coordinates $x = r \cdot \cos\theta, y = r \cdot \sin\theta, z = z$ (the meniscus is axisymmetric). Expressing r and θ as functions of x and y , i.e. $r = \sqrt{x^2 + y^2}, \theta = \arctan(y/x)$, the partial derivatives of the function $z(x,y)$ are:

$$\frac{\partial z}{\partial x} = \frac{dz}{dr} \cdot \frac{x}{r}, \quad \frac{\partial z}{\partial y} = \frac{dz}{dr} \cdot \frac{y}{r},$$

$$\frac{\partial^2 z}{\partial x^2} = \frac{d^2 z}{dr^2} \cdot \frac{x^2}{r^2} + \frac{dz}{dr} \cdot \frac{y^2}{r^3}, \quad \frac{\partial^2 z}{\partial y^2} = \frac{d^2 z}{dr^2} \cdot \frac{y^2}{r^2} + \frac{dz}{dr} \cdot \frac{x^2}{r^3}, \quad \frac{\partial^2 z}{\partial x \partial y} = \frac{d^2 z}{dr^2} \cdot \frac{xy}{r^2} - \frac{dz}{dr} \cdot \frac{xy}{r^3}.$$

Replacing these derivatives in Equation (8.3), the Young–Laplace equation written in cylindrical coordinates is:

$$\frac{\frac{d^2 z}{dr^2} + \frac{1}{r} \cdot \frac{dz}{dr} \cdot \left[1 + \left(\frac{dz}{dr} \right)^2 \right]}{\left[1 + \left(\frac{dz}{dr} \right)^2 \right]^{3/2}} = \pm \frac{p_0 - p_v - \rho_l g z + \frac{1}{2} \rho_l \Omega_1^2 \cdot r^2 - \frac{B^2(r)}{2\mu}}{\gamma_{lv}}, \quad (8.10)$$

for which the solution $z = z(r)$ is sought depending on the radial coordinate $r = \sqrt{x^2 + y^2}$. An equivalent formulation of Equation (8.10) is given in terms of the principal curvatures:

$$\frac{\frac{d^2 z}{dr^2}}{\left[1 + \left(\frac{dz}{dr} \right)^2 \right]^{3/2}} + \frac{\frac{1}{r} \cdot \frac{dz}{dr}}{\left[1 + \left(\frac{dz}{dr} \right)^2 \right]^{1/2}} = \pm \frac{p_0 - p_v - \rho_l g z + \frac{1}{2} \rho_l \Omega_1^2 \cdot r^2 - [B^2(r)/2\mu]}{\gamma_{lv}} \quad (8.11)$$

where

$$\frac{d^2z/dr^2}{[1+(dz/dr)^2]^{3/2}} = \frac{1}{R_1} \quad \text{and} \quad \frac{(1/r) \cdot (dz/dr)}{[1+(dz/dr)^2]^{1/2}} = \frac{1}{R_2},$$

but the most useful formulation is:

$$\frac{d^2z}{dr^2} = \pm \frac{p_0 - p_v - \rho_l g z + \frac{1}{2} \rho_l \Omega_1^2 \cdot r^2 - \frac{B^2(r)}{2\mu}}{\gamma_{lv}} \cdot \left[1 + \left(\frac{dz}{dr} \right)^2 \right]^{3/2} - \frac{1}{r} \cdot \frac{dz}{dr} \cdot \left[1 + \left(\frac{dz}{dr} \right)^2 \right]. \quad (8.12)$$

This is a nonlinear second-order differential equation and to obtain its solution $z = z(r)$ two conditions are needed, which, in association with Equation (8.12), give the BVP or initial value problem (IVP). In general, because of its nonlinearity, the problem does not have a solution expressed in an analytical form.

To solve the BVP (or IVP) it is necessary do a qualitative analysis and to develop specific numerical tools. To this end, Equation (8.12) is transformed into a nonlinear first-order system of differential equations. In the literature, two equivalent systems are known: one having three differential equations, and another having two differential equations. In both formulations, the angle ϕ between the tangent to the meniscus (at an arbitrary point) and the horizontal axis, called meridian angle [Boucher 1980], is involved.

First, Princen and Mason [Princen 1965] introduced the arc length s along the curve which generates the surface of revolution $z(r)$: $dr/ds = \cos\phi$, $dz/ds = \pm\sin\phi$ (the positive or negative signs depend on the axis frame convention in the same way as in Equation (8.1)). Taking into account that $dr/ds = \cos\phi$, $dz/ds = \sin\phi$ imply the curvatures $1/R_1 = d\phi/ds$ and $1/R_2 = (\sin\phi)/r$ (e.g. configuration Figure 8.1a), and $dr/ds = \cos\phi$, $dz/ds = -\sin\phi$ imply $1/R_1 = -d\phi/ds$, $1/R_2 = -(\sin\phi)/r$ (e.g. configuration Figure 8.1b)), Equation (8.11) is transformed into a system of three parametric differential equations:

$$\begin{cases} \frac{dr}{ds} = \cos\phi \\ \frac{dz}{ds} = \pm\sin\phi \\ \frac{d\phi}{ds} = -\frac{\sin\phi}{r} \pm \frac{p_0 - p_v - \rho_l g z + \frac{1}{2} \rho_l \Omega_1^2 \cdot r^2 - [B^2(r)/2\mu]}{\gamma_{lv}} \end{cases} \quad (8.13)$$

Later, Huh and Scriven [Huh 1969] eliminated the parameter s using the notation $dz/dr = \pm\tan\phi$ (with the sign convention mentioned above). Thus, Equation (8.11) was transformed into a system of two differential equations:

$$\begin{cases} \frac{dz}{dr} = \pm\tan\phi \\ \frac{d\phi}{dr} = \pm \frac{p_0 - p_v - \rho_l g z + \frac{1}{2} \rho_l \Omega_1^2 \cdot r^2 - [B^2(r)/2\mu]}{\gamma_{lv}} \cdot \frac{1}{\cos\phi} - \frac{1}{r} \cdot \tan\phi. \end{cases} \quad (8.14)$$

In order to make the analytical and numerical analysis easier, a dimensionless form of the Young–Laplace equation is also used, by introducing the following dimensionless parameters with L a characteristic dimension of the problem or the capillary constant of the material (see Chapter 2):

$$\tilde{r} = \frac{r}{L}; \quad \tilde{z} = \frac{z}{L}; \quad \phi(r) \rightarrow \phi(\tilde{r}), \tag{8.15}$$

which leads to:

$$\frac{dz}{dr} = \frac{d(\tilde{z} \cdot L)}{d(\tilde{r} \cdot L)} = \frac{d\tilde{z}}{d\tilde{r}}, \quad \frac{d^2z}{dr^2} = \frac{d}{dr} \left(\frac{dz}{dr} \right) = \frac{1}{L} \frac{d}{d\tilde{r}} \left(\frac{d\tilde{z}}{d\tilde{r}} \right) = \frac{1}{L} \frac{d^2\tilde{z}}{d\tilde{r}^2}.$$

Using the above dimensionless parameters, Equation (8.12) can be written as:

$$\frac{d^2\tilde{z}}{d\tilde{r}^2} = \pm \left[La - Bo \cdot \tilde{z} + \frac{1}{2}(We \cdot \tilde{r}^2 - Bo_{em}) \right] \cdot \left[1 + \left(\frac{d\tilde{z}}{d\tilde{r}} \right)^2 \right]^{3/2} - \frac{1}{\tilde{r}} \frac{d\tilde{z}}{d\tilde{r}} \left[1 + \left(\frac{d\tilde{z}}{d\tilde{r}} \right)^2 \right], \tag{8.16}$$

where $Bo = \rho_1 \cdot g \cdot L^2 / \gamma_{lv}$ denotes the Bond number, $La = (p_o - p_v) \cdot L / \gamma_{lv}$ the Laplace number, $We = \rho_1 \Omega_1 L^3 / \gamma_{lv}$ the Weber number and $Bo_{em} = (B^2(r) \cdot L) / (\mu \cdot \gamma_{lv})$ is the electromagnetic Bond number. Because after the dimensionless analysis ϕ depends on the non-dimensional parameter \tilde{r} , in the following $\tilde{\phi}$ is used instead of $\phi(\tilde{r})$.

Taking into account that:

$$\begin{aligned} \frac{dz}{dr} = \pm \tan \phi &\Rightarrow \frac{d\tilde{z}}{d\tilde{r}} = \pm \tan \tilde{\phi} \\ \frac{d^2\tilde{z}}{d\tilde{r}^2} = \frac{d}{d\tilde{r}} \left(\frac{d\tilde{z}}{d\tilde{r}} \right) &= \frac{d}{d\tilde{r}} (\pm \tan \tilde{\phi}) = \pm \frac{1}{\cos^2 \tilde{\phi}} \frac{d\tilde{\phi}}{d\tilde{r}} = \pm (1 + \tan^2 \tilde{\phi}) \frac{d\tilde{\phi}}{d\tilde{r}}, \end{aligned} \tag{8.17}$$

the following dimensionless form of the Young–Laplace equation is obtained:

$$\frac{d\tilde{\phi}}{d\tilde{r}} = \pm \left[La - Bo \cdot \tilde{z} + \frac{1}{2}(We \cdot \tilde{r}^2 - Bo_{em}) \right] \cdot \frac{1}{\cos \tilde{\phi}} - \frac{1}{\tilde{r}} \tan \tilde{\phi}. \tag{8.18}$$

Therefore, Equation (8.16) is transformed into the system:

$$\begin{cases} \frac{d\tilde{z}}{d\tilde{r}} = \pm \tan \tilde{\phi} \\ \frac{d\tilde{\phi}}{d\tilde{r}} = \pm \left[La - Bo \cdot \tilde{z} + \frac{1}{2}(We \cdot \tilde{r}^2 - Bo_{em}) \right] \cdot \frac{1}{\cos \tilde{\phi}} - \frac{1}{\tilde{r}} \tan \tilde{\phi}. \end{cases} \tag{8.19}$$

The mathematical models given by the systems (8.13), (8.14) or (8.19) are very useful for obtaining information concerning the meniscus behaviour (shape, monotony, attainment of the growth angle, etc.). They were successfully applied only after the development of computers powerful enough to permit the computation of menisci.

8.1.2 Initial and Boundary Conditions of the Meniscus Problem

The initial and/or boundary conditions required for solving the axisymmetric Young–Laplace equation are determined by the structural features of each specific configuration and will be analysed in the following sections for EFG, Cz, and dewetted Bridgman crystal growth techniques. In this section, common features corresponding to typical boundary conditions of the capillary problem are discussed: the *catching* and *wetting boundary conditions*.

The *catching boundary condition* is specific for materials that are wetted by the melt. It is used when one meniscus end is partially fixed, e.g. for the EFG technique the counter line of the meniscus surface is fixed by the internal or external edge counter (see Chapter 2, Figure 2.4b, d, j, k or Figure 2.4e, f). This condition can be expressed as:

$$z|_{r=r_0} = \text{const.},$$

where r_0 represents the radial coordinate of the point situated at the meniscus end, and the value of the constant depends on the position of the horizontal axis of the (rOz) frame, i.e. this constant is set to zero if the meniscus end is on the Or axis, or is equal to the distance between the horizontal axis Or and its parallel which passes through the meniscus end (see Chapter 2, section 2.6.1.1).

The *wetting boundary condition* is also known as the *angle of fixation boundary condition* because it expresses the angle made between the tangent to the meniscus at its endpoint situated at the base, and the tangent to the shaper or crucible wall (see also Chapter 2, section 2.6.1.2). For the axisymmetric Young–Laplace equation written for the configurations presented in Figure 2.4a, c, g, h, i (see Chapter 2) or Figure 8.18 (see dewetted Bridgman technique), the wetting boundary condition can be expressed as follows:

$$\left. \frac{dz}{dr} \right|_{r=r_0} = \tan\left(\theta - \frac{\pi}{2}\right)$$

where θ represents the wetting angle (see Chapter 1, and Figures 8.4 and 8.18).

From the physical point of view, the catching and wetting conditions cannot be applied simultaneously at the same point $r = r_0$. However, for certain configurations, it is useful from the mathematical point of view to perform calculations with a given angle applied at the catching condition point. Then the angle is varied in order to find a physically acceptable solution to the problem. In such cases, the systems (8.13), (8.14) or (8.19) have two initial conditions. Thus, an initial value problem is obtained and its unique solution represents the meniscus surface $z = z(r)$. The existence and uniqueness of the meniscus is assured on the basis of the Cauchy theorem, because functions from the right-hand terms of the system (8.13), (8.14) or (8.19) are real analytically. The meniscus can be computed numerically using Runge–Kutta method (see Appendix to this chapter in which the procedure for the fourth–order Runge–Kutta method is presented).

After the meniscus shape is obtained, the *growth angle criterion* should be imposed. It asserts that the crystal is obtained when the *growth angle* α is attained at the place where the meniscus contacts the crystal (see Chapter 1, section 1.3). This condition is expressed as

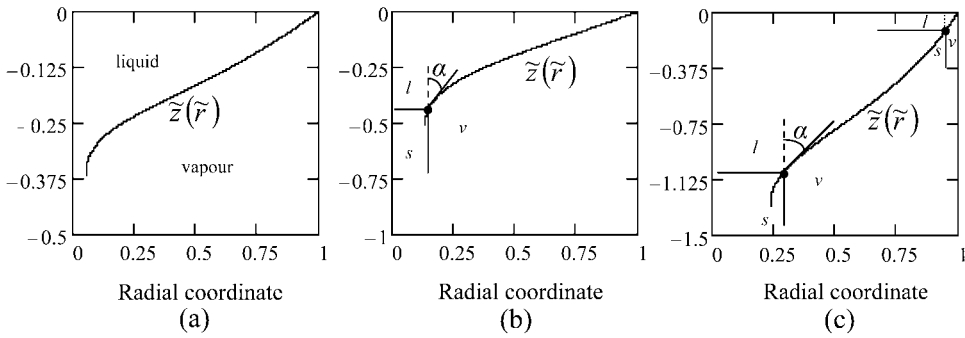


Figure 8.2 Numerical meniscus shape and attainment of the growth angle for InSb ($Bo = 3.84$, $\alpha = 25^\circ$): (a) $La = 0.105$: the growth angle cannot be achieved; (b) $La = 0.262$: the growth angle is achieved once; (c) $La = 0.393$: the growth angle is achieved twice.

$$\phi|_{r=r_c} = \frac{\pi}{2} - \alpha,$$

where r_c represents the crystal radius.

Even if the IVP of the Young–Laplace equation has a unique solution, it is nevertheless possible that this solution does not satisfy the condition for attainment of the growth angle. If this condition is satisfied then a crystal having a radius r_c can be obtained (Figure 8.2); otherwise, a crystal cannot be obtained.

The attainment of the growth angle is exemplified in Figure 8.2. More precisely, in the configuration shown in Figure 8.2a, there is no place along the meniscus where the angle is equal to α , so it is impossible to grow a crystal under conditions giving this meniscus. In Figure 8.2b, it is possible to grow a crystal from this meniscus. In Figure 8.2c, the growth angle can be achieved twice on the meniscus. This means that, under the same capillary conditions, it is possible to grow crystals with two different diameters. The choice is realized by heating or cooling the system in order to fix the height of the solid–liquid interface.

As already explained in Chapter 2, in some configurations, the wetting boundary condition does not exist (or it does so at infinity and hence cannot be used in numerical solutions; see section 8.2). In these cases, to solve the Young–Laplace equation, the growth angle should represent one boundary condition, and the second condition should be expressed using the meniscus height, which is unknown. These kinds of problems are very difficult from a mathematical and numerical point of view, so they should be treated separately, e.g. see section 8.2.

8.1.3 Approximate Solutions of the Axisymmetric Meniscus Problem

Some authors have proposed *simple approximations* of the axisymmetric Young–Laplace equation used especially for unbounded extent (i.e. Ω is an unbounded axisymmetric domain), when numerical solution of the BVP is very difficult [Huh 1969]. For example, in 1960 Nutt neglected the second curvature:

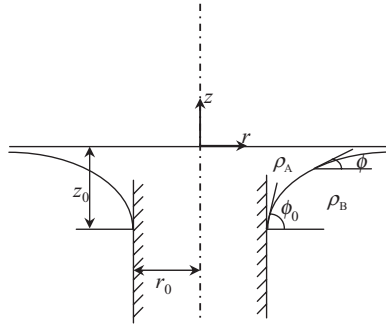


Figure 8.3 The meniscus for a vertical circular cylinder positioned in a fluid (Reprinted with permission from [Huh 1969], copyright (1969) Elsevier Ltd).

$$\frac{1}{R_2} = \frac{\frac{1}{r} \cdot \frac{dz}{dr}}{\left[1 + \left(\frac{dz}{dr}\right)^2\right]^{1/2}}$$

from Equation (8.11) [Nutt 1960], leading an analytical expression for the meniscus. More precisely, for the configuration presented in Figure 8.3, the Equation (8.11) is reduced to

$$\frac{\frac{d^2z}{dr^2}}{\left[1 + \left(\frac{dz}{dr}\right)^2\right]^{3/2}} = \frac{(\rho_B - \rho_A)gz}{\gamma_{lv}}$$

which is equivalent to:

$$\frac{d\phi}{dr} = \frac{(\rho_B - \rho_A)gz}{\gamma_{lv}} \cdot \frac{1}{\cos\phi}$$

where $dz/dr = +\tan\phi$ (the positive sign is due to the configuration). This equation can be integrated between r_0 and r (here $r > r_0$, see Figure 8.3), and the meniscus z can be expressed as a function of ϕ :

$$z(\phi) = -2\sqrt{\frac{\gamma_{lv}}{(\rho_B - \rho_A)g}} \cdot \sin\left(\frac{\phi}{2}\right).$$

Another approximation was reported by Tsivinski [Tsivinski 1962]. He considered both curvatures but expanded the curvature $1/R_2$ in a Taylor series, considering only the first two terms from the Taylor series:

$$\frac{1}{R_2} = \frac{1}{R_2}(h) + (z-h) \cdot \left. \frac{d}{dz} \left(\frac{1}{R_2} \right) \right|_{z=h},$$

where h represents the meniscus height. Using this approximation, Tsivinski obtained an analytical formula for the meniscus height as function of the crystal radius r_c and the growth angle α (for more details, see section 8.2):

$$h_T(r_c) = -\left(\frac{\cos \alpha}{2r_c}\right) \cdot \frac{\gamma_{lv}}{\rho_l g} + \sqrt{\left(\frac{\cos \alpha}{2r_c}\right)^2 \cdot \frac{\gamma^2}{\rho_l^2 g^2} - \frac{2\gamma}{\rho_l g} \cdot (\sin \alpha - 1)}.$$

This formula has been intensively cited and used for finding the analytical formulas of the meniscus. For example, Hurle obtained:

$$r(z) = r_c + \sqrt{\frac{2}{A} - h^2} - \sqrt{\frac{2}{A} - z^2} - \frac{1}{\sqrt{2A}} \cdot \ln \left| \frac{z \cdot \sqrt{2} + \sqrt{2 - A \cdot h^2}}{\sqrt{2} + \sqrt{2 - A \cdot z^2}} \right|,$$

where

$$A = \frac{1}{2} \left(\frac{\sin\left(\frac{\pi}{2} - \alpha\right)}{r_c \cdot h} + \frac{\rho_l g}{\gamma_{lv}} \right).$$

(see details in section 8.1) [Hurle 1983].

Other approximations of the axisymmetric Young–Laplace equation are based on Bessel functions [Boucher 1980, Ferguson 1912]. Boucher obtained a most useful mathematical approximation involving zero- and first-order modified Bessel functions:

$$z = \sqrt{1 + \cos \phi} \cdot \frac{K_0(r\sqrt{2})}{K_1(r\sqrt{2})}, \tag{8.20}$$

where

$$\frac{K_0(r\sqrt{2})}{K_1(r\sqrt{2})} \approx \frac{1}{\sqrt{1 + 1/(r\sqrt{2})}}$$

Equation (8.20) can be used to give $z = z(r)$ at constant ϕ , or $z = z(\phi)$ at constant r .

Comparisons between these analytical formulas [Hurle 1983] and the computed menisci reported by Huh and Scriven [Huh 1969] showed that the explicit approximations of the meniscus are adequate for the range of values of crystal radius and contact angle encountered in crystal growth.

The most recent approximation was given by Hernandez-Baltazar [Hernandez-Baltazar 2005] who solved the Young–Laplace equation with an elliptic representation, i.e. the principal curvatures

$$\frac{1}{R_1} = \frac{\frac{d^2 z}{dr^2}}{\left[1 + \left(\frac{dz}{dr}\right)^2\right]^{3/2}}, \quad \frac{1}{R_2} = \frac{\frac{1}{r} \cdot \frac{dz}{dr}}{\left[1 + \left(\frac{dz}{dr}\right)^2\right]^{1/2}}$$

were approximated by

$$\frac{1}{R_1} = \frac{a^4 b^4}{[a^4 z^2 + b^4 r^2]^{3/2}} \quad \text{and} \quad \frac{1}{R_2} = \frac{b^2}{[a^4 z^2 + b^4 r^2]^{3/2}},$$

assuming that the meniscus profile is very close to an elliptic profile with a , b representing the length of the semimajor (one half of the longest axis of the ellipse) and semiminor (one half of the shortest axis) axes of the ellipse centred at the origin. The elliptical analytical solution proposed by these authors is dependent on the parameter a in square form and its predictive capacity depends on a cubic expression. The parameters a and b are obtained from solving the Young–Laplace equation with the elliptical equation:

$$\frac{a}{b} + \frac{a^3}{b^3} = 2 + \beta^* \cdot a^2, \quad \text{where} \quad \beta^* = \frac{(\rho_B - \rho_A) \cdot g}{\gamma_{lv}}.$$

When the results of the analytical solution and the literature data for different profiles are compared, a correlation with acceptable error in the fifth digit is obtained. This means that the error in the parameter β^* , after applying the differential expression, would be less than 0.1%.

8.2 Analytical and Numerical Solutions for the Meniscus Equation in the Cz Method

For the Cz growth method (see Figure 8.4), the axisymmetric meniscus is given by the Young–Laplace equation (8.12). In the Cz process, the meniscus height h is controlled by heat transfer and the problem is to find the relation between the crystal radius and the meniscus height.

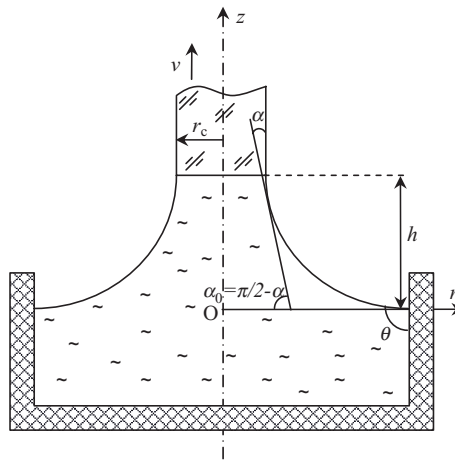


Figure 8.4 Axisymmetric model for a cylindrical crystal grown by the Cz method.

The pressure due to rotation in Cz is only a few pascals and is commonly neglected. If the growth process takes place without a magnetic field, Equation (8.12) becomes:

$$\frac{d^2z}{dr^2} = -\frac{(p_0 - p_v) - \rho_l g z}{\gamma_{lv}} \cdot \left[1 + \left(\frac{dz}{dr} \right)^2 \right]^{-3/2} - \frac{1}{r} \cdot \frac{dz}{dr} \cdot \left[1 + \left(\frac{dz}{dr} \right)^2 \right]. \tag{8.21}$$

The solution $z = z(r)$ of Equation (8.21) has to satisfy the following boundary conditions:

$$z(r_c) = h, \quad \frac{dz}{dr}(r_c) = -tg\alpha_0; \quad \alpha_0 \in (0, \pi/2), \tag{8.22}$$

where $r_c > 0$ is the crystal radius, $\alpha_0 = \pi/2 - \alpha$ where α is the growth angle, h is the meniscus height (an unknown in the problem if a crystal with given r_c is to be pulled). Moreover, if the meniscus extends untouched far enough outwards its equilibrium shape becomes effectively flat at some distance from the crystal. The meniscus may then, for all intents and purposes, be regarded as unbounded, i.e. as extending to infinity [Huh 1969]:

$$z|_{r \rightarrow \infty} = 0. \tag{8.23}$$

From this peculiarity (no curvature of the meniscus at $r \rightarrow \infty$) it follows that the pressure in the melt at $z = 0$ is equal to the vapour pressure $p_0 = p_v$.

Because of (8.23), it is very difficult to find a numerical method for solving the meniscus surface equation, (8.21). To avoid this inconvenience, many authors have tried to find sufficiently accurate analytical approximations to the real meniscus profile. The most often cited results are those reported by Tsivinski [Tsivinski 1962] which derived an analytical expression for the meniscus height (i.e. the unknown h from the boundary condition (8.22)), in a Czochralski configuration using a particular form of the meniscus equation (8.11):

$$-\frac{\frac{d^2z}{dr^2}}{\left[1 + \left(\frac{dz}{dr} \right)^2 \right]^{3/2}} - \frac{\frac{1}{r} \cdot \frac{dz}{dr}}{\left[1 + \left(\frac{dz}{dr} \right)^2 \right]^{1/2}} = \frac{\rho_l g z}{\gamma_{lv}}, \tag{8.24}$$

where

$$\frac{\frac{d^2z}{dr^2}}{\left[1 + \left(\frac{dz}{dr} \right)^2 \right]^{3/2}} = \frac{1}{R_1} \quad \text{and} \quad \frac{\frac{1}{r} \cdot \frac{dz}{dr}}{\left[1 + \left(\frac{dz}{dr} \right)^2 \right]^{1/2}} = \frac{1}{R_2}$$

represent principal curvatures. Tsivinski considered both curvatures but he expanded the curvature $1/R_2$ in a Taylor series at the point h , as follows:

$$\frac{1}{R_2} = \frac{1}{R_2}(h) + (z-h) \cdot \left. \frac{d}{dz} \left(\frac{1}{R_2} \right) \right|_{z=h}. \tag{8.25}$$

Using $1/R_2 = (\sin\phi)/r$, where ϕ is the angle between the tangent to the meniscus (at an arbitrary point) and the horizontal axis, the terms $(1/R_2)(h)$ and $(d/dz)(1/R_2)|_{z=h}$ from the above representation are obtained as function of the growth angle α and the crystal radius r_c :

$$\frac{1}{R_2}(h) = \frac{\sin\phi(h)}{r_c} = \frac{\sin\left(\frac{1}{2}\pi - \alpha\right)}{r_c} = \frac{\sin\alpha_0}{r_c},$$

$$\left.\frac{d}{dz}\left(\frac{1}{R_2}\right)\right|_{z=h} \cong \frac{(1/R_2)(h) - (1/R_2)(0)}{h} = \frac{(\sin\phi(h))/r_c - 0}{h} = \frac{\sin\left(\frac{1}{2}\pi - \alpha\right)}{r_c \cdot h}.$$

After computations, the following formula for the curvature $1/R_2$ is obtained:

$$\frac{1}{R_2} = \frac{\sin\left(\frac{1}{2}\pi - \alpha\right)}{r_c} \cdot \frac{z}{h}. \quad (8.26)$$

Thus, the meniscus equation (8.24) becomes

$$-\frac{z''}{[1+z'^2]^{3/2}} - \frac{\sin\left(\frac{1}{2}\pi - \alpha\right)}{r_c} \cdot \frac{z}{h} = \frac{\rho_l g z}{\gamma_{lv}}, \quad (8.27)$$

where $z' = dz/dr$ and $z'' = d^2z/dr^2$. Multiplying this equation by z' , and integrating between 0 and z gives:

$$-\frac{1}{\sqrt{1+z'^2}} - \frac{\sin\left(\frac{1}{2}\pi - \alpha\right)}{r_c \cdot h} \cdot \frac{z^2}{2} - \frac{\rho_l g}{\gamma_{lv}} \cdot \frac{z^2}{2} + \left.\left(\frac{1}{\sqrt{1+z'^2}}\right)\right|_{z=0} = 0. \quad (8.28)$$

Because $1/\sqrt{1+z'^2} = \cos\phi(r)$, it follows that:

$$-\cos\phi(r) - \frac{\sin\left(\frac{1}{2}\pi - \alpha\right)}{r_c \cdot h} \cdot \frac{z^2}{2} - \frac{\rho_l g}{\gamma_{lv}} \cdot \frac{z^2}{2} + 1 = 0. \quad (8.29)$$

For $z = h$, $\phi(h) = \frac{1}{2}\pi - \alpha = \alpha_0$, and hence Equation (8.29) will represent an equation of the second degree for the meniscus height h :

$$\frac{\rho_l g}{\gamma_{lv}} \cdot \frac{h^2}{2} + \frac{\sin\alpha_0}{2r_c} \cdot h - (1 - \cos\alpha_0) = 0. \quad (8.30)$$

Solving this equation, the following analytical approximations on the meniscus height [Tsvinski 1962] is obtained:

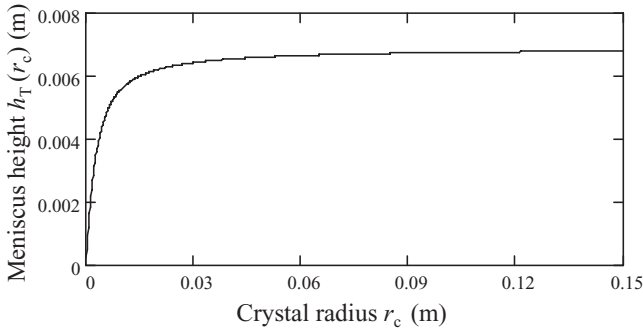


Figure 8.5 Meniscus height profile h_T as a function of the cylindrical silicon crystal radius r_c .

$$h_{1,2} = -\left(\frac{\sin \alpha_0}{2r_c}\right) \cdot \frac{\gamma_{lv}}{\rho_l g} \pm \sqrt{\left(\frac{\sin \alpha_0}{2r_c}\right)^2 \cdot \frac{\gamma_{lv}^2}{\rho_l^2 g^2} + \frac{2\gamma_{lv}}{\rho_l g} \cdot (1 - \cos \alpha_0)}. \quad (8.31)$$

It is easy to see that $h_{1,2}$ can be positive or negative, but for physical reasons only the positive meniscus will be considered:

$$h = -\left(\frac{\sin \alpha_0}{2r_c}\right) \cdot \frac{\gamma_{lv}}{\rho_l g} + \sqrt{\left(\frac{\sin \alpha_0}{2r_c}\right)^2 \cdot \frac{\gamma_{lv}^2}{\rho_l^2 g^2} + \frac{2\gamma_{lv}}{\rho_l g} \cdot (1 - \cos \alpha_0)}. \quad (8.32)$$

where α is the growth angle. This is equivalent to:

$$h_T(r_c) = -\left(\frac{\cos \alpha}{2r_c}\right) \cdot \frac{\gamma_{lv}}{\rho_l g} + \sqrt{\left(\frac{\cos \alpha}{2r_c}\right)^2 \cdot \frac{\gamma_{lv}^2}{\rho_l^2 g^2} + \frac{2\gamma_{lv}}{\rho_l g} \cdot (1 - \sin \alpha)} \quad (8.33)$$

which is used to estimate the meniscus height in diameter control techniques ([Bardsley 1974–2, Bardsley 1977, Dijk 1974, Johansen 1992]) (Figure 8.5), or for comparison with other analytic approximations [Bardsley 1974–1, Hurle 1981, Hurle 1983, Johansen 1987, Johansen 1992, Mika 1975, Tatartchenko 1993].

An analytical approximation of the meniscus profile can be obtained only for some particular cases. For example, Hurle considered a reduced form of Equation (8.28):

$$\frac{1}{\sqrt{1+z'^2}} + \left(\frac{\sin\left(\frac{1}{2}\pi - \alpha\right)}{r_c \cdot h} + \frac{\rho_l g}{\gamma_{lv}} \right) \cdot \frac{z^2}{2} - 1 = 0. \quad (8.34)$$

Writing the equation in the form:

$$\frac{1}{\sqrt{1+z'^2}} = 1 - A \cdot z^2,$$

where

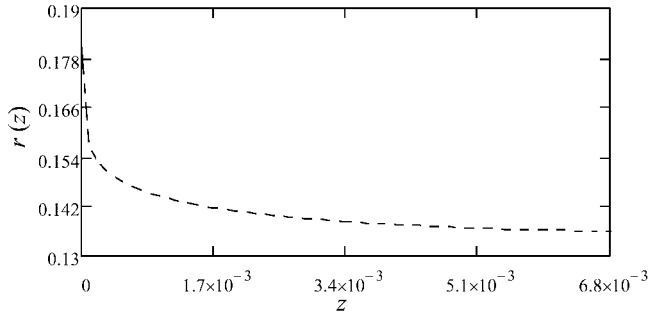


Figure 8.6 Meniscus profile $r_T(z)$ vs z .

$$A = \frac{1}{2} \left(\frac{\sin\left(\frac{1}{2}\pi - \alpha\right)}{r_c \cdot h} + \frac{\rho_l g}{\gamma_{lv}} \right), \tag{8.35}$$

the following ordinary differential equation is obtained:

$$\frac{1 - A \cdot z^2}{\sqrt{1 - (1 - A \cdot z^2)^2}} dz = dr.$$

After integrating between h and z , using $r(h) = r_c$, the following explicit analytical formula $r_T(z)$ for the meniscus is obtained:

$$r_T(z) = r_c + \sqrt{\frac{2}{A} - h^2} - \sqrt{\frac{2}{A} - z^2} - \frac{1}{\sqrt{2A}} \cdot \ln \left| \frac{z}{h} \cdot \frac{\sqrt{2} + \sqrt{2 - A \cdot h^2}}{\sqrt{2} + \sqrt{2 - A \cdot z^2}} \right|. \tag{8.36}$$

Replacing A and h by (8.35) and (8.33) respectively, the meniscus profile for a cylindrical silicon crystal of radius $r_c = 0.136\text{m}$ is shown in Figure 8.6.

The second analytical expression for the meniscus height reported in the literature is based on Bessel functions (see section 8.1.3) [Hurle 1983, Johansen 1992, Johansen 1994]:

$$h_B(r_c) = \sqrt{\frac{2\gamma_{lv}}{\rho_l g}} \cdot \sqrt{\frac{1 - \cos\left(\frac{1}{2}\pi - \alpha\right)}{1 + (1/r_c) \cdot \sqrt{\gamma_{lv}/(\rho_l g)}}}, \tag{8.37}$$

equivalent to

$$h_B(r_c) = \sqrt{\frac{2\gamma_{lv}}{\rho_l g}} \cdot \sqrt{\frac{1 - \sin \alpha}{1 + (1/r_c) \cdot \sqrt{\gamma_{lv}/(\rho_l g)}}}. \tag{8.37'}$$

Details of Bessel functions and how they are used to obtain Equation (8.34) will be given later, when a new analytical-numerical solution for computing the meniscus surface will be proposed.

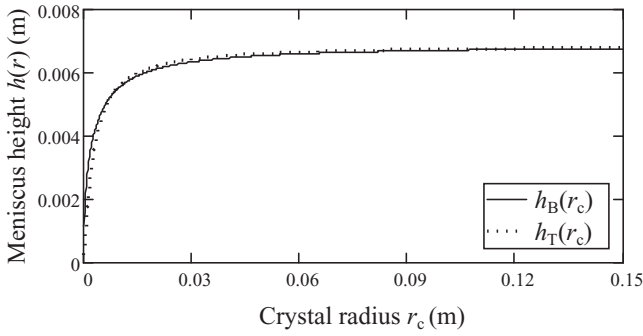


Figure 8.7 Meniscus heights h_T (8.33) and h_B (8.37) as function of the crystal radius r_c .

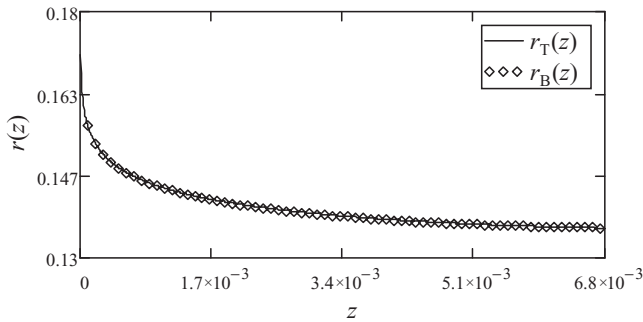


Figure 8.8 Meniscus profiles r_T (8.36) and r_B (8.38) vs z .

A comparison between Equations (8.33) and (8.37) can be seen in Figure 8.7. The figure shows accurate analytical approximations of the meniscus height as a function of the crystal radius. For small crystal radius the error is of the order 10^{-4} , but for large crystal radius, as in Cz crystal growth, the approximation is very good, which is why both formulas have been used by crystal growers. Moreover, for the second of the meniscus height formula $h_B(r_c)$ a similar analytical formula for the meniscus $r_B(z)$ can be found [Hurle 1983]:

$$r_B(z) = \frac{1}{2} \sqrt{\frac{\gamma_{lv}}{\rho_l g}} \cdot \left(P(z) + \sqrt{P^2(z) + \frac{3}{4} (\rho_l g / \gamma_{lv})^2 \cdot z^2 - 2} \right) \tag{8.38}$$

where $P(z)$ is given by

$$P(z) = r_c \sqrt{\frac{\rho_l g}{\gamma_{lv}}} + \frac{1}{\sqrt{1 + (1/r_c) \cdot (\gamma_{lv} / (\rho_l g))}} \cdot \left(\frac{1}{2r_c} \cdot \sqrt{\frac{\gamma_{lv}}{\rho_l g}} - \ln\left(\frac{z}{h_B(z)}\right) - \frac{3}{16} \left(1 + \frac{1}{r_c} \cdot \frac{\gamma_{lv}}{\rho_l g}\right) \cdot \left(\frac{\rho_l g}{\gamma_{lv}}\right) \cdot h_B^2(z) + \frac{3}{16} \cdot \frac{\rho_l g}{\gamma_{lv}} \cdot z^2 \right)$$

The comparison between Equations (8.36) and (8.38) can be seen in Figure 8.8.

Computations show that for the considered cylindrical silicon crystal of radius $r_c = 0.136 \text{ m}$, the errors between these two analytical formulas are of the order 10^{-5} .

The reason why researchers used the above approximations is that it is difficult to obtain a numerical solution because of the condition (8.23). In order to avoid this difficulty, Mika and Uelhoff [Mika 1975] proposed an analytical-numerical solution. More precisely, part of the solution for $r \rightarrow \infty$ (called asymptotic part of the solution) can be derived analytically, i.e. for $r \in [r^*; \infty)$, and the remaining part can be solved numerically using Runge–Kutta method on the finite range $r \in (0; r^*]$. The problem is to find the accurate range on which this analytical solution is available, and after that to find initial conditions for computing the numerical solution.

In the following, the asymptotic part of the solution, $r \in [r^*; \infty)$, obtained using modified Bessel functions [Mika 1975] is presented. For the second part of the solution, $r \in (0; r^*]$, mathematical tools for finding initial conditions in order to solve the IVP numerically are used.

The asymptotic solution can be obtained starting from Equation (8.21), in which $(dz/dr)^2$ is neglected because $dz/dr \ll 1$ at a large enough distance from the crystal, and $p_0 = p_v$:

$$\frac{d^2 z}{dr^2} = \frac{\rho_l g z}{\gamma_{lv}} - \frac{1}{r} \cdot \frac{dz}{dr}, \quad (8.39)$$

which can be rewritten in the form

$$r^2 \cdot \frac{d^2 z}{dr^2} + r \cdot \frac{dz}{dr} - r^2 \cdot \frac{\rho_l g}{\gamma_{lv}} \cdot z = 0. \quad (8.40)$$

In order to write this as a standard Bessel equation, $z(r)$ is transformed to $y(x)$ with: $r = x \cdot \sqrt{\gamma_{lv}/(\rho_l g)}$ and $z = y \cdot \sqrt{\gamma_{lv}/(\rho_l g)}$. Thus, Equation (8.40) becomes:

$$x^2 \cdot \frac{d^2 y}{dx^2} + x \cdot \frac{dy}{dx} - x^2 \cdot y = 0 \quad (8.41)$$

Equation (8.41) is called a homogeneous modified Bessel differential equation, being of the type:

$$x^2 \cdot y'' + x \cdot y' - (x^2 + n^2) \cdot y = 0, \quad (8.42)$$

with $n = 0$. From the theory of Bessel functions, it is known that the general solution is a linear combination between modified Bessel functions of the first and second order, respectively: $y(x) = C_1 \cdot I_n(x) + C_2 \cdot K_n(x)$, where C_1 and C_2 are constants which should be determined. The general solution of Equation (8.41) is:

$$y(x) = C_1 \cdot I_0(x) + C_2 \cdot K_0(x), \quad (8.43)$$

because $n = 0$. Moreover, it is known that for $x \gg n$ (this is available in Cz growth because for the asymptotic solution $r \in [r^*; \infty)$, and hence $r \gg 0$), the modified Bessel

functions become: $I_n(x) \approx e^x/\sqrt{2\pi x}$ and $K_n(x) \approx e^{-x}/\sqrt{2\pi x}$. Thus, the general solution (8.43) is

$$y(x) = C_1 \cdot \frac{e^x}{\sqrt{2\pi x}} + C_2 \cdot \frac{e^{-x}}{\sqrt{2\pi x}}. \tag{8.44}$$

Returning to the problem in $z(r)$, the following general solution for the asymptotic part of meniscus shape is obtained:

$$z(r) = \sqrt{\frac{\gamma_{lv}}{\rho_l g}} \cdot \left(C_1 \cdot \frac{\exp\left\{r \cdot \sqrt{\frac{\rho_l g}{\gamma_{lv}}}\right\}}{\sqrt{2\pi r} \sqrt{\frac{\rho_l g}{\gamma_{lv}}}} + C_2 \cdot \frac{\exp\left\{-r \sqrt{\frac{\rho_l g}{\gamma_{lv}}}\right\}}{\sqrt{2\pi r} \sqrt{\frac{\rho_l g}{\gamma_{lv}}}} \right). \tag{8.45}$$

The first modified Bessel function $I_0(r) = J_0(ir)$ is complex, but only the real part of the solution (8.45) is considered:

$$z(r) = \sqrt{\frac{\gamma_{lv}}{\rho_l g}} \cdot \left(C_2 \cdot \frac{\exp\left\{-r \sqrt{\frac{\rho_l g}{\gamma_{lv}}}\right\}}{\sqrt{2\pi r} \sqrt{\frac{\rho_l g}{\gamma_{lv}}}} \right), \tag{8.46}$$

which is equivalent to $y(x) = C_2 \cdot K_0(x)$, according to [Mika 1975].

The solution (8.46) satisfies the boundary condition (8.23):

$$z|_{r \rightarrow \infty} = 0.$$

In order to find the unique solution, the constant C_2 must be computed. For that, the continuity condition of the first derivative at the connection point r^* is imposed, i.e. the continuity of the first derivatives for asymptotic analytical and numerical solutions at r^* , $dz/dr|_{r=r^*} = -\tan\phi(r^*)$. Thus, deriving the asymptotic analytical solution $z(r)$ given by (8.46) and equating that with the corresponding derivative available for the numerical solution ($-\tan\phi(r^*)$), gives:

$$z(r) = \sqrt{\frac{\gamma_{lv}}{\rho_l g}} \cdot \frac{K_0\left(r \sqrt{\frac{\rho_l g}{\gamma_{lv}}}\right)}{K_1\left(r^* \sqrt{\frac{\rho_l g}{\gamma_{lv}}}\right)} \cdot \tan\phi(r^*). \tag{8.47}$$

Here the derivative property of the modified Bessel function: $(d/dx)(K_0(x)) = -K_1(x)$ is used. Moreover, in this computation the previously used approximation:

$$\frac{K_0(r)}{K_1(r)} \approx \frac{1}{\sqrt{1+(1/r)}}, \tag{8.48}$$

was considered. If $r = r^* = r_c$ in (8.47), and using the approximation (8.48), then the formula of the meniscus height given by (8.37) is obtained. Nowadays, it is not necessary to use approximation (8.48) because modern computers can compute modified Bessel functions; this makes it possible to compute the initial conditions:

$$z(r^*) = h^*, \quad \frac{dz}{dr}(r^*) = -\tan \phi(r^*), \quad (8.49)$$

necessary for solving numerically the nonlinear system of differential equations corresponding to Equation (8.21):

$$\begin{cases} \frac{dz}{dr} = -\tan \phi \\ \frac{d\phi}{dr} = -\frac{\rho_l \cdot g}{\gamma_{lv}} \cdot \frac{z}{\cos \phi} - \frac{1}{r} \cdot \tan \phi. \end{cases} \quad (8.50)$$

In what follows, the meniscus will be computed, using the analytical-numerical solution described above, for a cylindrical silicon crystal grown by the Cz technique.

First, it is necessary to find the region for which the asymptotic analytical solution is accurate. Using the material parameters of silicon and computing the modified Bessel functions

$$K_0\left(r\sqrt{\frac{\rho_l g}{\gamma_{lv}}}\right), \quad K_1\left(r\sqrt{\frac{\rho_l g}{\gamma_{lv}}}\right) \quad \text{for } r \in (0; \infty),$$

it follows that their ratio increases to 1 for $r \leq 3.7$ m, and after that the modified Bessel functions exponentially decay to zero, i.e. for $x \gg n$,

$$K_n(x) \approx \frac{e^{-x}}{\sqrt{(2/\pi) \cdot x}};$$

in our case $n = 0$ or 1 , and x represents $r\sqrt{\rho_l g / \gamma_{lv}}$. This shows that a crucible radius $0.25 \leq 3.7$ m and a value for r^* which is not far from the crucible radius, e.g. $r^* = 0.19$ m, should be considered, in order to have an almost flat meniscus. Hence, we set $r^* = 0.19$ m and then find h^* , i.e. the corresponding meniscus height, and $-\tan \phi(r^*)$, necessary for conditions (8.49).

Replacing $r = r^* = 0.19$ m in Equations (8.47) and (8.33) the following system is obtained:

$$\begin{cases} h^* = \sqrt{\frac{\gamma_{lv}}{\rho_l g}} \cdot \frac{K_0\left(r^* \sqrt{\frac{\rho_l g}{\gamma_{lv}}}\right)}{K_1\left(r^* \sqrt{\frac{\rho_l g}{\gamma_{lv}}}\right)} \cdot \tan \phi(r^*) \\ h^* = -\left(\frac{\sin \phi(r^*)}{2r^*}\right) \cdot \frac{\gamma_{lv}}{\rho_l g} + \sqrt{\left(\frac{\sin \phi(r^*)}{2r^*}\right)^2 \cdot \frac{\gamma_{lv}^2}{\rho_l^2 g^2} - \frac{2\gamma_{lv}}{\rho_l g} \cdot (\cos \phi(r^*) - 1)}. \end{cases} \quad (8.51)$$

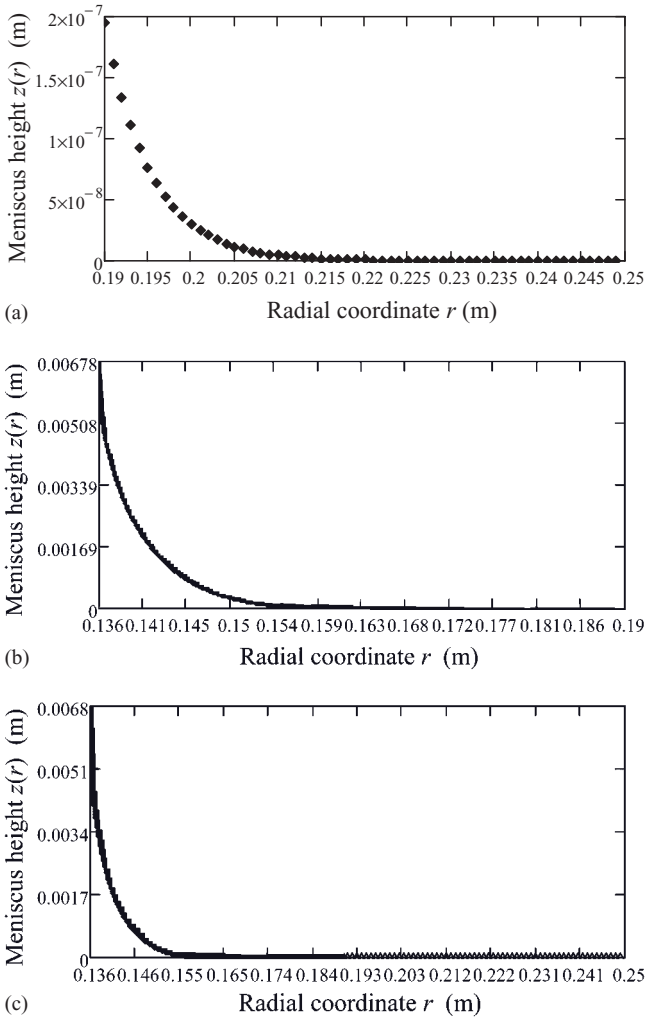


Figure 8.9 (a) Meniscus given by the asymptotic analytical solution on the interval $[0.19; 0.25]$. (b) Computed meniscus obtained by numerical solution of the initial value problem on the interval $[0; 0.19]$. (c) The analytical-numerical meniscus for a cylindrical silicon crystal grown in a crucible of radius 0.25 m.

In solving this system we considered those values of $\phi(r^*)$ that belong to the interval $(0, \frac{1}{2}\pi)$. For the above values, only one value is in the required interval: $\phi(r^*) = 7.2$ s. Replacing this in first or second equation gives $h^* = 0.2 \mu\text{m}$. In this way the initial condition is computed, which permits to find the numerical solution. The asymptotic analytical approximation of the meniscus is obtained by plotting function given by (8.47), as can be seen in Figure 8.9a. The numerical solution of the meniscus is obtained solving the system (8.50) with the boundary conditions (8.49). The computed meniscus is shown in Figure 8.9b. The union between the analytical and numerical menisci forms the final required meniscus (Figure 8.9c).

The error between the meniscus height $h = 0.0067$ m computed using the analytical-numerical solution, and those computed using only the analytical formulas h_T (8.32) and h_B (8.37), are of the order 10^{-5} , for a crystal radius $r_c = 0.0136$ m.

In the above analytical-numerical model, the idea reported in the literature concerning approximation of the meniscus using Bessel functions was used, but the first part of the meniscus (situated in the neighbourhood of the crucible) was obtained by computing modified Bessel functions, not using the approximation (8.48). From these calculations, initial conditions necessary to solve the IVP (8.49)–(8.50) were found, and the second part of the meniscus (situated near the crystal) was computed numerically. In comparison with previous approximations [Huh 1969, Hurle 1983, Mika 1975], this represents an improved result over the analytical-numerical method which gave errors of the order 10^{-4} .

As can be seen in the developments presented above, no exact solution of the meniscus shape, neither analytical nor numerical, can exist. Always an approximated part of the solution should be used and the difficulty is to keep this approximation as low as possible.

8.3 Analytical and Numerical Solutions for the Meniscus Equation in the EFG Method

The meniscus surface equation (8.3) and its corresponding boundary conditions for the EFG method are considered for sheets and cylindrical crystals. *Qualitative analyses* are performed, and when possible (i.e. in very particular cases) *analytical solutions* are given. The properties of the menisci obtained from the qualitative studies, are exemplified through *numerical examples*.

In the EFG technique, the main question is: what is the relation between the meniscus height h (which can be controlled through heat transfer) and the crystal sheet half-thickness or crystal rod radius?

8.3.1 Sheets

The central component of the EFG growth method is the die. The shape of the die defines the shape and the size of the meniscus, i.e. the liquid bridge retained between the die and the crystal (see Chapters 2 and 5). In order to obtain a sheet, the upper surface of the die has to be rectangular. The main characteristic of the sheet is its thickness (or half-thickness x_c). Then solutions $z = z(x)$ of Equation (8.3), depending only on the coordinate x , are sought. This means that the border effects (which occur on both edges of the sheet) are not considered. This approximation is equivalent to those given by Nutt [Nutt 1960] who neglected the curvature $1/R_2$ from Equation (8.1) written in the (xOz) frame (Figure 8.10). It is possible to consider the borders of the sheet as half-cylinders, and the meniscus computed for an EFG crystal rod can be used as a first approximation. However, the junction between the axisymmetric border meniscus and the two-dimensional sheet meniscus remains a problem.

Thus, the meniscus equation (8.1) without magnetic field and without rotation of the liquid becomes:

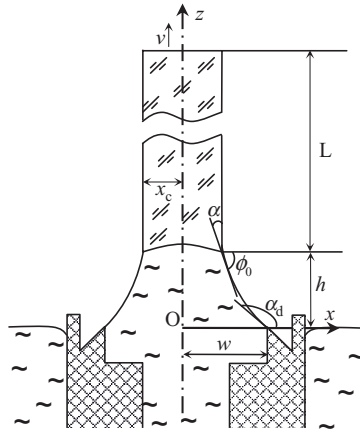


Figure 8.10 Two-dimensional model for a sheet grown by the EFG method.

$$\frac{\frac{d^2z}{dx^2}}{\left[1 + \left(\frac{dz}{dx}\right)^2\right]^{3/2}} = \frac{\rho_l g z - (p_0 - p_v)}{\gamma_{lv}}, \tag{8.52}$$

which is equivalent to

$$\frac{d^2z}{dx^2} = \frac{\rho_l g z - (p_0 - p_v)}{\gamma_{lv}} \cdot \left[1 + \left(\frac{dz}{dx}\right)^2\right]^{3/2}. \tag{8.53}$$

In the EFG method, the pressure p_0 is the pressure at the origin and it depends on the position of the liquid surface outside the die. For example, referring to Figure 8.10, because a liquid surface plane coinciding with the shaper edge plane has been chosen, $p_0 = p_v$, and hence Equation (8.53) becomes:

$$\frac{d^2z}{dx^2} = \frac{\rho_l g z}{\gamma_{lv}} \cdot \left[1 + \left(\frac{dz}{dx}\right)^2\right]^{3/2}. \tag{8.54}$$

The solution $z(x)$ of Equation (8.54) has to satisfy the following catching boundary condition:

$$z(w) = 0, \tag{8.55}$$

where $w > 0$ is the inner half-thickness of the die. It is assumed that the bottom line of the meniscus on the die is fixed on the edge of the die; i.e. $z(w) = 0$ and $z(x) > 0$ for $x < w$ (x close to w) [Braescu 2003].

At the other end of the meniscus, the growth angle criterion should be imposed, i.e.:

$$z(x_c) = h \quad \text{and} \quad \frac{dz}{dx}(x_c) = -\tan \alpha \tag{8.56}$$

where the meniscus height h and the sheet half-thickness x_c are unknown. In order to find the relation between h and x_c for a given inner die half-thickness w , an intermediate parameter α_d (see Figure 8.10) satisfying:

$$\frac{dz}{dx}(w) = \tan \alpha_d \quad (8.57)$$

is used, or ϕ_c if we denote by $\phi_c = \pi - \alpha_d$:

$$\frac{dz}{dx}(w) = -\tan \phi_c, \quad \phi_c \in \left(0; \frac{1}{2}\pi\right). \quad (8.58)$$

In the following, Equation (8.54) will be solved satisfying conditions (8.55) and (8.58) for a given die half-thickness w , and a given angle ϕ_c . After that, for the obtained meniscus $z(x)$, the growth angle criteria (8.56) will be imposed and the dependence of the sheet half-thickness x_c as a function of the meniscus height h will be found.

In the particular case of zero gravity the solution $z(x)$ can be expressed in an analytical form: Equation (8.54) becomes $d^2z/dx^2 = 0$ for which the solution is $z(x) = c_1 \cdot x + c_2$, where c_1 and c_2 can be determined from the conditions (8.55) and (8.58). In this way, the obtained *analytical solution*

$$z(x) = -(\tan \phi_c) \cdot x + w \cdot \tan \phi_c \quad (8.59)$$

shows that in zero gravity the meniscus is a straight line.

Imposing the growth angle criterion, the parameter ϕ_c is eliminated and the following dependence of the sheet half-thickness x_c as a function of the meniscus height h is obtained:

$$x_c(h) = w - \frac{h}{\tan \alpha}. \quad (8.60)$$

Using material parameters for silicon (growth angle $\alpha = 11^\circ = 0.1919$ radians), and a die half-thickness $w = 0.002$ m, the representation shown in Figure 8.11 is obtained.

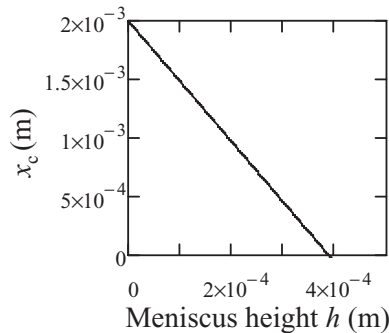


Figure 8.11 Dependence of the sheet half-thickness x_c as a function of the meniscus height h in zero gravity.

If gravity is considered, then *an analytical form of the meniscus cannot be obtained*, but *qualitatively* it is possible to get information about the shape of the meniscus, and *the meniscus shape can be computed* using Runge–Kutta method.

Thus, using the technique set out in the first section, the nonlinear Equation (8.54) is transformed into a nonlinear system of two differential equations:

$$\begin{cases} \frac{dz}{dx} = -\tan \phi \\ \frac{d\phi}{dx} = -\frac{\rho_l \cdot g \cdot z}{\gamma_{lv}} \cdot \frac{1}{\cos \phi} \end{cases} \tag{8.61}$$

for which the boundary conditions (8.55), (8.58) become:

$$z(w) = 0, \quad \phi(w) = \phi_c; \quad \phi_c \in (0, \pi/2). \tag{8.62}$$

The functions from the right-hand side of Equation (8.61) are defined for $z \in (-\infty; \infty)$, $\phi \in (-\pi/2; \pi/2)$ and are independent of x (the system is autonomous). These functions depend also on the material parameters $\rho_l \in (0; \infty)$, $\gamma_{lv} \in (0; \infty)$. The functions are real analytical, i.e. they can be expanded in a Taylor series in the neighbourhood of any point $(z, \phi, \rho_l, \gamma_{lv})$ from $D = (-\infty; +\infty) \times (-\pi/2; \pi/2) \times (0; +\infty) \times (0; +\infty)$. Therefore, for the Cauchy problem (8.61)–(8.62), all the conditions of the Cauchy–Lipschitz theorem concerning the existence and uniqueness of the solution of the problem (8.61)–(8.62) are satisfied. It follows that the problem (8.61)–(8.62) has a unique saturated solution defined on an interval $(a; b)$. The solution of (8.61)–(8.62) will be denoted by:

$$z = z(x; w, \phi_c, \gamma_{lv}, \rho_l), \quad \phi = \phi(x; w, \phi_c, \gamma_{lv}, \rho_l) \tag{8.63}$$

and depends on x and on the parameters $w, \phi_c, \gamma_{lv}, \rho_l$; a and b also depend on $w, \phi_c, \gamma_{lv}, \rho_l$ and satisfy $a < w < b$.

In general, the solution (8.63) cannot be expressed in an explicit form (because the system is nonlinear). For this reason, the behaviour of the solution will be analysed in the neighbourhood of w [Balint 2005].

From (8.61) and (8.62) we have:

$$\left. \frac{dz}{dx} \right|_{x=w} = -\tan \phi_c < 0, \tag{8.64}$$

which shows that there exists $\varepsilon' > 0$ such that for any $x \in (w - \varepsilon'; w]$ we have $dz/dx < 0$. It follows that the function $z = z(x; w, \phi_c, \gamma_{lv}, \rho_l)$ is strictly decreasing on the interval $(w - \varepsilon'; w]$ and is strictly positive on $(w - \varepsilon'; w)$:

$$z = z(x; w, \phi_c, \gamma_{lv}, \rho_l) > 0, \quad \forall x \in (w - \varepsilon'; w).$$

Taking into account the equality:

$$\frac{d^2z}{dx^2} = -\frac{1}{\cos^2 \phi} \cdot \frac{d\phi}{dx}$$

it follows that, in the neighbourhood of w , the meniscus is convex at any point, which is obvious from the Young–Laplace equation:

$$\frac{d^2z}{dx^2} = -\frac{1}{\cos^2\phi} \cdot \frac{d\phi}{dx} = \frac{1}{\cos^3\phi} \cdot \frac{\rho_l \cdot g \cdot z}{\gamma_{lv}} > 0.$$

The equality:

$$\frac{d\phi}{dx} = -\frac{\rho_l \cdot g \cdot z}{\gamma_{lv}} \cdot \frac{1}{\cos\phi}$$

shows that there exists $\varepsilon'' > 0$ such that on $(w - \varepsilon''; w)$ the function $\phi(x; w, \phi_c, \gamma_{lv}, \rho_l)$ is strictly decreasing and

$$\phi = \phi(x; w, \phi_c, \gamma_{lv}, \rho_l) > \phi_c, \quad \forall x \in (w - \varepsilon''; w).$$

The growth angle is achieved if the following equality holds:

$$\phi(x; w, \phi_c, \gamma_{lv}, \rho_l) = \frac{\pi}{2} - \alpha = \phi_0. \quad (8.65)$$

In order to obtain more information about the solution (8.63), an approximation of the solution (8.63) by Taylor polynomials, obtained by expansion in w , is considered:

$$\begin{aligned} z(x; w, \phi_c, \gamma_{lv}, \rho_l) &\approx z(w; w, \phi_c, \gamma_{lv}, \rho_l) \\ &+ \frac{dz}{dx}(w; w, \phi_c, \gamma_{lv}, \rho_l) \cdot (x - w) \\ &+ \frac{1}{2} \cdot \frac{d^2z}{dx^2}(w; w, \phi_c, \gamma_{lv}, \rho_l) \cdot (x - w)^2 \\ &+ \frac{1}{6} \cdot \frac{d^3z}{dx^3}(w; w, \phi_c, \gamma_{lv}, \rho_l) \cdot (x - w)^3, \end{aligned} \quad (8.66)$$

$$\begin{aligned} \phi(x; w, \phi_c, \gamma_{lv}, \rho_l) &\approx \phi(w; w, \phi_c, \gamma_{lv}, \rho_l) \\ &+ \frac{d\phi}{dx}(w; w, \phi_c, \gamma_{lv}, \rho_l) \cdot (x - w) \\ &+ \frac{1}{2} \cdot \frac{d^2\phi}{dx^2}(w; w, \phi_c, \gamma_{lv}, \rho_l) \cdot (x - w)^2. \end{aligned} \quad (8.67)$$

The coefficients of these polynomials are obtained from Equations (8.61) and conditions (8.62), and are given by:

$$z(w) = z(w; w, \phi_c, \gamma_{lv}, \rho_l) = 0; \quad (8.68)$$

$$z'(w) = \frac{dz}{dx}(w; w, \phi_c, \gamma_{lv}, \rho_l) = -\tan\phi_c; \quad (8.69)$$

$$z''(w) = \frac{d^2z}{dx^2}(w; w, \phi_c, \gamma_{lv}, \rho_l) = 0; \tag{8.70}$$

$$z'''(w) = \frac{d^3z}{dx^3}(w; w, \phi_c, \gamma_{lv}, \rho_l) = -\frac{1}{\cos^3 \phi_c} \cdot \frac{\rho_l \cdot g}{\gamma_{lv}} \cdot \tan \phi_c; \tag{8.71}$$

$$\phi(w) = \phi(w; w, \phi_c, \gamma_{lv}, \rho_l) = \phi_c; \tag{8.72}$$

$$\phi'(w) = \frac{d\phi}{dx}(w; w, \phi_c, \gamma_{lv}, \rho_l) = 0; \tag{8.73}$$

$$\phi''(w) = \frac{d^2\phi}{dx^2}(w; w, \phi_c, \gamma_{lv}, \rho_l) = \frac{1}{\cos^2 \phi_c} \cdot \frac{\rho_l \cdot g}{\gamma_{lv}} \cdot \sin \phi_c. \tag{8.74}$$

Replacing these coefficients into (8.66)–(8.67) gives the following approximations to the solution (8.63):

$$z(x; w, \phi_c, \gamma_{lv}, \rho_l) \approx -(\tan \phi_c) \cdot (x-w) - \frac{1}{6} \cdot \frac{1}{\cos^3 \phi_c} \cdot \frac{\rho_l \cdot g}{\gamma_{lv}} \cdot \tan \phi_c \cdot (x-w)^3, \tag{8.75}$$

$$\phi(x; w, \phi_c, \gamma_{lv}, \rho_l) \approx \phi_c + \frac{1}{2} \cdot \frac{1}{\cos^2 \phi_c} \cdot \frac{\rho_l \cdot g}{\gamma_{lv}} \cdot \sin \phi_c \cdot (x-w)^2. \tag{8.76}$$

These approximations are valid only for x close to w [Balint 2005]. This will be shown numerically for silicon sheets.

The attainment of the growth angle at a point $(0; w]$ means that the equation:

$$\phi_c + \frac{1}{2} \cdot \frac{1}{\cos^2 \phi_c} \cdot \frac{\rho_l \cdot g}{\gamma_{lv}} \cdot \sin \phi_c \cdot (x-w)^2 = \frac{\pi}{2} - \alpha \tag{8.77}$$

has at least one solution on $(0; w]$. Because

$$(x-w)^2 = \frac{\frac{1}{2} \pi - \alpha - \phi_c}{\frac{1}{2} \cdot \frac{\sin \phi_c}{\cos^2 \phi_c} \cdot \frac{\rho_l \cdot g}{\gamma_{lv}}},$$

it is easy to see that Equation (8.77) can have only one solution on $(0; w]$ if the following inequalities hold:

(i) $0 < \phi_c < \frac{1}{2} \pi - \alpha$

(ii) $w - \sqrt{\frac{\frac{1}{2} \pi - \alpha - \phi_c}{\frac{1}{2} \cdot \frac{\sin \phi_c}{\cos^2 \phi_c} \cdot \frac{\rho_l \cdot g}{\gamma_{lv}}}} > 0$

These inequalities express the range of the parameter ϕ_c for which the growth angle can be achieved. For example, using parameters for silicon and a die half-thickness

$w = 0.002\text{ m}$, the inequalities (i)–(ii) show that condition of the growth angle is satisfied for $1.11 \leq \phi_c < 1.3787$.

Indeed, considering 30 values of the parameter ϕ_c and integrating by Runge–Kutta the problem (8.61)–(8.62), it is found that the growth angle is achieved for $1.04 \leq \phi_c < 1.3787$. This proves that the above Taylor approximation is useful for finding the range of the parameter ϕ_c .

Concerning the meniscus shape: from Equations (8.75)–(8.76), it is easy to see that the functions $z(x; w, \phi_c, \gamma_{lv}, \rho_l)$, $\phi(x; w, \phi_c, \gamma_{lv}, \rho_l)$ are convex in the neighbourhood of w . The growth angle condition imposes the same monotony on the whole interval (x_c, w) for the function $\phi(x; w, \phi_c, \gamma_{lv}, \rho_l)$, i.e. $d\phi/dx < 0$. This implies:

$$\frac{d^2z}{dx^2} = -\frac{1}{\cos^2 \phi} \cdot \frac{d\phi}{dx} > 0,$$

i.e. the meniscus convexity on the interval (x_c, w) , as can be seen in Figure 8.12.

The couples (x_c, h) in which the growth angle is attained were computed for every parameter ϕ_c considered. Plotting these couples gives the dependence shown in Figure 8.13.

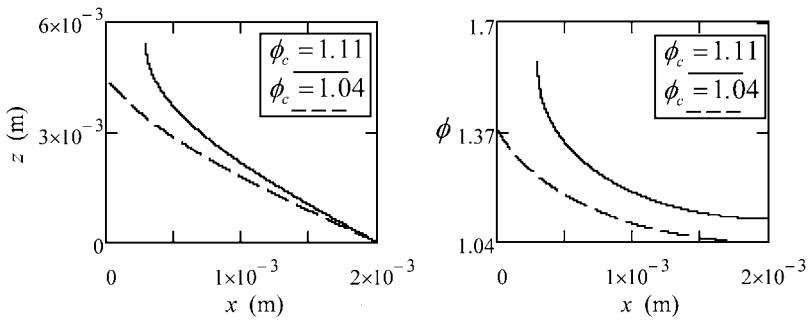


Figure 8.12 Numerical representation of the functions $z = z(x; w, \phi_c, \gamma_{lv}, \rho_l)$ and $\phi = \phi(x; w, \phi_c, \gamma_{lv}, \rho_l)$ for silicon sheets grown using a die with half-thickness $w = 0.002\text{ m}$, and $\phi_c = 1.04$ or 1.11 radians.

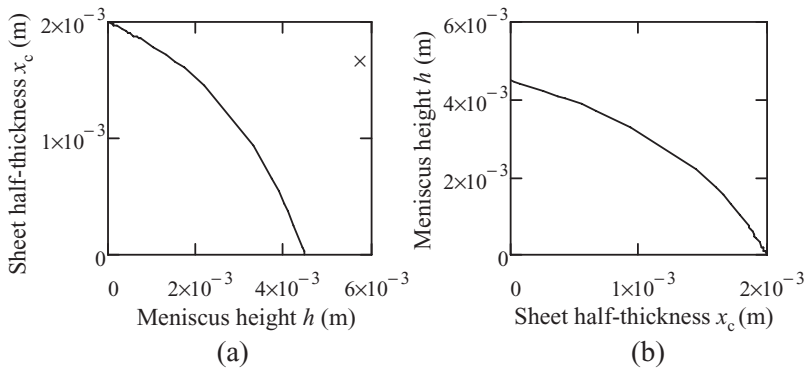


Figure 8.13 The computed dependencies $x_c(h)$ (a) and $h(x_c)$ (b).

Because an analytical expression fitting the above data is useful for practical crystal growers, the dependence of the sheet half-thickness x_c as function of the meniscus height h :

$$x_c(h) = \frac{0.002 - 0.42 \cdot h + 87 \cdot h^2 - 20500 \cdot h^3}{1 - 116.2 \cdot h + 35500 \cdot h^2 - 3825000 \cdot h^3}, \quad h \in [0; 0.0045], \quad (8.78)$$

and the dependence of the meniscus height h as function of the sheet half-thickness x_c :

$$h(x_c) = \frac{0.004 - 5.64 \cdot x_c + 2400 \cdot x_c^2 - 334000 \cdot x_c^3}{1 - 1044 \cdot x_c + 357000 \cdot x_c^2 - 3.86 \cdot 10^7 \cdot x_c^3 + 3 \cdot 10^8 \cdot x_c^4}, \quad x_c \in [0.0000012; 0.002], \quad (8.78^*)$$

are obtained, for a silicon sheet grown using a die half-thickness $w = 0.002$ m.

The above *qualitative analyses* show that the dependences $x_c(h)$ and $h(x_c)$ are decreasing functions. For the configuration shown in Figure 8.10, i.e. $p_o = p_v$, and zero gravity these dependences are linear functions, and the growth angle is always attained. In normal gravity conditions the above dependences are concave functions (the second derivative is negative), and the growth angle is attained if the parameter ϕ_c satisfies inequalities (i)–(ii).

8.3.2 Cylindrical Crystals

In order to obtain a cylindrical crystal a circular die is used (see Figure 8.14). In this case, the equation of the meniscus surface is the axisymmetric Young–Laplace equation (8.12), which becomes:

$$\frac{d^2z}{dr^2} = \frac{\rho_l g z - (p_o - p_v)}{\gamma_{lv}} \cdot \left[1 + \left(\frac{dz}{dr} \right)^2 \right]^{3/2} - \frac{1}{r} \cdot \frac{dz}{dr} \cdot \left[1 + \left(\frac{dz}{dr} \right)^2 \right], \quad (8.79)$$

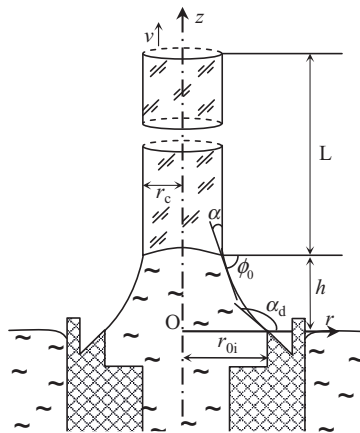


Figure 8.14 Axisymmetric model of a cylindrical crystal grown by the EFG method.

if the growth process takes place without a magnetic field and without rotation of the crucible [Borodin 1979, Braescu 2004–1, Braescu 2004–2, Brener 1979–1, Brener 1979–2]. In the configuration in Figure 8.14, the liquid surface plane coincides with the shaper edge plane and hence $p_o = p_v$. Equation (8.79) becomes:

$$\frac{d^2z}{dr^2} = \frac{\rho_l g z}{\gamma_{lv}} \cdot \left[1 + \left(\frac{dz}{dr} \right)^2 \right]^{3/2} - \frac{1}{r} \cdot \frac{dz}{dr} \cdot \left[1 + \left(\frac{dz}{dr} \right)^2 \right]. \quad (8.80)$$

The solution $z(r)$ of Equation (8.80) has to verify the following catching boundary condition:

$$z(r_{0i}) = 0, \quad (8.81)$$

where $r_{0i} > 0$ is the inner radius of the die. It is assumed that the bottom line of the meniscus on the die is fixed on the edge of the die; i.e. $z(r_{0i}) = 0$ and $z(r) > 0$ for $r < r_{0i}$ (r close to r_{0i}).

At the other end of the meniscus, the growth angle criteria should be imposed, i.e.:

$$z(r_c) = h \quad \text{and} \quad \frac{dz}{dr}(r_c) = -\tan \alpha \quad (8.82)$$

where the meniscus height h and the crystal radius r_c are unknown. For finding h and r_c for a given inner die radius r_{0i} , an intermediate parameter α_d will be used (see Figure 8.14) satisfying:

$$\frac{dz}{dr}(r_{0i}) = \tan \alpha_d, \quad (8.83)$$

or ϕ_c if we denote by $\phi_c = \pi - \alpha_d$:

$$\frac{dz}{dr}(r_{0i}) = -\tan \phi_c, \quad \phi_c \in \left(0; \frac{\pi}{2} \right). \quad (8.84)$$

In the following, Equation (8.80) satisfying conditions (8.81) and (8.84) will be solved for a given die radius r_{0i} and a given angle ϕ_c . After that, for the obtained meniscus $z(r)$, the growth angle criteria (8.82) will be imposed and the dependence of the crystal radius r_c as function of the meniscus height h will be found.

In the particular case of zero gravity the solution $z(r)$ can be expressed in an analytical form. Equation (8.80) becomes:

$$\frac{d^2z}{dr^2} + \frac{1}{r} \cdot \frac{dz}{dr} \cdot \left[1 + \left(\frac{dz}{dr} \right)^2 \right] = 0, \quad (8.85)$$

which is equivalent to

$$\frac{d}{dr} \left(\frac{r \cdot \frac{dz}{dr}}{\sqrt{1 + \left(\frac{dz}{dr} \right)^2}} \right) = 0, \quad \text{i.e.} \quad \frac{r \cdot \frac{dz}{dr}}{\sqrt{1 + \left(\frac{dz}{dr} \right)^2}} = c_1,$$

where c_1 is a constant. From this an analytical expression for the derivative of the function $z(r)$ is obtained:

$$\frac{dz}{dr}(r) = \pm \frac{c_1}{\sqrt{r^2 - c_1^2}}. \tag{8.86}$$

Imposing the condition (8.84) gives the value of the constant $c_1 = r_{0i} \cdot \sin \phi_c$ and the function $z(r)$ becomes:

$$z(r) = r_{0i} \cdot \sin \phi_c \cdot \int_r^{r_{0i}} \frac{1}{\sqrt{u^2 - r_{0i}^2 \cdot \sin^2 \phi_c}} du.$$

Thus, the *analytical expression of the meniscus* as function of the parameters is:

$$z(r) = r_{0i} \cdot \sin \phi_c \cdot \ln \frac{r_{0i} + \sqrt{r_{0i}^2 - r_{0i}^2 \cdot \sin^2 \phi_c}}{r + \sqrt{r^2 - r_{0i}^2 \cdot \sin^2 \phi_c}}, \tag{8.87}$$

for which the condition $r \in [r_{0i} \cdot \sin \phi_c, r_{0i}]$ is imposed, in order to assure the existence of the functions employed [Braescu 2005].

Imposing the growth angle criterion, the parameter ϕ_c can be eliminated and the dependence of the meniscus height as function of the crystal radius can be found. From the condition

$$\frac{dz}{dr}(r_c) = -\tan \alpha$$

we get

$$\sin \phi_c = \frac{r_c}{r_{0i}} \cdot \sin \alpha, \tag{8.88}$$

which substituted into (8.87) gives:

$$z(r_c) = r_c \cdot (\sin \alpha) \cdot \ln \frac{r_{0i} + \sqrt{r_{0i}^2 - r_c^2 \cdot \sin^2 \alpha}}{r_c + \sqrt{r_c^2 - r_c^2 \cdot \sin^2 \alpha}}.$$

Since $z(r_c) = h$, the analytical formula of the meniscus height as a function of the crystal radius is obtained:

$$h(r_c) = r_c \cdot (\sin \alpha) \cdot \ln \frac{r_{0i} + \sqrt{r_{0i}^2 - r_c^2 \cdot \sin^2 \alpha}}{r_c (1 + \cos \alpha)}. \tag{8.89}$$

Using material parameters for silicon (growth angle $\alpha = 11^\circ = 0.1919$ radians), and a die radius $r_{0i} = 0.002$ m, the representation for the curve (8.89) is found as shown in Figure 8.15.

If gravity is considered, then *an analytical form of the meniscus cannot be obtained*, but performing *qualitative studies* gives us information about the shape of the meniscus

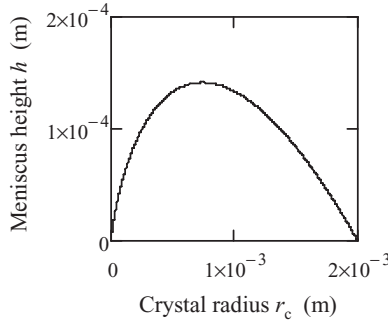


Figure 8.15 Meniscus height h as function of the crystal radius r_c in zero gravity.

which depends on the pressure, and the *meniscus shape* is computed using Runge–Kutta method.

Thus, using the technique presented in previous section, the nonlinear equation (8.60) is transformed into the following nonlinear system of two differential equations:

$$\begin{cases} \frac{dz}{dr} = -\tan \phi \\ \frac{d\phi}{dr} = -\frac{\rho_l \cdot g}{\gamma_{lv}} \cdot \frac{z}{\cos \phi} - \frac{1}{r} \cdot \tan \phi \end{cases} \quad (8.90)$$

for which the boundary conditions (8.81), (8.84) become [Braescu 2004–2]:

$$z(r_{0i}) = 0, \quad \phi(r_{0i}) = \phi_c; \quad \phi_c \in \left(0, \frac{\pi}{2}\right). \quad (8.91)$$

The functions from the right-hand member of Equations (8.90) are defined for $r \in (0; \infty)$, $z \in (-\infty; \infty)$, $\phi \in (-\pi/2; \pi/2)$. They are real analytic functions, i.e. can be expanded into Taylor series, and hence for the Cauchy problem (8.90)–(8.91) the conditions of existence and uniqueness of a solution are satisfied. It follows that the Cauchy problem (8.90)–(8.91) has a unique saturated solution defined on an interval $(a; b)$:

$$z = z(r; r_{0i}, \phi_c, \gamma_{lv}, \rho_l), \quad \phi = \phi(r; r_{0i}, \phi_c, \gamma_{lv}, \rho_l), \quad (8.92)$$

depending on r and on the parameters r_{0i} , ϕ_c , γ_{lv} , ρ_l . The interval extremities a and b depend on r_{0i} , ϕ_c , γ_{lv} , ρ_l as well and verify $0 < a < r_{0i} < b$ [Braescu 2004-2].

Generally, the solution (8.92) can not be expressed in an explicit form because the system is nonlinear; for this reason it is necessary to analyse the behaviour of the solution in the neighbourhood of r_{0i} .

From the system (8.90) and the conditions (8.91) the following inequalities can be obtained:

$$\left. \frac{dz}{dr} \right|_{r=r_{0i}} = -\tan \phi_c < 0, \quad (8.93)$$

$$\left. \frac{d\phi}{dr} \right|_{r=r_{0i}} = -\frac{1}{r_{0i}} \cdot \tan \phi_c < 0. \quad (8.94)$$

Inequality (8.93) shows that there exists $\varepsilon' > 0$ such that for $r \in (r_{0i} - \varepsilon'; r_{0i}]$, $dz/dr < 0$. It follows that the function $z = z(r; r_{0i}, \phi_c, \gamma_{lv}, \rho_l)$ is strictly decreasing on $(r_{0i} - \varepsilon'; r_{0i}]$ and is strictly positive on $(r_{0i} - \varepsilon'; r_{0i})$:

$$z = z(r; r_{0i}, \phi_c, \gamma_{lv}, \rho_l) > 0, \quad \forall r \in (r_{0i} - \varepsilon'; r_{0i}).$$

The inequality $d\phi/dr|_{r=r_{0i}} < 0$ shows that the function $\phi = \phi(r; r_{0i}, \phi_c, \gamma_{lv}, \rho_l)$ is strictly decreasing on $(r_{0i} - \varepsilon''; r_{0i}]$ and

$$\phi = \phi(r; r_{0i}, \phi_c, \gamma_{lv}, \rho_l) > \phi_c, \quad \forall r \in (r_{0i} - \varepsilon''; r_{0i}).$$

In addition, since

$$\frac{d^2z}{dr^2} = -\frac{1}{\cos^2 \phi_c} \cdot \frac{d\phi}{dr} > 0$$

in the neighbourhood of r_{0i} , it results that the function $z(r; r_{0i}, \phi_c, \gamma_{lv}, \rho_l)$ is convex in the neighbourhood of r_{0i} .

In order to get more information about the solution (8.92), it will be approximated by Taylor polynomials obtained by expansion in r_{0i} :

$$\begin{aligned} z(r; r_{0i}, \phi_c, \gamma_{lv}, \rho_l) &\approx z(r_{0i}; r_{0i}, \phi_c, \gamma_{lv}, \rho_l) + \frac{dz}{dr}(r_{0i}; r_{0i}, \phi_c, \gamma_{lv}, \rho_l) \cdot (r - r_{0i}) \\ &\quad + \frac{1}{2} \cdot \frac{d^2z}{dr^2}(r_{0i}; r_{0i}, \phi_c, \gamma_{lv}, \rho_l) \cdot (r - r_{0i})^2 \\ &\quad + \frac{1}{6} \cdot \frac{d^3z}{dr^3}(r_{0i}; r_{0i}, \phi_c, \gamma_{lv}, \rho_l) \cdot (r - r_{0i})^3, \end{aligned} \quad (8.95)$$

$$\begin{aligned} \phi(r; r_{0i}, \phi_c, \gamma_{lv}, \rho_l) &\approx \phi(r_{0i}; r_{0i}, \phi_c, \gamma_{lv}, \rho_l) + \frac{d\phi}{dr}(r_{0i}; r_{0i}, \phi_c, \gamma_{lv}, \rho_l) \cdot (r - r_{0i}) \\ &\quad + \frac{1}{2} \cdot \frac{d^2\phi}{dr^2}(r_{0i}; r_{0i}, \phi_c, \gamma_{lv}, \rho_l) \cdot (r - r_{0i})^2. \end{aligned} \quad (8.96)$$

The coefficients of these polynomials are obtained from (8.90) and (8.91), being given by [Braescu 2004-2] as:

$$z(r_{0i}) = z(r_{0i}; r_{0i}, \phi_c, \gamma_{lv}, \rho_l) = 0; \quad (8.97)$$

$$z'(r_{0i}) = \frac{dz}{dr}(r_{0i}; r_{0i}, \phi_c, \gamma_{lv}, \rho_l) = -\tan \phi_c; \quad (8.98)$$

$$z''(r_{0i}) = \frac{d^2z}{dr^2}(r_{0i}; r_{0i}, \phi_c, \gamma_{lv}, \rho_l) = \frac{1}{r_{0i}} \cdot \frac{\sin \phi_c}{\cos^3 \phi_c}; \quad (8.99)$$

$$z'''(r_{0i}) = \frac{d^3 z}{dr^3}(r_{0i}; r_{0i}, \phi_c, \gamma_{lv}, \rho_l) = -2 \cdot \frac{\sin^3 \phi_c}{\cos^5 \phi_c} \cdot \frac{1}{r_{0i}^2} - \frac{\sin \phi_c}{\cos^5 \phi_c} \cdot \frac{1}{r_{0i}} - \frac{1}{\cos^2 \phi_c} \left[\frac{\rho_l \cdot g}{\gamma_{lv}} \cdot \frac{\sin \phi_c}{\cos^2 \phi_c} + \frac{1}{r_{0i}^2} \cdot \tan \phi_c \right]; \quad (8.100)$$

$$\phi(r_{0i}) = \phi(r_{0i}; r_{0i}, \phi_c, \gamma_{lv}, \rho_l) = \phi_c; \quad (8.101)$$

$$\phi'(r_{0i}) = \frac{d\phi}{dr}(r_{0i}; r_{0i}, \phi_c, \gamma_{lv}, \rho_l) = -\frac{\sin \phi_c}{\cos \phi_c} \cdot \frac{1}{r_{0i}}; \quad (8.102)$$

$$\phi''(r_{0i}) = \frac{d^2 \phi}{dr^2}(r_{0i}; r_{0i}, \phi_c, \gamma_{lv}, \rho_l) = \frac{\rho_l \cdot g}{\gamma_{lv}} \cdot \frac{\sin \phi_c}{\cos^2 \phi_c} + \frac{1}{r_{0i}^2} \cdot \tan \phi_c + \frac{\sin \phi_c}{\cos^3 \phi_c} \cdot \frac{1}{r_{0i}^2}. \quad (8.103)$$

Because

$$\phi''(r_{0i}) = \frac{\rho_l \cdot g}{\gamma_{lv}} \cdot \frac{\sin \phi_c}{\cos^2 \phi_c} + \frac{1}{r_{0i}^2} \cdot \tan \phi_c + \frac{\sin \phi_c}{\cos^3 \phi_c} \cdot \frac{1}{r_{0i}^2} > 0$$

and

$$\phi'(r_{0i}) = -\frac{\sin \phi_c}{\cos \phi_c} \cdot \frac{1}{r_{0i}} < 0,$$

the function:

$$\begin{aligned} \phi(r; \phi_c, \gamma_{lv}, \rho_l) &\approx \phi_c - \frac{\sin \phi_c}{\cos \phi_c} \cdot \frac{1}{r_{0i}} \cdot (r - r_{0i}) \\ &+ \frac{1}{2} \cdot \left(\frac{\rho_l \cdot g}{\gamma_{lv}} \cdot \frac{\sin \phi_c}{\cos^2 \phi_c} + \frac{1}{r_{0i}^2} \cdot \tan \phi_c + \frac{\sin \phi_c}{\cos^3 \phi_c} \cdot \frac{1}{r_{0i}^2} \right) \cdot (r - r_{0i})^2 \end{aligned} \quad (8.104)$$

has a minimum which is achieved at the point $r_{\min} > r_{0i}$:

$$r_{\min} = r_{0i} - \frac{\phi'(r_{0i})}{\phi''(r_{0i})},$$

i.e. the polynomial function of second degree $\phi(r; r_{0i}, \phi_c, \gamma_{lv}, \rho_l)$ decreases until r_{\min} and increases after that.

The position of r_{\min} shows that the function $\phi(r; r_{0i}, \phi_c, \gamma_{lv}, \rho_l)$ decreases and is convex on $(0; r_{0i}]$. This implies convexity of the meniscus, too. Indeed, because $\phi(r; r_{0i}, \phi_c, \gamma_{lv}, \rho_l)$ decreases, $d\phi/dr < 0$, and hence

$$\frac{d^2 z}{dr^2} = -\frac{1}{\cos^2 \phi_c} \cdot \frac{d\phi}{dr} > 0 \text{ on } (0; r_{0i}],$$

which proves convexity of the function $z(r; r_{0i}, \phi_c, \gamma_{lv}, \rho_l)$.

Concerning the growth angle condition: from the monotonicity of $\phi(r; r_{0i}, \phi_c, \gamma_{lv}, \rho_l)$, the growth angle can be achieved in $(0; r_{0i})$ only if the contact angle ϕ_c is in $(0; \pi/2 - \alpha]$. Thus if $\phi_c = \pi/2 - \alpha$, then the growth angle is achieved in r_{0i} . If $\phi_c < \pi/2 - \alpha$, then the growth angle can be attained on $(0; r_{0i})$ only once (because $\phi(r; r_{0i}, \phi_c, \gamma_{lv}, \rho_l)$ decreases). Imposing the growth angle condition on the function $\phi(r; r_{0i}, \phi_c, \gamma_{lv}, \rho_l)$, the following equation is obtained:

$$\frac{1}{2} \left(\frac{\rho_l \cdot g}{\gamma_{lv}} \cdot \frac{\sin \phi_c}{\cos^2 \phi_c} + \frac{1}{r_{0i}^2} \cdot \tan \phi_c + \frac{\sin \phi_c}{\cos^3 \phi_c} \cdot \frac{1}{r_{0i}^2} \right) \cdot (r - r_{0i})^2 - \frac{\sin \phi_c}{\cos \phi_c} \cdot \frac{1}{r_{0i}} \cdot (r - r_{0i}) + \phi_c = \frac{\pi}{2} - \alpha$$

which should have one root in $(0; r_{0i})$. This condition can be satisfied if:

- (i) $\Delta = \left(\frac{\sin \phi_c}{\cos \phi_c} \cdot \frac{1}{r_{0i}} \right)^2 - 2 \left(\frac{\rho_l \cdot g}{\gamma_{lv}} \cdot \frac{\sin \phi_c}{\cos^2 \phi_c} + \frac{1}{r_{0i}^2} \cdot \tan \phi_c + \frac{\sin \phi_c}{\cos^3 \phi_c} \cdot \frac{1}{r_{0i}^2} \right) \cdot \left(\phi_c - \frac{\pi}{2} + \alpha \right) > 0,$
- (ii) $\frac{\frac{\sin \phi_c}{\cos \phi_c} \cdot \frac{1}{r_{0i}} - \sqrt{\Delta}}{\frac{\rho_l \cdot g}{\gamma_{lv}} \cdot \frac{\sin \phi_c}{\cos^2 \phi_c} + \frac{1}{r_{0i}^2} \cdot \tan \phi_c + \frac{\sin \phi_c}{\cos^3 \phi_c} \cdot \frac{1}{r_{0i}^2}} < 0.$

These inequalities express the range of the parameter ϕ_c for which the growth angle can be achieved. For example, using parameters for silicon and a die radius $r_{0i} = 0.002$ m, the inequalities (i)–(ii) show that the growth angle condition can be satisfied for $0 < \phi_c < 1.378$. Indeed, considering 30 values of the parameter ϕ_c and integrating by Runge–Kutta for the problem (8.90)–(8.91), the growth angle is achieved for $0.01 \leq \phi_c < 1.378$. The previous described convexity and the monotonicity of the functions $z = z(r; r_{0i}, \phi_c, \gamma_{lv}, \rho_l)$, $\phi = \phi(r; r_{0i}, \phi_c, \gamma_{lv}, \rho_l)$ can be seen in Figure 8.16. For every considered parameter ϕ_c , the couples (r_c, h) in which the growth angle is achieved were computed. Plotting these couples gives the dependence showing Figure 8.17.

Because an analytical expression fitting the above data is useful for practical crystal growers, the dependence of the meniscus height h as function of the crystal radius r_c :

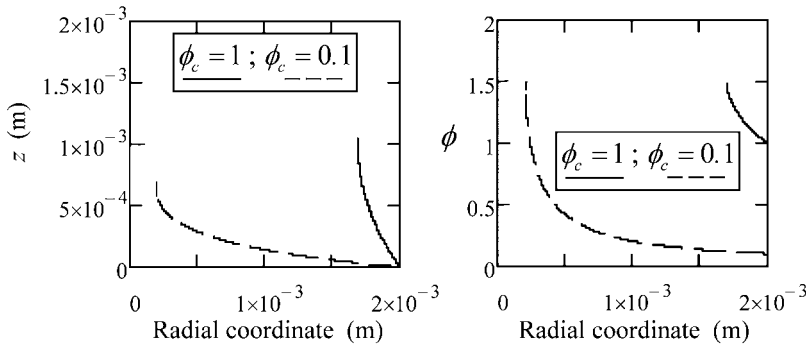


Figure 8.16 Numerical representation of the functions $z = z(r; r_{0i}, \phi_c, \gamma_{lv}, \rho_l)$ and $\phi = \phi(r; r_{0i}, \phi_c, \gamma_{lv}, \rho_l)$ for cylindrical silicon rods grown using a die radius $r_{0i} = 0.002$ m, and $\phi_c = 1; 0.1$ radians.

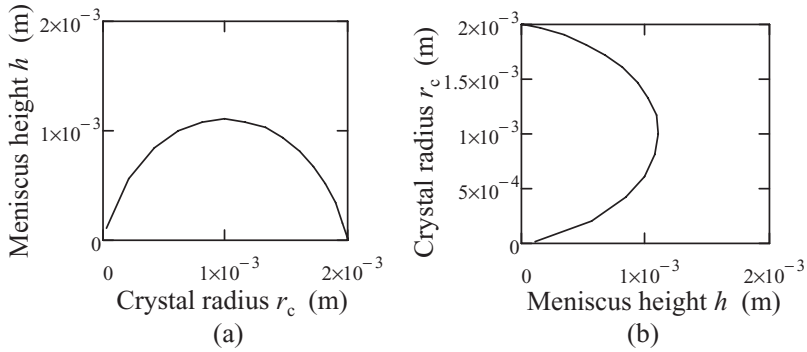


Figure 8.17 The dependencies $h(r_c)$ (a) and $r_c(h)$ (b).

$$h(r_c) = \frac{0.002 + 0.0009 \ln r_c + 0.00017 \ln^2 r_c + 1.2 \times 10^{-5} \ln^3 r_c + 3.26 \times 10^{-7} \ln^4 r_c}{1 + 0.60 \ln r_c + 0.14 \ln^2 r_c + 0.015 \ln^3 r_c + 0.0006 \ln^4 r_c},$$

$$h \in [0; 0.0011],$$

and the dependence of the crystal radius r_c as function of the meniscus height h are obtained for a cylindrical silicon crystal grown using a die radius $r_{0i} = 0.002$ m.

The above *qualitative analyses* show that the dependencies $r_c(h)$ and $h(r_c)$ are parabolic functions. For the configuration presented in Figure 8.14, i.e. $p_O = p_v$, and zero gravity, the growth angle is always attained for $r \in [r_{0i} \sin \phi_c, r_{0i}]$. On Earth, the growth angle is achieved if the parameter ϕ_c satisfies inequalities (i)–(ii).

8.4 Analytical and Numerical Solutions for the Meniscus Equation in the Dewetted Bridgman Method

Dewetted Bridgman is a crystal growth technique in which the crystal is detached from the crucible wall by a liquid free surface at the level of the solid–liquid interface, called *liquid meniscus*, which creates a gap between the crystal and the ampoule (Figure 8.18).

The dewetting is explained in Chapter 6 and involves the wetting angle θ , the growth angle α , possible modification of these parameters due to pollution of the melt by the gas phase and possible pressure difference between the hot and cold sides of the crucible.

There are two problems of interest in dewetting (see Chapter 6):

- What is the gap thickness e , therefore the crystal radius $r_c = r_a - e$?
- What is the shape of the meniscus? This shape is related to the stability of the process.

In order to understand the process which leads to a crystal with a constant radius under normal gravity, analytical and numerical studies of axisymmetric meniscus shapes must be made and the dependence of the meniscus shape on the pressure difference must be established, starting from the Young–Laplace equation of a capillary surface (8.11) written in agreement with the above configuration [Duffar 2000]:

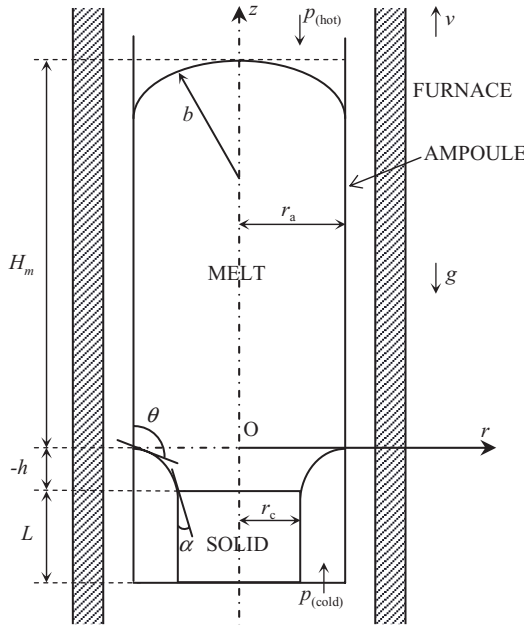


Figure 8.18 Schematic dewetted Bridgman crystal growth system.

$$\frac{\frac{d^2z}{dr^2}}{\left[1 + \left(\frac{dz}{dr}\right)^2\right]^{3/2}} + \frac{\frac{1}{r} \cdot \frac{dz}{dr}}{\left[1 + \left(\frac{dz}{dr}\right)^2\right]^{1/2}} = \frac{p_0 - p_v - \rho_l g z}{\gamma_{lv}}$$

Here, the external pressure on the melt $p_v = p_{\text{cold}}$ and the internal pressure applied on the liquid, p_0 is defined as:

$$p_0 = p_{\text{hot}} + \rho_l g H_m + \frac{2\gamma_{lv}}{b},$$

where p_{hot} and p_{cold} are the vapour pressure at the hot and cold sides of the sample and b is the radius of curvature at the apex of the liquid. Thus the Young–Laplace equation can be written as follows:

$$\frac{\frac{d^2z}{dr^2}}{\left[1 + \left(\frac{dz}{dr}\right)^2\right]^{3/2}} + \frac{\frac{1}{r} \cdot \frac{dz}{dr}}{\left[1 + \left(\frac{dz}{dr}\right)^2\right]^{1/2}} = \frac{\rho_l g (H_m - z) - \Delta p}{\gamma_{lv}} + \frac{2}{b}, \quad (8.105)$$

where $\Delta p = p_{\text{cold}} - p_{\text{hot}}$ represents the pressure difference between the cold and hot sides of the sample and the term $2/b$ is due to the curvature at the top which depends on the

wetting angle θ and on the crucible radius r_a [Duffar 1997]. Under microgravity this can be written as follows:

$$\frac{1}{b} = -\frac{\cos\theta}{r_a}.$$

What is specific for dewetted Bridgman is that the contribution due to the curvature $2/b$ at the top of the free liquid must be considered in Equation (8.105). It is important to emphasize that for crucibles with a reasonable practical radius (larger than the melt capillary constant), the curvature of the upper free liquid surface is very small in normal gravity conditions, and hence it can be neglected. This is not true in microgravity conditions, which is why these cases are treated separately in what follows.

From the physical point of view, the dewetting phenomenon is governed by the Young–Laplace equation through the Bond (Bo), and Laplace (La) dimensionless numbers. Thus, using the dimensionless numbers (8.15) obtained by using the ampoule radius r_a as length scale, Equation (8.110) becomes [Epure 2010]:

$$\frac{\frac{d^2\tilde{z}}{d\tilde{r}^2}}{\left[1 + \left(\frac{d\tilde{z}}{d\tilde{r}}\right)^2\right]^{3/2}} + \frac{\frac{1}{\tilde{r}} \cdot \frac{d\tilde{z}}{d\tilde{r}}}{\left[1 + \left(\frac{d\tilde{z}}{d\tilde{r}}\right)^2\right]^{1/2}} = [Bo(\tilde{H}_m - \tilde{z}) - La - 2\cos\theta], \quad (8.106)$$

where $\tilde{H}_m = H_m/r_a$, $Bo = \rho_l \cdot g \cdot r_a^2 / \gamma_{lv}$, and $La = \Delta p \cdot r_a / \gamma_{lv}$.

8.4.1 Zero Gravity

In zero gravity conditions, the dimensionless Young–Laplace equation becomes:

$$\frac{\frac{d^2\tilde{z}}{d\tilde{r}^2}}{\left[1 + \left(\frac{d\tilde{z}}{d\tilde{r}}\right)^2\right]^{3/2}} + \frac{\frac{1}{\tilde{r}} \cdot \frac{d\tilde{z}}{d\tilde{r}}}{\left[1 + \left(\frac{d\tilde{z}}{d\tilde{r}}\right)^2\right]^{1/2}} = [-La - 2\cos\theta], \quad (8.107)$$

for which the following wetting boundary condition must be satisfied:

$$\frac{d\tilde{z}}{d\tilde{r}}(1) = \tan\left(\theta - \frac{\pi}{2}\right), \quad \theta \in \left(\frac{\pi}{2}, \pi\right) \quad (8.108)$$

and the choice of axis gives $\tilde{z}(1) = 0$.

Equation (8.107) can be written as

$$\frac{\tilde{r} \cdot \frac{d^2\tilde{z}}{d\tilde{r}^2} + \frac{d\tilde{z}}{d\tilde{r}} \cdot \left[1 + \left(\frac{d\tilde{z}}{d\tilde{r}}\right)^2\right]}{\left[1 + \left(\frac{d\tilde{z}}{d\tilde{r}}\right)^2\right]^{3/2}} = -(La + 2\cos\theta) \cdot \tilde{r}$$

which is equivalent to

$$\frac{d}{d\tilde{r}} \left(\frac{\tilde{r} \cdot \frac{d\tilde{z}}{d\tilde{r}}}{\sqrt{1 + \left(\frac{d\tilde{z}}{d\tilde{r}}\right)^2}} \right) = -(La + 2 \cos \theta) \cdot \tilde{r}.$$

Integrating, we obtain the analytical expression for the derivative of the function $\tilde{z}(\tilde{r})$:

$$\frac{d\tilde{z}}{d\tilde{r}}(\tilde{r}) = \frac{-\tilde{r}^2 \cdot \cos \theta - \tilde{r}^2 \cdot (La/2) + c_1}{\sqrt{\tilde{r}^2 - (-\tilde{r}^2 \cdot \cos \theta - \tilde{r}^2 \cdot (La/2) + c_1)^2}}. \tag{8.109}$$

The constant c_1 is determined from the boundary condition $(d\tilde{z}/d\tilde{r})(1) = \tan(\theta - \pi/2)$. It follows that

$$\frac{d\tilde{z}}{d\tilde{r}}(\tilde{r}) = \frac{-\tilde{r}^2 \cdot \cos \theta - \tilde{r}^2 \cdot (La/2) + (La/2)}{\sqrt{\tilde{r}^2 - (-\tilde{r}^2 \cdot \cos \theta - \tilde{r}^2 \cdot (La/2) + (La/2))^2}}. \tag{8.110}$$

Further, the analytical expression of the meniscus can be obtained by integration. The integral can be expressed using elementary functions only in some particular cases.

8.4.1.1 Case I: $La = 0, g = 0$

Integrating Equation (8.110) gives:

$$\tilde{z}(\tilde{r}) = \frac{1}{\cos \theta} \cdot \sqrt{1 - \tilde{r}^2 \cos^2 \theta} + c_2. \tag{8.111}$$

Using the boundary condition $\tilde{z}(1) = 0$, the analytical expression of the meniscus surface in zero gravity when $La = 0$ is obtained:

$$\tilde{z}(\tilde{r}) = \frac{1}{\cos \theta} \cdot (\sqrt{1 - \tilde{r}^2 \cos^2 \theta} - \sin \theta), \tag{8.112}$$

where $\tilde{r} \in [0, 1]$. Dewetting occurs when the growth angle α is achieved at least at one point on the meniscus surface, i.e. when the equation:

$$\tilde{\phi}(\tilde{r}) = (\pi/2) - \alpha \tag{8.113}$$

has at least one solution in the range $(0, 1)$; where $\tilde{\phi}$ is the angle between the plane $\tilde{z} = 0$ and the tangent plane to the meniscus. For this angle the equality $\tan \tilde{\phi} = d\tilde{z}/d\tilde{r}$ holds, and hence information concerning attainment of the growth angle is given by the equation:

$$\tan \tilde{\phi} = \frac{-\tilde{r}^2 \cdot \cos \theta}{\sqrt{\tilde{r}^2 - (-\tilde{r}^2 \cdot \cos \theta)^2}}$$

from whence:

$$\sin \tilde{\phi} = -\tilde{r} \cdot \cos \theta \tag{8.114}$$

which is equivalent to

$$\tilde{\phi} = \arcsin(-\tilde{r} \cdot \cos \theta), \quad (8.115)$$

for any $\tilde{r} \in [0, 1]$. What is remarkable is that Equation (8.115) gives a condition for dewetting that depends on the growth angle α and contact angle θ . From the positivity of the derivative

$$\frac{d\tilde{\phi}}{d\tilde{r}} = -\frac{\cos \theta}{\sqrt{1 - \tilde{r}^2 \cos^2 \theta}} > 0, \quad \theta \in \left(\frac{\pi}{2}, \pi\right)$$

it follows that the function $\tilde{\phi}(\tilde{r})$ is strictly increasing for $\tilde{r} \in [0, 1]$. Considering this monotonicity and the boundary condition $(d\tilde{z}/d\tilde{r})(1) = \tan(\theta - \pi/2)$ which is equivalent to $\tilde{\phi}(1) = (\pi/2) - \alpha$, the growth angle $(\pi/2) - \alpha$ can be achieved if $\tilde{\phi}(\tilde{r})$ decreases from $\theta - (\pi/2)$ to $(\pi/2) - \alpha$. This means that $(\pi/2) - \alpha < \theta - (\pi/2)$ and hence $\alpha + \theta > \pi$. In the opposite case, when $\alpha + \theta < \pi$, the growth angle cannot be achieved because of the monotonicity of $\tilde{\phi}(\tilde{r})$.

Assuming that the growth angle can be achieved, i.e. $\alpha + \theta > \pi$, Equations (8.113) and (8.114) give:

$$\sin((\pi/2) - \alpha) = -(1 - \tilde{e}) \cdot \cos \theta$$

where \tilde{e} represents the nondimensional gap thickness and $\tilde{r}_c = 1 - \tilde{e}$ the nondimensional crystal radius. The following *nondimensional gap thickness formula* [Duffar 1997] results:

$$\tilde{e} = \frac{\cos \theta + \cos \alpha}{\cos \theta} \quad (8.116)$$

valid under *zero gravity* conditions, $La = 0$, and $\alpha + \theta > \pi$.

We now have a remarkable new result concerning the meniscus shape. Because $\tan \tilde{\phi} = d\tilde{z}/d\tilde{r}$ and $d\tilde{\phi}/d\tilde{r} > 0$, the second derivative is:

$$\frac{d^2\tilde{z}}{d\tilde{r}^2} = \frac{d}{d\tilde{r}} \left(\frac{d\tilde{z}}{d\tilde{r}} \right) = \frac{d}{d\tilde{r}} (\tan \tilde{\phi}) = \frac{1}{\cos^2 \tilde{\phi}} \cdot \frac{d\tilde{\phi}}{d\tilde{r}}$$

This equation proves that $d^2\tilde{z}/d\tilde{r}^2 > 0$, and hence under *zero gravity* and $La = 0$, the *meniscus is globally convex* for any $\tilde{r} \in [0, 1]$.

8.4.1.2 Case II: $La \neq 0$, $g = 0$

To obtain the meniscus equation, Equation (8.110) should be integrated, but if $La \neq 0$ this integral can not be expressed using elementary functions. In order to obtain information about the meniscus shape, attainment of the growth angle, and gap thickness, a qualitative study is necessary.

Introducing $\tan \tilde{\phi} = d\tilde{z}/d\tilde{r}$ in Equation (8.110) gives:

$$\sin \tilde{\phi} = -(\cos \theta) \cdot \tilde{r} - \frac{La}{2} \cdot \tilde{r} + \frac{La}{2} \cdot \frac{1}{\tilde{r}}, \quad (8.117)$$

which is equivalent to

$$\tilde{\phi} = \arcsin\left(-(\cos\theta) \cdot \tilde{r} - \frac{La}{2} \cdot \tilde{r} + \frac{La}{2} \cdot \frac{1}{\tilde{r}}\right), \quad (8.118)$$

for any $\tilde{r} \in [0, 1]$. In a similar way to previous calculations, the sign of the derivative $d\tilde{\phi}/d\tilde{r}$ will give information about the shape of the meniscus, and about the condition that must be imposed on the sum of the wetting and growth angles to ensure that attainment of the growth angle is feasible. Deriving the relation (8.118) gives:

$$\frac{d\tilde{\phi}}{d\tilde{r}} = \left[\frac{1}{\sqrt{1 - \left(-(\cos\theta) \cdot \tilde{r} - \frac{La}{2} \cdot \tilde{r} + \frac{La}{2} \cdot \frac{1}{\tilde{r}}\right)^2}} \right] \cdot \left[\left(-\cos\theta - \frac{La}{2}\right)\tilde{r}^2 - \frac{La}{2} \right] \cdot \frac{1}{\tilde{r}^2}. \quad (8.119)$$

The sign of this derivative depends on the sign of the expression depending on \tilde{r} and La :

$$E(\tilde{r}, La) = \left(-\cos\theta - \frac{La}{2}\right)\tilde{r}^2 - \frac{La}{2}. \quad (8.120)$$

The following three cases should be considered:

- If $La \in (-\infty; 0]$, then $E(\tilde{r}, La) > 0$ and hence $d\tilde{\phi}/d\tilde{r} > 0$. Moreover,

$$\frac{d^2\tilde{z}}{d\tilde{r}^2} = \frac{1}{\cos^2\tilde{\phi}} \cdot \frac{d\tilde{\phi}}{d\tilde{r}} > 0,$$

i.e. the meniscus is globally convex, and the growth angle can be achieved only if $\alpha + \theta > \pi$.

- If $La \in (0; -2\cos\theta)$, then the meniscus changes its curvature (concave to convex) at the point $\tilde{r}_1 = \sqrt{La/(-2 \cdot \cos\theta - La)}$, i.e. $E(\tilde{r}_1, La) = 0$, which is equivalent to

$$\frac{d\tilde{\phi}}{d\tilde{r}}(\tilde{r}_1) = \frac{d^2\tilde{z}}{d\tilde{r}^2}(\tilde{r}_1) = 0,$$

and the growth angle can be achieved either once or twice, depending on its value.

- If $La \in [-2\cos\theta; +\infty)$, then $E(\tilde{r}, La) < 0$ and hence $d\tilde{\phi}/d\tilde{r} < 0$. In this case the meniscus is globally concave, i.e. $d^2\tilde{z}/d\tilde{r}^2 < 0$, and the growth angle can be achieved only if $\alpha + \theta < \pi$.

The above ranges for the pressure difference give information about the meniscus shape and the corresponding cases $\alpha + \theta < \pi$ or $\alpha + \theta > \pi$, in which the growth angle can be achieved or, in other words, when dewetting is feasible.

Assuming that La , θ , and α are chosen such that the growth angle can be achieved, the growth angle condition (8.113) is satisfied somewhere along the meniscus. From (8.117):

$$\sin\left(\frac{\pi}{2} - \alpha\right) = -(\cos\theta) \cdot (1 - \tilde{e}) - \frac{La}{2} \cdot (1 - \tilde{e}) + \frac{La}{2} \cdot \frac{1}{(1 - \tilde{e})}, \quad (8.121)$$

from which the following *gap thickness formulas* available in *zero gravity* [Duffar 1997] are obtained:

$$\tilde{e}_1 = \frac{\cos\alpha + 2 \cdot \cos\theta + La + \sqrt{\cos^2\alpha + La^2 + 2 \cdot La \cdot \cos\theta}}{La + 2 \cdot \cos\theta}, \tag{8.122}$$

$$\tilde{e}_2 = \frac{\cos\alpha + 2 \cdot \cos\theta + La - \sqrt{\cos^2\alpha + La^2 + 2 \cdot La \cdot \cos\theta}}{La + 2 \cdot \cos\theta}, \tag{8.123}$$

The gap formula (8.122) is valid when the growth angle is reached on the convex part of the meniscus, and formula (8.123) is valid when attainment of the growth angle takes place on the concave part of the meniscus. More precisely, the numerical results obtained by solving the problem (8.90)–(8.91) by the Runge–Kutta method for InSb crystals grown in zero gravity by the dewetted Bridgman technique (the parameters for InSb are those presented in [Balint 2008, Braescu 2008-2]), confirm the results obtained from the qualitative study:

- If $La \in (-\infty; 0]$, then the meniscus is globally convex and the growth angle can be achieved once. When the growth angle is reached the gap thickness is given by \tilde{e}_1 , as in (8.122). The numerical results reveal this behaviour for $La = -0.655 \in (-\infty; 0]$ and $\theta + \alpha = 160^\circ + 25^\circ > \pi$, as can be seen in Figure 8.19. The figure shows that the meniscus is globally convex and that the growth angle is achieved. The computed gap thickness $\tilde{e} = 1 - \tilde{r}_{c1} = 1 - 0.97915 = 0.02085$ is equal to the value given by formula (8.122), i.e. $\tilde{e}_1 = 0.02085$.
- If $La \in (0; -2\cos\theta)$, then the meniscus is concave–convex (i.e it has a point of inflexion). If the growth angle is attained on the concave part the gap thickness is given by \tilde{e}_2 in (8.123); if on the convex part, the gap thickness is given by \tilde{e}_1 in (8.122). The numerical results confirm this behaviour. The menisci are concave–convex and the growth angle can be achieved either once or twice: (a) for $\theta + \alpha = 112^\circ + 25^\circ < \pi$ and $La = 0.105 \in (0; -2\cos\theta) = (0; 0.749)$ the growth angle is not achieved (see Figure

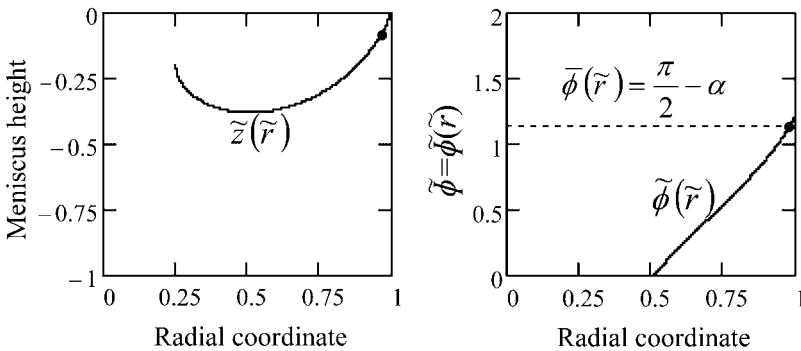


Figure 8.19 Meniscus shape $\tilde{z}(\tilde{r})$ and meniscus angle $\tilde{\phi}(\tilde{r})$ corresponding to $La = -0.655$ and $\theta + \alpha = 160^\circ + 25^\circ$ for InSb, $g = 0$. The place where the growth angle $(\pi/2) - \alpha = 1.13446$ radians) is reached is shown by the black dot.

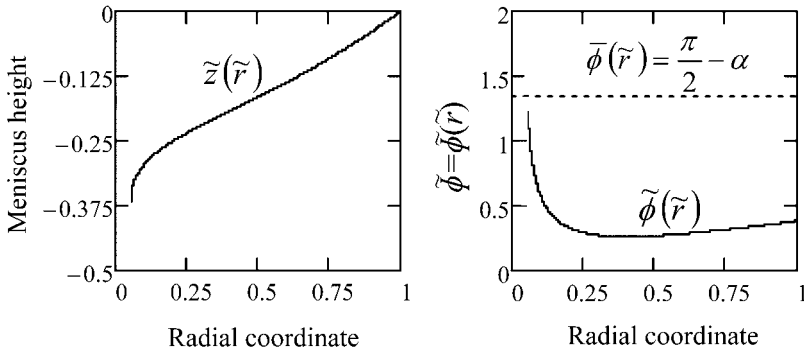


Figure 8.20 Meniscus shape $\tilde{z}(\tilde{r})$ and meniscus angle $\tilde{\phi}(\tilde{r})$ corresponding to $La = 0.105$ and $\theta + \alpha = 112^\circ + 25^\circ$ for $lnSb$, $g = 0$. The growth angle cannot be achieved.

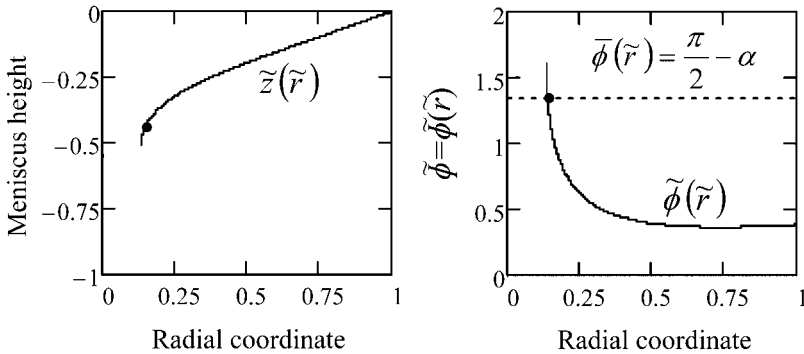


Figure 8.21 Meniscus shape $\tilde{z}(\tilde{r})$ and meniscus angle $\tilde{\phi}(\tilde{r})$ corresponding to $La = 0.262$ and $\theta + \alpha = 112^\circ + 25^\circ$ for $lnSb$, $g = 0$. The place where the growth angle $(\pi/2) - \alpha = 1.13446$ radians is achieved is shown by the black dot.

8.20), but for $La = 0.262 \in (0; 0.749)$ the growth angle is achieved once, as can be seen in Figure 8.21; (b) for $\theta + \alpha = 160^\circ + 25^\circ > \pi$ and $La = 0.393 \in (0; -2\cos\theta) = (0; 1.879)$ the growth angle is achieved twice (Figure 8.22). If the growth angle is achieved on the concave part of the meniscus, then the computed gap thickness in Figure 8.21 $\tilde{e} = 1 - \tilde{r}_{c1} = 1 - 0.1505 = 0.8494$ is equal to $\tilde{e}_2 = 0.8494$ given by (8.123) and in Figure 8.22, $\tilde{e} = 1 - \tilde{r}_{c1} = 1 - 0.2819 = 0.7181$ is equal to \tilde{e}_2 . If the growth angle is reached on the convex part of the meniscus, then the computed gap thickness $\tilde{e} = 1 - \tilde{r}_{c2} = 1 - 0.9374 = 0.0626$ is equal to $\tilde{e}_1 = 0.0626$ given by (8.122), as can be seen in Figure 8.21.

- If $La \in [-2\cos\theta; +\infty)$, then the meniscus is concave and the growth angle can be achieved once. When the growth angle is attained the gap thickness is given by \tilde{e}_2 in (8.123). The numerical results show that the meniscus is concave, and that the growth angle is achieved for $\theta + \alpha = 112^\circ + 25^\circ < \pi$, $La = 0.85 \in [-2\cos\theta; +\infty) = [0.749; +\infty)$ (Figure 8.23). The computed gap thickness $\tilde{e} = 1 - \tilde{r}_{c2} = 1 - 0.4573 = 0.5427$ is equal to \tilde{e}_2 as given by (8.123).

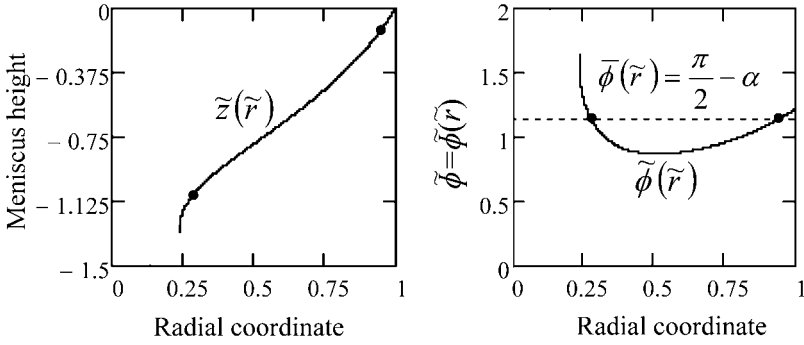


Figure 8.22 Meniscus shape $\tilde{z}(\tilde{r})$ and meniscus angle $\tilde{\phi}(\tilde{r})$ corresponding to $La = 0.393$ and $\theta + \alpha = 160^\circ + 25^\circ$ for $InSb$, $g = 0$. The places where the growth angle $(\pi/2) - \alpha = 1.13446$ radians) is achieved are shown by the black dots.

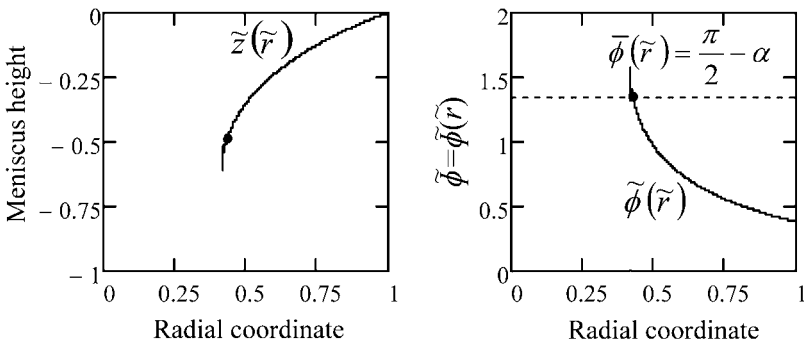


Figure 8.23 Meniscus $\tilde{z}(\tilde{r})$ and meniscus angle $\tilde{\phi}(\tilde{r})$ corresponding to $La = 0.85$ and $\theta + \alpha = 112^\circ + 25^\circ$ for $InSb$, $g = 0$. The place where the growth angle $(\pi/2) - \alpha = 1.13446$ radians) is achieved is shown by the black dot.

8.4.2 Normal Gravity

Under normal gravity conditions, for a crucible radius larger than the capillary constant of the material, the curvature of the upper free liquid surface can be neglected (it is very small), and hence the Young–Laplace equation (8.105) becomes:

$$\frac{d^2\tilde{z}}{d\tilde{r}^2} = [Bo \cdot (\tilde{H}_m - \tilde{z}) - La] \cdot \left[1 + \left(\frac{d\tilde{z}}{d\tilde{r}} \right)^2 \right]^{3/2} - \frac{1}{\tilde{r}} \left[1 + \left(\frac{d\tilde{z}}{d\tilde{r}} \right)^2 \right] \cdot \frac{d\tilde{z}}{d\tilde{r}}, \quad (8.124)$$

where the axisymmetric solution $\tilde{z} = \tilde{z}(\tilde{r})$ has to satisfy the following boundary condition:

$$\frac{d\tilde{z}}{d\tilde{r}}(1) = \tan\left(\theta - \frac{\pi}{2}\right), \quad \theta \in \left(\frac{\pi}{2}, \pi\right). \quad (8.125)$$

and, by the choice of origin, $\tilde{z}(1) = 0$.

Using the technique presented in section 8.1, the nonlinear equation (8.124) is transformed into the following nonlinear system of two differential equations:

$$\begin{cases} \frac{d\tilde{z}}{d\tilde{r}} = \tan\tilde{\phi} \\ \frac{d\tilde{\phi}}{d\tilde{r}} = [Bo \cdot (\tilde{H}_m - \tilde{z}) - La] \cdot \frac{1}{\cos\tilde{\phi}} - \frac{1}{\tilde{r}} \cdot \tan\tilde{\phi} \end{cases} \quad (8.126)$$

for which the boundary condition (8.125) becomes [Balint 2008, Braescu 2008-2]:

$$\tilde{z}(1) = 0, \quad \tilde{\phi}(1) = \theta - \frac{\pi}{2}; \quad \theta \in \left(\frac{\pi}{2}, \pi\right). \quad (8.127)$$

The functions on the right-hand side of Equations (8.126) are real analytic, i.e. they can be expanded in Taylor series, and the conditions of existence and uniqueness of a solution are satisfied for the problem (8.126)–(8.127). The meniscus shape is described by the solution

$$\tilde{z} = \tilde{z}(\tilde{r}; \theta, La, Bo, \tilde{H}_m), \quad \tilde{\phi} = \tilde{\phi}(\tilde{r}; \theta, La, Bo, \tilde{H}_m)$$

which depends on \tilde{r} and on the parameters $\theta, La, Bo, \tilde{H}_m$. In what follows, this solution is denoted by $\tilde{z} = \tilde{z}(\tilde{r}), \tilde{\phi} = \tilde{\phi}(\tilde{r})$.

Because of the high nonlinearity of the problem, *an analytical formula for the meniscus cannot be obtained*, hence analytical and numerical studies of meniscus shapes are necessary. With this aim, the dependence of meniscus shape on the pressure difference will be established, and inequalities of the pressure intervals which assure the feasibility of dewetting will be determined.

Because of the different behaviours of the meniscus shape in the cases $\alpha + \theta < \pi$, and $\alpha + \theta > \pi$, as already shown in zero gravity, qualitative studies will be performed on each case separately. Recent experimental developments [Sylla 2008–1], confirmed by thermodynamic analysis [Sylla 2008–2], show that contamination of the system during the growth process may greatly increase the wetting angle, leading to an unexpected inequality between the wetting angle θ and growth angle α , i.e. $\alpha + \theta > \pi$.

8.4.2.1 Case I: $\alpha + \theta < \pi$

In order to make a qualitative study of the meniscus shape (convex, concave–convex, convex–concave, concave) as a function of the Laplace number, the function $\tilde{z} = \tilde{z}(\tilde{r})$ is approximated by a Taylor polynomial of third degree $T_{\tilde{z}}^3(\tilde{r})$ in the neighbourhood of $\tilde{r} = 1$. To establish the inequalities of the pressure intervals (i.e. La numbers) which assure the feasibility of dewetting, the information obtained from Taylor approximation (approximate meniscus) will be combined with properties deduced from the problem (8.126)–(8.127) which describes the shape of the real meniscus. Thus, approximating the function $\tilde{z} = \tilde{z}(\tilde{r})$ by a Taylor polynomial of third degree $T_{\tilde{z}}^3(\tilde{r})$ in the neighbourhood of $\tilde{r} = 1$, accurate qualitative results are obtained only in a sufficiently small neighbourhood of r_a . The third-order Taylor polynomial $T_{\tilde{z}}^3(\tilde{r})$ which approximates the meniscus surface $\tilde{z} = \tilde{z}(\tilde{r})$ is given by:

$$T_{\tilde{z}}^3(\tilde{r}) = \tilde{z}'(1) \cdot (\tilde{r} - 1) + \frac{\tilde{z}''(1)}{2} \cdot (\tilde{r} - 1)^2 + \frac{\tilde{z}'''(1)}{6} \cdot (\tilde{r} - 1)^3 \quad (8.128)$$

where $\tilde{z}'(1)$, $\tilde{z}''(1)$, $\tilde{z}'''(1)$ represent the first-, second- and third-order derivatives of the function $\tilde{z} = \tilde{z}(\tilde{r})$ at $\tilde{r} = 1$, and are obtained from the system (8.126) and boundary conditions (8.127) as follows [Braescu 2008-2]:

$$\tilde{z}'(1) = A_{\tilde{z}}^1 = -\frac{\cos\theta}{\sin\theta}, \quad (8.129)$$

$$\tilde{z}''(1) = -A_{\tilde{z}}^2 \cdot La + B_{\tilde{z}}^2 = -\frac{1}{\sin^3\theta} \cdot La + \frac{\cos\theta}{\sin^3\theta} + \frac{Bo \cdot \tilde{H}_m}{\sin^3\theta}, \quad (8.130)$$

$$\begin{aligned} \tilde{z}'''(1) &= A_{\tilde{z}}^3 \cdot La^2 - B_{\tilde{z}}^3 \cdot La + C_{\tilde{z}}^3 \\ &= -\frac{3 \cdot \cos\theta}{\sin^5\theta} La^2 + \left(\frac{6 \cdot \cos^2\theta}{\sin^5\theta} + \frac{1}{\sin^3\theta} + \frac{6 \cdot Bo \cdot \tilde{H}_m \cdot \cos\theta}{\sin^5\theta} \right) La \\ &\quad + \frac{1}{\sin^3\theta} \cdot \left[-\frac{3 \cdot Bo^2 \cdot \tilde{H}_m^2 \cdot \cos\theta}{\sin^2\theta} - \frac{3 \cdot \cos^3\theta}{\sin^2\theta} - 2 \cdot \cos\theta + \frac{Bo \cdot \cos\theta}{\sin\theta} \right. \\ &\quad \left. - \frac{6 \cdot Bo \cdot \tilde{H}_m \cdot \cos^2\theta}{\sin^2\theta} - Bo \cdot \tilde{H}_m \right]. \end{aligned} \quad (8.131)$$

The concavity or convexity of the meniscus $\tilde{z} = \tilde{z}(\tilde{r})$ in a sufficiently small neighbourhood of 1 is given by the sign of the second derivative of the approximated meniscus $\tilde{z}_T(\tilde{r}) = T_{\tilde{z}}^3(\tilde{r})$:

$$\begin{aligned} \frac{d^2 T_{\tilde{z}}^3}{d\tilde{r}^2} &= -A_{\tilde{z}}^2 \cdot La + B_{\tilde{z}}^2 + [A_{\tilde{z}}^3 \cdot La^2 - B_{\tilde{z}}^3 \cdot La + C_{\tilde{z}}^3] \cdot (\tilde{r} - 1) \\ &= E_{\tilde{z}}^2 + E_{\tilde{z}}^3 \cdot (\tilde{r} - 1). \end{aligned} \quad (8.132)$$

The sets of La values that define convex, concave–convex, convex–concave and concave shapes of the approximated menisci are determined by the following inequalities:

- if $E_{\tilde{z}}^2 > 0$ and $E_{\tilde{z}}^4 < 0$ (or $E_{\tilde{z}}^2 > 0$ and $E_{\tilde{z}}^4 > 1$), then the approximated meniscus is convex;
- if $E_{\tilde{z}}^2 > 0$ and $0 < E_{\tilde{z}}^4 < 1$, then the approximated meniscus is concave–convex;
- if $E_{\tilde{z}}^2 < 0$ and $0 < E_{\tilde{z}}^4 < 1$, then the approximated meniscus is convex–concave;
- if $E_{\tilde{z}}^2 < 0$ and $E_{\tilde{z}}^4 < 0$ (or $E_{\tilde{z}}^2 < 0$ and $E_{\tilde{z}}^4 > 1$), then the approximated meniscus is concave;

where $E_{\tilde{z}}^4 = 1 - (E_{\tilde{z}}^2 / E_{\tilde{z}}^3)$.

Dewetting occurs if the growth angle α is achieved at some point in the interval (0, 1), which is given by the solution of the equation:

$$\tilde{\phi}(\tilde{r}) = \frac{\pi}{2} - \alpha \quad \text{or} \quad \frac{dT_{\tilde{z}}^3}{d\tilde{r}} = \tan\left(\frac{\pi}{2} - \alpha\right). \quad (8.133)$$

Because $\alpha + \theta < \pi$, the boundary condition for $\tilde{\phi}(\tilde{r})$ shows that the growth angle $(\pi/2) - \alpha$ can be achieved only if $\tilde{\phi}(\tilde{r})$ decreases, i.e. $d\tilde{\phi}/d\tilde{r} < 0$. On the other hand,

$$\frac{d\tilde{\phi}}{d\tilde{r}}(1) = E_{\tilde{z}}^2 \cdot \sin^2(\theta) \quad \text{and} \quad \frac{d^2T_{\tilde{z}}^3}{d\tilde{r}^2}(1) = E_{\tilde{z}}^2.$$

Hence, if $\tilde{\phi}(\tilde{r})$ decreases then

$$\frac{d^2T_{\tilde{z}}^3}{d\tilde{r}^2}(1) = E_{\tilde{z}}^2 < 0$$

and the real meniscus should be concave in the neighbourhood of 1. For this reason, in what follows special attention is paid to the convex–concave (S-shaped), and concave meniscus shapes. Moreover, the inequality $E_{\tilde{z}}^2 > 0$, which appears in both cases, gives the values of La resulting in a concave meniscus at 1:

$$La > \frac{B_{\tilde{z}}^2}{A_{\tilde{z}}^2} = \cos\theta + Bo \cdot \tilde{H}_m. \tag{8.134}$$

The inequality (8.134) states that the gas pressure difference should be larger than the hydrostatic pressure plus a term which depends on the capillary parameters.

For certain values of La , the growth angle can be achieved twice for a convex–concave approximated meniscus (Equation (8.133) has two solutions), and once for a concave approximated meniscus (Equation (8.133) has one solution). These values of La are given by the following statements (for details see [Braescu 2008-2]):

- *Statement 1:* The set of La values for which the growth angle α can be achieved once on the approximated meniscus is defined by the inequality:

$$F_{\tilde{z}}^1 = \left(A_{\tilde{z}}^1 - \frac{\cos\alpha}{\sin\alpha} \right) \cdot \left[\frac{1}{2} \cdot E_{\tilde{z}}^3 - E_{\tilde{z}}^2 + A_{\tilde{z}}^1 - \frac{\cos\alpha}{\sin\alpha} \right] < 0. \tag{8.135}$$

- *Statement 2:* The set of La values for which the growth angle α can be achieved twice in the interval $(0, 1)$ on the approximated meniscus is defined by the following inequalities:

$$F_{\tilde{z}}^2 = (E_{\tilde{z}}^2)^2 - 2 \cdot E_{\tilde{z}}^3 \cdot \left(A_{\tilde{z}}^1 - \frac{\cos\alpha}{\sin\alpha} \right) > 0, \tag{8.136}$$

$$F_{\tilde{z}}^3 = \frac{A_{\tilde{z}}^1 - \frac{\cos\alpha}{\sin\alpha}}{E_{\tilde{z}}^3} > 0, \tag{8.137}$$

$$F_{\tilde{z}}^4 = \frac{F_{\tilde{z}}^1}{F_{\tilde{z}}^3} > 0, \tag{8.138}$$

$$F_{\tilde{z}}^5 = \frac{E_{\tilde{z}}^2}{E_{\tilde{z}}^3} \in (0, 1). \tag{8.139}$$

- *Statement 3:* For $\alpha + \theta < \pi$:

- (i) If the real meniscus is concave at 1, then $La > Bo \cdot \tilde{H}_m + \cos\theta$;
- (ii) If the real meniscus is convex at the triple point r_c in which the growth angle is achieved, then $La < Bo \cdot (\tilde{H}_m - \tilde{h}) - \cos\alpha$.

Inequalities (i) and (ii) define the interval La_1 for which dewetted Bridgman growth is feasible with a convex–concave (S-shaped) meniscus. Moreover they show that the value $La_{(\text{concave})}$ for which the meniscus is concave can be deduced from the pressure difference values $La_{(\text{convex–concave})}$ for which the meniscus is S-shaped.

The range La_1 can be refined by using the approximation $\tilde{\phi}_r(\tilde{r})$ of the function $\tilde{\phi}(\tilde{r})$, and the condition for attainment of the growth angle on the approximate meniscus $\tilde{z}_r(\tilde{r})$.

- **Statement 4:** A refined range La^{approx} of the interval La_1 , for which dewetted Bridgman with convex–concave meniscus is feasible and the growth angle is achieved, is determined by the following inequalities:

- (i) $Bo \cdot \tilde{H}_m + \cos\theta < La < Bo \cdot (\tilde{H}_m - \tilde{h}) - \cos\alpha$,
- (ii) $F_z^1(La) = \left(A_z^1 - \frac{\cos\alpha}{\sin\alpha} \right) \cdot \left[\frac{1}{2} \cdot E_z^3 - E_z^2 + A_z^1 - \frac{\cos\alpha}{\sin\alpha} \right] < 0$,
- (iii) $Bo \cdot (\tilde{H}_m - \tilde{h}) - \frac{\cos\alpha}{\tilde{r}_1(La)} > La$,

where $\tilde{r}_1(La)$ represents the real root of the equation

$$\frac{1}{2} \cdot E_z^3 - E_z^2 + A_z^1 - \frac{\cos\alpha}{\sin\alpha} = 0$$

and is in (0, 1) [Braescu 2008-2].

Inequalities (i) are related to the shape of the meniscus: concave at 1 and convex later. The inequality (ii) $F_z^1(La) < 0$ indicates that the growth angle α is achieved once on the approximated meniscus. Inequality (iii) shows that in $\tilde{r}_1(La)$ the approximated meniscus is convex.

In the following, numerical results are obtained by solving the problem (8.126)–(8.127) for InSb crystals grown in normal gravity by the dewetted Bridgman process [Balint 2008, Braescu 2008-2].

Inequalities (i)–(ii), from Statement 4 give the La range [51.353; 52.617]. Through inequality (iii) this is refined to $La^{\text{approx}} = [51.353; 52.589]$ which represents the range of the Laplace number for which dewetted Bridgman growth with a convex–concave meniscus is possible and where the growth angle is achieved. Numerically integrating the system (8.126)–(8.127) for different values of the La from the refined range La^{approx} , gives $La^{\text{real}} = [51.726; 52.458]$ which represents the real range of the pressure difference that gives a convex–concave real meniscus where the growth angle is attained twice (Figure 8.24). If $La^{\text{real}} \geq 52.46$ then the real meniscus is concave and the growth angle is achieved only once, as can be seen in Figure 8.25.

Figures 8.24 and 8.25 show that the approximated meniscus given by the third-degree Taylor polynomial $T_z^3(\tilde{r})$ is accurate only in the neighbourhood of 1. However, experimental values of the gap thickness are always much smaller than 1 mm (see Chapter 6). The points marked on the figures represent the points at which the growth angle is achieved.

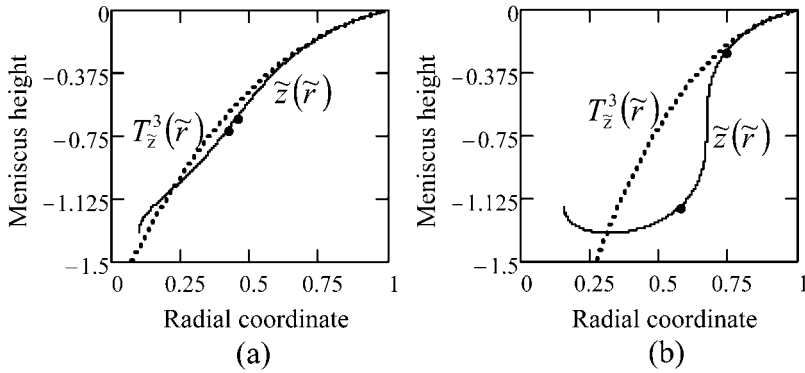


Figure 8.24 Approximated menisci $T_{\tilde{z}}^3(\tilde{r})$ (dotted line) and real (numerical) convex-concave menisci $\tilde{z}(\tilde{r})$ corresponding to $La = 51.726$ (a) and $La = 52.446$ (b) for $InSb$, $\tilde{F}_m = 10.9$. The places where the growth angle $(\pi/2) - \alpha = 1.13446$ radians) is achieved are shown by the black dots.

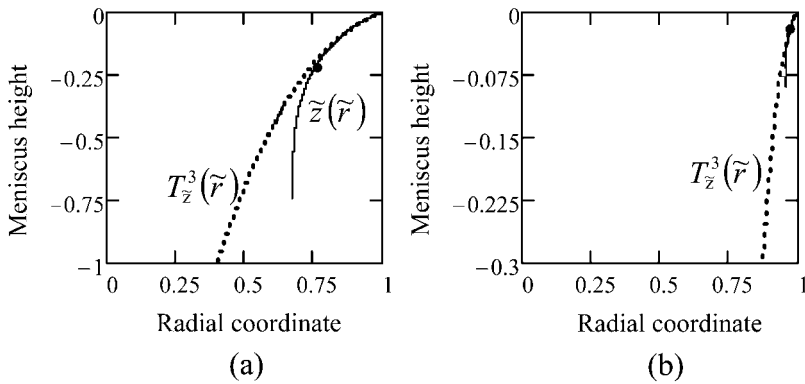


Figure 8.25 Approximated menisci $T_{\tilde{z}}^3(\tilde{r})$ (dotted line) and real (numerical) concave menisci $\tilde{z}(\tilde{r})$ corresponding to $La = 52.46$ (a) and $La = 64.167$ (b) for $InSb$, $\tilde{F}_m = 10.9$. The places where the growth angle $(\pi/2) - \alpha = 1.13446$ radians) is achieved are shown by the black dots.

8.4.2.2 Case II: $\alpha + \theta > \pi$

During the growth process of classical semiconductors grown in uncoated ampoules (i.e. $\alpha + \theta < \pi$), contamination of the system may greatly increase the wetting angle, leading to an unexpected sum of the wetting angle θ and growth angle α , i.e. $\alpha + \theta > \pi$. For this reason, the dependence of the meniscus shape on the pressure difference is studied, in order to get conditions that allow dewetting for classical semiconductors grown in uncoated crucibles with contamination (or in coated crucibles). To study the meniscus shape qualitatively as a function of the Laplace number, only the properties obtained from the problem (8.126)–(8.127) are used. In the case $\alpha + \theta > \pi$, the meniscus height increases

if La increases, hence the Taylor polynomial approximations cannot be used because they are valid only in a small neighbourhood of 1 (this is the opposite behaviour to the previous case $\alpha + \theta < \pi$, where increasing La leads to a decrease of the meniscus).

Thus, considering the inequality $\alpha + \theta > \pi$ and boundary condition for $\tilde{\phi}(\tilde{r})$, $\tilde{\phi}(1) = \theta - (\pi/2)$, it follows that the growth angle $(\pi/2) - \alpha$ can be achieved if $\tilde{\phi}(\tilde{r})$ decreases from $\theta - (\pi/2)$ to $(\pi/2) - \alpha$, i.e. $d\tilde{\phi}/d\tilde{r} > 0$. On the other hand, from Equations (8.126):

$$\frac{d\tilde{\phi}}{d\tilde{r}}(1) = [Bo \cdot (\tilde{H}_m - \tilde{z}(1)) - La] \cdot \frac{1}{\cos\tilde{\phi}(1)} - \frac{1}{\tilde{r}} \cdot \tan\tilde{\phi}(1),$$

and using the boundary conditions $\tilde{z}(1) = 0$, $\tilde{\phi}(1) = \theta - (\pi/2)$, gives:

$$\frac{d\tilde{\phi}}{d\tilde{r}}(1) = \frac{1}{\sin\theta} [Bo \cdot \tilde{H}_m - La + \cos\theta]. \quad (8.140)$$

As $d\tilde{\phi}/d\tilde{r}(1) > 0$, the following inequality for the pressure difference is obtained:

$$La < Bo \cdot \tilde{H}_m + \cos\theta, \quad (8.141)$$

for which the growth angle can be achieved.

Concerning the meniscus shape, because

$$\frac{d^2\tilde{z}}{d\tilde{r}^2}(1) = \frac{1}{\cos^2\tilde{\phi}(1)} \cdot \frac{d\tilde{\phi}}{d\tilde{r}}(1),$$

$d^2\tilde{z}/d\tilde{r}^2 > 0$ in the neighbourhood of 1, which means that the growth angle can be achieved if the meniscus is convex in the neighbourhood of 1.

Then, for a pressure difference which satisfies the inequality (8.141) the meniscus is convex in the neighbourhood of 1 (this includes globally convex or concave–convex menisci), and the growth angle can be achieved.

Numerical results obtained by solving the problem (8.126)–(8.127) for InSb crystals grown on the ground by the dewetted Bridgman process for high apparent wetting angle (i.e. the contamination case $\theta + \alpha = 160^\circ + 25^\circ > \pi$) prove that if the pressure difference satisfies the inequality (8.141), i.e. $La < 49.794$, then the meniscus is globally convex (Figure 8.26) or concave–convex (see Figure 8.27; it is difficult to see this shape on the figure, but it can be seen in the numerical results) and the growth angle is achieved once.

Further, there are cases in which the meniscus is concave at 1 and the growth angle can be achieved. There are two possible situations: (i) convex–concave meniscus, and (ii) globally concave meniscus.

For the *convex–concave meniscus* there is a point of inflexion \tilde{r}_1 , i.e. $(d^2\tilde{z}/d\tilde{r}^2)(\tilde{r}_1) = 0$. This condition implies that $(d\tilde{\phi}/d\tilde{r})(\tilde{r}_1) = 0$ because

$$\frac{d^2\tilde{z}}{d\tilde{r}^2} = \frac{1}{\cos^2\tilde{\phi}} \cdot \frac{d\tilde{\phi}}{d\tilde{r}}.$$

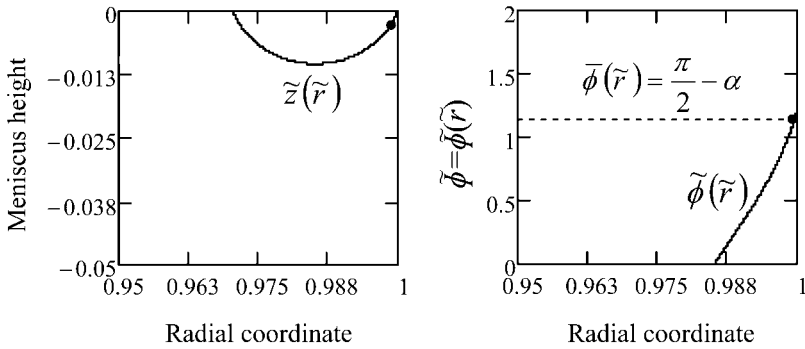


Figure 8.26 Meniscus shape $\tilde{z}(\tilde{r})$ and meniscus angle $\tilde{\phi}(\tilde{r})$ corresponding to $La = -13.095$ and $\theta + \alpha = 160^\circ + 25^\circ > \pi$ for $lnSb$, $\tilde{H}_m = 10.9$. The place where the growth angle $((\pi/2) - \alpha = 1.13446$ radians) is reached is shown by the black dot.

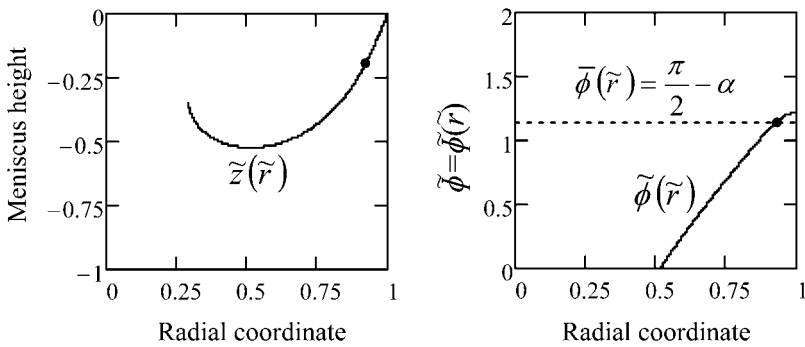


Figure 8.27 Meniscus $\tilde{z}(\tilde{r})$ and meniscus angle $\tilde{\phi}(\tilde{r})$ corresponding to $La = 49.788$ and $\theta + \alpha = 160^\circ + 25^\circ > \pi$ for $lnSb$, $\tilde{H}_m = 10.9$. The place where the growth angle $((\pi/2) - \alpha = 1.13446$ radians) is achieved is shown by the black dot.

Because the meniscus is concave at 1, i.e. $d\tilde{\phi}/d\tilde{r} < 0$ in the neighbourhood of 1, the meniscus is concave for $\tilde{r} \in [\tilde{r}_1; 1]$ and the function $\tilde{\phi}(\tilde{r})$ decreases. Attainment of the growth angle may be possible on the convex meniscus, i.e. on the left side of \tilde{r}_1 the meniscus is convex and $d\tilde{\phi}/d\tilde{r} > 0$. This proves that the growth angle can be achieved if the function $\tilde{\phi}(\tilde{r})$ is concave and its maximum is $(\tilde{r}_1; \tilde{\phi}(\tilde{r}_1))$. This gives a condition on the second derivative $(d^2\tilde{\phi}/d\tilde{r}^2)(\tilde{r}) < 0$ for $\tilde{r} \in (\tilde{r}_1 - \epsilon; \tilde{r}_1 + \epsilon)$. Thus, deriving the second equation

$$\frac{d\tilde{\phi}}{d\tilde{r}} = [Bo \cdot (\tilde{H}_m - \tilde{z}) - La] \cdot \frac{1}{\cos\tilde{\phi}} - \frac{1}{\tilde{r}} \cdot \tan\tilde{\phi}$$

from Equations (8.126), and replacing \tilde{r} by \tilde{r}_1 , we get:

$$\frac{d^2\tilde{\phi}}{d\tilde{r}^2}(\tilde{r}_1) = \left(\frac{1}{\tilde{r}_1^2} - Bo \cdot \frac{1}{\cos\tilde{\phi}(\tilde{r}_1)} \right) \cdot \tan\tilde{\phi}(\tilde{r}_1) \tag{8.142}$$

which must be negative. As $\tilde{\phi}(\tilde{r}_1) \in (\theta - (\pi/2); (\pi/2))$ and $\tilde{r}_1 < 1$, from (8.142) we have that $\tilde{r}_1 > \sqrt{(1/Bo) \cdot \sin \theta}$, which gives the following limit for the ampoule radius:

$$1 > \sqrt{(1/Bo) \cdot \sin \theta}. \tag{8.143}$$

Moreover, since $(d\tilde{\phi}/d\tilde{r})(\tilde{r}_1) = 0$ the following inequality for the pressure difference is obtained:

$$La < Bo \cdot \tilde{H}_m - Bo \cdot z(\tilde{r}_1). \tag{8.144}$$

Here $\tilde{z}(\tilde{r}_1)$ is unknown but $\tilde{z}(\tilde{r}_1) < 0$, and hence if

$$La < Bo \cdot \tilde{H}_m \tag{8.145}$$

then inequality (8.144) is always satisfied.

In conclusion, for a convex–concave meniscus, the growth angle can be achieved (the crystal can be obtained) if inequalities (8.143) and (8.145) are satisfied. In practice, it is not certain whether the growth angle is always attained; this depends on the material and process parameters.

Numerical results obtained by solving the problem (8.126)–(8.127) for InSb crystals grown under normal gravity by the dewetted Bridgman process for the case $\theta + \alpha = 160^\circ + 25^\circ > \pi$, show that if $La = 50.679 < Bo \cdot \tilde{H}_m = 50.733$ and $1 > \sqrt{(1/Bo) \cdot \sin \theta} = 0.271$, then the meniscus is convex–concave and the growth angle is achieved on the convex part of the meniscus (Figure 8.28).

For the globally concave meniscus $d\tilde{\phi}/d\tilde{r} < 0$, and hence the function $\tilde{\phi}(\tilde{r})$ decreases on the interval (0; 1); because $(\pi/2) - \alpha < \theta - (\pi/2)$ the growth angle cannot be achieved on the globally concave meniscus. Numerical results show that for $La = 51.504 > Bo \cdot \tilde{H}_m = 50.733$ Pa the meniscus is globally concave and the growth angle is not achieved (Figure 8.29).

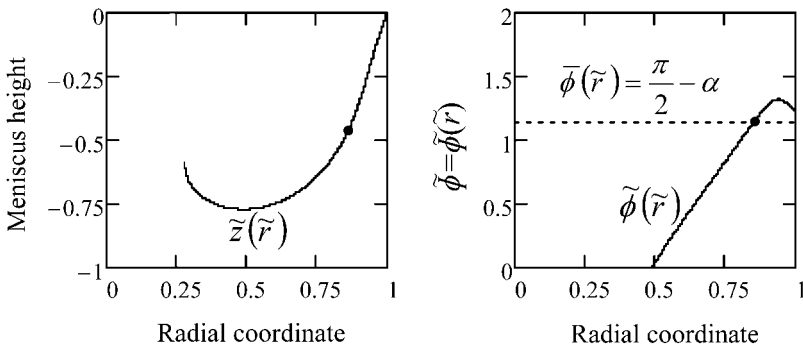


Figure 8.28 Convex–concave meniscus shape $\tilde{z}(\tilde{r})$ and meniscus angle $\tilde{\phi}(\tilde{r})$ corresponding to $La = 50.679$ and $\theta + \alpha = 160^\circ + 25^\circ > \pi$ for InSb, $\tilde{H}_m = 10.9$. The place where the growth angle $(\pi/2) - \alpha = 1.13446$ radians is reached is shown by the black dot.

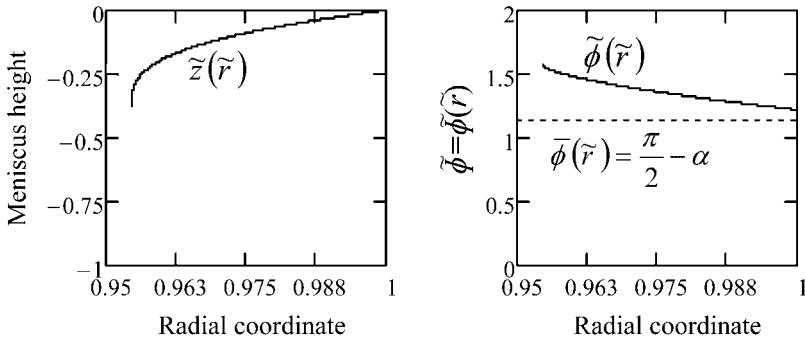


Figure 8.29 Globally concave meniscus shape $\tilde{z}(\tilde{r})$ and meniscus angle $\tilde{\phi}(\tilde{r})$ corresponding to $La = 51.504$ and $\theta + \alpha = 160^\circ + 25^\circ > \pi$ for $InSb$, $H_m = 10.9$. The growth angle $((\pi/2) - \alpha = 1.13446$ radians) cannot be achieved.

The above analytical and numerical studies of meniscus shapes were performed in order to derive the conditions which allow dewetting and lead to a crystal with a constant radius under normal gravity. The results are useful for *in situ* control of the process and show the importance of a careful calculation of the meniscus shapes for the optimization of stable dewetted Bridgman growth.

8.5 Conclusions

In this chapter, mathematical and numerical analyses of the BVP for the Young–Laplace equation have been presented as an essential part of capillarity problems and processes. First, a mathematical formulation of the capillary problem and the BVP for the Young–Laplace equation in the three-dimensional and axisymmetric cases was presented.

After that, the problems were formulated for the Cz, EFG and dewetted Bridgman growth techniques. For the configurations and specific boundary conditions considered, analytical solutions of the meniscus were found in some special cases. Due to the high nonlinearity of these problems in general cases, the solutions were approached qualitatively and proved by numerical computations using the Runge–Kutta method. From these analytical and numerical studies, information useful for practical crystal growers was reported: meniscus shapes for different growth conditions, the range of some parameters for which the growth angle is achieved (i.e. a crystal is obtained), the dependencies between the meniscus height and the crystal thickness. A relevant computer program (in Mathcad) is presented in the Appendix .

Because of the nonlinearity of the Young–Laplace equation, no simple solution of the problem exists in most cases. It is always necessary to perform a qualitative analysis, which is problem dependent. After that a numerical solution can be sought. However, as shown for the Cz technique, there are configurations for which no exact solution is available.

Appendix: Runge–Kutta Methods

The Runge–Kutta methods are single-step methods which approximate solutions of first-order differential equations (or systems) with given initial conditions. They are based on the Taylor series method in which derivatives are approximated by the forward difference and at the same time, keep the desirable property of higher-order local truncation error [Braescu 2008–1]. These facts imply a better convergence to the solution.

In practice, there are some particular forms of the Runge–Kutta method: the second-order method RK2, the third-order method RK3, the fourth-order (standard) method RK4 and the fifth-order Runge–Kutta–Fehlberg method RKF5. The RK4 method is discussed in more details in the next section, as it is the most commonly used.

A.1 Fourth-Order Runge–Kutta Method (RK4)

Considering the initial value problem:

$$y'(x) = f(x, y)$$

$$y(x_0) = y_0$$

where $f: (a; b) \times (c; d) \rightarrow \mathbb{R}$ is an indefinite derivable function and $x_0 \in (a; b)$, $y_0 \in (c; d)$. The solution $y(x)$ of IVP can be computed numerically using RK4 method along the interval $[x_0; x_N]$ which is divided in N equidistant subintervals. The RK4 method for this problem is summarized by the following equation with differences:

$$y_i = y_{i-1} + \frac{1}{6}(k_1 + 2k_2 + 2k_3 + k_4), i = 1, \dots, N$$

where $x_i = x_{i-1} + h$, $i = 1, \dots, N$, h represents the step-size (equidistant nodes are considered), $h = \frac{x_N - x_0}{N}$; x_N is the end value of the interval; x_0 is the first value of the interval, N represents the number of the solution values in the interval $[x_0, x_N]$; y_i is the approximation of $y(x_i)$; and ...

$$k_1 = h \cdot f(x_{i-1}, y_{i-1}),$$

$$k_2 = h \cdot f\left(x_{i-1} + \frac{h}{2}, y_{i-1} + \frac{k_1}{2}\right),$$

$$k_3 = h \cdot f\left(x_{i-1} + \frac{h}{2}, y_{i-1} + \frac{k_2}{2}\right),$$

$$k_4 = h \cdot f(x_{i-1} + h, y_{i-1} + k_3).$$

Thus the current value y_i is determined by the previous value y_{i-1} , to which is added an estimated slope $\frac{1}{6}(k_1 + 2k_2 + 2k_3 + k_4)$ which represents the weighted average of slopes:

- k_1 is the slope at the beginning of the interval;
- k_2 is the slope at the midpoint of the interval, using the slope k_1 for determining the value of y at the point $x_{i-1} + (h/2)$ by Euler's method (first-order Runge–Kutta method);

- k_3 is the slope at the midpoint of the interval, but now using the slope k_2 for determining the value of y at the point $x_{i-1} + (h/2)$ by Euler's method;
- k_4 is the slope at the end of the interval with its y -value predicted by k_3 .

In summary, each value of k_i gives an estimate of the size of the y -jump made by the actual solution across the whole width of the interval. The first one uses Euler's method, the next two use estimates of the solution slope at the midpoint, and the last one uses an estimate of the slope at the endpoint. Each k_i uses the earlier k_i as a basis for its prediction of the y -jump. The local truncation error for RK4 is of the order $O(h^5)$.

A.1.1 RK4 Procedure

Input a, b, c, N, f // a, b, c are the problem-dependent values of x_0, x_N and y_0 //

Runge-Kutta4(c, a, b, N, f)

```

 $x_0 \leftarrow a$ 
 $x_N \leftarrow b$ 
 $y_0 \leftarrow c$ 
 $h \leftarrow \frac{|x_N - x_0|}{N}$ 
for  $i \in 1..N$ 
     $k_1 \leftarrow h \cdot f(x_{i-1}, y_{i-1})$ 
     $k_2 \leftarrow h \cdot f\left(x_{i-1} + \frac{h}{2}, y_{i-1} + \frac{k_1}{2}\right)$ 
     $k_3 \leftarrow h \cdot f\left(x_{i-1} + \frac{h}{2}, y_{i-1} + \frac{k_2}{2}\right)$ 
     $k_4 \leftarrow h \cdot f(x_{i-1} + h, y_{i-1} + k_3)$ 
     $y_i \leftarrow y_{i-1} + \frac{1}{6}(k_1 + 2k_2 + 2k_3 + k_4)$ 
     $y_i \leftarrow y_{i-1} + h$ 
augment  $(x, y)$ 
    
```

S: = Runge-Kutta4(c, a, b, N, f).

This method is relatively easy to implement and gives good accuracy, but as it is a constant step size method, the calculation time may become very long, especially if a very small step size is needed. Thus, in order to reduce computation time, an *adaptive step size* version of the Runge-Kutta method can be used. The general formula for the adaptive step size Runge-Kutta method is given by:

$$y_{i+1} = y_i + \sum_{n=1}^6 c_n k_n$$

where:

$$k_1 = h \cdot f(x_i, y_i)$$

$$k_n = h \cdot f \left(x_i + a_n \cdot h, y_i + \sum_{m=1}^{n-1} b_{nm} k_m \right), n = 2, \dots, 6$$

with local truncation error of order $O(h^6)$.

Several sets of a_n , b_{nm} and c_n coefficients and computer algorithms for implementation of this method were reported, e.g. those suggested by Cash and Karp [Cash 1990].

Thus, in the *adaptive Runge–Kutta* method, the step size is controlled so that the results are within the desired accuracy. This is why the numerical computations in Chapter 8 are performed using the *adaptive RK4 method*.

Runge–Kutta methods are available in all standard computer mathematical toolboxes such as Matlab, Mathcad, Mathematica, Maple etc. The use of a Runge–Kutta fourth-order method with fixed integration step (a routine called *rkfixed*), and with step-size adaptation (*Rkadapt*) is shown here for Mathcad.

A.2 Rkfixed and Rkadapt Routines for Solving IVP

The case of cylindrical rods grown in zero gravity using the EFG technique (the configuration presented in Figure 8.14) is considered as an example. Equation (8.86) with the initial condition (8.81) is solved numerically and the solutions obtained using the routines *rkfixed* and *Rkadapt* are compared with the analytical solution (8.87).

Thus, the following IVP is solved numerically:

$$\frac{dz}{dr}(r) = -\frac{r_{0i} \cdot \sin \phi_c}{\sqrt{r^2 - (r_{0i} \cdot \sin \phi_c)^2}} \quad (\text{A8.1})$$

$$z(r_{0i}) = 0 \quad (\text{A8.2})$$

The exact solution represents the analytical expression of the meniscus as function of the parameter ϕ_c :

$$z(r) = r_{0i} \cdot \sin \phi_c \cdot \ln \frac{r_{0i} (1 + \cos \phi_c)}{r + \sqrt{r^2 - r_{0i}^2 \cdot \sin^2 \phi_c}}, \quad r \in (r_{0i} \cdot \sin \phi_c, r_{0i}] \quad (\text{A8.3})$$

The obtained solution of *rkfixed* and *Rkadapt* routines is a matrix with two columns (independent variable values, and the corresponding solution function values). The arguments list of these procedures is as follows:

$$\text{rkfixed}(\text{init}, x_1, x_2, N, D) \text{ and } \text{Rkadapt}(\text{init}, x_1, x_2, N, D)$$

where:

- *init* is either a vector of n real initial values, where n is the number of unknowns, or a single scalar initial value, for a single ordinary differential equation (ODE);
- x_1 and x_2 are real, scalar initial and end points of the interval over which the solution to the ODE(s) will be evaluated;
- N is the integer number of points beyond the initial point at which the solution is to be approximated;

- D is a derivative vector function of the form $D(x, y)$ specifying the right-hand side of the system.

A.2.1 Example of Implementation in Mathcad

```

r0i := 0.002 [m]
phi_c := 1.3 [rad]
a := r0i; c := 0 // initial value given at the beginning of the interval //
b := r0i * sin(phi_c) + 10^-9 // final value of the interval //
N := 1000 // number of the solution value in the interval [a, b] //
init := c

D(x, y) := (-r0i * sin(phi_c) / sqrt(x^2 - (r0i * sin(phi_c))^2))

S_fixed := rkfixed(init, a, b, N, D)
R_fixed := S_fixed^(0)  Z_fixed := S_fixed^(1)
S_adapt := Rkadapt(init, a, b, N, D)
R_adapt := S_adapt^(0)  Z_adapt := S_adapt^(1)
    
```

S_fixed =			S_adapt =		
	0	1		0	1
...
990	0.001927846	0.000475318	990	0.001927846	0.000475318
991	0.001927773	0.000478036	991	0.001927773	0.000478036
992	0.0019277	0.000480909	992	0.0019277	0.000480909
993	0.001927628	0.000483968	993	0.001927628	0.000483968
994	0.001927555	0.000487253	994	0.001927555	0.000487253
995	0.001927482	0.000490826	995	0.001927482	0.000490826
996	0.001927409	0.000494776	996	0.001927409	0.000494776
997	0.001927336	0.000499258	997	0.001927336	0.000499258
998	0.001927263	0.00050457	998	0.001927263	0.00050457
999	0.00192719	0.000511483	999	0.00192719	0.000511479
1000	0.001927117	0.000532588	1000	0.001927117	0.000526005

A.2.2 Conclusion

Comparing the solution obtained by *rkfixed* (i.e. RK4), *Rkadapt* and the analytical solution, it is easy to see that *Rkadapt* gives better results. In seeking the computed value of the function at the endpoint b of the interval, it can be observed that the difference between the exact solution and the approximate solutions are in the fourth digit for *rkfixed*, and the sixth digit for *Rkadapt*. Note that the error can be decreased by increasing N .

The *exact solution* is given by Equation (A8.3). At the end point of the interval the exact solution is:

$$z(b) = z(r_{0i} \cdot \sin(\phi_c) + 10^{-9}) = 0.0005263903.$$

The *approximate solution* given by the *rkfixed* routine, computed at the endpoint *b*, is:

$$z_{\text{fixed}} = 0.000532588 \text{ // the last value from the table S_fixed corresponding to } b \text{ //}$$

The *approximate solution* given by the *Rkadapt* routine, computed at the endpoint *b*, is:

$$z_{\text{adapt}} = 0.000526005 \text{ // the last value from the table S_adapt corresponding to } b \text{ //}$$

After plotting the menisci obtained numerically (Figure A8.1a), it is difficult to see a difference of the order of the fourth or sixth digit and for this reason an enlarged image is shown in Figure A8.1b.

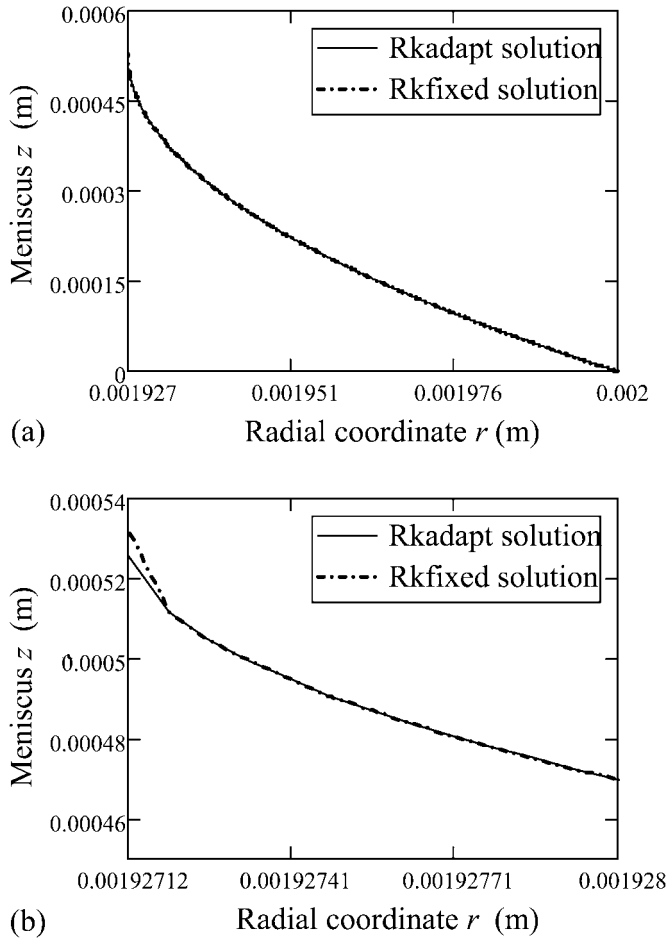


Figure A8.1 (a) Approximated menisci obtained by RK4 (dotted line) and adaptive RK4 (full line). (b) Approximated menisci obtained by RK4 (dotted line) and adaptive RK4 (enlargement of Figure A8.1a).

References

- [Balint 2005] Balint S., Braescu L., Balint A.M., Szabo R., *J. Cryst. Growth* **283** (2005) 15.
- [Balint 2008] Balint S., Braescu L., Sylla L., Epure S., Duffar T., *J. Cryst. Growth* **310** (2008) 1564.
- [Bardsley 1974] Bardsley W., Cockayne B., Green G.W., Hurle D.T.J., Joyce G.C., Roslington J.M., Tufton P.J., Webber H.C., Healey M., *J. Cryst. Growth* **24–25** (1974) 369.
- [Bardsley 1977-1] Bardsley W., Hurle D.T.J., Joyce G.C., *J. Crystal Growth* **40** (1977) 13.
- [Bardsley 1977-2] Bardsley W., Hurle D.T.J., Joyce G.C., Wilson G.C., *J. Cryst. Growth* **40** (1977) 21.
- [Borodin 1979] Borodin V.A., Brener E.A., Tatarchenko V.A., *Acta Phys. Sci. Hungar.* **47** (1979) 151.
- [Boucher 1980] Boucher E.A., Jones T.G.J., *J. Chem. Soc. Faraday I* **76** (1980) 1419.
- [Braescu 2003] Braescu L., Balint A.M., Balint S., *J. Cryst. Growth* **259** (2003) 121.
- [Braescu 2004-1] Braescu L., Balint A.M., Balint S., *J. Cryst. Growth* **268** (2004) 284.
- [Braescu 2004-2] Braescu L., Balint A.M., Balint S., *J. Cryst. Growth* **269** (2004) 617.
- [Braescu 2005] Braescu L., *Nonlinear Stud.* **12**(4) (2005) 361.
- [Braescu 2008-1] Braescu L., Balint St., Bonchis N., Kaslik E., *Numerical Methods* (undergraduate course in English), West University Publishing House, Timisoara, Romania (2008).
- [Braescu 2008-2] Braescu L., *J. Colloid Interface Sci.* **319** (2008) 309.
- [Brener 1979-1] Brener E.A., Tatarchenko V.A., *Acta Phys. Sci. Hungar.* **47** (1979) 133.
- [Brener 1979-2] Brener E.A., Tatarchenko V.A., *Acta Phys. Sci. Hungar.* **47** (1979) 139.
- [Cash 1990] Cash J.R., Karp A.H., *ACM Trans. Math. Software* **16** (1990) 201–222.
- [Clanet 2002] Clanet C., Quere D., *J. Fluid Mech.* **460** (2002) 131.
- [Dijk 1974] Dijk H.J.A., Goorissen J., Gross U., Kersten R., Pistorius J., *Acta Electron.* **17** (1974) 45.
- [Duffar 1997] Duffar T., Boiton P., Dusserre P., Abadie J., *J. Cryst. Growth* **179** (1997) 397.
- [Duffar 2000] Duffar T., Dusserre P., Picca F., Lacroix S., Giacometti N., *J. Cryst. Growth* **211** (2000) 434.
- [Epure 2010] Epure S., PhD Thesis, Grenoble Institute of Technology, France and West University of Timisoara, Romania (2010).
- [Ferguson 1912] Ferguson A., *Phil. Mag.* **24** (1912) 837.
- [Finn 1986] Finn R., *Equilibrium capillary surfaces*, Springer-Verlag, New York (1986), pp. 1–16.
- [Gartner 1972] Gartner K.J., Rittinghaus K.F., Seeger A., Uelhoff W., *J. Cryst. Growth* **13–14** (1972) 619.
- [Gartner 1973] Gartner K.J., Uelhoff W., *Optik* **37** (1973) 15.
- [Hartland 1976] Hartland S., Hartley R.W., *Axisymmetric Fluid-Liquid Interfaces*, Elsevier, Amsterdam (1976).
- [Hauksbee 1709] Hauksbee F., *Physico-Mechanical Experiments*, London (1709), pp. 139–169.
- [Hernandez-Baltazar 2005] Hernandez-Baltazar E., Gracia-Fadrique J., *J. Colloid Interface Sci.* **287** (2005) 213.
- [Huh 1969] Huh C., Scriven L.E., *J. Colloid Interface Sci.* **30** (1969) 323.
- [Hurle 1981] Hurle D.T.J., *Advances in Colloid and Interface Science* **15** (1981) 101.
- [Hurle 1983] Hurle D.T.J., *J. Crystal Growth* **63** (1983) 13.
- [Johansen 1987] Johansen T.H., *J. Crystal Growth* **80** (1987) 343.
- [Johansen 1992] Johansen T.H., *J. Cryst. Growth* **118** (1992) 353.
- [Johansen 1994] Johansen T.H., *J. Crystal Growth* **141** (1994) 484.
- [Landau 1971] Landau L.D., Lifchits E.M., *Mécanique des Fluides* (Mir, Moscow, 1971 (in French)).
- [Laplace 1806] Laplace P.S., *Traité de Mécanique Céleste; Suppléments au Livre X, Oeuvres Complètes Vol. 4*, Gauthier-Villars, Paris (1806).
- [Mika 1975] Mika K., Uelhoff W., *J. Crystal Growth* **30** (1975) 9.
- [Nutt 1960] Nutt C.W., *Chem. Eng. Sci.* **12** (1960) 133.

- [O’Kane 1972] O’Kane D.F., Kwap T.W., Gulitz L., Bednowitz A.L., *J. Cryst. Growth* **13–14** (1972) 624.
- [Princen 1965] Princen H.M., Mason S.G., *J. Colloid Sci.* **20** (1965) 246.
- [Sachs 1980] Sachs E.M., Surek T., *J. Cryst. Growth* **50** (1980) 114.
- [Sylla 2008-1] Sylla L., Duffar T., *Mater. Sci. Eng. A* **495** (2008) 208–214.
- [Sylla 2008-2] Sylla L., *PhD thesis, INP-Grenoble* (2008) (in French).
- [Tatartchenko 1993] Tatarchenko Y.A., *Shaped Crystal Growth*, Kluwer, Dordrecht (1993), pp. 19–167.
- [Tsivinski 1962] Tsivinski S.V., *Inzheherno Fiz. Zhur.* **5** (1962) 59.
- [Young 1805] Young T., *Phil. Trans. R. Soc. London* **95** (1805) 65.

Index

Note: page numbers in italics refer to figures and tables

- actuator performance analysis 154–6
- ADC (automatic diameter control) 116
- adhesion energy 3, 6, 11
 - halide/ceramic systems 27
 - oxide/metal systems 26
 - vertical Bridgman (VB) technique 360–3
- alloys
 - contact angles 15, 19, 21, 22–4, 22, 24, 25
 - dewetted vertical Bridgman (VB) technique 380, 381, 382
 - shaped crystal growth 110
 - surface tension vs composition 416, 417
 - thermocapillary convection 224, 459, 459, 460
 - see also* intermetallics *and under the names of specific alloys*
- aluminium components 106
- aluminium nitride substrates 23, 24
- aluminium oxide
 - crystal growth 70, 71, 76, 77, 78, 79
 - surface tension 18
- automated control *see* control systems
- automated crystal seeding 320–1
- automatic diameter control (ADC) 116

- batch disturbance rejection 194, 196–8, 198, 199
- Biot numbers 206, 206
- Bond number 59, 73, 415
- boron nitride substrate 24–5, 25
- boron oxide layer 24, 117–18, 138
- boron trioxide encapsulant 367, 371–2, 373
- borothermic reactions 230
- Bridgman method *see* vertical Bridgman (VB) technique
- Burton–Prim–Slichter equation 100–1

- cadmium telluride
 - contact angles 19, 21, 25
 - surface tension 18

- calcium chloride encapsulant 367
- capillarity, definitions 1–4
- capillary constant 60
- capillary crystal tubes 331–2, 332, 333
- capillary flow *see* Marangoni convection
- capillary length 3, 135
- capillary pressure 3
- capillary problem 59–62
 - mathematical formulation 468–76
 - TPS 81–92
- capillary shaping techniques (CST) 51–3
 - classification of methods xxviii
 - schematic representation 62
 - see also under the names of particular techniques*
- capillary stability *see* dynamic stability
- carbon-based substrates 21–3, 22, 23, 26, 27, 27
- carbothermic reactions 230
- Cassie's equation 12
- chemical contamination 397–9, 398, 399
 - see also* oxygen partial pressure
- chemocapillary convection 414
- classification of methods xxviii
- closed-loop simulations 160, 161
- composite materials, contact angles 11–12, 12
 - contact angles 4–27
 - composite materials 11–12, 12
 - composite wetting 9–10, 10
 - dynamics of wetting 12–16
 - halide/ceramic systems 27
 - heterogeneous surfaces 11–12, 11, 12
 - hysteresis 9
 - measurement 16–17, 17
 - metastable and stable 6, 7
 - molten metals on oxides 18–20
 - oxide/carbon systems 26
 - oxide/metal systems 18–20, 25–6, 26, 27
 - roughness effect 8–11, 9, 10

- semiconductors
 - on carbon-based substrates 21–3
 - on nitrides 23–5
 - on oxides 17–21, 19
- sharp edges effect 8–9, 8
- sticking 11
- system size effects 6
- thermodynamics 5–12
- vertical Bridgman (VB) technique 358–60, 360, 361
- Young's and Young–Dupré equations 5–6
- contamination *see* chemical contamination
- control systems
 - actuator performance analysis 154–6
 - components 122–3, 122
 - control inputs 124
 - Czochralski technique 124–32
 - feedforward control 125–6
 - FZ technique 264, 266–7
 - measurement issues 130–2
 - model-based 123–4, 126–7, 127–9
 - multiloop control system 127–8
 - vs PID control 121–2
 - PID control approaches 161–70, 162, 164
 - process dynamics analysis 150–4
 - shaped crystal growth 319–32
 - capillary crystal tubes 331–2
 - stability 127
 - stability analysis-based 78–80, 79
 - Verneuil technique 78–80
- convective flow *see* Marangoni convection
- copper
 - capillary shaping 95–7
 - growth angles 36
- core-doped fibres 316–19, 317, 318
- corundum *see* aluminium oxide
- crystal diameter measurement 117–18
- crystal interface height
 - heater power relation 151
 - pulling speed relation 151–2, 152
- crystal interface radius
 - control based on 161–3
 - heater power relation 151, 154–6, 155, 156, 157
 - pulling speed relation 151–2, 152, 153, 154–6, 154, 156, 157
- crystal length
 - hydromechanical–geometrical model 134–5
 - parametized control model 171–6
- crystal radius
 - and differential weight gain 119
 - flatness-based controller 175–81, 178, 179
 - and growth rate 118, 175–81, 180
 - measurement issues 130–1
- crystal seeding, automated 320–1
- crystal slope angle 29–30, 62–3, 133, 137
- crystal surface modelling 261–2, 261, 263
- crystal surface orientation
 - thermal behaviour modelling 147–8, 147
 - thermal–geometry interactions 157–60, 159, 160
- crystallization front displacement rate 63
- curved interface shape 143–4, 143, 157, 158
- FZ technique 222
 - nonlinear observer design 192–3, 193
- cylindrical crystals
 - edge-defined film-fed growth (EFG) 493–500, 496, 499
 - Verneuil technique 76, 77
- Czochralski technique
 - advanced techniques 181–98
 - analytical-numerical model 449–52, 450, 451, 476–86
 - capillary shaping parameters 66, 68
 - capillary stability 68–9
 - control approaches 124–32
 - control issues 116–24
 - crystal growth furnace 144
 - defect structures 69–70
 - dynamic stability 55, 57, 65–9
 - gas bubbles 246, 247, 297, 298
 - growth striations 191, 193, 195
 - heat stability 65
 - linear observer design 182–3
 - meniscus surface equation 476–86
 - model-based control 126
 - nonlinear observer design 183–94, 187, 190, 195
 - origin xxiii, xxv
 - schematic representation 53
 - shaped crystal growth 69
 - stability analysis 65–9
 - temperature distribution 65–8
 - thermocapillary convection 448–56, 452
 - magnetic field damping 451–6, 453, 454, 455, 456
 - vapor pressure controlled 117, 118
 - see also* liquid encapsulated Cz (LEC) method
- Czochralski–Gomperz technique 107
- defect structures 54
 - Czochralski technique 69–70
 - edge-defined film-fed growth (EFG) 285–6, 286
 - FZ technique 208, 210, 210
 - micro-pulling down technique (μ -PD) 342
 - vertical Bridgman (VB) technique 361, 362, 363

- dendritic web growth 280, 286–8, 287
- dewetted vertical Bridgman (VB) technique 373–408, 375
- chemical contamination 397–9, 398, 399
- configurations 394
- crucible material and wetting properties of melt 388–9
- crucible roughness effect 377, 378, 379, 395–7, 395, 396
- gallium antimonide 383, 385
- germanium 380–2
- growth atmosphere and pollution 390–3, 391
- growth velocity 392
- indium antimonide 383–6
- interface shape 392–4, 394
- meniscus shape 506, 507, 508, 513, 515, 516, 517
- meniscus surface equation 500–17
- microgravity conditions 374–8, 397–401
- modelling 394–404, 500–17
- normal gravity conditions 378–9, 388, 388–94
- pressure difference across meniscus 389, 399–402, 400
- residual gases 402–3, 404
- sample and growth procedure 390
- schematic 501
- stability analysis 401, 404–7, 405
- surface morphology 388, 389, 392
- surface ridges 376, 376, 377
- diameter control 116–17
- diameter measurement 117–18
- dislocation defects
- edge-defined film-fed growth (EFG) 285
 - FZ technique 208, 210, 210
 - micro-pulling down technique (μ -PD) 342
 - vertical Bridgman (VB) technique 361, 362, 363
- distributed-parameter models 126–7
- dopant distribution
- core-doped fibres 316–19
 - periodically doped structures 312–15, 313
 - time dependency 415
 - see also* dopant striations
- dopant striations
- FZ technique 219, 418, 419, 435, 438
 - magnetic field effect 445
 - vibration effect 446, 447
- dynamic stability 54–65
- Czochralski technique 65–9
 - FZ technique 80–1, 225
 - Kyropoulos technique 69–70
 - TPS 55, 57, 81–93
 - Verneuil technique 57, 71–80
- edge stabilized/supported ribbon *see* String Ribbon™
- edge-defined film-fed growth (EFG) 107, 278, 278, 280, 297, 298
- analytical-numerical model 284, 486–500
 - applicable materials 279
 - core-doped fibres 318
 - cylindrical crystals 493–500, 493, 496, 499
 - defect structures 285–6, 286
 - gas bubbles 297, 298
 - meniscus surface equation 486–500
 - periodically doped structures 312–13, 313
 - polygonal crystals 282–3
 - sapphire crystals 293–4
 - sheets, crystal 486–93, 487, 488, 492
 - Si crystals 281–6, 283
 - thermocapillary convection 456–7
- electrodynamical forces, RF-induced 218–19, 222, 223, 225
- EM field modelling 254
- encapsulation *see* liquid encapsulation
- equipment–process model 144–6, 145
- external triple point (ETP) modelling 253, 253
- feedback controller 121, 122, 123, 172–6
- feedforward control 122, 123, 125–6
- flatness-based controller 172–5, 175, 179, 180, 181
- floating zone (FZ) crystal growth *see* FZ technique
- force acting on the load cell 130–1, 138–9
- forces acting on the melt zone 210–11
- forward problem (control systems) 125
- Froude number 59
- FZ technique 203–70
- alternative heating methods 242
 - applicable materials 204, 205
 - basic process 208–10, 209
 - configurations 205
 - control systems 266, 266–7
 - dopant striations 219, 418, 419, 435, 438
 - dynamic stability 80–1, 225
 - experiment and numerical results compared 216–20, 218
 - forces acting on the melt zone 210–11
 - grid processing algorithms 262, 263, 264–5
 - growth angle 38–9, 211, 212
 - growth striations 219, 418
 - heat balance 206
 - image furnaces 230–40, 237, 238
 - laboratory reference system (LRS) 249
 - laser heating 240–1
 - machine in operation 217
 - maximum zone height 204–6, 205
 - melting the feed rod 208, 213–14, 214

- metallic melts 220–30, 220, 221
 - ambient atmosphere effect 228–30
 - convective flow 222–6, 223
 - curved interface shape 222
 - melt composition changes 226, 227, 228
 - melt refining 229–30
 - metal–vapour reactions 229–30
 - temperature distribution 221
 - travelling solvent method (TSFZ) 226–8
 - modelling 247–70, 266, 267
 - molten zone shape 249–57, 256, 257, 258
 - needle-eye process 208–14, 209, 247–70
 - numerical analysis 247–70
 - optical and RF induction heating
 - compared 225–6, 226
 - origin *xxv*, *xxvii*
 - pedestal method 205, 206, 214–15, 215
 - quasi-square cross-section crystals 215–16, 216
 - RF heating 207–30, 209, 250
 - schematic representation 55
 - set up 207–8, 220
 - shape stability 80–1, 211–13, 213
 - silicon 207–20
 - solutocapillary convection 460
 - thermocapillary convection 223–5, 223, 417–48
 - vertical cross-section 250
- gallium antimonide
 - contact angles 19, 21, 24, 25
 - dewetted crystal growth experiments 383, 385
 - growth angles 36
 - surface tension 18, 416
 - gallium antimony alloy
 - contact angles 21
 - surface tension vs composition 416, 417
 - gallium arsenide
 - capillary shaping 99–100
 - contact angles 19, 25
 - growth angles 36
 - surface tension 18, 416
 - gallium indium antimony alloy 377
 - gallium indium arsenic alloy, contact angles 22
 - gas bubbles 297, 298
 - FZ technique 246, 247
 - growth from an element of shape (GES) 309
 - variable shaping technique (VST) 303
 - Gemini (dual ribbon growth) 289, 289
 - germanium
 - capillary shaping 99–100
 - contact angles
 - carbon-based substrates 23
 - nitride substrates 23–4, 24, 25
 - oxide substrates 19, 20, 20, 21
 - dewetted crystal growth experiments 380–2
 - growth angles 36
 - shaped crystal growth 105, 108
 - surface tension 18, 416
 - germanium antimony alloy 380, 381, 382
 - germanium gallium alloy 380, 381
 - germanium silicon alloy
 - composition and surface tension 416
 - contact angles 15, 19, 22, 23–4, 24, 25, 25
 - thermocapillary convection 459, 459, 460
 - GES *see* growth from an element of shape (GES)
 - Gomperz's method *xxiii*, *xxvi*
 - growth angles 28–44
 - boundary condition 61–2
 - constant growth angle approximation 39–40
 - estimation and verification 40–4
 - FZ technique 38–9, 211, 212
 - interfacial energies 29–35
 - mathematical representation 40, 40
 - measurement 35–8
 - nonconstant 193–4, 194
 - relative orientations of the three interfaces 34
 - in simulations of crystal growth 38–44
 - values for various materials 36
 - growth from an element of shape (GES) 307–12
 - growth striations 309
 - multicomponent oxide crystal growth 313–14, 313
 - periodically doped structures 313–15, 315, 316
 - sapphire 308, 310, 311
 - growth rate 30, 38
 - calculation 189
 - control 117, 128–9, 176–81, 178, 179
 - and crystal radius 118, 175–81, 180
 - fluctuations 435, 436, 437
 - hydromechanical–geometrical model 134, 137
 - thermal behaviour modelling 142
 - growth striations
 - Czochralski technique 191, 193, 195
 - FZ technique 219, 418, 435–9, 440, 441
 - GES 309
 - Marangoni convection 415
 - vertical Bridgman (VB) technique 393
- halide/ceramic systems, contact angles 27
 - heat transfer modelling 41
 - Czochralski technique 119–21, 146–7

- FZ technique 206, 222–4, 254–5
 vertical Bridgman (VB) technique 357–8
- heater power
 control input 124, 128–9, 151, 154–6, 155, 156, 157, 179
 crystal interface radius relation 151–2, 155, 156, 157
- Herring equation 28, 33
- horizontal ribbon growth (HRG) 292
- hydromechanical–geometrical model 133–42
 assumptions 133
 nonlinear model-based control 171–6
 quantities used 134
- image furnaces 230–40, 231, 233
 control systems 234–6
 FZ technique 230–40, 237, 238
 light sources 232, 234
 mirror focusing properties 234, 235
 mirror materials 232, 234
 temperature measurements 234–5, 239–40
- image processing 130
- impurity distribution
 Czochralski technique 448
 FZ technique 225
 time dependency 415
 TPS 100–3, 101, 103, 104
see also growth striations
- indium antimonide
 contact angles 19, 25
 dewetted crystal growth experiments 383–6
 growth angles 36
 surface tension 18
- indium phosphide
 contact angles 19, 25
 growth angles 36
- interface shape modelling 143–4, 143
 oxide melts 243–5, 243, 244
- interfacial attachment 44
- interfacial energies 1–3, 4
 growth angles 19–35
 vertical Bridgman (VB) technique 360–1, 359
- intermetallics
 FZ technique 220–30, 220, 221
 ambient atmosphere effect 228–30
 convective flow 222–6, 223
 curved interface shape 222
 melt composition changes 226, 227, 228
 melt refining 229–30
 metal–vapour reactions 229–30
 temperature distribution 221
 travelling solvent method (TSFZ) 226–8
- internal triple point (ITP) modelling 253–4, 253, 254
- inverse problem (control systems) 125
- Kronecker delta 58
- Kyropoulos technique 53, 69–70
- Laplace capillary equation 3, 3, 60
- Laplace constant 135
- laser heated pedestal growth (LHPG) 346
- laser heating 240–1, 241, 245
- lateral photovoltage scanning (LPS) 219–20, 219
- lift ratio 171, 173, 175, 176–7
- linear observer design 182–3
- linear system model analysis 148–50
 comparison with nonlinear modelling 148, 149, 155–6
 controller choice 154
 dynamic characteristics 152–4, 153, 155
 full state and second-order 151–2, 151
- liquid encapsulated Cz (LEC) method 117
 hydromechanical–geometrical model 135, 138–9
 nonlinear control design 172, 178, 180, 181
 nonlinear observer design 188, 191, 191
 weight-based control 165
- liquid encapsulation
 VB technique 366–73
 crystals grown 367
 solid–liquid–salt triple point region 370
 surface and wetting properties 370
- liquid/vapour interface 4, 29
see also meniscus shape
- lithium chloride–potassium chloride
 encapsulant 367, 368–71, 369
- lithium fluoride
 growth angles 36
 surface tension 18
- lithium niobate
 growth angles 36
 micro-pulling down technique (μ -PD) 344–6, 345, 346
 surface tension 18
- local shaping technique (LST) 308
- Luenberger observer 182–3
- lumped-parameter models 125, 126, 128–9
- Lyapunov equations 57–8
- magnetic fields
 thermocapillary convection damping
 Czochralski technique 449, 451–6, 453, 454, 455, 456
 FZ technique 443–5, 444, 446

- Marangoni convection 223–4, 223, 413–60
 azimuthal temperature distribution 431–2, 432
 centrifugal instability 429
 Czochralski technique 448–56, 452
 damping 443–8
 magnetic fields 443–5, 444, 446
 vibration 445–6, 447
 edge-defined film-fed growth (EFG) 456–7
 elliptic instability 429, 430
 experimental set up 425, 425, 426, 427, 439
 flow and temperature fields 423, 423
 flow transitions 426–9, 428
 fluid dynamics 422–35
 full float zones 435
 FZ technique 417–48
 growth rate fluctuations 435, 437, 438
 growth striations 415
 half-zone model 417, 418, 422–35, 422, 424
 instability mechanisms 429–31, 430, 431
 magnetic field damping 443–5, 444, 446
 mode appearance coefficient (MAC) 432–3, 433
 numerical simulations 439–41
 oscillatory flow 415, 426, 428, 429, 431, 434
 frequency 433–5, 434
 oxide melts 244–5, 244
 oxygen partial pressure effect 419–22, 421
 partially confined half-zone (PCHZ)
 configuration 429–31, 430
 schematic representation 414, 418
 solutocapillary convection 457–60, 459
 supercritical Marangoni numbers 431–5
 temperature oscillations 431–2, 432, 435, 436
 three-dimensional numerical
 simulations 439–41, 442
 vertical Bridgman (VB) technique 362–3, 364, 457
 vibration damping 445–6, 447
- Marangoni number 414–15
 critical 415, 435–41
 vs the Prandtl number 441, 442
 flow transitions 426
 supercritical 431–5
- materials
 edge-defined film-fed growth (EFG) 279
 FZ technique 204, 205
 micro-pulling down technique (μ -PD) 334–5
- mathematical models 123–4, 132–50, 465–517
 capillary problem 468–76
 Czochralski technique 476–86
 dewetted vertical Bridgman (VB)
 technique 395–405, 500–17
 edge-defined film-fed growth (EFG) 284, 285, 486–500
 meniscus problem 38–44, 472–6
 melt volume 259, 260
 melting temperatures 206
 meniscus mass 135–6
 meniscus profile curves 43, 330, 331
 meniscus shape 59–60, 465–7, 466
 Czochralski technique 476–86, 479, 480, 481, 485
 and heat balance 121
 mathematical models 38–44, 133–5, 472–6
- meniscus surface equation 60–1
 Czochralski technique 476–86
 dewetted vertical Bridgman (VB)
 technique 500–17
 edge-defined film-fed growth (EFG) 486–500, 488, 492
- Mesa Crucible 289–90, 290
- metal substrates 25–6, 26, 27, 27
- metallic melts
 contact angles 17–18
 FZ technique 220–30, 220, 221
 ambient atmosphere effect 228–30
 convective flow 222–6, 223
 curved interface shape 222
 melt composition changes 226, 227, 228
 melt refining 229–30
 metal–vapour reactions 229–30
 temperature distribution 221
 travelling solvent method (TSFZ) 226–8
 oxidation 18–19, 20
 wetting behaviour 13–14, 19
- metals 105, 106, 110
- microgravity conditions 205–6
 dewetted vertical Bridgman (VB) technique 374–8, 398–400
 FZ technique 237, 237, 238
 TPS 95–100, 96, 97, 98, 99, 100
- micro-pulling down technique (μ -PD) 333–46, 337
 applicable materials 334–5
 BGO fibre crystals 343, 343, 344
 crucible–melt relation 339–40
 LN fibres 344–6, 345, 346
 meniscus representation 340
 YAG garnet crystals 340–3, 341, 342
- mirror furnaces *see* image furnaces
- model-based control 123–4, 126–7, 127–30
 vs PID control 121–2
- modelling *see* mathematical models
- molten zone shape, FZ technique 249–57, 256, 257, 258
- multiloop control system 127–8

- nitride substrates 23–5, 24, 25
 noncapillary shaping (NCS) 299–307, 299, 300
 core-doped fibres 318–19, 319
 sapphire 301, 302
 domes 305–7, 305, 306
 variable cross-section 303–7, 303, 304
 nonlinear dynamics 157–60, 159, 160, 161
 nonlinear model-based control 170–81
 nonlinear modelling, comparison with linear modelling 148, 149, 155–6
 nonlinear observer design 183–94, 187, 190, 195
 numerical analysis 476–517
 see also mathematical models
- ‘observability’ 132
 ‘observer’ 131–2, 131
 open melting front 252
 optical heating 230–47
 optical imaging 130
 optical material parameters 237–9, 238, 239
 oscillatory flow 225, 426, 429, 431–4, 435
 see also Marangoni convection
 oxide melts 242–7
 ambient atmosphere effect 245–7, 246, 247
 contact angles
 carbon-based substrates 26, 27
 metal substrates 25–6, 26, 27
 convective flow 244
 wetting behaviour 14, 14, 15
 oxide substrates 17–21, 19, 20
 oxygen partial pressure
 contact angle effect 18–19, 20, 21, 26, 392, 399
 FZ technique 245–7
 surface tension relation 416, 421
 thermocapillary convection 419–22
- Péclet–Marangoni number 414
 periodically doped structures 312–15, 313
 phase boundaries 251–4
 photovoltaics (PV) 280, 283, 287
 PID control
 based on crystal radius estimation 161–3, 162, 164
 based on weight measurement 164–70, 165, 166
 FZ technique 266, 266–7, 267
 optimization 169–70
 shaped crystal growth 331–2
 vs model-based control 121–2
 plate-shaped crystals
 automated growth 325–8
 micro-pulling down technique (μ -PD) 337, 338
 Verneuil technique 78
 Prandtl number 222
 Marangoni convection dependence 414, 423–4, 423, 441, 442, 443
 process dynamics analysis 150–4
 pulling speed
 control input 124, 129, 134, 154–6, 177, 179
 crystal interface height relation 151–2, 152
 crystal interface radius relation 151–2, 152, 154–6, 156, 157
 PID-based control 162, 162, 163, 164
 vs melt surface temperature 197
 PV (photovoltaics) 280, 283, 287
- radiation heating 230–41
 radiofrequency heating *see* RF heating
 rare earth (RE)–transition metal
 compounds 204, 230
 reactive spreading 14–16, 15, 16
 semiconductors on carbon-based substrates 22, 23
 semiconductors on nitrides 23–5
 reference trajectory calculation 122
 crystal length parametrized control model 173, 174
 nonlinear observer design 187, 187
 PID control 163, 165, 166
 Reynolds–Marangoni number 414
 RF heating
 FZ technique 207–30, 249–50
 induced electrodynamic forces 218–19, 222, 223, 225
 micro-pulling down technique (μ -PD) 334–5, 338
 RGS (ribbon growth on substrate) 290–2, 291
 RHP (right-half-plane) characteristic 151
 ribbon growth 60–1, 280
 classification of technologies 280–1, 281
 dendritic web growth 286–8, 287
 edge-defined film-fed growth (EFG) 281–2
 FZ technique 80–1
 residual stresses 282
 ribbon edge instability 282
 Si crystals 280–2
 TPS 93, 99–100, 100
 ribbon growth on substrate (RGS) 290–2, 291
 ribbon-to ribbon (RTR) technique 80–1
 right-half-plane (RHP) characteristic 151
 rotation rate
 Czochralski technique 124
 FZ technique 224–5, 244

- roughness *see* surface roughness
- RTR (ribbon-to ribbon) technique 80–1
- ruby 240, 316
- Runge–Kutta Methods 518–22
- sapphire
- core-doped fibres 317, 317, 318
 - edge-defined film-fed growth (EFG) 293–4, 318, 329
 - growth angles 35–6, 36, 94, 94
 - growth from an element of shape (GES) 307–12, 308, 310, 311
 - noncapillary shaping (NCS) 299–307, 301, 302
 - domes 305–7, 305, 306
 - variable cross-section 303–7, 303, 304
 - optical-grade fibre 294
 - periodically doped structures 313
 - shaped crystal growth 292–332, 329
 - TPS 103, 104
 - variable shaping technique (VST) 295–7
 - Verneuil technique 70
- secondary radiation 240
- semiconductors
- adhesion energy 11
 - anomalous behaviour 166–9
 - contact angles
 - on carbon-based substrates 21–3, 22
 - nitrides substrates 23–5, 24, 25
 - oxide substrates 17–21, 19, 20
 - growth angles 31–2
 - surface tension 18
 - wetting behaviour 13–14
 - see also under the names of specific materials*
- sessile drop technique 16–17, 17
- shape stability *see* dynamic stability
- sheets, crystal, EFG technique 486–93, 487, 488, 492
- Siemens process 207
- silica, surface tension 18
- silica substrates 19–21
 - contact angles 17–18, 19
- silicon
- closed shapes 282–6
 - contact angles
 - carbon-based substrates 22, 23
 - nitride substrates 23, 24, 25, 25
 - oxide substrates 19, 20–1
 - dendritic web growth 286–8
 - edge-defined film-fed growth (EFG) 281–6, 283
 - FZ technique 207–20
 - growth angles 36
 - Marangoni convection 419–22, 420, 421
 - ribbon growth 280–2, 285
 - shaped crystal growth 109–10, 109, 279–92
 - String Ribbon™ 288–90, 288, 289
 - surface tension 18, 416, 420–2, 421
 - thermocapillary convection 448
 - TPS 102–3, 103, 104
- Silicon Film™ 290–1
- silicon nitride substrates 23, 24
- silicon on cloth (SOC) 109
- Smith equation 6
- SOC (silicon on cloth) 109
- solid/liquid interface energy 2, 2, 4, 29, 31–2
- solid/liquid interface shape 38–44, 140–1
 - see also* meniscus shape
- solid/liquid/vapour triple phase line (TPL) 5–6, 5, 28
- solid/vapour interface energy 4, 29–31, 31–2
- solid/vapour interface shape 38–44, 44
- solutocapillary convection 414–15, 457–60
- spoke patterns 448–9
- stability analysis *see* dynamic stability
- Stefan condition 41
- Stepanov techniques 107, 277–8, 298
- sticking behaviour 11
 - see also* adhesion energy
- striations *see* growth striations
- String Ribbon™ 288–90, 288, 289
- surface energy 1–2, 4
- surface roughness
 - contact angles 8–11, 9, 10
 - dewetted vertical Bridgman (VB) technique 377, 378, 379, 395–7, 395, 397
- surface tension
 - composition dependence 416, 417
 - and impurities 416, 416, 420–2, 421
 - measurement 16–17, 17
 - temperature dependence 416, 420–2, 421
 - values for various compounds 18
 - vs* surface energy 4
- technique of pulling from shaper *see* TPS
- temperature field 41, 63
 - Czochralski technique 65–8, 143–4
 - FZ technique 219, 220, 221, 250–1, 255, 258, 262
 - image furnaces 235, 240
 - Marangoni convection 423, 432, 432, 441, 452, 454, 455
- temperature measurements 234
- thermal behaviour modelling 142–8, 197–8
- thermal interface curvature 356–8, 357, 358
- thermal-geometry interactions 157–60, 159, 160, 196

- thermocapillary convection *see* Marangoni convection
- Tiller's criterion 225
- TPL *see* solid/liquid/vapour triple phase line (TPL)
- TPS
 - capillary shaping theory 81–92
 - boundary conditions 83, 86, 87, 89, 92
 - capillary coefficients 93
 - experimental tests 94–100
 - definition 104
 - dynamic stability 55, 57, 92–3
 - history 104–8
 - peculiarities 110–11
 - schematic representation 56
 - shaped metal profiles 106
- tracking observer 187
- travelling solvent FZ method (TSFZ) 226–8
- triple phase line *see* solid/liquid/vapour/triple phase line (TPL)
- TSFZ (travelling solvent FZ method) 226–8
- tubular crystals 105, 106
 - automated growth 321–5, 329, 331–2, 331
 - defect structures 285–6, 286
 - edge-defined film-fed growth (EFG) 282–4, 283, 285
 - growth from an element of shape (GES) 308
 - Verneuil technique 77–8, 78
- two shaping elements technique (TSET) 109–10
- two-loop control 176–81, 179, 180, 181
- vapor pressure controlled Czochralski (VCz) method 117, 118
- variable shaping technique (VST)
 - gas bubbles 303
 - sapphire 295–7, 296, 303
- VB technique *see* vertical Bridgman (VB) technique
- VCz (vapor pressure controlled Czochralski) method 117, 118
- Verneuil technique 70–1
 - capillary shaping parameters 72, 73, 75
 - cylindrical crystals 76, 77
 - dynamic stability 57, 71–80
 - origin *xxiii*, *xxiv*
 - plate-shaped crystals 78
 - schematic representation 54
 - shaped crystal growth 76–80
- stability analysis-based automation 78–80, 79
- tubular crystals 77–8, 78
- vertical Bridgman (VB) technique 355–73
 - contact angles 358–9, 360, 361
 - crystal–crucible adhesion 359–63
 - defect structures 361, 362, 363
 - dewetting process *see* dewetted vertical Bridgman (VB) technique
 - dislocation defects 363
 - growth striations 392
 - interfacial energies 359–60, 359
 - liquid encapsulation 366–73, 369
 - crystals grown 367
 - solid–liquid–salt triple point region 370
 - surface and wetting properties 370
 - origin *xvi*
 - set up 356
 - spurious nucleation on crucible walls 363, 365–6, 365, 366
 - thermal interface curvature 356–8, 357, 358
 - thermocapillary convection 362–3, 364, 457
 - thermomechanical detachment 362–3, 364
- view factor 146–7, 148
- VST *see* variable shaping technique (VST)
- Weber number 59
- weight measurement 118, 119
 - evaluation 130–1
 - hydromechanical–geometrical model 138–42
 - right-half-plane zero characteristics 126
- weight-based control 164–70, 165, 166
 - crystal seeding 320–1
 - plate enlargement 325–6, 326, 328
 - in situ correction 326–7
 - steady state growth 328–31
 - tube enlargement 322–5, 322, 324, 325
- Wenzel Equation 8
- wetting behaviour 5
 - heterogeneous surfaces 11–12
 - nonreactive spreading 13–14
 - reactive spreading 14–16, 15, 16
 - see also* contact angles
- work of adhesion 3
- work of cohesion 2
- Young–Dupré equation 6
- Young–Laplace equation 38, 40, 135, 466, 468–86
- Young's equation 5–6